Outer Continental Shelf Environmental Assessment Program

Final Reports of Principal Investigators

Volume 72 December 1990

U.S. DEPARTMENT OF COMMERCE
National Oceanic and Atmospheric Administration
National Ocean Service
Office of Oceanography and Marine Assessment
Ocean Assessments Division
Alaska Office

U.S. DEPARTMENT OF THE INTERIOR
Minerals Management Service
Alaska OCS Region
OCS Study, MMS 90-0096

"Outer Continental Shelf Environmental Assessment Program Final Reports of Principal Investigators" ("OCSEAP Final Reports") continues the series entitled "Environmental Assessment of the Alaskan Continental Shelf Final Reports of Principal Investigators."

It is suggested that reports in this volume be cited as follows:

Colony, R. 1985. A Markov model for nearshore sea ice trajectories. U.S. Dep. Commer., NOAA, OCSEAP Final Rep. 72: 1–55.

Newton, J. L. 1982. Temperature and salinity structure of the wintertime Bering Sea marginal ice zone. U.S. Dep. Commer., NOAA, OCSEAP Final Rep. 72: 57–119.

Pritchard, R. S., and D. J. Hanzlick. 1987. Interpolation, analysis, and archival of data on sea ice trajectories and ocean currents obtained from satellite-linked instruments. U.S. Dep. Commer., NOAA, OCSEAP Final Rep. 72: 121–238.

Pritchard, R. S., and D. R. Thomas. 1985. Chukchi Sea ice motions, 1981–82. U.S. Dep. Commer., NOAA, OCSEAP Final Rep. 72: 239–255.

Reimnitz, E., E. W. Kempema, and P. W. Barnes. 1986. Anchor ice and bottom-freezing in high-latitude marine sedimentary environments: observations from the Alaskan Beaufort Sea. U.S. Dep. Commer., NOAA, OCSEAP Final Rep. 72: 257–281.

Kempema, E. W., E. Reimnitz, and R. E. Hunter. 1986. Flume studies and field observations of the interaction of frazil ice and anchor ice with sediment. U.S. Dep. Commer., NOAA, OCSEAP Final Rep. 72: 283–330.

Reimnitz, E., and E. W. Kempema. 1986. Field observations on slush ice generated during freezeup in Arctic coastal waters. U.S. Dep. Commer., NOAA, OCSEAP Final Rep. 72: 331–355.

Shapiro, L. H. 1987. Mechanical properties of sea ice and sea ice deformation in the nearshore zone. U.S. Dep. Commer., NOAA, OCSEAP Final Rep. 72: 357–584.

Stringer, W. J. 1988. Remote sensing data acquisition, analysis, and archival. U.S. Dep. Commer., NOAA, OCSEAP Final Rep. 72: 585–634.

OCSEAP Final Reports are published by the U.S. Department of Commerce, National Oceanic and Atmospheric Administration, National Ocean Service, Ocean Assessments Division, Alaska Office, Anchorage, and primarily funded by the Minerals Management Service, U.S. Department of the Interior, through interagency agreement.

Requests for receipt of OCSEAP Final Reports
on a continuing basis should be addressed to:

NOAA–OMA–OAD
Alaska Office
Federal Bldg., U.S. Courthouse Room A13
222 West Eighth Ave., #56
Anchorage, AK 99513–7543

OUTER CONTINENTAL SHELF ENVIRONMENTAL ASSESSMENT PROGRAM

Final Reports of Principal Investigators

Volume 72

December 1990

U.S. DEPARTMENT OF COMMERCE
National Oceanic and Atmospheric Administration
National Ocean Service
Office of Oceanography and Marine Assessment
Ocean Assessments Division
Alaska Office

U.S. DEPARTMENT OF THE INTERIOR
Minerals Management Service
Alaska OCS Region
OCS Study, MMS 90-0096

Anchorage, Alaska

The facts, conclusions, and issues appearing in these reports are based on research results of the Outer Continental Shelf Environmental Assessment Program (OCSEAP), which is managed by the National Oceanic and Atmospheric Administration, U.S. Department of Commerce, and funded (wholly or in part) by the Minerals Management Service, U.S. Department of the Interior, through an Interagency Agreement.

The content of these reports has not been altered from that submitted by the Principal Investigators. In some instances, grammatical, spelling, and punctuation errors have been corrected to improve readability; some figures and tables have been enhanced to improve clarity in reproduction.

Outer Continental Shelf Environmental Assessment Program

Final Reports of Principal Investigators

VOLUME 72 DECEMBER 1990

CONTENTS

A MARKOV MODEL FOR NEARSHORE SEA ICE TRAJECTORIES

by

Roger Colony

Polar Science Center
University of Washington
Seattle, Washington 98105

Final Report
Outer Continental Shelf Environmental Assessment Program
Research Unit 654

February 1985

ACKNOWLEDGMENTS

This study was funded by the Minerals Management Service, Department of the Interior, through an Interagency Agreement with the National Oceanic and Atmospheric Administration, Department of Commerce, as part of the Outer Continental Shelf Environmental Assessment Program under Contract Number 83-ABC-00358.

I thank my colleagues Alan Thorndike, Norbert Untersteiner, and Richard Moritz for their helpful reviews and discussions.

ABSTRACT

A probabilistic model of sea ice trajectories has been completed under NOAA/Ocean Assessments Division Contract No. 83-ABC-00358. In this model: (1) an ice parcel is given an initial position and season, (2) the ice parcel is moved from one position to another based on conditional probabilities, and (3) the ice parcel either melts or permanently leaves the region of interest. The statistics of sea ice motion over short periods of time are derived from observations of the motion of individual ice floes. These short term statistics define a stochastic process from which long term statistics can be deduced. This model is distinct from deterministic models which may be used in forecast (or hindcast) mode or as the basis for a Monte Carlo simulation.

The model has important implications regarding the transport of oil by sea ice. Model results are shown for probable motions originating at Prudhoe Bay and Peard Bay. Included as an appendix are the FORTRAN computer programs used in this study. With slight modification these programs can be used to study other regions.

TABLE OF CONTENTS

INTRODUCTION

Oil spilled in the frozen sea environment is trapped by a network of ridges and other roughness elements common to sea ice. The subsequent transport of oil is then almost wholly dependent on the motion of the sea ice cover. The day-to-day motion of this ice cover is primarily due to the synoptic surface winds, transient and quasi-stationary ocean currents, and effects of horizontal stresses within the cover. For pack ice the *rms* daily motion is about 7 km. The long term temporal mean is about 1-2 km d^{-1}, depending on location. On intermediate time scales, say of one to twelve months, there are significant departures from the long term mean motion. These departures are large enough to interact with the field of mean motion, resulting in a wide range of possible oil spill trajectories.

In this report a stochastic kinematic model of oil spill trajectories is described. The treatment is stochastic since it emphasizes the range of possible paths the oil may take, and their probabilities. It is kinematic because it is based only on observations of ice motion. The model is not dynamic in that no balance of forces is explicitly considered. Rather, the appropriate physics for the atmosphere-ocean-ice system are represented by the kinematics.

A stochastic model for future oil spills is required because the state of the atmosphere, in particular surface winds, cannot be predicted beyond a few days. Apart from the intrinsic instability of the global atmospheric state, there is often merit in the stochastic modelling of large and rather complex processes. The model presented is appealing because it is dependent only on a small number of input parameters which are both physically meaningful and experimentally accessible.

The model is based on a Markov process in which the state is defined by the position of the oil. The ice drift data are used to construct the elementary transition probabilities which express the probability that the oil moves from one location to any other in a given short time interval. The statistical properties of the long term trajectories are deduced from the transition probabilities. In formulating the model, the following items are prescribed:

1) the oil spill is initiated at a particular time and position,
2) in a unit time step, the change in position is given in terms of probabilities which depend only on position and season,
3) the trajectory "ends" when the ice either melts or leaves the modelled region.

The initial state, transition probabilities, and final state are described by a Markov process. Applying a well developed calculus, one can address variations of the question: *If a particle occupies region* Ω *at time* t, *what is the probability that it will be in region* Ω' *at time* t'?

Two study regions are analyzed, the Beaufort Sea and the Chukchi Sea. The strong mean westward surface current near Pt. Barrow allows these two regions to be analyzed separately. Specific results are shown for oil spills assumed to originate at Prudhoe Bay and Peard Bay.

MATHEMATICAL MODEL

The mathematical model is adapted from Colony and Thorndike (1985), hereafter abbreviated CT. The authors select an ice particle, say an area of ice containing an oil spill, and define a stochastic process which expresses the motion of that particle from one location to another. Following that approach the study region is divided into a number of cells labelled with the integers 1, 2, ..., N (see Figure 1). These integers define the set of *transient states*

$$\mathbf{T} = \{1, 2, \ldots, N\} \qquad \text{(transient states)}.$$

In the model the location of the ice particle at time t is expressed only in terms of the cell which it occupies. This *state* of the particle is a random variable, $X(t)$, which assumes the integer values of the set $\mathbf{T}$. Thus $X(5) = 53$ is a statement that the selected ice particle occupies the cell labelled 53 at time $t = 5$. The probability of this event is denoted as $Pr[X(5) = 53]$.

The probability of the ice particle moving from one cell to another requires a statement of conditional probability. Here $Pr[\text{event } a \mid \text{event } b]$ will denote the probability that event a occurs, given that event b occurs. The probability that the ice particle occupies cell j at time t_{k+1} given that it occupied cell i at time t_k is

$$p_{ijk} = Pr[X(t_{k+1}) = j \mid X(t_k) = i], \; i,j \in \mathbf{T} .$$

The probability that the ice particle occupying cell i at time t_k melts in the interval (t_k, t_{k+1}) is

$$q_{ijk} = Pr[X(t_{k+1}) = j \mid X(t_k) = i], \; i \in \mathbf{T}, \; j \in \mathbf{A}_m .$$

The set of *absorbing states* for melting,

$$\mathbf{A}_m = \{N+1, N+2, \ldots, N+M\} \ ,$$

identify particular regions in which the ice melts. Thus we can distinguish between ice melting in ecologically sensitive regions from ice melting in more benign regions. Once the ice has melted the trajectory is terminated.

The trajectory is also terminated when the ice particle exits the model region without melting. For example, the ice particle may exit to the north or to the west of the model region. The exit probabilities are given as

$$r_{ijk} = Pr\,[X(t_{k+1}) = j \mid X(t_k) = i]\ , i \in T,\ \in \mathbf{A}_e$$

The set of exit states are denoted by the integers

$$\mathbf{A}_e = \{N+M+1, N+M+2, \ldots, N+M+E\}.$$

Again, the integers in $\mathbf{A}_e$ are associated with the different ways in which the ice can exit the modelled region.

All of these probabilities are organized into the *transition probability matrix*

$$A_k = \begin{bmatrix} p_{ijk} & q_{ijk} & r_{ijk} \\ 0 & I & 0 \\ 0 & 0 & I \end{bmatrix} \begin{matrix} i \in \mathbf{T} \\ i \in \mathbf{A}_m \\ i \in \mathbf{A}_e \end{matrix}$$
$$\begin{matrix} j \in \mathbf{T} & j \in \mathbf{A}_m & j \in \mathbf{A}_e \end{matrix} \qquad k = 0,1,2,\ldots$$

This matrix, together with a statement of the probability distribution at time t_o, describes a discrete time, finite state, terminating, Markov process. The mathematics of this process is well developed, for instance, by Karlin and Taylor (1975).

The transitional probability matrix $\{a_{ijk}\} = A_k$, gives the one step conditional probability. If we consider the n step conditional probability, we have

$$a_{ijk}^{(n)} = Pr\,[X(t_{k+n}) = j \mid X(t_k) = i]\ , i,j \in T \cup \mathbf{A}_m \cup \mathbf{A}_e$$

and it can be shown that

$$\{a_{ijk}{}^{(n)}\} = A_k A_{k+1} \cdots A_{k+n} \ .$$

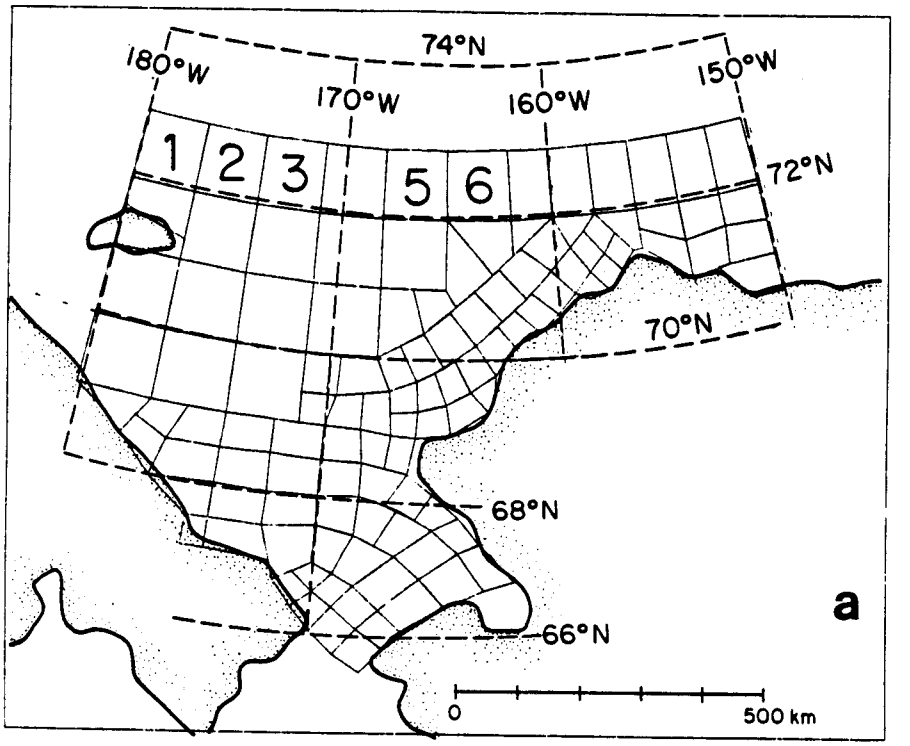

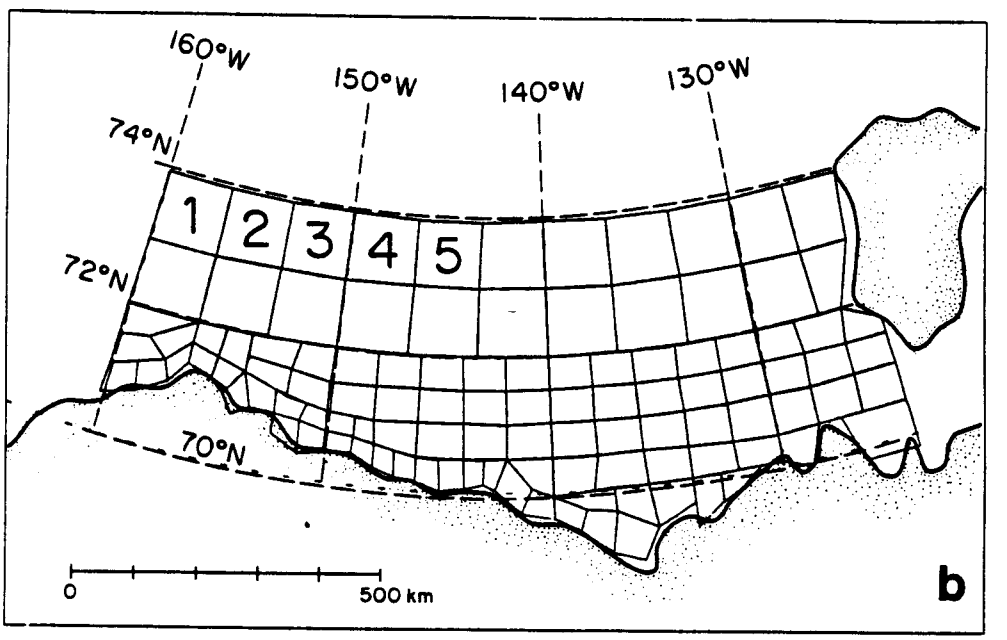

Figure 1. (a) The study region for the Chukchi Sea, N = 109. (b) The study region for the Beaufort Sea, N = 108.

DISTRIBUTION OF 30 DAY MOTIONS

The transition probability matrix is physically a well defined notion. By that we mean one could conduct an experiment to determine this matrix to within arbitrary sampling errors. This experiment would define the probability density function $f_k(\mathbf{y}|\mathbf{x})da$ giving the probability of moving from location $\mathbf{x}$ to a differential area $\mathbf{y}\,da$ in the time interval (t_k, t_{k+1}). The probability of moving from one cell to some other is then

$$p_{ijk} = \int_{\text{cell } i} \int_{\text{cell } j} f_k(\mathbf{y}|\mathbf{x})\, d\mathbf{y}\, d\mathbf{x} / \text{area of cell i}$$

In general, $f_k(\mathbf{y}|\mathbf{x})$ is dependent on both initial position $\mathbf{x}$ and time t_k. Note that $\int_{\text{model region}} f_k(\mathbf{y}|\mathbf{x})d\mathbf{y} \leq 1$; ice at time t_k may not exist in the model region at time t_{k+1}.

A number of experiments have already been conducted. Drifting data buoys were a part of many research programs; AIDJEX, OCSEAP, and LOREX, to cite a few. Since 1979 the Arctic Buoy Program has sought to monitor the fields of surface atmospheric pressure and sea ice motion, Untersteiner and Thorndike (1982). Observations from these programs form a data base to study the variability of ice motion. For example, Figure 2 shows 48 observations of 30 day sea ice motion as analyzed by Thorndike and Colony (1983). From these data one can begin to approximate the probability density function $f_k(\mathbf{y}|\mathbf{x})$.

The variability of sea ice motion can also be studied by mathematical models, both kinematic and dynamic. These range from the most simple, Thorndike and Colony (1982) to rather complex (Liu and Leendertse, 1981; Pritchard and Kolle, 1981). All of these models have a common theme -- sea ice motion is a response to the surface winds and upper ocean currents. Thorndike and Colony (1982) claim, for example, that at some distance from the coast, sea ice motion and geostrophic winds have a squared correlation of about 0.75. Figure 3 bears this out for the two locations (74° N, 160° W) and (74° N, 140° W). Thomas and Pritchard (1979) calculate monthly displacements based on a *free drift model*. A free drift model balances the forces due to air stress, water stress, sea surface tilt, and Coriolis force but neglects the force due to horizontal stresses within the ice cover. Figure 4 shows the model results for the 32 months of March in the period 1946-1977. The agreement between Figure 2 and Figure 4 is remarkable.

Colony and Thorndike modelled the one step motions with a homogeneous, isotropic, bivariate Gaussian distribution. For the greater part of the Arctic Basin this assumption is valid. Thorndike (1982), for example, demonstrated that many features in the Arctic surface weather patterns could be explained in terms of a simple homogeneous, isotropic, Gaussian process.

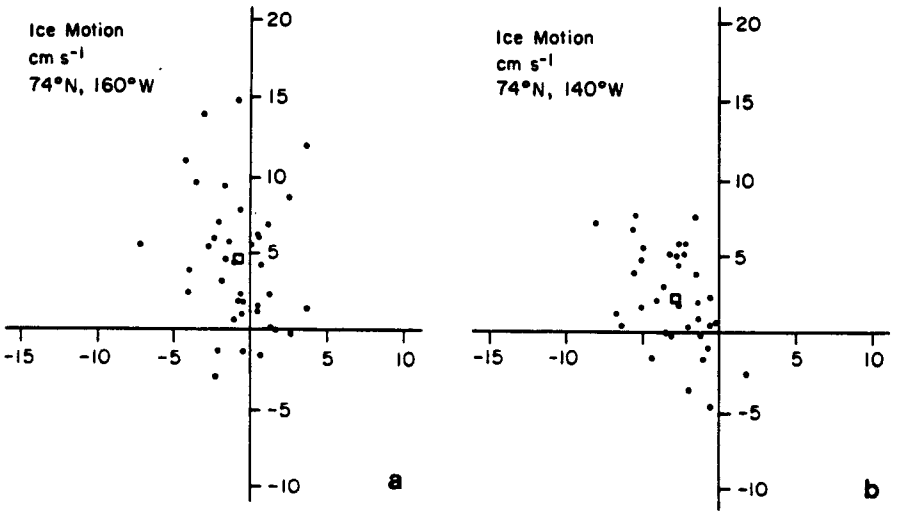

Figure 2. (a) Thirty day averaged ice motions at 74°N, 160°W for the period 1 Feb. 1979-30 Dec. 1981. The horizontal axis denotes motion parallel to the Greenwich longitude, the vertical axis denotes motion parallel to 90°E longitude. (b) Thirty day averaged ice motions at 74°N, 140°W for the period 1 Feb. 1979-30 Dec. 1981.

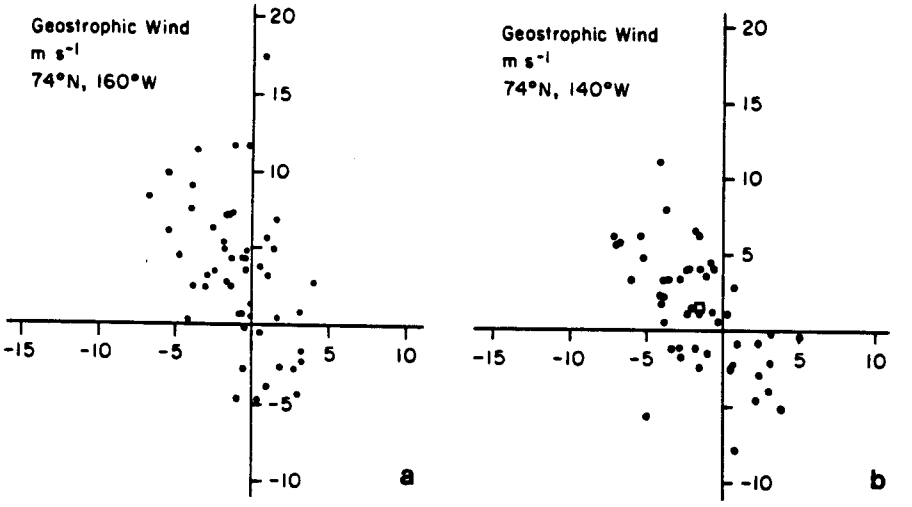

Figure 3. (a) Thirty day averaged geostrophic winds at 74°N, 160°W for the period 1 Feb. 1979-30 Dec. 1981. The horizontal axis denotes motion parallel to the Greenwich longitude, the vertical axis denotes motion parallel to 90°E longitude. (b) Thirty day averaged geostrophic winds at 74°N, 140°W for the period 1 Feb. 1979-30 Dec. 1981.

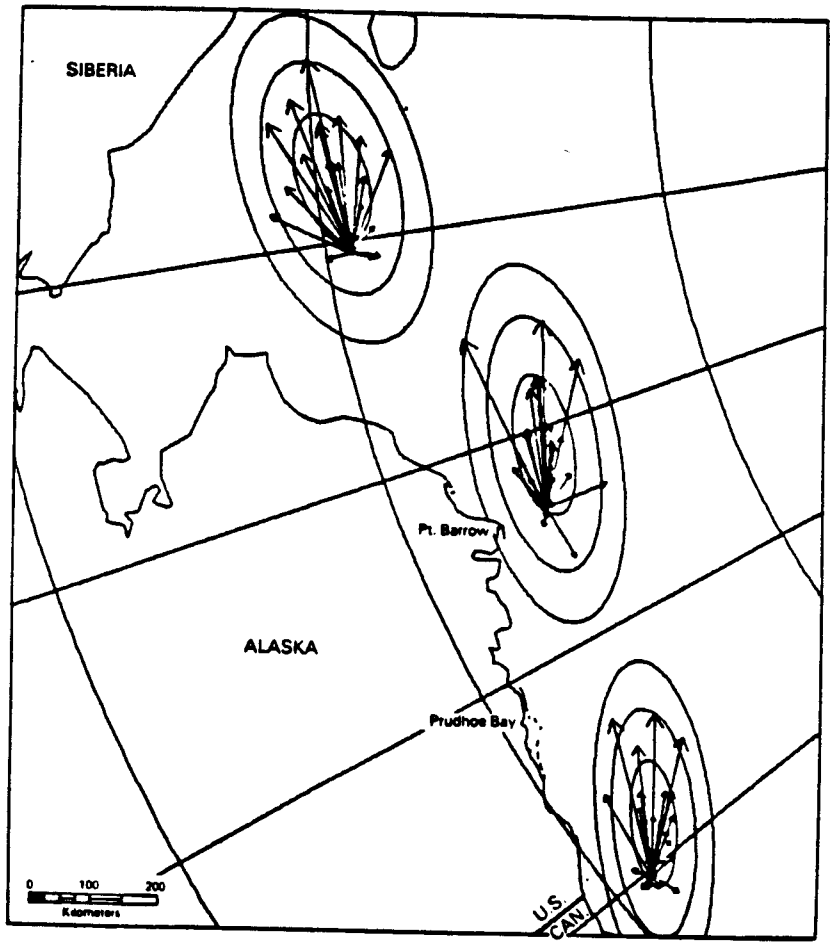

Figure 4. Free drift calculations of monthly motion using surface winds from the 32 Marches. Based on a Gaussian distribution, the elliptical isopleths of probability density delineate areas containing 50%, 90%, and 99% probabilities; taken from Thomas and Pritchard (1979).

Figures 2-4 suggest however that an anisotropic description of 30 day motions is necessary for the Beaufort and Chukchi Sea regions. The extent and importance of spatial and temporal variability of the statistics is not resolved by the data.

For this study the true probability density function, $f_k(\mathbf{y}|\mathbf{x})$ is approximated by the bivariate Gaussian distribution

$$g(\mathbf{y}\,;\,\mathbf{x}_0, B) = (2\pi)^{-1}\,|B\,|^{-1/2}\exp\{-\frac{1}{2}\,(\mathbf{y}-\mathbf{x}_0)^T\,B^{-1}(\mathbf{y}-\mathbf{x}_0)\}\ .$$

Here $\mathbf{x}_0 = \mathbf{x}+\mathbf{u}$ is the mean position at the end of the 30 day motion and B is the covariance matrix between the components of displacement. This formulation allows for an inhomogeneous, anisotropic, description of probable motion. There are several *a priori* justifications for choosing the Gaussian distribution. For example, the net motion over a time interval may be regarded as the sum of several independent events. Then the Gaussian distribution is a consequence of the Central Limit Theorem, (see Vanmarcke, 1983).

The mean 30 day motion, $\mathbf{u}$, is obtained from observations of buoy motions described in Colony and Thorndike (1984). The results are shown in Figure 5. The covariance matrix is defined such that the principal axis is aligned with $\mathbf{u}$. The motion variance in this principal direction is defined as σ_1^2. The motion variance in the perpendicular direction is taken to be $\sigma_2^2=\frac{\sigma_1^2}{4}$. This gives a ratio of 2:1 for the major and minor axis of the ellipse defined by $(\mathbf{y}-\mathbf{x}_0)^T B^{-1}(\mathbf{y}-\mathbf{x}_0)$ = constant. The total is chosen such that $\sigma_1^2 + \sigma_2^2 = \sigma^2 = 1.25\times10^4\ \mathrm{km}^2$; e.g., $\sigma_1^2 = 10^4\ \mathrm{km}^2$ and $\sigma_2^2 = .25\times10^4\ \mathrm{km}^2$ This model is not in contradiction with the data of Figure 2 or the calculations of Figure 4.

THERMODYNAMICS

When the ice cover melts, the trapped oil is free to disperse. Because the physics of oil transport, dispersion, and weathering is different in the open ocean than in sea ice, this analysis ends once the ice melts. To simply say that the ice cover melts misrepresents the complicated thermodynamic and morphological seasonal changes of sea ice in the marginal seas. A number of processes can be identified in the seasonal breakup of sea ice: oceanic heat flux, radiative and convective heat fluxes to the atmosphere, mechanical breaking of large ice floes, and large scale advection of sea ice. These processes are difficult to observe in the harsh and dynamic environment of the marginal seas. So, rather than theorize about these processes, we will again turn to observations.

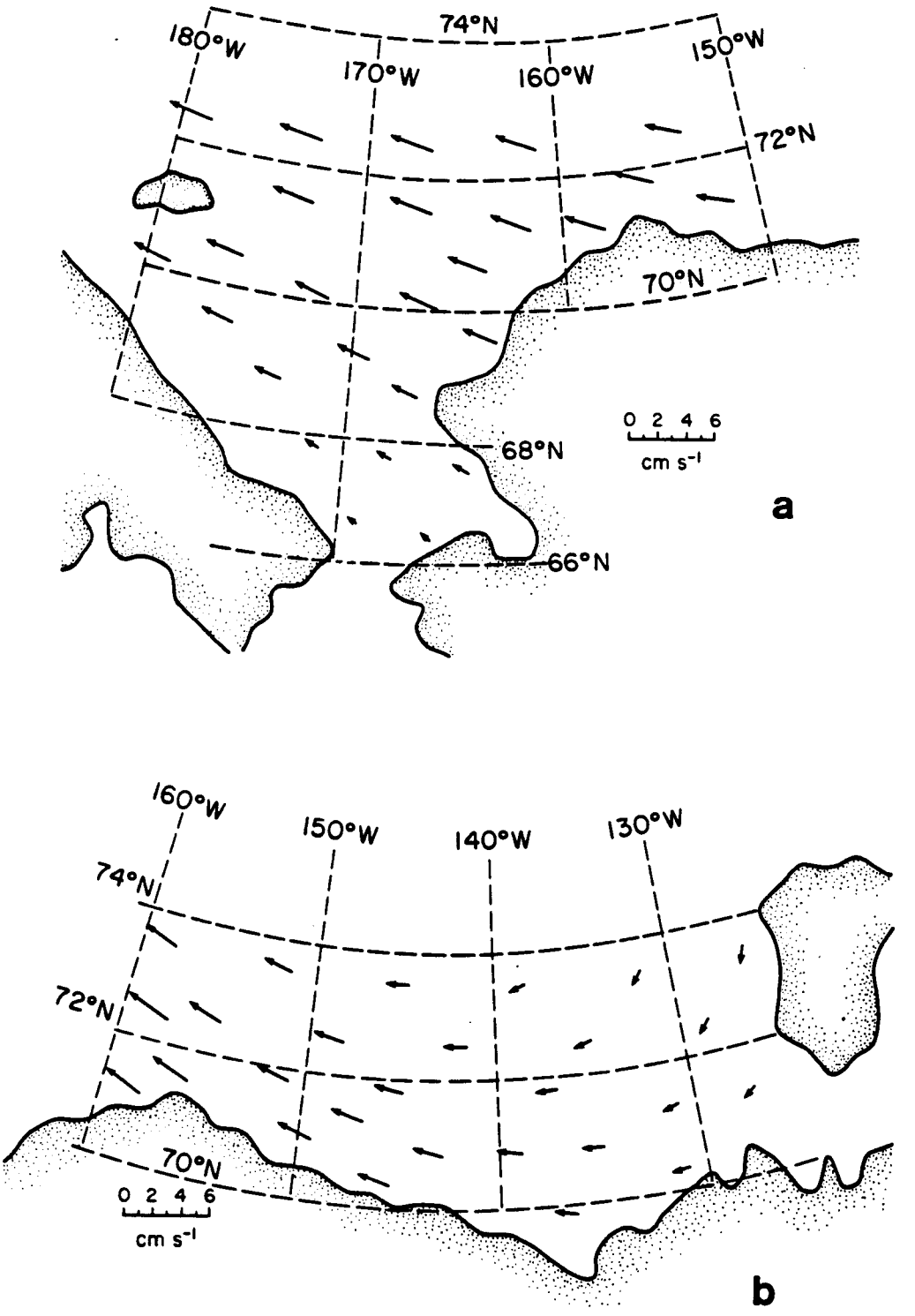

Figure 5. Illustration of the field of mean 30-day motions for (a) the Chukchi Sea and (b) the Beaufort Sea as obtained from observations. The analysis procedure is from Colony and Thorndike (1984).

Observations of ice edge position and ice concentration have been made for a number of years. Webster (1982) analyzed these data for a 29 year period (1953-1981); the results are compiled in La Belle *et al.* (1983). Figure 6 shows the number of occurrences, in per cent of total years, of the ice edge being south of a set of contour lines on the 1st of August. For the present study, the 50% ice edge position will characterize the melting process. If an ice particle moves south of this 50% contour, then it will be regarded as melted; if it stays north of the 50% contour, it remains frozen. This simplification of the melting process almost certainly introduces large errors. For example, the interannual variability of ice edge position is largely due to the natural variability of ice motion. In this study, however, the position of the ice edge is presumed to be independent of the history of motion. Therefore, the results must be viewed with caution.

CALCULATION OF A_k

The procedure for estimating the elements of the transition probability matrix, A_k follows CT. The bivariate Gaussian distribution describes the provisional motion from one location to another. If this provisional motion places the ice in a region of open water or if it places the ice outside the model region, then the distribution function is adjusted. For illustration, consider motion originating from the center of cell i. This location is denoted by $\square$

The provisional motion during a unit time interval is shown in Figure 7. These figures show the probability that the ice moves:

a) from $\square$ to cell j = $\int_{cell\ j} g(\mathbf{y}; \square + \overline{\mathbf{u}}, B)d\mathbf{y}$, $j \in T$

b) from $\square$ to melt region j = $\int_{region\ j} g(\mathbf{y}; \square + \overline{\mathbf{u}}, B)d\mathbf{y}$, $j \in \mathbf{A}_m$

c) from $\square$ to exit region j = $\int_{region\ j} g(\mathbf{y}; \square + \overline{\mathbf{u}}, B)d\mathbf{y}$, $j \in \mathbf{A}_e$

d) from $\square$ to the coast = $\int_{coast} g(\mathbf{y}; \square + \overline{\mathbf{u}}, B)d\mathbf{y}$

The regions are taken so as to not intersect and furthermore the union of the regions is taken to include all points $\mathbf{y}$. The first three of the integrals are related to p_{ijk}, q_{ijk}, and r_{ijk}, respectively. Sea ice cannot, however, move onto the coastal regions; it is restrained by the effects of internal ice stresses. In this model the ice is assumed to remain at the initial location, $\square$

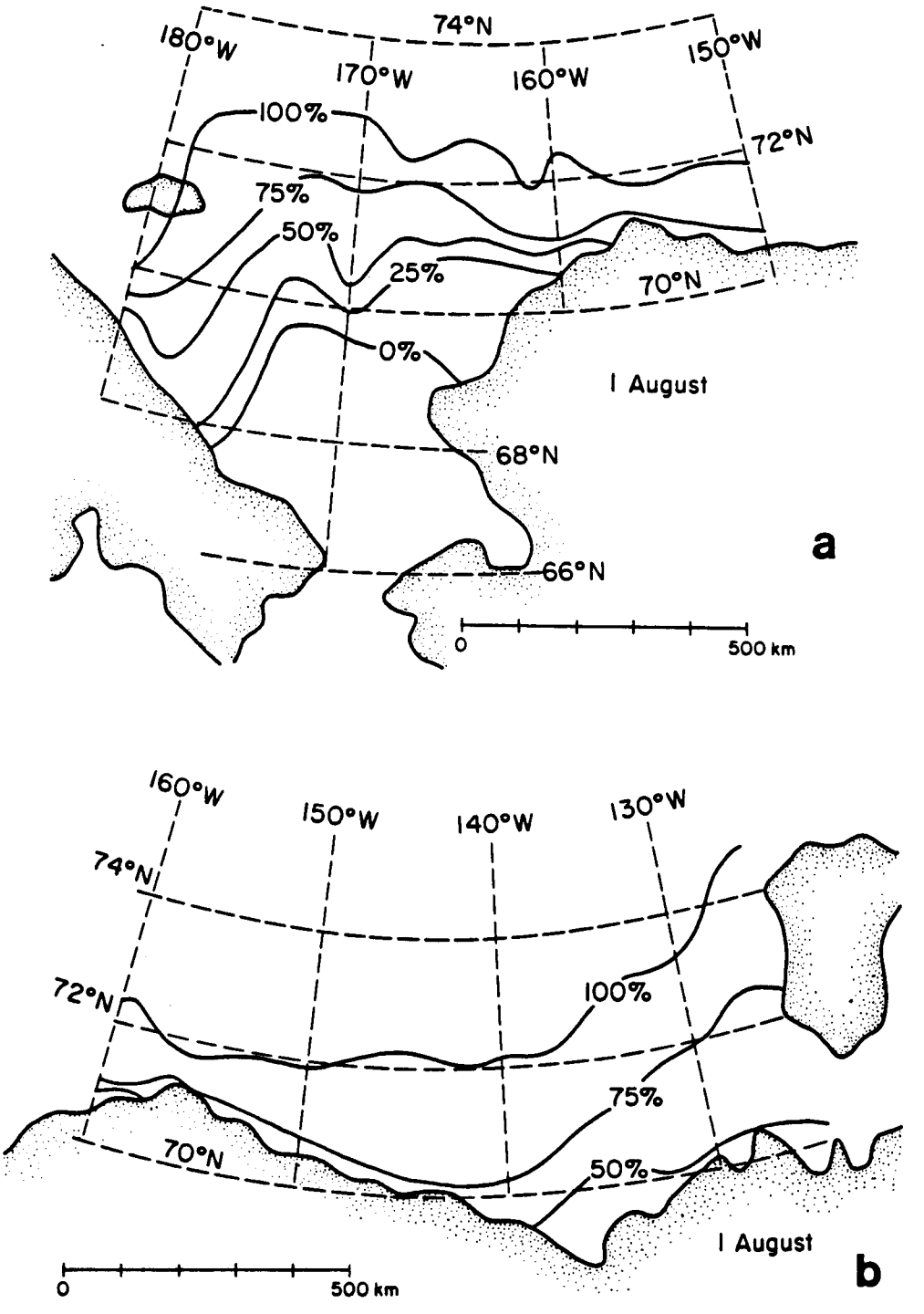

Figure 6. Probabilities in percent of ice edge location on 1 August in the Chuckchi Sea (a) and in the Beaufort Sea (b). The ice edge was never found to be south of the line marked 0%. The ice edge was always found to be south of the line marked 100%. One half of the ice edge observations were found to be south of the line marked 50%, taken from LaBelle *et al* (1983) and Webster (1982).

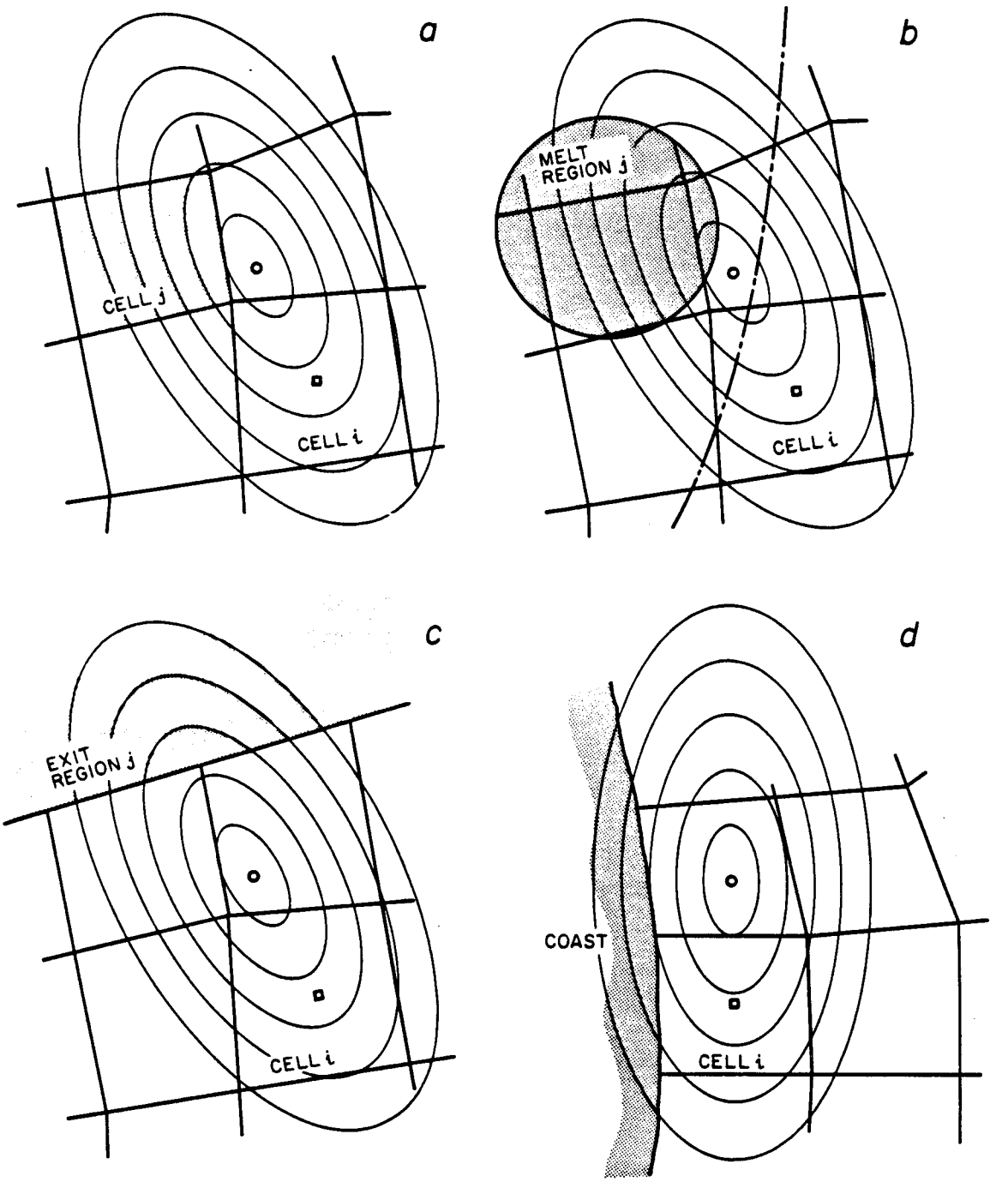

Figure 7. Illustration of provisional motion originating from ▫ during a time step (t_k, t_{k+1}). The ellipses are contour lines of the Gaussian probability density function. (a) motion from ▫ to cell j, (b) motion from ▫ to melt region j, (c) motion from ▫ to exit region j, (d) motion from ▫ which encounters the coast.

The model resolves ice particle position only in that it occupies a cell. The true ice particle position in cell i is taken to be a random variable having uniform distribution; for example,

$$p_{ijk} = \int_{\text{cell } j} \int_{\text{cell } i} g(\mathbf{y};\ \mathbf{x} + \overline{\mathbf{u}}\ ,\ B)d\mathbf{x}d\mathbf{y} / \text{area of cell } i$$

Details of this formulation are given in CT.

RESULTS

If oil is spilled in Peard Bay on the first of April, where is the sea ice apt to transport the oil? Will this sea ice melt and release the oil in an ecologically sensitive area? A quantitative response to these questions must involve a statement of probability of occurrence. In the context of the model, the results will focus on the matrix $\{a_{ijk}{}^{(n)}\}$.

The results can be generalized and more easily understood by introducing the vector

$$S(n) = (s_1(n), s_2(n), \cdots, s_N(n), \cdots, s_{N+M+E}(n))$$

where

$$s_j(n) \equiv Pr[X(t_n) = j]\ ,\ j \in T\ U\ \mathbf{A}_m\ U\ \mathbf{A}_e$$

If, as above, the oil is spilled in Peard Bay at time t_o, then $S(0) = (0, 0, \cdots, 0, 1, 0, \cdots, 0)$; the probability of oil being at j = Peard Bay is equal to unity. The time evolution of S is then

$$S(1) = S(0)A_0\ ,\ S(2) = S(1)A_1 = S(0)A_0A_1\ ,\ S_{(n)} = S(0)A_0A_1 \cdots A_{n-1}$$

In the case above, $S(n)$ is simply the row of $\{a_{ijo}^{(n)}\}$ corresponding to the Peard Bay location. The generalization is that $S(0)$ is defined in probabilistic terms. Thus oil spilled in the Beaufort Sea can be modelled in the Chukchi Sea by specifying the probable way in which oil is transported from the Beaufort Sea into the eastern portion of the Chukchi Sea.

In displaying the results it is convenient to normalize the elements of S by the area of each cell,

$$\tilde{s}_j(n) = s_j(n) / \text{area of cell } j,\quad j \in T$$

The $\tilde{s}_j(n)$ now have units of km^{-2} and collectively they can be regarded as an approximation to the probability density function for ice particle position at time t_n. These functions are shown in Figure 8 for n = 1, 2, 3, 4, 5. The contour lines shown in Figure 8 are subjectively drawn.

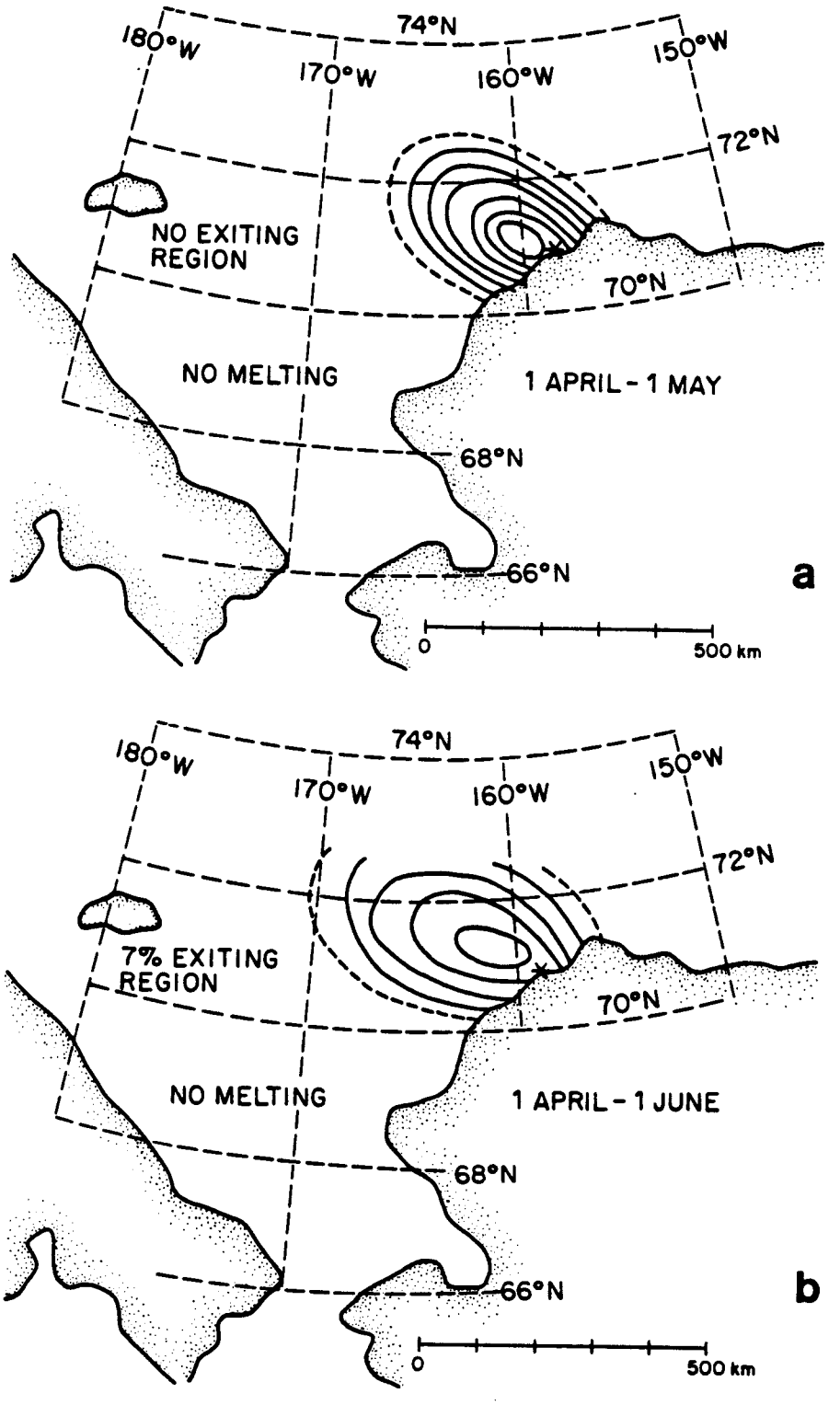

Figure 8. The probability density function for the position of oil spilled in Peard Bay on 1 April for: (a) 1 May, (b) 1 June, (c) 1 July, (d) 1 August and (e) 1 September, and (f) 1 October. The dotted line shows the 50% ice edge location. The solid contour levels are at $4\times10^{-6}km^{-2}$, $8\times10^{-6}km^{-2}$, $12\times10^{-6}km^{-2}$, and so on. The dashed contour is at $2\times10^{-6}km^{2}$. The probability of the ice having melted or having exited the region are shown.

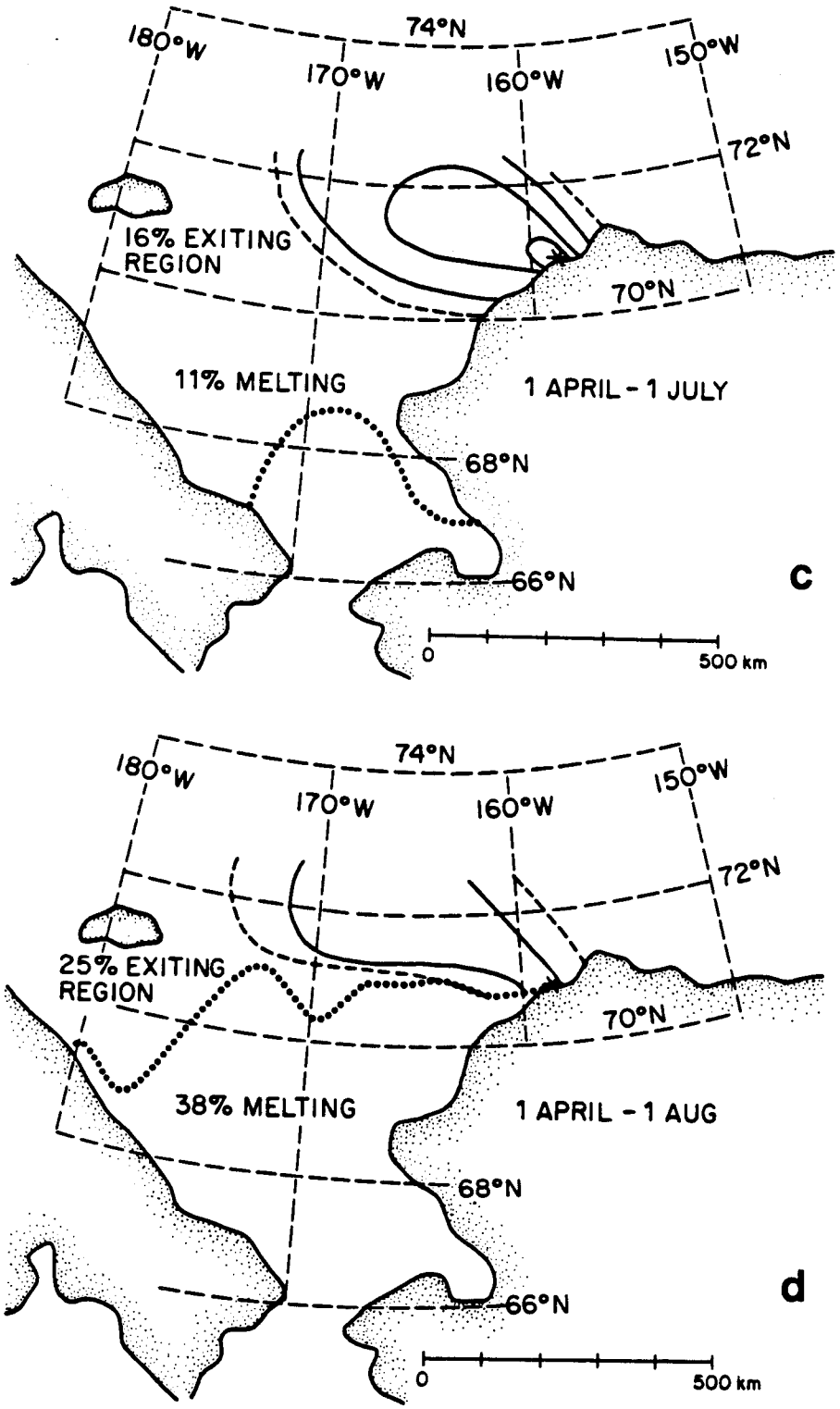

Figure 8. continued

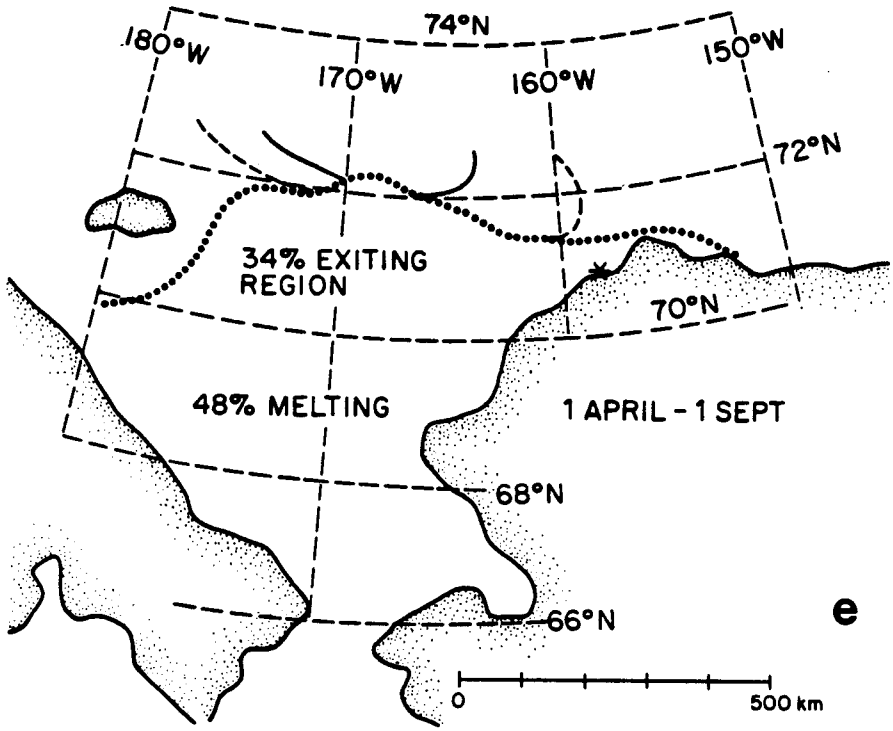

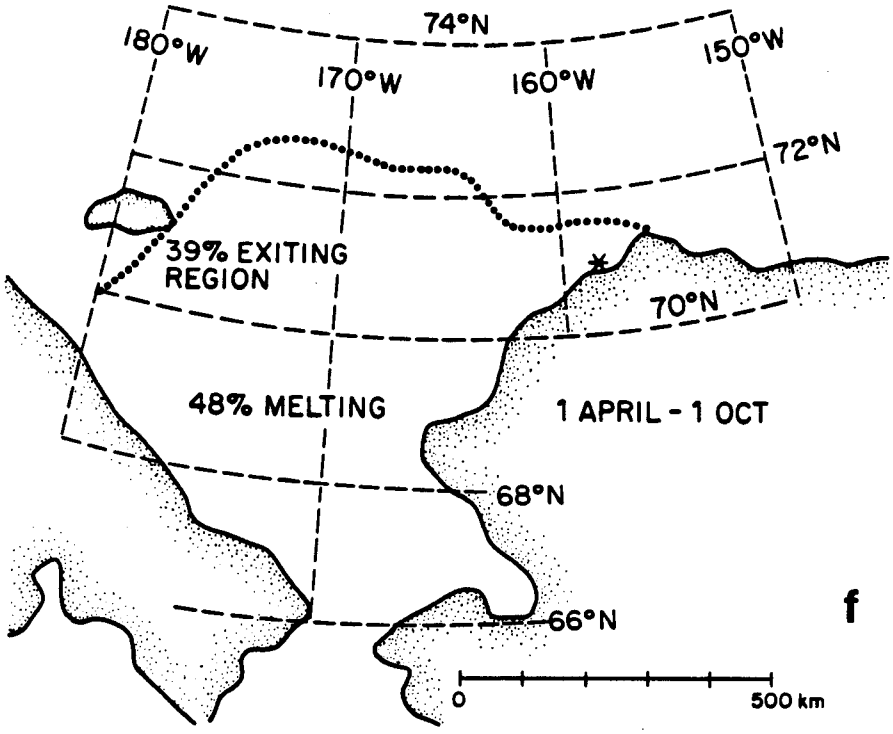

Figure 6. continued

It should be noted that the contour lines in Figure 8 are somewhat different from those in Figures 4 and 7. In Figure 8 the isopleths are of probability density function. The dashed contour represents a value of $2\times10^{-6}\,km^{-2}$; successive solid contours represent values of 4×10^{-6}, 8×10^{-6}, $12\times10^{-6}\,km^{-2}$, and so on. The ellipses shown in Figures 4 and 7 are lines of constant $(\mathbf{y}-\mathbf{x}_0)^T B^{-1} (\mathbf{y}-\mathbf{x}_0)$ which for the Gaussian distribution are also lines of constant probability density. These ellipses, of course, do not show the uniform increments of the density function illustrated in Figure 8.

The density function shown by Figure 8 can be used to estimate the probability of oil spilled in Peard Bay being transported to any area of the study region. This simply requires the integration of the density function over the desired area. For example, if the density had a uniform value of $2\times10^{-6}\,km^{-2}$ over a region of 100 km square, then the probability of the oil occupying that area would be $(2\times10^{-6}\,km^{-2}) \times (100^2 km^2) = 0.02$. Figure 9 shows the probability density function associated with a spill in Prudhoe Bay.

CONCLUSIONS

The probable motion and melting of sea ice has been modelled with special emphasis on its ability to transport oil. The model is focused on a time scale of several months and a length scale of several hundred kilometers. On those scales an oil spill has great latitude in possible trajectories. On time scales of several days the model is not appropriate, because successive steps are not independent. On these time scales, one of several available dynamic models should be used.

The question of model verification is always appropriate. The Markov hypothesis (independent increments) has been tested and for practical purposes successive 30-day motions are uncorrelated. Furthermore, the observed 60-day motions are in qualitative agreement with those predicted by the model. The question of intermodel comparison is more difficult to answer. Agreement between the results of two models can be used as support for both sets of modelling assumptions. Differences between the results may help diagnose and correct shortcomings in one approach or the other.

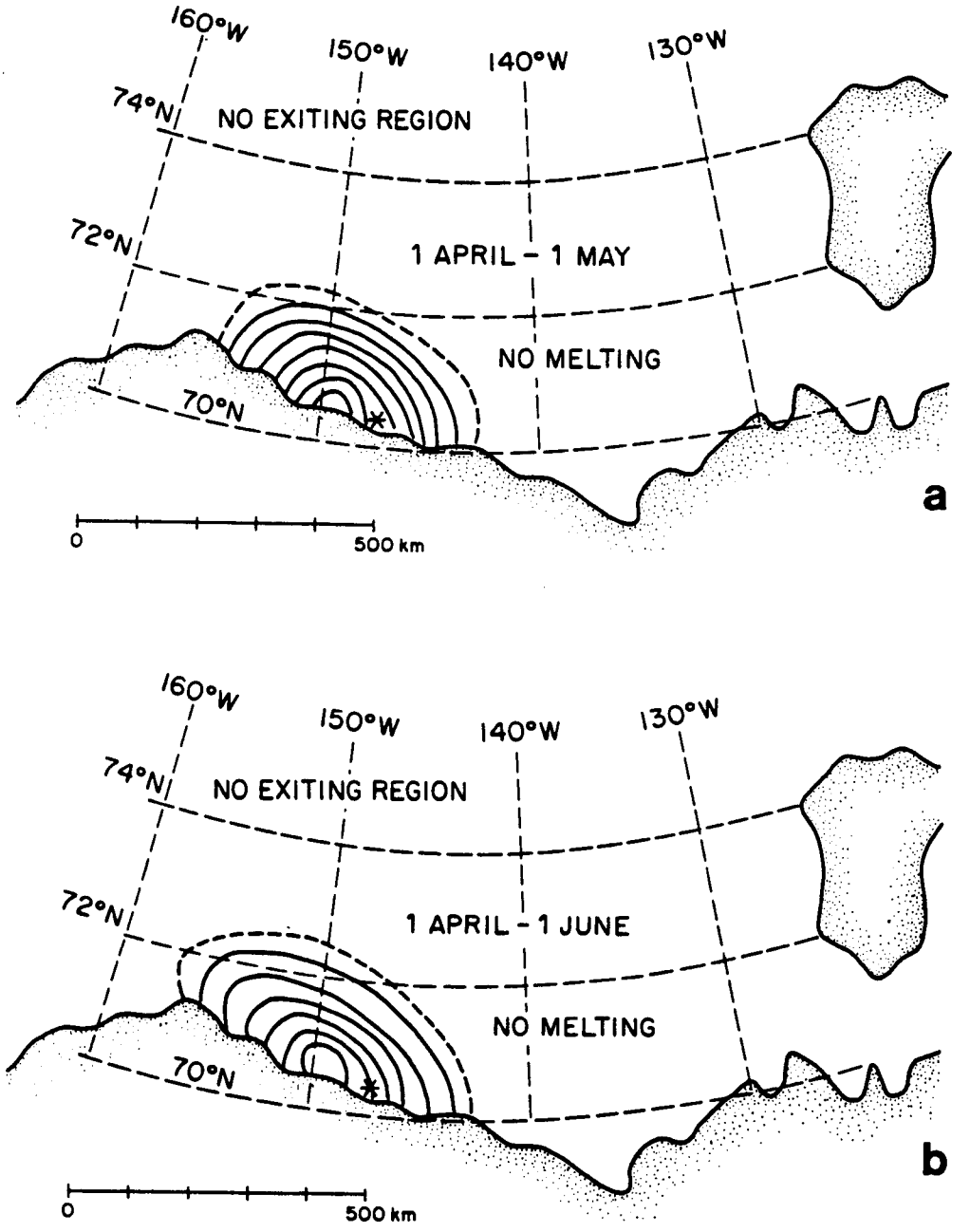

Figure 9. The probability density function for the position of oil spilled in Prudhoe Bay on 1 April for: (a) 1 May, (b) 1 June, (c) 1 July, (d) 1 August, (e) 1 September, and (f) 1 October. The dotted line shows the 50% ice edge location. The solid contour levels are at $4\times10^{-6}km^{-2}$, $8\times10^{-6}km^{-2}$, $12\times10^{-6}km^{-2}$, and so on. The dashed contour is at $2\times10^{-6}km^{2}$. The probability of the ice having melted or having exited the region are shown.

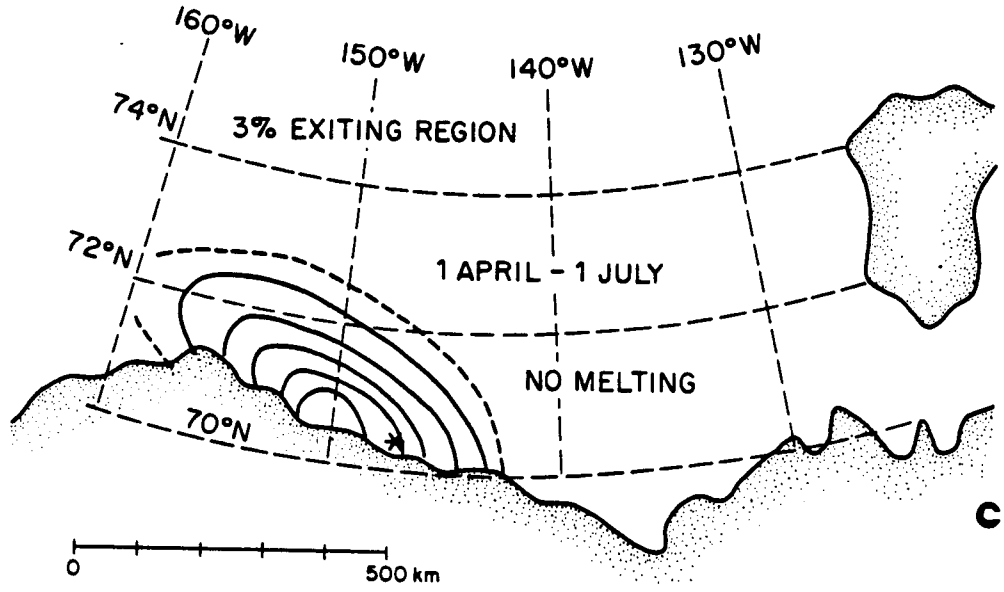

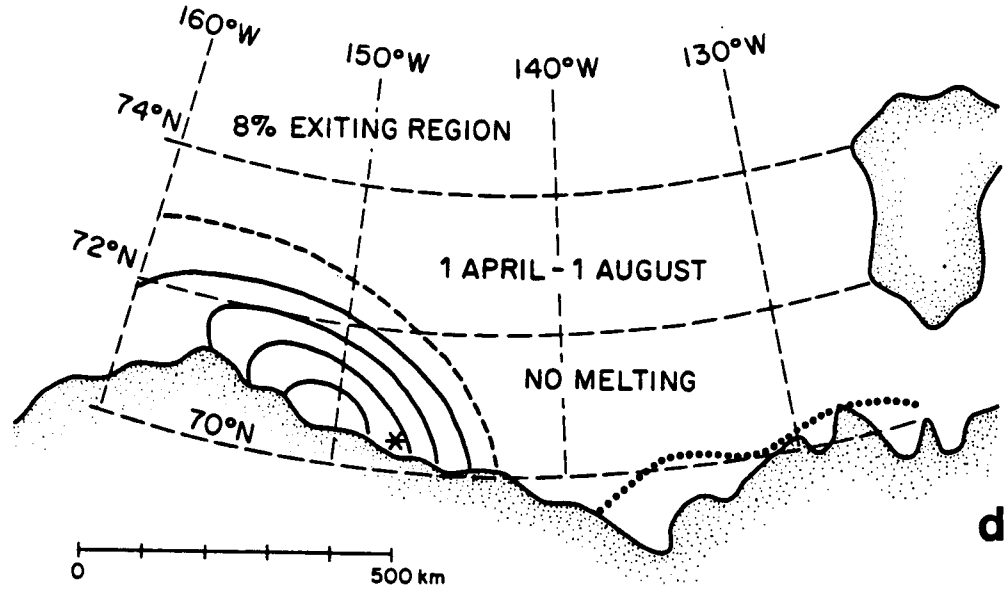

Figure 9. continued

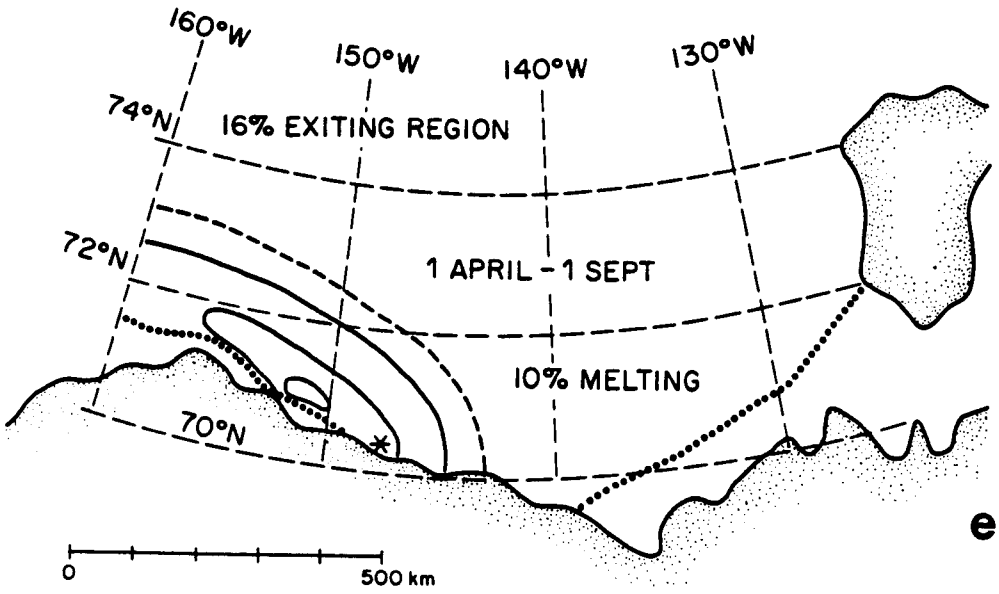

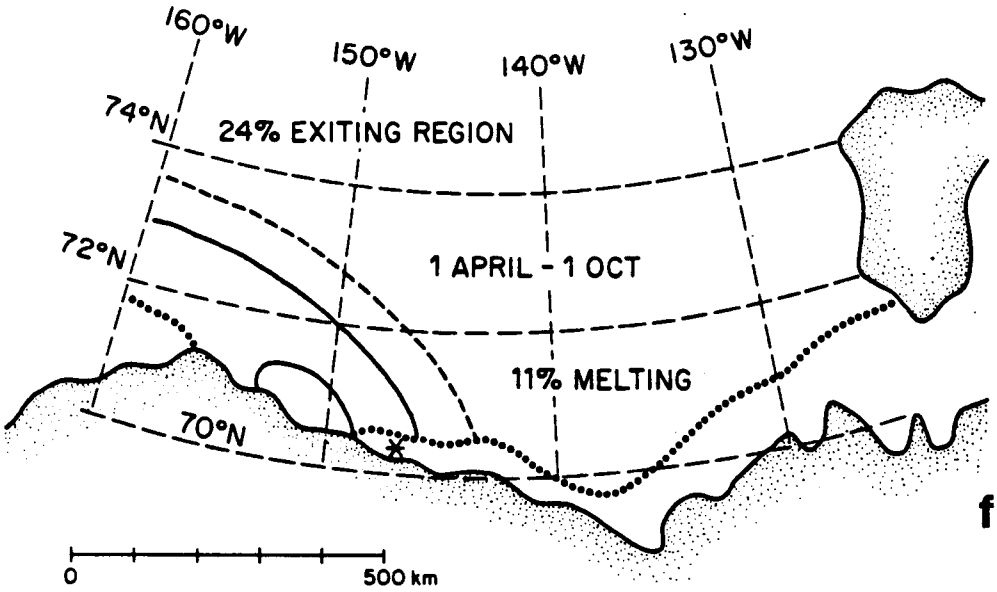

Figure 9. continued

REFERENCES CITED

Colony, R. and A. S. Thorndike, 1984. An estimate of the mean field of sea ice motion, *J. Geophys. Res., 89* (C6), 10623-10629.

Colony, R. and A. S. Thorndike, 1985. Sea ice motion as a drunkard's walk, *J. Geophys. Res.*, 90 (C1), 965-974.

Karlin, S. and H. M. Taylor, 1975. *A First Course in Stochastic Processes,* Academic Press, New York, 557 pages.

LaBelle, J. C., J. L. Wise, R. P. Voelker, R. H. Schulze, and G. M. Wohl, 1983. *Alaska Marine Ice Atlas,* Arctic Environmental Information and Data Center, University of Alaska, Anchorage, Alaska.

Liu, S. K. and J. J. Leendertse, 1981. A three-dimensional oil-spill model with and without ice cover. International Symposium on Mechanics of Oil Slicks, International Association of Hydraulic Research, Paris, 1981, 249-265.

Pritchard, R. S. and J. J. Kolle', 1981. Modelling sea ice trajectories for oil spill tracking. Final report to U.S. Department of Transportation, U.S. Coast Guard, Flow Research Company, Kent, Washington.

Thomas, D. R. and R. S. Pritchard, 1979. Beaufort and Chukchi Sea Ice Motion, Part 1: Pack Ice Trajectories. Flow Research Report No. 133, Flow Research Company, Kent, Washington.

Thorndike, A. S., 1982. Statistical properties of the atmospheric pressure field over the Arctic Ocean, *J. Atmos. Sci., 39* (10), 2229-2238.

Thorndike, A. S. and R. Colony, 1982. Sea ice motion in response to geostrophic winds, *J. Geophys. Res., 87* (C8), 5845-5852.

Thorndike, A. S. and R. Colony, 1983. Objective analysis of atmospheric pressure and sea ice motion over the Arctic Ocean. Seventh International Conference on Port and Ocean Engineering Under Arctic Conditions, Helsinki, Finland.

Untersteiner, N. and A. S. Thorndike, 1982. The Arctic Data Buoy Program. *Polar Record, 21,* 127-135.

Vanmarke, E., 1983. *Random Fields: Analysis and Synthesis,* MIT Press, Cambridge, Mass., 382 pages.

Webster, B. D., 1982. Empirical probabilities of the ice limit and fifty percent ice concentration boundary in the Chukchi and Beaufort Seas. National Weather Service, U. S. National Oceanic and Atmospheric Administration, Anchorage, Alaska. NOAA Technical Memorandum NWS AR-34, 9 pages.

APPENDIX.
DATA PROCESSING FOR
THE RANDOM TRANSPORT OF OIL BY SEA ICE

Esther A. Munoz
Polar Science Center
University of Washington,
Seattle, Washington

In this section the programs used to model oil spill trajectories are presented. The two initial input files required to run the model are the coordinates of the four vertices that define the cells into which the region of interest has been partitioned and the data set of mean ice velocity for the region.

Program MEANICE interpolates ice velocity to the center point of each cell, from which program PIJ generates the transition probability matrix (TPMX) for moving from one transient state to another or from a transient state to an absorbing state. Program PIJ requires the additional input files containing the probabilities of melting in each cell during a given month and the coordinates of the vertices of the melt and exit regions. A TPMX is generated for each season, after which all are compiled into one large file which becomes the input to programs APOWER and MARKOV. The set of probable trajectories beginning in cell A at time T terminating after N steps is calculated by APOWER. Program MARKOV calculates the time to reach an absorbing state and the probable number of visits to any other cell given that the trajectory originated in cell I.

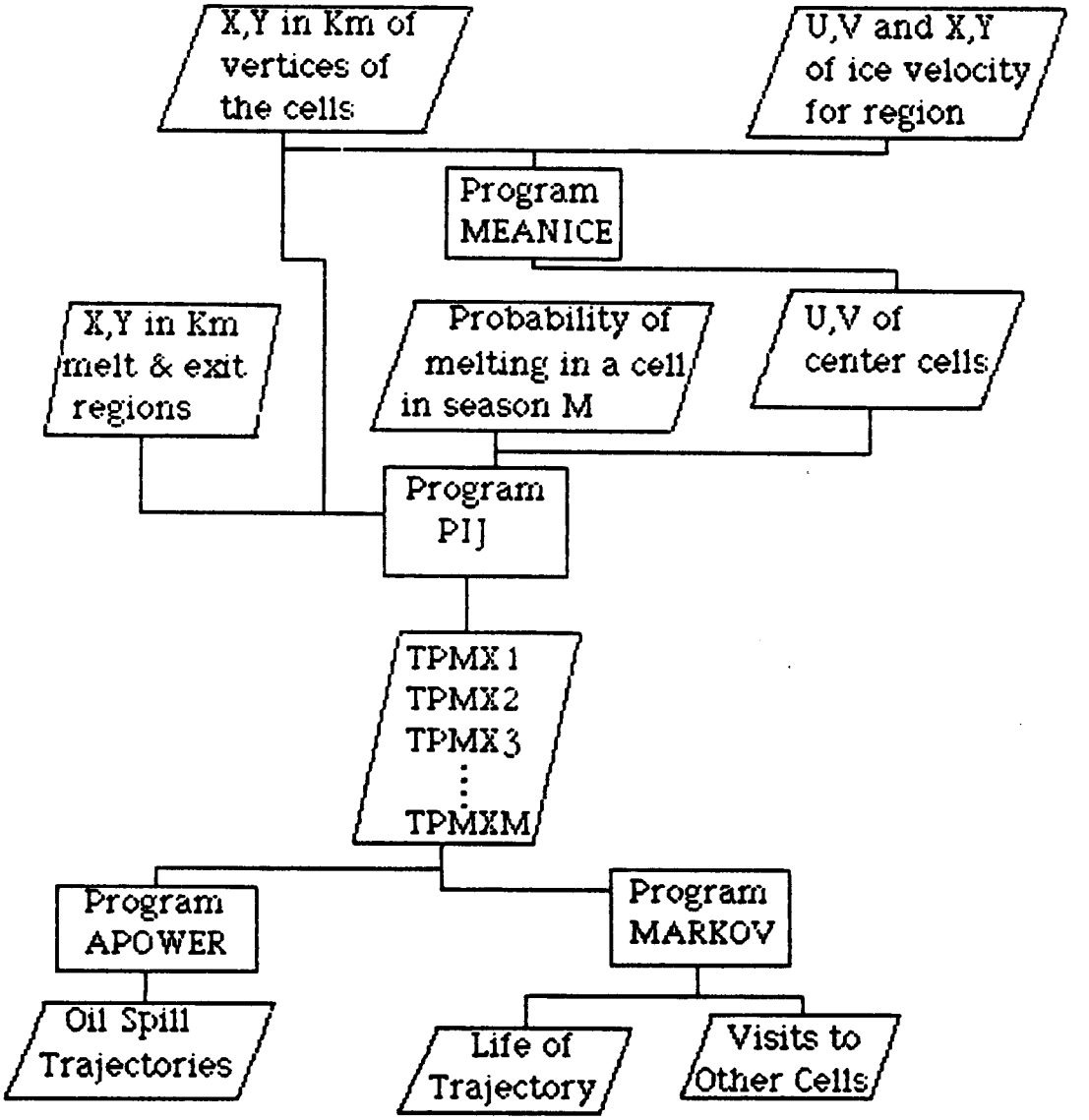
X,Y in Km of vertices of the cells
U,V and X,Y of ice velocity for region
Program MEANICE
X,Y in Km melt & exit regions
Probability of melting in a cell in season M
U,V of center cells
Program PIJ
TPMX1
TPMX2
TPMX3
TPMXM
Program APOWER
Program MARKOV
Oil Spill Trajectories
Life of Trajectory
Visits to Other Cells

```
      PROGRAM MEANICE (INPUT,OUTPUT,TAPE1,TAPE2,TAPE3)
C
C     PROGRAM MEANICE INTERPOLATES MEAN ICE MOTION FROM A
C     A MEAN FIELD TO THE CENTER OF EACH CELL.
C
C
      IMPLICIT COMPLEX (Z)
      COMMON /EGRAD/ EUX,EUY,EVX,EVY,EDIV,EVOR
C     INPUT FILE1 -- CONTAINS THE X,Y COORDINATES IN KILOMETERS
C                    OF THE CENTER POINT OF EACH CELL
      DIMENSION Z2X(130)
C
C     INPUT FILE2 -- CONTAINS ICE MOTION DATA
C                    NUMBER OF DAYS OF DATA FOR POINT -- NUX
C                    POSITION X,Y IN KILOMETERS -- ZX
C                    U,V IN CM/SEC -- ZU
C
C     OUTPUT FILE3 -- CONTAINS THE (U,V) MEAN ICE VELOCITIES
C                     IN CM /SEC AT THE CENTER OF EACH CELL
      DIMENSION ZUS(130)
C
      DIMENSION NUX(111), ZX(111), ZU(111)
      DIMENSION ZG(111), SIGD(111)
      DIMENSION ZIX(50), ZIU(50), ZIG(50), SIGI(50)
      REAL LHS(100,100),RHS(100,6),ALP(100,6),CHECK(100)
      DIMENSION COR(100,100), ERUV(100), LCELL(50), IPR(100)
C
C     NI = NUMBER OF CELLS
      NI = 108
      DO 5 I=1,NI
           READ (1) Z2X(I)
 5    CONTINUE
C
C
C     ND = NUMBER OF DATA POINTS.
      ND = 111
      DO 25 I=1,ND
           READ (2) NUX(I),ZX(I),ZU(I)
 25   CONTINUE
C
C
      DEL = 10
      DELC = DEL*100000
      CALL DATAER (NUX,SIGD,ND)
      PRINT 325, (I,NUX(I),ZX(I),ZU(I),SIGD(I),I=1,ND)
C
      DO 300 IX=1,NI
           ZZX = Z2X(IX)
C
C     SELECT DATA TO USE IN INTERPOLATION
           XCUT = 500
 50        NU = 0
           DO 75 IB=1,ND
C     IF LESS THAN 30 BUOY DAYS OF DATA ARE AVAILABLE FOR
C     THIS DATA POINT, DO NOT USE IT.
                IF (NUX(IB) .LT. 30) GO TO 75
                IF (CABS(ZZX-ZX(IB)).GT.XCUT) GO TO 75
                NU = NU+1
                LCELL(NU) = IB
                ZIX(NU) = ZX(IB)
                ZIU(NU) = ZU(IB)
                SIGI(NU) = SIGD(IB)
 75        CONTINUE
           IF (NU.GE.20) GO TO 100
           IF (XCUT.GT.2000.0) STOP
           XCUT = 1.5*XCUT
```

```
          GO TO 50
C
  100     N2U = 2*NU
          PRINT 350, IX,NU,(LCELL(I),I=1,NU)
C
          CALL SLHS (ZIX,SIGI,NU,LHS)
          CALL SRHS (ZZX,ZIX,NU,RHS,1)
          ZX1 = ZZX+DEL*(1.0,0.0)
          CALL SRHS (ZX1,ZIX,NU,RHS,3)
          ZX2 = ZZX+DEL*(0.0,1.0)
          CALL SRHS (ZX2,ZIX,NU,RHS,5)
C
          DO 150 I=1,N2U
               DO 125 K=1,6
                    ALP(I,K) = RHS(I,K)
  125          CONTINUE
               DO 130 J=1,N2U
                    COR(I,J) = LHS(I,J)
  130          CONTINUE
  150     CONTINUE
C
C     GLESOM IS FROM BOEING MATH LIBRARY
          CALL GLESOM (LHS,100,N2U,IPR,ALP,6,DI)
          IF (ABS(DI).LT.0.5) STOP
C
          DO 175 K=1,2
               PRINT 375, K,(ALP(I,K),I=1,N2U)
  175     CONTINUE
C
          CALL ERROR (ALP,RHS,N2U,ERUU(IX))
C
          DO 275 K=1,3
               K2 = 2*K
               K1 = K2-1
               U = 0
               V = 0
               DO 200 I=1,NU
                    I2 = 2*I
                    I1 = I2-1
                    ZALPU = CMPLX(ALP(I1,K1),-ALP(I2,K1))
                    U = U+ZALPU*ZIU(I)
                    ZALPV = CMPLX(ALP(I1,K2),-ALP(I2,K2))
                    V = V+ZALPV*ZIU(I)
  200          CONTINUE
               IF (K.EQ.2) GO TO 225
               IF (K.EQ.3) GO TO 250
               UC = U
               VC = V
               ZUS(IX) = CMPLX(U,V)
               GO TO 275
C
  225          DUDX = (U-UC)/DELC
               DVDX = (V-VC)/DELC
               GO TO 275
C
  250          DUDY = (U-UC)/DELC
               DVDY = (V-VC)/DELC
  275     CONTINUE
          DIV = DUDX+DVDY
          VOR = DVDX-DUDY
          PRINT 400, IX,ZZX,ZUS(IX),ERUU(IX)
          PRINT 425, DUDX,DVDX,DUDY,DVDY,DIV,VOR
          PRINT 450, EUX,EUY,EVX,EVY,EDIV,EVOR
          WRITE (3) ZZX,ZUS(IX),ERUU(IX),DUDX,DVDX,DUDY,DVDY,DIV,VOR
  300 CONTINUE
      STOP
```

```
C
 325  FORMAT (41H1 INPUT DATA FOR MEAN FIELD INTERPOLATION//(2I6,2F15.0,
     $2F15.2,F15.6))
 350  FORMAT (19H0 INTERPOLATION PT.I5,5X,I5,10H DATA USED,2014/(44X,
     $2014))
 375  FORMAT (I5,10F12.7/(5X,10F12.7))
 400  FORMAT (26H0 INTERPOLATED VELOCITY AT I5,4F12.3,F12.6)
 425  FORMAT (28H0 VELOCITY GRADIENTS (1/SEC),3X,6E12.3)
 450  FORMAT (25H0 GRADIENT ERROR VARIANCE,6X,6E12.3)
      END



      SUBROUTINE SLHS(Z,SIGI,NU,LHS)
      COMPLEX Z(NU),DZ
      REAL LHS(100,100),SIGI(100)
C     CONSTRUCT LEFT HAND SIDE MATRIX LHS FOR INTERPOLATION
C     CORRELATE ALL PAIRS OF VELOCITY COMPONENTS
C
      QSQ = 4
      DO 25 I=1,NU
           I2 = I+I
           I1 = I2-1
           LHS(I1,I1) = 1.+SIGI(I)/QSQ
           LHS(I2,I2) = 1.+SIGI(I)/QSQ
           LHS(I1,I2) = LHS(I2,I1) = 0.
           IF (I.EQ.NU) GO TO 50
           IP1 = I+1
           DO 20 J=IP1,NU
                J2 = J+J
                J1 = J2-1
                DZ = Z(I)-Z(J)
                R = CABS(DZ)
                C = REAL(DZ)/R
                S = AIMAG(DZ)/R
                B1 = BPARLU(R)
                B2 = BPERPU(R)
                LHS(I1,J1) = C*C*B1+S*S*B2
                LHS(I1,J2) = LHS(I2,J1) = C*S*(B1-B2)
                LHS(I2,J2) = S*S*B1+C*C*B2
                LHS(J1,I1) = LHS(I1,J1)
                LHS(J2,I2) = LHS(I2,J2)
                LHS(J2,I1) = LHS(I2,J1)
                LHS(J1,I2) = LHS(I1,J2)
 20         CONTINUE
 25   CONTINUE
 50   RETURN
      END



      SUBROUTINE SRHS(ZX,Z,NU,RHS,L)
      COMPLEX ZX,Z(NU),DZ
      REAL RHS(100,6)
C     CONSTRUCT MULTIPLE RIGHT HAND SIDE RHS FOR INTERPLORATION .  THE
C     COLUMNS INDEXED BY L REFER TO THE U COMPONENT AT (GX,GY),(GX+1,GY)
C     ,(GX,GY+1), AND THE V COMPONENT AT THE SAME POINTS.
      DO 50 I=1,NU
           I2 = I+I
           I1 = I2-1
           DZ = ZX-Z(I)
           R = CABS(DZ)
           IF (R.LT.0.1) GO TO 25
           C = REAL(DZ)/R
           S = AIMAG(DZ)/R
           B1 = BPARLU(R)
```

```
            B2 = BPERPU(R)
            RHS(I1,L) = C*C*B1+S*S*B2
            RHS(I2,L) = RHS(I1,L+1) = C*S*(B1-B2)
            RHS(I2,L+1) = S*S*B1+C*C*B2
            GO TO 50
C
 25         RHS(I1,L) = 1
            RHS(I2,L+1) = 1
            RHS(I2,L) = RHS(I1,L+1) = 0
 50    CONTINUE
       RETURN
       END



       SUBROUTINE ERROR(A,S,N,EUU)
C      CALCULATE THE VELOCITY INTERPOLATION ERROR VARIANCE
       COMMON /EGRAD/ EUX,EUY,EVX,EVY,EDIV,EVOR
       REAL A(100,6),S(100,6),EU(6),E(6,6)
C
       DO 50 K=1,6
            EU(K) = 1
            DO 25 I=1,N
                 EU(K) = EU(K)-A(I,K)*S(I,K)
 25         CONTINUE
 50    CONTINUE
       EUU = EU(1)+EU(2)
       DEL = 10
       B12 = BPARLU(DEL)
       B13 = BPERPU(DEL)
       DEL2 = 1.41214*DEL
       B23 = 0.5*(BPARLU(DEL2)+BPERPU(DEL2))
       B26 = 0.5*(BPARLU(DEL2)-BPERPU(DEL2))
       E(1,1) = E(2,2) = E(3,3) = E(4,4) = E(5,5) = E(6,6) = 1
       E(1,4) = E(4,1) = E(1,5) = E(5,1) = E(1,6) = E(6,1) = 0
       E(2,4) = E(4,2) = E(2,5) = E(5,2) = 0
       E(3,4) = E(4,3) = E(3,6) = E(6,3) = 0
       E(1,2) = E(2,1) = B12
       E(1,3) = E(3,1) = B13
       E(2,3) = E(3,2) = E(5,6) = E(6,5) = B23
       E(2,6) = E(6,2) = E(3,5) = E(5,3) = B26
       E(4,6) = E(6,4) = B12
       E(4,5) = E(5,4) = B13
       DO 100 KI=1,6
            DO 90 KJ=1,6
                 DO 75 I=1,N
                      E(KI,KJ) = E(KI,KJ)-A(I,KI)*S(I,KJ)
 75              CONTINUE
 90         CONTINUE
 100   CONTINUE
C      SIG = STANDARD DEVIATION OF ONE VELOCITY COMPONENT (M/S)
       SIG = 0.02
       EUX = E(1,1)+E(2,2)-2.*E(1,2)
       EUY = E(1,1)+E(3,3)-2.*E(1,3)
       EVX = E(4,4)+E(5,5)-2.*E(4,5)
       EVY = E(4,4)+E(6,6)-2.*E(4,6)
       RETURN
       END



       SUBROUTINE DATAER(NDAYS,SIGD,N)
C      SIGD IS THE VARIANCE OF THE MEASUREMENT ERROR FOR
C      SINGLE COMPONENT OF VELOCITY AT THE DATA POINT
       DIMENSION NDAYS(N), SIGD(N)
       DATA TCORR/5.0/
```

```
      SIG2 = 25
      DO 25 I=1,N
           SIGD(I) = 1000
           IF (NDAYS(I).EQ.0) GO TO 25
           SIGD(I) = SIG2/NDAYS(I)*TCORR
25    CONTINUE
      RETURN
      END


      FUNCTION BPARLU(R)
      A = 1500.
      B = (R/A)**2
      BPARLU = EXP(-B)
      RETURN
      END


      FUNCTION BPERPU(R)
      A = 1500.
      B = (R/A)**2
      BPERPU = (1.-2.*B)*EXP(-B)
      RETURN
      END


      SUBROUTINE VIPDA(A,KA,B,KB,N,CC)
      REAL A(1),B(1)
      DOUBLE PRECISION C
      C = DBLE(CC)
      DO 25 I=1,N
           II = 1+(I-1)*KA
           IJ = 1+(I-1)*KB
           C = C+A(II)*B(IJ)
           CC = C
25    CONTINUE
      RETURN
      END
```

```
      PROGRAM PIJ (INPUT,OUTPUT,TAPE1,TAPE2,TAPE3,TAPE4,TAPE5)
C
C     PROGRAM PIJ GENERATES THE TRANSITION PROBABILITY MATRIX.
C
C
C     INPUT FILE1 -- CONTAINS THE (X,Y) COORDINATES IN KILOMETERS
C                    OF THE VERTICES OF EACH CELL (ZCELL)
C                    THE NOTATION ON VERTICES IS TO NUMBER
C                    THEM COUNTER-CLOCKWISE
C     INPUT FILE2 -- CONTAINS THE (X,Y) COORDINATES IN KILOMETERS
C                    OF THE VERTICES OF EACH MELT AND EXITREGIONS (ZCELL)
C                    THE NOTATION IS EXACTLY THE SAME AS
C                    FOR THE TRANSIENT STATES
      COMPLEX ZCELL(4,130)
C
C
C     INPUT FILE3 -- CONTAINS THE (U,V) MEAN ICE MOTIONS IN
C                    CM / SEC  (THIS FILE IS THE OUTPUT FILE OF
C                    PROGRAM MEANICE)
      COMPLEX UM, XM(130)
C
C     OUTPUT FILE4 -- OUTPUTS THE TRANSITIONAL PROBABILITY MATRIX
      REAL P(130)
C
C     INPUT FILE5 -- CONTAINS THE PROBABILITY OF MELTING IN A CELL
C
C
C     ZP IS A PARTITION OF EACH CELL
      COMPLEX ZP(25,130)
C     A IS THE AREAS OF THE PARTIONS OF THE CELLS AND TA IS THE
C     TOTAL AREA OF THE CELLS
      REAL A(25,130)),TA(130)
C
      COMMON /SEP/ VAR2D,VAR1,VAR2
      COMPLEX DIJ
      LOGICAL KPP
C
C
C
      KPP = .T.
      S2MAX = 10.0
      NCELL = 108
      NEXIT = 8
      NMELT = 1
C     M SQUARED IS THE NUMBER OF PARTITIONS TO DIVIDE EACH CELL
      M = 4
      M2 = M*M
C     NDATE IS THE DATE OF THE MELT SEASON FOR WHICH THIS TRANSITION
C     PROBABILITY MATRIX IS BEING GENERATED
      NDATE = 0110
C     30 DAY ANISOTROPHIC, INHOMOGENEOUS COVARIANCE
      DAYS = 30
      DELT = DAYS*24*60*60
      DSQBAR = 2.5E+4
      VAR2D = DSQBAR/2
      VAR1 = 0.8*VAR2D
      VAR2 = 0.2*VAR2D
      SIG2D = SQRT(VAR2D)
      PRINT 125, DSQBAR,VAR2D,SIG2D,DAYS
C
C
      NCELLE = NCELL+NEXIT
      NCELLA = NCELL+NEXIT+NMELT
      DO 25 I=1,NCELL
           READ (1,150) (ZCELL(K,I),K=1,4)
           READ (3) UM
```

```
          XM(I) = DELT*UM/1.0E+5
          CALL DIVIDE (ZCELL(1,I),ZCELL(2,I),ZCELL(3,I),ZCELL(4,I),ZP(1,I),
     $    A(1,I),TA(I),M)
          PRINT 175, I,M,(ZCELL(K,I),K=1,4),TA(I),XM(I)
 25   CONTINUE
C
      DO 50 I=1,NEXIT
          II = NCELL+I
          READ (2,150) (ZCELL(K,II),K=1,4)
          CALL DIVIDE (ZCELL(1,II),ZCELL(2,II),ZCELL(3,II),ZCELL(4,II),ZP(1
     $    ,II),A(1,II),TA(II),M)
          PRINT 200
 50   PRINT 175, I,M,(ZCELL(K,II),K=1,4),TA(II)
C
C     CALCULATE THE PROBABILITY OF MOVING FROM CELL(I) TO CELL(J)
C
      PRINT 225
      DO 100 I=1,NCELL
          DO 75 J=1,NCELLE
              P(J) = 0
              DIJ = ZCELL(1,I)+XM(I)-ZCELL(1,J)
              S2 = DIJ*CONJG(DIJ)
              IF (S2/VAR2D.GT.S2MAX.AND.J.LE.NCELL) GO TO 75
C
              CALL INTG (ZP(1,I),ZP(1,J),A(1,I),A(1,J),TA(I),M2,XM(I),
     $        P(J))
C
 75       CONTINUE
          IF (KPP) CALL PRINTP (P,NCELLE,I)
          CALL NORM (P,NCELLE,I)
          IF (NMELT.GT.0) CALL MELT (P,NCELLE,I,NDATE,NMELT)
          IF (KPP) CALL PRINTP (P,NCELLA,I)
          WRITE (4) (P(J),J=1,NCELLA),TA(I)
 100  CONTINUE
      STOP
C
C
 125  FORMAT (27H1 MEAN SQUARED SEPARATION =E10.3,5X,15H  2D VARIANCE =E
     $10.3,5X,20H  ROOT OF VARIANCE =F6.0,5X,F10.0,14H DAY TIME STEP//)
 150  FORMAT (5X,8F10.4)
 175  FORMAT (5H0 CELL215,8F8.0,E11.3,2F8.0)
 200  FORMAT (17H0 ABSORBING STATE)
 225  FORMAT (31H1 TRANSITION PROBABILITY MATRIX)
      END



      SUBROUTINE DIVIDE(ZA,ZB,ZC,ZD,ZX,A,TA,M)
C     SUBDIVIDE THE CELL WITH VERTICES ZA,ZB,ZC,ZD INTO
C     M**2 SUB-CELLES EACH HAVING CENTER AT ZX AND AREA A
      IMPLICIT COMPLEX (Z)
      DIMENSION ZX(25), Z(6,6), A(25)
      N = M+1
      DEL = 1.0/M
      DO 25 J=1,N
          ALP = (J-1)*DEL
          ZL = ZA+ALP*(ZD-ZA)
          ZR = ZB+ALP*(ZC-ZB)
          DO 25 I=1,N
              BET = (I-1)*DEL
 25   Z(I,J) = ZL+BET*(ZR-ZL)
      K = 0
      TA = 0
      DO 50 I=1,M
          DO 50 J=1,M
              K = K+1
```

```
                ZX(K) = (Z(I,J)+Z(I+1,J)+Z(I,J+1)+Z(I+1,J+1))/4
                A(K) = AREA(Z(I,J),Z(I+1,J),Z(I+1,J+1),Z(I,J+1))
                TA = TA+A(K)
 50     CONTINUE
        RETURN
        END



        FUNCTION AREA(Z1,Z2,Z3,Z4)
C       DETERMINE THE AREA OF THE QUADRALATERAL
        IMPLICIT COMPLEX (Z)
        ZA = -Z2*CONJG(Z3)+Z1*CONJG(Z3-Z2)
        ZB = -Z3*CONJG(Z4)+Z2*CONJG(Z4-Z3)
        ZC = -Z4*CONJG(Z1)+Z3*CONJG(Z1-Z4)
        ZD = -Z1*CONJG(Z2)+Z4*CONJG(Z2-Z1)
        AREA = AIMAG(ZA+ZB+ZC+ZD)/4
        RETURN
        END



        SUBROUTINE INTG(ZA,ZB,AA,AB,TA,M2,ZM,PJ)
C       ZA , ZB ARE PARTITIONS OF CELL(A) , CELL(B)
C       SUM IS THE INTEGRAL OF F ( X GIVEN Y ) DX FOR X IN CELL B
C       WHERE F IS THE PROBABILITY DENSITY FUNCTION
        IMPLICIT COMPLEX (Z)
        COMMON /SEP/ VAR2D,VAR1,VAR2
        DIMENSION ZA(M2), ZB(M2), AA(M2), AB(M2)
        TWOPIS = 2.*3.1415927*SQRT(VAR1*VAR2)
        TSUM = 0.0
        DO 50 I=1,M2
             SUM = 0
             DO 25 J=1,M2
                  ZD = ZA(I)+ZM-ZB(J)
                  ZP = ZM/CABS(ZM)*CONJG(ZD)
                  X1 = REAL(ZP)
                  X2 = AIMAG(ZP)
                  S2 = (X1**2/VAR1+X2**2/VAR2)/2.
                  IF (S2.GT.5.0) GO TO 25
                  SUM = SUM+AB(J)*EXP(-S2)
 25          CONTINUE
             TSUM = TSUM+SUM*AA(I)
 50     CONTINUE
        TSUM = TSUM/TWOPIS/TA
        PJ = TSUM
        RETURN
        END



        SUBROUTINE NORM(P,N,ICELL)
        REAL P(N)
        PT = 0
        DO 25 I=1,N
 25     PT = PT+P(I)
        PT1 = 1-PT
        IF (ABS(PT1).GT.0.00) PRINT 50, ICELL,PT
C       LUMP DEFICIT PROBABILITY INTO ORIGINATING CELL
C       TO SIMULATE ICE STRESS
        P(ICELL) = P(ICELL)+PT1
        RETURN
C
C
 50     FORMAT (5H0 CELL15,22H HAS TOTAL PROBABILITYE12.3)
        END
```

```
      SUBROUTINE PRINTP(P,N,ICELL)
      DIMENSION P(N), PK(130), IK(130)
      K = 0
      DO 25 I=1,N
           IF (P(I).EQ.0.0) GO TO 25
           K = K+1
           IK(K) = I
           PK(K) = P(I)
 25   CONTINUE
      PRINT 50, ICELL,(IK(J),PK(J),J=1,K)
      RETURN
C
C
 50   FORMAT (5H0 CELL15,14H PROBABILITIES/(5X,10(I5,F7.4)))
      END



      SUBROUTINE MELT(P,NE,ICELL,NDATE,NMELT)
C     MODEL MELTING AS INDEPENDENT OF SEASON
C
      DIMENSION P(130), IM(130), MM(130), PM(130)
C
      IF (ICELL.GT.1) GO TO 50
 25   READ (5,150,END=125) IDATE,NIM
      PRINT 150, IDATE,NIM
      READ (5,175,END=125) (IM(K),MM(K),PM(K),K=1,NIM)
      IF (IDATE.NE.NDATE) GO TO 25
      PRINT 200, (IM(K),MM(K),PM(K),K=1,NIM)
 50   CONTINUE
C
      DO 75 K=1,NMELT
 75   P(NE+K) = 0
      DO 100 KK=1,NIM
           K = IM(KK)
           AMELT = P(K)*PM(KK)
           P(K) = P(K)-AMELT
           MK = MM(KK)
           P(NE+MK) = P(NE+MK)+AMELT
 100  CONTINUE
 125  RETURN


 150  FORMAT (2I5)
 175  FORMAT (2I5,F5.2)
 200  FORMAT (28H1 PROBABILITY OF SUMMER MELT//(5H  CELL15,22H  INTO ABSO
     $RBING STATE15,20H  WITH PROBABILITY =F8.3))
      END
```

```
      PROGRAM APOWER (INPUT,OUTPUT,TAPE1,TAPE2,TAPE3)
C
C     PROGRAM APOWER FINDS THE PROBABILITY AND DENSITY FUNCTIONS
C     FOR ICE MOVING FROM CELL A TO ANY OTHER CELL OR STATE IN
C     TIME = NSTEPS MONTHS
C
C
C     INPUT FILE1 -- IS THE TRANSITIONAL PROBABILITY MATRICES
C                    GENERATED BY PROGRAM PIJ
C
C     OUTPUT FILE2 -- IS THE PROBABILITY FUNCTION FOR EACH TIME STEP
C                     OF MOVING FROM A TRANSIENT STATE (A CELL) TO
C                     ANOTHER TRANSIENT OR AN ABSORBING STATE
C
C     OUTPUT FILE3 -- IS THE CUMULATIVE DENSITY FUNCTION
C
C
      COMMON NP,NR,P(130,130),AN1(130,130),R(130,10),TA(130),MONTH
      LOGICAL NEXTP
C
C     NUMBER OF CELLS
      NP = 108
C     NUMBER OF EXIT REGIONS
      NEXIT = 8
C     NUMBER OF MELT REGIONS
      NMELT = 1
      NR = NEXIT+NMELT
      N = NP+NR
      N1 = NP+1
C
C     MONTH IS INITIAL TIME
      MONTH = 4
C     NUMBER OF MONTHS TO FOLLOW ICE MOTION
      NSTEPS = 8
      NTT = NSTEPS+MONTH-1
C
      CALL FINDP (.T.,MONTH,NEXTP)
      CALL READTP (.T.,N,N1)
      CALL INITIAL (N,N1)
C
C
      DO 25 NT=2,NTT
           MONTH = MONTH+1
           IF (MONTH.EQ.13) MONTH = 1
           CALL FINDP (.F.,MONTH,NEXTP)
           IF (NEXTP) CALL READTP (.F.,N,N1)
           CALL AIJN (NT)
 25   CONTINUE
      STOP
      END



      SUBROUTINE READTP(LTPM,N,N1)
      LOGICAL LTPM
      COMMON NP,NR,P(130,130),AN1(130,130),R(130,10),TA(130),MONTH
      DIMENSION IJ(130), PJ(130)
C
      DO 25 I=1,NP
           READ (1) (P(I,J),J=1,NP),(R(I,J),J=1,NR),TA(I)
 25   CONTINUE
C
      DO 50 I=1,NP
           DO 50 J=N1,N
                P(I,J) = R(I,J-NP)
 50   CONTINUE
```

```
C
      IF (.NOT.LTPM) RETURN
      PRINT 125
      DO 100 I=1,NP
           K = 0
           SUMP = 0
           DO 75 J=1,NP
                IF (P(I,J).EQ.0.0) GO TO 75
                K = K+1
                IJ(K) = J
                PJ(K) = P(I,J)
                SUMP = SUMP+P(I,J)
 75        CONTINUE
           PRINT 150, I,SUMP
 100  PRINT 175, (IJ(J),PJ(J),J=1,K),(J,R(I,J),J=1,NR)
      RETURN
C
 125  FORMAT (31H0 TRANSITION PROBABILITY MATRIX)
 150  FORMAT (5H0 BOX15,25H TRANSITION PROBABILITIES,5X,20H TOTAL PROBAB
     $ILITY =F10.4)
 175  FORMAT (10(I5,F7.4))
      END



      SUBROUTINE INITIAL(N,N1)
      COMMON NP,NR,P(130,130),AN1(130,130),R(130,10),TA(130),MONTH
C
      DO 25 I=N1,N
           DO 25 J=1,N
 25   P(I,J) = 0
      DO 50 I=N1,N
 50   P(I,I) = 1
      DO 75 I=1,N
           DO 75 J=1,N
                AN1(I,J) = P(I,J)
 75   CONTINUE
      WRITE (2) MONTH,AN1
      RETURN
      END



      SUBROUTINE AIJN(NT)
      COMMON NP,NR,P(130,130),AN1(130,130),R(130,10),TA(130),MONTH
      REAL AN(130,130),AD(130),AT(130)
      LOGICAL LAN,LAT
C
      LAN = .F.
      N = NP+NR
C
      DO 25 I=1,N
           DO 25 J=1,N
                AN(I,J) = 0
                DO 25 K=1,N
                     AN(I,J) = AN(I,J)+AN1(I,K)*P(K,J)
 25   CONTINUE
      WRITE (2) MONTH,AN
C
      IF (.NOT.LAN) GO TO 75
      DO 50 I=1,N
           PRINT 175, I,NT,(AN(I,J),J=1,N)
 50   CONTINUE
 75   CONTINUE
      LAN = .F.
C
```

```
      LAT = .F.
      DO 125 I=1,N
           AT(I) = 0
           DO 100 J=1,N
                AT(I) = AT(I)+AN(I,J)
 100       AN1(I,J) = AN(I,J)
           IF (ABS(AT(I)-1.0).GT.0.00001) LAT = .T.
 125  CONTINUE
      IF (LAT) PRINT 200, (AT(I),I=1,N)
C     PRINT THE PROBABILITIES AND DENSITY FUNCTION FOR INITIAL
C     INITIAL CELL I
      I = 85
      PRINT 175, I,NT,(AN(I,J),J=1,N)
      DO 150 J=1,NP
 150  AD(J) = AN(I,J)/TA(J)
      PRINT 225, I,NT,(AD(J),J=1,NP)
      WRITE (3) I,MONTH,(AD(J),J=1,NP)
      RETURN
C
 175  FORMAT (11H0 FROM CELL15,5X,8H IN STEP15/(10F10.4))
 200  FORMAT (10E10.2)
 225  FORMAT (11H0 FROM CELL15,5X,8H IN STEP15/(10E10.2))
      END



      SUBROUTINE FINDP(FIRST,M,NEXTP)
C
C     FIND THE TRANSITION PROBABILITY MATRIX FOR MONTH (M)
C     CHUKCHI SEA  M = 1,2,3,4,5, 11,12  = EQUAL WINTER
C     M = 6 (JULY), M = 7 (AUG), M = 8 (SEPT),
C     M = 9 (OCT), M = 10 (NOV)
C
      DIMENSION JMON(11)
      LOGICAL FIRST,NEXTP
      DATA JMON(1),JMON(7),JMON(8),JMON(9),JMON(10),JMON(11)/10HWINTER
     $   ,10HWINTER    ,10HAUGUST    ,10HSEPTEMBER ,10HOCTOBER   ,
     $10HWINTER    /
C
C
      IF (.NOT.FIRST) GO TO 100
      REWIND 1
      IFIRST = M+1
      IF (IFIRST.LT.8.OR.IFIRST.GT.10) IFIRST = 0
 25   READ (1) IDATE,NPTS
      IF (IDATE.EQ.IFIRST) GO TO 75
      DO 50 I=1,NPTS
           READ (1)
 50   CONTINUE
      GO TO 25
C
 75   IDM = IDATE
      IF (IDATE.EQ.0) IDM = 1
      PRINT 150, JMON(IDM)
      RETURN
 100  CONTINUE
      IF (M.LE.6.OR.M.GE.10) GO TO 125
      NEXTP = .T.
      IF (M.EQ.11) REWIND 1
      READ (1) IDATE
      IDM = IDATE
      IF (IDATE.EQ.0) IDM = 1
      PRINT 150, JMON(IDM)
      RETURN
 125  NEXTP = .F.
      RETURN
```

```
C
  150  FORMAT (/,* MONTH IS *,A10)
       END
```

```
      PROGRAM MARKOV (INPUT,OUTPUT,TAPE1,TAPE2,TAPE3)
C
C
C     PROGRAM MARKOV GIVES THE PROBABILITY OF ENTERING ANY TRANSIENT
C     OR ABSORBING STATE GIVEN AN INITIAL TRANSIENT STATE
C
C
C     INPUT FILE1 -- TRANSITIONAL PROBABILITY MATRIX
C
C     OUTPUT FILE2 -- PROBABILITY OF VISITING ANY OTHER CELL IN NSTEPS
C
C     OUTPUT FILE3 -- PROBABILITY OF REACHING AN ABSORBING STATE
C                     IN NSTEPS
C
      COMMON NQ,NR,Q(120,120),QK(120,120),R(120,10)
C
C     NUMBER OF CELLS
      NQ = 108
C     NUMBER OF ABSORBING STATES
      NR = 9
      NSTEPS = 60
C
C
      CALL READTP (.T.)
      CALL IMQ (.F.)
      CALL VISITS (.F.,.F.,.F.)
      CALL LIFE
      CALL FATE
      CALL MORT (NSTEPS)
      STOP
      END



      SUBROUTINE READTP(LTPM)
      LOCAL LTPM
      COMMON NQ,NR,Q(120,120),QK(120,120),R(120,10)
      DIMENSION IJ(120), QJ(120)
C
      REWIND 1
      DO 25 I=1,NQ
 25   READ (1) (Q(I,J),J=1,NQ),(R(I,J),J=1,NR)
C
      IF (.NOT LTPM) RETURN
      PRINT 100
      DO 75 I=1,NQ
           K = 0
           SUMQ = 0
           DO 50 J=1,NQ
                IF (Q(I,J).EQ.0.0) GO TO 50
                K = K+1
                IJ(K) = J
                QJ(K) = Q(I,J)
                SUMQ = SUMQ+Q(I,J)
 50        CONTINUE
           PRINT 125, I,SUMQ
 75   PRINT 150, (IJ(J),QJ(J),J=1,K),(J,R(I,J),J=1,NR)
      RETURN
C
 100  FORMAT (31H1 TRANSITION PROBABILITY MATRIX)
 125  FORMAT (5H0 BOX15,25H TRANSITION PROBABILITIES,5X,20H TOTAL PROBAB
     $ILITY =F10.4)
 150  FORMAT (10(I5,F7.4))
      END
```

```
      SUBROUTINE IMQ(LCHECK)
      LOGICAL LCHECK
      COMMON NQ,NR,Q(120,120),QK(120,120),R(120,10)
      REAL IPR(120),QC(120)
C
      DO 50 I=1,NQ
           DO 25 J=1,NQ
                Q(I,J) = -Q(I,J)
 25        QK(I,J) = 0
           Q(I,I) = 1+Q(I,I)
 50   QK(I,I) = 1
      WRITE (3) Q
C
      CALL LEQT1F (Q,NQ,NQ,120,QK,0,IPR,IER)
      PRINT 125, IER
      CALL READTP (.F.)
C
      IF (.NOT.LCHECK) RETURN
      REWIND 3
      READ (3) Q
      DO 100 I=1,NQ
           DO 75 J=1,NQ
                QC(J) = 0
                DO 75 K=1,NQ
 75        QC(J) = QC(J)+Q(I,K)*QK(K,J)
           QC(I) = QC(I)-1
 100  PRINT 150, I,(QC(J),J=1,NQ)
C
      RETURN
C
 125  FORMAT (13H0 FROM LEQT1F I10)
 150  FORMAT (I5,10E10.3/(5X,10E10.3))
      END



      SUBROUTINE VISITS(LNUM,LPROB,LVNUM)
      COMMON NQ,NR,Q(120,120),QK(120,120),R(120,10)
      LOGICAL LNUM,LPROB,LVNUM
      REAL RHOV(120),SVV(120)
C
      IF (.NOT.LNUM) GO TO 50
      PRINT 225
      DO 25 I=1,NQ
 25   PRINT 250, I,(QK(I,J),J=1,NQ)
 50   CONTINUE
C
      IF (.NOT.LPROB) GO TO 125
      PRINT 275
      DO 100 I=1,NQ
           DO 75 J=1,NQ
                GJ = QK(J,J)-1
                RHOJ = GJ/(1+GJ)
 75        RHOV(J) = (1-RHOJ)*QK(I,J)
           GI = QK(I,I)-1
           RHOI = GI/(1+GI)
           RHOV(I) = RHOI
 100  PRINT 300, I,(RHOV(J),J=1,NQ)
 125  CONTINUE
C
      IF (.NOT.LVNUM) GO TO 200
      PRINT 325
      DO 175 I=1,NQ
           DO 150 J=1,NQ
                FAC = 2*QK(J,J)-1
```

```
 150       SUU(J) = SQRT(QK(I,J)*FAC-QK(I,J)**2)
 175   PRINT 350, I,(SUU(J),J=1,NQ)
 200   CONTINUE
       RETURN
C
 225   FORMAT (30H1 THE MATRIX QK = INV( I - Q )///)
 250   FORMAT (36H0 EXPECTED NUMBER OF VISITS FROM BOX15/(10F6.1,5X,10F6.
      $1))
 275   FORMAT (36H1 RHO(I,J) = G(I,J) / ( 1-RHO(J,J) )/54H  WHERE G(I,J)
     -  $IS THE EXPECTED NUMBER OF VISITS N.GT.0//)
 300   FORMAT (52H0 PROBABILITY OF VISITING A BOX GIVEN A START AT I =I5,
      $/(10F6.3,5X,10F6.3))
 325   FORMAT (45H1 THE MATRIX QK * ( 2*DIAG(NK) - I ) - SQ(QK)///)
 350   FORMAT (53H0 ROOT OF VARIANCE OF NUMBER OF VISITS FROM STATE I =I5
      $,/(10F6.1,5X,10F6.1))
       END



       SUBROUTINE LIFE
C      TAU(I) IS THE TIME TO EXIT OR MELT
C      GIVEN THE PROCESS STARTS IN STATE I
C
       COMMON NQ,NR,Q(120,120),QK(120,120),R(120,10)
       COMMON /FUNP/ TAU(120),VTAU(120),SIGT(120),RS(120,10)
C
       DO 25 I=1,NQ
            TAU(I) = 0
            DO 25 J=1,NQ
 25    TAU(I) = TAU(I)+QK(I,J)
       PRINT 100, (TAU(I),I=1,NQ)
C
       DO 75 I=1,NQ
            VTAU(I) = -TAU(I)-TAU(I)**2
            DO 50 J=1,NQ
 50         VTAU(I) = VTAU(I)+2*QK(I,J)*TAU(J)
 75    SIGT(I) = SQRT(VTAU(I))
       PRINT 125, (SIGT(I),I=1,NQ)
       REWIND 2
       WRITE (2) (TAU(I),I=1,NQ)
       WRITE (2) (VTAU(I),I=1,NQ)
       RETURN
C
 100   FORMAT (30H0 LIFE EXPECTANCY FROM STATE I/(10F10.1))
 125   FORMAT (50H0 ROOT OF VARIANCE OF LIFE EXPECTANCY FROM STATE I/
      $(10F10.1))
       END



       SUBROUTINE FATE
C      RS(I,J) IS THE PROBABILITY THAT THE ICE EXITS
C      OR MELTS AT J GIVEN THE PROCESS STARTS AT STATE I
C
       COMMON NQ,NR,Q(120,120),QK(120,120),R(120,10)
       COMMON /FUNP/ TAU(120),VTAU(120),SIGT(120),RS(120,10)
C
       DO 50 J=1,NR
            DO 25 I=1,NQ
                 RS(I,J) = 0
                 DO 25 K=1,NQ
 25         RS(I,J) = RS(I,J)+QK(I,K)*R(K,J)
 50    PRINT 75, J,(RS(I,J),I=1,NQ)
       WRITE (2) ((RS(I,J),I=1,NQ),J=1,NR)
       RETURN
C
```

```
 75   FORMAT (41H0 PROBABILITY OF REACHING ABSORBING STATE15,13H FROM ST
     $ATE I/(10F10.4))
      END


      SUBROUTINE MORT(NSTEP)
C     QNR(I,J) IS THE PROBABILITY THAT ABSORBING STATE J
C     IS REACHED FROM STATE I IN EXACTLY N STEPS
C
      COMMON NQ,NR,Q(120,120),QK(120,120),R(120,10)
      REAL QNR(120,10),QNRX(120,10),SQNR(120,10)
C
      IF (NSTEP.EQ.0) RETURN
      REWIND 3
      PRINT 250
      NT = 1
      DO 25 I=1,NQ
           DO 25 J=1,NR
                QNR(I,J) = R(I,J)
 25   SQNR(I,J) = QNR(I,J)
      GO TO 150
C
 50   NT = NT+1
      DO 75 I=1,NQ
           DO 75 J=1,NR
 75   QNRX(I,J) = QNR(I,J)
      DO 125 I=1,NQ
           DO 125 J=1,NR
                QNR(I,J) = 0
                DO 100 K=1,NQ
 100            QNR(I,J) = QNR(I,J)+Q(I,K)*QNRX(K,J)
 125  SQNR(I,J) = SQNR(I,J)+QNR(I,J)
 150  CONTINUE
      IF (MOD(NT,6).NE.0) GO TO 200
      DO 175 J=1,NR
           PRINT 275, J,NT,(QNR(I,J),I=1,NQ)
 175  PRINT 300, J,NT,(SQNR(I,J),I=1,NQ)
 200  DO 225 J=1,NR
           WRITE (3) J,NT,(QNR(I,J),I=1,NQ)
 225  WRITE (3) J,NT,(SQNR(I,J),I=1,NQ)
      IF (NT.LT.NSTEP) GO TO 50
      RETURN
C
 250  FORMAT (1H1,20X,38H MORTALITY TABLES FOR INITIAL STATES I//)
 275  FORMAT (40H0 PROBABILITY OF BEING ABSORBED IN STATE15,13H IN TIME
     $STEP15/(20F6.3))
 300  FORMAT (40H0 PROBABILITY OF BEING ABSORBED IN STATE15,13H BY TIME
     $STEP15/(20F6.3))
      END
```

```
      PROGRAM PLOTMAP(INPUT,OUTPUT,TAPE6=OUTPUT,TAPE1,
     *TAPE2,TAPE3,TAPE4)
C
C
C     PROGRAM PLOTMAP USES THE NCAR PLOTTING PACKAGES AND
C     PRODUCES VARIOUS PLOTS.
C
C     INPUT FILE1 -- CONTAINS THE X,Y COORDINATES OF THE VERTICES
C                    OF EACH CELL
C     INPUT FILE2 -- CONTAINS THE X,Y COORDINATES OF THE CENTER
C                    OF EACH CELL
C     INPUT FILE3 -- CONTAINS COORDINATES FOR THE ICE EDGE AT VARIOUS
C                    SEASONS
C     INPUT FILE4 -- OUTPUT FILE OF PROGRAMS PIJ, APOWER, OR
C                    MARKOV CONTAINING NUMBERS TO BE PLOTTED AT
C                    THE CENTER OF EACH CELL
C
      DIMENSION PL1(2), PL2(2), PL3(2), PL4(2)
      CHARACTER*1 ISEA, ICELL, NUM, IVEC, ICIR, ICE, IDEC
      BOOLEAN IGPAT
C
C
      COMMON /IPCONR/ SIZEL,SIZEM,SIZEP,NLA,XTL,YBT,SIDE,NREP,NCRT,
     *                ILAB,NULBLL,IOFFD,EXT,IOFFP,SPVAL,IOFFM,
     *                ISOLID,IHILO
      COMMON /IPSUPM/ IPEN1,IPEN2,ILABEL,IGPAT
      COMMON /CENTER/ CX(150), CY(150), NMBRBXS
      COMMON /CENTERK/ CKX(150), CKY(150)
      COMMON /POINTS/ PX(6), PY(6)
C
C
C     ****************************************************************
C
C     IS THIS PLOT OF THE BEAUFORT SEA?  IF 'NO', THE CHUKCHI
C     SEA IS ASSUMED.
      ISEA = 'Y'
C
C
C     HOW MANY PLOTS WILL BE MADE?
      NPLOTS = 1
C     IF YOU WANT TO PLOT CELLS:
      ICELL = 'N'
C     IF YOU WANT THE CELLS NUMBERED:
      NUM = 'N'
C     IF YOU WANT TO PLOT VECTORS:
      IVEC = 'N'
C     IF YOU WANT TO PLOT VARIANCE CIRCLES:
      ICIR = 'N'
C     IF YOU WANT A 10 CHARACTER LABEL ON YOUR VECTOR PLOT:
      LABEL = 10H
C     IF YOU WANT TO PLOT THE ICE EDGE:
      ICE = 'N'
C     IF YOU WANT TO PLOT A DECIMAL PARAMETER:
      IDEC = 'Y'
C     IF YOU WANT A 10 CHARACTER LABEL ON YOUR DECIMAL PLOT:
      LABEL2 = 10H
C
C     ****************************************************************
C
C
      ILABEL = 0
      IGPAT = O"1400"
C
C
      DO 300 IREPEAT = 1,NPLOTS
      IF(ISEA .EQ. 'Y')THEN
```

```
C           PROJECTION FOR THE BEAUFORT SEA.
            PL1(1) = 71.0
            PL1(2) = -165.0
            PL2(1) = 71.0
            PL2(2) = -120.
            PL3(1) = 68.0
            PL3(2) = -142.
            PL4(1) = 77.
            PL4(2) = -142.
            CALL SUPMAP (1, 72.5, -142.5, 0.,
     *           PL1, PL2, PL3, PL4, -5,
     *           10, 0, 1, IER)
            NMBRBXS = 108
            SCALEY = -159.
            SCALEX = 69.
            RF = .078577 / 998.5
       ELSE
C           PROJECTION FOR THE CHUKCHI SEA.
            PL1(1) = 70.0
            PL1(2) = 176.0
            PL2(1) = 70.0
            PL2(2) = -146.
            PL3(1) = 64.5
            PL3(2) = -168.
            PL4(1) = 75.
            PL4(2) = -170.
            CALL SUPMAP (1, 70.0, -165., 0.,
     *           PL1, PL2, PL3, PL4, -5,
     *           10, 0, 1, IER)
            NMBRBXS = 109
            SCALEY = -163.
            SCALEX = 68.
            RF = .096262 / 1220.439
       ENDIF
C
C
       IMARK = 6H'KRL'U
       CALL SUPCON(SCALEX,SCALEY,PX(1),PY(1))
       DO 50 I = 1,5
            PX(I+1) = PX(I) + (100. * RF)
            PY(I+1) = PY(1)
            CALL PWRY(PX(I),PY(I),IMARK,1,0,90,0)
 50    CONTINUE
       CALL PWRY(PX(6),PY(6),IMARK,1,0,90,0)
       PPY = PY(6) - .002
       CALL PWRY(PX(6),PPY,7H 500 KM,7,0,180,0)
       CALL CURVE(PX,PY,6)
C
C
C
            IF(IREPEAT .GT. 1)GO TO 275
            IF(IVEC .EQ. 'Y' .OR.
     *         IDEC .EQ. 'Y' .OR.
     *         NUM  .EQ. 'Y' )THEN
               DO 250 I = 1,NMBRBXS
                    READ(2,910,END=150)X,Y
                    CKX(I) = X
                    CKY(I) = Y
                    CALL COORD(X,Y,XLAT,XLON)
                    CALL SUPCON(XLAT,XLON,CX(I),CY(I))
 250           CONTINUE
            ENDIF
 275        IF(ICELL .EQ. 'Y')CALL CELLS
            IF(NUM .EQ. 'Y')CALL BXNUMBR(ISEA)
            IF(IVEC .EQ. 'Y')CALL XVECTOR(LABEL,ICIR)
            IF(IDEC .EQ. 'Y')CALL DECIMAL(LABEL2)
```

```
          IF(ICE .EQ. 'Y')CALL EDGE(ISEA)
C
          CALL FRAME
 300  CONTINUE
 910  FORMAT (30X,2F10.0)

 150  STOP
      END



      SUBROUTINE CELLS
C
C   CELLS READS THE COORDINATES (IN KM) AND PLOTS
C     THE CELLS THEY DEFINE
C
      DIMENSION XLAT(5), XLON(5)
      DIMENSION X1(4), Y1(4)
C
C
      REWIND 1
  50  READ(1,900,END=200)(X1(I),Y1(I),I=1,4)
C  C  PRINT 900, (X1(I),Y1(I),I=1,4)
      DO 100 I = 1,4
           CALL COORD(X1(I),Y1(I),X,Y)
           CALL SUPCON(X,Y,XLAT(I),XLON(I))
 100  CONTINUE
      XLAT(5) = XLAT(1)
      XLON(5) = XLON(1)
      CALL CURVE(XLAT,XLON,5)
      GO TO 50
C
C
 900  FORMAT (5X,8F10.4)
 200  RETURN
      END



      SUBROUTINE BXNUMBR(ISEA)
C
C     BXNUMBR PLOTS THE NUMBER OF THE CELL IN ITS CENTER
C
      CHARACTER*1 ISEA
      COMMON /CENTER/ CX(150), CY(150), NMBRBXS
C
C
      DO 100 NB = 1,NMBRBXS
           IF(NB .GT. 109 .AND. ISEA .EQ. 'N')GO TO 100
           XPT = CX(NB)
           YPT = CY(NB)
           ENCODE(3,910,IDATA)NB
           CALL PWRY(XPT,YPT,IDATA,3,0,0,1)
 100  CONTINUE
C
C
 910  FORMAT (I3)
      RETURN
      END



      SUBROUTINE EDGE(ISEA)
C
C
      CHARACTER*1 ISEA
```

```
      DIMENSION X(100), Y(100)
      COMMON /DATE/ ISTEP
C
C
      REWIND 3
      IF(ISEA .EQ. 'Y')THEN
           ELON1 = 360. - 160.
           ELON2 = 360. - 120.
      ELSE
           ELON1 = 180.
           ELON2 = 360. - 150.
      ENDIF
C
C
      MON = ISTEP + 1
 25   READ(3,900,END=1000)IDAY,IM,NP,NT
      IF(IM .NE. MON .OR. IDAY .NE. 01)THEN
           DO 30 I = 1,NP
                READ(3,910)
 30        CONTINUE
           GO TO 25
      ENDIF
      NPTS = 0
      DO 50 I = 1,NP
           READ(3,910,END=1000)XLAT, XLON
           IF(XLON .LT. 0.0)XLON = 360. + XLON
           IF(XLON .LT. ELON1 .OR.
     *        XLON .GT. ELON2)GO TO 50
           NPTS = NPTS + 1
           PRINT 920,NPTS,XLAT,XLON,B
           CALL SUPCON(XLAT,XLON,X(NPTS),Y(NPTS))
 50   CONTINUE
C
C
      IF(NPTS .EQ. 0)GO TO 100
      CALL CURVE(X,Y,NPTS)
 100  IF(NT .GT. 1)GO TO 25
 900  FORMAT (2I2,I4,I2)
 910  FORMAT(2F7.2)
 920  FORMAT (I10,3F7.2)
 1000 RETURN
      END
      SUBROUTINE COORD(X,Y,XLT,XLN)
      PI = 3.14159265 / 180.0
      R = 110.949
C
C
      XLT = 90. - ((SQRT(X**2 + Y**2)) / R)
      XR = X * PI
      YR = Y * PI
      YY = ATAN2(YR,XR)
      XLN = YY / PI
      RETURN
      END
      SUBROUTINE COORD2(A,B,X,Y)
      PI = 0.017453293
      R = 110.949
      D = R * (90.-A)
      X = D * COS(B*PI)
      Y = D * SIN(B*PI)
      RETURN
      END
      SUBROUTINE DECIMAL(LABEL)
C
      COMMON /POINTS/ PX(6), PY(6)
C
```

```
      COMMON /CENTER/ CX(150), CY(150), NMBRBXS
      COMMON /DATE/ ISTEP
      DIMENSION PARA(150), MONTHS(12)
C
      DATA MONTHS / 5HJAN   , 5HFEB   , 5HMAR   , 5HAPR   ,
                    5HMAY   , 5HJUNE  , 5HJULY  , 5HAUG   ,
                    5HSEPT  , 5HOCT   , 5HNOV   , 5HDEC    /
C
      NALL = NMBRBXS
      DO 50 I = 1,NALL
           PARA(I) = -9999.
 50   CONTINUE
C
      READ(4)ICELL,ISTEP,(PARA(I),I=1,NALL)
      IF(EOF(4))1000,200,1000
 200  DO 250 I = 1,NALL
           IF(PARA(I) .LT. -9000.)GO TO 250
           XPT = CX(I)
           YPT = CY(I)
           IPARA = INT (1.0E+7 * PARA(I))
           IF(I .LT. 10)PRINT *, PARA(I), IPARA
           ENCODE(3,910,IDATA)IPARA
           CALL PWRV(XPT,YPT,IDATA,3,0,180,1)
 250  CONTINUE
      IDAY = 1
      MON1 = 4
      MON2 = ISTEP + 1
      ENCODE(30,920,IDAT)IDAY, MONTHS(MON1),
                         IDAY, MONTHS(MON2),ICELL
      PRINT 920,IDAT
      PNT =  PY(1) -.005
      CALL PWRV(PX(1),PNT,IDAT,30,2,180,2)
 910  FORMAT (I3)
 920  FORMAT (I1,1X,A5,1X,I1,1X,A5,1X,1X,I2,5X)
 1000 RETURN
      END
      SUBROUTINE XVECTOR(LABEL,IC)
C
C
      CHARACTER*1 IC
      COMMON /CENTER/ CX(150), CY(150), NMBRBXS
      COMMON /CENTERK/ CKX(150), CKY(150)
      DIMENSION X(150), Y(150)
      DIMENSION X1(150), Y1(150)
      DIMENSION DIAMETR(150), NDIA(150)
      DIMENSION PX(2), PY(2)
C
C
      RO = 50
      SIGMA = 5
      IEX = 6H"PRL"X
      ICIRCLE = 6H"PGU"Y
      XFACTOR = 27.
      RFACTOR = .4
      DO 50 I = 1,NMBRBXS
           X(I) = -9999.
 50   CONTINUE
C
C
      IF(IC .EQ. 'Y')THEN
              DO 75 I = 1,NMBRBXS
                   READ(4)IJ,NDIA(I),XXX,YYY,X1(I),Y1(I)
 75           CONTINUE
      ELSE
           DO 80 I = 1,NMBRBXS
                   READ(4)SX,SY,X2,Y2
```

```
                    X1(I) = X2
                    Y1(I) = Y2
 80         CONTINUE
      ENDIF
      DO 100 NB = 1,NMBRBXS,2
           X2 = (X1(NB)*XFACTOR) + CKX(NB)
           IF(NB .GT. 109)GO TO 100
           Y2 = (Y1(NB)*XFACTOR) + CKY(NB)
           CALL COORD(X2,Y2,X3,Y3)
           CALL SUPCON(X3,Y3,X(NB),Y(NB))
 999  FORMAT(I5,4F12.3,/,6F12.3)
           IF(IC .EQ. 'Y')THEN
                IF(NDIA(NB) .EQ. 0)THEN
                     DIAMETR(NB) = 0.0
                     GO TO 100
                ENDIF
                IF(NDIA(NB) .LT. 31)THEN
                     DIAMETR(NB) = -9999.
                     GO TO 100
                ENDIF
                DIAMETR(NB) = SQRT((RO*SIGMA)/(FLOAT(NDIA(NB))))
           ENDIF
 100  CONTINUE
C
C
 200  DO 250 I = 1,NMBRBXS
           IF(X(I) .LT. -9000.)GO TO 250
           PX(1) = CX(I)
           PY(1) = CY(I)
           PX(2) =  X(I)
           PY(2) =  Y(I)
           CALL CURVE(PX,PY,2)
           IF(IC .EQ. 'Y')THEN
                IF(DIAMETR(I) .EQ. 0.0)GO TO 250
                IF(DIAMETR(I) .LT. -9000.)THEN
C  C   C   C   C   C   C   CALL PWRX(CX(I),CY(I),IEX,6,0,135,1)
                     GO TO 250
                 ENDIF
                SIZ = DIAMETR(I) * RFACTOR
                CALL PWRX(PX(2),PY(2),ICIRCLE,6,SIZ,135,1)
           ENDIF
 250  CONTINUE
      ENCODE(10,910,IDAT)LABEL
      CALL PWRY(.14,.205,IDAT,10,2,135,0)
 900  FORMAT (/,5X,2I10,/,2F12.2,/)
 910  FORMAT (A10)
      RETURN
      END
```

TEMPERATURE AND SALINITY STRUCTURE OF THE WINTERTIME BERING SEA MARGINAL ICE ZONE

by

John L. Newton

Science Applications, Inc.
1200 Prospect Street
La Jolla, California 92038

Final Report
Outer Continental Shelf Environmental Assessment Program
Research Unit 616

July 1982

ACKNOWLEDGMENTS

The winter 1980 CTD data were collected jointly by the Naval Postgraduate School and Science Applications, Inc., on the Winter 1980 Arctic West Cruise of the USCGC *Polar Star*.

The Arctic Submarine Laboratory of the Naval Ocean Systems Center, San Diego, CA, provided the icebreaker services and logistical support for the field measurements. The field work and preliminary analysis were also supported by Office of Naval Research Contract N00014-80-C-0368, with Science Applications, Inc., La Jolla, CA. This analysis and report were prepared under NOAA Contract NA81RAC00154.

ABSTRACT

Wintertime CTD sections across the Marginal Ice Zone (MIZ) of the Central Bering Sea shelf are analyzed and compared with fall CTD data. During the wintertime at depths shallower than 75 m, the water column was homogeneous and near freezing. Between the 75 and about 125 m isobaths, the structure was essentially two-layer with a cool-fresh upper layer overlying a warmer more saline bottom layer. Upper layer temperatures were significantly (>0.1^{o}C) above freezing for a distance of 50-100 km into the ice pack. The horizontal temperature and salinity gradients are intensified during the winter in the region of the ice edge. Correspondingly, the baroclinic currents in the upper layer appear to be strengthened and to follow along the ice edge. Fall to March comparisons do not reflect total changes in heat and salt content in the MIZ over a season. The changes are investigated to identify the important ice-ocean interactions.

Changes in temperature and salinity between fall and winter in the region of the MIZ indicate a heat loss of about 3.7 x 10^4 cal/cm^2 of which 60-66% occurred in the upper layer and 34-40% in the lower layer; and reduction in salt content of 2.4 g/cm^2 with 54-56% in the upper layer and 44-46% in the lower layer. The changes in total heat and salt content can be attributed to a heat loss through the surface (85% of the total heat change) plus a heat loss (15% of the total) and freshening due to ice melt of about 1 m averaged over the 200 km MIZ. Regression analysis of heat and salt content change in 25 km intervals along the MIZ are consistent with the concept of a direct surface exchange of heat plus heat loss and freshening by ice melt. The slope of the regression (equivalent to ρL, the density of ice times the latent heat of fusion) averaged about 62 cal/cm^3; the intercept (equivalent to direct surface heat loss) was 3.1 x 10^4 [cal/cm^2] for the total heat loss and 2 x 10^4 [cal/cm^2] for the upper layer. Changes in the temperature and salinity of the upper layer were significantly correlated with a slope of $\cong$ 2.5^{o}C/ppt, consistent with modification by ice melting. From fall to late March about 1 m of ice appears to have melted in the 200 km wide MIZ. This is equivalent to a southward movement of 0.5 m thick ice into the MIZ at about 8 cm/sec over a two month period.

TABLE OF CONTENTS

LIST OF FIGURES

LIST OF FIGURES (continued)

LIST OF FIGURES (continued)

LIST OF TABLES

1. INTRODUCTION

During March 1980, Conductivity and Temperature versus Depth (CTD) profiles were obtained along two sections which crossed the Bering Sea Marginal Ice Zone (MIZ) over the southeastern and central shelf. Preliminary results from these measurements have been presented by Newton and Andersen, 1980 and Paquette and Bourke, 1980. These sections supplement the relatively meager data base presently available to study the physical oceanographic processes relevant to the characteristics of the wintertime Bering Sea MIZ.

The purpose of this report is to present a detailed analysis of these sections within the context of recent physical oceanographic studies of the Bering Sea MIZ. The structure and characteristics of these sections will be compared to that of some pertinent sections from other seasons. Finally, these analyses and comparisons will form the basis for a discussion of some potentially important physical oceanographic process in the Bering Sea MIZ.

2. OCEANOGRAPHIC BACKGROUND

Kinder and Schumacher, 1981a, described the hydrographic structure of the Southeastern Bering Sea Shelf, southeast of St. Matthew Island. They identified three domains on the shelf based on the vertical hydrographic structure (Figure 2.1). This brief summary, following Kinder and Schumacher, 1981a, particularly reflects summertime conditions. In the shallow coastal domain, depths less than 50 m, the vertical structure is homogeneous with very little vertical stratification. During the late summer, temperatures are usually high (8-12^{o}C) and salinities are low (<31.5 ppt). The middle domain, between the 50 m and 100 m isobaths, is characterized by a two-layer structure with high stratification. Bottom temperatures remain cool (-1 to 3^{o}C) throughout the summer and salinities are about 31.5 ppt. Lying seaward of the 100 m isobath, the outer domain has a three-layer structure, mixed surface and bottom layers and a stratified interior, with moderate stratification. Salinities in the outer domain are high, greater than 32 ppt and temperatures fall in the 3 to 6^{o}C range. The three domains are separated

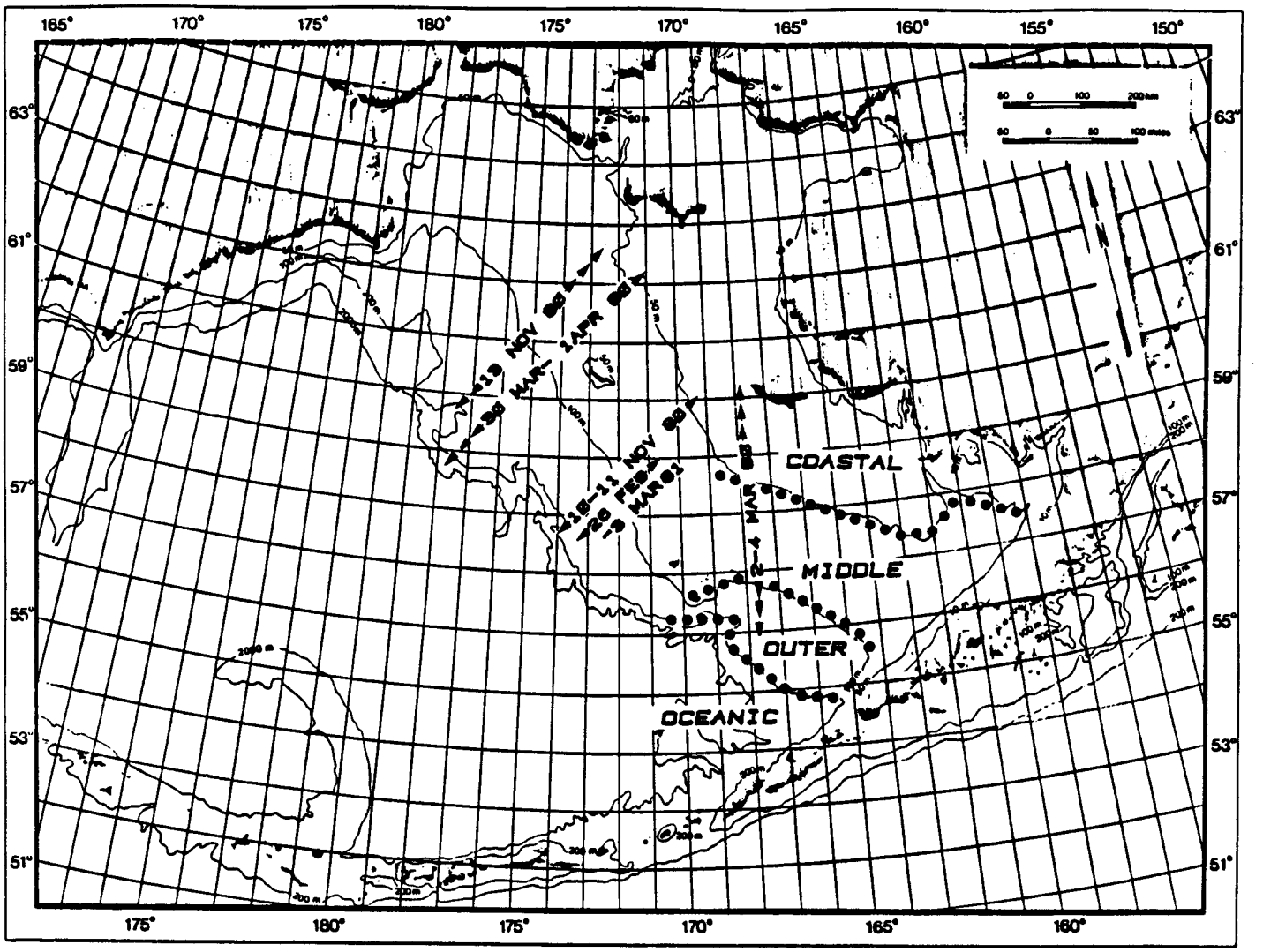

Figure 2.1. Location and orientation of CTD sections discussed in this report. The hydrographic domains of the southeastern Bering Sea Shelf from Kinder and Schumacher (1981a) are indicated.

by fronts, an inner front along the 50 m isobath, a middle front at about the 100 m depth contour and a shelf break front which separates the seaward extent of the outer domain from the oceanic waters of the deep Bering Sea.

Kinder and Schumacher, 1981a, identified several physical processes which act to form or alter the hydrographic structure over the shelf. Local changes in water mass characteristics can be caused by cooling and heating at the sea surface, evaporation and precipitation and the effects of ice melting and freezing. Because of the small mean flow on the shelf the impact of local processes are believed to be more important than changes due to advection. Vertical mixing due to tides and winds is one of the processes which determine the vertical hydrographic structure. In the coastal domain tide and wind stirring is sufficient to overcome buoyancy addition and thus maintain the vertically homogeneous structure. The deeper depths of the middle domain prevent tide and wind mixing from stirring the entire water column. The result is a wind stirred upper layer separated from a tidally mixed bottom layer by a sharp pycnocline region. In the outer domain the tide-mixed and wind-mixed layers do not meet thus leaving an interior stratified region.

Kinder and Schumacher, 1981a, indicate that during the winter, waters over most of the shelf are vertically homogeneous. They note two exceptions: warm saline water from the oceanic domain which intrudes onto the shelf along the bottom into the outer domain, and a low salinity lens of meltwater which can stratify the water.

The circulation over the southeastern Bering shelf (Kinder and Schumacher, 1981b) approximately corresponds to the hydrographic domains described above. In the outer regime (depths >100 m) the mean flow is about 1-5 cm/sec directed northwesterly along the isobaths and appears to be in geostrophic balance. The mean flow in the middle regime, between the 50 and 100 m depth contours, has a random direction and low speed (<0.5 cm/sec). Near the inner front, along the 50 m isobath, the average circulation is in counterclockwise with speeds of 1-5 cm/sec. The majority (60 to 90%) of the horizontal kinetic energy over the shelf is tidal with 80% of this tidal energy in the semidiurnal band.

3. DATA

The Winter 1980 data were collected during the March 1980 Bering Sea Cruise of the USCGC POLAR STAR (Newton and Andersen, 1980). A total of 83 CTD stations were occupied, of which 29 (stations 3-16 and 67-83) were located in or near the MIZ and will be emphasized here. Table 3.1 lists the positions and the date-time of occupation for these stations. A Neil Brown CTD (MK III microstructure profiler) interfaced to a Hewlett Packard 9835B desktop calculator was used to collect the data. Nansen bottles were employed to obtain independent checks on temperature and salinity. Newton and Andersen, 1980, describe the data collection procedures and cruise operations in more detail.

CTD data appropriate for comparison to these winter 1980 transects were obtained by Muench, 1981. Five CTD sections selected for discussion are located in Figure 2.1 and listed below. For ease of reference they are identified by season (W = Winter, F = Fall) and year (1980 or 1981). In chronological order these sections are:

W-80A (Newton and Andersen, 1980): A north-south line of CTD stations across the southeastern Bering Sea Shelf MIZ.

W-80B (Newton and Andersen, 1980): A northeasterly tending CTD section across the central Bering Sea shelf MIZ northwest of St. Matthew Island.

F-80A (Muench, 1981): A northeasterly directed transect of CTD stations across the central Bering Sea shelf southwest of St. Matthew Island.

F-80B (Muench, 1981): A line of CTD stations across the central Bering Sea shelf nearly coincident with section W-80B.

W-81 (Muench, 1981): Wintertime CTD stations which repeated a part of the F-80A transect.

Table 3.1. Station Data for Winter 1980 CTD Observation

W-80A

STATION	POSITION		DATE	TIME(Z)	DEPTH(m)
1	54-20.0N	166-17.0W	29 FEB 80	0019	778
2	54-36.0	166-12.0		0236	403
3	56-15.0	167-16.0		1230	128
4	56-23.5	167.08.0		1502	112
5	56-30.0	167-12.0		1636	126
6	56-37.0	167-14.0		1720	102
7	56-47.5	167.20.0	29 FEB 80	1849	91
8	56-50.0	167-23.0	1 MAR 80	0054	82
9	57-01.0	167-30.4		0239	79
10	57-14.5	167-39.7		0625	77
11	57-35.7	167-55.0		1143	73
12	57-57.0	168-10.0	1 MAR 80	2038	72
13	58-30.0	168-16.0	3 MAR 80	0400	59
14	59-05.0	168-08.0	3 MAR 80	1830	42
15	59-36.0	168-10.0	3 MAR 80	2348	40
16	59-52.1	168-16.5	4 MAR 80	0406	37

W-80B

STATION	POSITION		DATE	TIME(Z)	DEPTH(m)
67	61-36.0	172-08.0	28 MAR 80	1915	58
68	61-19.0	172-52.0	29 MAR 80	2030	64
69	61-01.0	173-40.0	30 MAR 80	2002	65
70	60-42.0	174-25.0	31 MAR 80	1109	89
71	60-24.0	175-08.0	31 MAR 80	2111	108
72	60-03.5	175-57.5	1 APR 80	0514	126
73	60-01.0	176-04.0	1 APR 80	0621	128
74	59-54.0	176-30.0	1 APR 80	1553	133
75	59-49.0	176-30.0	1 APR 80	2025	139
76	59-45.0	176-35.0	2 APR 80	0028	137
77	59-42.0	176-45.0		0159	139
78	59-39.0	176-53.0		0412	151
79	59-33.0	177-02.0		0916	152
80	59-29.0	177-07.0		1031	149
81	59-26.0	177-14.0		1136	159
82	59-20.0	177-24.0		1327	170
83	59-16.0	177-45.0	2 APR 80	1537	278

4. ANALYSIS OF MARCH 1980 CTD SECTIONS

4.1 Introduction

In this section, the two March 1980 MIZ CTD transects will be described individually. As indicated above, the CTD transects will be identified by season and year. Thus W-80A and W-80B (winter, 1980) are the transects across the southeastern Bering shelf and central Bering shelf, respectively, that were obtained during March 1980.

The analysis for each cross section includes:

- A description of the vertical temperature and salinity structure,
- Calculation of the horizontal property gradients along the section,
- An analysis of the temperature-salinity correlations including their relationship to the freezing point,
- Calculation of stratification parameters, and
- A short summary discussion.

4.2 Section W-80A

Section W-80A was occupied during the period 29 February to 3 March 1980. This section crossed the southeastern Bering Sea shelf between the 125 and 50 m depth contours (Figure 2.1); and thus extended from the outer shelf hydrographic domain, across the middle shelf into the coastal domain (Kinder and Schumacher, 1981a). Vertical cross sections of temperature and salinity along the southward end of this transect are shown in Figures 4.1a and b. The ice edge was located between Stations 9 and 10 over water of about 80 m depth.

The vertical structure along section W-80A generally corresponded to the hydrographic domains described by Kinder and Schumacher, 1981a. Seaward of Station 7, the vertical temperature and salinity structure could be characterized as three layered; a nearly homogeneous surface layer and a mixed bottom layer which is occasionally warm and saline (Stations 3 and 4) due to

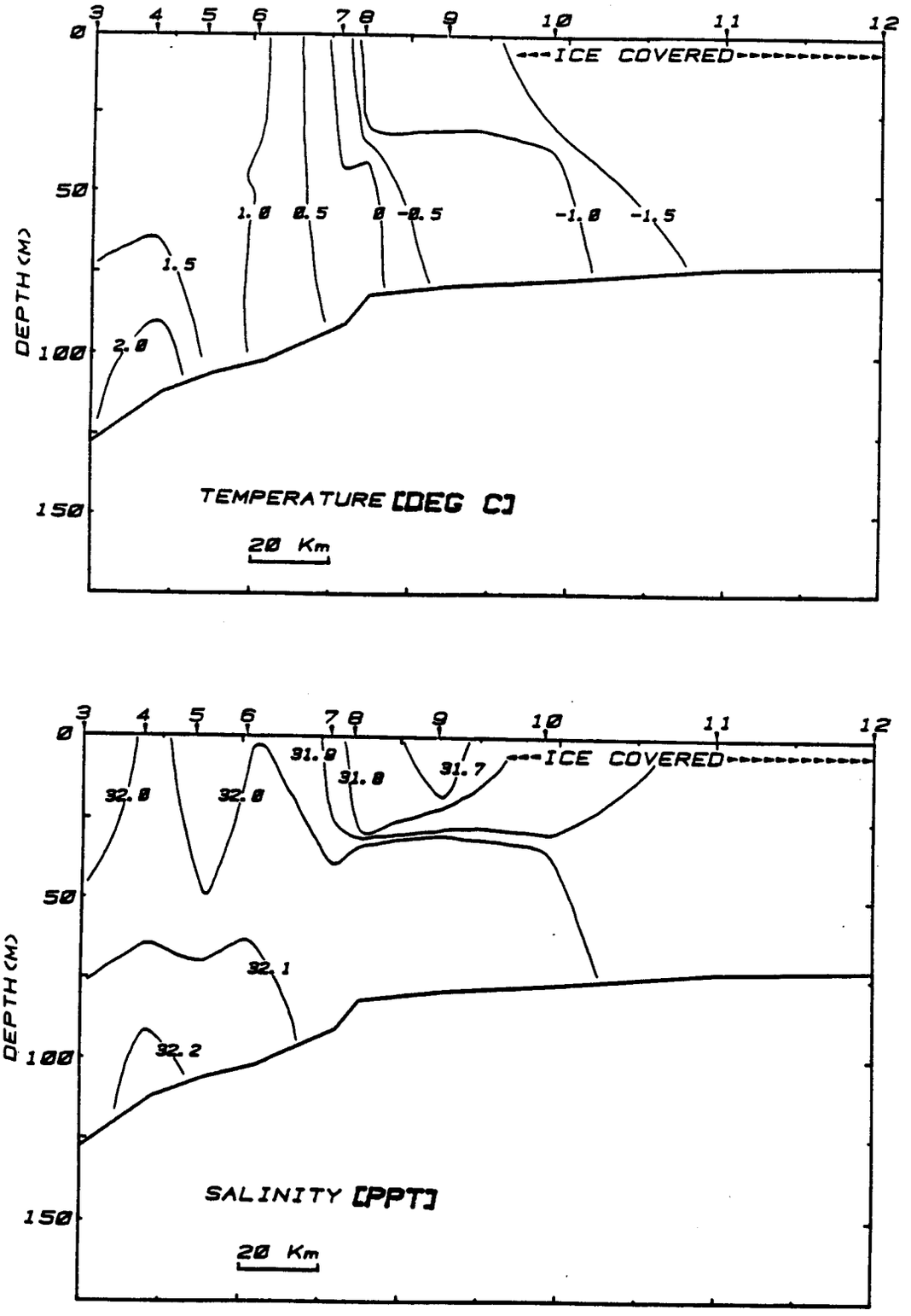

Figure 4.1. Vertical distribution of temperature (a) and salinity (b) across the southeastern Bering Sea shelf obtained during 29 Feb - 3 Mar 1980. W-80A.

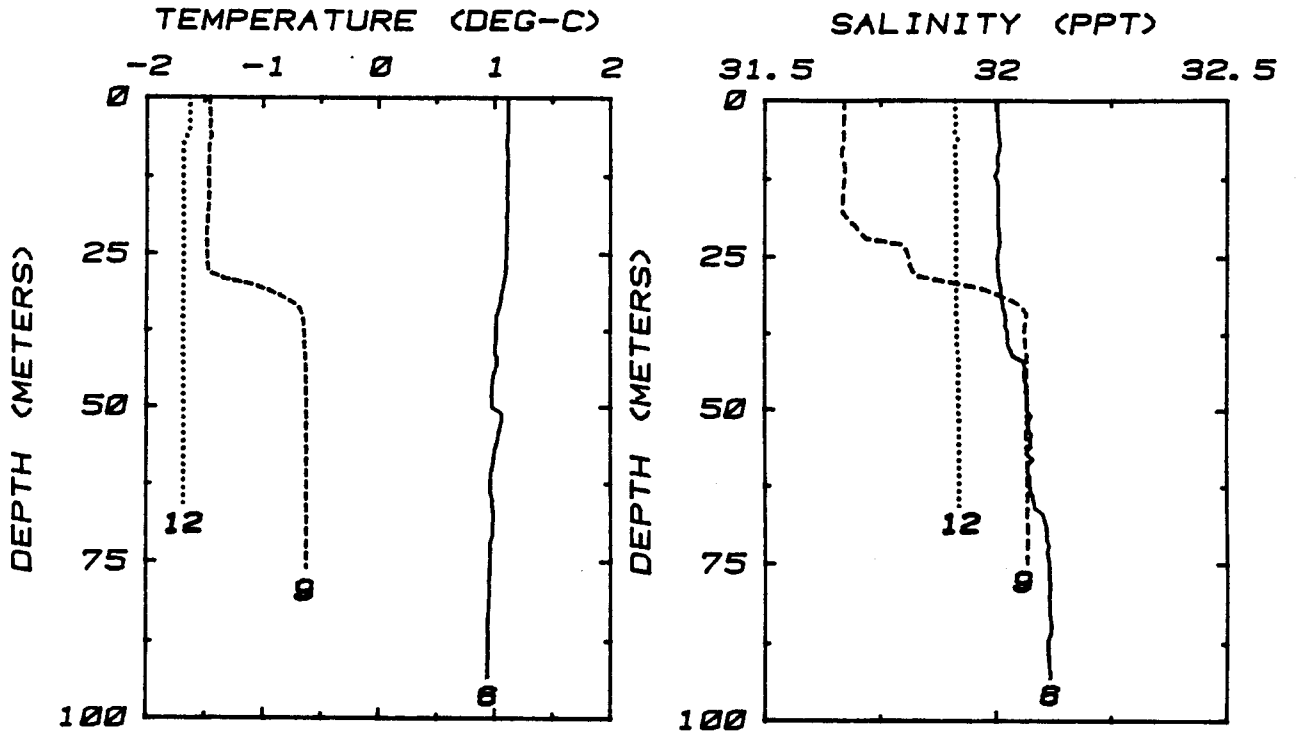

Figure 4.2. Vertical profiles of temperature and salinity at three representative stations along Section W-80A; Stations 6, 9 and 12.

an intrusion of Bering Sea water onto the shelf along the bottom, which were separated by middle layer which displayed small scale structure. This vertical structure (c.f. Station 6, Figure 4.2) is typical of the outer-shelf domain (Kinder and Schumacher, 1981a). From Station 7 northward through Station 10, the vertical structure was two-layered (Station 9, Figure 4.2) corresponding to the middle shelf hydrographic domain. The vertical temperature and salinity distributions at Station 11 and northward were essentially vertically homogeneous (Station 12, Figure 4.2) characteristic of the coastal domain.

The surface- and bottom-layer temperature and salinity are plotted versus distance along the section in Figure 4.3. The transition from the three-layer outer- to the two-layer middle-shelf domains occurred between Stations 6 and 7 within a few km of the 100 m contour. The transition from the middle-shelf to the vertically homogeneous coastal structure occurred between Stations 10 and 11, about 100 km north of the 100 m contour in water

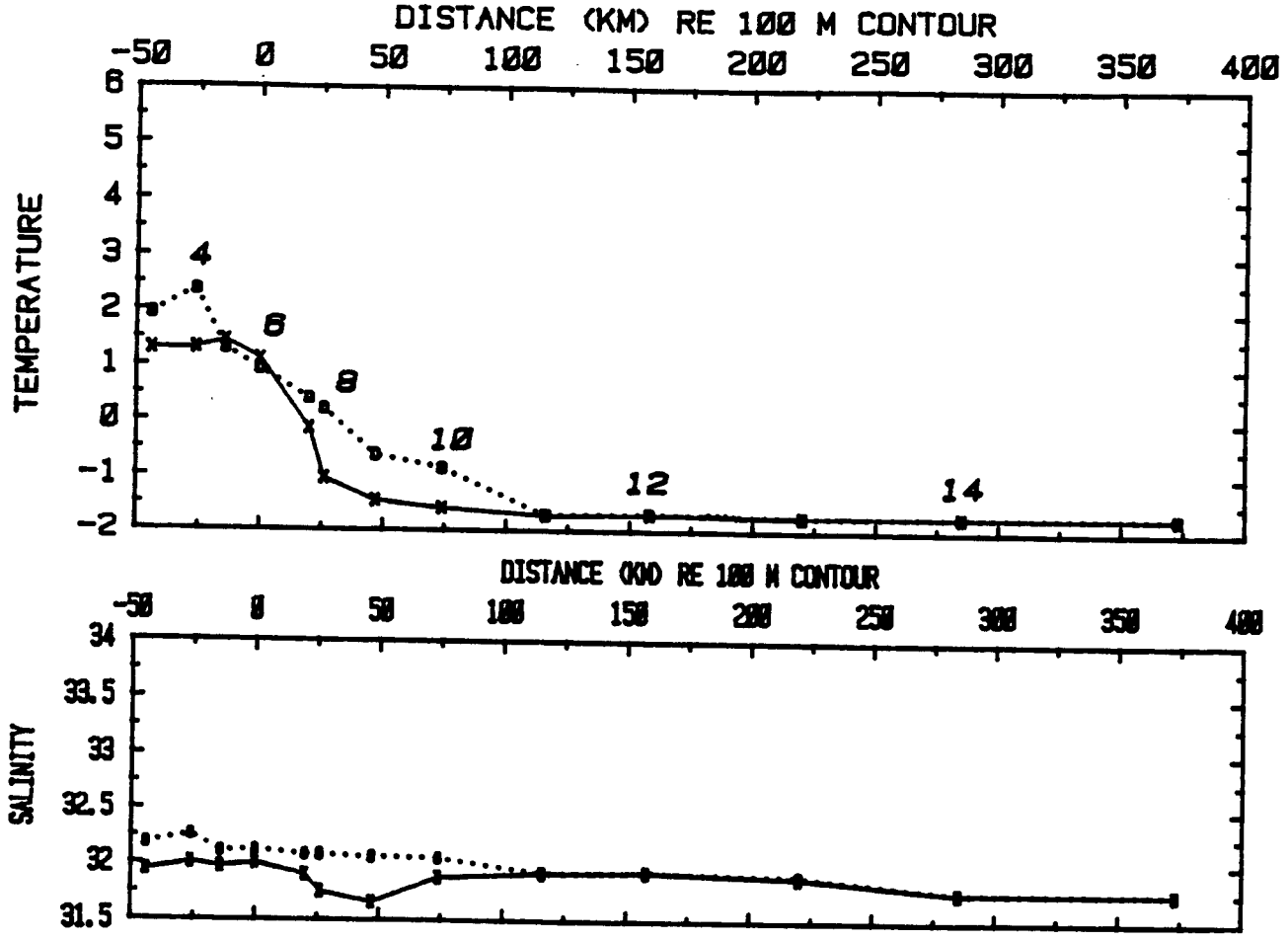

Figure 4.3. Section W-80A. Surface (x—x) and lower (0···0) layer temperature (^{o}C) and salinity (ppt) versus distance (km) along section W-80A relative to the 100 m isobath.

of 75 m depth. In the upper layer temperature decreased from +1.4^{o}C to <-1.5^{o}C over a 60 m distance between Stations 5 and 9 (a regression slope of -5.3 x 10^{-2}^{o}C/km) with a corresponding salinity decrease from 32.0 ppt to 31.7 ppt (a regression slope of -6 x 10^{-3} ppt/km). In the lower layer, property changes along the section were more gradual. Between Station 3 and 11, a distance of 160 km temperature decreased nearly linearly from +2.0^{o}C to <-1.5^{o}C (a regression slope of -2.6 x 10^{-2}^{o}C/km) while salinity decreased from 32.2 ppt to 31.9 ppt (a regression slope of -2 x 10^{-3} ppt/km).

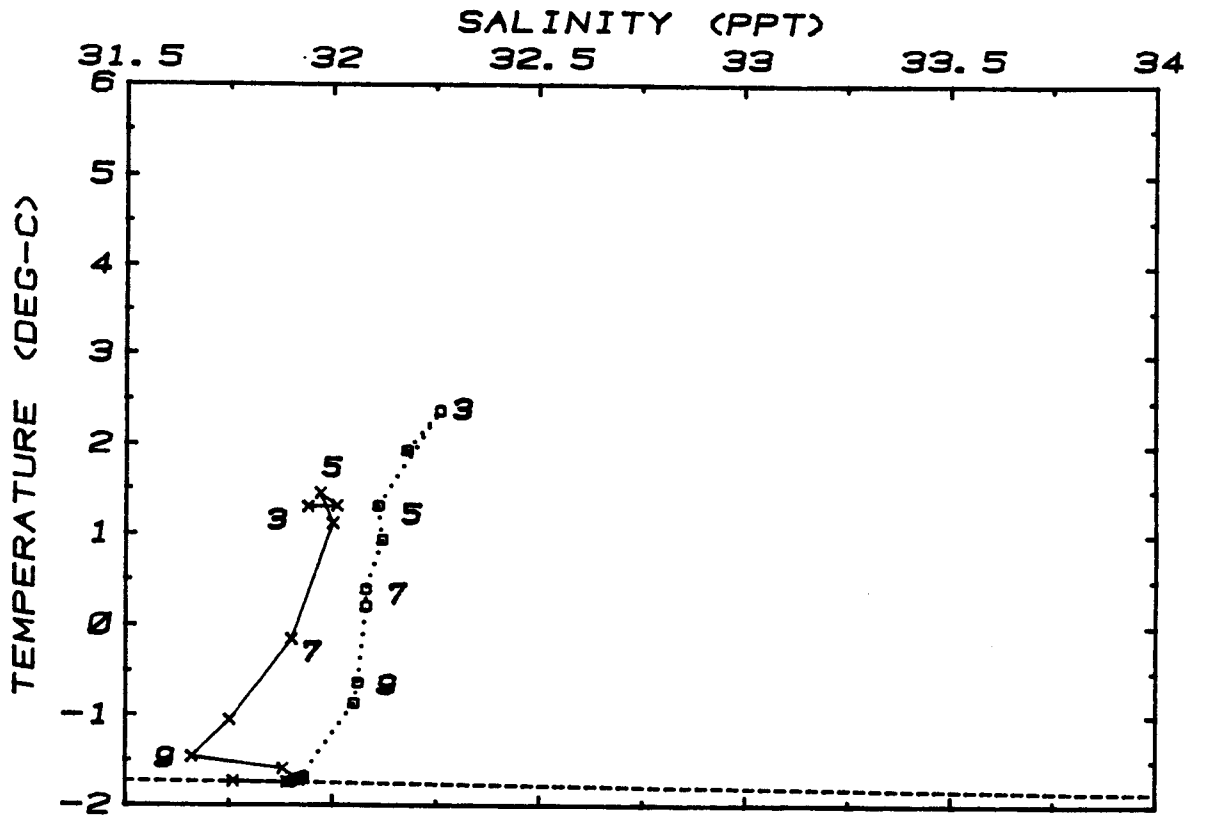

Figure 4.4. Temperature - salinity characteristics along Section W-80A plotted in the T-S plane proceeding from open water northward for upper (x—x) and lower (0···0) layer.

Figure 4.4 compares the temperature and salinity characteristics of the upper and lower layers along the section in the T-S plane. Progressing from the outer shelf through the middle shelf domain, the lower layer cools to the freezing point and freshens along a nearly linear T-S correlation (with a regression slope of $\frac{dT}{dS}$ = 13.6). The T-S correlation for the upper layer has an inflection point at Station 9. Seaward of this point (Stations 5-9) the T-S correlation has a slope of dT/dS = 8.5; while northward to Station 11 the slope is ∿-1.

Figure 4.5 shows the temperature of the upper and lower layers relative to the freezing point calculated from the observed salinity using the formula of Doherty and Kester, 1974. It is interesting to note that the upper layer temperature is above the freezing point well in under the ice edge, at least to Station 10 and perhaps north of this.

The degree of vertical stratification was estimated as

$$\Delta\sigma_t \simeq \beta\Delta S - \alpha\Delta T \ , \qquad (1)$$

where

$\Delta\sigma_t$ = Sigma-T difference between upper and lower layer,

ΔS = Salinity difference between upper and lower layer,

ΔT = Temperature difference between upper and lower layer,

$\beta = \frac{1}{\sigma t}\frac{\partial \sigma t}{\partial S} \simeq + 0.80 \text{ ppt}^{-1}$, and

$\alpha = \frac{-1}{\sigma t}\frac{\partial \sigma t}{\partial T} \simeq + 0.053^{o}C^{-1}$.

In the outer shelf domain vertical stratification (Figure 4.6) was about .10 to .20 σt units, and generally decreased toward the north. Within the middle shelf domain, stratification increased to $\sim$.3 σ_T units due to the freshening in the upper layer at Stations 7 through 10 (Figures 4.3 and 4.4). At Station 11 and northward vertical stratification was essentially zero.

4.3 Section W-80B

Section W-80B was occupied during 30 Mar - 2 Apr 80. This section crossed the central Bering Sea shelf from the 170 m contour northward to a water depth of about 70 m. The ice edge was located at Station 79 over water of about 150 m depth. Vertical distributions of temperature and salinity along this transect are shown in Figures 4.7a and b.

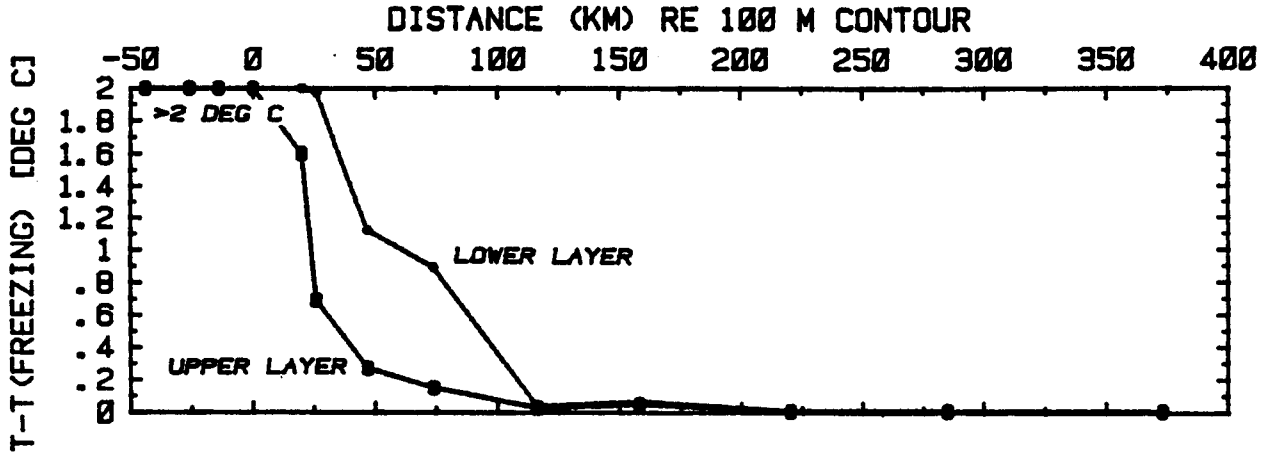

Figure 4.5. Upper (o—o) and lower (*···*) layer temperatures expressed as the departure from the freezing point (Doherty and Kester, 1974) versus distance (km) along Section W-80A relative to the 100 m isobath.

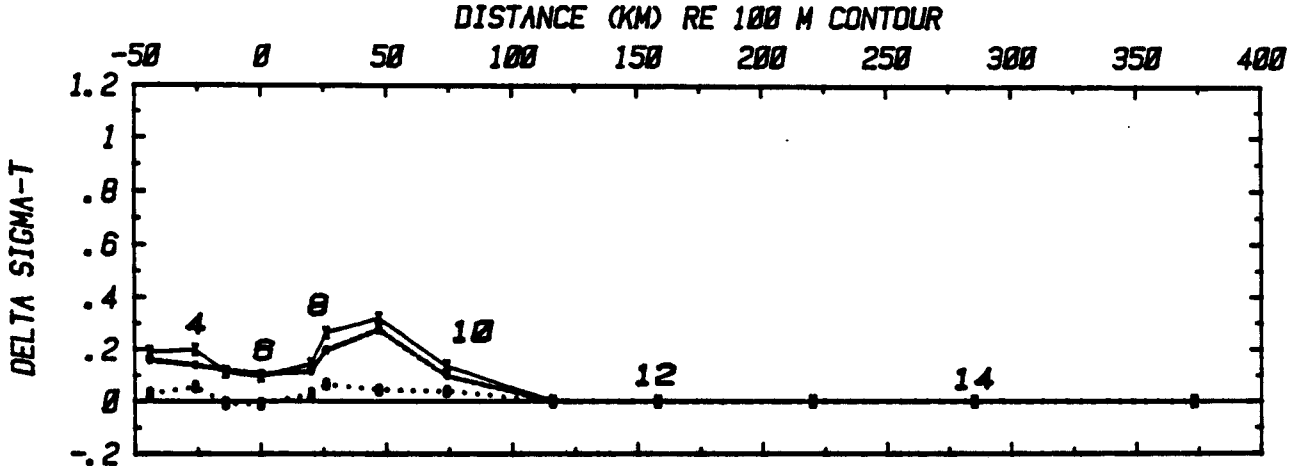

Figure 4.6. Section W-80A, vertical stratification versus distance (km) along the section relative to the 100 m isobath. The individual components, $\alpha\Delta T$ (0···0) and $\beta\Delta S$ (x—x) as well as the total stratification $\beta\Delta S - \alpha\Delta T$ are plotted in units of sigma-T.

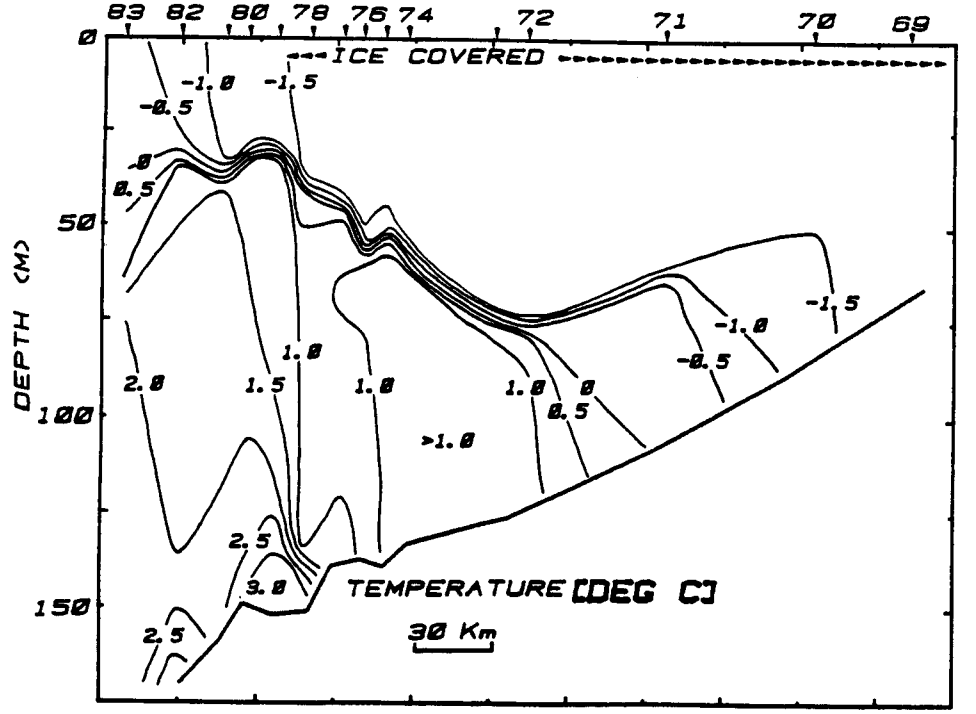

(a)

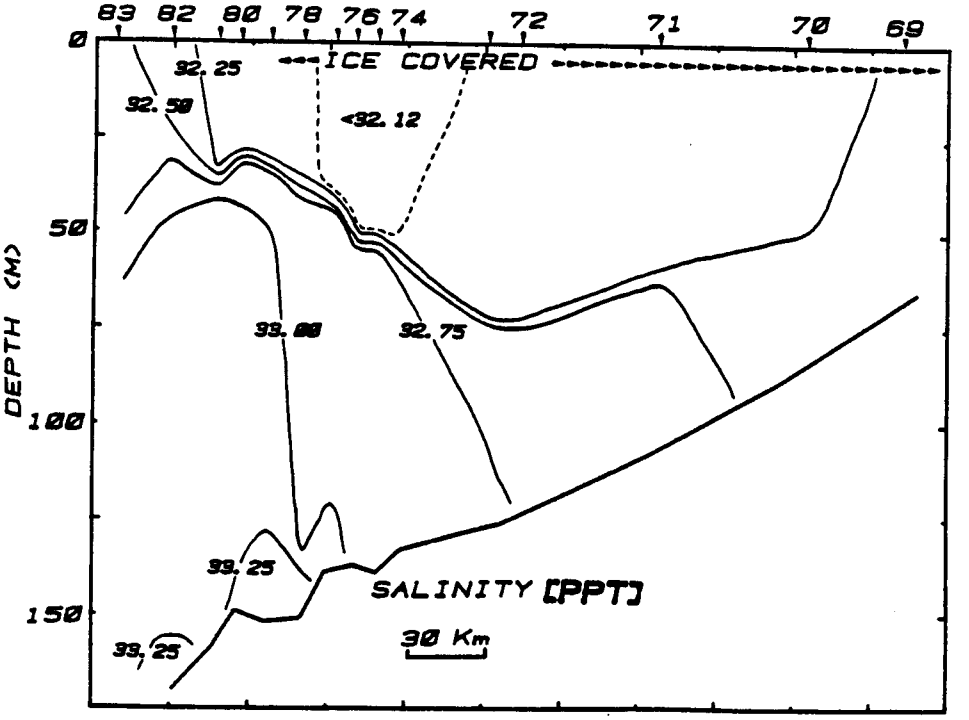

(b)

Figure 4.7. Vertical distribution of temperature (a) and salinity (b) across the central Bering Sea Shelf obtained during 30 Mar - 2 Apr 1980. W-80B.

The vertical structure along Section W-80B northward of the 125 m depth contour was analogous to that of Section W-80A described above. At Station 69 and northward in water depths of ∿70 m, the water column is nearly homogeneous in temperature with minimal stratification ($\Delta\sigma_t$ < ∿0.05) as shown by the profile at Station 68 (Figure 4.8). At Stations 70-73, bounded by the 75 and 125 m depth contours, the vertical structure was 2-layer with a 50 to 70 m thick homogeneous layer of cool fresh water overlying a warmer more saline layer which extended to the bottom (profile 72, Figure 4.8). Seaward of Station 73 over water depths greater than 125 m, the vertical structure became very complex but generally can be characterized as;

- A relatively cool, homogeneous surface layer which extended from Station 74 seaward about 60 km to Station 82. Progressing toward open water this layer thinned from 50 to 25 m, warmed from -1.6°C to -1.3°C, and increased in salinity from ∿32.1 to >32.2 ppt. Below the homogeneous surface layer was a pycnocline of 10-20 m thickness across which the majority of the vertical temperature and salinity change occurred.
- Extending from the base of the pycnocline, at a depth of 40-60 m, to depths of 80-120 m was a layer displaying temperature and salinity structure which consisted of small vertical scale (few m's) temperature minima/maxima with amplitudes of a few tenths of a degree centigrade.
- A nearly homogeneous layer with temperature of about 1°C extended from the base of the small-scale structure layer to the bottom at Stations 74-76 and to about 130 m at Stations 77 and 78.
- At the extreme south end of the section (at Stations 77-83) a warm (>3.0°C) saline (>33.5 ppt) layer of about 20 m thickness extended into onto the shelf along the bottom.

Figure 4.9 plots the surface and bottom layer temperature and salinity versus distance along the section. The transition from essentially homogeneous to the two-layer structure occurred near Station 69, about 50 km north of the 100 m curve in about 70 m of water. The transition from a simple two-layer

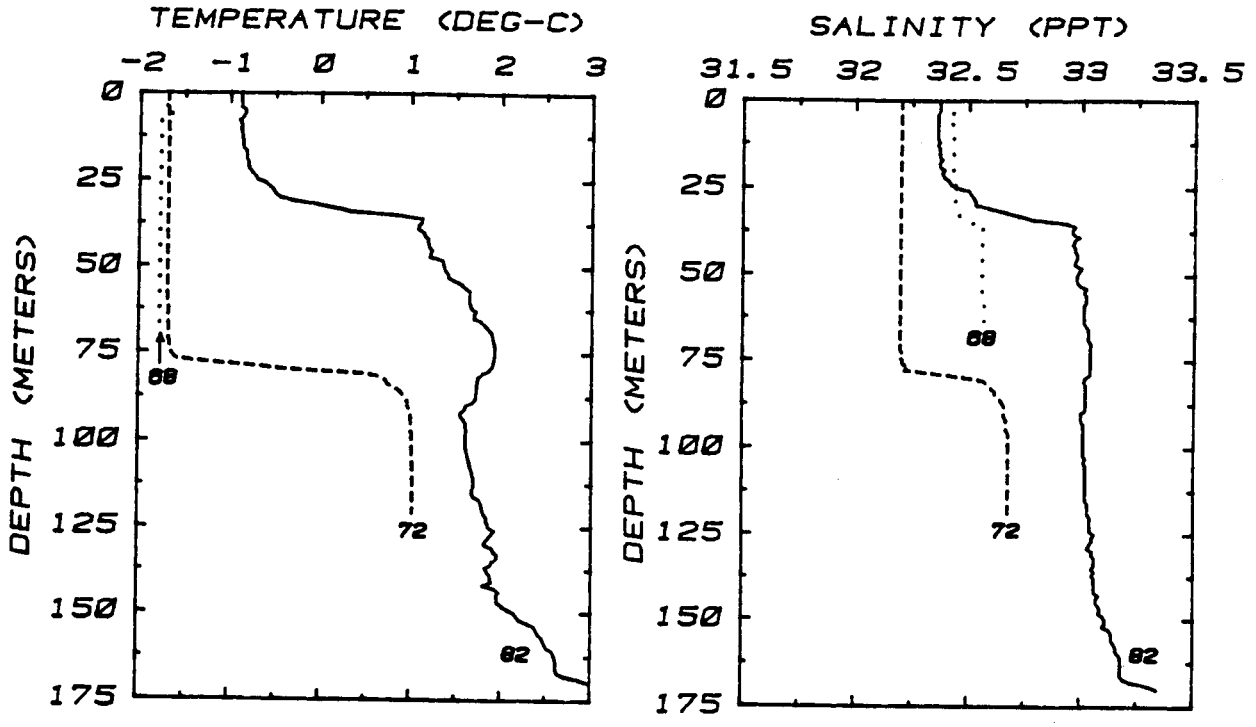

Figure 4.8. Vertical profiles of temperature and salinity at three representative stations along Section W-80B; Stations 82, 72 and 68.

system to the complex multilayer structure at the seaward end of the section took place near Station 74, 150 km seaward of the 100 m isobath. Upper layer temperature decreased from ∿-.4 to <-1.5°C between Stations 83 and 77 a distance of 74 km (a regression slope of -1.6×10^{-2}°C/km) with the corresponding salinity decreasing from 32.6 to 32.1 ppt (a slope of -6×10^{-3} ppt/km). The lower layer evidenced a greater total change in temperature and salinity along the section than the upper layer, however the changes took place over a greater distance (250 km from Station 83 to Station 70), thus the horizontal gradients, $\frac{dS}{dX} = -4 \times 10^{-3}$°C/km and $\frac{dT}{dX} = -1.9 \times 10^{-2}$°C/km were similar.

The T-S characteristics of the surface and bottom layer along section W-80B are shown in Figure 4.10. Between stations 83 and 77, the surface

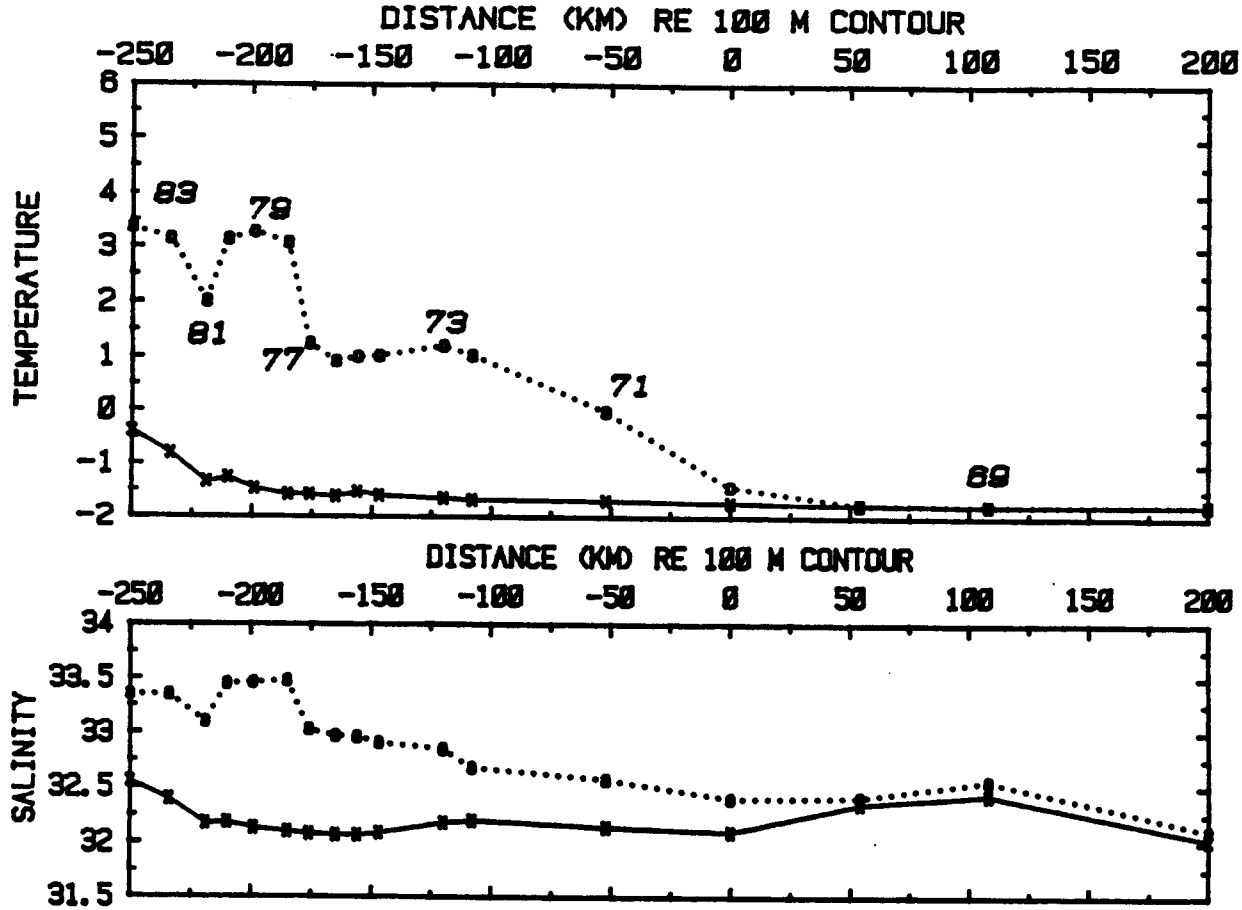

Figure 4.9. Surface (x—x) and lower (0···0) layer temperature (^{o}C) and salinity (ppt) versus distance (km) along Section W-80B relative to the 100 m isobath.

layer cools and freshens along a nearly linear T-S correlation with a regression slope dT/dS = +2.6^{o}C/ppt. The slope of the T-S correlation for the lower layer, Stations 70 through 83, is about 4.0^{o}C/ppt.

The surface and bottom layer temperature, relative to the freezing point (Doherty and Kester, 1974), are plotted in Figure 4.11. The surface layer remained greater than .1^{o}C above freezing for a distance of 100 km under the ice to Station 72. At Station 68 and northward, in the nearly vertically homogeneous region, both near-surface and near-bottom waters were essentially at the freezing point.

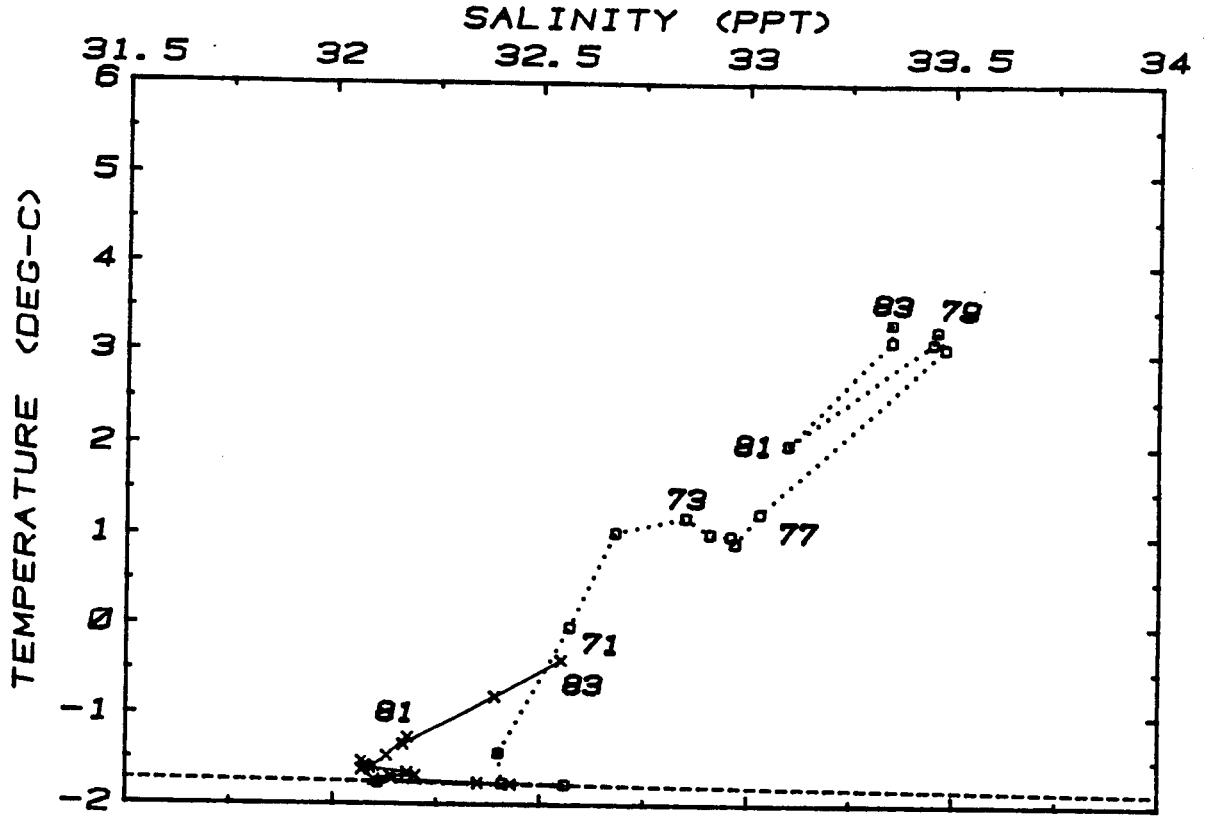

Figure 4.10. Temperature-salinity characteristics along Section W-80B plotted in the T-S plane proceeding from open water northward for the upper (x—x) and lower (0···0) layer.

Figure 4.12 plots the vertical density stratification along the section, computed by Equation (1), along with individual contributions to the density of the vertical temperature and salinity changes. Both temperature and salinity increased with depth at all stations along the section, thus the vertical salinity gradient, the major contributor, tended to stabilize the water column while the lesser effect of the vertical temperature gradient was destabilizing. The total density stratification was greatest ($\sim$0.8 σ_t units) near the ice edge due to relatively high bottom layer salinities and perhaps coincidentally a slightly freshened surface layer. Northward, through the two-layer region, density stratification decreased to a minimum 50 km north of the 100 m contour at Station 69.

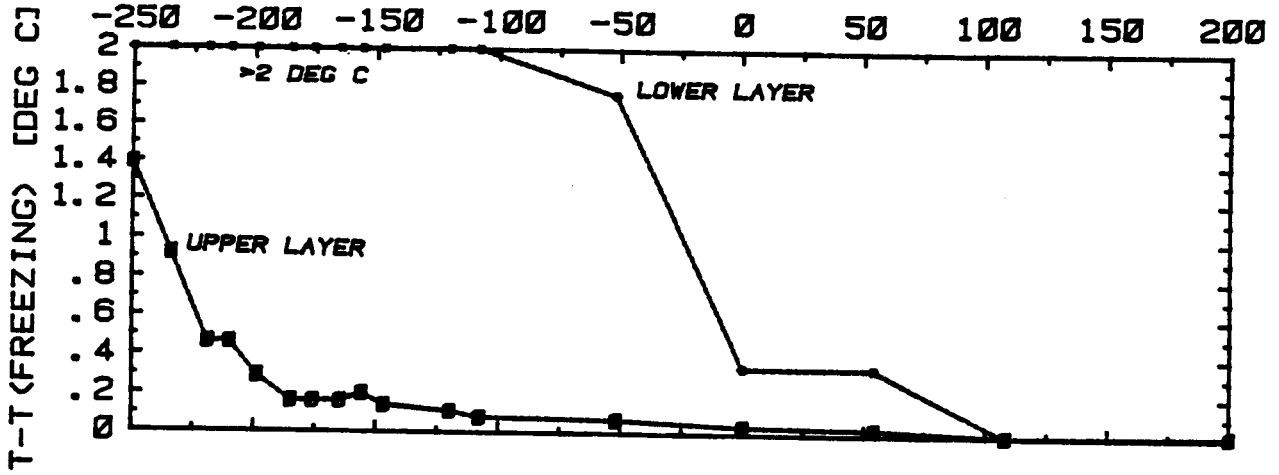

Figure 4.11. Upper (o—o) and lower (*...*) layer temperatures, expressed as the departure from the freezing point (Doherty and Kester, 1974) versus distance (km) along Section W-80B relative to the 100 m isobath.

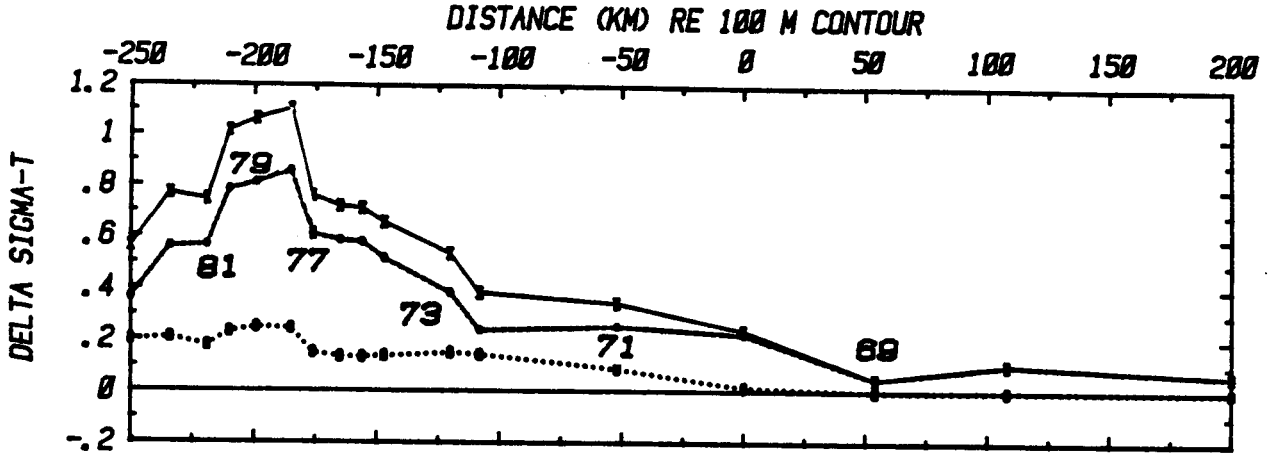

Figure 4.12. Vertical stratification versus distance (km) along Section W-80B relative to the 100 m isobath. The individual components $\alpha\Delta T$ (0···0) and $\beta\Delta S$ (x—x) as well as the total stratification, $\beta\Delta S - \alpha\Delta T$ are plotted in units of Sigma-T.

5. COMPARISONS WITH FALL 1980, WINTER 1981 CTD SECTIONS

5.1 Fall 1980, Winter 1981 CTD Sections

This section briefly describes the structure and T-S characteristics of the fall and winter data collected in 1980 and 1981 (Muench, 1981) in a format similiar to Section 4. These results will be used in later sections to describe the regional wintertime structure and compare fall to winter conditions.

- F-80A. The F-80A section crossed the central shelf southwest of St. Matthew Island (Figure 2.1). The vertical distribution of temperature, salinity and density (sigma-t) for this section has been described by Muench (1981). The water column was essentially two-layer with an interface at 50 to 60 m depth. Upper and lower layer temperature (^{o}C) and salinity (ppt) versus distance along the section are shown in Figure 5.1. Upper and lower layer temperature decrease from $4^{o}C$ near the shelf break northward to a minimum near Stations 7 and 8. Salinity decreases monotonically toward the north. From Station 1, north to Station 8, the horizontal gradients of temperature and salinity in the lower layer ($-1.3 \times 10^{-2}{}^{o}C/km$ and -5×10^{-3} ppt/km) were slightly greater than corresponding upper layer gradients ($-1.0 \times 10^{-2}{}^{o}C/km$ and -3×10^{-3} ppt/km). Stratification decreased from 0.4 sigma-t units at Station 1 to essentially 0 at Station 9 and northward (Figure 5.2) with both temperature (decreasing with depth) and salinity (increasing with depth) acting to stabilize the water column.

  The temperature-salinity characteristics of the upper and lower layers proceeding from deepwater northward are shown in Figure 5.3. Seaward of Stations 7 and 8, the T-S slope was positive ($\frac{dT}{dS} = +2.8^{o}C/ppt$ for upper and $+2.6^{o}C/ppt$ for lower layer). North of Station 8 the slope was negative, $\frac{dT}{dS} = -1.2^{o}C/ppt$.

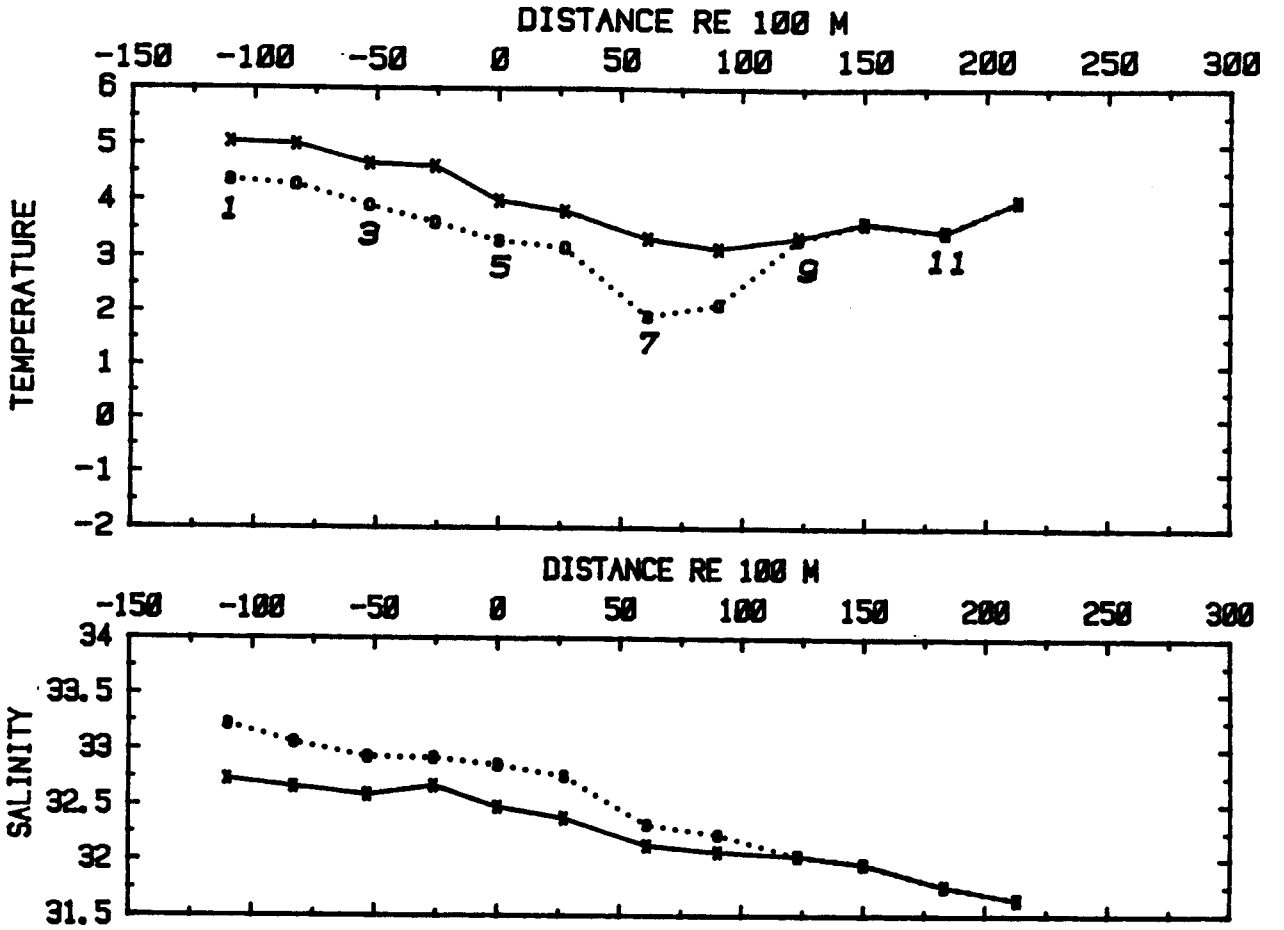

Figure 5.1. F-80A. Surface (x—x) and lower (0···0) layer temperature (°C) and salinity (ppt) versus distance (km) relative to the 100 m isobath along the Section.

- F-80B. This section lies about 300 km northwest of the F-80A section described above (Figure 2.1). Figures 5.4 through 5.6 show the upper and lower layer temperature (°C) and salinity (ppt) versus distance (km), the vertical stratification, and T-S characteristics along the section. Though the temperatures along this section tended to be lower than along F-80A, the horizontal gradients and the shape of the T-S correlations were similar. Both upper and lower layer temperatures decreased (-7×10^{-3}°C/km and -9×10^{-3}°C/km respectively) from near the shelf edge northward to Station 20. From Station 20 northward temperature increased in both the upper ($+5 \times 10^{-3}$°C/km) and lower ($+9 \times 10^{-3}$°C/km) layers. Salinity decreased monotonically (-3×10^{-3}

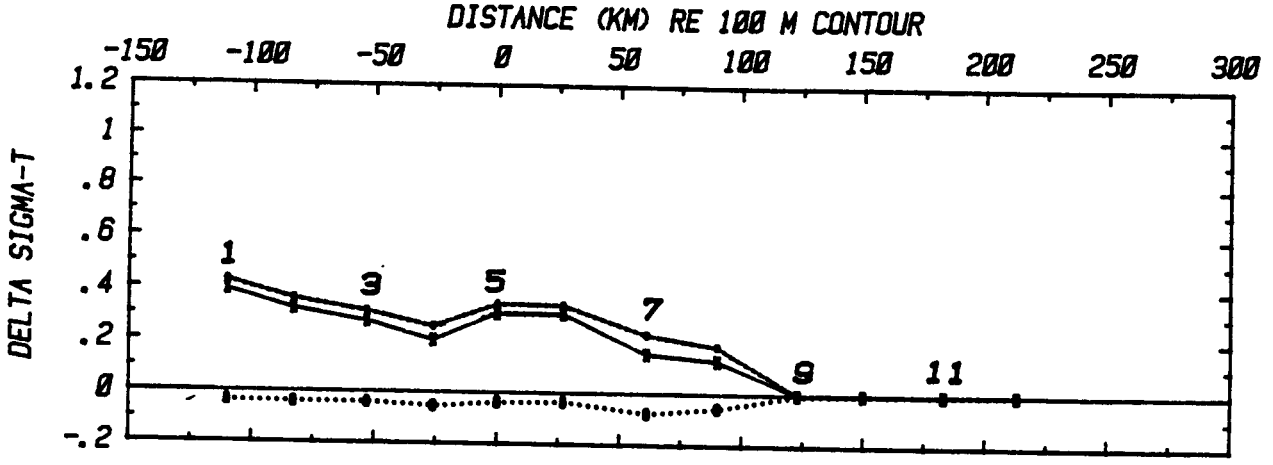

Figure 5.2. F-80A. Vertical stratification versus distance (km) relative to the 100 m isobath. The individual components, $\alpha\Delta T$ (0···0) and $\beta\Delta S$ (x–x) and the total stratification, $\beta\Delta S$-$\alpha\Delta T$ are plotted in units of Sigma-T.

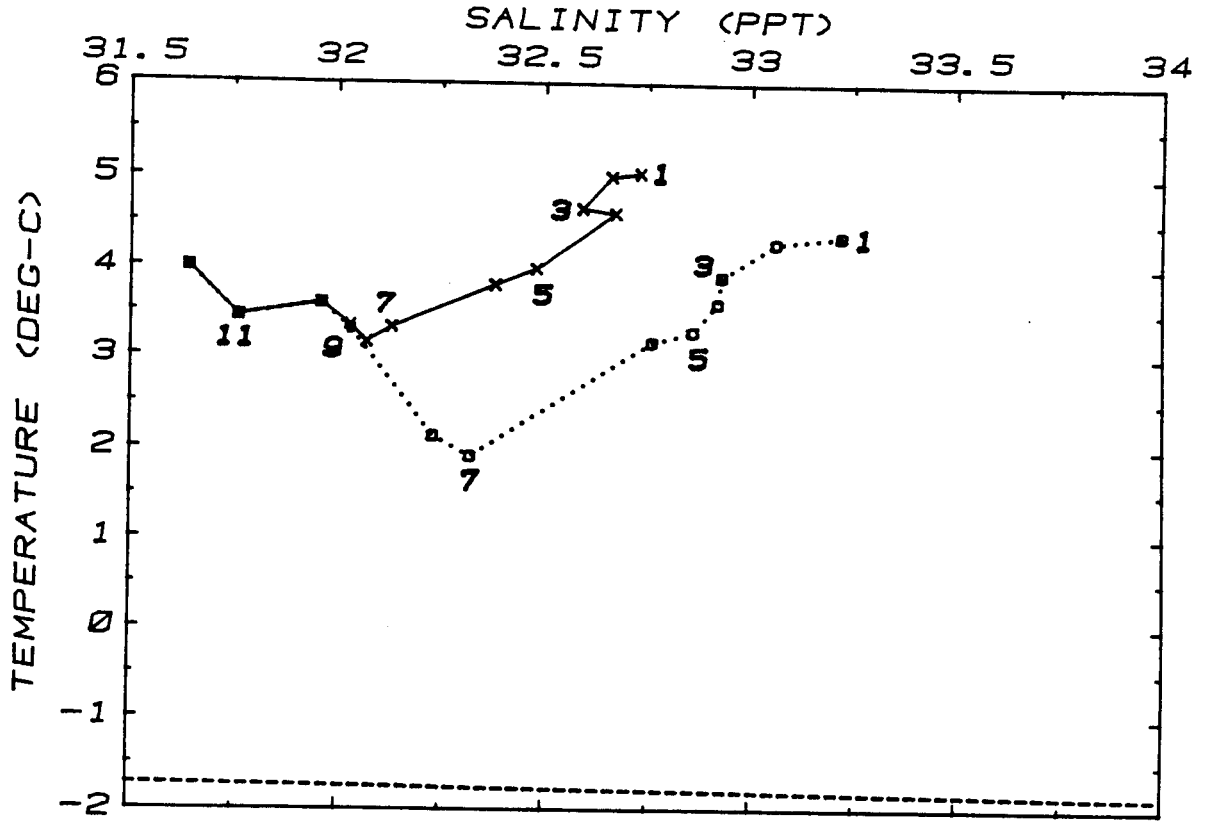

Figure 5.3. F-80A. Temperature-salinity characteristics proceeding from deepwater northward for upper (x–x) and lower (0···0) layers.

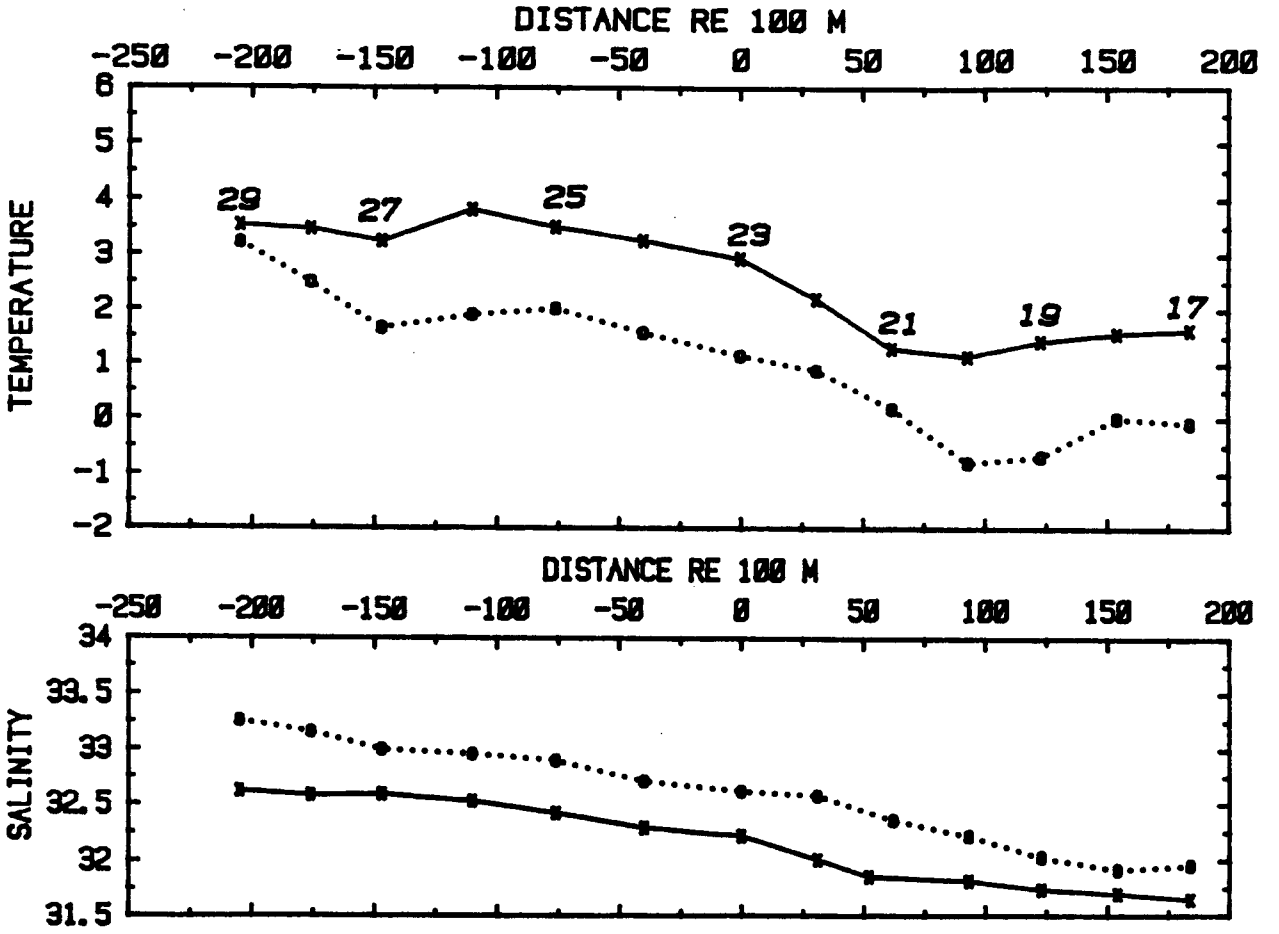

Figure 5.4. F-80B. Surface (x—x) and lower (0···0) layer temperature (°C) and salinity (ppt) versus distance (km) relative to the 100 m isobath along the Section.

ppt/km in both layers) northward along the section. The slopes of the T-S correlations were similar to those along Section F-80A; dT/dS = +2.7°C/ppt (upper layer) and +2.9°C/ppt (lower layer) south of the temperature minimum (Station 20) and dT/dS = -3.0°C/ppt north of the temperature minimum.

Vertical stratification (Figure 5.5) was two-layer throughout the section. Stratification decreased from 0.5 sigma-t units near the shelf edge to about 0.3 sigma-t units at the north end of the section. Both the vertical temperature and salinity gradients were stabilizing.

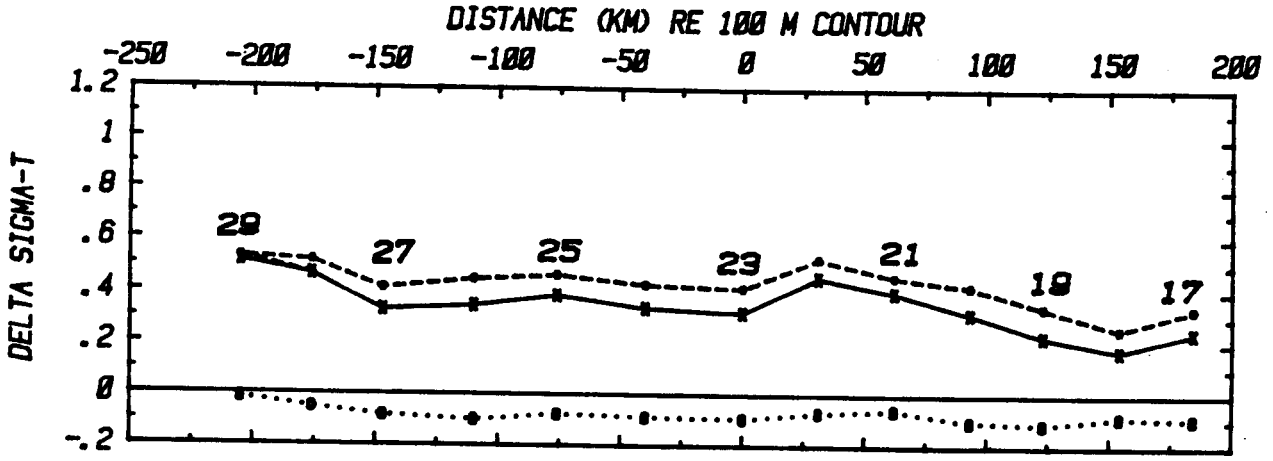

Figure 5.5. F-80B. Vertical stratification versus distance (km) relative to the 100 m isobath. The individual components, $\alpha\Delta T$ (0···0) and $\beta\Delta S$ (x–x) and the total stratification, $\beta\Delta S$-$\alpha\Delta T$ are plotted in units of Sigma-T.

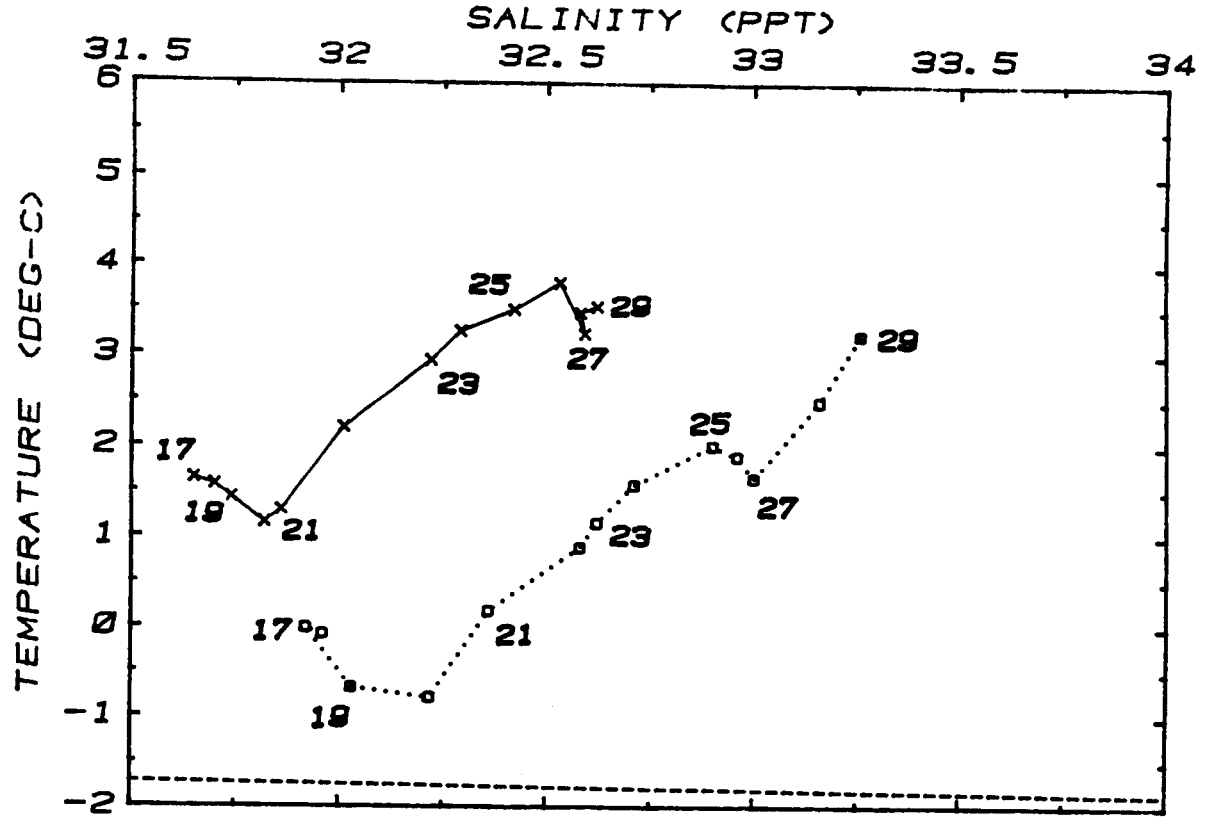

Figure 5.6. F-80B. Temperature-salinity characteristics proceeding from deepwater northward for upper (x–x) and lower (0···0) layers.

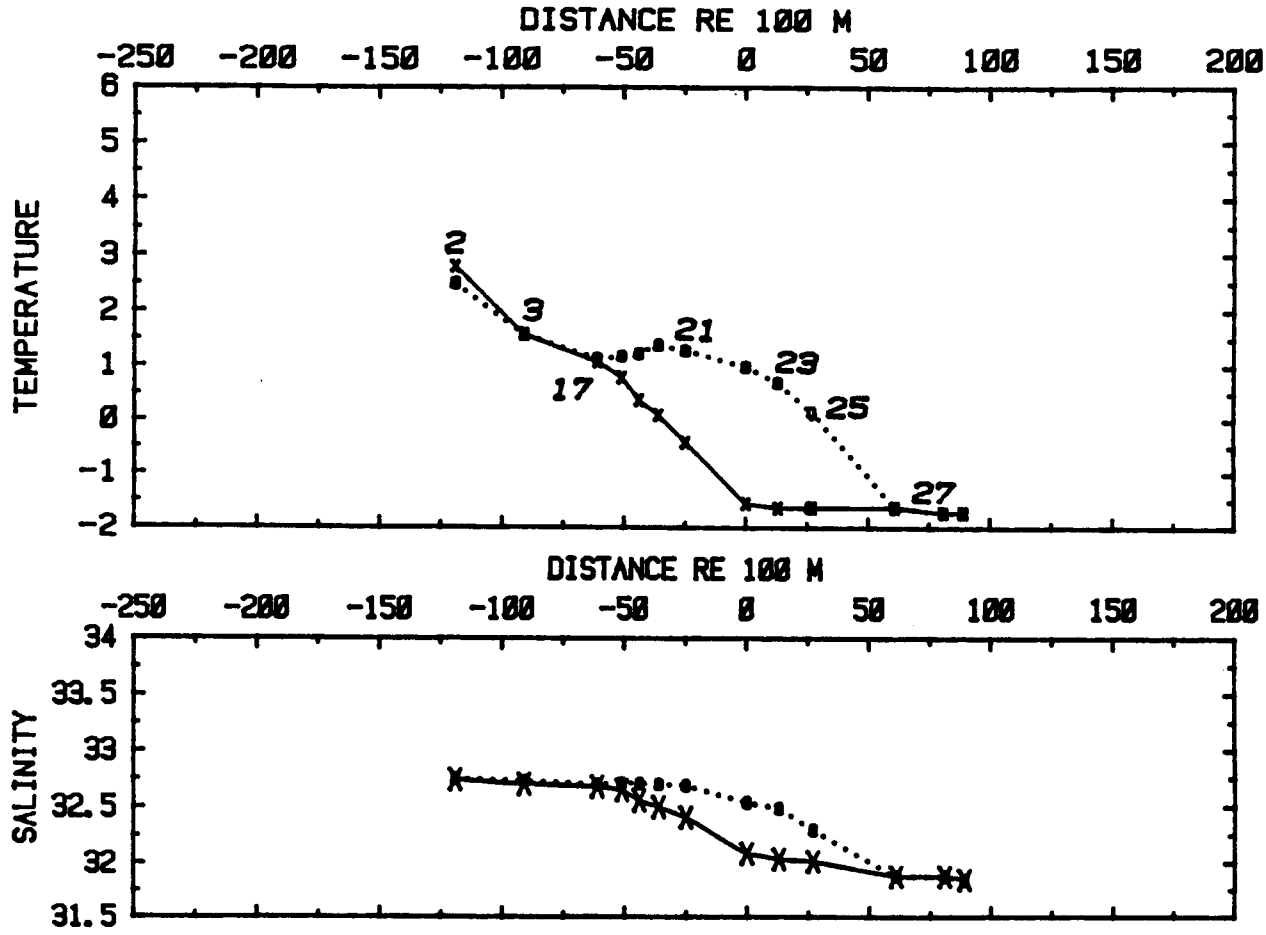

Figure 5.7. W-81. Surface (x—x) and lower (0···0) layer temperature (^{o}C) and salinity (ppt) versus distance (km) relative to the 100 m isobath along the Section.

- W-81. This section essentially repeats the F-80A section (Figure 2.1). Proceeding north from Station 2 toward the ice edge (Figure 5.7) upper layer temperature decreased (-4.4 x 10^{-2}^{o}C/km) to near the freezing point as salinity also decreased (-1 x 10^{-2} ppt/km). Lower layer temperature and salinity decreased to the north but over a greater horizontal distance (1.0 x 10^{-2}^{o}C/km and 4 x 10^{-3} ppt/km respectively). Vertical stratification was essentially zero at the seaward and northward end of the section (Figure 5.8) with a maximum of 0.2 sigma-t units occurring near the 100 m isobath. The along-section T-S correlations (Figure 5.9) are positive (dT/dS = +4.4^{o}C/ppt (upper layer) and +2.6^{o}C/ppt (lower layer).

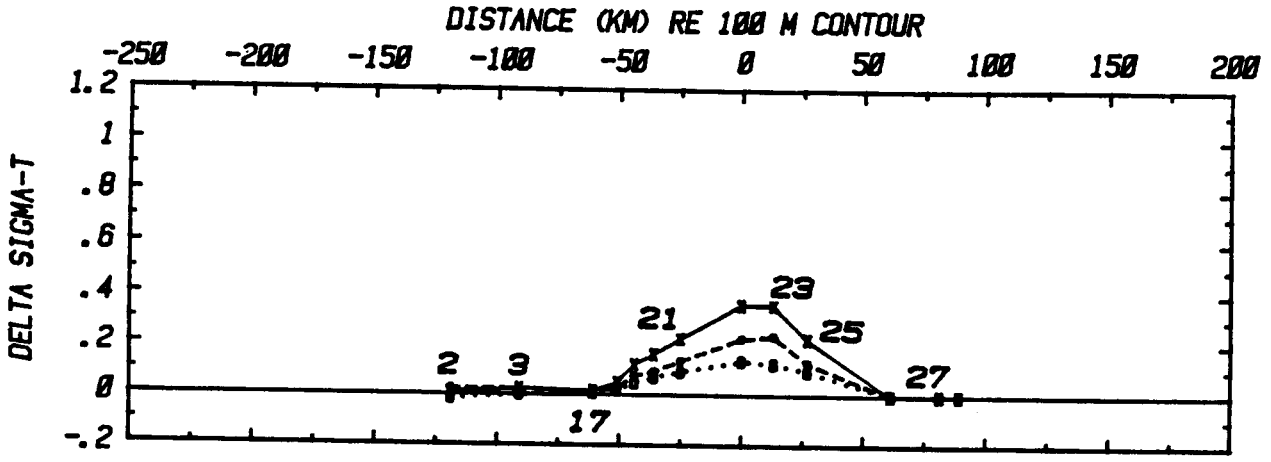

Figure 5.8. W-81. Vertical stratification versus distance (km) relative to the 100 m isobath. The individual components, $\alpha\Delta T$ (0···0) and $\beta\Delta S$ (x–x) and the total stratification, $\beta\Delta S$-$\alpha\Delta T$ are plotted in units of Sigma-T.

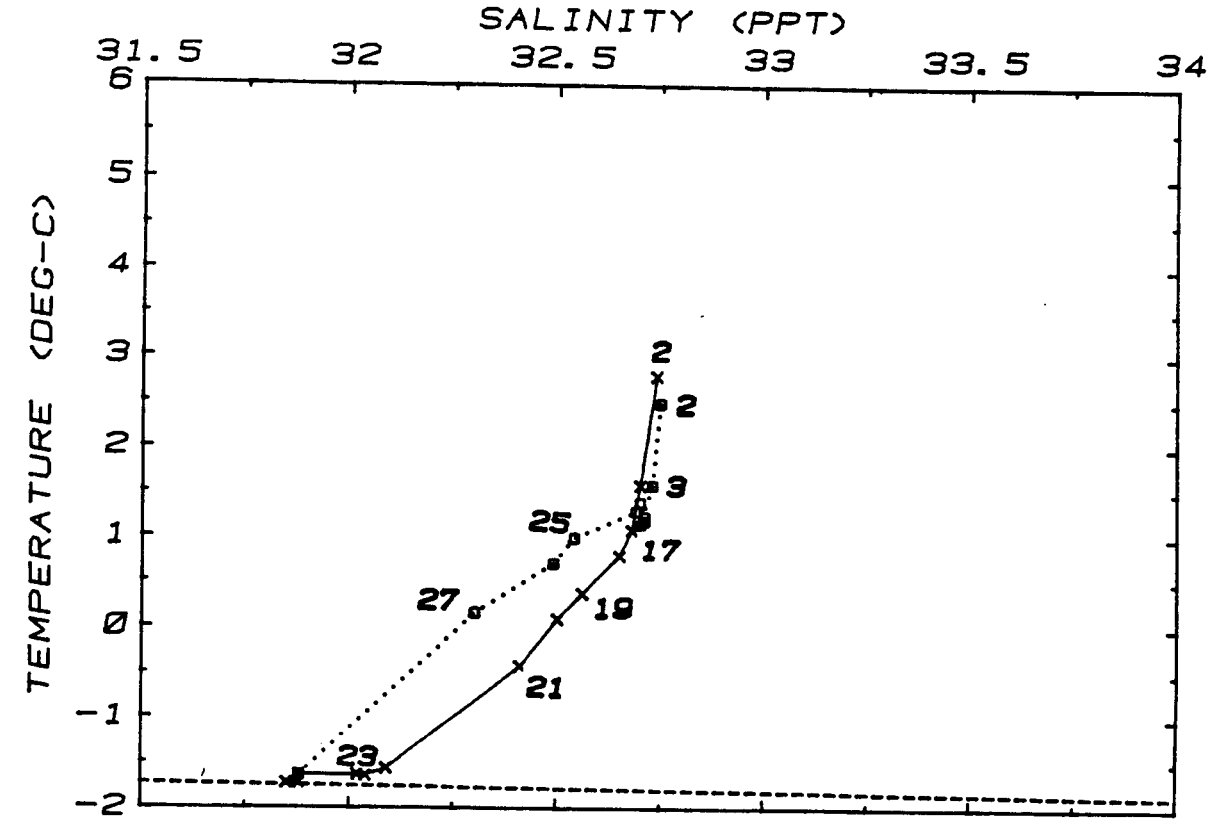

Figure 5.9. W-81. Temperature-salinity characteristics proceeding from deepwater northward for upper (x–x) and lower (0···0) layers.

5.2 Regional Characteristics of the Wintertime Hydrographic Structure

Three of the CTD sections discussed above, W-80A, W-81 and W-80B, crossed the Bering Sea MIZ at about 250 km intervals from the southeastern shelf (W-80A) to the central shelf (W-80B). Noting that the middle section (W-81) is from a different year, these sections will be discussed as a group to provide a regional description of the temperature, salinity and density structure of the MIZ.

Figure 5.10 shows the location of the three sections and plots the approximate position of the ice edge based on the Navy-NOAA Joint Ice Center analyses for 26 Feb and 4 Mar 1980, coincident with Section W-80A, 25 Mar and 1 Apr 1980, coincident with Section W-80B, and 3 and 10 Mar 1981 corresponding to Section W-81. Over the southeastern shelf, east of 172°W, the ice edge during these periods was positioned over rather shallow water, 50-100 m, and showed a significant amount of variability (∿200 km) in the north-south direction. West of 172°W, over the central and eastern shelf, the ice edge positions for these periods tended to be nearly coincident. West of 172°W the ice edge occurred over deeper water and appeared to be nearly aligned with the 200 m isobath.

Wintertime hydrographic structure in the MIZ based on the 1980-81 data generally could be characterized as two-layer (Figures 4.1a and b, 4.7a and b and Muench, 1981). The upper layer was on the order of 50 m thick and the lower layer was usually 25-75 m in vertical extent. The temperature and salinity of the upper and lower layers along the shelf is plotted in Figures 5.11a and b and 5.12a and b. The heavy line segments indicate where the contoured values occur along the sections. Dashed lines are used to connect equal values along the shelf but should not be construed as contours because of the wide spacing (∿250 km) of the CTD lines. The temperature of the upper layer changed from cool (<-1.5°C) to relatively warm (>0°C) over a distance of about 50 km. This relatively sharp horizontal temperature gradient was coincident with a salinity change (Figure 5.11b) of 0.25 ppt or greater over the same distance. This temperature and salinity front occurred roughly coincident with the ice edge (Figure 5.10) and thus, proceeding westward, tended to be positioned over progressively deeper water. North of the -1.7°C isoline in Figure 5.11a,

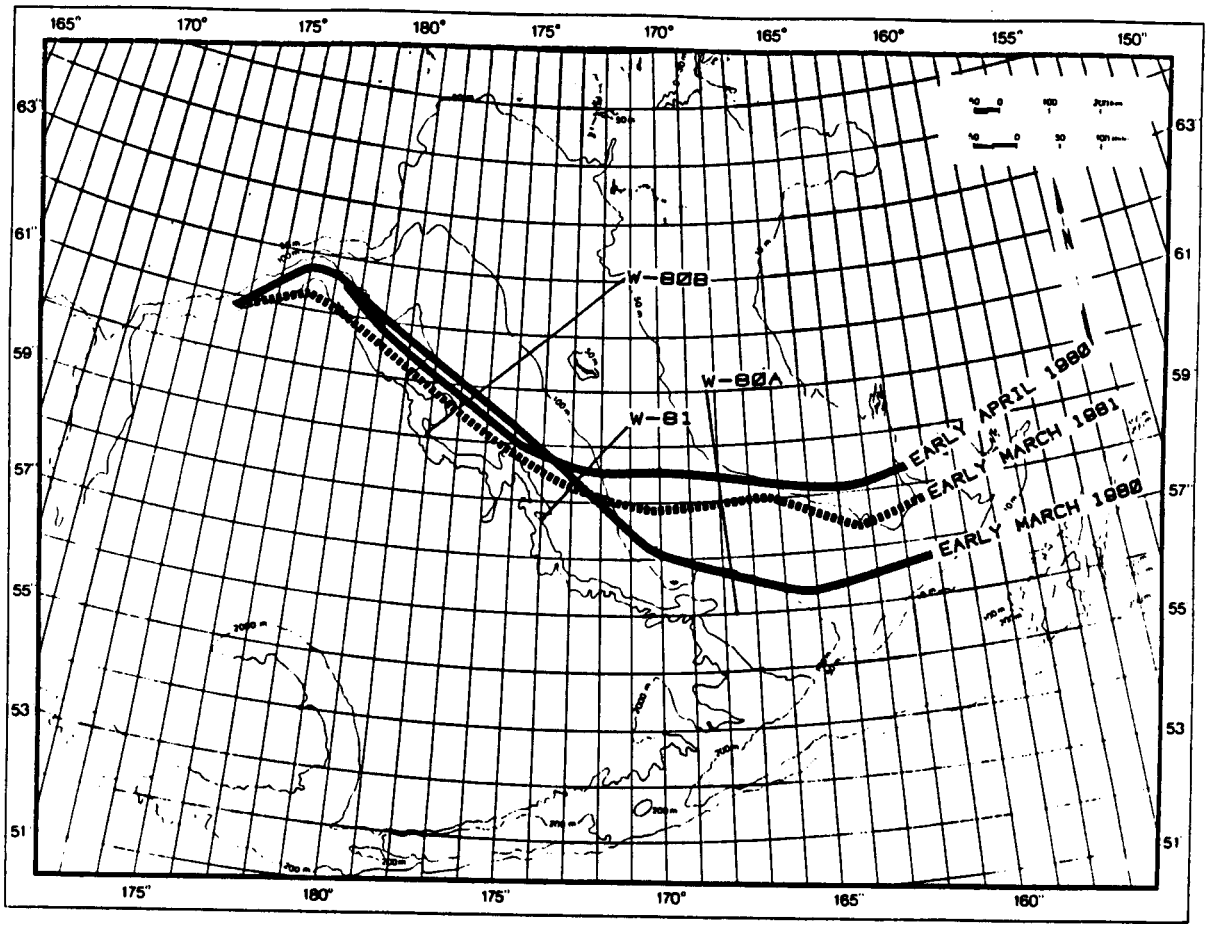

Figure 5.10. Approximate location of the ice edge based on NAVY-NOAA Joint Ice Center analyses for (1) Early March 1980 (26 Feb and 4 Mar; Section W-80A), (2) Early April 1980 (25 Mar and 1 Apr; Section W-80B), and (3) Early March 1981 (3 Mar and 10 Mar; Section W-81).

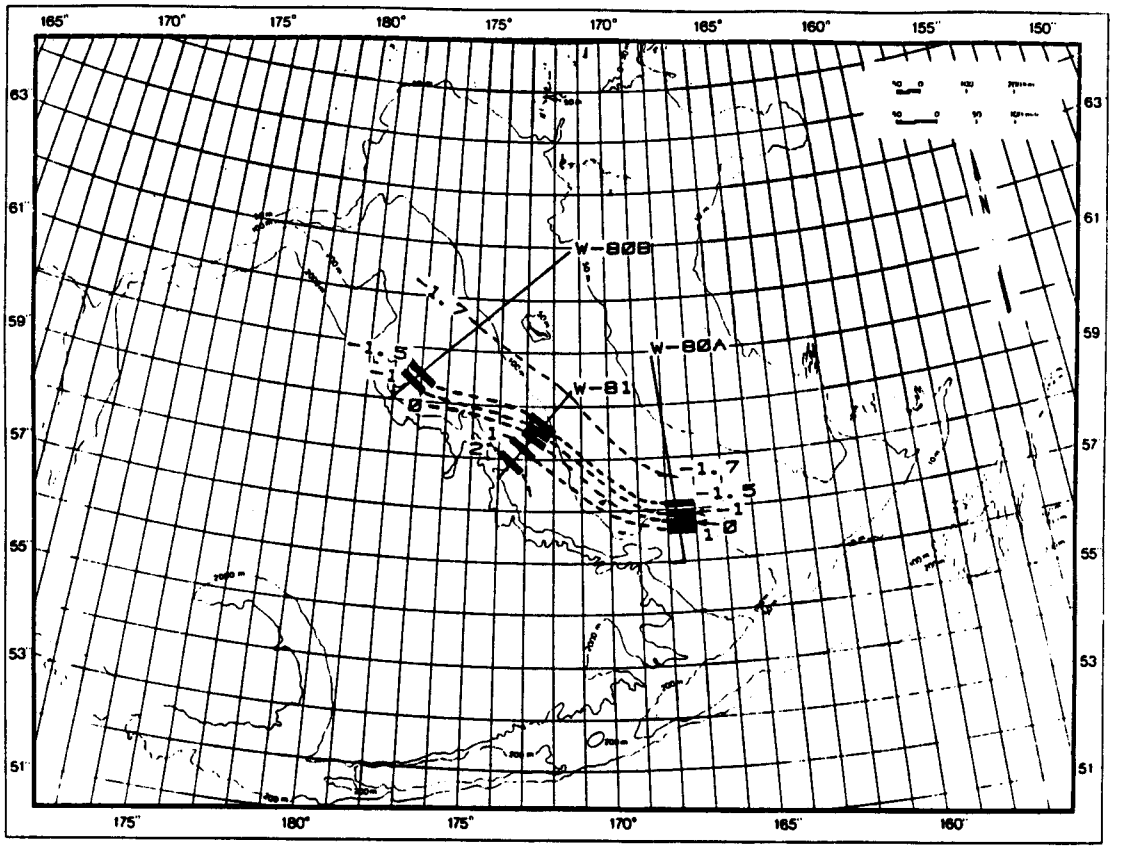

Figure 5.11a. Upper layer temperature (°C)

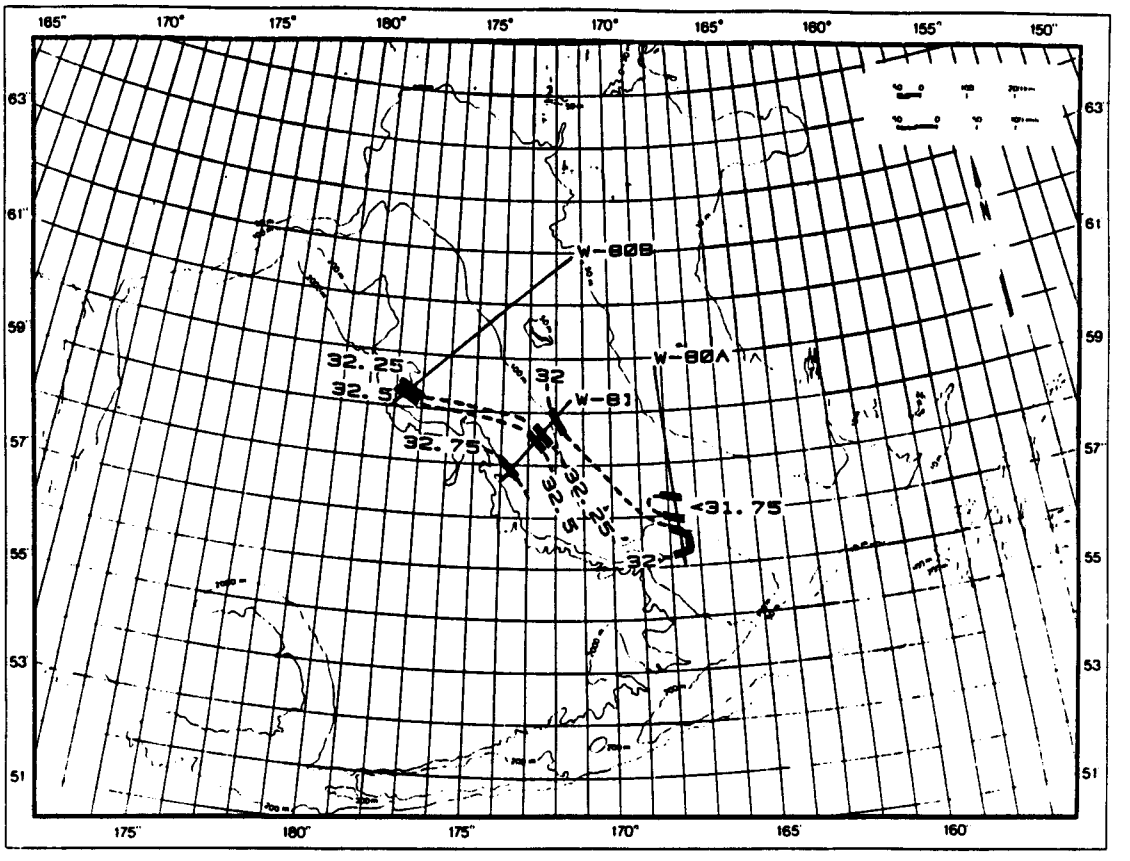

Figure 5.11b. Upper layer salinity (°/oo)

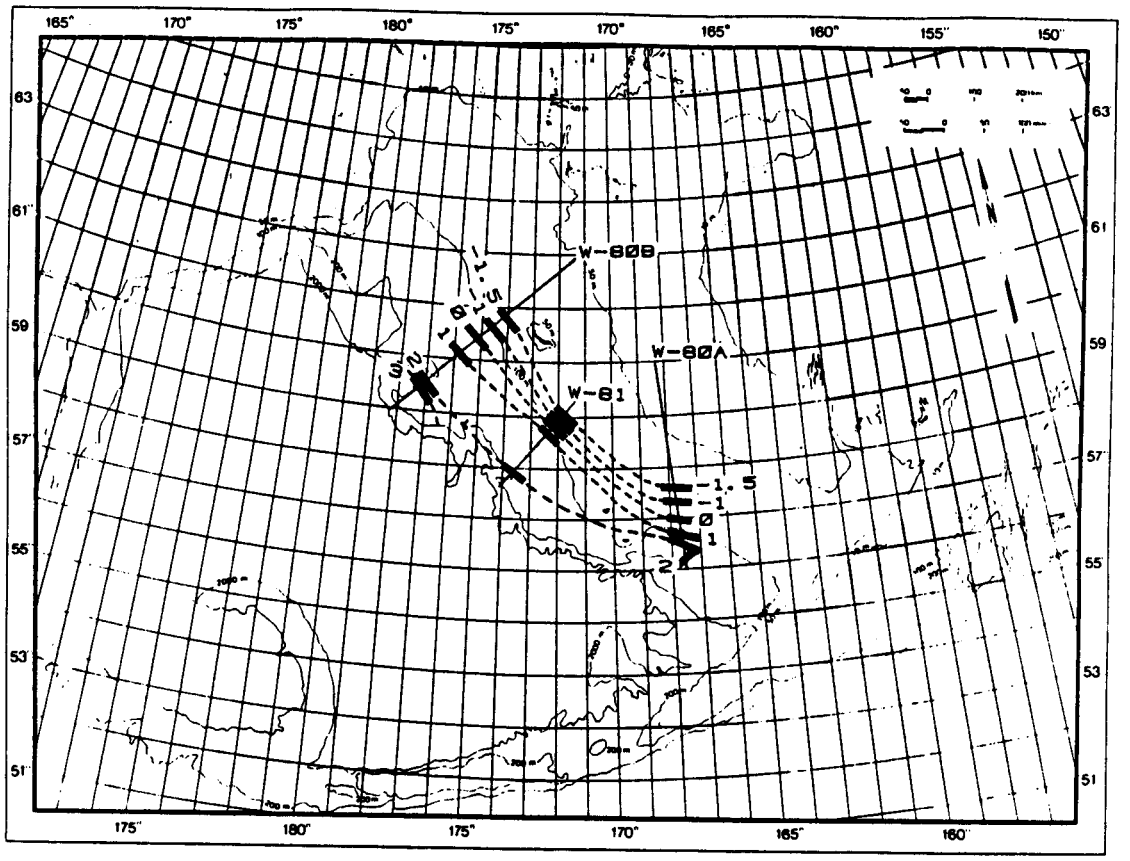

Figure 5.12a. Lower layer temperature (°C)

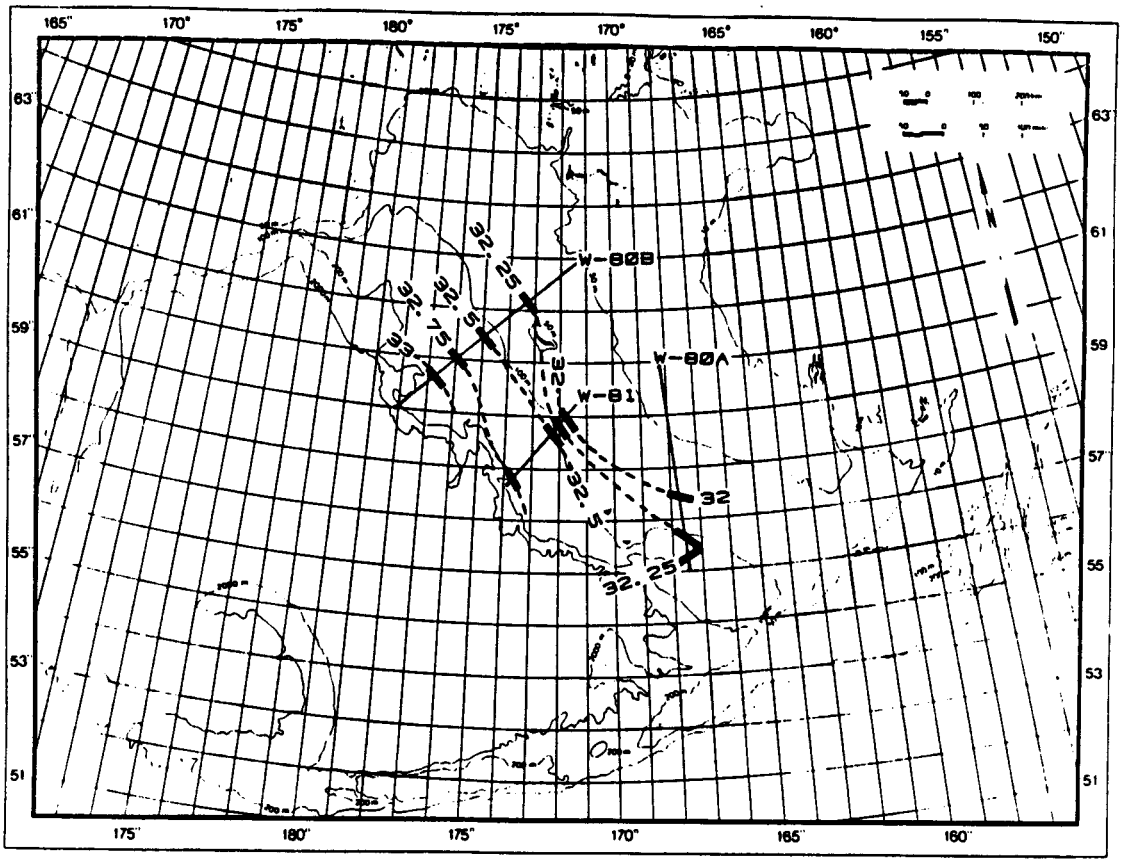

Figure 5.12b. Lower layer salinity (°/oo)

surface layer temperatures were essentially at the freezing point for the associated salinity. South of the -1.7°C isoline to the ice edge, a distance of 50 to 200 km, upper layer temperatures were significantly elevated (>0.10°C) above their freezing point.

Throughout the MIZ lower layer temperatures and salinities (Figure 5.12a and b) were greater than those of the upper layer. Lower layer temperature and salinity for the 1980 sections changed more regularly in the north-south direction and did not show a sharp transition or front. Section W-81 however, did have a high gradient region in the lower layer for both temperature and salinity at about the 100 m contour.

Though temperature increased with depth, the effect on density of the increased salinity resulted in a stably stratified water column throughout the MIZ. The stability, expressed as the difference in sigma-t between the lower and upper layer is plotted in Figure 5.13. North of about the 75 m contour, the water column is essentially vertically homogeneous. Stratification increases south toward the ice edge, reaching a maximum (Δsigma-t $\sim$.3 in W-80A, W-81 and Δsigma-T = $\sim$.8 in W-80B) near the ice margin.

The dynamic height of the surface (0 db) relative to 50 db is plotted in Figure 5.14. The strongest baroclinic current shear (closely spaced isolines) occurred near the ice edge over the central shelf (W-81 and W-80B). Computed baroclinic currents in this region were on the order of 3-4 cm/sec. North of the ice margin baroclinic currents were weak (<1 cm/sec on the average) and possibly evidenced some eddy-like motions (for example in the north part of Section W-80B).

5.3 Seasonal Changes in Heat and Salt

Two pairs of CTD sections provide a measure of winter to fall and fall to winter changes in heat and salt content within the Bering Sea MIZ. These pairs are W-80B and F-80B (April 1980 and November 1980, separated by 227 days) which crossed the central shelf northwest of St. Matthew Island and F-80A and W-81 (November 1980 and March 1981, separated by 112 days) which crossed the central shelf southeast of St. Matthew Island.

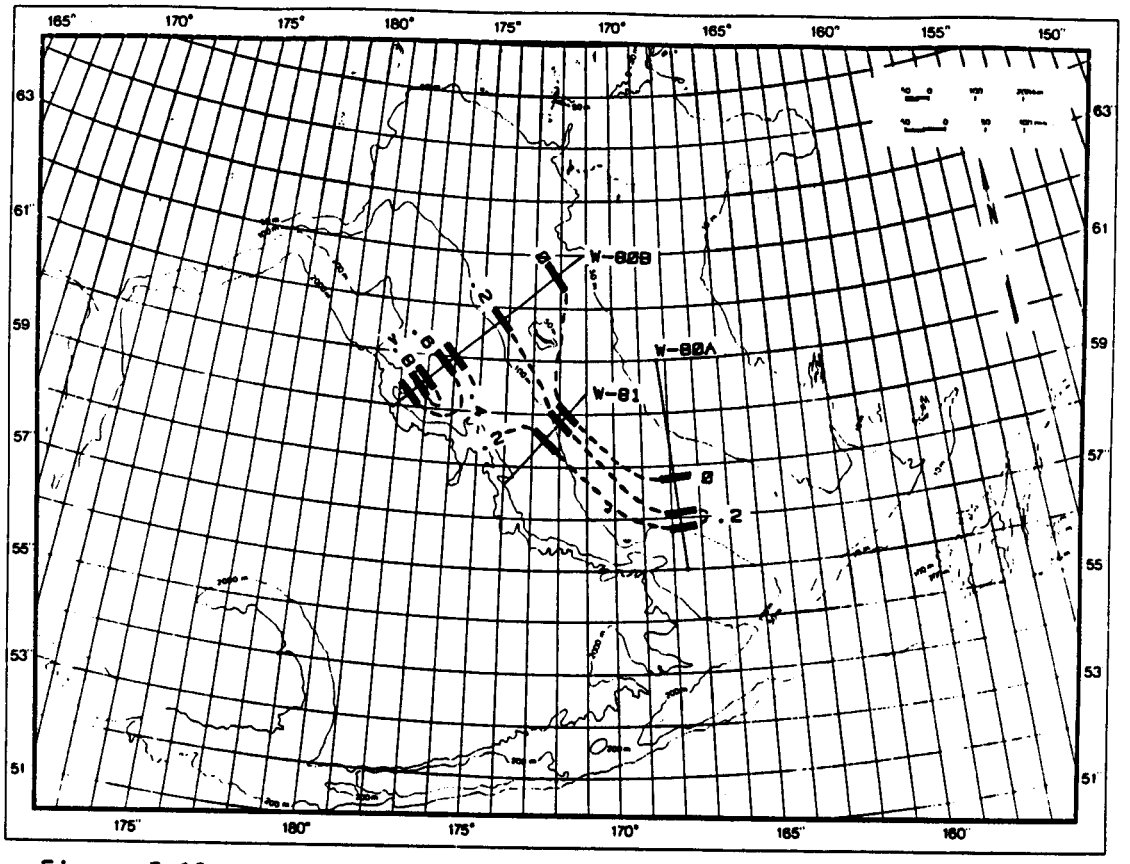

Figure 5.13. Vertical stratification, sigma-t difference between lower and upper layers.

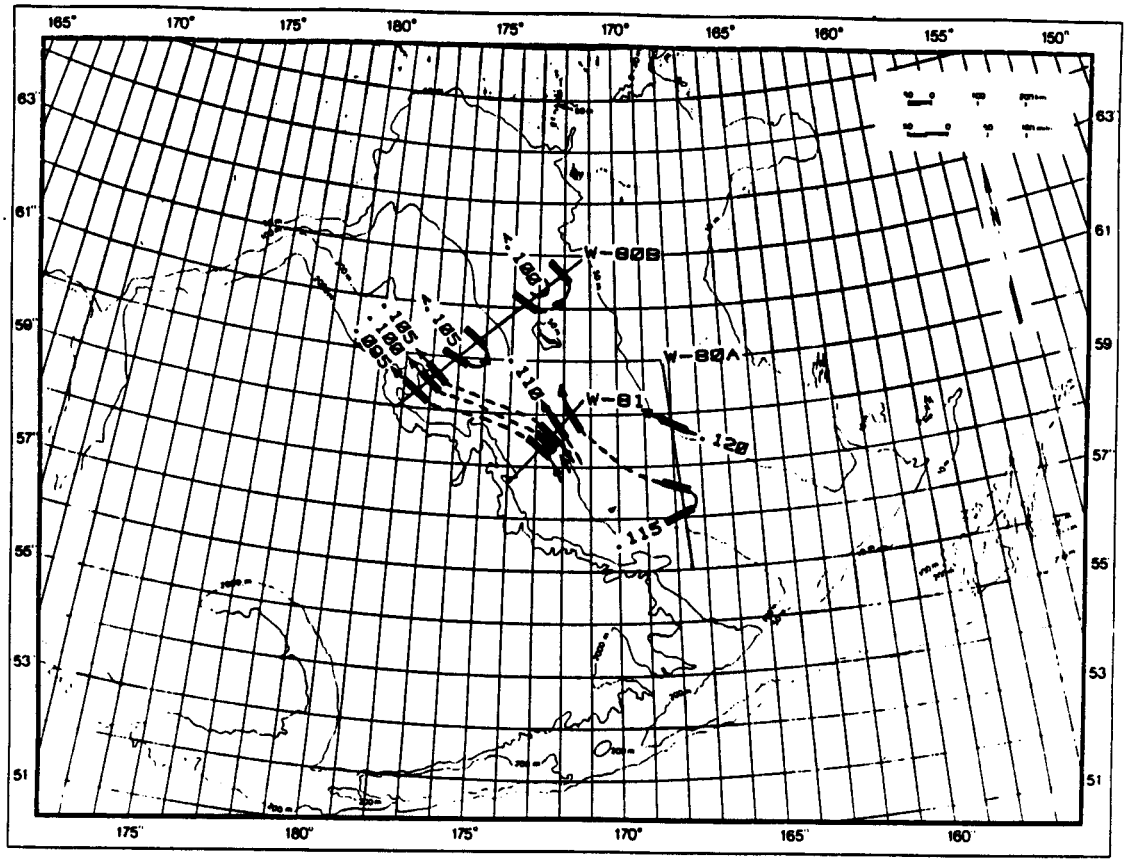

Figure 5.14. Dynamic height (dyn-m) relative to 50 db

Figures 5.15a and b plot the lines of stations which make up the W-80B — F-80B and F-80A — W-81 sections and indicate the position of the 100 m isobath. For this comparison these station lines were divided into 25 km intervals. A single hydrographic station within an interval was assumed to be representative of conditions within that segment; two or more stations within an interval were averaged to provide temperature and salinity profiles typical of the interval. The station lines making up each comparison were matched at the 100 m isobath for the purpose of the following calculations.

For each 25 km interval the change in heat content between fall and winter was calculated as:

$$\Delta H_{F\rightarrow W} = \rho C_p \int_0^D (T_W - T_F)\, dz \quad , \tag{2}$$

where $\Delta H_{F\rightarrow W}$ [cal] is the change heat content of a column of water 1 cm^2 in area of height D[cm] between winter 1980 and the subsequent fall 1980 (W-80B → F-80B) or winter 1981 as the previous fall (W-81 ← F-80A)

ρ[gm/cm^3] is the density, $\cong 1.03$ gm/cm^3

C_p[cal/gm-^oC] is the specific heat, $\cong 0.94$ cal/gm-^oC

D[cm] is depth of the water, and

T_W , T_F are the Winter and Fall temperature [^oC] profiles as a function of depth [z].

The above computation was carried out for each 25 km interval along both pairs of sections. Separate calculations were made for the mixed surface layer, for

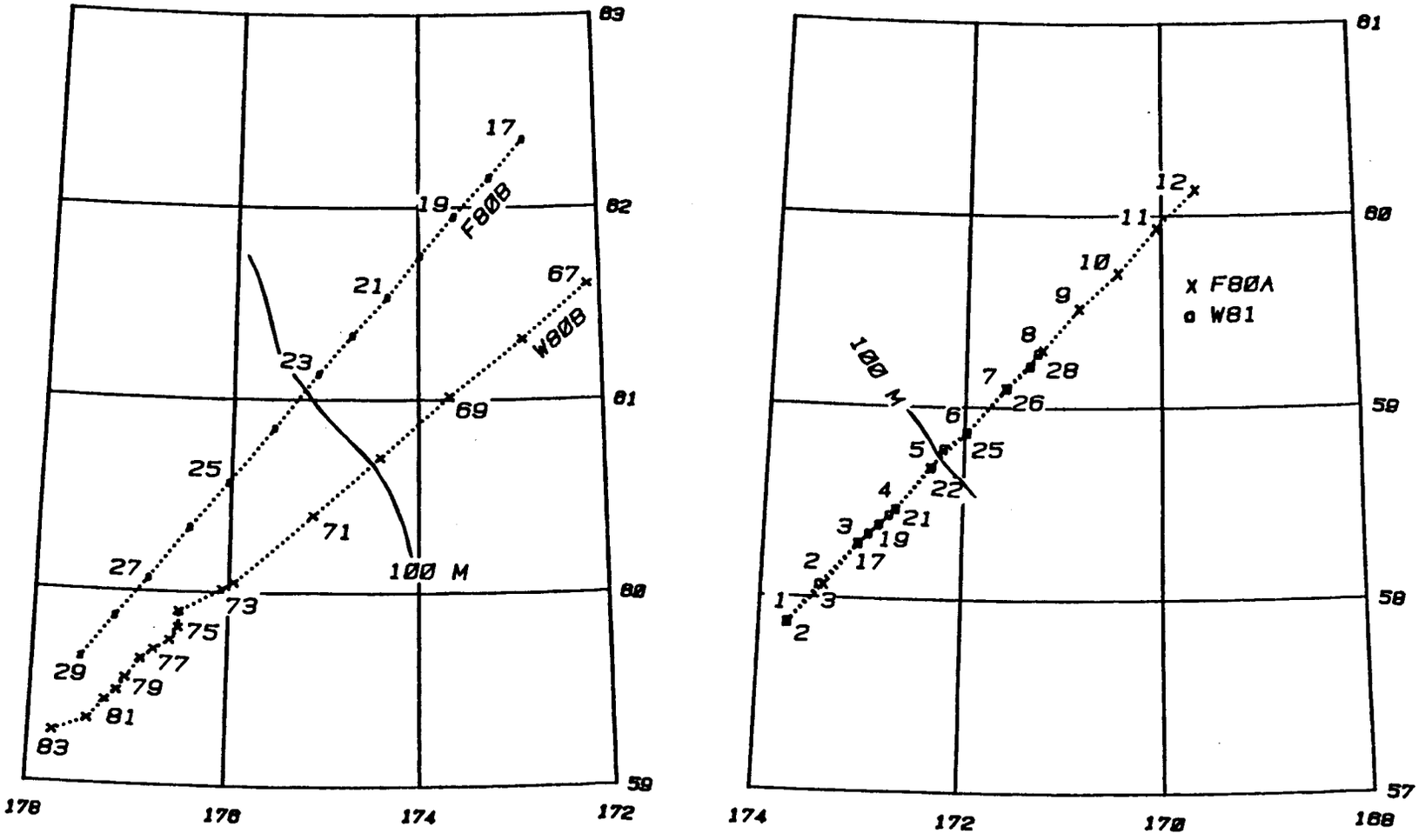

Figure 5.15. Positions of CTD stations for (a) F-80A and W-81 and (b) F-80B and W-80B sections.

water column from the base of the surface layer to the ocean bottom and for their sum, the total change in heat content. The results are plotted in Figures 5.16a and b.

Similarly, the change in salt content was computed for the same cases by:

$$\Delta S_{F\to W} = \rho \cdot 10^{-3} \int_0^D (S_W - S_F)\, dz \qquad (3)$$

where $\Delta S_{F\to W}$ [gm] is the change in salt content of a column of water 1 cm^2 in area of height D[cm].

ρ[gm/cm^3] is the density, $\cong$1.03 gm/cm^3,

D[cm] is the depth of the water, and

S_F , S_W are the Fall and Winter salinity (ppt) profiles as a function of depth [z].

The equivalent thickness of ice melting ($\Delta S<0$) or freezing ($\Delta S>0$) required to produce the change in salt content was estimated by:

$$i = 10^3 \Delta S/[.9(\bar{S}-Si)] \qquad (4)$$

where i is the thickness of ice melt (or freezing)

ΔS [gm] is the change in salt content over the appropriate layer

Si (g/kg) is the salinity of the ice [$\cong$7 g/kg]

$\bar{S}$ (g/kg) is the average initial salinity of the layer, and

.9 is the density of sea ice [gm/cm^3] .

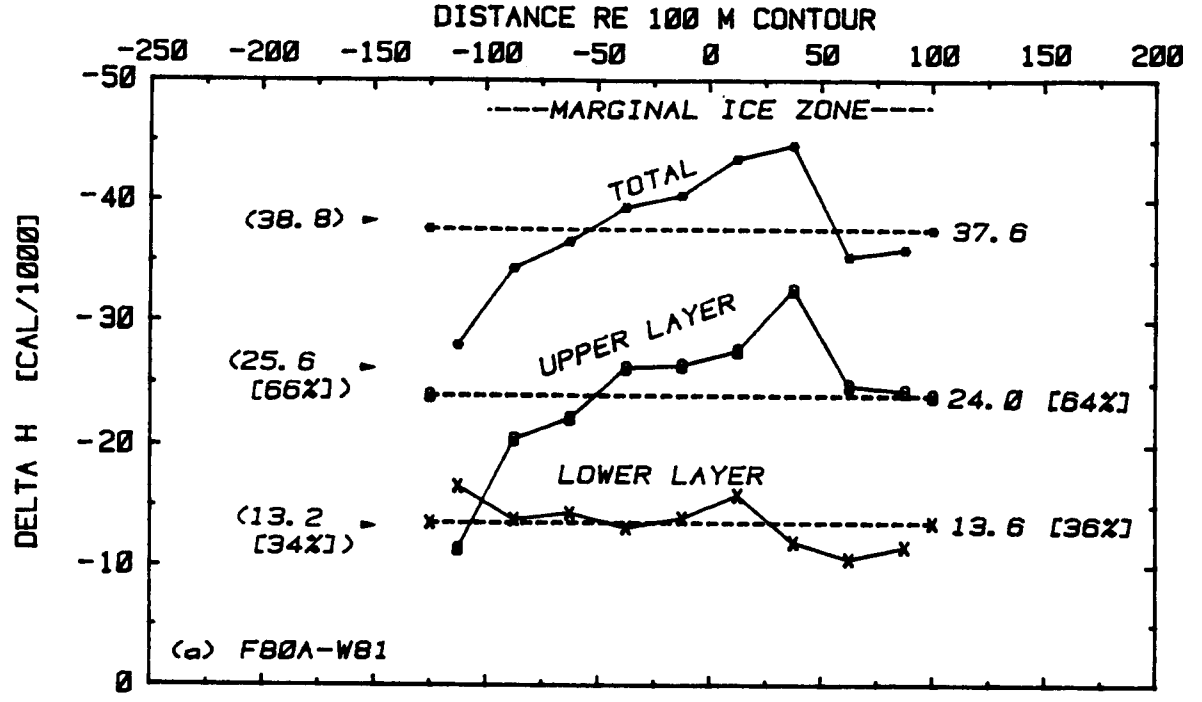

(a)

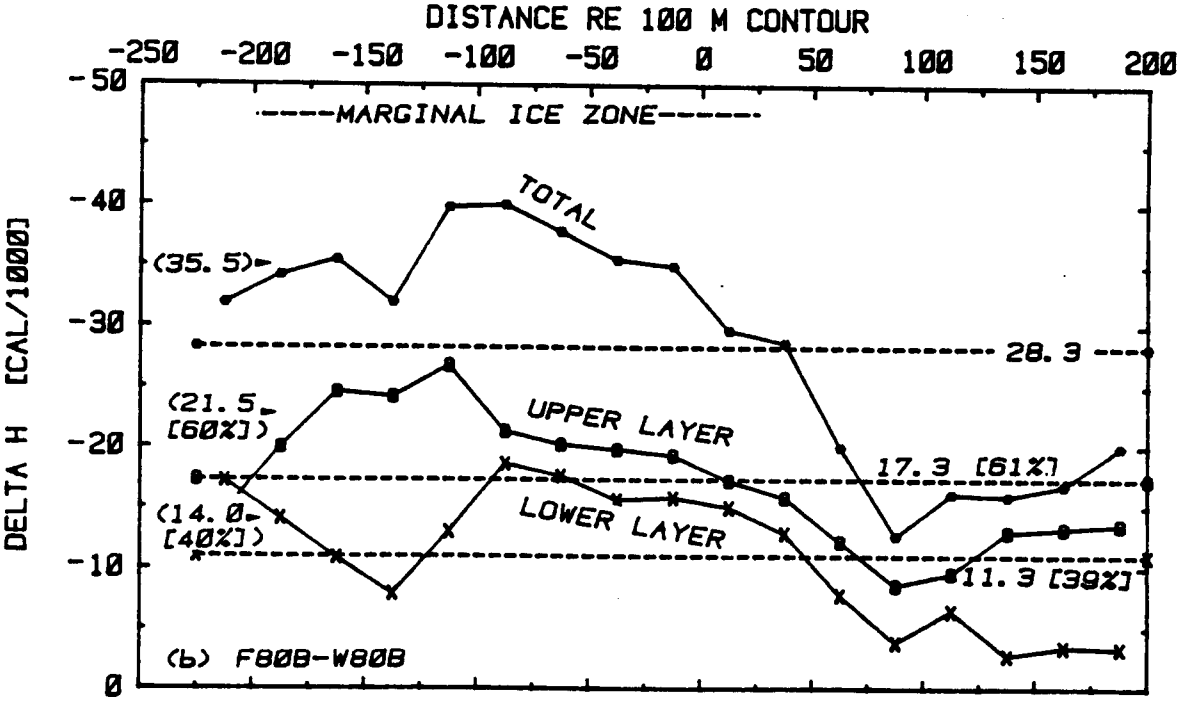

(b)

Figure 5.16. Change in heat content, $\Delta H[Cal/cm^2]$, for 25 km intervals; (a) F-80A – W-81 and (b) F-80B – W-80B. Along section averages are shown for the total section length (dashed lines) and for the MIZ (averages shown in parentheses).

The change in salt content [gm] and the equivalent dilution/concentration by ice melting/freezing expressed in meters are plotted in Figures 5.17 and 5.18 a and b.

The F-80A – W-81 comparison, a 225 km line approximately centered on the 100 m isobath, is limited by the length of the W-81 CTD section, obtained when the wind pushed the ice northward. Except for the southern most 25 km segment which appears to be influenced by the oceanic domain this section can be considered to have crossed the MIZ. The total change in heat content averaged over the MIZ portion of this section was 3.88×10^4 cal/cm^2 during the November 80 to March 81 (112 day) period. Of this total change in heat content, 2.55×10^4 cal/cm^2 [66%] occurred in the upper layer and 1.36×10^4 cal/cm^2 [34%] were extracted from the lower layer extending from the base of the surface layer to the bottom. The heat loss was a maximum in the 25-50 km interval north of the 100 m isobath and decreased to the north and south (Figure 5.16a). The change in salt content averaged along the MIZ portion of this section (Figure 5.17a) was 2.3 g/cm^2 of which 1.3 gm/cm^2 [56%] was due to freshening of the surface layer in the winter and 1.0 gm/cm^2 [44%] was a result of lower layer freshening. Except for the seaward 25 km interval, which might have been influenced by oceanic domain waters the salt deficit was a maximum just north of the 100 m isobath, coincident with the maximum in the heat loss (Figure 5.16a). The salt deficit (Figure 5.17a) is converted to equivalent meters of ice melt/freezing in Figure 5.18a. The maximum salt deficit, at 25-50 km north of the 100 m isobath, is equivalent to the melting of 1.6 m of ice per cm^2.

The F-80B – W-80B comparison covers a line of nearly 400 km across the MIZ onto the Bering shelf. North of the interval which lies 25-50 km north of the 100 m contour, the salt deficit is positive (Figure 5.17b) suggestive of freezing conditions during the winter of 1980. Thus the MIZ will be considered to be the region from 200 km seaward of the 100 m depth contour to 25 km shelfward of the 100 m isobath. This also corresponds to that region where the wintertime (W-80B) upper (and lower) layer temperatures were significantly above (>+0.10°C) freezing (Figure 4.11). The total change in heat content from fall 1980 to winter 1981 was 3.55×10^4 cal/cm^2 averaged over the section with 2.15×10^4 cal/cm^2 [60%] of the change in the upper layer

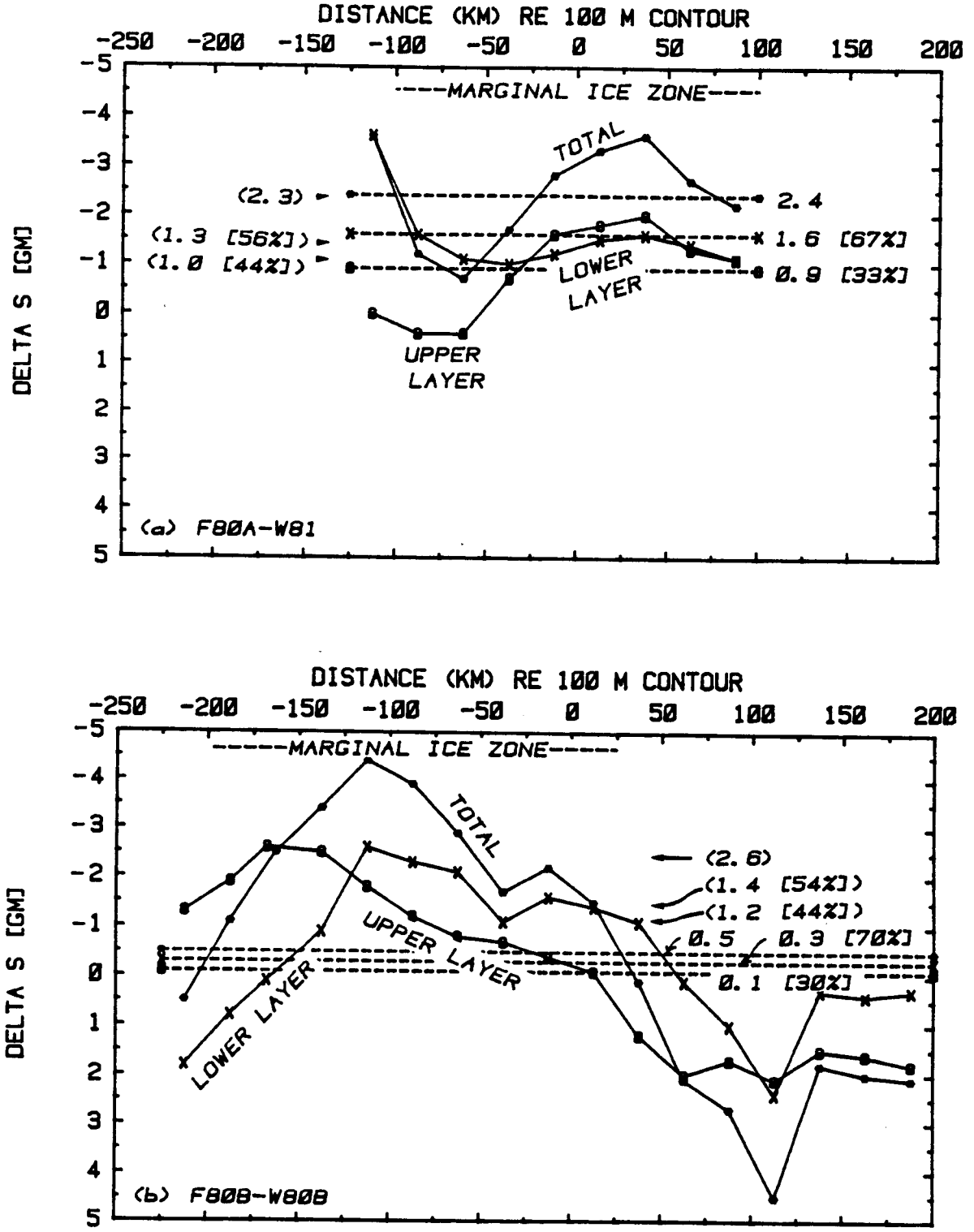

Figure 5.17. Change in salt content, $\Delta S[gm/cm^2]$, for 25 km intervals. (a) F-80A – W-81 and (b) F-80B – W-80B. Along section averages are shown for the total section length (dashed lines) and for the MIZ (averages shown in parentheses).

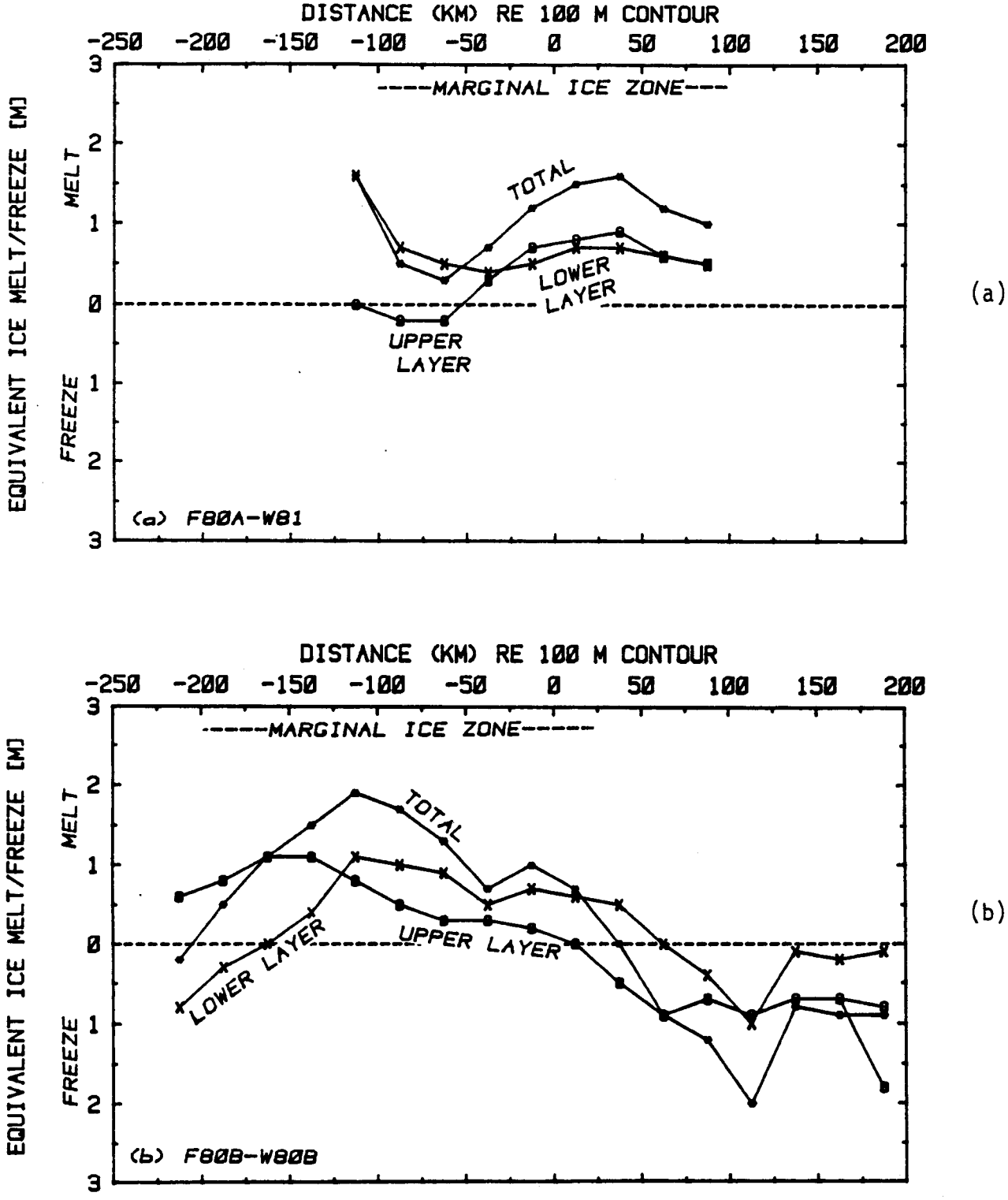

Figure 5.18. The thickness of ice at 7°/oo in meters which must melt (-) or freeze (+) to produce the observed change in salt content; (a) F-80A — W-81 and (b) F-80B — W-80B.

and a 1.40×10^4 cal/cm^2 [40%] of the change in the water column extending from the base of the upper layer to the bottom. The maximum heat content change occurred about 100 km seaward of the 100 m isobath. The average salt deficit in winter was 2.6 gm/cm^2 with 1.4 gm/cm^2 [54%] in the upper layer and 1.2 gm [46%] from below the pycnocline. The maximum in wintertime salt deficit (Figure 5.17b) occurred coincident with the maximum in the heat loss at about 100 km seaward of the 100 m isobath. The maximum total salt deficit was equivalent to the melting of 1.9 m of ice per cm^2 area.

Table 5.1 summarizes the average changes in heat and salt content across the MIZ for the two comparisons. The total change in heat content was about the same (within 10%) for both comparisons. Just over 60% of the total change in heat content was a result of heat extracted from the upper layer and the remainder (a little under 40%) occurred at depths below the pycnocline. Similarly, the change in total salt content was within 15% for the two comparisons with just over 50% of the salt deficit attributed to the upper layer and somewhat less than 50% due to freshening of the waters below the pycnocline.

A simple box model of heat and salt exchange in the MIZ which neglects advection is sketched in Figure 5.19. During the fall to winter period heat will be lost: (1) from the upper layer through surface exchange and (2) from the lower layer by a two step process of first mixing of the warm lower layer waters into the upper layer and then exchange through the surface. The melting of ice in the MIZ will (3) extract heat from the upper layer and (4) from the lower layer in the presence of vertical mixing. Accompanying the heat loss associated with ice melt will be a reduction in the salt content of the (5) upper and (6) lower layer due to the addition of fresh water. For this simple model the change in heat and salt content (expressed as equivalent ice melt) from fall to winter can be expressed as:

$$\Delta H_{F \rightarrow W} = \Delta H_0 + \rho L i \qquad (5)$$

where $\Delta H_{F \rightarrow W}$ total change in heat content [cal] per cm^2 area

Table 5.1. Summary of Changes in Heat and Salt Content from Fall to Winter Averaged Across the MIZ Portion of the Sections

		F80A-W81	F80B-W80B
Change in Heat Content [Cal/cm^2]	Total	3.88×10^4 (100%)	3.55×10^4 (100%)
	Upper Layer	2.56×10^4 (66%)	2.15×10^4 (60%)
	Lower Layer	1.32×10^4 (34%)	1.40×10^4 (40%)
Change in Salt Content [gm/cm^2] (Equivalent Thickness of Ice Melting)	Total	2.3 (1.00 m) (100%)	2.6 (1.10 m) (100%)
	Upper Layer	1.0 (0.48 m) (44%)	1.4 (0.57 m) (54%)
	Lower Layer	1.3 (0.52 m) (56%)	1.2 (0.53 m) (46%)

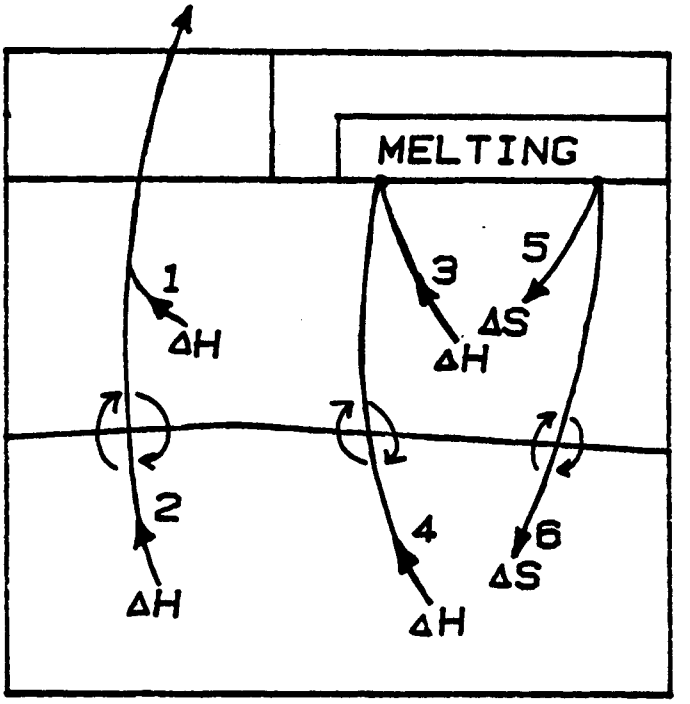

Figure 5.19. Schematic of changes in heat and salt content due to surface exchange and ice melting. Advective effects are neglected.

ΔH_0 change in heat content due to surface exchange [cal] per cm^2 area

ρLi change in heat content due to ice melting [cal]; ρ = density of ice [g/cm^3]; L = latent heat of fusion for sea ice [cal/gm]; i = ice thickness [cm] per cm^2 area melting.

The latent heat of fusion of sea ice, L, which is the number of calories necessary to melt one gram of sea ice, is a variable function of the temperature and salinity of the ice (c.f. Zubov, 1943, Table 40). For example in the rather narrow temperature range of -1 to -2°C and salinity range of 6 to 8 ppt, L varies from 47 to 68 cal/gm. Choosing L = 60 cal/gm and using the values from Table 5.1, estimates for the terms in expression (5) are shown in Table 5.2.

Based on the average changes in heat and salt content from fall to winter and the assumptions above it appears that of the total heat loss, about 85% is due to surface exchange (with about 2/3 of this heat loss from the upper layer and 1/3 from the lower layer). About 15% of the total heat loss can be associated with the process of the melting of sea ice in the MIZ.

As it appears that the changes in heat content are, at least visually (Figures 5.17, 5.18 and 5.19), somewhat correlated with the changes in salt content along the sections, it may be possible to estimate the terms in equation (5) by a linear regression using the individual data pairs for each 25 km interval. The regression, $y = a + bx$, was computed for each section on the data from the upper layer, lower layer and total water column with $y = \Delta H_{F \rightarrow W}$, X = i, and thus a estimates ΔH_0 and b estimates ρL. The results of the regression analyses are summarized in Table 5.3. With one exception (the F-80B — W-80B total case) the correlations between $\Delta H_{F \rightarrow W}$ and i for the upper layer and the total water column were significantly different from zero at the 5% confidence level. The correlations for the lower layer data were not significantly different from zero.

Table 5.2. Estimates of the Heat Balance Terms [Cal/cm^2] in Equation (8) Based on the Averaged Data in Table 5.1

		$\Delta H_{F \to W}$	ΔH_0	ρL_i
F80A-W81	Total	3.88×10^4	3.34×10^4	0.54×10^4
	Upper Layer	2.56×10^4	2.30×10^4	0.26×10^4
	Lower Layer	1.32×10^4	1.04×10^4	0.28×10^4
F80B-W80B	Total	3.55×10^4	2.96×10^4	0.59×10^4
	Upper Layer	2.15×10^4	1.86×10^4	0.29×10^4
	Lower Layer	1.40×10^4	1.11×10^4	0.29×10^4

Table 5.3. Summary of Parameters for Regression Analysis of ΔH Versus i (Equation 1) for the 25 km Intervals Across the MIZ

		F80A → W81	F80B → W80B	Combined F80A-W81 & F80B-W80B
Total	n	8	9	17
	r	0.72*	0.64	0.53*
	ΔH_0	3.28×10^4	3.03×10^4	3.23×10^4
	ρL	59.4	44.8	43.7
Upper Layer	n	8	9	17
	r	0.86*	0.82*	0.62*
	ΔH_0	2.13×10^4	1.79×10^4	2.0×10^4
	ρL	91.1	62.8	65.3
Lower Layer	n	8	9	17
	r	0.13	0.52	0.45
	ΔH_0	1.21×10^4	1.18×10^4	1.14×10^4
	ρL	18.9	43.2	40.6

*Correlation coefficient significantly different from zero at the 5% significance level.

n = number of pairs

c = correlation coefficient

ΔH_0 = the intercept

ρL = the slope of the regression line

The correlation between the temperature and salinity changes within each 25 km interval from fall to winter conditions are shown in Figure 5.20 for the upper mixed layer and for the lower layer, extending from the base of the upper layer to the bottom. Changes in upper layer temperatures ranged from -3.4°C to -5.5°C with salinity differences of -0.06 ppt to +0.52 ppt. There was a positive correlation between the temperature and salinity differences ($r = 0.75$, significantly different from 0 at the 1% significance level) with the slope, $\Delta T/\Delta S \cong 2.47^{o}C/ppt$. Temperature and salinity differences for the lower layers ranged from -0.9°C to -4.0°C and -0.08 ppt to +0.54 ppt respectively. These ΔT-ΔS pairs were also positively correlated ($r = 0.81$, different from zero at the 1% confidence level) with a slope of $\Delta T/\Delta S \cong 4.7^{o}C/ppt$. If the important processes for altering the surface layer temperature and salinity in the MIZ are ice melting and surface exchange then the temperature and salinity changes can be determined from:

$$\underset{\left[\begin{array}{l}\text{heat}\\ \text{content,}\\ \text{fall}\end{array}\right]}{\rho C_p a d T_W} = \underset{\left[\begin{array}{l}\text{heat}\\ \text{content,}\\ \text{winter}\end{array}\right]}{\rho C_p a d T_F} - \underset{\left[\begin{array}{l}\text{surface}\\ \text{exchange}\end{array}\right]}{\Delta H_0} - \underset{\left[\begin{array}{l}\text{heat used to melt}\\ \text{i thickness of ice}\end{array}\right]}{\rho_i L i a} \qquad (6)$$

where

$\rho, \rho i$ = density of water, ice

C_p = specific heat of water

a = area (km^2)

d = layer depth

T_W = average upper layer temperature, winter

T_F = average upper layer temperature, fall

ΔH_0 = surface heat exchange

Li = latent heat of fusion of sea ice, and

i = thickness of ice melt.

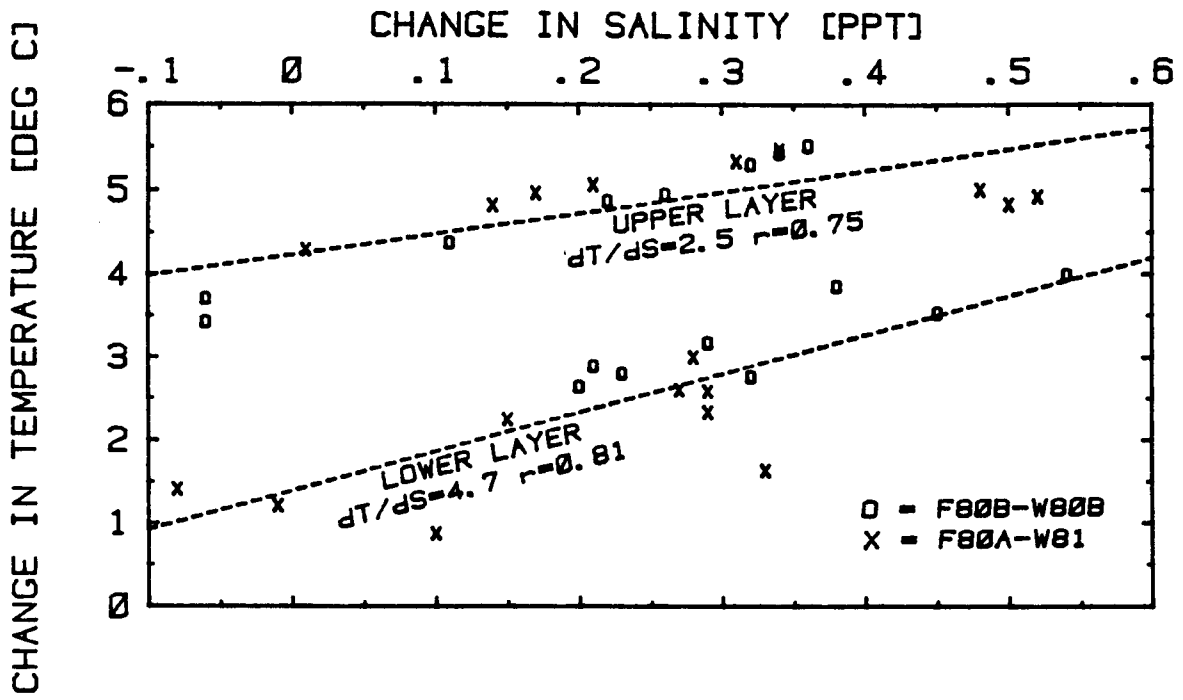

Figure 5.20. Correlation between the temperature and salinity changes within each 25 km interval for the upper layer and the water column from the base of the upper layer to the bottom (average ΔT and ΔS) for both comparisons.

The temperature change can be expressed as,

$$\Delta T = T_W - T_F = - \Delta H_0 / \rho C_p d - i \left[\frac{\rho_i L i}{\rho C_p d} \right] \tag{7}$$

For salinity,

$$\rho a d S_F 10^{-3} = \rho a (d+i)\ S_W 10^{-3} \tag{8}$$

where S_F, S_W = average upper layer salinities in fall and winter

$$\Delta S = S_W - S_F = S_F \left(\frac{d}{d+i}\right) - S_F = S_F \frac{i}{d+i} \cong S_F \frac{i}{d} \tag{9}$$

For this expression, the salinity of the melting ice is taken as zero and the layer depth is held constant. Both the temperature and salinity of the upper layer will vary as the amount of ice melt (i). The term ΔH_0, the surface exchange will probably be about constant across the 200 km MIZ.

Combining (7) and (9)

$$\Delta T = - \Delta H_0/\rho C_p d - \Delta S \frac{\rho i}{\rho} \frac{Li}{C_p S_p} \tag{10}$$

The slope of the ΔT - ΔS correlation in the upper layer should approximately be given by

$$\frac{\rho i}{\rho} \frac{Li}{C_p S_F} \cong 2.4^{o}C/ppt \tag{11}$$

with

$$\rho i/\rho \cong .9,\ C_p = .94 \frac{Cal}{g\text{-}^{o}C},\ Li = 80 \frac{Cal}{gm},\ S_p = 31 \text{ ppt},$$

which is approximately equal to the slope in Figure 5.20. A more detailed derivation of this slope can be found in Gade, 1979. The temperature-salinity changes in the lower layer appear to be correlated but along a steeper slope ($\sim$4.7^{o}C/ppt) suggesting a different mechanism.

6. DISCUSSION AND CONCLUSIONS

Wintertime hydrographic structure over the southeast and central Bering Sea shelf, based on this 1980-81 data, conforms in many respects to the domains proposed by Kinder and Schumacher, 1981a for the southwestern shelf. During winter over the central shelf, the boundary between the vertically homogeneous coastal domain and the two-layer middle domain appears to occur at about the 75 m isobath (Figure 5.13). This boundary may be farther south, over deeper water, than during summer where it is coincident with the 50 m contour. This would suggest that wintertime mixing processes such as due to tides and stirring by the relative movement of ice over the water aided by negative buoyancy addition at the surface by the cooling and freezing process, are able to completely mix the water column to a deeper depth than the summertime combination of wind and tidal mixing. During wintertime the middle domain, with a characteristic two-layer structure, extended from about the 75 m contour to the 100 m contour over the southeastern shelf. Over the central shelf the two layer structure extended seaward of the 100 m contour, to depths of 125 to 150 m.

During winter the temperature and salinity of both the upper and lower layers decrease to the north. Surface layer temperatures remained significantly (>.1^{o}C) above freezing for distances of 50 to 100 km into the ice pack. The horizontal gradients of temperature and salinity in the upper layer (-2 to -5 x 10^{-2} ^{o}C/km and -6 to -10 x 10^{-3} ppt/km) tended to be greater than the corresonding gradients in the lower layer (-1 to -3 x 10^{-2} ^{o}C/km and -1 to -4 x 10^{-3} ppt/km). The greatest upper layer horizontal property gradients occurred coincident with the approximate position of ice edge (compare Figures 5.10 and 5.11a and b). The horizontal changes in T-S properties were similar along the two central shelf sections ($dT/dS \cong 3$ to 4 ^{o}C/ppt). Although both temperature and salinity decrease northward along the sections their effects on the horizontal density gradient are not completely compensating. The reduction in density due to the salinity decrease is greater than the increase in density due to the temperature decrease ($\Delta S/\Delta T \cong 1/4$; $\beta\Delta S/\alpha\Delta T \cong 4$). As a result there is a horizontal density gradient associated with the ice edge which in turn indicates a baroclinic flow in the upper layer directed to the northwest along the ice edge (Figure 5.14).

Fall to winter comparisons can be made by comparing sections W-80B → F-80B and F-80A → W-81. Although changes over the fall to late March period do not reflect total changes in the MIZ over a season, they may reflect some of the important ice-ocean processes and interactions. During fall, the temperatures in the upper layer were in the +2 to +5°C range (Figures 5.1 and 5.4). Upper layer temperatures were a maximum in the south and decreased to the north at about -1×10^{-2} °C/km. Lower layer temperatures were about 1 to 2°C/km lower than in the upper layer and also decreased to the north along nearly the same slope. The salinities along the fall sections (Figures 5.1 and 5.4) also decreased to the north (about 3 to 5×10^{-3} ppt/km) with the lower layer salinities .25 to .5 ppt greater than in the upper layer. Both the vertical temperature (negative) and salinity (positive) gradients were stabilizing. During wintertime the following changes in the temperature and salinity structure were evident. Upper layer temperatures and salinities decreased and the horizontal property gradients increased by a factor of 2 to 4, especially in the region of the ice edge. In the lower layer temperature and salinity also decreased along the sections but significant changes in the horizontal gradients were not so evident. During winter the vertical temperature gradient becomes positive and is a destabilizing component in the vertical density gradient.

The changes in heat and salt content from fall to winter in the MIZ computed for the two comparison sections lead to the following conclusions:

- The total change in heat content averaged along the MIZ portion of the sections was about 3.7×10^4 cal/cm^2 (Figure 5.16) of which 60 to 66% occurred in the upper layer and 34 to 40% occurred in the lower layer.
- The total change in salt content averaged along the MIZ portion of the sections was about 2.4 gm/cm^2 (Figure 5.17), equivalent to the melting of 1 m of ice, of which 54 to 56% occurred in the upper layer and 44 to 46% occurred in the lower layer.
- Combining the above results with the assumption that the latent heat of fusion for sea ice is about 60 cal/gm suggests that

approximately 15% of the total heat loss is used in the melting of ice and 85% is due to surface exchange (Table 5.2).

- Treating each 25 km interval as an individual estimate of the heat and salt changes given by $\Delta H_{F \to W} = \Delta H_0 + \rho L i$ (Eq. 5) and inputting computed values of $\Delta H_{F \to W}$ and i estimates of ΔH_0 (the intercept) and ρL (the slope) were made using regression techniques (Table 5.3) to check the consistency of the observations against this relationship. Correlations were positive and significant at the 5% level for the upper layer cases and two of three of the cases using the total water column. Estimates of the slope, ρL, ranged from 44 to 91 [cal/cm^3] with an average of about 62 [cal/cm^3]; estimates of the intercept, ΔH_0, were 3.1×10^4 [cal/cm^2] for the total water column and 2.0×10^4 [cal/cm^2] for the upper layer.

- The correlation between the changes in temperature and salinity (Figure 5.20) from fall to winter show a slope, $\Delta T/\Delta S \cong 2.5$ for the upper layer consistent with dilution and cooling by ice melt. The slope for the lower layer, $\Delta T/\Delta S \cong 4.7$ is different suggesting another mechanism, perhaps vertical mixing, may also play a role in determining the lower layer properties.

Both comparisons indicate that by late March about 1 m of ice on the average has melted over a band of 200 km in north-south extent. Using an average thickness of 0.5 m, this equates to a 400 km band of ice advecting south and melting in the MIZ. If southward movement of ice into the MIZ and subsequent melting has taken place over a two month period then the southernly rate of ice movement is about 8 cm/sec. For comparison Muench and Ahlnas, 1976, estimated the southward movement of ice into the MIZ at about 18 cm/sec.

7. REFERENCES CITED

Doherty, B. J., and D. R. Kester. 1971. Freezing point of seawater. J. Mar. Res. 32(2): 285-300.

Gade, H. B. 1979. Melting of ice in sea water: a primitive model with application to antarctic ice shelves and icebergs. J. Phys. Oceanogr. 9(1): 189-198.

Kinder, T. H., and J. D. Schumacher. 1981a. Hydrographic structure over the continental shelf of the southeastern Bering Sea. In The Eastern Bering Sea Shelf: Oceanography and Resources, Vol. I, D. W. Hood and J. A. Calder, eds., 1339 pp.

Kinder, T. H., and J. D. Schumacher. 1981b. Circulation over the continental shelf of the southeastern Bering Sea. In The Eastern Bering Sea Shelf: Oceanography and Resources, Vol. I, D. W. Hood and J. A. Calder, eds., 1339 pp.

Muench, R. D. 1981. Physical oceanographic investigations in the Bering Sea marginal ice zone (draft). SAI/NW-81-250-04, 50 pp.

Muench, R. D., and K. Ahlnas. 1976. Ice movement and distribution in the Bering Sea from March to June 1974. J. Geophys. Res. 81(24): 4467-4476.

Newton, J. L., and B. G. Andersen. 1980. MIZPAC 80A; USCGC Polar Star (WAGB-10) Arctic West Operations. March 1980: Bering Sea. Cruise report and preliminary oceanographic results. SAI-202-80-460-LJ, 32 pp.

Zubov, N. N. 1943. Arctic ice. 491 pp. Transl. USAF Cambridge Research Center, ed., U.S. Navy Electronic Laboratory.

INTERPOLATION, ANALYSIS, AND ARCHIVAL OF DATA ON SEA ICE TRAJECTORIES AND OCEAN CURRENTS OBTAINED FROM SATELLITE-LINKED INSTRUMENTS

by

Robert S. Pritchard and Dennis J. Hanzlick

IceCasting, Inc.
11042 Sand Point Way, N.E.
Seattle, Washington 98125–5846

Final Report
Outer Continental Shelf Environmental Assessment Program
Research Unit 683

April 1987

ACKNOWLEDGMENTS

This study was funded by the Minerals Management Service, Department of the Interior, through an interagency agreement with the National Oceanic and Atmospheric Administration, Department of Commerce, as part of the Outer Continental Shelf Environmental Assessment Program. The analysis and report were prepared according to NOAA Contract WASC-86-00043.

TABLE OF CONTENTS

LIST OF FIGURES

LIST OF TABLES

1. INTRODUCTION

This final report is submitted to NOAA to describe the work performed by IceCasting, Inc.(ICI) under NOAA contract No. WASC-86-00043. The broad objectives of the study were to analyze data taken by ice drifting buoys in Norton Sound and the Chukchi Sea during 1981-82, to describe the atmospheric and oceanic features that occurred during these field programs, and to provide the data in a revised format to NODC. The two field projects that collected these data were conducted by Dr. R. S. Pritchard, now with ICI, and others at Flow Research Company (Flow), and were sponsored by NOAA through the OCSEAP program, as part of RU567. The field program in Norton Sound was jointly sponsored by OCSEAP and a consortium of oil companies.

Both of these field projects used the NOAA Tiros satellite system to receive data. A combination of ARGOS and air-droppable TAD(A) buoys was used, with additional sensors on some buoys to measure environmental parameters. The experiments were designed to obtain broad spatial coverage throughout the winter. Eleven buoys were deployed at three different times in Norton Sound and six were deployed at two different times in the Chukchi Sea.

Under RU567 the data were obtained and validated, but not analyzed. The data were submitted to the National Oceanographic Data Center (NODC) to be archived, but file formats have since changed (from File Type 056 to 156), and standardization of these formats precluded including these data. Therefore, the first objective of the work was to modify the raw data to fit into the File Type 156, and to submit the results for a final quality

assurance check and archival in the NODC data bank. The second objective was to describe the ice behavior and the environmental conditions that existed during the field programs.

In section 2, we discuss the background leading to this work. In section 3, the tasks performed during the study are described. In section 4, the analytical methods used are presented. The discussion is focused on the method of Optimal Interpolation because the method has recently been adapted for analyzing sea ice motion data in the presence of tidal oscillations. In sections 5 and 6, we describe the ice behavior and the environmental conditions that existed in the Norton Sound and Chukchi Sea, respectively. In section 7, the work is summarized.

2. BACKGROUND

The MMS and OCSEAP are responsible for obtaining enough information about the environmental conditions in each lease sale area to ensure that exploration and production of hydrocarbons will be safe and will not have an unacceptable impact on the environment. This responsibility has many aspects, and the data to be analyzed here relate to several of them.

The ice motions and ice conditions affect when and how operations can proceed at a site which might be threatened at some time during the operation. Both variables also affect the design of structures that can operate at each site because thicker ice or multi-year ice can exert larger forces on a structure than thinner or first-year ice, and because the ice strength increases with increasing strain rates.

If a drilling accident were to occur, and oil were released into the ocean, on or under the ice, then the impact of this release must be understood. Since oil may be transported by both the ocean and the ice, it is critical to understand the relationship between wind, water and ice motions.

Observations of the winds, currents and ice motions are of direct value, but the history of accurate, season-long observations is short and they are expensive to make. Therefore, OCSEAP has relied on mathematical and computer models of the ice and ocean dynamics to estimate the expected range of behavior over the lifetime of production from a lease sale area (e.g., Pritchard, 1979; Thomas and Pritchard, 1979, 1982; Liu and Leendertse, 1984). Observations are used primarily to validate

and tune the models, although Colony and Thorndike (1985) have estimated the range of ice motions using a statistical model based directly on observed motions.

The data to be analyzed here are from field experiments that were designed so that ice and ocean dynamics models could be tested and their performance verified. The two largest external driving forces (air and water drag) depend on the winds and currents relative to the ice (e.g. Pritchard, 1981; McPhee, 1982). Therefore, these field experiments measured both winds (or barometric pressure from which winds could be determined) and currents at selected locations.

For the Chukchi Sea experiment, where the large-scale wind fields are driven primarily by gradients in the barometric pressure field, barometers were used to supplement the hemispheric barometric pressure fields normally estimated by the National Meteorological Center (NMC). For the Norton Sound experiment, gradient winds give a less accurate measure of local winds (Kozo, 1984), so winds were measured directly using an anemometer and vane on a 3-m-tall mast.

The ocean currents at the bottom of the mixed layer (some 6- to 10-m below the ice in the shallow waters of both Norton Sound and the Chukchi Sea) were measured relative to the ice by suspending a current meter below the ice floe on which the buoy was deployed. This allowed the absolute current to be determined, if the ice velocity were known, by adding the two quantities vectorially.

If the ice trajectories, and the winds and currents that drive the ice, are determined for each day, then we have a

consistent set of variables to describe the synoptic-scale processes that control long-term behavior. On short time scales, the tides cause ice and water movements. Usually these motions are small over periods longer than a day when compared to the wind- and current-driven drift, although Liu and Leendertse (1984) have concluded that Norton Sound currents result from tidal residuals. Here, we assume that the short-term tidal and inertial oscillations have only a small effect on the daily processes, and so they can be filtered out of the data without affecting the analysis of the synoptic-scale processes.

Table 1 shows the buoys that were deployed, their initial locations, sensors, and start/finish dates of transmission. The dates begin late in 1981 and end by the summer of 1982.

Table 1. Buoy Locations, Sensors, and Launch and End Dates.

Buoy ID	Rough Location	Barom.	Anemom. & Vane	Current Meter	Compass	Dates Launch	Dates End
3607	Norton Sound		x	x	x	2/06	2/19
3608	Norton Sound		x	x	x	2/24	6/11
3609	Norton Sound		x	x	x	2/27	4/06
3610	Norton Sound					12/18	1/16
3611	Norton Sound					12/17	6/29
3612	Norton Sound					1/31	5/31
3613	Norton Sound					2/26	4/11
3614	Norton Sound					3/02	6/15
3615	Norton Sound					3/02	3/25
3616	Norton Sound					3/03	6/18
3617	Norton Sound					3/03	6/11
3620	Chukchi					1/30	2/15
3621	Chukchi					12/19	2/17(a)
3622	Chukchi	x				2/09	6/12
3623	Chukchi			x		2/11	7/13
3624	Chukchi			x		2/15	5/03
3625	Chukchi	x		x		2/16	5/08

Note (a) This buoy continued to transmit until 1983.

Trip reports and a description of buoy operations can be found in Thomas and Pritchard (1982). For completeness, we briefly discuss here the data and the methods used to retrieve the raw data using the NOAA satellites.

The positions of the drifting buoys were measured at irregular intervals throughout the day depending on the timing of satellite passes. The ARGOS and TAD(A) buoys transmitted a short, roughly 400 MHz burst at one minute intervals. This signal was received by the NOAA satellites and transmitted to the Gilmore Creek receiving station, which then re-transmitted it to Service Argos, Toulouse, where it was processed. Buoy positions were determined by observing the Doppler shift in signal frequency. As each satellite passed overhead (at satellite noon, it viewed each buoy for up to twelve minutes), multiple transmissions were received and used by Service Argos to estimate position. The sensor data were encoded into the signal, with 256 bits transmitted each time. Those buoys that contained sensors also contained a clock. At 2-hour intervals, the buoy interrogated each sensor and stored the observations in memory. Wind vectors and current meter speeds were averaged over a 9-minute period and then stored. Current meter directions and barometric pressure were sensed instantaneously at the sampling times and stored. Four sets of sensor observations were stored in memory and transmitted sequentially to the satellite receiver to provide redundancy in the system. In this way each sensor observation was saved and transmitted for a 6-hour period, thereby greatly increasing the probability that a satellite would receive the signal.

Reynolds and Pease (1984) also deployed an array of six ARGOS drifting buoys in Norton Sound during January and February 1982. Their experiment was located approximately between the Norton Sound and Chukchi Sea regions being reported here. Four of the PMEL platforms drifted through the Bering Strait, and in response to alternating winds and currents, oscillated through the strait three or more times. Their other two platforms oscillated north and south on the same time scales, but remained near the western Norton Sound area (Pease and Salo, 1987).

3. APPROACH

The objectives of the project were satisfied by dividing the work into the following four tasks.

Task 1. Acquire data from the University of Rhode Island (URI).

A magnetic tape containing all data from the two field experiments was provided to the ICI investigators by Ms. Nancy Clayton, URI. The tape blocking was chosen after consulting with Mr. Pat McCafferty, Flow, to ensure that the data could be read from the magnetic tape into the Flow MASSCOMP computer. The Norton Sound data were written in the older file type 056 format, which interspersed records describing the buoy positions, wind speed and direction, relative currents, ice floe orientation, and other measurements, so that one file was available for each buoy. The Chukchi Sea data were written in a modified file type 156 format, with separate files for position, barometric pressure, and current for each buoy.

During this project, the barometric pressure data were averaged over two-hour time periods to obtain estimates at about the same sampling rate as the other variables. These average values were stored at NODC. This filtering process retained all essential information because there are no significant physical processes responding above this frequency.

The raw data were examined for erroneous points by plotting the time history for each position and sensor. Figure 3.01 shows a typical plot of the position estimates from Service Argos, with dots at each time. Similar plots were used to peruse the sensor

data. The time scale represents a decimal measure of time in Julian days. The Julian time of t=1.000 day corresponds to January 1, 1982 at 0000 GMT. Plots have been scaled to present 30-days of data, roughly a month, on a page. For convenience, Table 3.1 presents the Julian time at the start of each month for which data were obtained.

Table 3.1. Relationship Between Julian times and Calendar Dates. All times correspond to 0000 GMT on the dates shown.

Calendar Date	Julian Time
Dec 1, 1981	-30.
Jan 1, 1982	1.
Feb 1, 1982	32.
Mar 1, 1982	60.
Apr 1, 1982	91.
May 1, 1982	121.
Jun 1, 1982	152.
Jul 1, 1982	182.
Aug 1, 1982	213.
Sep 1, 1982	244.
Oct 1, 1982	274.
Nov 1, 1982	305.
Dec 1, 1982	335.
Jan 1, 1983	366.
Feb 1, 1983	397.
Mar 1, 1983	425.

Task 2. Calculate interpolated positions for sensor data points for which such information is missing; and calculate absolute current speeds from current meter and buoy position records.

Approximately 10-12 position measurements are obtained each day. These data points are usually obtained during a twelve to sixteen hour period, with little data available during the remainder of the day. These positions are estimated at irregularly spaced intervals (from a few minutes to more than 6 hours apart), while the current meter measurements are obtained at regular 2-hour intervals. This data sampling density is adequate for determining the buoy (and ice floe) trajectories and

the velocities, but a sophisticated analytical technique is required. Accurate ice velocity estimates are important because they are used in conjunction with the relative current measurements to estimate absolute currents. Ice motion data can contain tidal oscillations with a spatial amplitude on the order of 10Km. The peak velocity of such a diurnal signal is about 60cm/s. This tidal component is larger than the longer-term, daily average values. A similar argument can be made concerning the semi-diurnal tidal component.

The ice velocity can be accurately estimated at 2-hour intervals because the tidal oscillations are periodic and well-known, and because the atmospheric forces and ocean currents which drive the ice vary on time scales longer than tidal. However, internal ice stresses can vary rapidly, creating an ice stress divergence force that accelerates the ice on shorter-term time scales. We have assumed that the short-term ice motions caused by the ice stress divergence are small and that the associated ice velocity component is also small compared to daily and tidal components. There are no independent data available to test this assumption.

The buoy position data were used to obtain a uniformly-spaced sequence of buoy position and velocity. The Optimal Interpolation method (OI) to be presented in section 4 was used to estimate the buoy positions at 3-hour intervals. The ice velocity was estimated at the same times by forming the difference between interpolated positions and dividing by the averaging interval. Linear interpolation was then used to

calculate the ice velocity associated with each current meter measurement.

The calculated position history of buoy 3608 is presented in Figure 3.02. The data used to calculate these positions are presented in Figure 3.01. The two histories may be compared directly. The OI fit is very good, with the interpolated data curve overlaying the raw data points. The high frequency tidal and inertial oscillations are described accurately, as are the longer-term variations.

The ocean current velocity, c, is estimated by adding the ice velocity, v_i, to the relative velocity, v_r, measured by the current meter

$$c = v_i + v_r \quad . \tag{3.1}$$

The ice velocity, v_i, can be estimated from the buoy positions using the relation,

$$v_i(t) = \frac{x(t+\Delta) - x(t-\Delta)}{2\Delta} \tag{3.2}$$

where Δ equals one-half of the velocity averaging interval. The method of optimal linear interpolation allows the positions to be calculated at any time.

Figure 3.03 shows the velocity of buoy 3608, calculated from the OI position history. Until about Jd 90 (see Table 3.1 for calendar dates associated with the Julian Day), this buoy was located near the mouth of Norton Sound where the diurnal tide is large. The presence of this large tidal velocity, which appears as a rather small oscillation in position, required that we use the sophisticated OI analysis, or else the ocean current estimates would have been swamped by uncertainty. Other simpler

techniques, such as linear interpolation between adjacent data points, could have been used to estimate sensor positions, but the OI method allowed us to estimate both position and velocity at the same time.

Task 3. Describe atmospheric and oceanic features and motions extant during the buoy deployment period.

The winds and currents provide two of the external forces that cause the ice cover to move and deform. The ice responds quickly to changes in these forces so that quasi-static behavior may be assumed on time scales of about a day (e.g. Pritchard, 1981). In addition, tidal forcing and inertial oscillations can drive ice motions at time scales as short as 6-12 hours. But it is the daily and longer-term variations that this project originally sought to measure, and it is these time scales on which our attention is focused. Thus, the time histories of winds and currents have been filtered to isolate the synoptic-scale behavior from the shorter term variations. Daily values of the ice velocities, winds, and currents were determined using a 48-hour cosine bell filter (e.g., Bendat and Piersoll, 1980; Bloomfield, 1976).

In Norton Sound, the wind speed and direction at each of the met-ocean buoys were measured directly by an anemometer and vane mounted on a 3-meter-tall mast. The winds were then calculated directly by forming the vector.

In the Chukchi Sea, the two barometers were not adequate to determine winds. To estimate the winds at the respective buoys,

we acquired data from the NOAA Pacific Marine Environmental Laboratory (PMEL), and used their METLIB software package (Macklin, et. al., 1984). Specifically, we obtained atmospheric pressure data on a section of the FNOC 63x63 northern hemisphere grid. This section covered the entire Bering and Chukchi sea region. The data had been interpolated by PMEL to one-quarter of the original grid size, and thus the grid spacing was about 90 km in the Chukchi. We extracted a subsection of the data which covered only the region of interest and used the METLIB program to calculate surface winds. The surface winds were estimated by multiplying the gradient winds by 0.70 and rotating the wind vector 30 degrees to the left. These values are consistent with the results of earlier studies of wind reduction ratios and indraft angles in the Arctic (Overland, 1985). A time series of winds at a selected location in the Chukchi was generated, and these data were compared against pressure map contours and surface observations as a check that the output winds were representative of the actual winds. Finally, a time series of winds along the drift tracks of the buoys was calculated.

Task 4. Prepare digital data in appropriate file type (FT 156) for archival at NODC.

The original FT 156 was not compatible with the data generated by this project because there was no field to accept the currents. Therefore, two new record types (E and F) were developed by the PI and Ms. Nancy Clayton of URI to allow us to archive data from drifting buoys with current meters. Mr. Steve Patterson, NODC, was consulted to ensure that the new formats

would be acceptable to NODC, and Dr. Jawed Hameedi, COTR, also concurred. The Data Documentation forms for this data set are presented in Appendix A.

The raw current meter measurements describe the ocean current velocity relative to the ice velocity. This relative velocity was considered to be too difficult to use by other investigators, and so the absolute ocean current was calculated and stored instead. However, the absolute current is a derived variable, and one that depends strongly on the method used to estimate ice velocity. Therefore, the FT 156 format also contains the ice velocity that was used to calculate the absolute current. The ice velocity was included to allow other investigators to reconstruct the original data set if desired, and therefore to use alternate methods to analyze the data.

A magnetic tape was generated in the format of File Type 156 and sent to the COTR for quality assurance testing by URI and transmittal to NODC. This tape satisfied the first of two deliverable products required under terms of the contract. This final report satisfies the second, and final, deliverable product of the project.

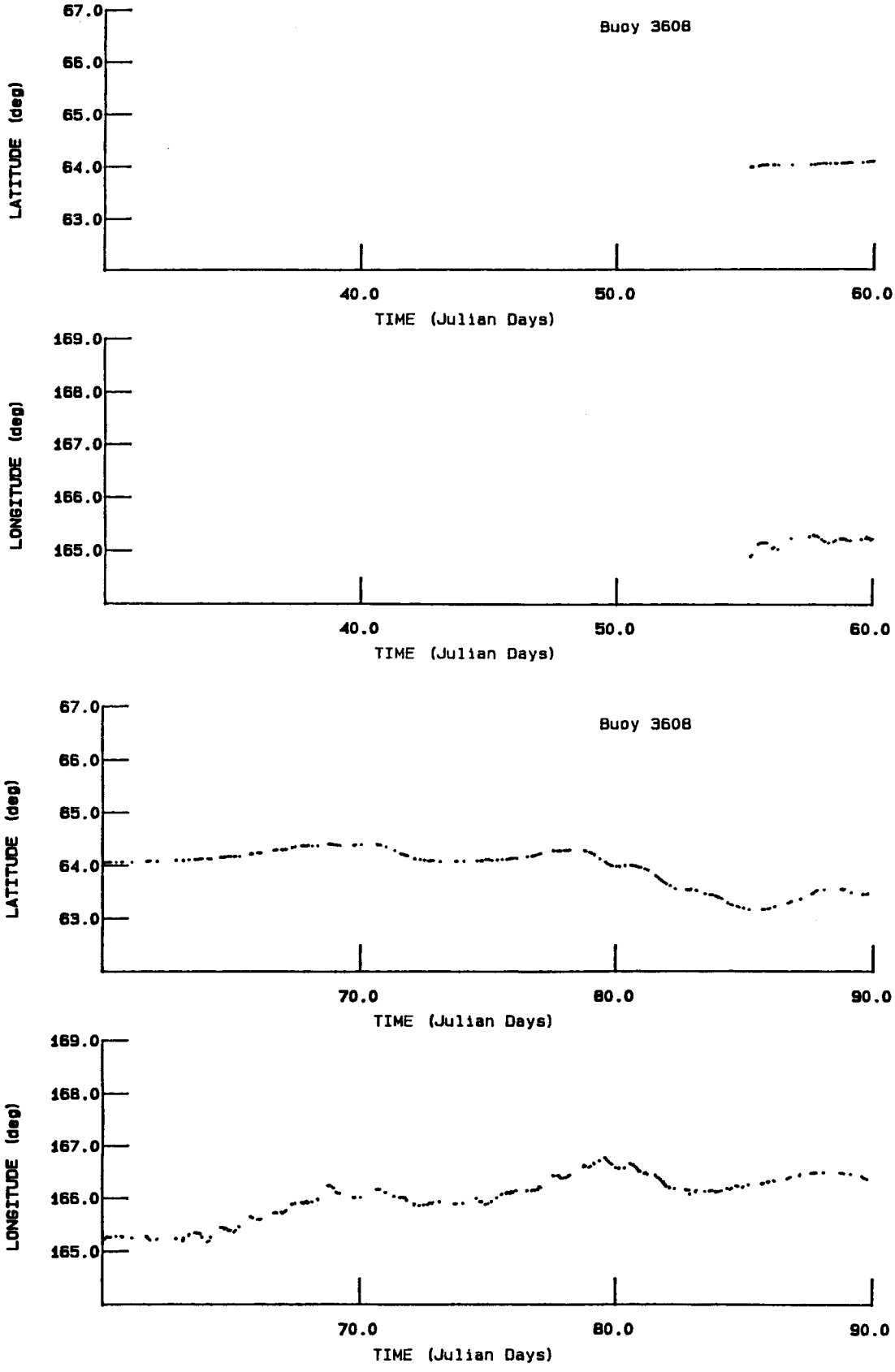

Figure 3.01. Buoy 3608 Raw Position Measurements.

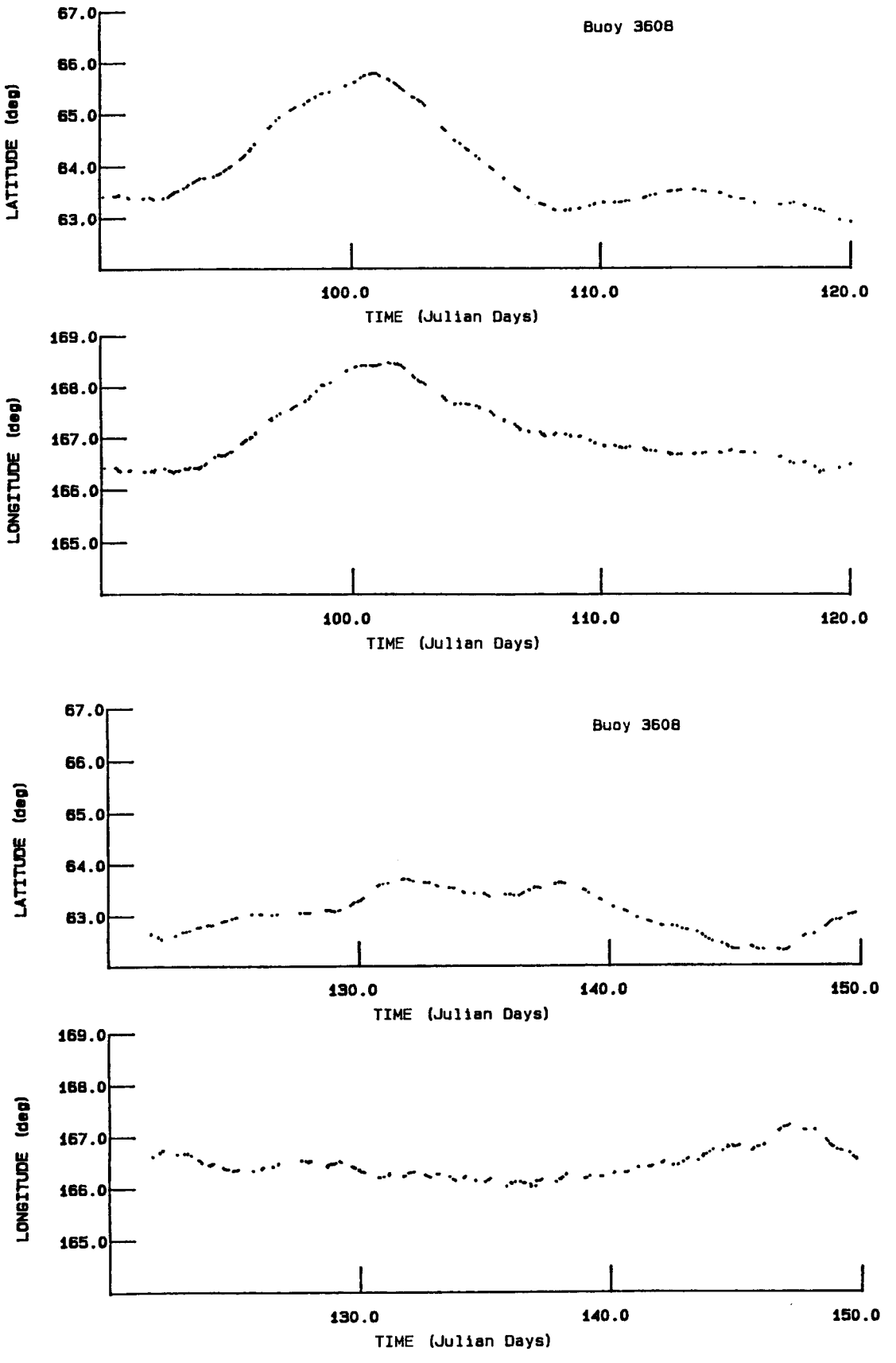

Figure 3.01. Buoy 3608 Raw Position Measurements (cont.)

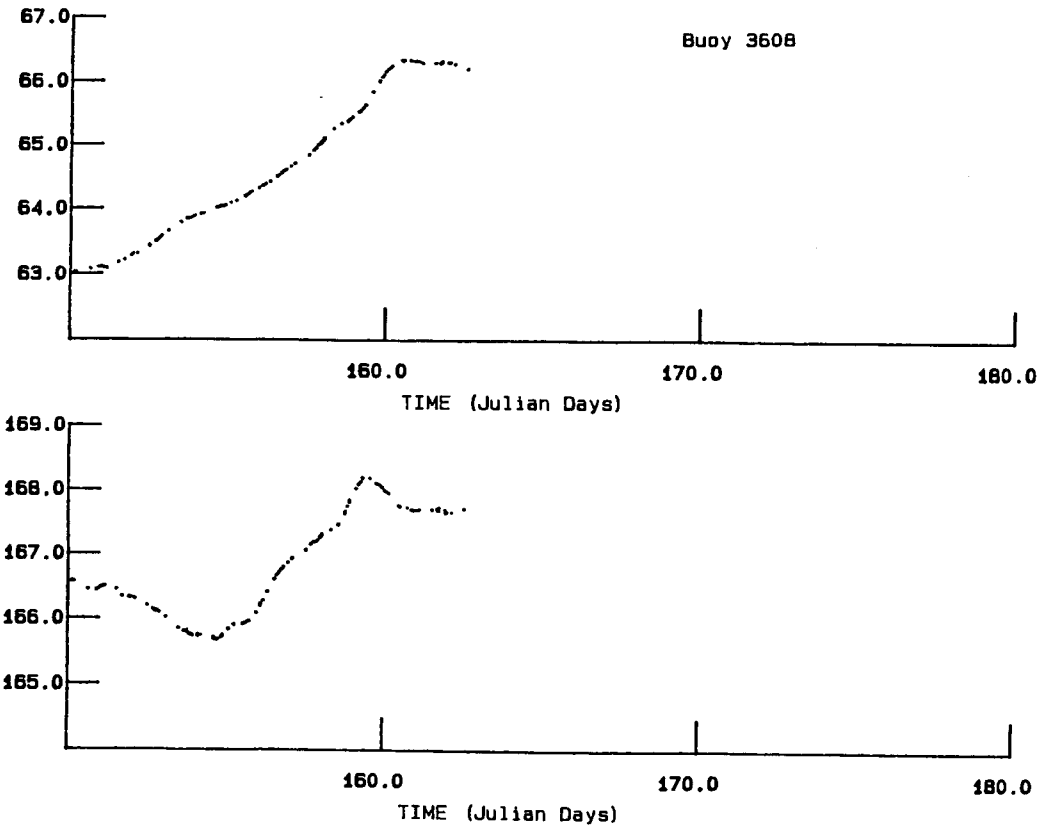

Figure 3.01. Buoy 3608 Raw Position Measurements (concl'd).

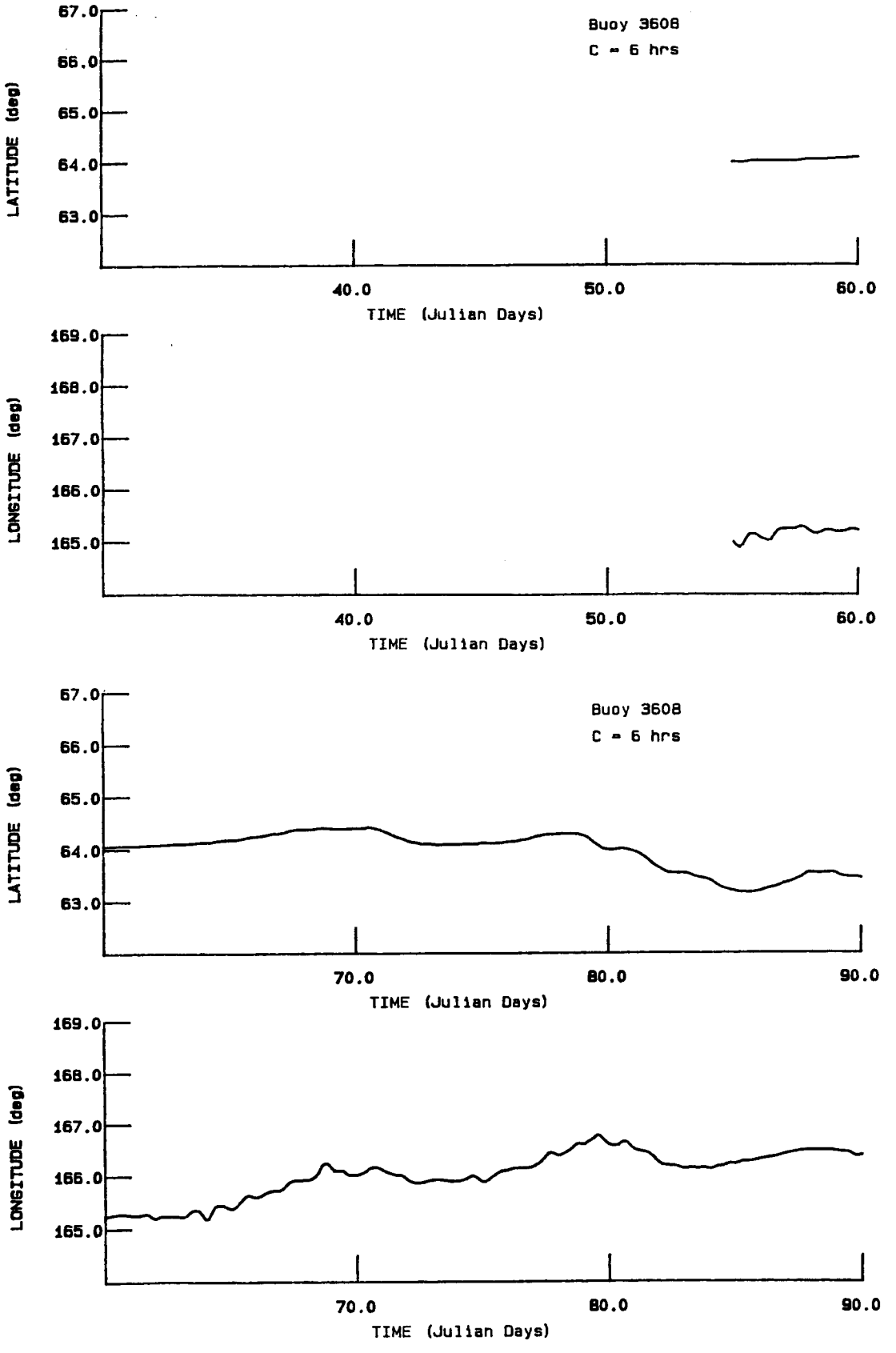

Figure 3.02. Buoy 3608 Interpolated Position Time History.

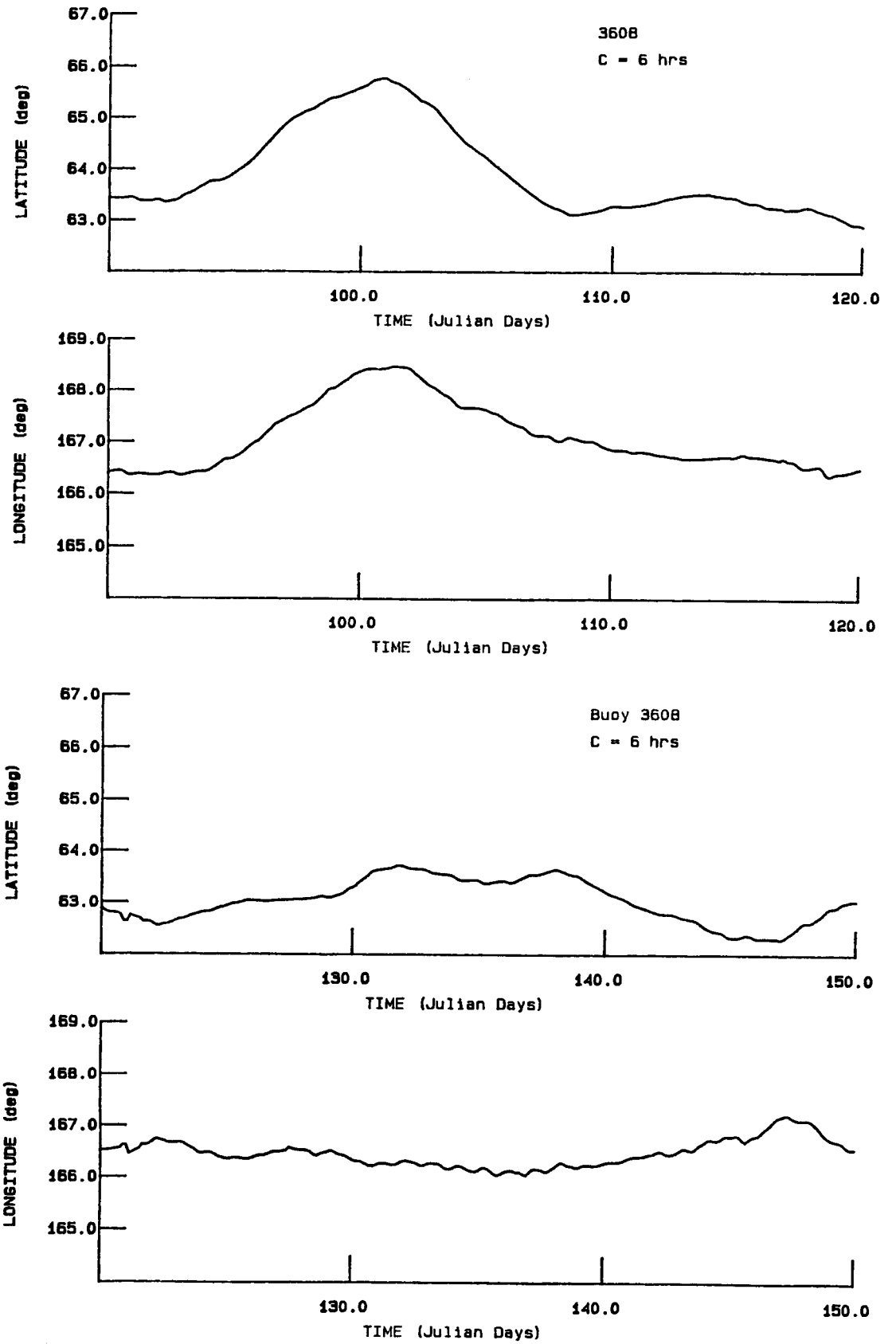

Figure 3.02. Buoy 3608 Interpolated Position Time History (cont.).

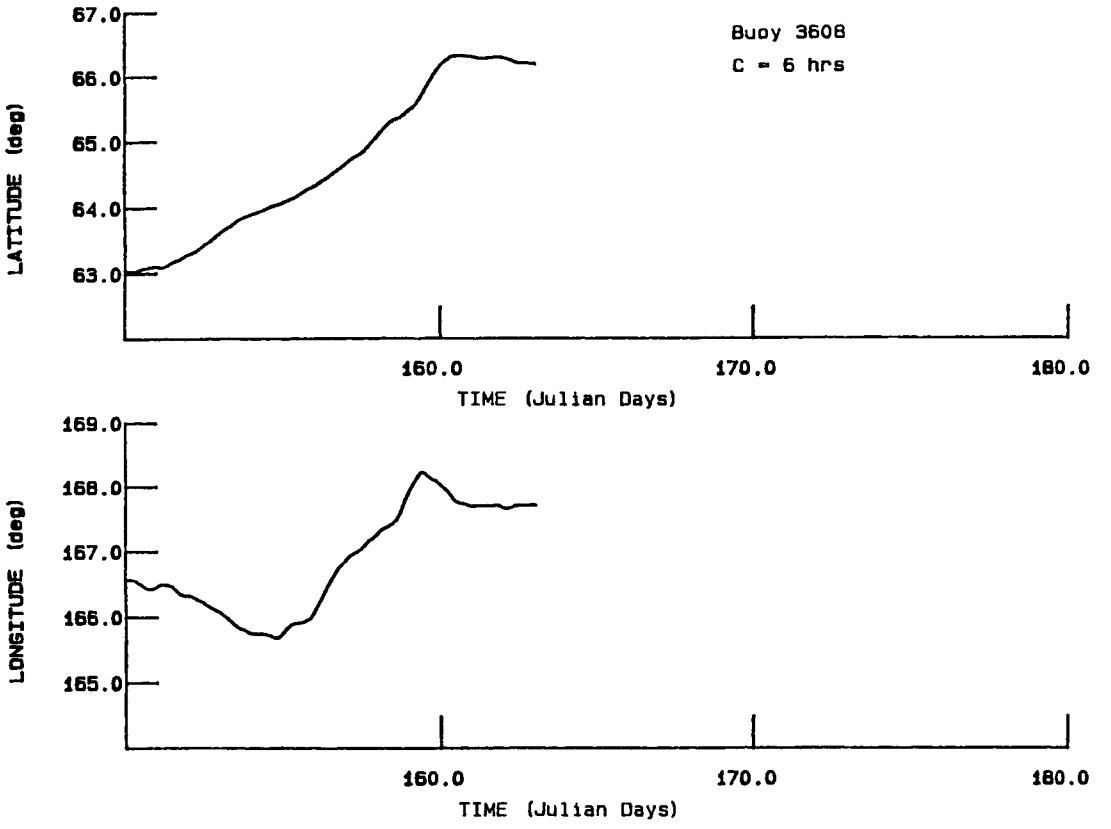

Figure 3.02. Buoy 3608 Interpolated Position Time History (concl'd).

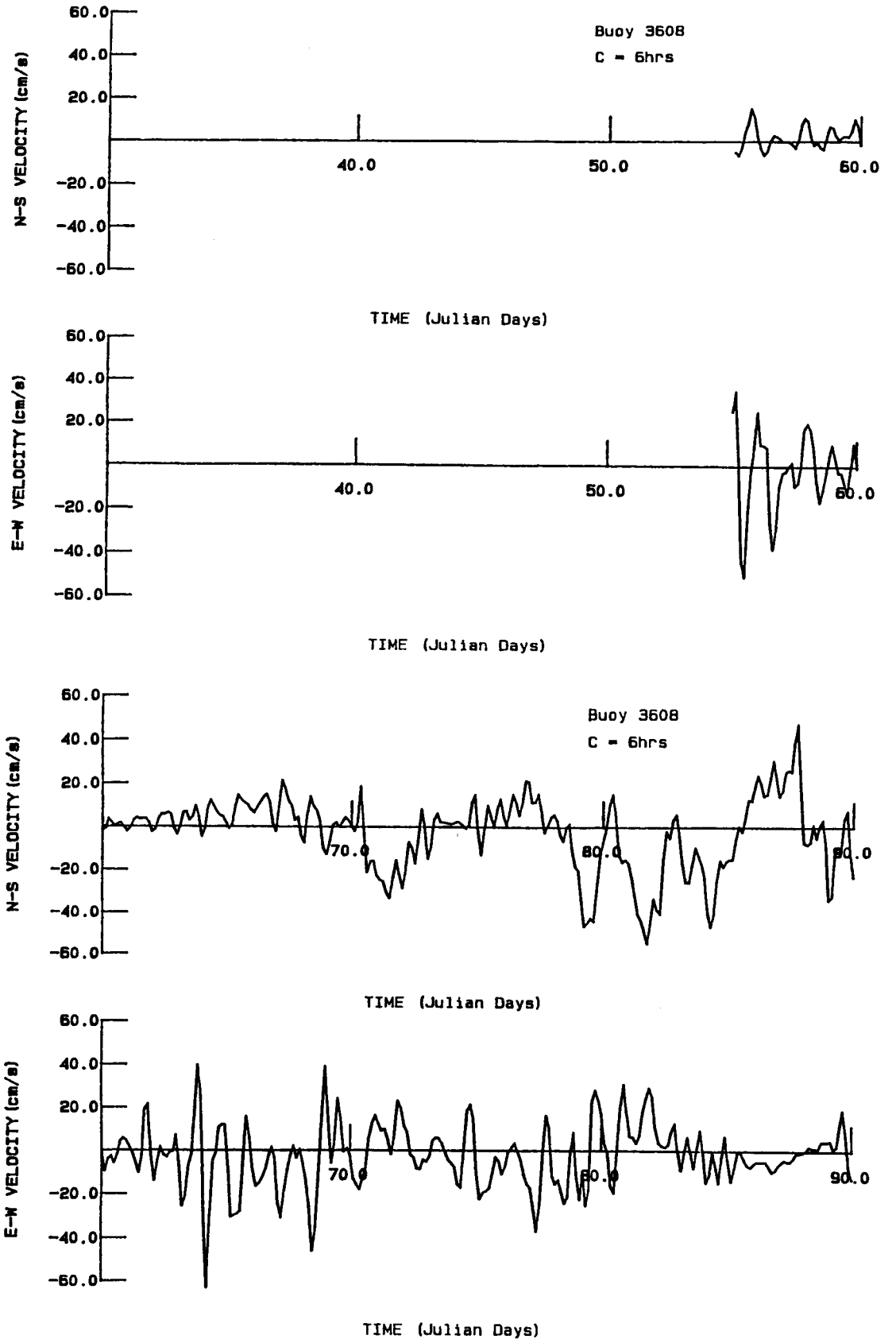

Figure 3.03. Buoy 3608 Velocity Time History Calculated from Interpolated Position History.

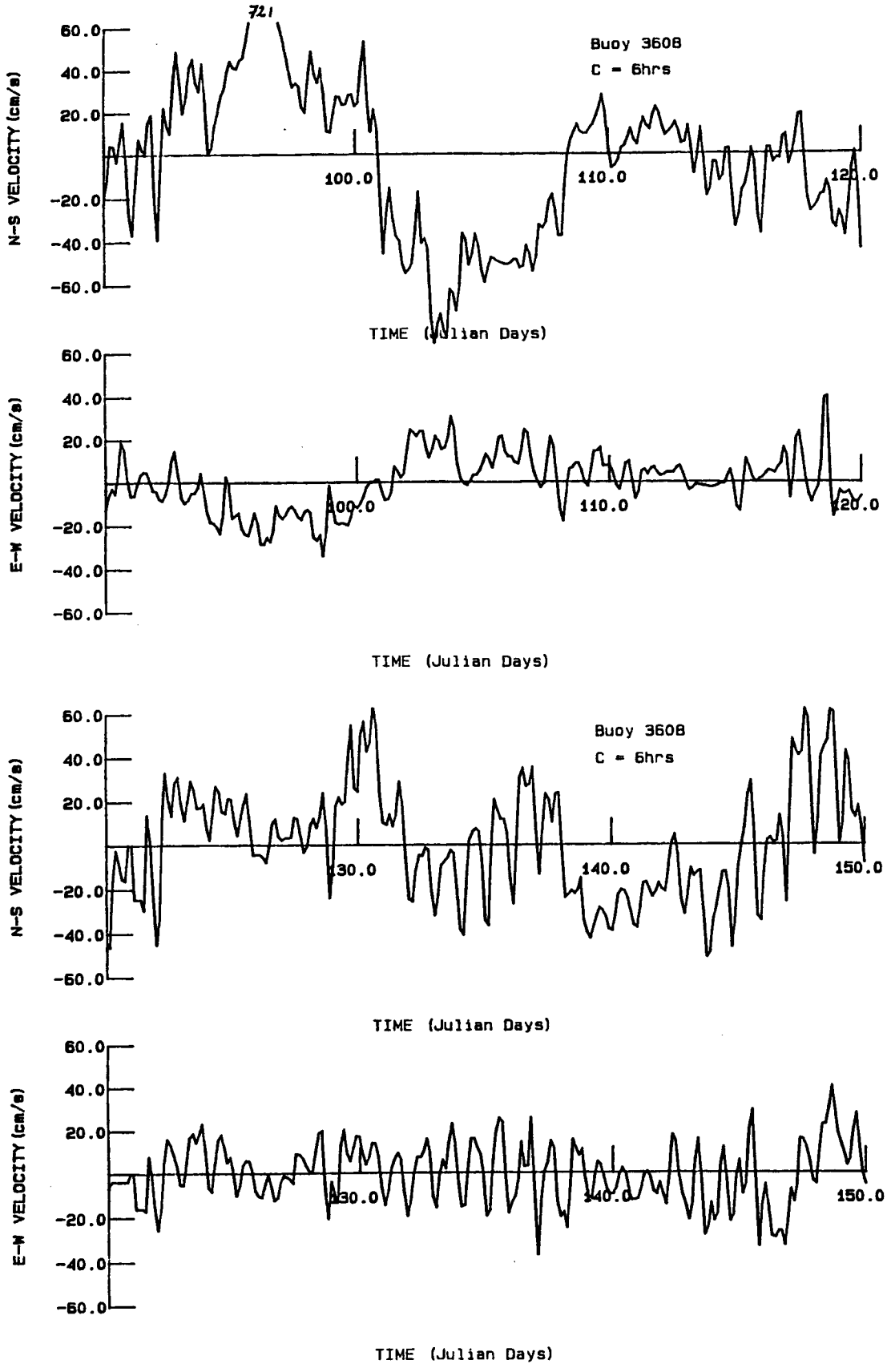

Figure 3.03. Buoy 3608 Velocity Time History Calculated from Interpolated Position History (cont.).

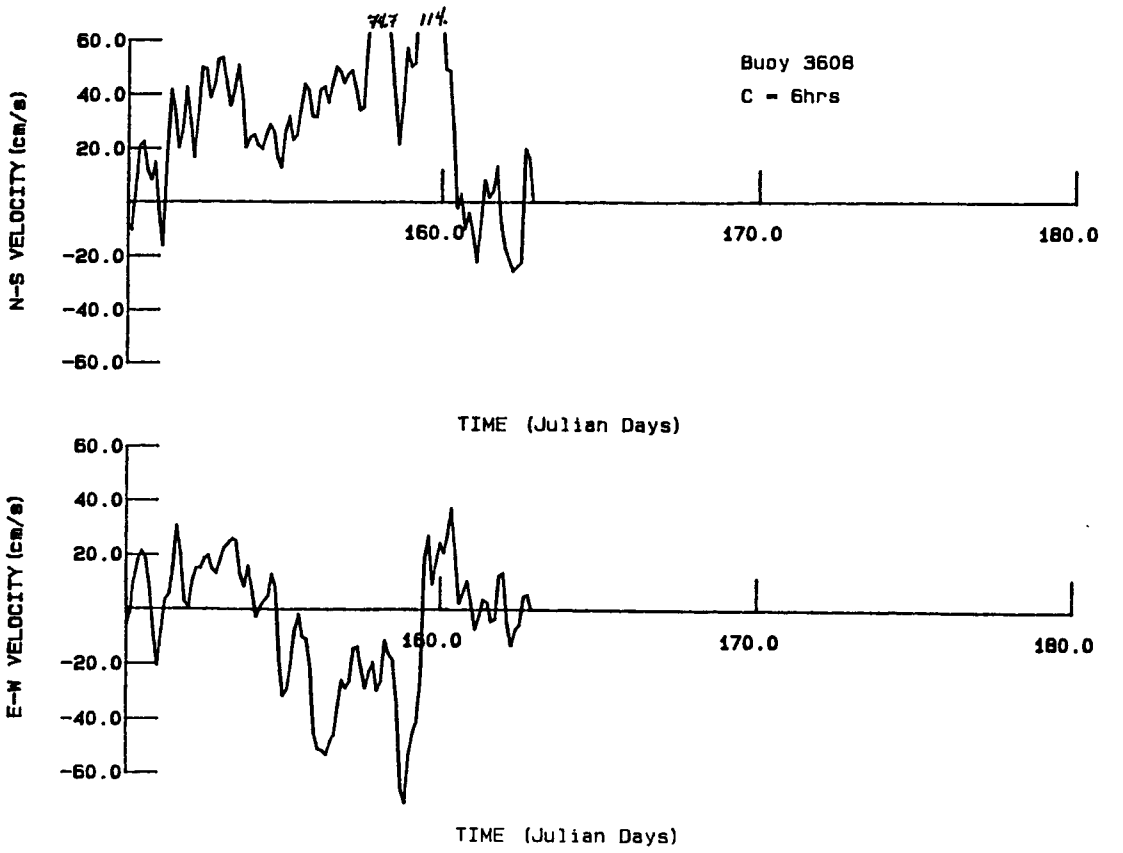

Figure 3.03. Buoy 3608 Velocity Time History Calculated from Interpolated Position History (concl'd).

4. ANALYTICAL METHODS

4.1. Optimal Interpolation

Assume that the set of N data points z_i, obtained from an experiment, represents one realization of a random process in time. The data values z_i are measurements of the dependent variable x that we wish to estimate. Since the data result from one realization of the random process, we consider the statistical properties of the process. The expectation E(x) is a time-dependent ensemble average of all values that the random variable may take weighted by the probability of occurrence. The second moment $E(x^2)$, the expectation of the square of x is found similarly. The variance of the random variable x, denoted by σ_x^2, is the mean squared deviation from its mean. The variance is related to the first two moments by (e.g. Gelb, 1974)

$$\sigma_x^2 = E(x^2) - [E(x)]^2. \qquad (4.1)$$

For simplicity, we assume that the average value of the data has been subtracted from the z_i. Our attention is focused on estimating variations about the average, and we assume that the average is added back at the end of the analysis.

4.1.1. Estimating Position. Let x represent either the latitude ϕ or the longitude λ, and consider each variable separately. We estimate the value of x by forming a linear combination of measured values

$$\hat{x}(t) = \sum_i \alpha_i(t)\, z_i \qquad (4.2)$$

where the coefficients α_i are determined at each time. The relationships that determine the coefficients result from the

assumptions used to make the estimate optimal.

The error between the estimate $\hat{x}$ and the true value x is

$$\varepsilon = \hat{x} - x. \tag{4.3}$$

The expectation of the square of the error ε may be expressed as a function of the coefficients as

$$E(\varepsilon^2) = E\left(\left[\sum_i \alpha_i(t)\, z_i - x\right]^2 \right). \tag{4.4}$$

This second moment is minimized at each time to determine the optimal estimate. The minimum value is found by taking the derivative of $E(\varepsilon^2)$ with respect to each coefficient α_j. As a result, for each value of j=1,2,..N, we obtain

$$\sum_i \alpha_i(t)\, E(z_i z_j) - E(x z_j) = 0 \tag{4.5}$$

where the order of the ensemble average and the summation are interchanged because both are linear operators.

The measurements differ from the value x_i (which is the value of x at time t_i) by the measurement error ε_i so that

$$z_i = x_i + \varepsilon_i. \tag{4.6}$$

The measurement errors are taken into account by expanding

$$E(z_i z_j) = E(x_i x_j) + E(x_i \varepsilon_j) + E(\varepsilon_i x_j) + E(\varepsilon_i \varepsilon_j) \tag{4.7}$$

and

$$E(x z_j) = E(x x_j) + E(x \varepsilon_j).$$

But if the error ε_j is uncorrelated with the variable x, and with other errors ε_i, then

$$\begin{aligned} E(x_i \varepsilon_j) &= 0 \\ E(\varepsilon_i x_j) &= 0 \\ E(x \varepsilon_j) &= 0 \end{aligned} \tag{4.8}$$

and

$$E(\varepsilon_i \varepsilon_j) = \sigma^2 \delta_{ij}$$

where σ is the standard deviation of the measurement errors. Substituting back into the equations governing the coefficients α_i gives

$$\sum_i \alpha_i \left[E(x_i x_j) + \sigma^2 \delta_{ij} \right] - E(x x_j) = 0 \qquad (4.9)$$

where the coefficients $\alpha_i(t)$ are evaluated at any time t by likewise evaluating the function x(t) at the same time.

The second moment of the process $E(x x_j)$ must be specified independently to solve for the coefficients α_i. If the process is stationary, then the correlation between x and x_j is a function of the time difference $t-t_j$. Previous experiments with different functional forms led us to assume that

$$E(x x_j) = \sigma_x^2 \, R(t-t_j) \qquad (4.10)$$

where the autocovariance function R is the error function

$$R(t-t_j) = \exp\left[-|t-t_j|/C \right]^2. \qquad (4.11)$$

The parameter C is a constant that defines the decay of the correlation with time, and σ_x is the standard deviation of x.

This form of the autocovariance function cannot describe the ice motions completely because the motions include both tidal and inertial oscillations (roughly 12 and 24 hour periods) and wind-driven variations (roughly 2-10 day periods). We tried to use an autocovariance function that included both the tidal cosine functions and the longer-term exponential decay, but the OI method failed. The problem arose when two or more data points were too-highly correlated. Even when data were pre-conditioned by averaging nearby data points, the system of linear equations was ill-conditioned, and could not be solved for the

coefficients. To circumvent this problem, the smaller time constants shown in Table 4.1 were used, but the local mean and trend were removed from the signal at each time. This step allowed us to track the short-term oscillations, independent of any knowledge of longer-term behavior. The excellent visual comparison of the interpolated values (Fig. 3.01) with the raw position data (Fig. 3.02) confirm that this approach was reasonable.

4.1.2. Parameters for Sea Ice Motions. The parameter C of the autocovariance function used to estimate either latitude or longitude histories (4.11) typically had a value of 6 hours. This value was chosen primarily by experimenting with the data. First, since roughly 12 data points were available daily, the highest frequency oscillations that could be resolved had a period of about 4 hours, which required C to be at least this order of magnitude. Second, the autocorrelation function for sea ice motions is unknown so we could not objectively define the independent time scale. Third, we tried several values of C ranging from 6 hours to 2 days and found that the power spectral density was unchanged if 6 or 12 hours was used, and that high frequency oscillations were reduced if longer times were used. Therefore, we chose C to be either 6 or 12 hours for most buoys, and used a larger value only when buoy transmissions were irregular or less frequent than normal. The final test on this choice was visual. If the resulting graphs of interpolated positions appeared to describe behavior in a reasonable way, then that set of parameter values was used. The normal position measurement errors were estimated to be 300 meters based on

measurements taken prior to deployments. Buoy 3620 transmitted irregularly and the pre-deployment measurements indicated that errors were on the order of 2km. Table 4.1 describes the constant values used for each buoy.

Table 4.1. Optimal Interpolation Parameters. The constant C represents the autocovariance time constant in equation (4.11), and E represents the estimated standard measurement error.

Buoy	C(hr)	E(km)
3607	6	.3
3608	6	.3
3609	6	.3
3610	12	.3
3611	48	.3
3612	6	.3
3613	6	.3
3614	6	.3
3615	6	.3
3616	12	.3
3617	6	.3
3620	48(a)	2.
3621	12	.3
3622	6	.3
3623	12	.3
3624	6	.3
3625	6	.3

Note (a). The latitude time constant was 48hr, while the longitude time constant was 72hr.

4.1.3. Error Estimate. The variance in the error is estimated by determining the expectation of the square error, given by equation (4.4). The binomial product is expanded into

$$E(\mathcal{E}^2) = E(\hat{x}\hat{x}) - 2E(\hat{x}x) + E(xx). \qquad (4.12)$$

Expanding the first term gives

$$E(\hat{x}\hat{x}) = \sum_j \alpha_j \sum_i \alpha_i \, E(z_i z_j) \qquad (4.13)$$

which by equation (4.5) reduces to

$$E(\hat{\hat{x}}x) = \sum_j \alpha_j E(xz_j) \qquad (4.14)$$

Similarly, the second term may be expanded into

$$E(\hat{x}x) = \sum_i \alpha_i E(xz_i). \qquad (4.15)$$

The combination of the three terms is written as

$$E(\varepsilon^2) = \sigma_x^2 [\ 1 - \sum_i \alpha_i R(t-t_i)\ ]. \qquad (4.16)$$

4.1.4. Optimal Estimation of Velocity from Position Measurements. Gandin (1965, pp. 69-70) states that any linear combination of values determined from an optimal estimate at different times is also an optimal estimate of the variable defined by the same linear combination. Therefore, if the velocity is estimated as the difference between two position estimates separated in time by an increment, then this velocity is also an optimal estimate. Furthermore, if the time increment is reduced in the limit to zero, then the resulting derivative is the optimal estimate of the rate of change of position. This important property implies that we can use the optimal estimate of the positions determined from the position measurements to obtain our optimal velocity estimate, and this result holds whether we calculate a time-averaged velocity (as the difference between two positions separated by a time increment 2Δ) or an instantaneous velocity (as the local slope of the position function). In either case, we use a linear combination of position measurements.

Our attention turns toward determining the velocity from the set of position data. Since (4.2) is a continuous function of time, the expression may be differentiated to determine the

velocity. This derivative gives the instantaneous velocity, or the slope of the position curve

$$\hat{v} = \sum_i \beta_i z_i . \tag{4.17}$$

where

$$\beta_i = d\alpha_i/dt \tag{4.18}$$

is the derivative of the coefficients in the linear position estimate. These derivatives may be determined by taking the time derivative of (4.9) which defines the coefficients α_i. The velocity coefficients β_i therefore satisfy

$$\sum_i \beta_i E(z_i z_j) - d[E(xz_j)]/dt = 0 \tag{4.19}$$

where the derivative of the autocorrelation may be determined explicitly by differentiating (4.10) and (4.11). This allows the slope of the position curve to be determined explicitly in terms of the position measurements. There is no need to approximate the velocity as a difference between two position estimates divided by the time interval.

In the above discussion, the instantaneous velocity, the slope of the position function, was estimated. In the next paragraphs we study the average velocity over a time interval 2Δ, which is estimated by forming the difference between positions separated by this time interval divided by 2Δ. The average velocity over a time interval 2Δ is the difference in position divided by the time interval

$$\bar{v}(t) = \frac{x(t+\Delta) - x(t-\Delta)}{2\Delta} \tag{4.20}$$

The coefficients needed to estimate the average velocity using

(4.17) are no longer the time derivatives of α_i, but are the differences between the coefficients in the position estimate

$$\beta_i(t) = \frac{\alpha_i(t+\Delta) - \alpha_i(t-\Delta)}{2\Delta}. \qquad (4.21)$$

The time-shifted coefficients can be determined explicitly at each time when the average velocity is to be estimated.

The expectation of the square of the velocity error $E(\hat{v}-v)^2$ is found using the same analytical methods presented in section 4.1.3 for the position. The result is

$$\frac{E(\hat{v}-v)^2}{\sigma_x^2} = \frac{1-R(2\Delta)}{2\Delta^2} - \sum_i \beta_i \frac{R(t+\Delta-t_i)-R(t-\Delta-t_i)}{2\Delta} \qquad (4.22)$$

The velocity calculated by forming differences of the position estimates was insensitive to the choice of averaging times ranging from 10min to 2hrs. This result occurred because of the values of the time constant C used in the OI analysis, and does not imply that shorter-term peaks do not exist. In fact, we know that local cracking of the ice and other processes can cause the ice to accelerate on shorter time scales, but these individual motions are generally small and within the 300-m measurement error of the buoys. We ignored them because the ARGOS-based measurement system cannot describe them accurately.

The position measurements are provided as latitude and longitude values and the estimates described previously are valid for estimating these geographic coordinates and the time rate of change of them. However, the velocity components must be transformed into rates of change of distance along the earth's

surface if we are to give physical meaning to the velocity components. The northward velocity component is determined from the rate of change of latitude by

$$v_y = \rho \, d\Phi/dt \tag{4.23}$$

and the eastward velocity component is determined from the rate of change of longitude by

$$v_x = -\rho \cos\Phi \, d\lambda/dt \tag{4.24}$$

where Φ is the latitude, λ is the longitude (measured positive westward), and we have assumed that the earth is a sphere of radius ρ. The average velocity components are determined by replacing these derivatives with differences and using the average latitude in the cosine function.

4.2. Complex Regression

To evaluate the relative importance of the wind and current on the ice motions, we study the correlations between these variables. Furthermore, since free-drift sea ice models suggest (e.g. Pritchard, 1984) that the ice motion relative to the ocean current (the variable v_r measured by the current meters) is a known function only of the wind, we wish to compare the ice velocity to the relative current velocity.

Although the correlation between two scalar variables is well-understood, it is not so simple to compare two vector variables. The respective correlations between the various velocity components do not give a particularly clear understanding of the relationship between the vectors themselves. To circumvent this difficulty, we use the complex regression, which allows us to study the relationship between pairs of two-dimensional vectors.

The ice velocity vector v may be regressed onto the wind vector w by introducing the linear relationship

$$v = Aw + B \tag{4.25}$$

where A and B are complex constants. The regression is obtained by determining the values A and B that give the best fit to the data in a least squares sense. This is accomplished in the usual way, except that care is required to include the complex conjugate as necessary.

The two complex constants must satisfy the relationships

$$A \sum w_i w_i^* + B \sum w_i^* = \sum v_i w_i^* \tag{4.26}$$

$$A \sum w_i + B N = \sum v_i \tag{4.27}$$

where w_i^* is the complex conjugate of w_i. These equations can be solved for coefficients A and B using standard complex algebra.

The mean-squared error between all data points and the regression curve is

$$\sigma_\varepsilon^2 = \sum \varepsilon_i \varepsilon_i^* / N \tag{4.28}$$

where $\varepsilon_i = v_i - (Aw_i + B)$ is the error at each data point.

The variance explained by the regression is equal to the total variance of the variable

$$\sigma_v^2 = \sum v_i v_i^* / (N-1) \tag{4.29}$$

less the unexplained variance shown in the error. Therefore, the variance explained by the regression σ is

$$\sigma^2 = \sigma_v^2 - N\sigma_\varepsilon^2/(N-1). \tag{4.30}$$

A similar analysis may be performed for each pair of two-dimensional vectors.

5. RESULTS: NORTON SOUND

5.1. Ice Trajectories

Eleven buoys were deployed in Norton Sound during three different time periods. The deployment pattern was designed to obtain ice motion, wind and current data over broad areas throughout the winter. The ice trajectories for each buoy, obtained after filtering tidal and other high frequency oscillations from the data, are presented in Appendix B.

In general within Norton Sound, the ice drifts westward, until it passes a line roughly connecting Nome and the Yukon delta. Then the ice tends to move northward and southward in episodes of roughly 3-15 days. These large-scale reversals appear to be related primarily to the currents existing at the time. Since the long-term average current is northward, one should expect this to be the direction most likely taken by the ice floes. This conjecture is confirmed by the drift of buoys 3608, 3611, 3613, and 3616. However, the southward movement of buoy 3612 shows that other trajectories are possible.

The slow westward drift of ice as indicated by the movement of buoys 3607 and 3609 points toward Norton Sound as a site for production of sea ice and its subsequent export into the northern Bering Sea where it is transported by the prevailing winds and currents. The strong north-south movements of buoy 3609 as it neared the mouth of Norton Sound indicate that the circulation inside the sound is different from that on the eastern Bering Sea proper.

These trends agree with observations by other investigators taken during different years (e.g. Stringer and Henzler, 1981; Thomas and Pritchard, 1981), and with the PMEL buoy data taken concurrently (Reynolds and Pease, 1984).

5.2. High Frequency Oscillations

High frequency oscillations in the ice motion arise from tidal and inertial oscillations, and from ice stress divergence. In Norton Sound we assume that ice stress divergence is not important, although nearshore ice motions can feel its influence.

The tidal oscillations in the northeastern Bering Sea and Norton Sound introduce large periodic oscillations to the ice velocity. Figures 3.03 and 5.01 depict the ice velocity observed by buoys 3608 and 3609, respectively. These results are consistent with the observations of Salo, Schumacher and Coachman (1983) and Mofjeld (1984) who have studied the tidal behavior in this region. The power spectral densities of the ice velocity for all three current meter buoys are presented in Figures 5.02 - 5.04.

5.3. Wind, Current and Ice Velocity

Buoys 3607 and 3609 were deployed in the interior of Norton Sound, while 3608 was deployed near the mouth of the sound. In addition to position measurements, these three buoys provided measurements of ocean current, wind, and air temperature every two hours.

Buoy 3607 transmitted for 13 days after deployment on February 6, and in that time, moved roughly 50 km southwestward.

The drift track showed one lateral excursion of 20 km which appeared to be due to a reversal of the wind over a 10-day period. Winds were northward over the first half of the deployment interval, shifting to southward during the second half. Both the currents and the ice drift reflected some influence of the wind, but neither was solely wind-driven (Fig. 5.05). The spectrum of ice velocity (Fig. 5.02) showed energy at the diurnal tidal frequency and also at frequencies less than about 0.5 cycles/day. The ice velocity time history indicated that the tidally-driven motion of buoy 3607 was mainly east-west, along the axis of Norton Sound. The trajectory of buoy 3607 thus reflects the influence of the winds at longer periods and currents at tidal periods.

Buoy 3608 was deployed on the ice near the mouth of Norton Sound on February 24 (Jd 55) and provided position and wind data until June 11 (Jd 162). The current meter operated until about Jd 100, ceased, and then resumed again for eight days just after Jd 150. The mean wind direction was toward the south, but there were intervals of strong winds toward the north (Fig. 5.06). For the first two weeks, the ice moved northwest out of Norton Sound, and then moved southward until about Jd 90. Beginning on Jd 92, when a major reversal of both the wind and current toward the north occurred, the ice moved over 250 km northward into Bering Strait by Jd 100. Both wind and current reversed again, and the ice moved about the same distance southward by Jd 110. After oscillating primarily north and south outside the mouth of Norton Sound, the ice began a major northward translation on Jd 147 and

passed through Bering Strait on about Jd 158. The wind and current reversed and set northward at the same time. The ice velocity during the major north-south episodes reached nearly 100cm/s. Currents relative to the ice remained small, generally less than 10cm/s, indicating that the currents and the ice moved similarly. Thus, the wind, current, and ice motion in the vicinity of Bering Strait tended to coincide. The reason is that all are likely related to the large scale, alongshore atmospheric pressure gradient. This agrees with Aagaard, et. al. (1985), who found that the meridional wind was well-correlated with the steric height difference between the Bering and Chukchi seas.

Buoy 3609 recorded wind and position data for five weeks beginning on February 27 (Jd 58). During that time, the net drift was about 120 km westward, ending at the mouth of the sound. Most of this westward translation took place in the first 20 days. Stick plots (Fig. 5.07) suggest only a weak relationship between the wind and the ice velocity for the first 20 days. The winds were primarily north-south while the ice motion was primarily toward the west. After about March 21 (Jd 80), the ice velocity showed a very different pattern which was characterized by three episodes of northward movement separated by three episodes of southward movement. Each episode lasted between two and three days. The concurrent winds were weak and variable. These ice motions after March 21 were clearly dominated by the stronger north-south currents outside of Norton Sound. The current meter of buoy 3609 failed about a week after deployment, so that there is no information about water motion over most of the deployment interval. However, the spectrum of

ice velocity (Fig. 5.02) showed energy at both the diurnal and semi-diurnal tidal frequencies, which in turn implies that the currents influenced the ice motion in this frequency range.

5.4. Correlations

Since free-drift models of ice motion indicate that the ice velocity relative to the current v_r is a function of wind velocity w, the correlation between these two variables is an indicator of the effect of the wind on the ice drift. Table 5.1 shows that 27, 35, and 0% of the relative ice velocity variance is related to the wind by this measure. This is less that the correlation between the ice velocity and wind directly, and the difference is probably caused by the correlation between wind and current.

A regression of the ice velocity onto the wind and current at buoy 3608 showed that the current accounted for 80% of the variance in the ice motion (see Table 5.1), while the wind accounted for 43% for the interval when current measurements were available. This implies that the current affected the ice motion significantly more than did the wind. The spectrum of ice velocity showed that most of the energy was at periods of about 5 days and longer, and that there was a relatively small contribution due to the diurnal tides. Similar correlations occur for buoys 3607 and 3609.

These correlations show that the current provides the dominant driving force for the longer-term ice motions.

Table 5.1. Comparison Between Wind, Ice Velocity, and Current for Norton Sound Drifting Buoys. Linear Regression Constants for Ice Velocity onto Wind (V-W), Ice Velocity onto Current (V-C), Current onto Wind (C-W), and Relative Current onto Wind (R-W). The parameters in this table satisfy $A = m \exp(i\theta)$ and $B = b_r + ib_i$, where A and B are used in equation (4.25), σ_y^2 and σ_x^2 are the variance of the dependent and independent variable respectively in the linear fit, and f is the fraction of variance of x described by y.

Buoy	N	m	θ	b_r	b_i	σ_y^2	σ_x^2	f
3607	15							
V-W		1.33	-25.9	-1.27	.56	94.2	23.0	.39
V-C		.89	28.3	-.11	1.46	94.2	70.2	.56
C-W		.97	-66.5	-2.15	-.98	70.2	23.0	.25
R-W		.87	-159.5	-.88	-1.55	54.2	23.0	.27
3608	54							
V-W		3.43	-.5	-3.46	8.80	650.2	24.2	.43
V-C		1.03	2.9	-1.26	2.75	650.2	487.3	.80
C-W		2.65	-6.6	-2.14	6.16	487.3	24.2	.34
R-W		.70	-166.0	.32	-.72	32.7	24.2	.35
3609	6							
V-W		1.35	-92.8	-.54	-1.59	28.7	7.8	.37
V-C		.81	15.0	-1.43	-3.14	28.7	34.3	.73
C-W		1.14	-111.9	1.05	1.66	34.3	7.8	.12
R-W		.31	113.1	.75	3.79	4.1	7.8	.00

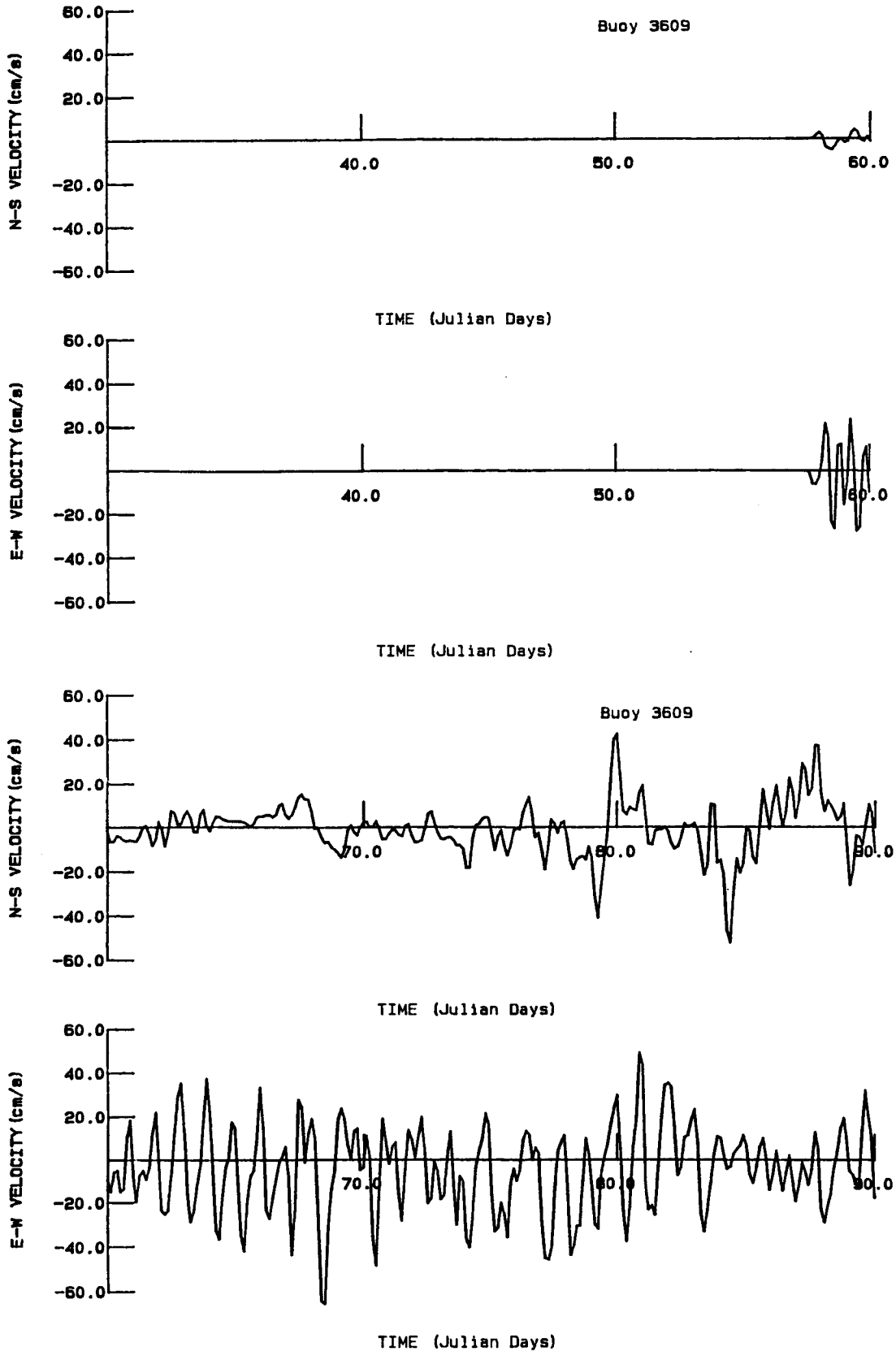

Figure 5.01. Buoy 3609 Velocity Time History Calculated from Interpolated Position History.

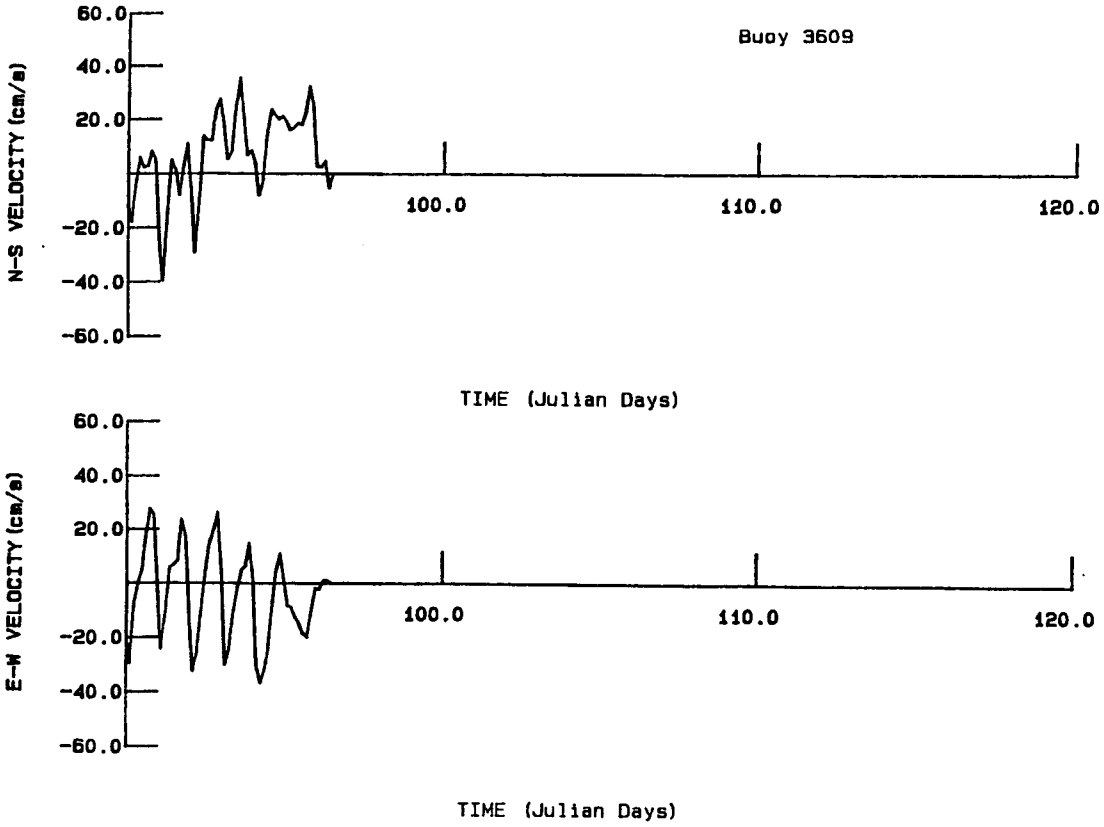

Figure 5.01. Buoy 3609 Velocity Time History Calculated from Interpolated Position History (concl'd).

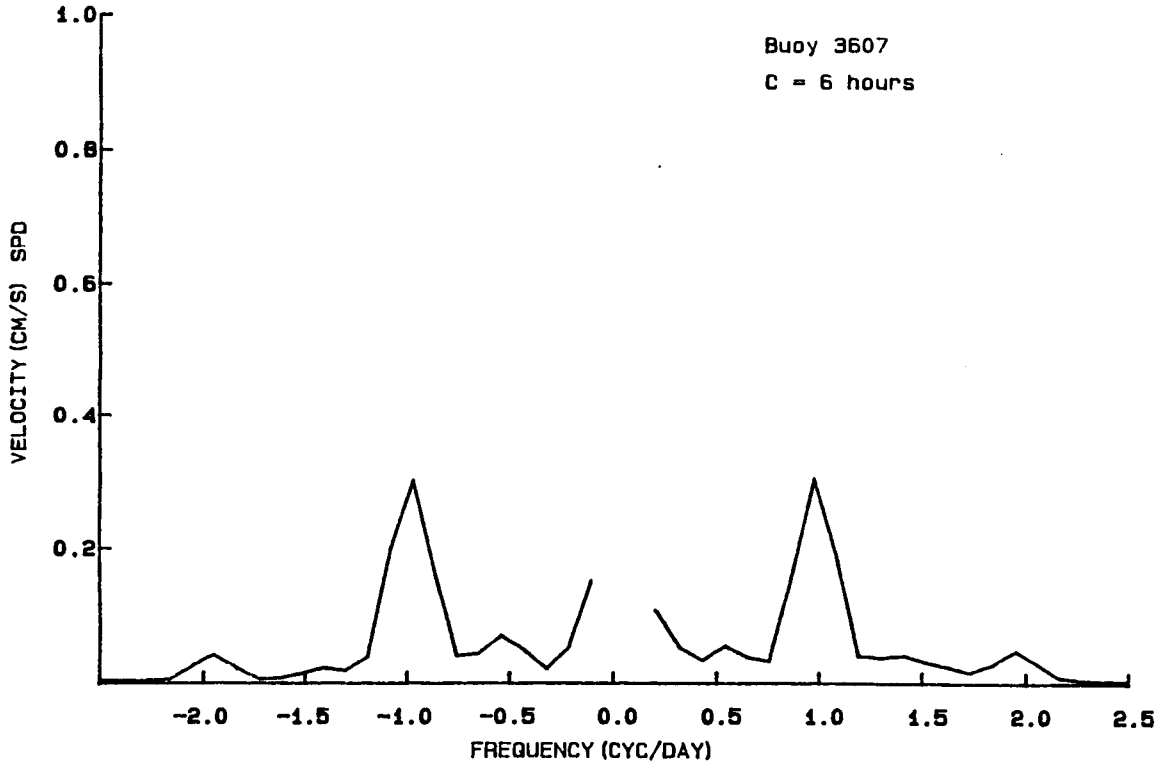

Figure 5.02. Buoy 3607 Ice Velocity Power Spectral Density.

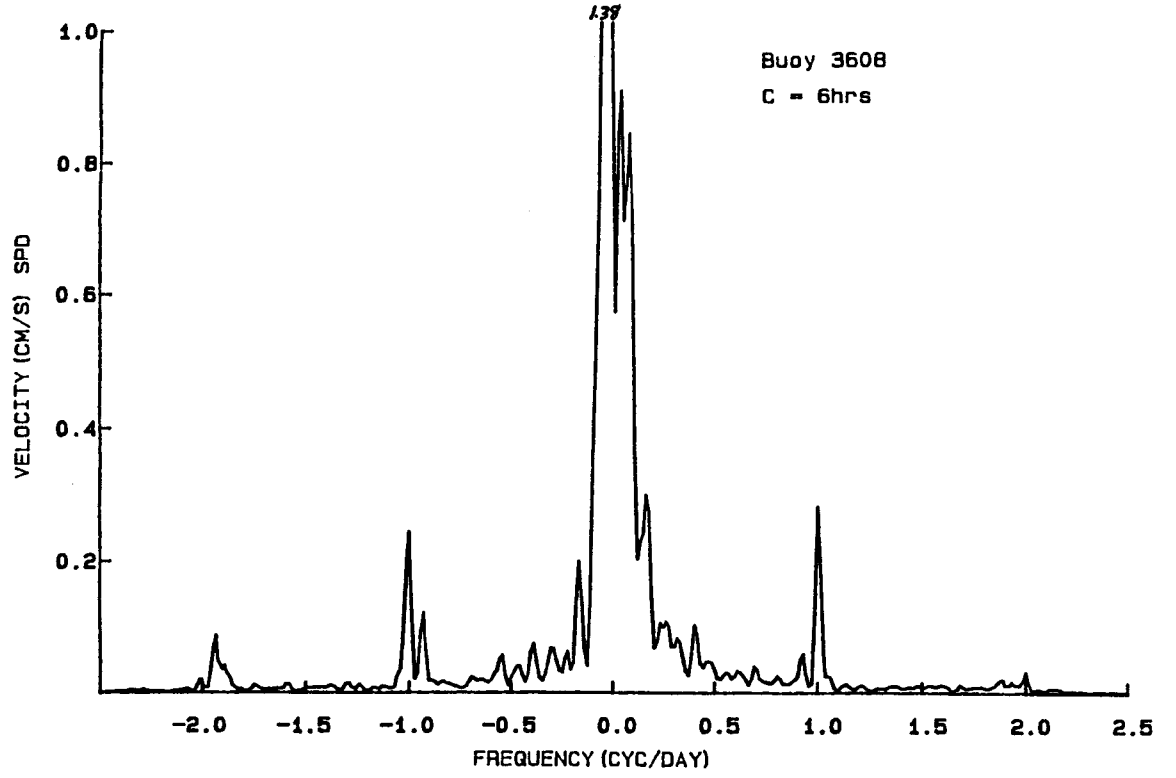

Figure 5.03. Buoy 3608 Ice Velocity Power Spectral Density.

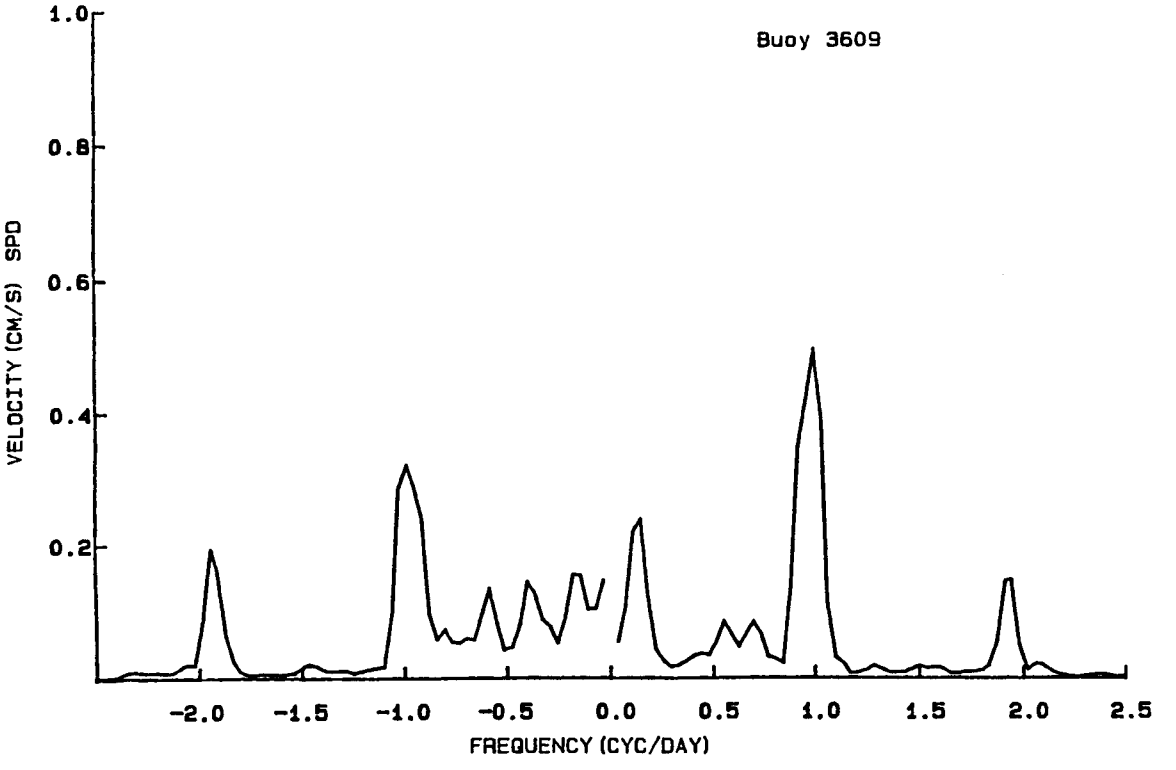

Figure 5.04. Buoy 3609 Ice Velocity Power Spectral Density.

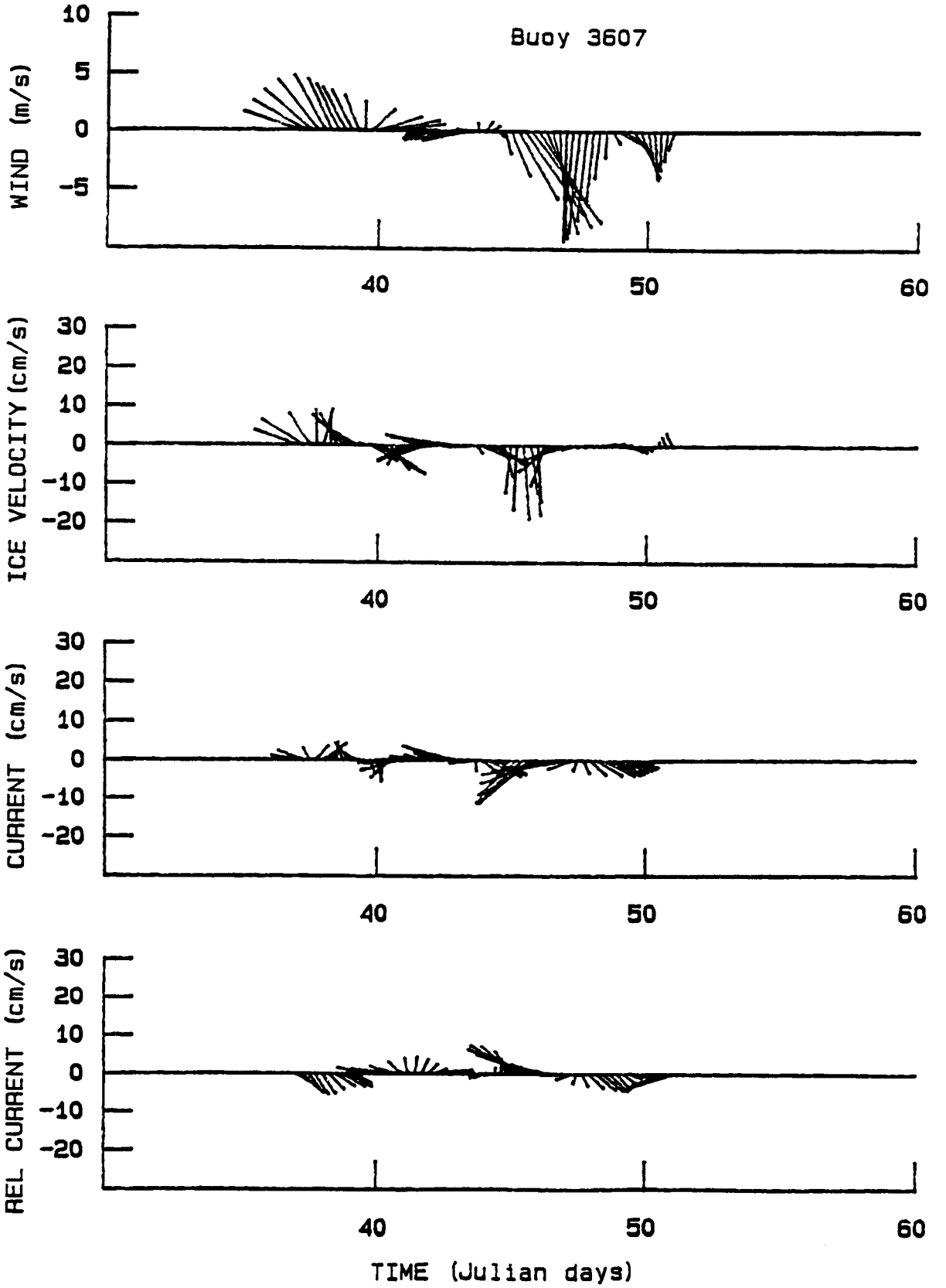

Figure 5.05. Buoy 3607 Stick Plots of Daily Average Wind, Ice Velocity, Current, and Relative Current.

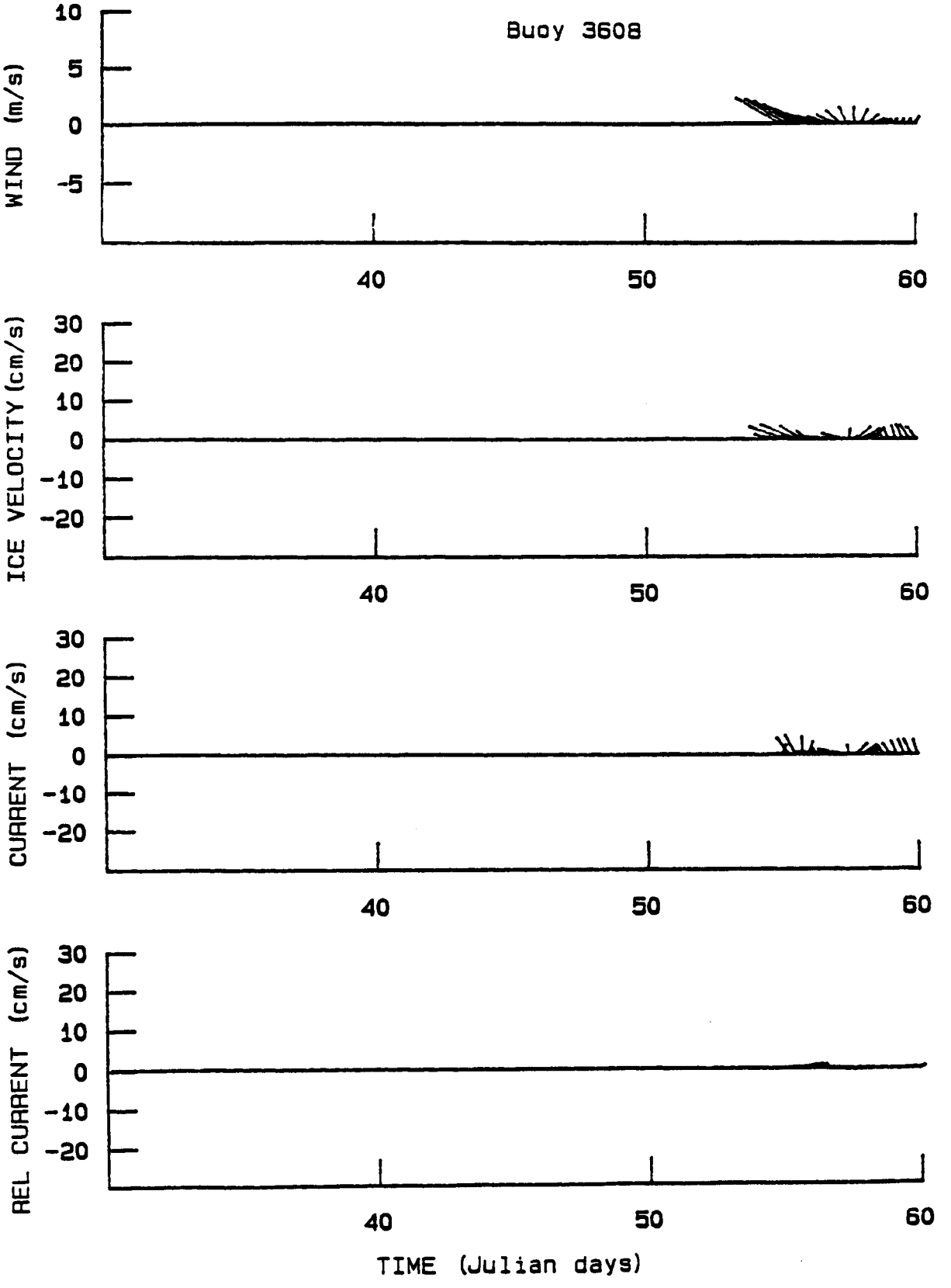

Figure 5.06. Buoy 3608 Stick Plots of Daily Average Wind, Ice Velocity, Current, and Relative Current.

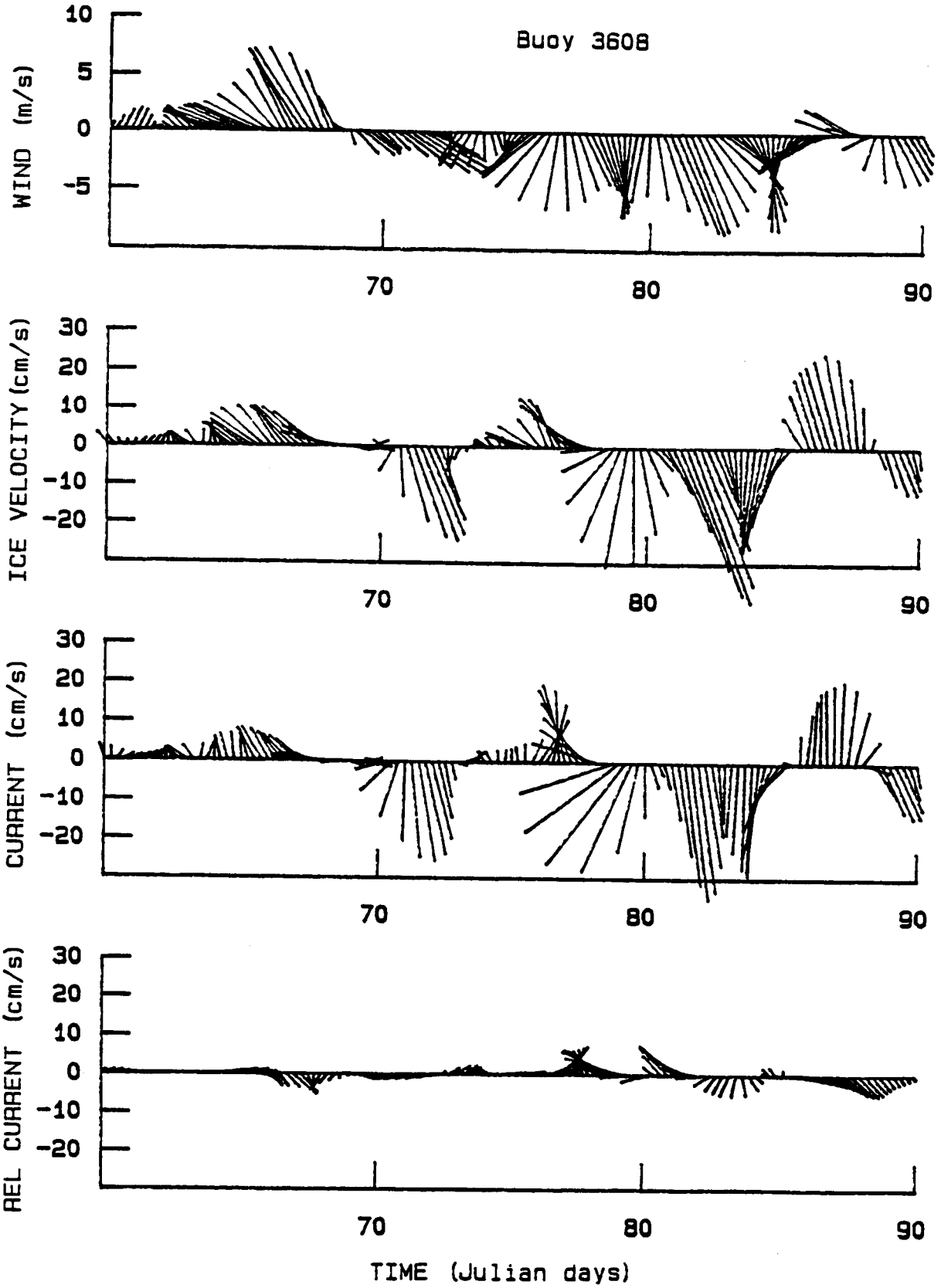

Figure 5.06. Buoy 3608 Stick Plots of Daily Average Wind, Ice Velocity, Current, and Relative Current (cont.).

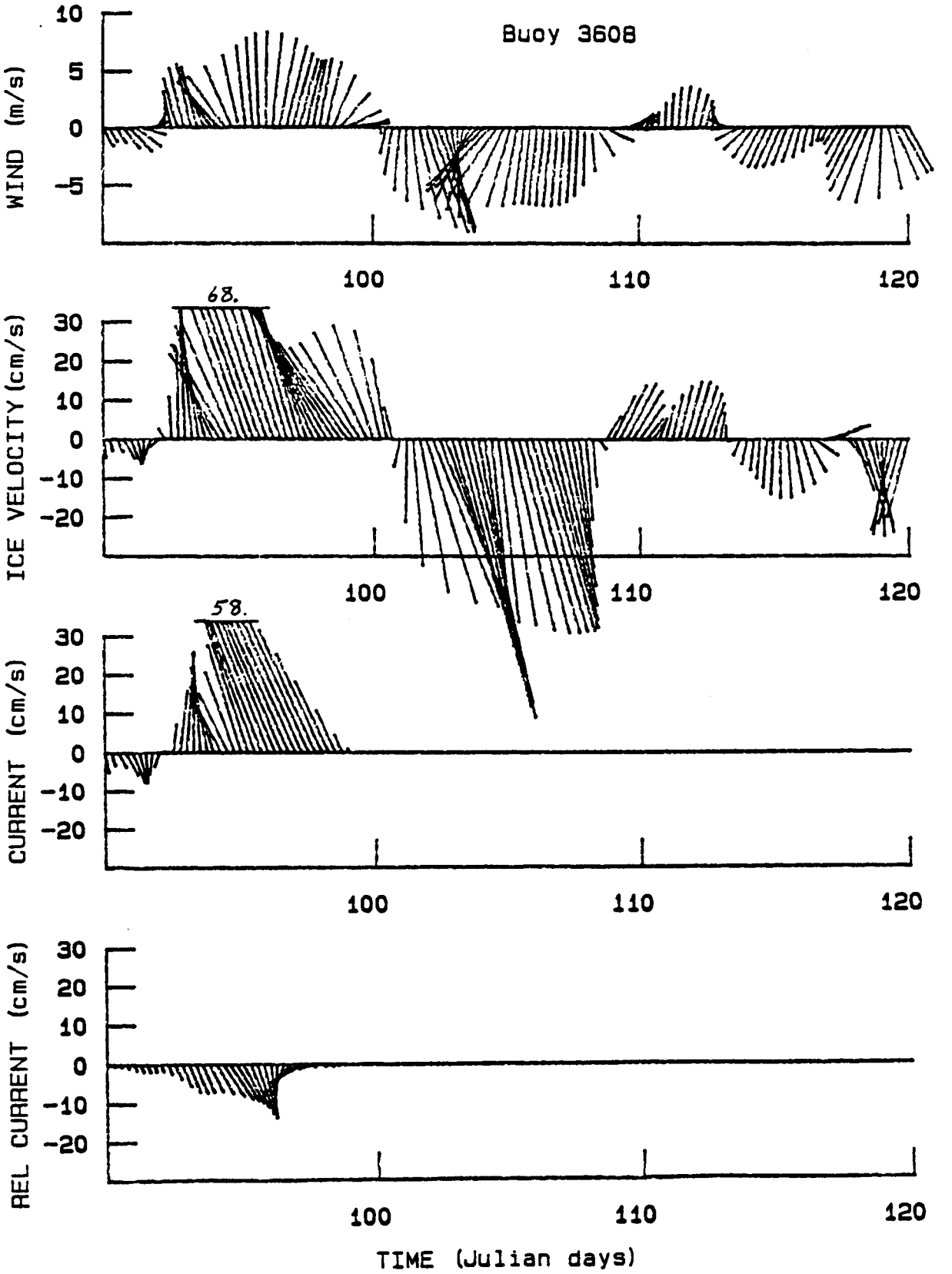

Figure 5.06. Buoy 3608 Stick Plots of Daily Average Wind, Ice Velocity, Current, and Relative Current (cont.).

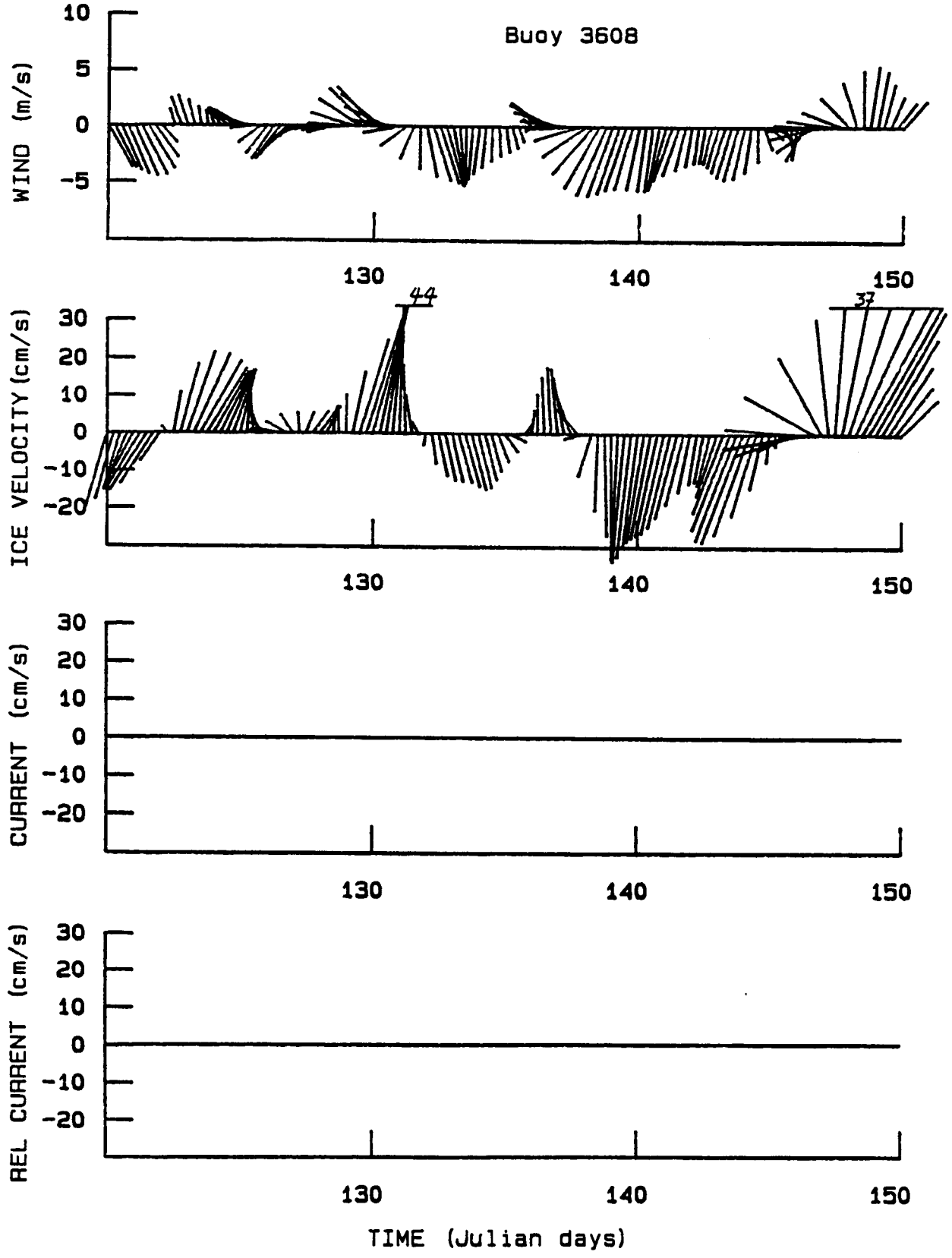

Figure 5.06. Buoy 3608 Stick Plots of Daily Average Wind, Ice Velocity, Current, and Relative Current (cont.).

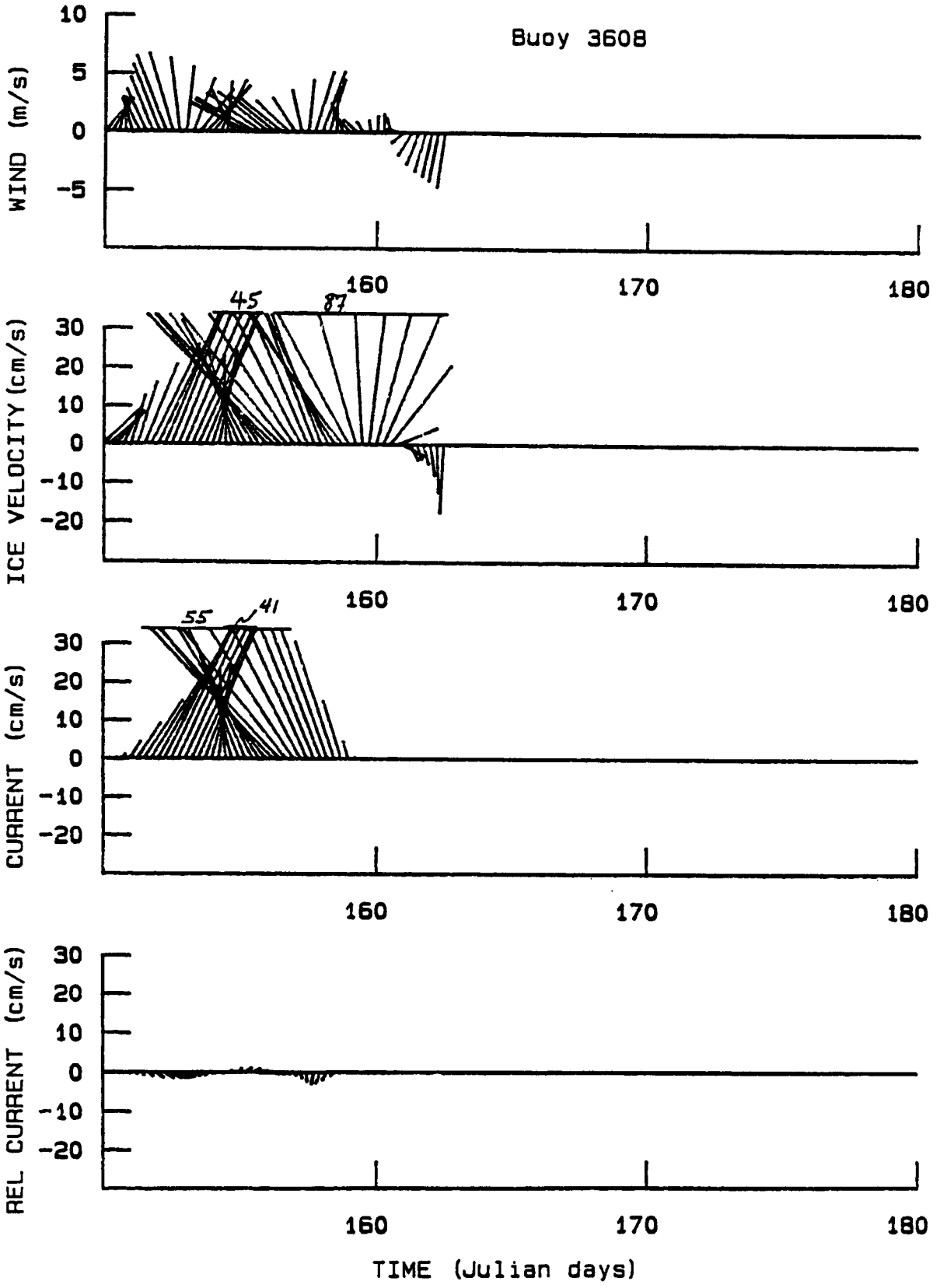

Figure 5.06. Buoy 3608 Stick Plots of Daily Average Wind, Ice Velocity, Current, and Relative Current (concl'd).

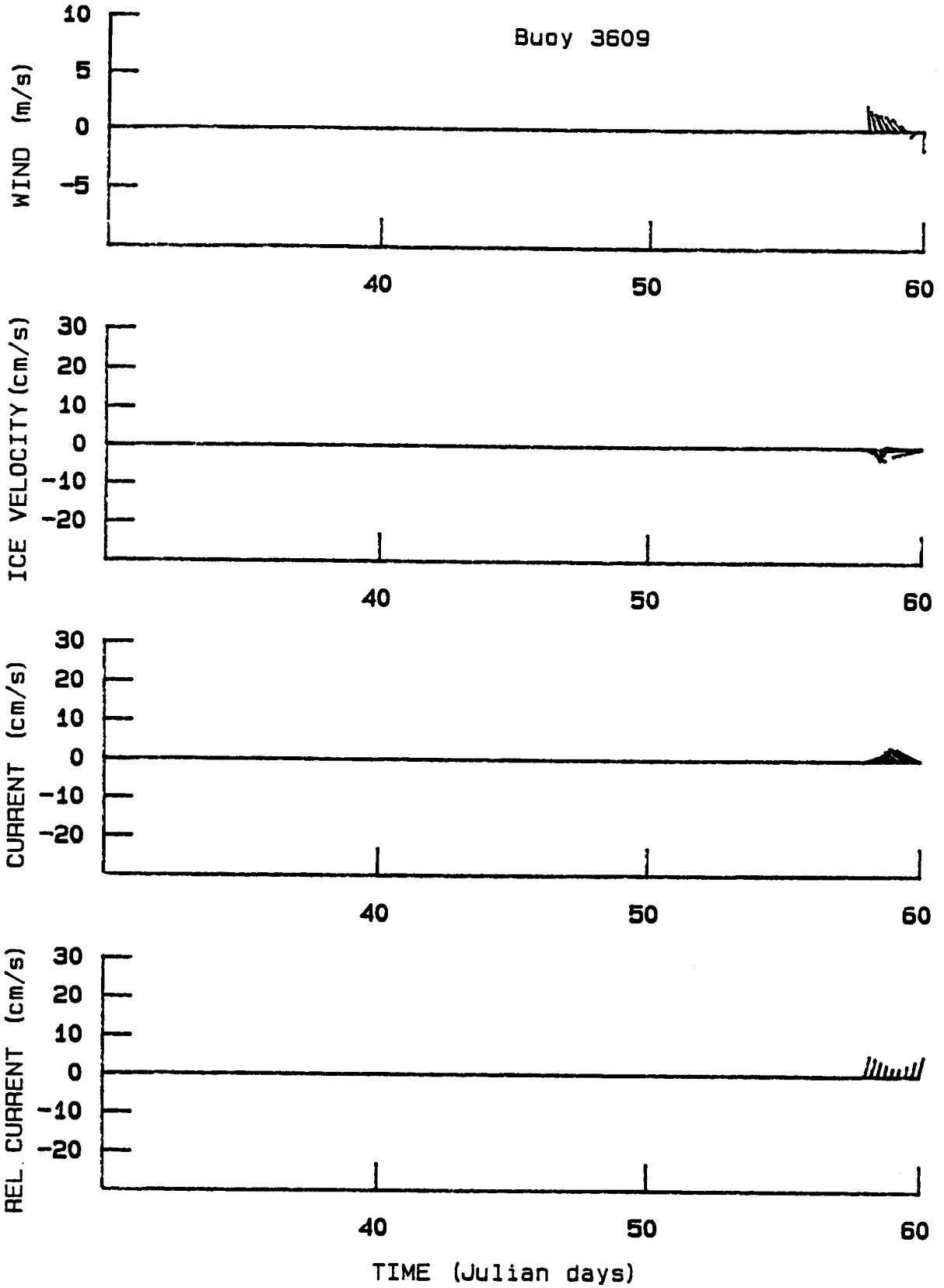

Figure 5.07. Buoy 3609 Stick Plots of Daily Average Wind, Ice Velocity, Current, and Relative Current.

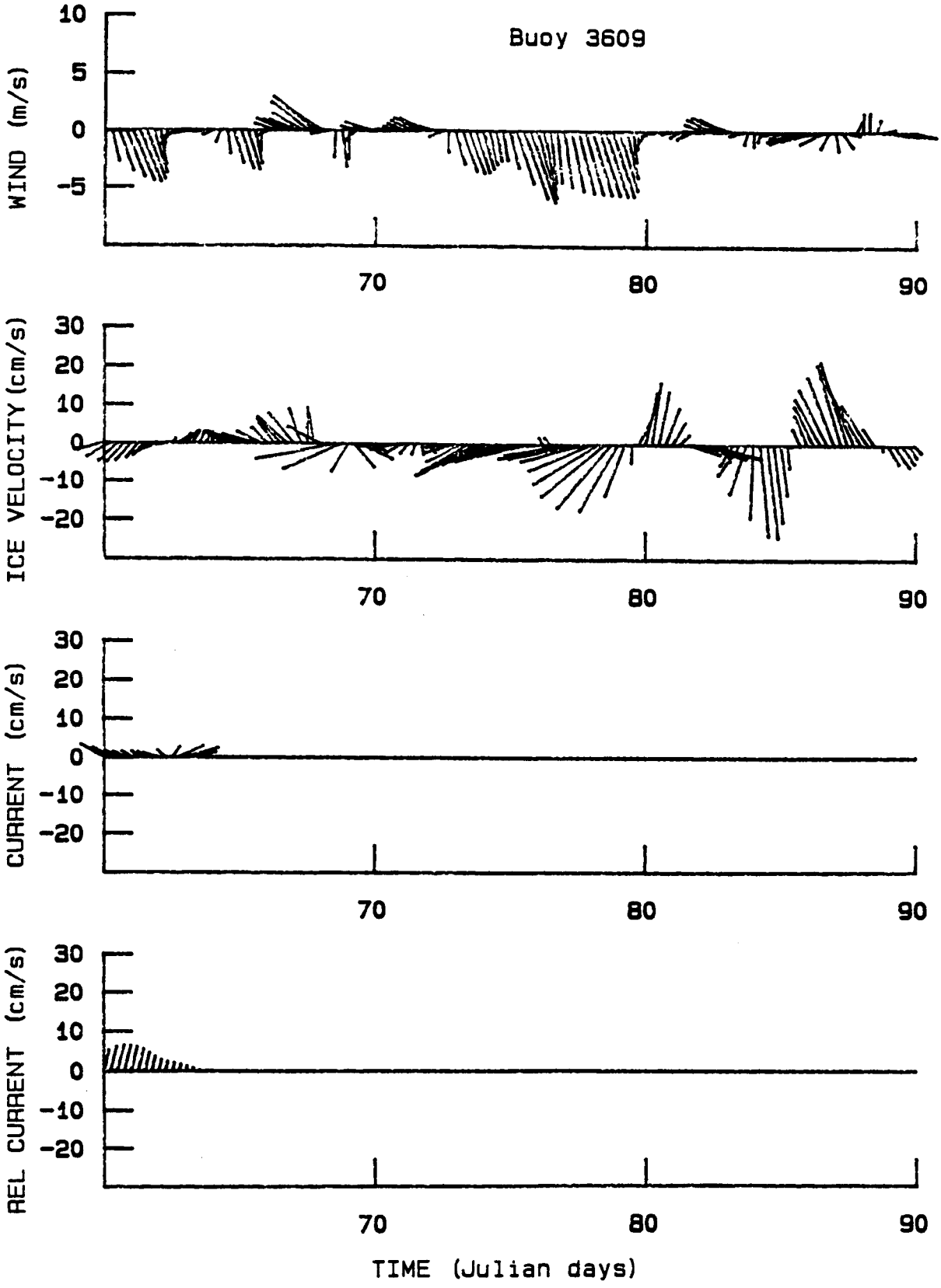

Figure 5.07. Buoy 3609 Stick Plots of Daily Average Wind, Ice Velocity, Current, and Relative Current (cont.).

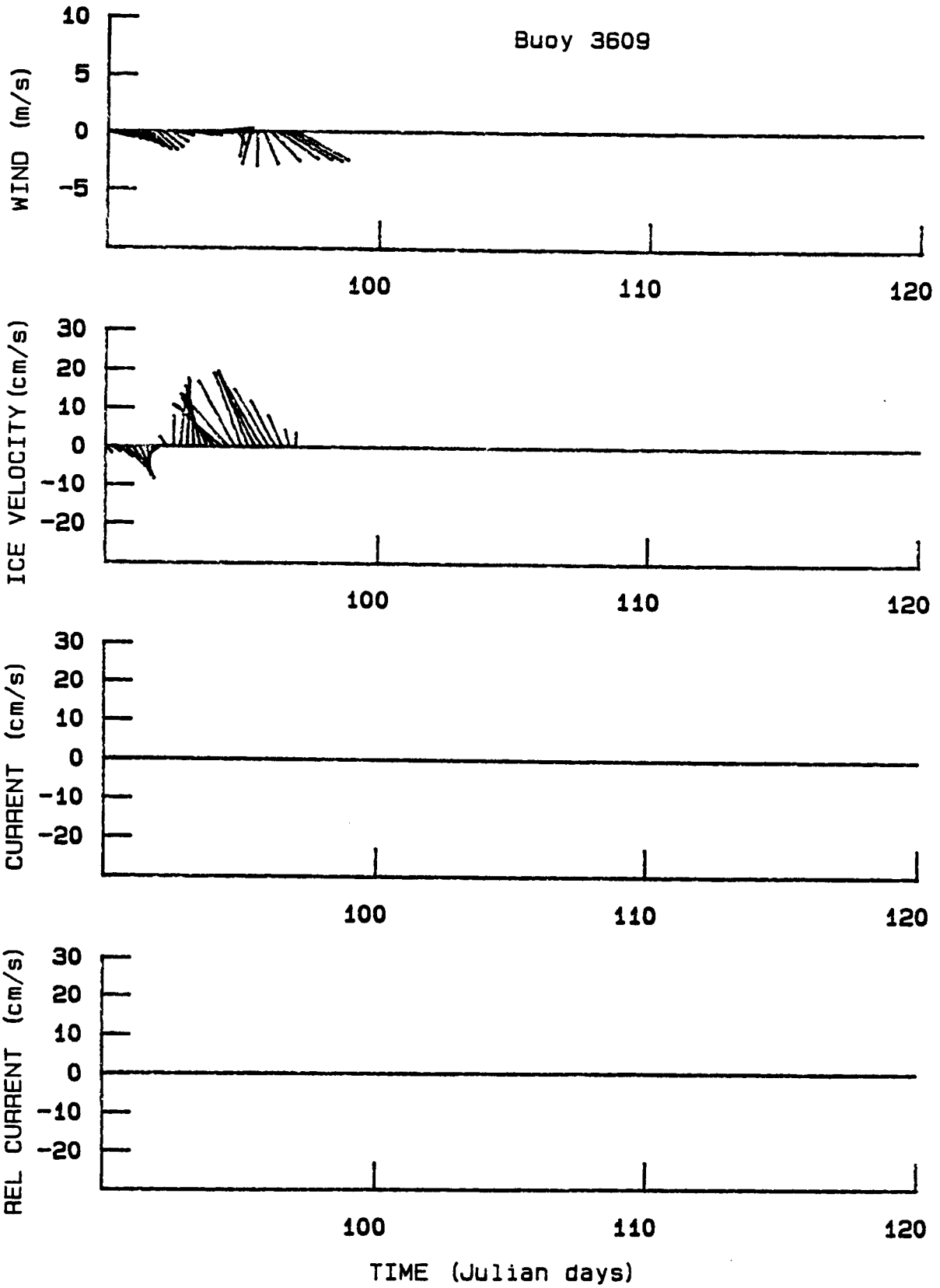

Figure 5.07. Buoy 3609 Stick Plots of Daily Average Wind, Ice Velocity, Current, and Relative Current (concl'd.).

6. RESULTS: CHUKCHI SEA

6.1. Ice Trajectories

Six buoys were deployed during two different time periods. The plan was to measure simultaneously the high speed nearshore motions and also the motions farther offshore that are more representative of the central Chukchi Sea. Multiple deployments were intended to allow buoys to occupy the region of interest for a longer period of time, after the first set drifted away. The ice trajectories for each buoy, obtained after filtering tidal and other high frequency oscillations from the data, are presented in Appendix B. These figures were copied from an earlier report on this work by Pritchard and Thomas (1985).

In general, the ice cover drifted toward the northwest, moving roughly 650km during a 6-month time period. Near the northwest Alaskan coast, the ice made numerous excursions alongshore, each excursion as large as 100km and lasting from about 3 to 10 days.

Figure 6.01 shows a typical position time history determined from the OI analysis. The shorter-term variations in Chukchi Sea ice motions are quite different from those of Norton Sound ice. The raw data (Figure 6.02) are jumpy, that is, they appear to have random errors on the order of 2km. But these are the same buoys and we expect the measurement error to be about 0.3km. We attribute the jumpiness to local ice deformations associated with rafting and ridging processes. Here the ice is 1-2m thick, even before it is deformed. The ice strength therefore allows ice stress divergence to be large enough that it can alter, or even

dominate, the force balance. Since local deformations can occur in a few hours or less, these processes can generate motions on shorter time scales than do tidal oscillations.

Figure 6.03 shows a plot of (ice) velocity for buoy 3625. The velocity is typically smaller than that for the Norton Sound buoys because tides and inertial oscillations are absent. The power spectral densities for buoys 3623, 3624 and 3625 (Figures 6.04-6.06, respectively) confirm the absence of any significant energy at the tidal or inertial frequencies. Rather, the energy appears to be confined to periods greater than about 2.5 days.

6.2 Wind, Current, and Ice Velocity

Three buoys, 3623, 3624, and 3625 included current meters suspended 10-m below the top surface of the ice, so that relative current measurements as well as position data were obtained. Buoy 3625 also included a barometer. Buoy 3624 drifted offshore of Cape Lisburne and Point Hope. Buoy 3625 drifted in the vicinity of Icy Cape, and buoy 3623 drifted offshore of Wainwright. All were deployed within about 50km of shore and tended to stay within roughly 150km of shore.

Buoy 3623 provided current measurements from February 11 (Jd 42) to March 1 (Jd 60), although position data extended until Jd 162. The ice trajectory tended to align with the coast, but with time the buoy migrated offshore, reaching a maximum of about 200 km on Jd 115 before moving back toward shore. From Jd 42 to Jd 60, the winds were typically less than 5m/s, and though variable, tended to align with the coast (Fig. 6.07). The ice moved eastward at up to 25cm/s until Jd 46 and then reversed

direction, slowing to a halt on Jd 50. It began moving eastward again on Jd 52 and again achieved speeds of about 25cm/s. There was no consistent relationship to the wind. Between Jd 42 and Jd 47 the current turned from offshore to northeastward alongshore, reaching a maximum speed of 35cm/s. The current reversed abruptly on Jd 47 and slowed from a maximum of 30cm/s to nearly zero by Jd 50, when it again reversed abruptly and set northeastward at speeds of 35cm/s until the end of the data on Jd 60. The relative current time history closely resembled that of the absolute current, which suggests that ice strength prevented the ice from responding in a free-drift mode to the sharp reversals and high currents.

While at first glance, the pattern of current reversals might correspond to the passage of an eddy, simultaneous current reversals at the locations of buoys 3624 and 3625 point rather to there being a dramatic change in atmospheric pressure and subsequent large-scale response of the ocean current. In fact, the barometer on buoy 3625 registered a low of 1005 mbar on Jd 49 and an increase to 1045 mbar by Jd 54. A barometer on another buoy farther offshore, 3622, registered a similar pattern. Even so, the data indicate that the current rather than the wind dominated the ice motion. Regression of the ice velocity onto the wind and the current showed that the current explained about three times as much of the variability of the ice velocity as did the wind.

Buoy 3624 yielded position and current measurements from February 15 (Jd 46) until May 1 (Jd 121). Over that interval,

the trajectory was characterized primarily by north-south excursions of roughly 200km, but also showed some westward movement. In addition, both wind and current vectors were oriented primarily north-south and displayed several reversals (Fig. 6.08). While there were some wind and ice velocity events which were coincident, there was no consistent relationship between the two. On the other hand, there was clearly a close relationship between the ice velocity and current over the entire data record, and the unambiguous evidence indicates that the current totally dominated the ice motion. One isolated example is that between Jd 46 and Jd 49, both the current and the ice velocity set southward at up to 50cm/s, while the wind was toward the northwest. Calculations over the entire record indicate that the current could account for about 93% of the variance in the ice velocity, while the wind could account for only 2% (see Table 6.1). However, it would be wrong to say that there were no instances in which the wind and current contributions were additive. The general conclusion is that buoy 3624 tracked the barotropic current which represented the oceanic response to large-scale atmospheric pressure fluctuations.

Buoy 3625 provided current measurements from February 16 (Jd 47) to March 8 (Jd 67), although the position data extended longer. Between Jd 52 and Jd 61, the ice moved northeastward alongshore at speeds of 10-20cm/s, and afterwards, it reversed direction and traveled slightly north of westward. The wind was offshore toward the northwest until Jd 61, when it changed direction toward the southwest, approximately alongshore

(Fig. 6.09). Wind speeds were generally in the range of 5-10m/s. Currents were northward to northeastward until about Jd 61, when there was a slow shift to northwestward flow. The relative current was variable and weak (less than 5cm/s) until about Jd 61 when it increased to about 10cm/s and became oriented more nearly in opposition to the wind. The change in the wind near Jd 61 was due to the passage of a front which accompanied an eastward moving low-pressure disturbance north of Alaska which was also reflected in the barometer records from buoys 3622 and 3625. Until about Jd 61, the current appeared to dominate the motion of the ice, but after that, the ice motion was clearly dominated by the wind. In fact, the wind and the current each explained about 75% of the variance in the ice velocity. This means that wind and current had nearly equal influence, but this wind correlation probably arose from its correlation with the current.

These three buoys were spaced about 150 km apart along the northwest coast of Alaska, but they still displayed some common behavior. The ice velocity and current reversal on about Jd 50 was reflected clearly in the data from 3623 and 3624, and weakly in the data from 3625. Between Jd 50 and Jd 60, all three buoys executed alongshore motion away from Bering Strait. From the trajectory plots, it is apparent that all three moved alongshore in unison between Jd 90 and Jd 100, and then reversed direction between Jd 100 and Jd 110. Recall that buoy 3608 in the northeast Bering Sea executed these same motions between Jd 90 and Jd 110. While local wind forcing must have some influence,

the evidence is strong that the ice along the coastline from Norton Sound to Barrow responds primarily to very large-scale barotropic current events which are driven by barometric pressure differences.

Table 6.1. Comparison Between Wind, Ice Velocity, and Current for Chukchi Sea Drifting Buoys. Linear Regression Constants for Ice Velocity onto Wind (V-W), Ice Velocity onto Current (V-C), Current onto Wind (C-W), and Relative Current onto Wind (R-W). The parameters in this table satisfy $A = m \exp(i\theta)$ and $B = b_r + ib_i$, where A and B are used in equation (4.25), σ_y^2 and σ_x^2 are the variance of the dependent and independent variable respectively in the linear fit, and f is the fraction of variance of x described by y.

Buoy	N	m	θ	b_r	b_i	σ_y^2	σ_x^2	f
3623	18							
V-W		1.48	-46.2	5.09	.30	91.1	8.4	.15
V-C		.32	-13.6	-.70	-.29	91.1	411.8	.44
C-W		2.62	-19.4	15.08	7.83	411.8	8.4	.09
R-W		1.46	7.9	9.99	7.52	243.8	8.4	.02
3624	78							
V-W		.41	-79.3	-2.05	1.91	324.8	62.5	.02
V-C		.89	-10.8	-2.40	.20	324.8	383.9	.93
C-W		.29	-92.8	.14	2.05	383.9	62.5	.00
R-W		.14	130.4	2.19	.14	40.6	62.5	.02
3625	19							
V-W		1.45	-70.8	-.16	-3.10	89.2	33.2	.77
V-C		.99	14.2	1.70	-3.79	89.2	67.8	.72
C-W		1.12	-84.1	-1.03	2.49	67.8	33.2	.60
R-W		.44	145.0	-.88	5.59	27.3	33.2	.19

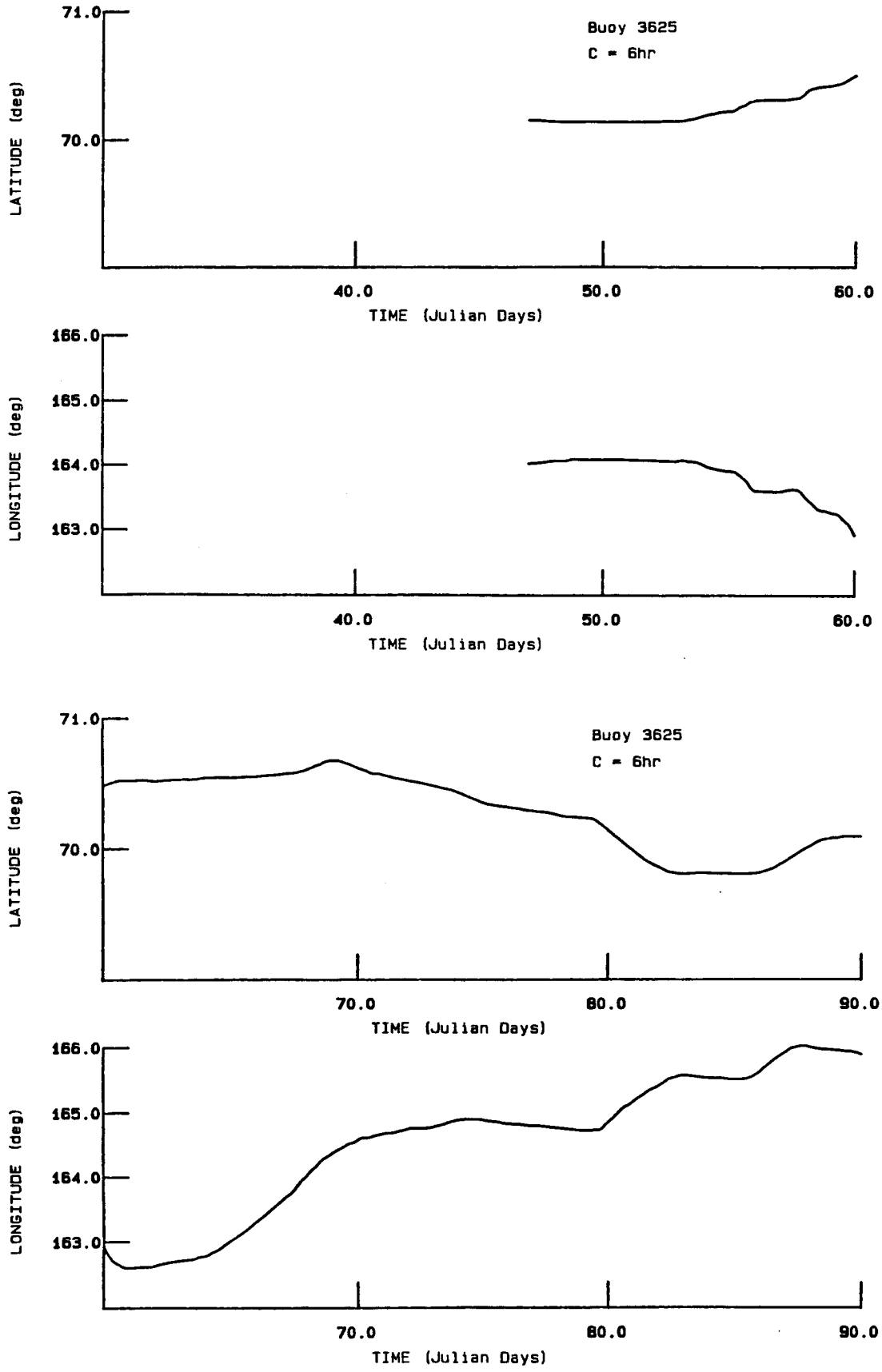

Figure 6.01. Buoy 3625 Interpolated Position Time History.

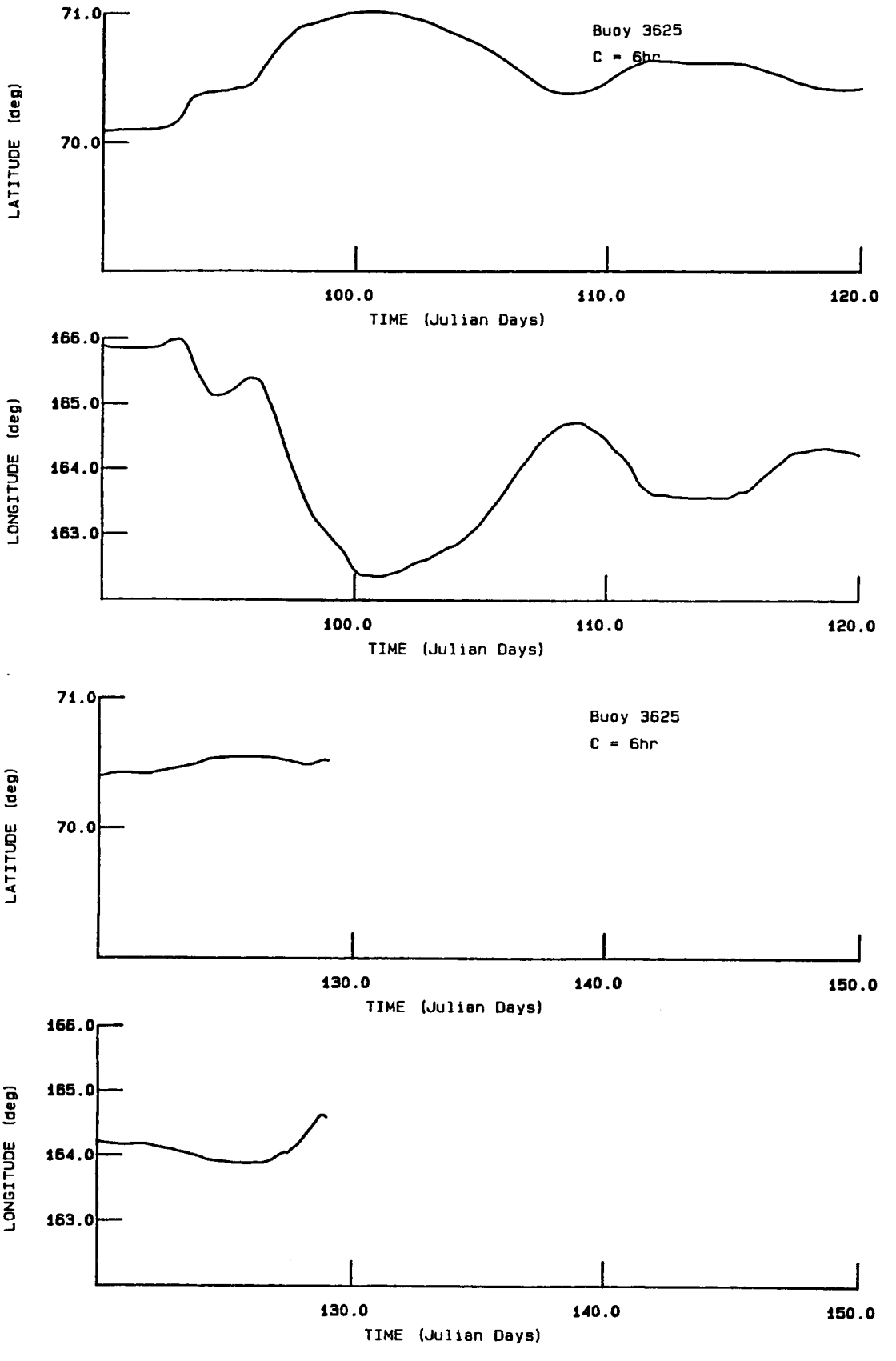

Figure 6.01. Buoy 3625 Interpolated Position Time History (concl'd).

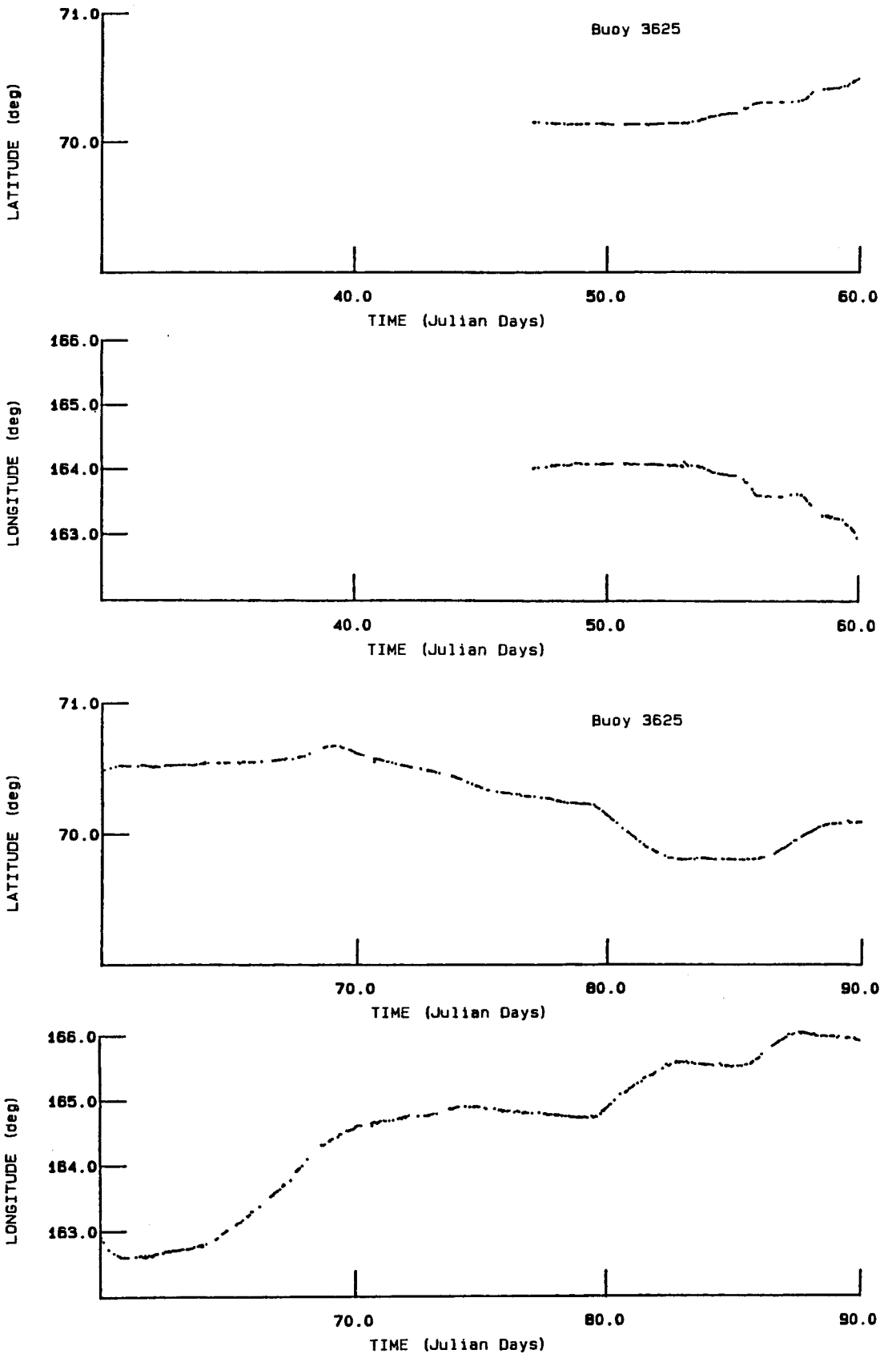

Figure 6.02. Buoy 3625 Raw Position Measurements.

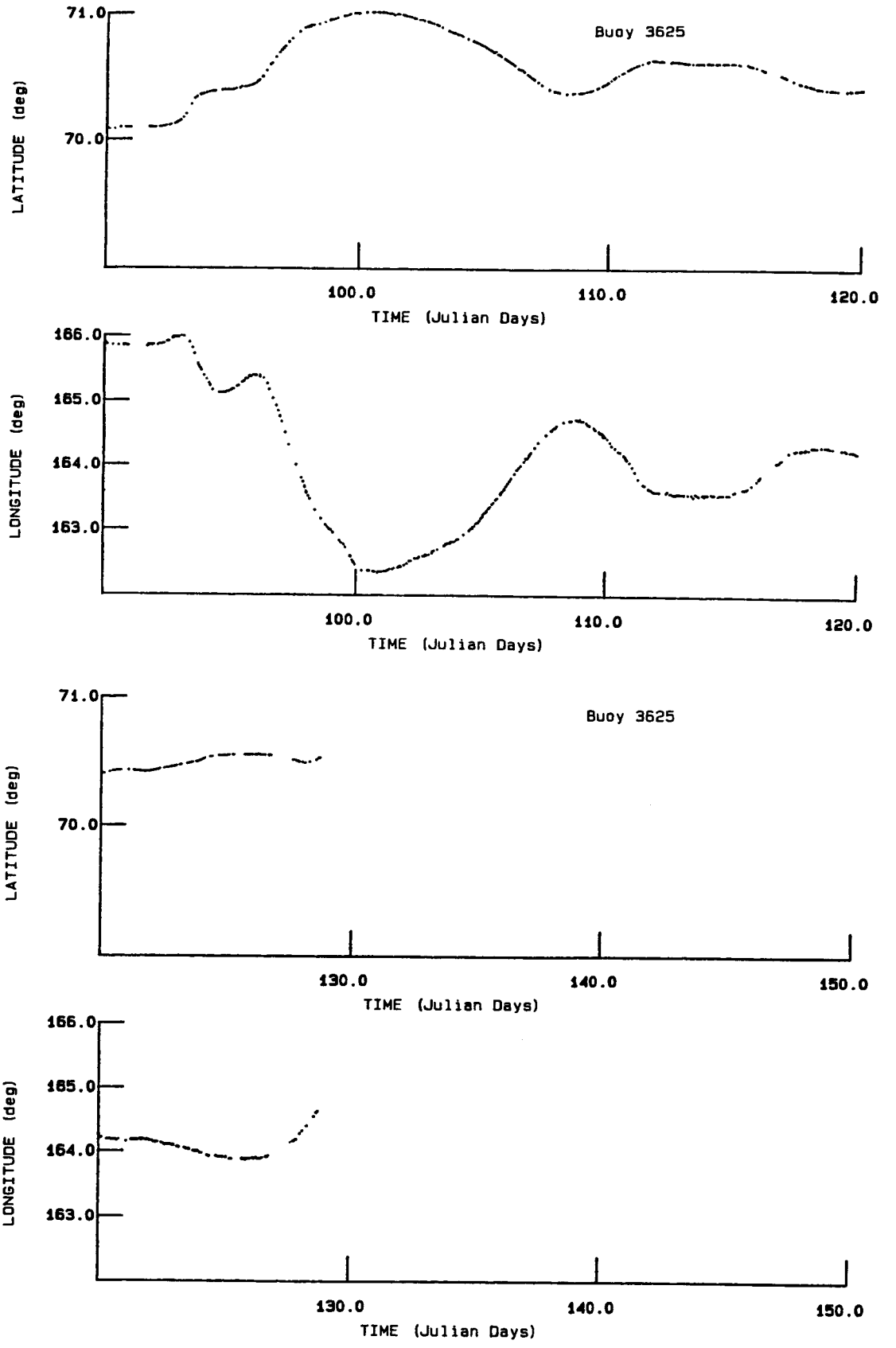

Figure 6.02. Buoy 3625 Raw Position Measurements (concl'd).

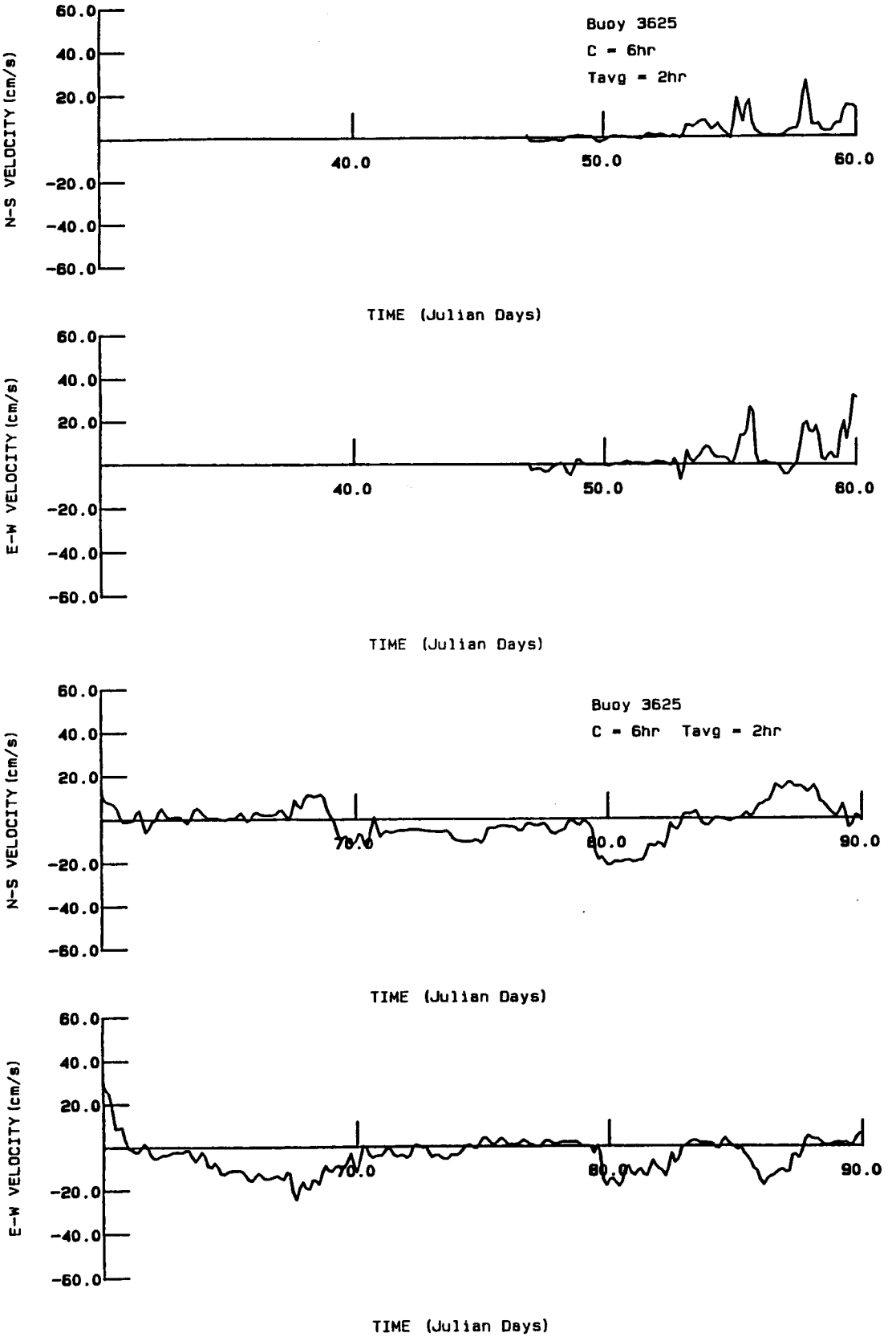

Figure 6.03. Buoy 3625 Velocity Time History Calculated from Interpolated Position History.

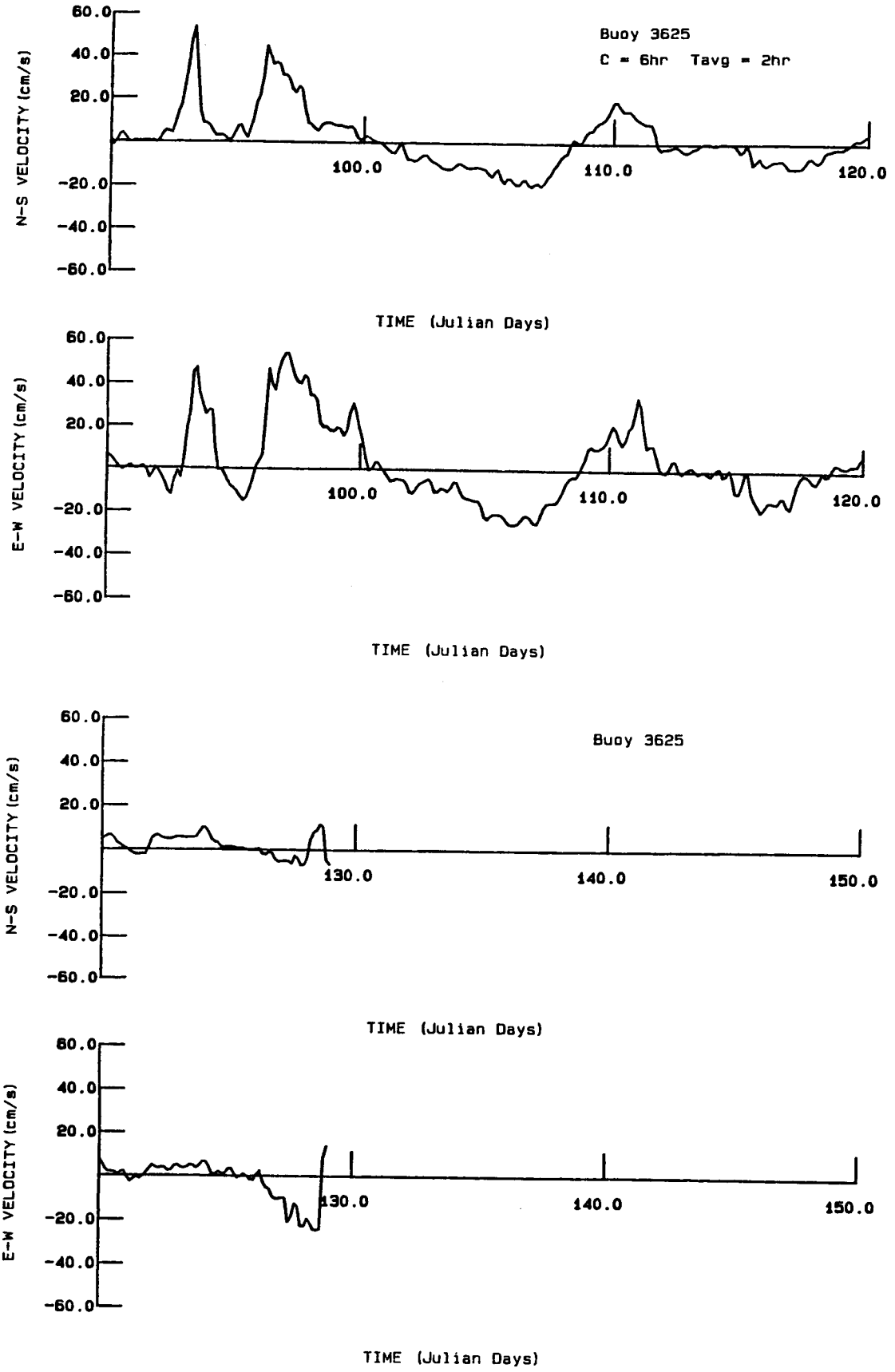

Figure 6.03. Buoy 3625 Velocity Time History Calculated from Interpolated Position History (concl'd).

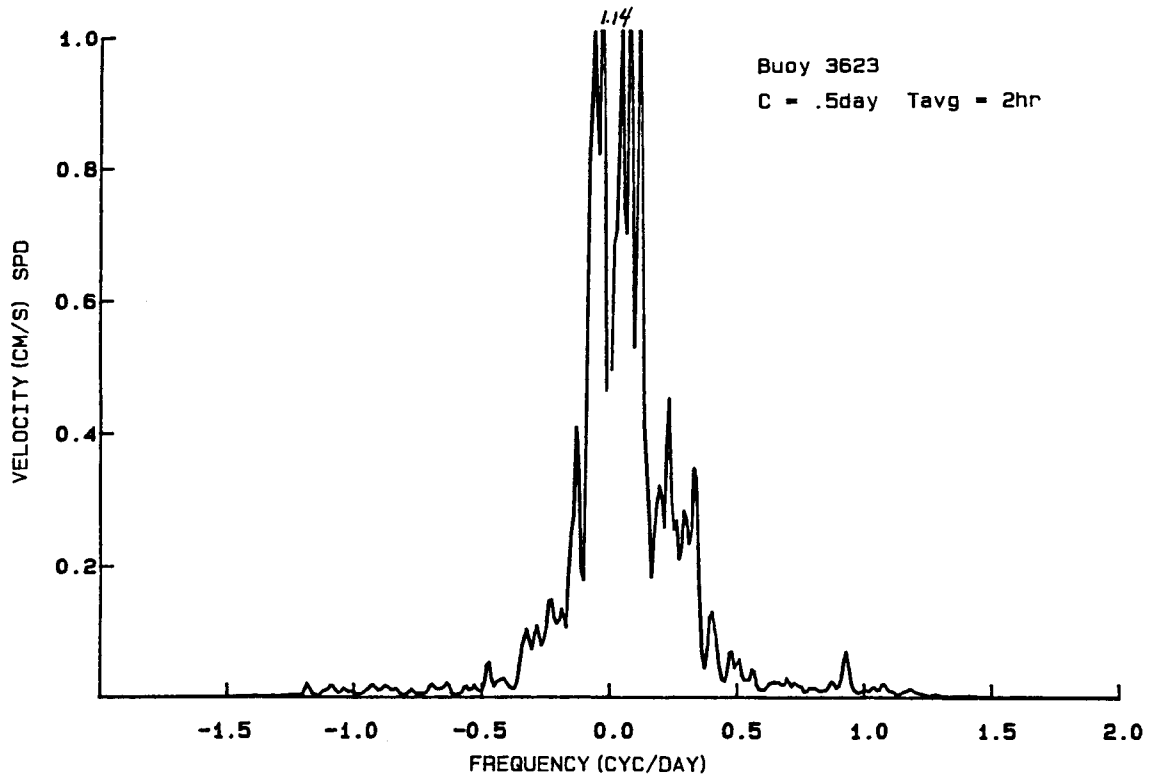

Figure 6.04. Buoy 3623 Ice Velocity Power Spectral Density.

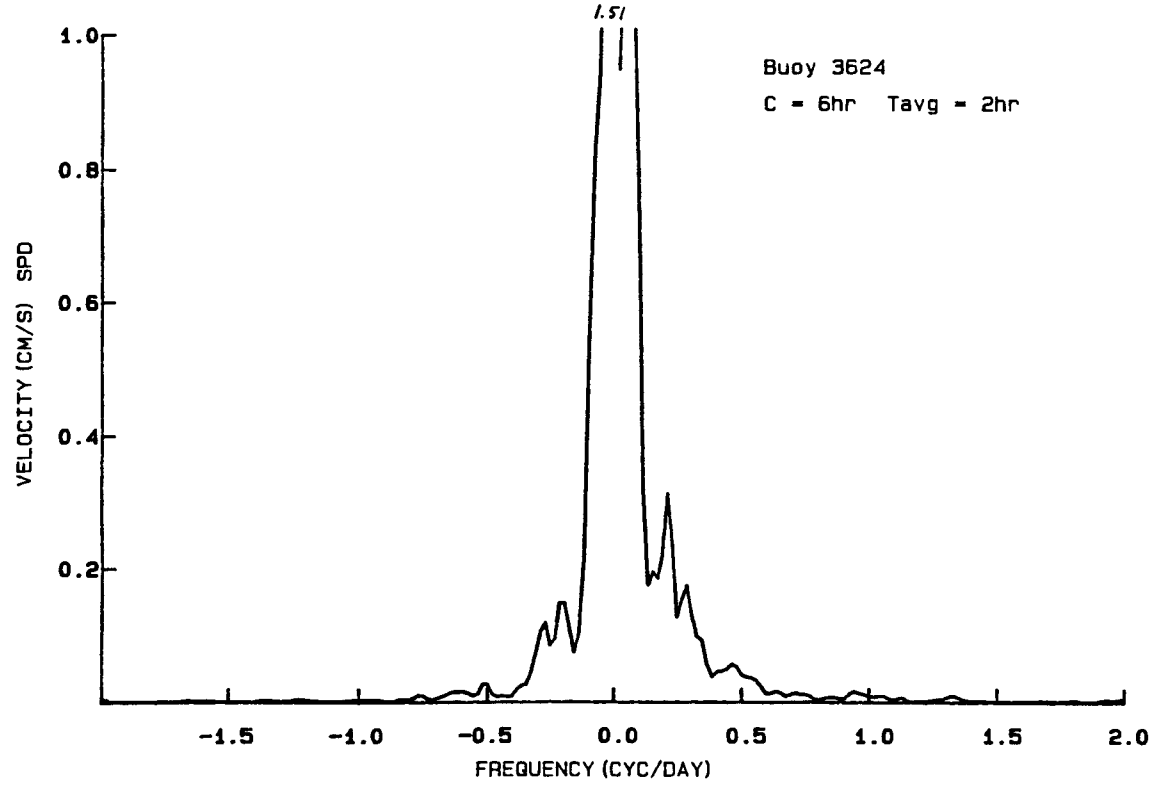

Figure 6.05. Buoy 3624 Ice Velocity Power Spectral Density.

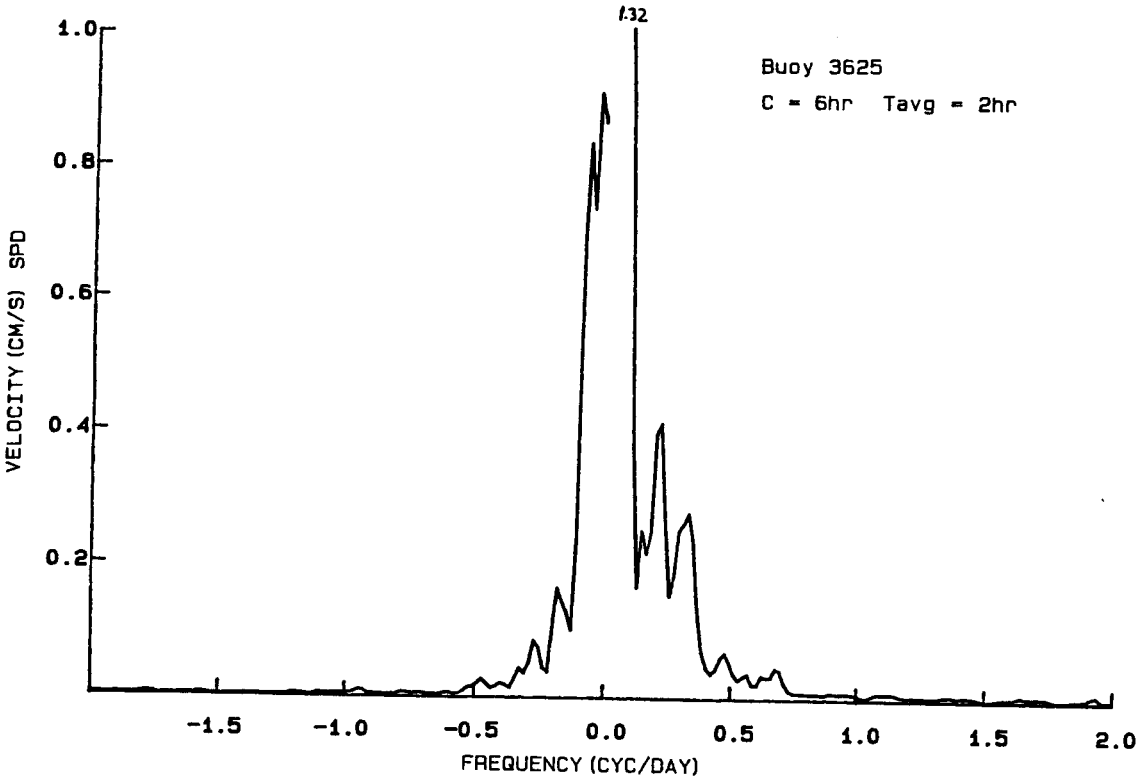

Figure 6.06. Buoy 3625 Ice Velocity Power Spectral Density.

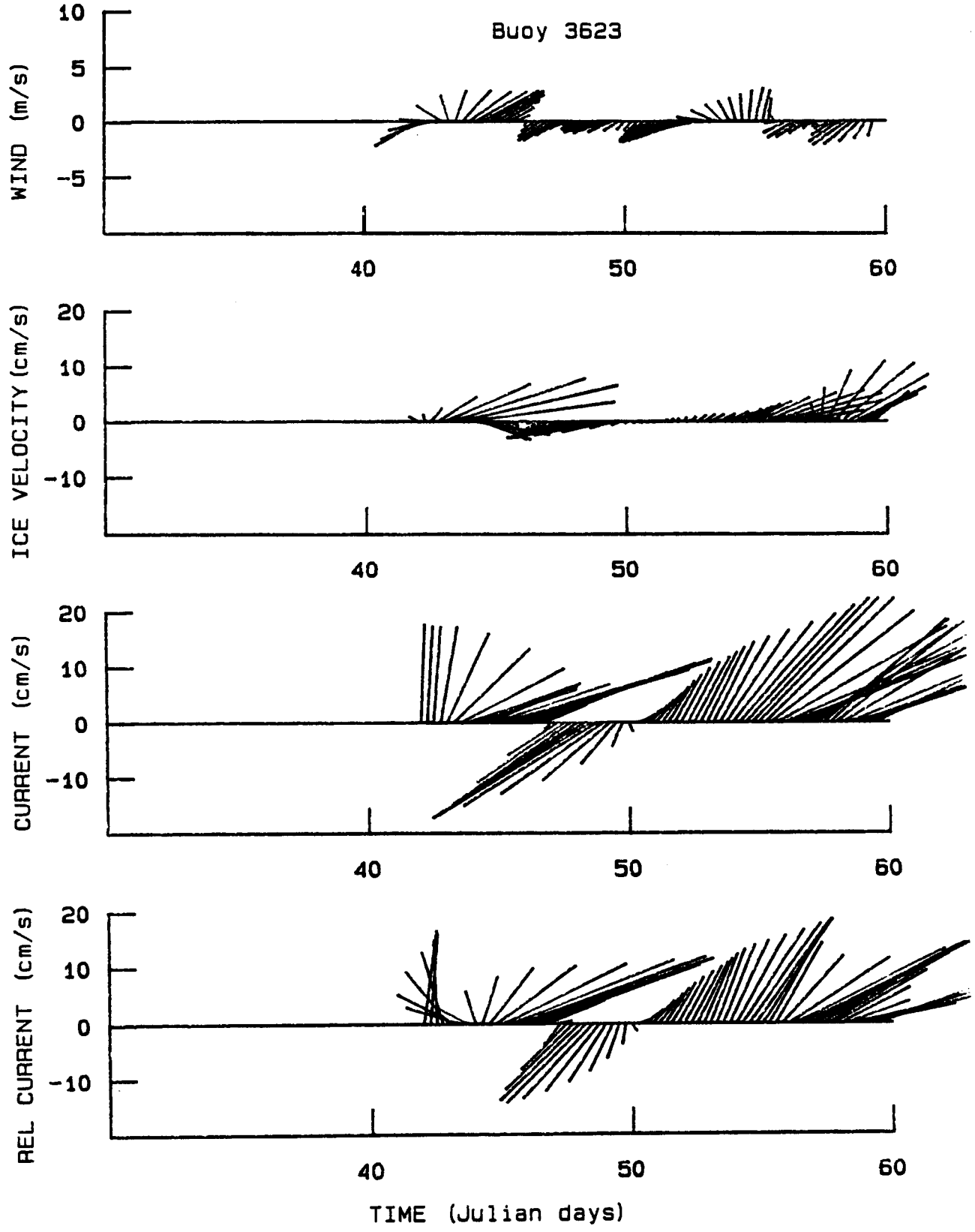

Figure 6.07. Buoy 3623 Stick Plots of Daily Average Wind, Ice Velocity, Current, and Relative Current.

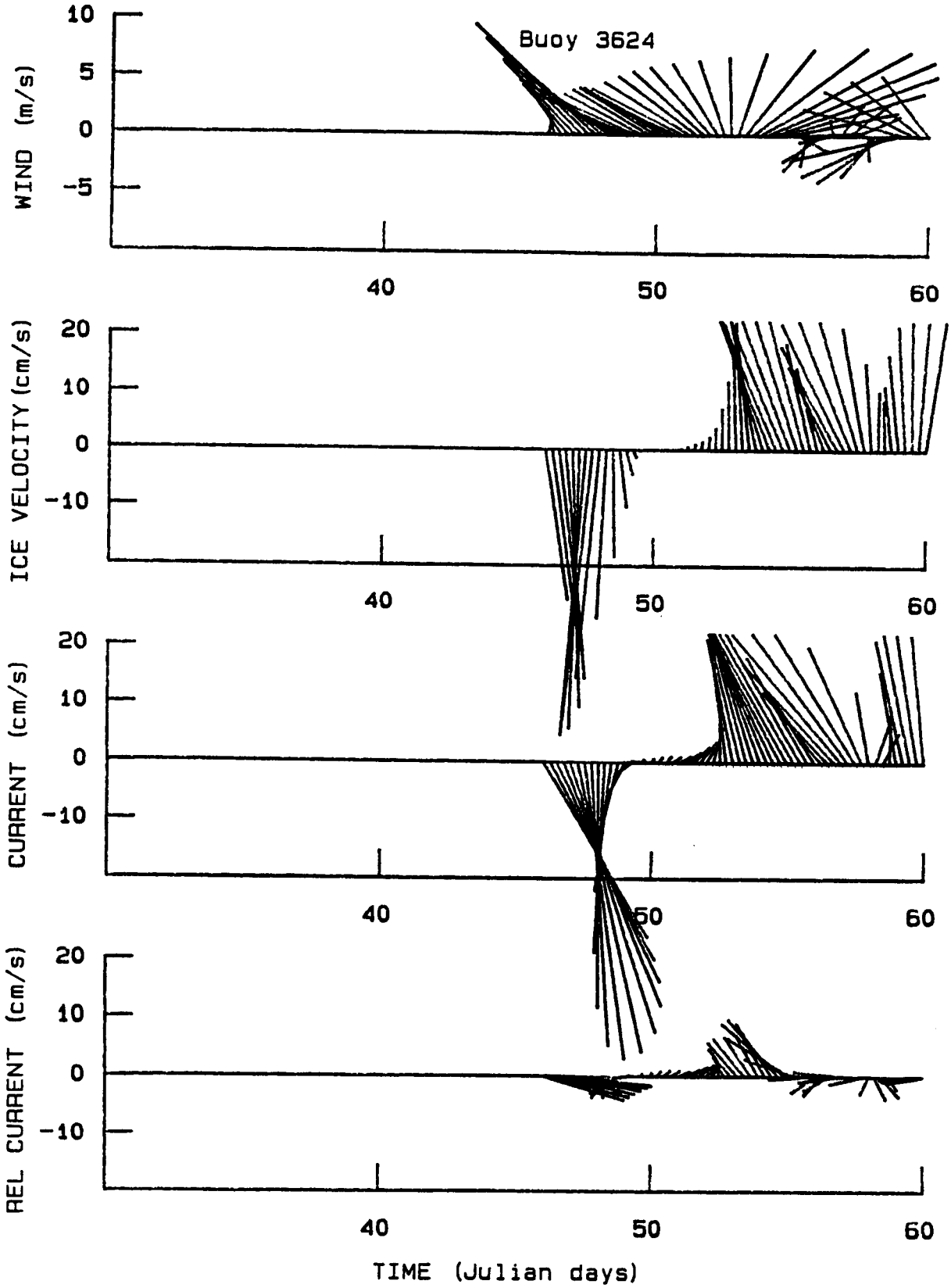

Figure 6.08. Buoy 3624 Stick Plots of Daily Average Wind, Ice Velocity, Current, and Relative Current.

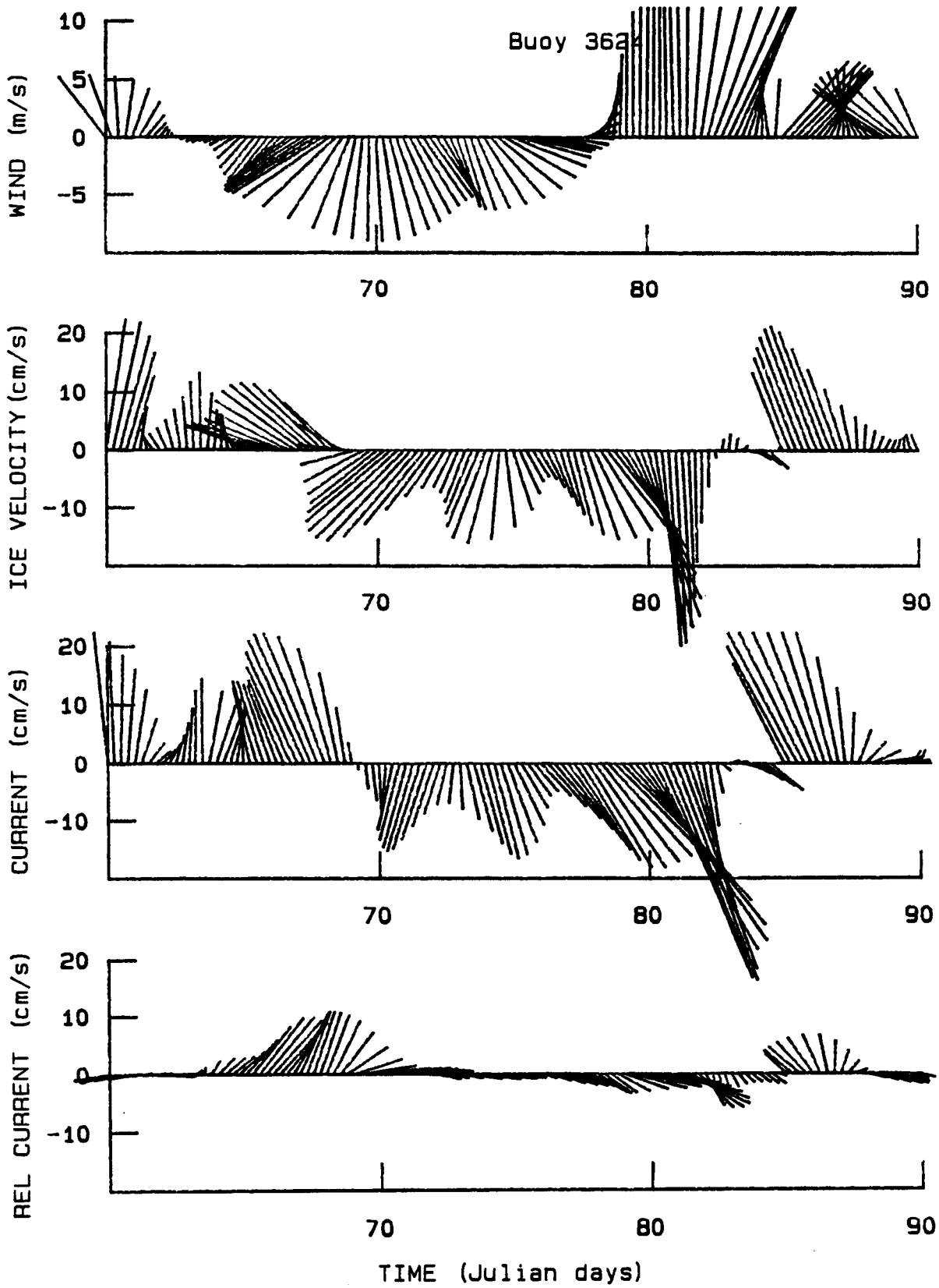

Figure 6.08. Buoy 3624 Stick Plots of Daily Average Wind, Ice Velocity, Current, and Relative Current.

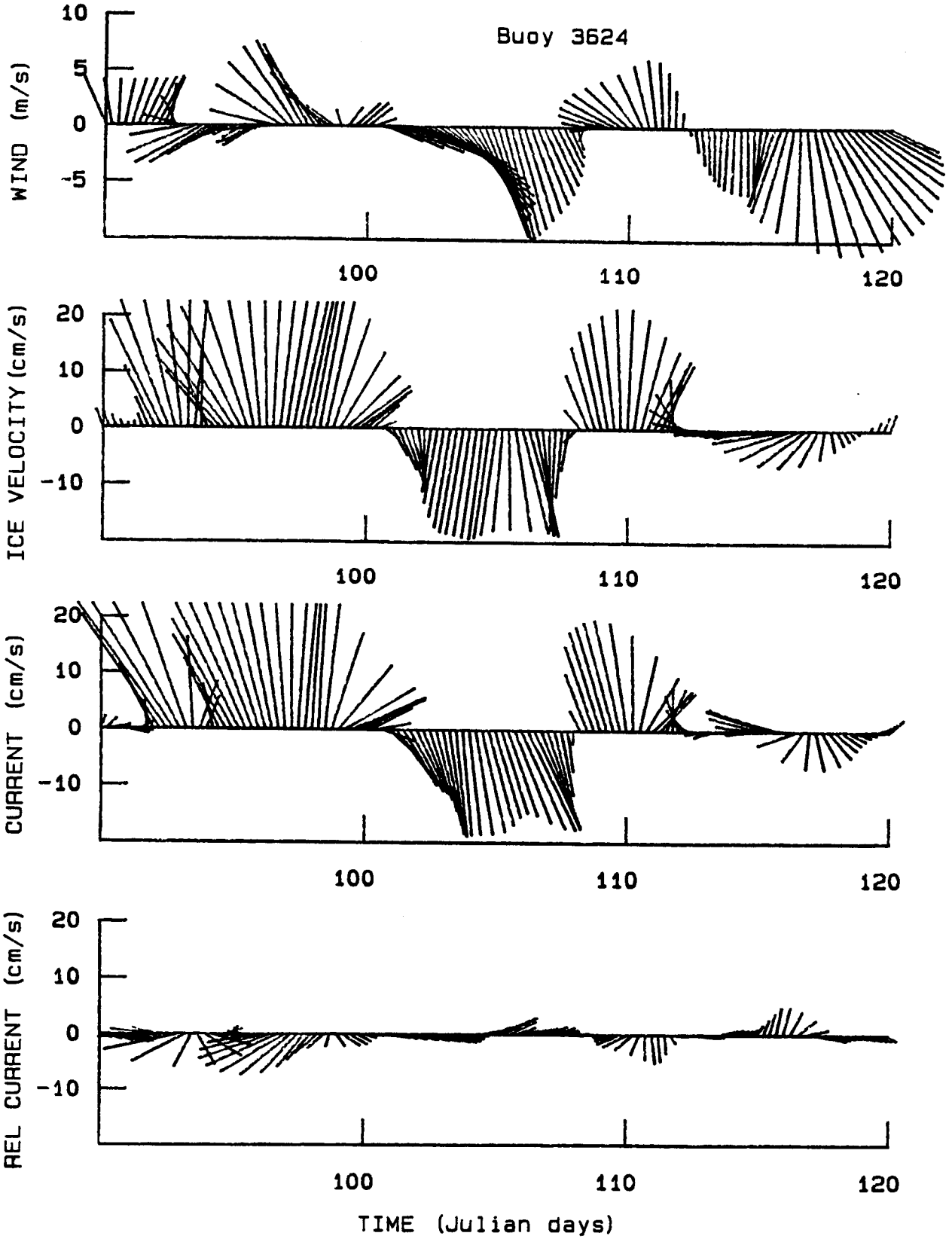

Figure 6.08. Buoy 3624 Stick Plots of Daily Average Wind, Ice Velocity, Current, and Relative Current.

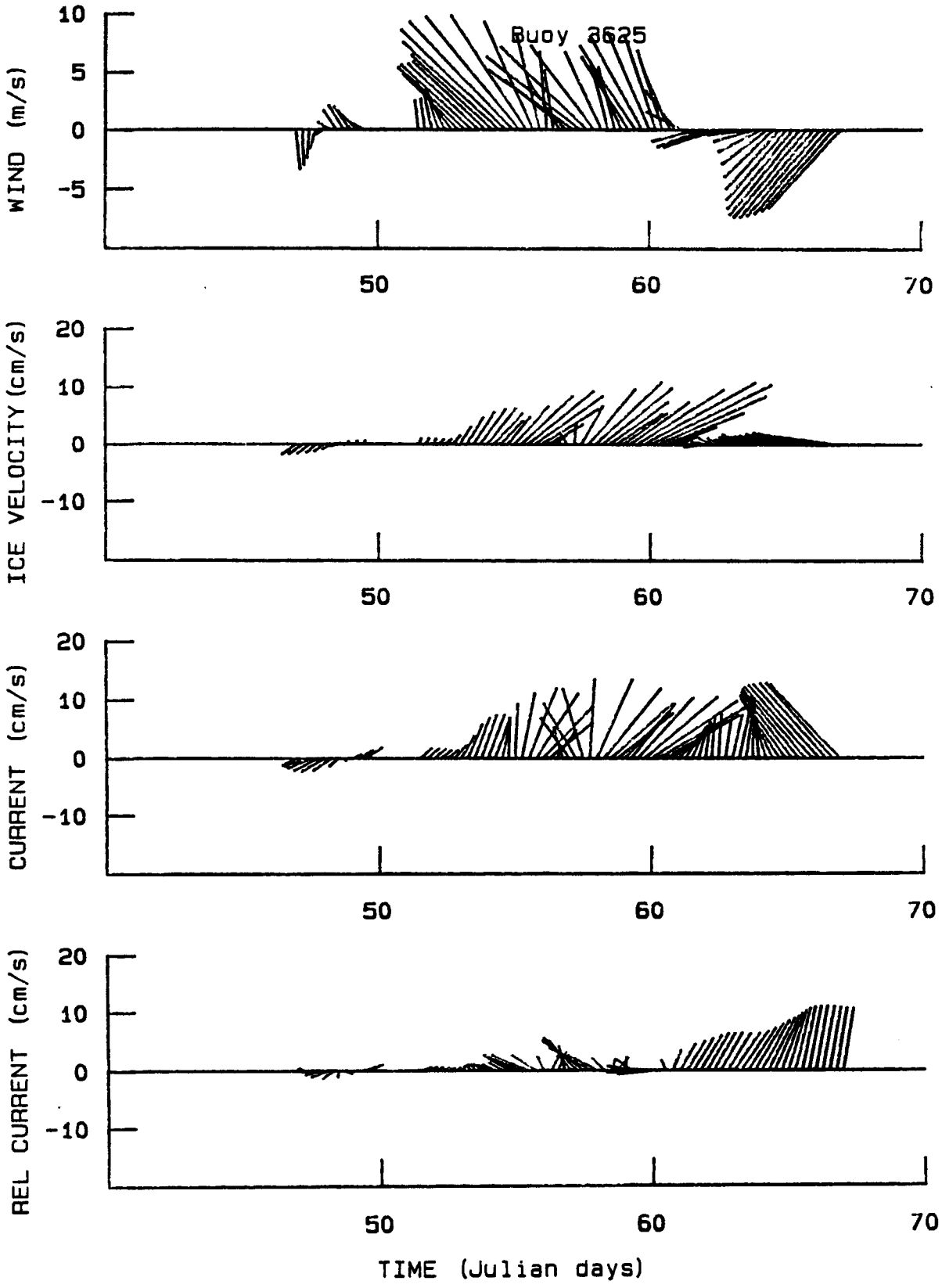

Figure 6.09. Buoy 3625 Stick Plots of Daily Average Wind, Ice Velocity, Current, and Relative Current.

7. SUMMARY

The motions of seventeen Argos buoys deployed on the Norton Sound and Chukchi Sea ice cover have been estimated using the method of optimal interpolation (OI). This is an objective technique that minimizes the expected error in the position estimate, takes account of measurement errors, and calculates the probable error in each position and velocity estimate.

The average ice velocity over a 2-hour time interval was determined as the spatial separation between two successive interpolated positions divided by the time increment. The expected error in these velocity estimates was also minimized by the OI technique. Relative currents were measured by the current meters drifting with the ice. Absolute ocean currents were determined by adding the ice velocity vectors and the relative current vectors.

The position and ice velocity estimates allowed the data to be archived in the new standard format of File Type 156. The existing NODC File Type 156 format was modified to accept ocean current data. A Record Type E was introduced to describe surface conditions, including winds and barometric pressures. A Record Type F was introduced to describe subsurface conditions, including ocean currents. Each data record included a position estimate, and a flag to indicate if this estimate was a measured raw position determined by Service ARGOS or a calculated position estimated by the OI procedure. Ice velocity estimates were included in Record Type F to allow reconstruction of the relative current measured by current meters suspended from the ice.

Ice motion histories show that diurnal tidal oscillations dominate the short-term velocity behavior in Norton Sound. There is a small semi-diurnal tidal component in Norton Sound that increases in the Bering Strait. In contrast, there is no significant tidal velocity component in the Chukchi Sea.

The atmospheric and oceanic conditions that existed during the field program have been described. High frequency variations were removed by filtering with a 48-hour cosine bell filter, and attention was focused on daily and longer behavior. We have analyzed the wind and current data and supplemented them with winds calculated from the NMC barometric pressure maps.

It is generally agreed that on time scales of roughly a day to a few weeks, the winds and currents provide the major external forces that drive the ice. When internal ice stress divergence is negligible, free-drift should provide a good approximation to the force balance. Under free-drift conditions, the ice velocity should be approximately equal to the vector sum of the ocean current and a linear function of the wind.

A complex regression analysis was used to determine what portion of the ice motions were described by the winds and currents using a free-drift model. Specifically, correlations between daily ice velocity and absolute current, and between the relative current (the current relative to the ice velocity) and the wind were determined to characterize the respective portions of the driving force contributed by ocean currents and wind. The three Norton Sound buoys showed that from 56 to 80% of the daily ice velocity variance were explained by the current. The wind contributed 0 to 35%. Similar calculations for the three Chukchi

Sea buoys showed that the current explained from 44 to 93% of the ice velocity variance, while the wind explained from 2 to 19%. In both cases, the current was found to be the more important factor in moving the ice. There was also evidence that some of the current-driven ice drift events were nearly simultaneous from Norton Sound to Barrow, which suggests that the ice was driven by barotropic currents that were caused by large-scale atmospheric pressure differences.

Although we have found that the currents provide the largest driving force to the ice cover in these regions, there remains a substantial part of the velocity variance that is not correlated with the winds or currents. These differences might be attributed to internal ice stress divergence, non-geostrophic currents, or other unknown processes. At this time, we do not know which processes are most important, but all are plausible.

More work is needed to understand how and why the ice behaves as it does, especially in the Chukchi Sea where the ice stress divergence can dominate the force balance. While the scope of the present work was largely limited to providing a basic description of the buoy movements and the concurrent physical setting, it did provide information on the relative importance of winds and currents on ice motions. These results can help guide the more sophisticated numerical studies that are needed to model the essential processes. The longer range goal should be to simulate and predict ice motions in these smaller geographic regions where ice stress divergence is important.

8. REFERENCES CITED

Aagaard, K., A.T. Roach, and J.D. Schumacher (1985) "On the Wind-driven Variability of the Flow through Bering Strait", J. Geophys. Res., vol. 90, no. C1, pp. 7213-7221.

Bendat, J. S., and Piersoll, A. G. (1980) Engineering Applications of Correlation and Spectral Analysis, John Wiley & Sons, New York.

Bloomfield, P. (1976) Fourier Analysis of Time Series: An Introduction, John Wiley & Sons, New York.

Colony, R., and Thorndike, A. S. (1985) "Sea Ice Motion as a Drunkard's Walk," J. Geophys. Res., vol. 90, no. C1, pp. 965-974.

Gandin, L. S. (1965) "Objective Analysis of Meteorological Fields," translated from Russian by Israel Program for Scientific Translation, Jerusalem, available from NTIS as No. TT65-50007.

Gelb, A., Kasper, J. F., Jr., Nash, R. A., Jr., Price, C. F., Sutherland, A. A., Jr. (1974) Applied Optimal Estimation, The M.I.T. Press, Cambridge, MA.

Kozo, T. L. (1984) "Mesoscale Meteorology of the Norton Sound Region," U. S. Dept. Commerce, NOAA, OCSEAP Final Report 39, pp. 1-102.

Liu, S.-K., and Leendertse, J. J. (1984) "Modeling of the Alaskan Coastal Waters," in Three-dimensional Shelf Models, Americal Geophysical Union, Washington, D.C.

Macklin, S. A., Brown, R. L., Gray, J., and Lindsay, R. W. (1984) "METLIB - II - A Program Library for Calculating and Plotting Atmospheric and Oceanic Fields," NOAA Technical Memorandum ERL PMEL-54, Pacific Marine Environmental Laboratory, Seattle, WA, 53pp.

McPhee, M. G. (1979) "The Effect of the Oceanic Boundary Layer on the Mean Drift of Pack Ice: Application of a Simple Model," J. Glaciol., vol. 9, pp. 388-400.

McPhee, M. G. (1982) "Sea Ice Drag Laws and Simple Boundary Layer Concepts, including Application to Rapid Melting," Report 82-4, Cold Regions Research and Engineering Laboratory, Hanover, NH.

Mofjeld, H. O. (1984) "Recent Observations of Tides and Tidal Currents from the Northeastern Bering Sea Shelf," Pacific Marine Environmental Laboratory, NOAA Technical Memorandum ERL PMEL-57, Seattle, WA.

Overland, J. E. (1985) "Atmospheric Boundary Layer Structure and Drag Coefficients over Sea Ice," J. Geophys. Res., vol. 90, no. C5, pp. 9029-9049.

Pease, C. H., and Salo, S. (1987) "Sea Ice Drift near Bering Strait during 1982," to appear in J. Geophys. Res., Special Issue on Marginal Ice Zones.

Pritchard, R. S. (1979) "Transport and Behavior of a Prudhoe Bay Oil Spill," in Proceedings of a Workshop on Oil in Ice held in Toronto on October 10-11, (Sponsored by University of Toronto and CANMAR).

Pritchard, R. S. (1981) "Mechanical Behavior of Pack Ice," in Mechanics of Structured Media, Part A, (ed) A. P. S. Selvadurai, Elsevier, Amsterdam. pp. 371-405.

Pritchard, R. S. (1984) "Beaufort Sea Ice Motions," in The Alaskan Beaufort Sea, (eds) P. W. Barnes, D. M. Schell, and E. Reimnitz, Academic Press, Orlando, pp. 95-113.

Pritchard, R. S., and Thomas, D. R. (1985) "Chukchi Sea Ice Behavior, 1981-82," Flow Technical Report No. 323, Flow Industries, Kent, WA.

Reynolds, M., and Pease, C. H. (1984) "Drift Characteristics of Northeastern Bering Sea Ice during 1982," NOAA Technical Memorandum ERL PMEL-55, Pacific Marine Environmental Laboratory, Seattle, WA, 135pp.

Stringer, W. J., and Henzler, R. D. (1981) "Ice Displacement Vectors Measured in Norton Sound and the Adjacent Bering Sea 1973-1979," Report to NOAA/OCSEAP on contract no. 03-5-022-55 for RU 267, University of Alaska, Geophysical Institute, Fairbanks, AK.

Thomas, D. R., and Pritchard, R. S. (1979) "Beaufort and Chukchi Sea Ice Motion - Part 1. Pack Ice Trajectories," Flow Research Report No. 133, Flow Research Company, Kent, WA.

Thomas, D. R., and Pritchard, R. S. (1981) "Norton Sound and Bering Sea Ice Motion; 1981," Flow Research Report No. 209, Flow Research Company, Kent, WA.

Thomas, D. R., and Pritchard, R. S. (1982) "The Transport and Behavior of Oil Spilled In and Under Sea Ice," Annual Report to Outer Continental Shelf Environmental Assessment Program on Research Unit 567, National Oceanic and Atmospheric Administration, Boulder, CO.

APPENDIX A

NODC File Type 156 Data Documentation Forms

ACCESSION NUMBER

DATA DOCUMENTATION FORM

NOAA FORM 24-13
(4-77)

U.S. DEPARTMENT OF COMMERCE
NATIONAL OCEANIC AND ATMOSPHERIC ADMINISTRATION
NATIONAL OCEANOGRAPHIC DATA CENTER
RECORDS SECTION
WASHINGTON, DC 20235

FORM APPROVED
O.M.B. No. 41-R2651
EXPIRES 1-81

(While you are not required to use this form, it is the most desirable mechanism for providing the required ancillary information enabling the NODC and users to obtain the greatest benefit from your data.)

This form should accompany all data submissions to NODC. Section A, Originator Identification, must be completed when the data are submitted. It is highly desirable for NODC to also receive the remaining pertinent information at that time. This may be most easily accomplished by attaching reports, publications, or manuscripts which are readily available describing data collection, analysis, and format specifics. Readable, handwritten submissions are acceptable in all cases. All data shipments should be sent to the above address.

A. ORIGINATOR IDENTIFICATION

THIS SECTION MUST BE COMPLETED BY DONOR FOR ALL DATA TRANSMITTALS

1. NAME AND ADDRESS OF INSTITUTION, LABORATORY, OR ACTIVITY WITH WHICH SUBMITTED DATA ARE ASSOCIATED

IceCasting, Inc.
11042 Sand Point Way N.E.
Seattle, WA 98125-5846

2. EXPEDITION, PROJECT, OR PROGRAM DURING WHICH DATA WERE COLLECTED

Norton Sound and
Chukchi Sea

3. CRUISE NUMBER(S) USED BY ORIGINATOR TO IDENTIFY DATA IN THIS SHIPMENT

NORTON or CHUKCHI

4. PLATFORM NAME(S)

3607, 3608, 3609, 3610, 3611, 3612, 3613, 3614, 3615, 3616, 3617, 3620, 3621, 3622, 3623, 3624, &3625

5. PLATFORM TYPE(S) *(E.G., SHIP, BUOY, ETC.)*

Drifting Buoy

6. PLATFORM AND OPERATOR NATIONALITY(IES)

PLATFORM	OPERATOR
USA	USA

7. DATES

FROM: MO/DAY/YR	TO: MO/DAY/YR
12/09/81	6/29/82

8. ARE DATA PROPRIETARY?

☒ NO ☐ YES

IF YES, WHEN CAN THEY BE RELEASED FOR GENERAL USE? YEAR ____ MONTH ____

9. ARE DATA DECLARED NATIONAL PROGRAM (DNP)?
(I.E., SHOULD THEY BE INCLUDED IN WORLD DATA CENTERS HOLDINGS FOR INTERNATIONAL EXCHANGE?)

☒ NO ☐ YES ☐ PART *(SPECIFY BELOW)*

10. PERSON TO WHOM INQUIRIES CONCERNING DATA SHOULD BE ADDRESSED WITH TELEPHONE NUMBER *(AND ADDRESS IF OTHER THAN IN ITEM-1)*

Robert S. Pritchard
(206)363-3394

11. PLEASE DARKEN ALL MARSDEN SQUARES IN WHICH ANY DATA CONTAINED IN YOUR SUBMISSION WERE COLLECTED.

GENERAL AREA

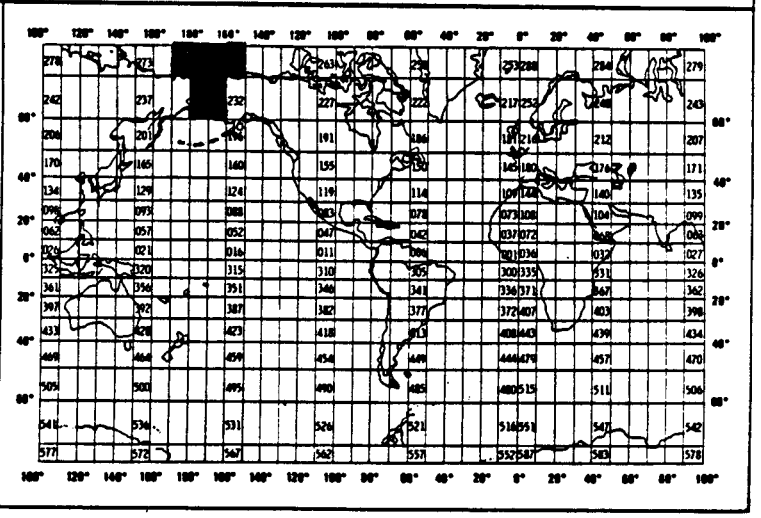

NOAA FORM 24-13

B. SCIENTIFIC CONTENT

NAME OF DATA FIELD	REPORTING UNITS OR CODE	METHODS OF OBSERVATION AND INSTRUMENTS USED (SPECIFY TYPE AND MODEL)	ANALYTICAL METHODS (INCLUDING MODIFICATIONS) AND LABORATORY PROCEDURES	DATA PROCESSING TECHNIQUES WITH FILTERING AND AVERAGING
Latitude/ Longitude	Deg,Min,Sec	Raw Position Determined by Service ARGOS. Buoys mfg. by Polar Research Laboratory	Calculated position is determined using Optimal Interpolation to estimate position of sensor data.	Ref: Pritchard and Hanzlick (1987)
Anemometer Ht.	Meters	Nominal 3-meter mast on top of ice.		Wind Velocity vector is the average of 32 samples taken during 9-minute period preceding observation time. Obs. at 2-hr intervals.
Wind Velocity Speed Direction	 m/s deg	Weathermeasure Model W203 Anemometer Model W204 Vane		
Atmospheric Pressure	millibars	Paroscientific barometer		Barometric pressure is average of all samples taken during 2-hr period centered on obs. time.
Air Temperature	C	Yellow Springs Instruments Thermolinear Thermistor		Instantaneous sample.
Compass Bearing	Deg	PRL fluxgate compass		Instantaneous sample.
Current Meter Depth	Meters	Nominal length of tether cable from top of ice.		
Ice Velocity Speed Direction	 cm/s Deg	Calculated from position.estimated from Optimal Interpolation.	Values are representative of 2-hr averages centered on obs. time.	Ref: Pritchard and Hanzlick (1987)

NOAA FORM 24-13

B. SCIENTIFIC CONTENT

NAME OF DATA FIELD	REPORTING UNITS OR CODE	METHODS OF OBSERVATION AND INSTRUMENTS USED (SPECIFY TYPE AND MODEL)	ANALYTICAL METHODS (INCLUDING MODIFICATIONS) AND LABORATORY PROCEDURES	DATA PROCESSING TECHNIQUES WITH FILTERING AND AVERAGING
Absolute Current Velocity Speed Direction	 cm/s Deg	Marinco Model Q-9 Savonius Rotor Current Meter tethered to Drifting Buoy on Ice.	Meter measures current relative to ice. Abs. current is calculated by adding ice velocity to rel.current vel. Ref: Pritchard and Hanzlick (1987)	Rel. current speed is average of samples during 9 minutes preceding obs. time. Rel. current direction is instantaneous sample. Direction is measured relative to buoy orientation and added to compass bearing to obtain Rel. Current Dir.
References ---------- (see attached list) Thomas and Pritchard (1982) describes the field program and hardware. Pritchard and Thomas (1985) describes Chukchi Sea ice motions. Pritchard and Hanzlick (1987) describes analytical methods, environmental conditions during the experiment, and the resulting ice behavior.				

NOAA FORM 24-13

REFERENCES

Pritchard, R. S., and Hanzlick, D. J. (1987a) "Sea Ice Trajectories and Ocean Currents 1981-1982: Norton Sound and Chukchi Sea," Final Report to OCSEAP/NOAA under Contract WASC-86-00043. Also printed as Technical Report Number ICI-RPT-87010, IceCasting, Inc., Seattle, WA.

Pritchard, R. S., and Thomas, D. R. (1985) "Chukchi Sea Ice Motions, 1981-82," Flow Technical Report Number 323, Flow Industries, Inc., Kent, WA.

Thomas, D. R., and Pritchard, R. S. (1982) "The Transport and Behavior of Oil Spilled In and Under Sea Ice," Annual Report to OCSEAP on RU567, NOAA, Boulder, CO. Also printed as Flow Research Report Number 240, Flow Research Company, Kent, WA.

C. DATA FORMAT

COMPLETE THIS SECTION FOR PUNCHED CARDS OR TAPE, MAGNETIC TAPE, OR DISC SUBMISSIONS.

1. LIST RECORD TYPES CONTAINED IN THE TRANSMITTAL OF YOUR FILE
GIVE METHOD OF IDENTIFYING EACH RECORD TYPE

HEADER Record	"A" in column 10
LAUNCH SUMMARY Record	"B" in column 10
SURFACE DATA Record	"E" in column 10
SUBSURFACE CURRENT Record	"F" in column 10

2. GIVE BRIEF DESCRIPTION OF FILE ORGANIZATION

Thirty six files on tape. File 1 contains a list of file names. Files 2-18 contain data for buoys 3607-3625, respectively. Each of these 17 data files is File Type 156. The second set of 18 files is an exact duplicate of the first set of 18 files, to be used in case an original is damaged. The enclosed Table 1 describes the number of lines, words, and bytes in each file.

The tape is UNLABELED.

3. ATTRIBUTES AS EXPRESSED IN ☐ PL-1 ☐ ALGOL ☐ COBOL ☒ FORTRAN ☐ _____ LANGUAGE

4. RESPONSIBLE COMPUTER SPECIALIST:
NAME AND PHONE NUMBER Robert S. Pritchard (206)363-3394
ADDRESS IceCasting, Inc. 11042 Sand Point Way N.E.
Seattle, WA 98125-5846

COMPLETE THIS SECTION IF DATA ARE ON MAGNETIC TAPE

5. RECORDING MODE
☐ BCD ☐ BINARY
☐ ASCII ☒ EBCDIC
☐ _____

6. NUMBER OF TRACKS (CHANNELS)
☐ SEVEN
☒ NINE
☐ _____

7. PARITY
☒ ODD
☐ EVEN

8. DENSITY
☐ 200 BPI ☒ 1600 BPI
☐ 556 BPI
☐ 800 BPI
☐ _____

9. LENGTH OF INTER-RECORD GAP (IF KNOWN) ☒ 3/4 INCH
standard ☐ _____

10. END OF FILE MARK ☐ OCTAL 17
standard ☐ unknown

11. PASTE-ON-PAPER LABEL DESCRIPTION *(INCLUDE ORIGINATOR NAME AND SOME LAY SPECIFICATIONS OF DATA TYPE, VOLUME NUMBER)*
Robert S. Pritchard
IceCasting, Inc.
Ice motion, wind, barometric pressure, and current data from 17 drifting buoys in Norton Sound and the Chukchi Sea during 1981-82.

12. PHYSICAL BLOCK LENGTH IN BYTES
1600

13. LENGTH OF BYTES IN BITS
8

NOAA FORM 24-13

Table 1. A brief description of files containing data for drifting buoys 3607-3625.

file #	lines	words	bytes	FILE NAME	Comments
1	18	18	107	list	1st set of files
2	483	4360	39108	n3607	
3	2718	23062	220143	n3608	
4	1011	8393	81876	n3609	
5	64	396	5169	n3610	
6	417	2625	33762	n3611	
7	1017	6554	82362	n3612	
8	502	3377	40647	n3613	
9	1127	6959	91272	n3614	
10	278	1744	22503	n3615	
11	967	6480	78312	n3616	
12	1076	6514	87141	n3617	
13	20	136	1591	n3620	
14	3875	21476	313846	n3621	
15	2557	18173	207088	n3622	
16	1109	8298	89800	n3623	
17	1783	13487	144394	n3624	
18	2132	15429	172663	n3625	
19	18	18	107	list	duplicate set of files
20	483	4360	39108	n3607	
21	2718	23062	220143	n3608	
22	1011	8393	81876	n3609	
23	64	396	5169	n3610	
24	417	2625	33762	n3611	
25	1017	6554	82362	n3612	
26	502	3377	40647	n3613	
27	1127	6959	91272	n3614	
28	278	1744	22503	n3615	
29	967	6480	78312	n3616	
30	1076	6514	87141	n3617	
31	20	136	1591	n3620	
32	3875	21476	313846	n3621	
33	2557	18173	207088	n3622	
34	1109	8298	89800	n3623	
35	1783	13487	144394	n3624	
36	2132	15429	172663	n3625	

RECORD FORMAT DESCRIPTION

Record Name: HEADER

14.Field Name	15.Position From 1- in Bytes	16.Length Bytes	17.Attributes	18.Use and Meaning
File Type	1	3	A1	'156'
File Identifier	4	6	A6	'NORTON' or 'CHUKCH' depending on location
Record Type	10	1	A1	'A'
Drogue Number	11	5	I5	3607, 3608,...3625
Drogue Type	16	5	A5	'NORTN' or 'CHUKC' to identify station
Principal Investigator	21	15	A15	'R.S. Pritchard '
Institution or Agency	36	15	A15	'IceCasting, Inc'
Platform Name	51	12	A12	' ADAP '
Buoy Number	63	4	I4	Same as Drogue Number
Blanks	67	14	14X	

RECORD FORMAT DESCRIPTION

Record Name: LAUNCH SUMMARY

14.Field Name	15.Position From 1- in Bytes	16.Length Bytes	17.Attributes	18.Use and Meaning
File Type	1	3	A1	'156'
File Identifier	4	6	A6	'NORTON' or 'CHUKCH' depending on location
Record Type	10	1	A1	'B'
Drogue Number	11	5	I5	3607, 3608,...3625
Launch Position				
Latitude	16	7	3I2,A1	DDMMSS plus 'N' or 'S' for hemisphere
Longitude	23	8	I3,2I2,A1	DDDMMSS plus 'E' or 'W' for hemisphere
End Position				
Latitude	31	7	3I2,A1	DDDMMSS plus 'N' or 'S' for hemisphere
Longitude	38	8	I3,2I2,A1	DDMMSS plus 'E' or 'W' for hemisphere
Launch Date(GMT)	46	6	3I2	YYMMDD
Launch Time(GMT)	52	4	2I2	HHXX hours and minutes
End Date(GMT)	56	6	3I2	YYMMDD
End Time(GMT)	62	4	2I2	HHXX hours and minutes
Drogue Depth	66	4	I4	Not Used
Observation Frequency	70	4	I4	Not Used
Blanks	74	7	7X	

RECORD FORMAT DESCRIPTION

Record Name: SURFACE DATA

14.Field Name	15.Position From 1- in Bytes	16.Length Bytes	17.Attributes	18.Use and Meaning
File Type	1	3	A3	'156'
File Identifier	4	6	A6	'NORTON' or 'CHUKCH' depending on location
Record Type	10	1	A1	'A'
Drogue Number	11	5	I5	3607, 3608,...3625
Position				
Latitude	16	7	3I2,A1	DDMMSS plus 'N' or 'S' for hemisphere
Longitude	23	8	I3,2I2,A1	DDDMMSS plus 'E' or 'W' for hemisphere
Observed Date(GMT)	31	6	3I2	YYMMDD
Observed Time(GMT)	37	4	2I2	HHXX hours and minutes
Anemometer Height	41	3	I3	xxx-meters to tenths
Wind Speed	44	3	I3	xxx-meters/sec to tenths
Wind Direction	47	4	I4	xxxx-degrees to tenths cw from North, Direction From
Atmospheric Pressure	51	6	I6	xxxxxx-millibars to hundredths
Air Temperature	57	4	I4	xxxx-Deg C to tenths
Compass Bearing of Surface Unit	61	4	I4	xxxx-degrees to tenths cw from North
Blanks	65	11	11X	
Position Code	76	1	A1	'M' for raw position from ARGOS, 'C' for Optimal Interpolation Estimate
Sequence Number	77	4	I4	xxxx-data card number, in ascending order

RECORD FORMAT DESCRIPTION

Record Name: SUBSURFACE CURRENT

14.Field Name	15.Position From 1- in Bytes	16.Length Bytes	17.Attributes	18.Use and Meaning
File Type	1	3	A3	'156'
File Identifier	4	6	A6	'NORTON' or 'CHUKCH' depending on location
Record Type	10	1	A1	'F'
Drogue Number	11	5	I5	3607, 3608,...3625
Position				
Latitude	16	7	3I2,A1	DDMMSS plus 'N' or 'S' for hemisphere
Longitude	23	8	I3,2I2,A1	DDDMMSS plus 'E' or 'W' for hemisphere
Observed Date(GMT)	31	6	3I2	YYMMDD
Observed Time(GMT)	37	4	2I2	HHXX hours and minutes
Ice Velocity				
Speed	41	5	I5	xxxxx-cm/sec to tenths
Direction	46	4	I4	xxxx-Degrees to tenths cw from North, Direction Toward
Current Meter Depth	50	4	I4	xxxx-meters to tenths
Absolute Current				
Speed	54	5	I5	xxxxx-cm/sec to tenths
Direction	59	4	I4	xxxx-Degrees to tenths cw from North, Direction Toward
Current Meter Depth	63	4	I4	Not Used
Absolute Current				
Speed	67	5	I5	Not Used
Direction	72	4	I4	Not Used
Position Code	76	1	A1	'M' for raw position from ARGOS, 'C' for Optimal Interpolation Estimate
Sequence Number	77	4	I4	xxxx-data card number, in ascending order

APPENDIX B

Sea Ice Trajectories

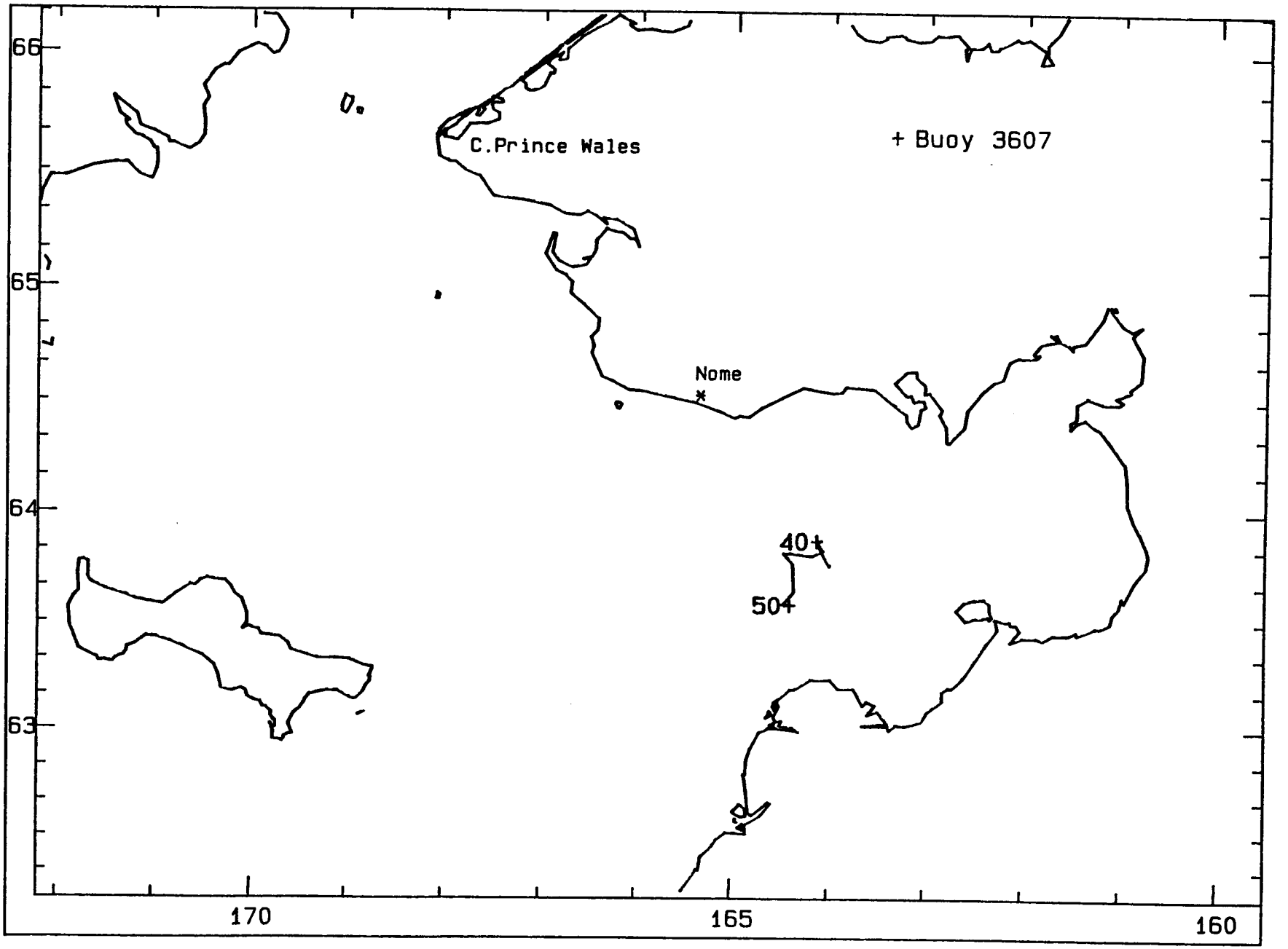
66
65
64
63
170
165
160
C.Prince Wales
+ Buoy 3607
Nome
40+
50+

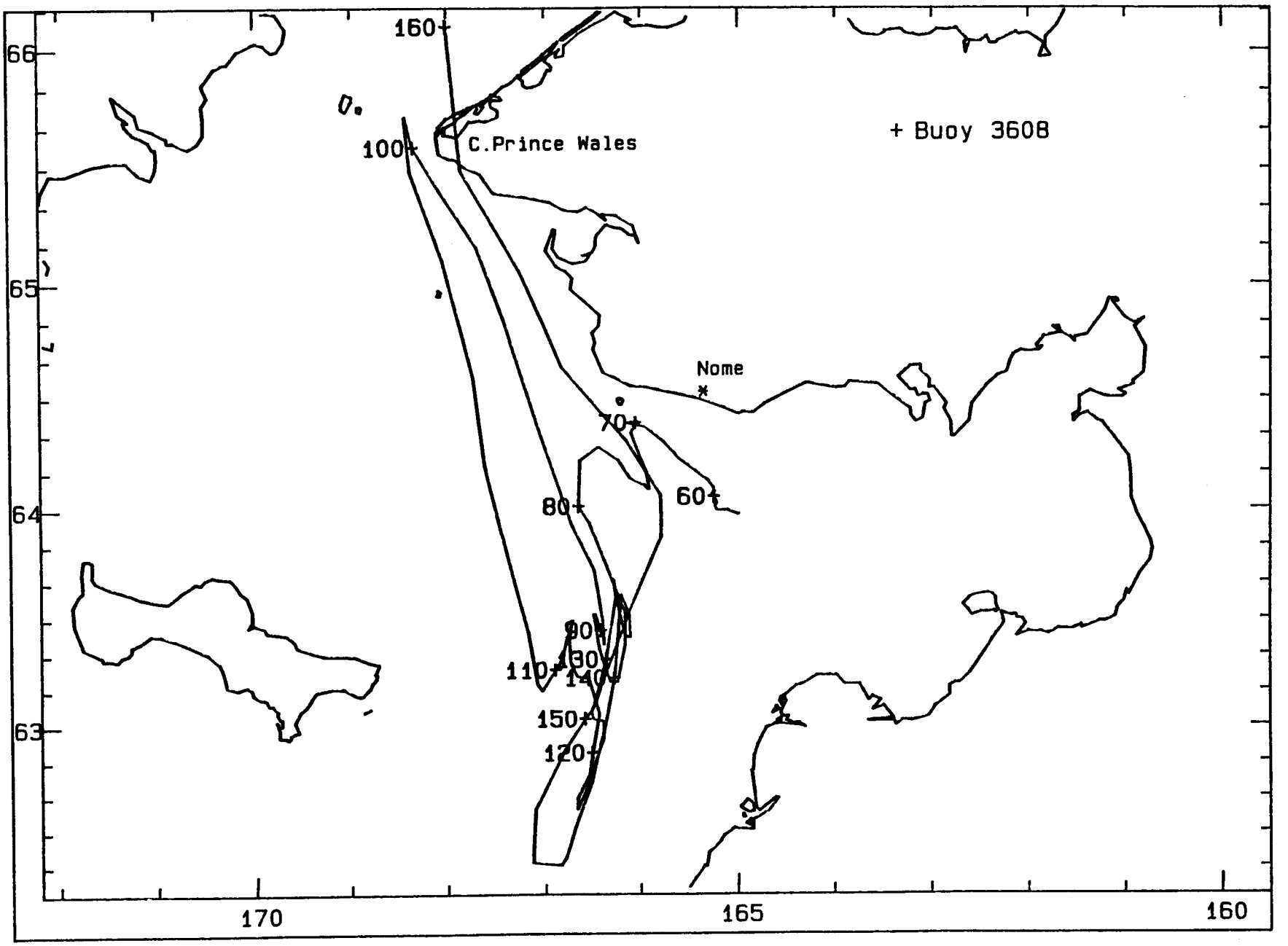
160
0
100
C.Prince Wales
+ Buoy 3608
Nome
70
60
80
90
110
130
140
150
120
66
65
64
63
170
165
160

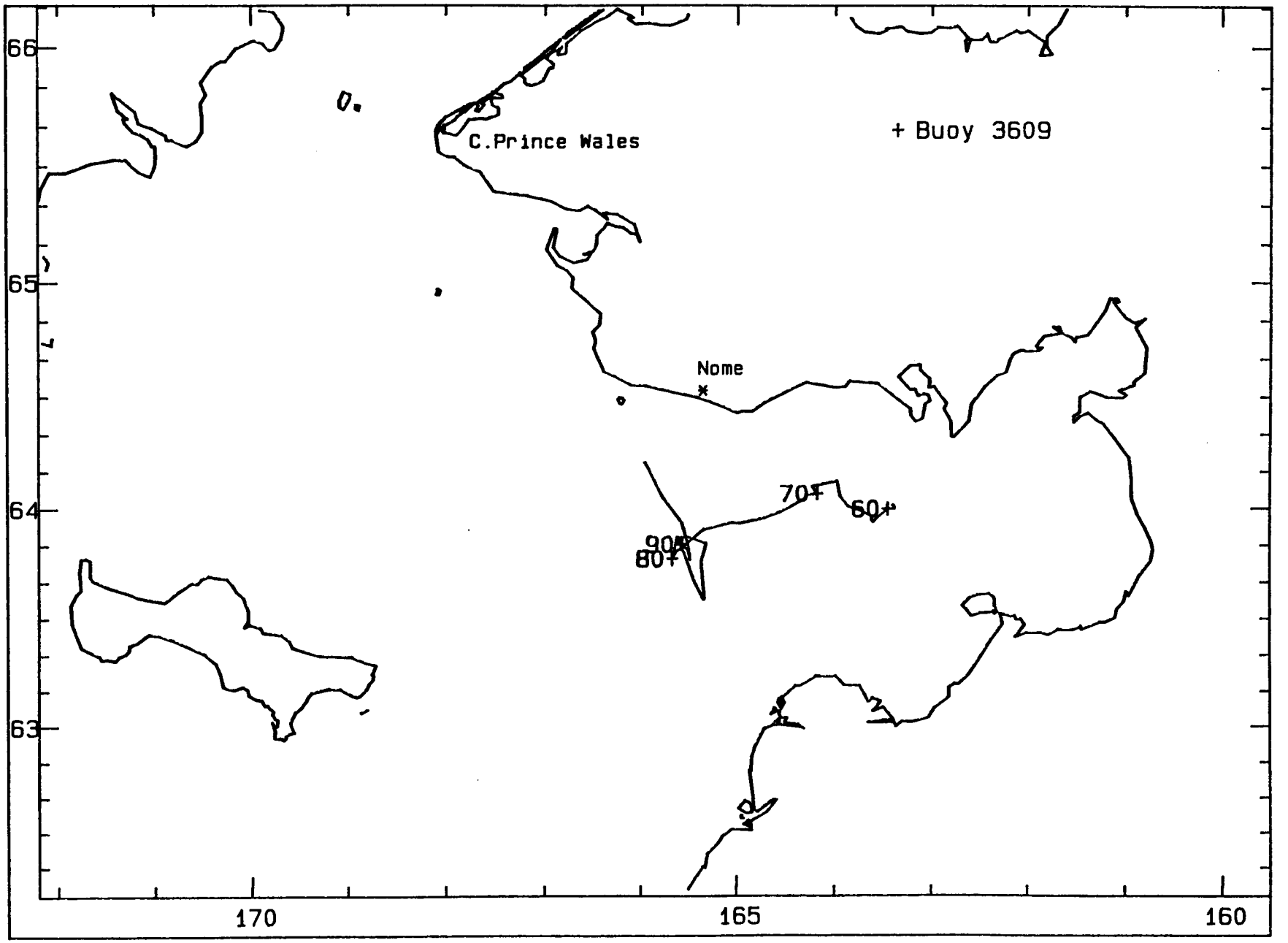
66
65
64
63
170
165
160
C.Prince Wales
+ Buoy 3609
Nome
70
60
90
80

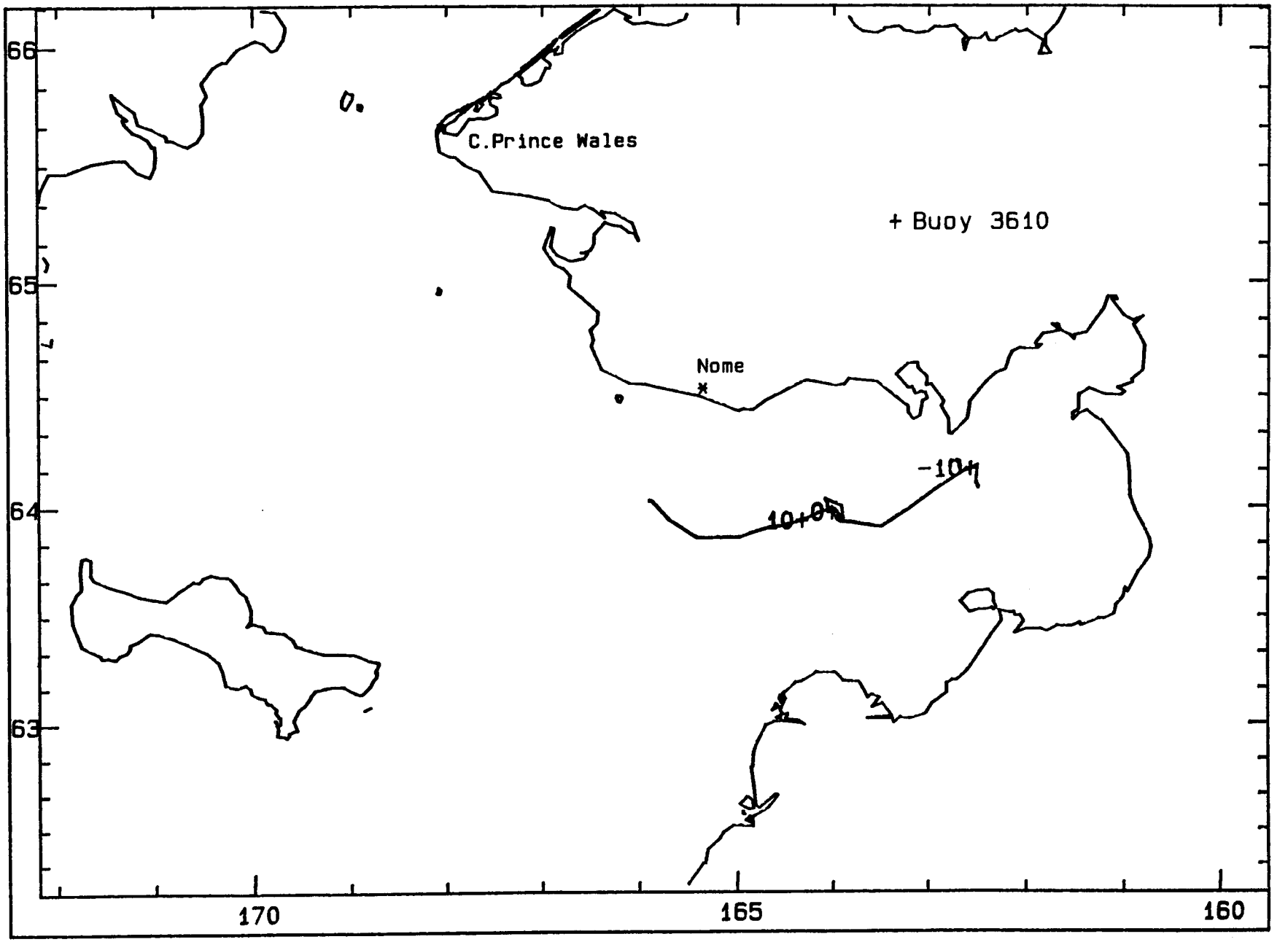
66
65
64
63
170
165
160
C.Prince Wales
+ Buoy 3610
Nome
-10
-10

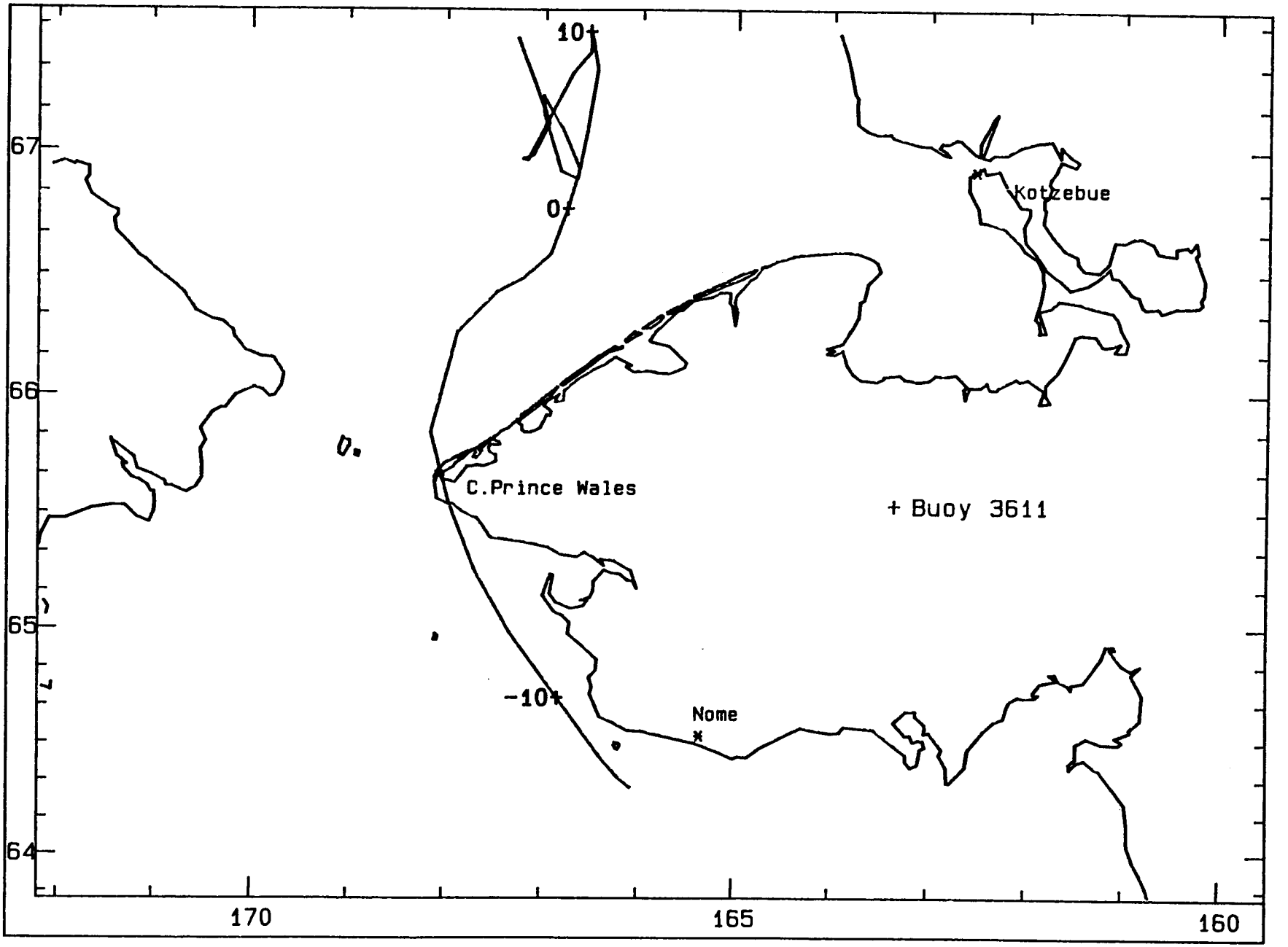
10+
0+
-10+
67
66
65
64
170
165
160
Kotzebue
C.Prince Wales
Nome
+ Buoy 3611

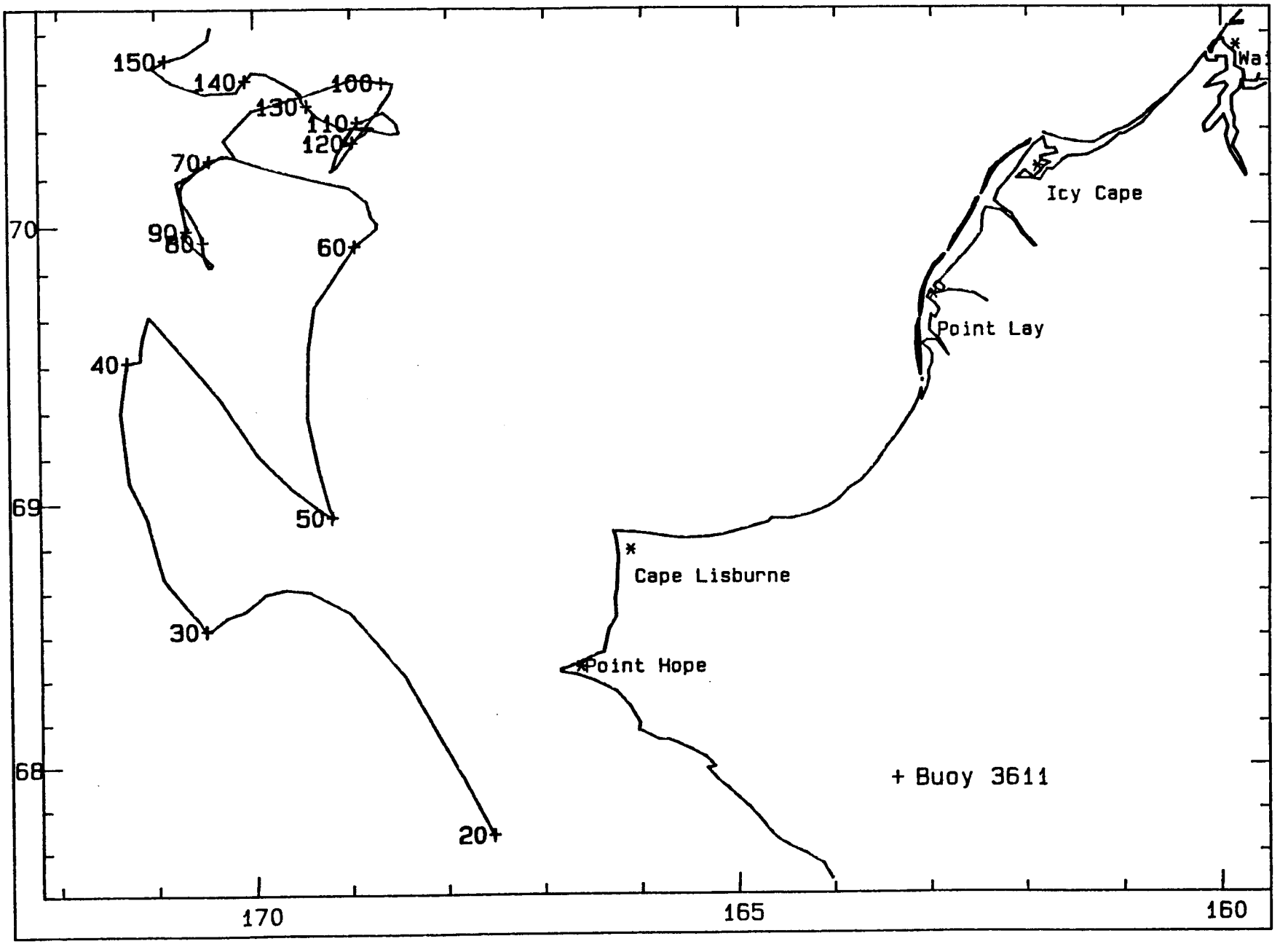
150+
140+
100+
130+
110+
120+
70+
90+
80+
60+
40+
50+
30+
20+
70
69
68
170
165
160
Icy Cape
Point Lay
Cape Lisburne
Point Hope
+ Buoy 3611

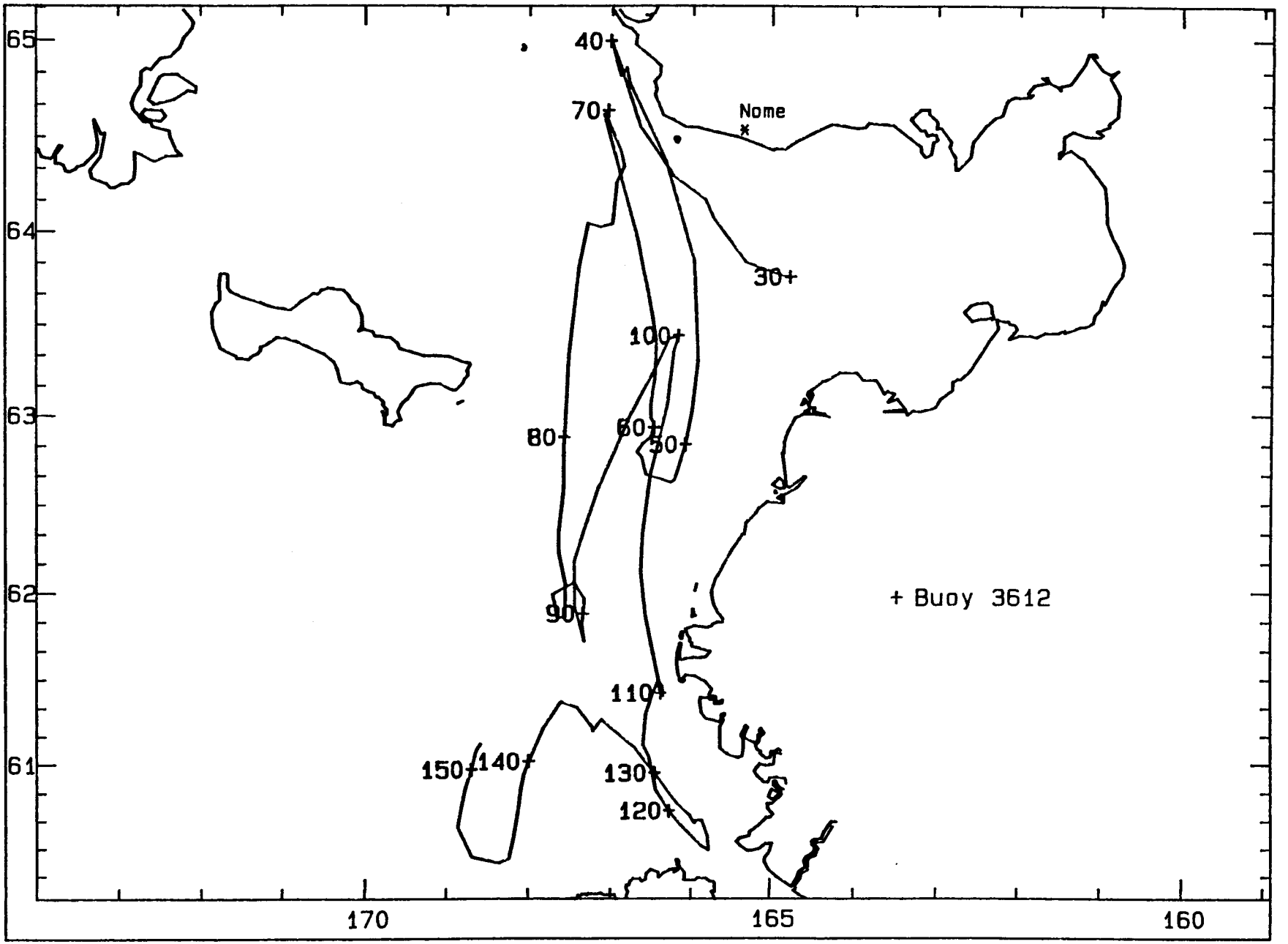
65
64
63
62
61
170
165
160
Nome
40+
70+
30+
100+
80+
60+
50+
90+
110+
150+
140+
130+
120+
+ Buoy 3612

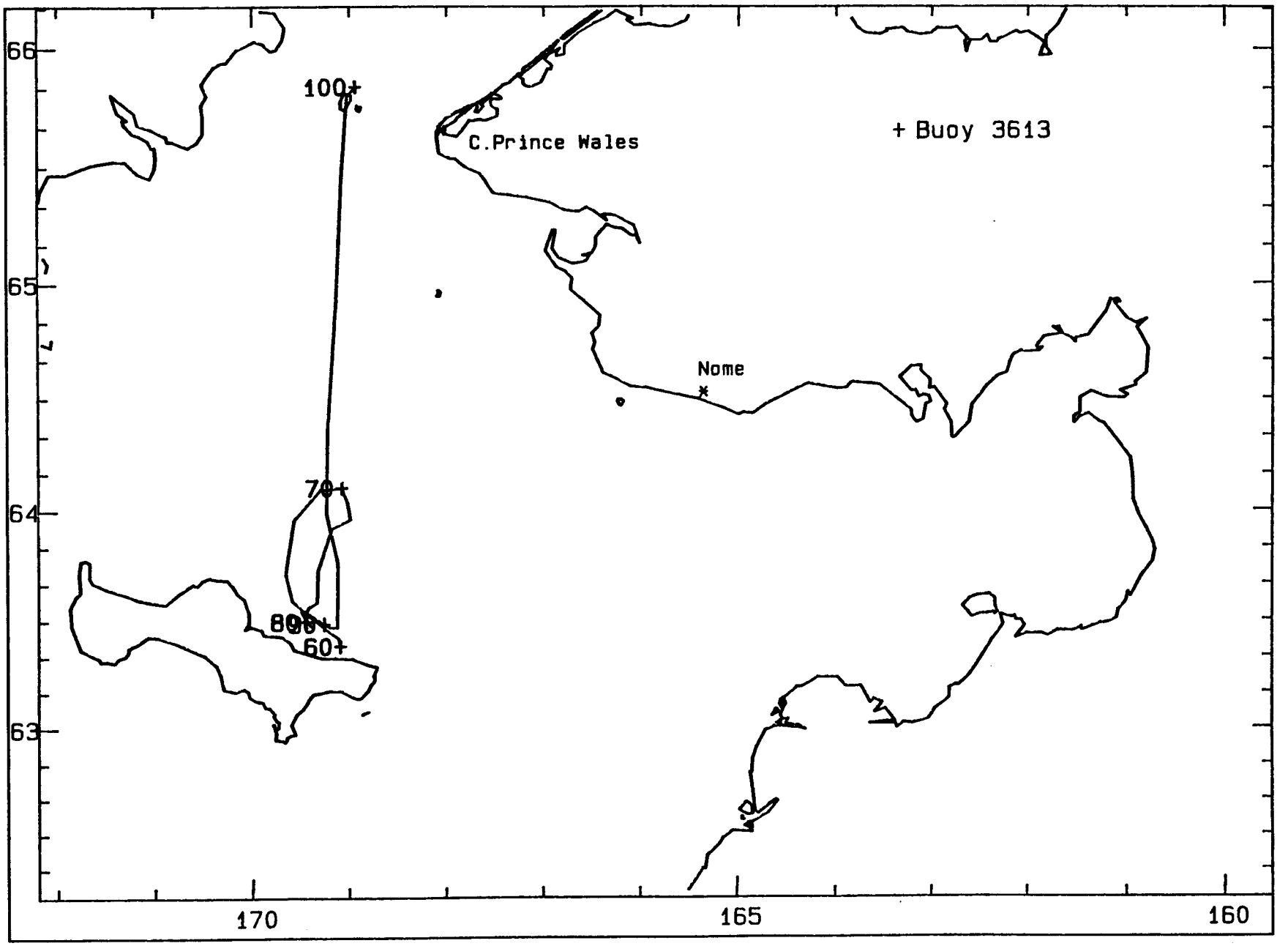
66
65
64
63
100+
70+
60+
C.Prince Wales
+ Buoy 3613
Nome
170
165
160

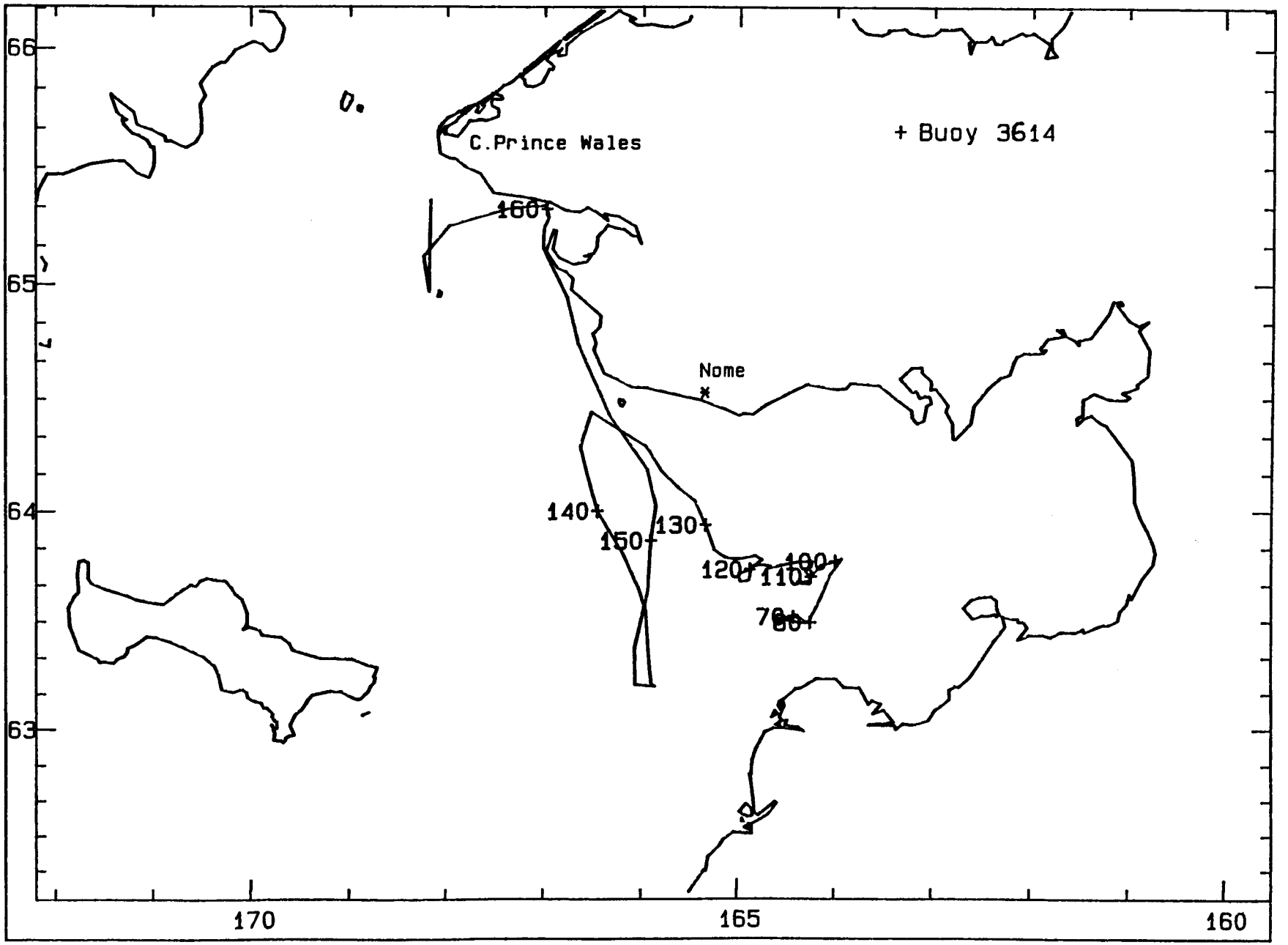
66
65
64
63
170
165
160
C.Prince Wales
+ Buoy 3614
160+
Nome
140+
150+
130+
120+
110+
100+
70+
80+

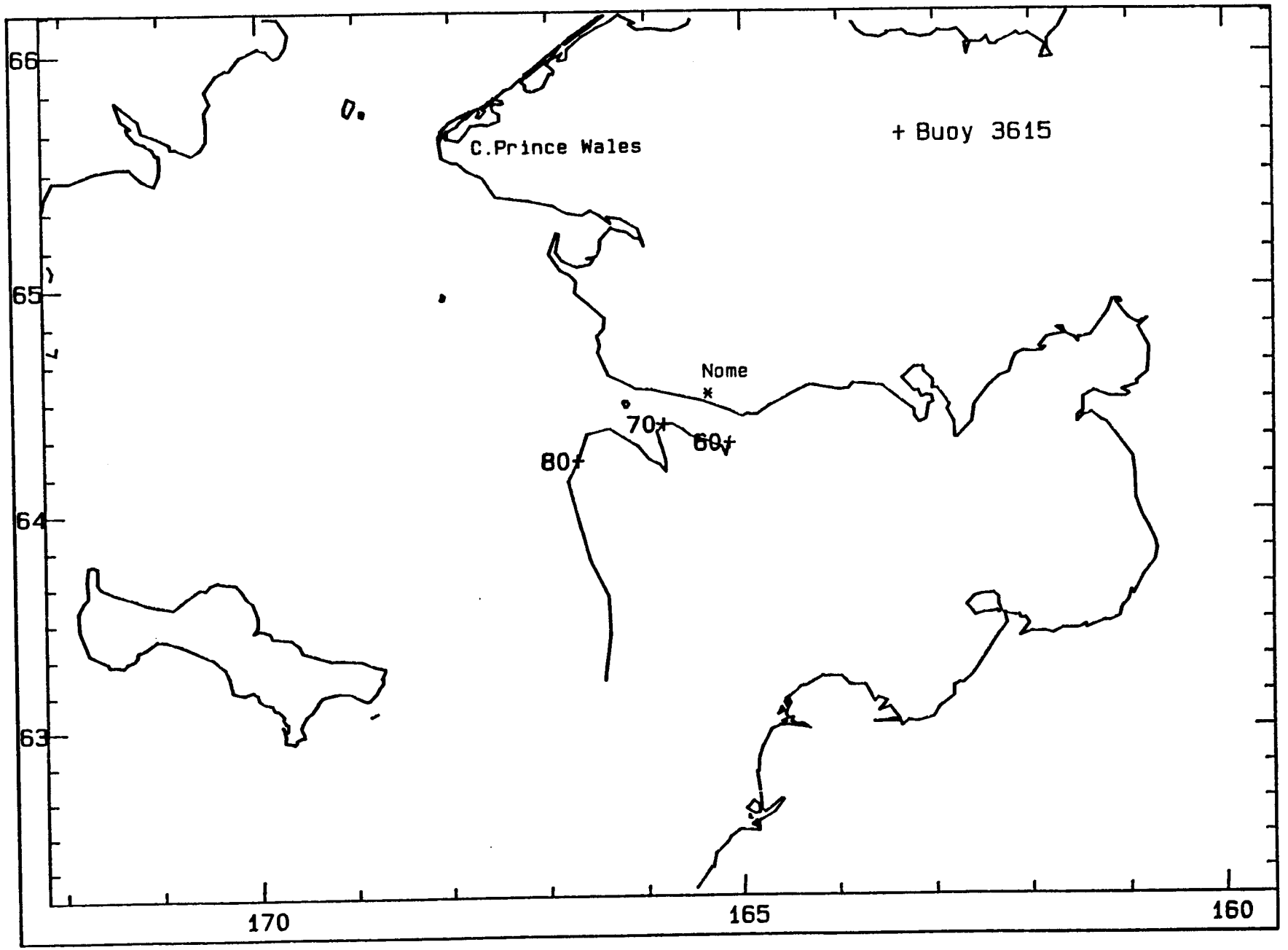
66
65
64
63
170
165
160
C.Prince Wales
+ Buoy 3615
Nome
70
60
80

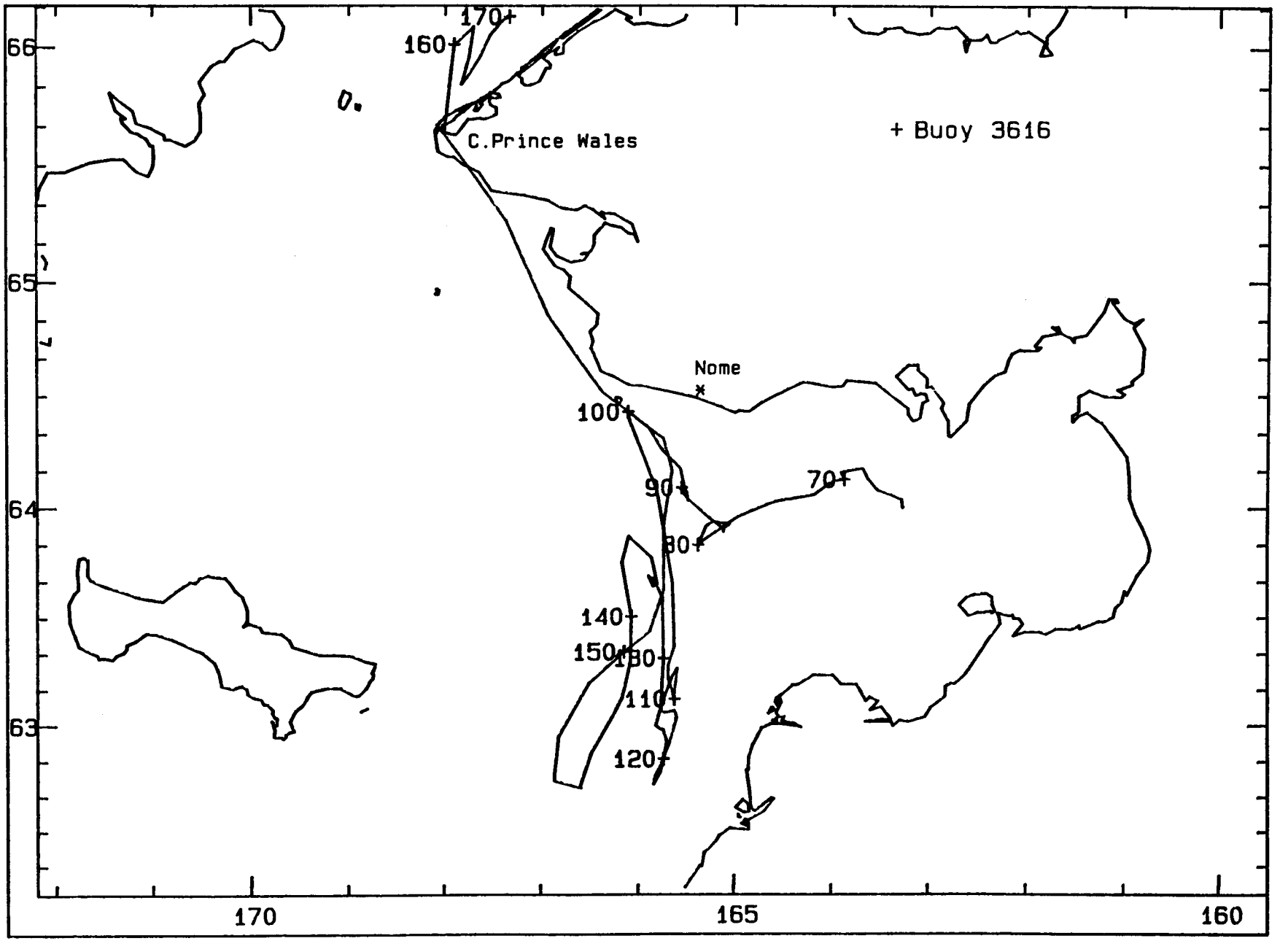
66
65
64
63
170
165
160
170+
160+
0.
C.Prince Wales
+ Buoy 3616
Nome
100+
90+
70+
80+
140+
150+
130+
110+
120+

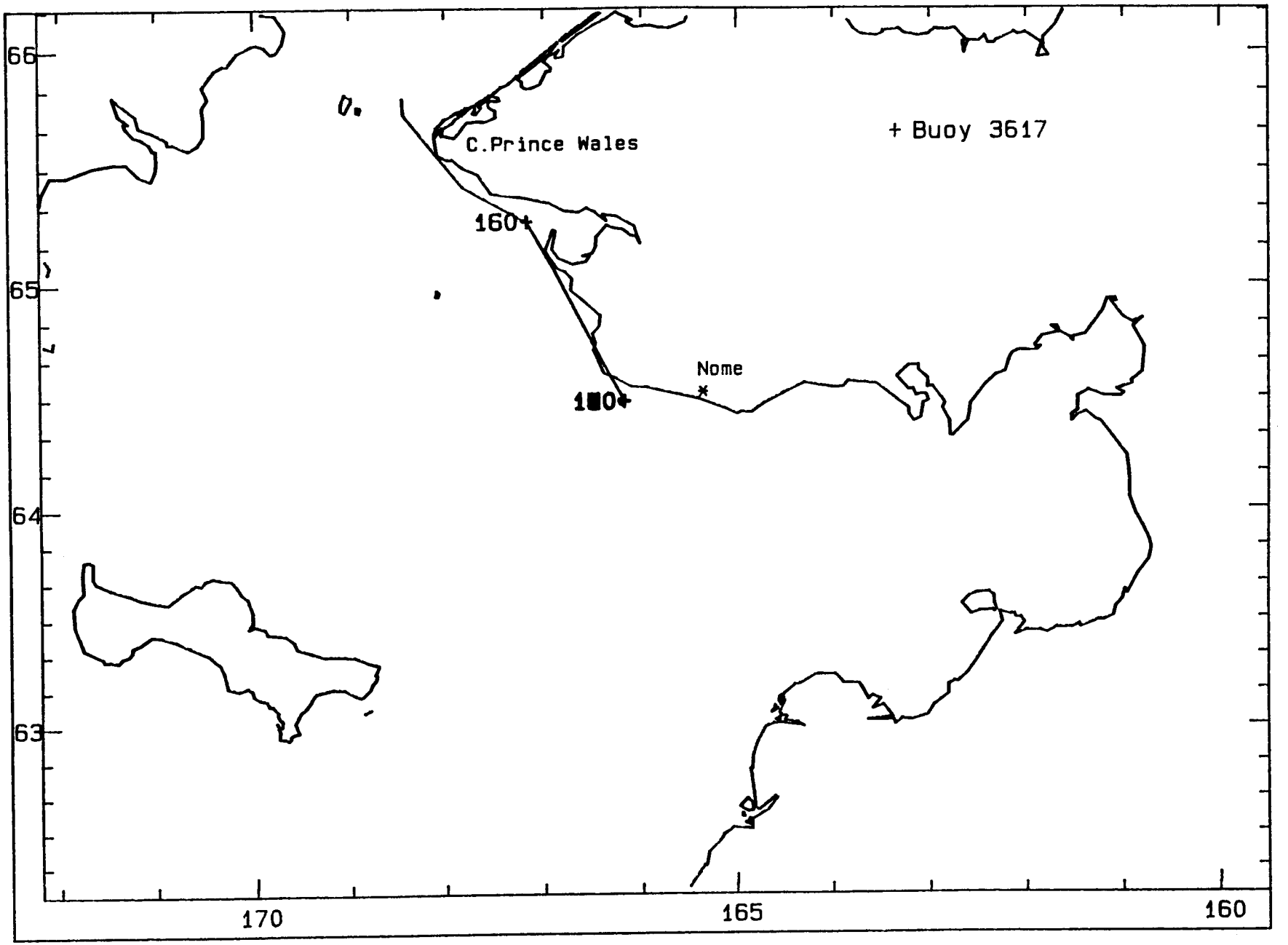
66
65
64
63
170
165
160
C.Prince Wales
+ Buoy 3617
160
Nome
180

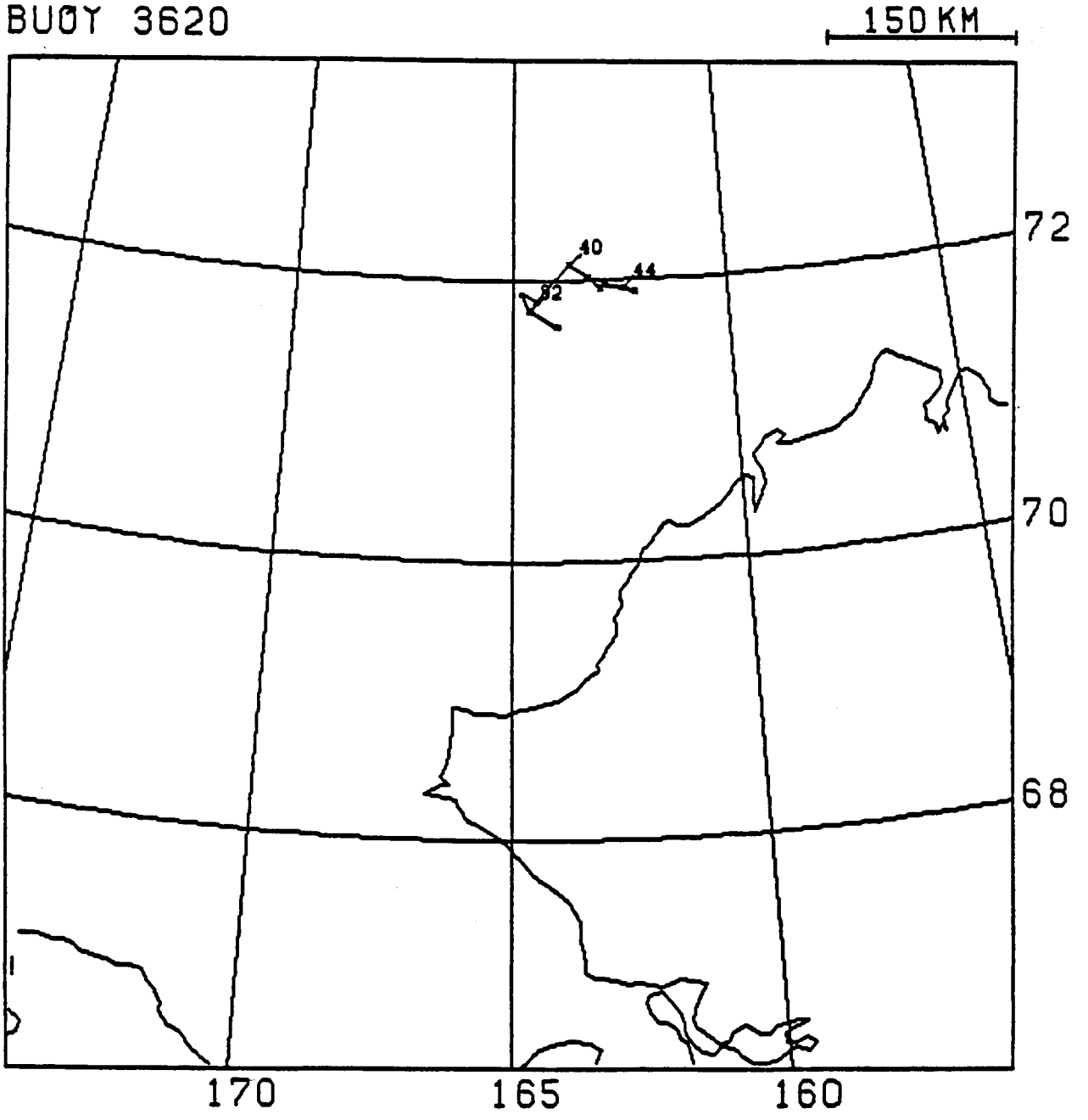
BUOY 3620
150 KM
72
70
68
170
165
160
40
44
32

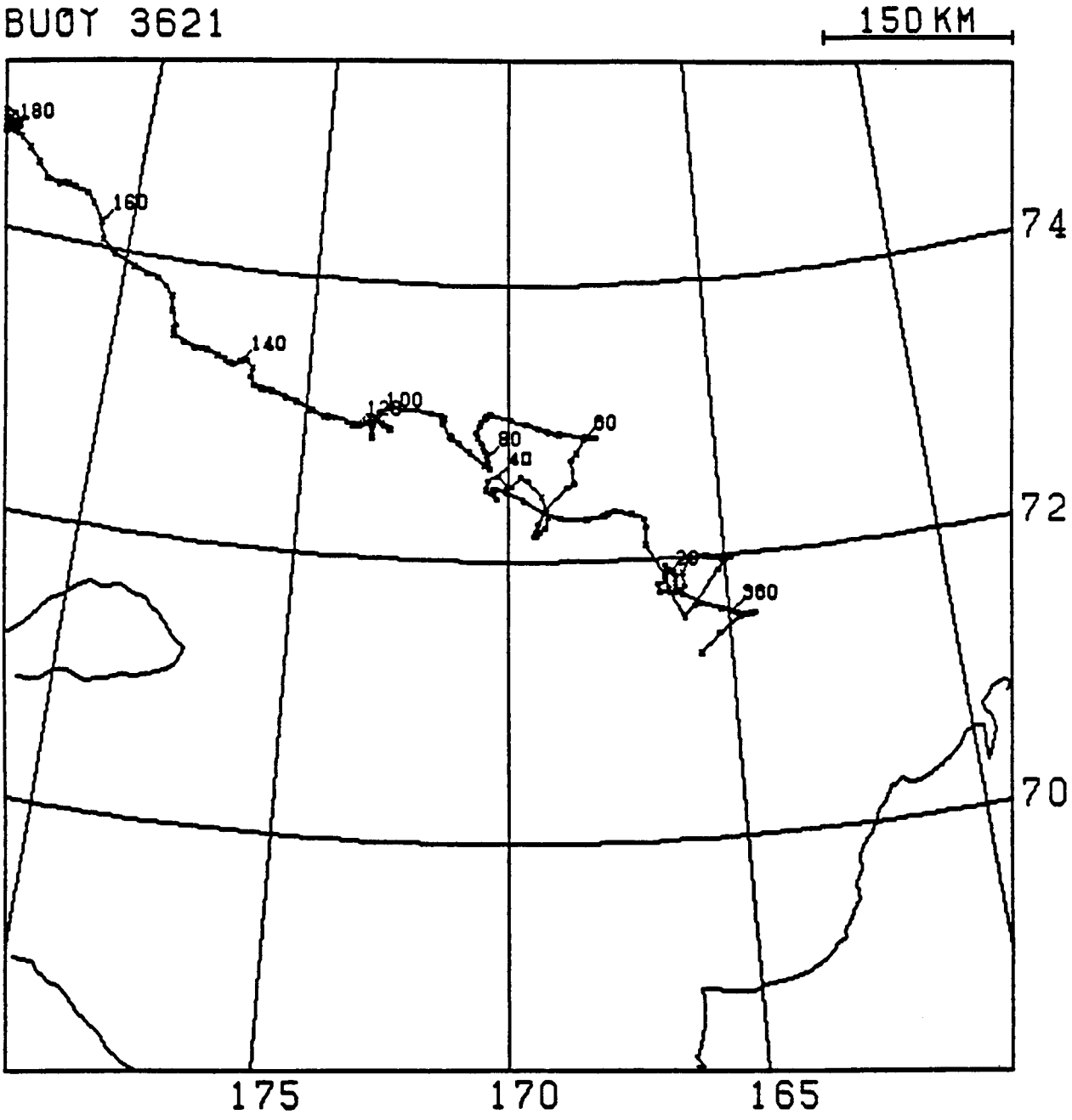
BUOY 3621
150 KM
180
160
140
120
100
80
60
40
20
360
74
72
70
175
170
165

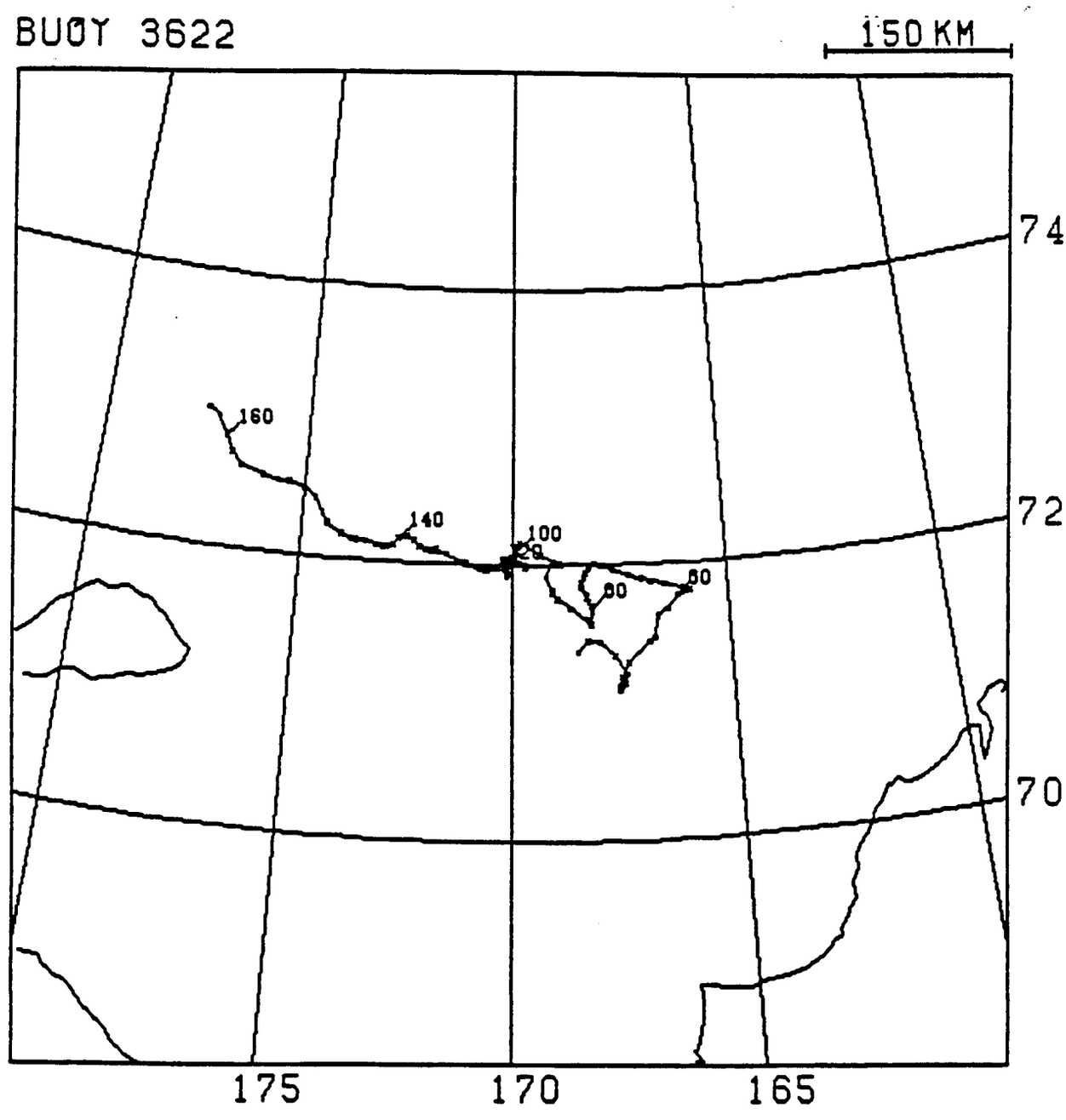
BUOY 3622
150 KM
74
72
70
160
140
100
80
60
175
170
165

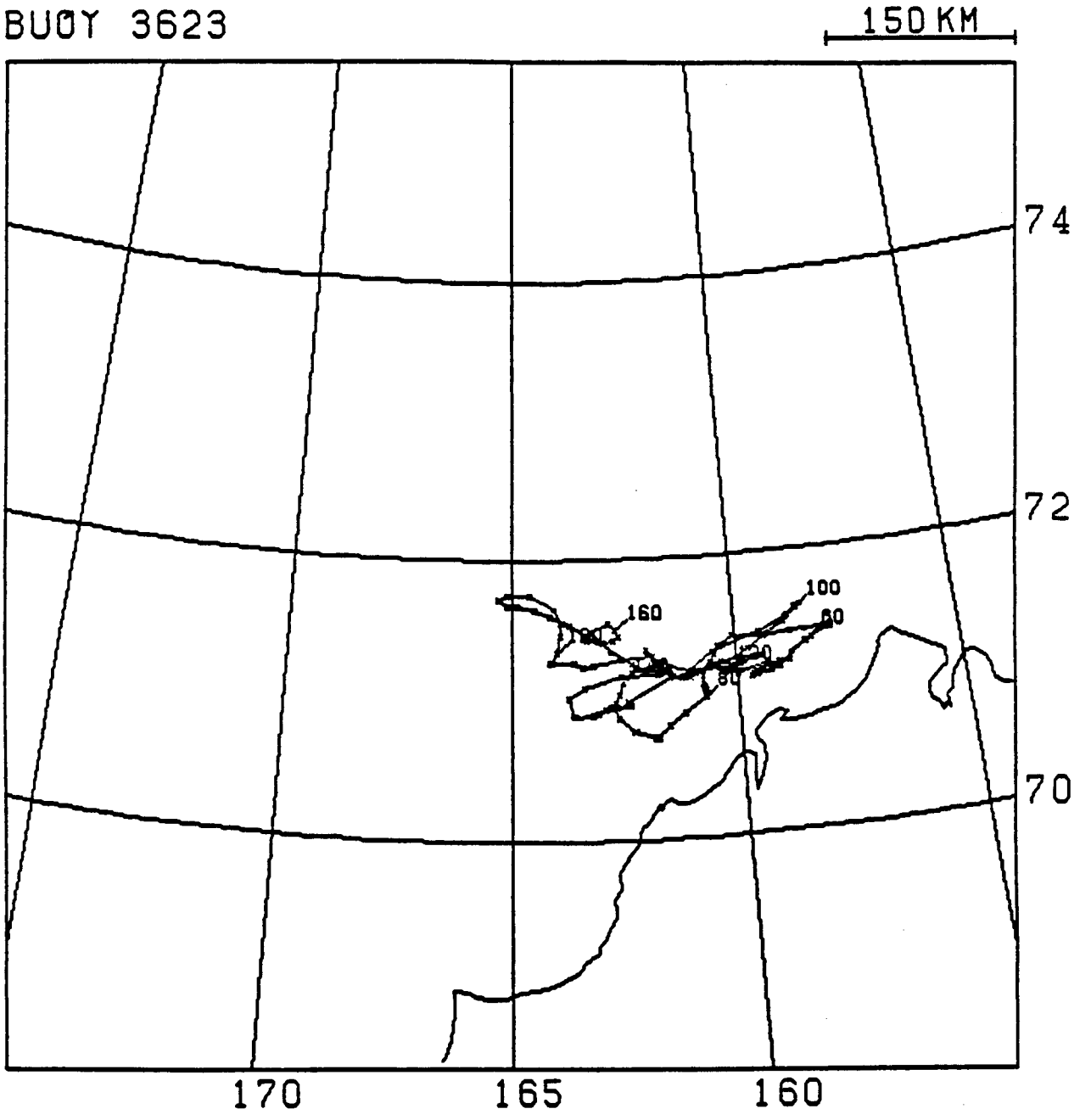
BUOY 3623
150 KM
74
72
70
170
165
160
160
100
80

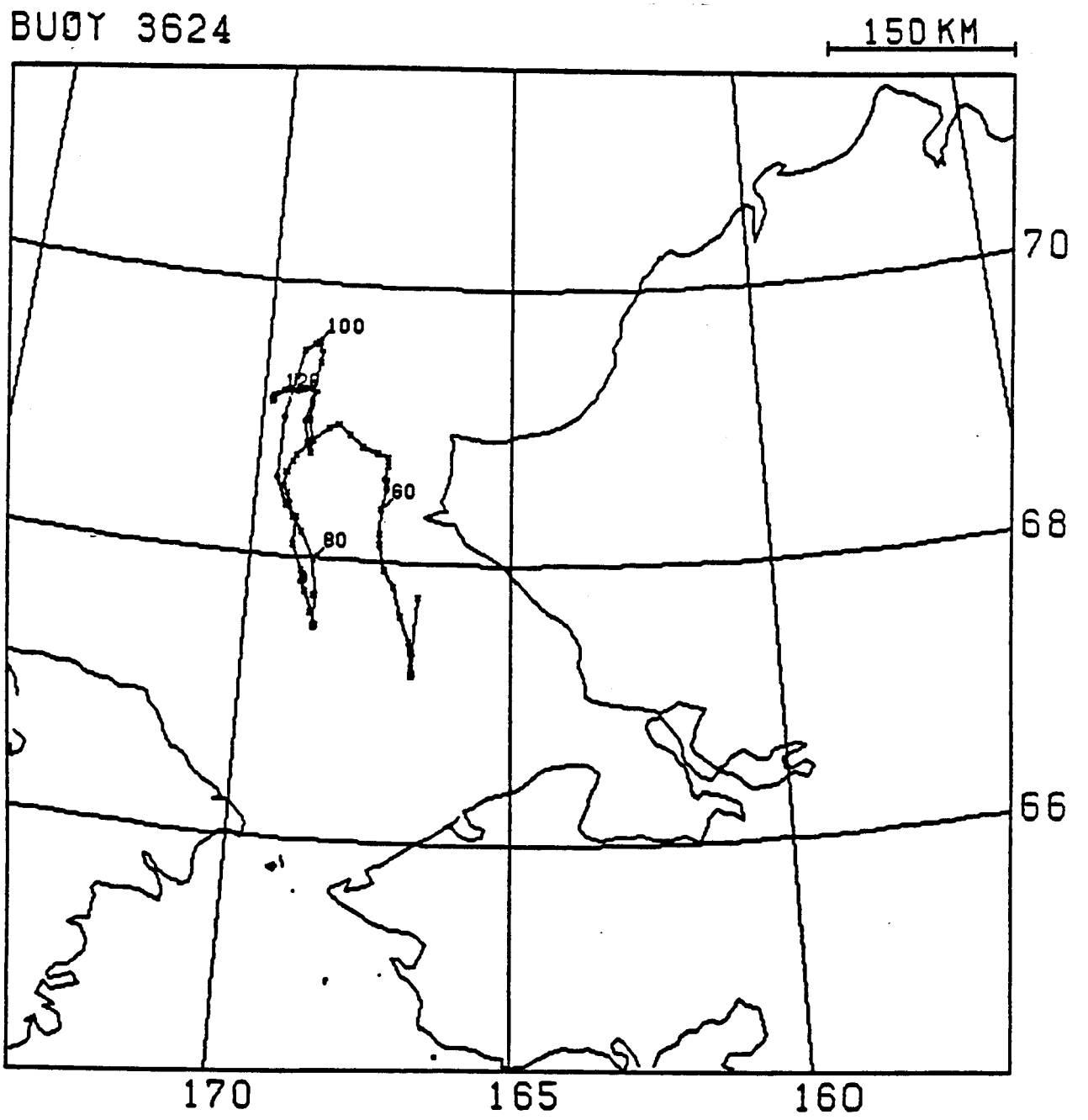
BUOY 3624
150 KM
70
68
66
100
125
60
80
170
165
160

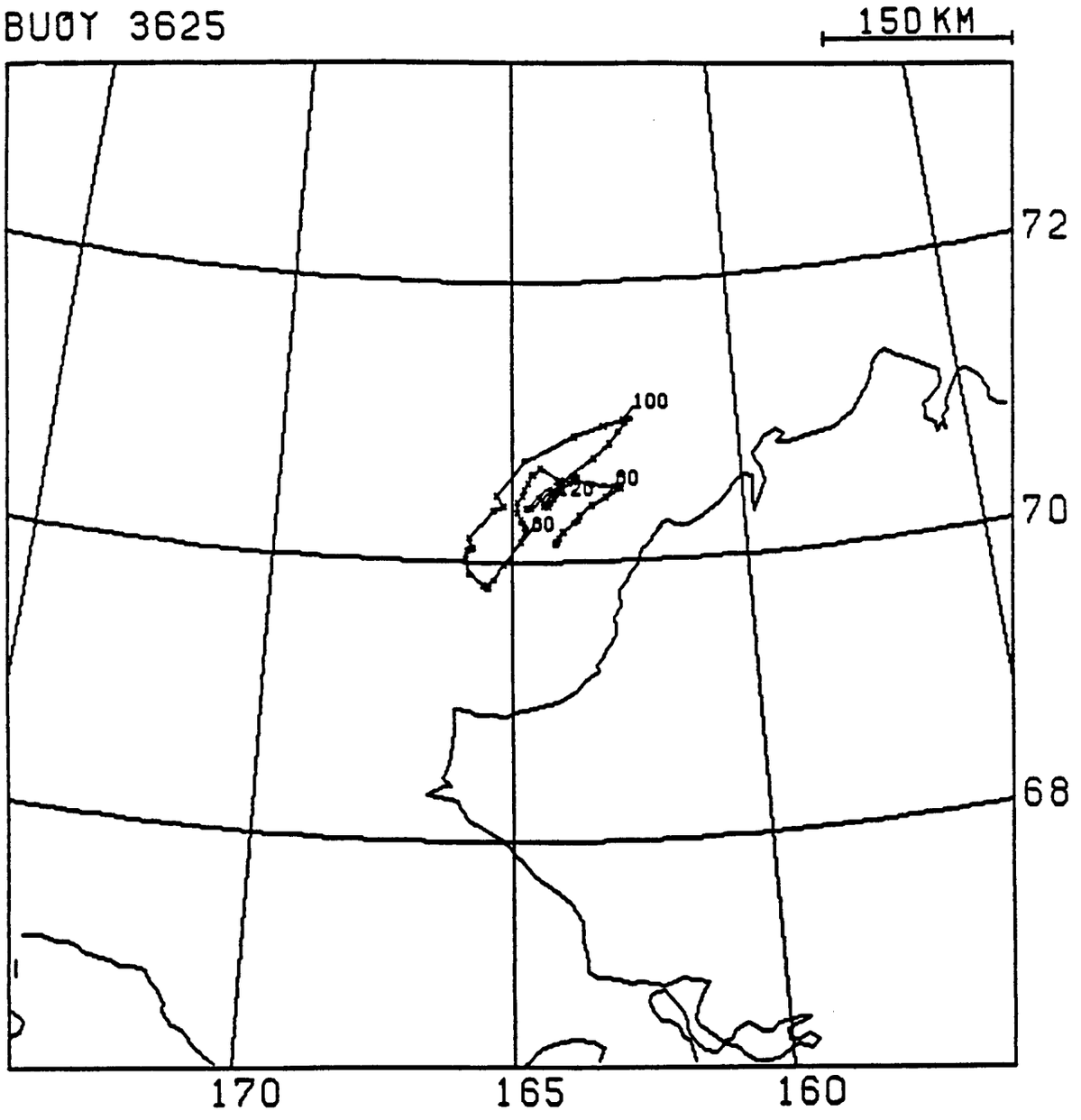
BUOY 3625
150 KM
72
70
68
100
80
60
170
165
160

CHUKCHI SEA ICE MOTIONS, 1981–82

by

Robert S. Pritchard and D. R. Thomas

Flow Industries, Inc.
Research and Technology Division
21414 – 68th Avenue South
Kent, Washington 98032

Final Report
Outer Continental Shelf Environmental Assessment Program
Research Unit 567

March 1985

TABLE OF CONTENTS

INTRODUCTION

During the winter of 1981-1982, six ice drifting buoys were deployed off the northwest coast of Alaska in the Chukchi Sea. The purpose of the work was to determine ice motions in the mobile region within about 150 km of shore, to measure ice motions further offshore, and also to measure barometric pressures and under-ice ocean currents. These data were expected to be valuable to analysts attempting to understand the forces that drive the nearshore ice at high speeds alongshore. The ice motion observations also extend the limited data base of direct measurements of Chukchi Sea ice motions.

The buoy deployment operations were presented by Thomas and Pritchard (1982). Briefly, two buoys were deployed in December 1981, and four more buoys were deployed in February 1982. Three of the latter buoys had current meters suspended 10 m below the top surface of the ice. Two of the latter buoys also contained barometers to measure atmospheric barometric pressure.

The Argos buoys, current meters, barometers and associated hardware were described in detail by Thomas and Pritchard (1982).

This report is a brief narrative description of the observed ice motions and currents.

RESULTS

The trajectories of each buoy deployed on the ice cover are presented in Figures 1 through 6. The ice motion histories were calculated using smoothed estimates of position. The smoothed positions were determined by passing a moving 48-hour cosine-bell filter over the data and calculating a position at 0000 GMT of each day. This analysis technique was used by Thomas and Pritchard (1981) to analyze ice drift behavior in Norton Sound. The position estimates each day are indicated by an 'x' on the trajectories. The date is indicated by a number determined by counting the days consecutively throughout the year, beginning with January 1 as day 1. Days in December 1981 lie in the interval of 335-365, and days in January 1982 begin with 1. Thus, January 31, 1982 is day 31, etc.

Several basic ice motion patterns are seen. The buoys further from shore (Figures 2 and 3) tend to drift fairly steadily offshore towards the west and

northwest. These buoys were deployed about 200 km away from shore. The rest of the buoys deployed nearer shore (Figures 1, 4, 5, and 6) drifted back and forth alongshore. The net motion of each nearshore buoy was much less than the total distance traveled.

The ice behavior is best viewed by breaking the time into episodic intervals. Then, at any selected time there is often a strong correlation between the motions of the buoys. For example, between days 60 and 80 all buoys, including the two further offshore, moved in a semicircular pattern to the northwest, then southwest and finally southeast.

The current meters suspended from buoys numbered 3623, 3624 and 3625 provided 9-min average current speeds and instantaneous direction readings every two hours (see Thomas and Pritchard, 1982, for descriptions of the hardware). The results are presented as stick plots in Figures 7 through 9. Each relative current vector represents the current velocity seen by an observer moving with the ice. This is different from the measurements taken by a fixed current meter. The absolute current is found by adding the ice velocity to the relative current. For example, if the ice is drifting freely with the ocean current, then the relative current would be zero.

The relative currents can be compared only until about day 66, after which the current meters on buoys numbered 3623 and 3625 stopped working. Until this failure, the currents offshore of Pt. Hope (Figure 8) and the currents offshore of Icy Cape (Figure 9) are similar. The currents offshore of Wainwright and west of Barrow (Figure 7) are not at all similar. The ice motions at all three sites appear to be similar from Figures 4 through 6. We may not be able to estimate ice velocities from these figures, however. After two of the current meters failed, the third buoy (see Figure 5 for positions and Figure 8 for relative current) continued to move about 200 km north and south offshore of Pt. Hope and Cape Lisburne. The currents during these excursions do not appear to be strongly correlated with the ice motions. From these observations, we conclude that the ice motion was not primarily driven by the local ocean currents. This conclusion differs from that of Reimer et al. (1979), who concluded that the ice in this region was strongly driven by the currents, at least when currents were large.

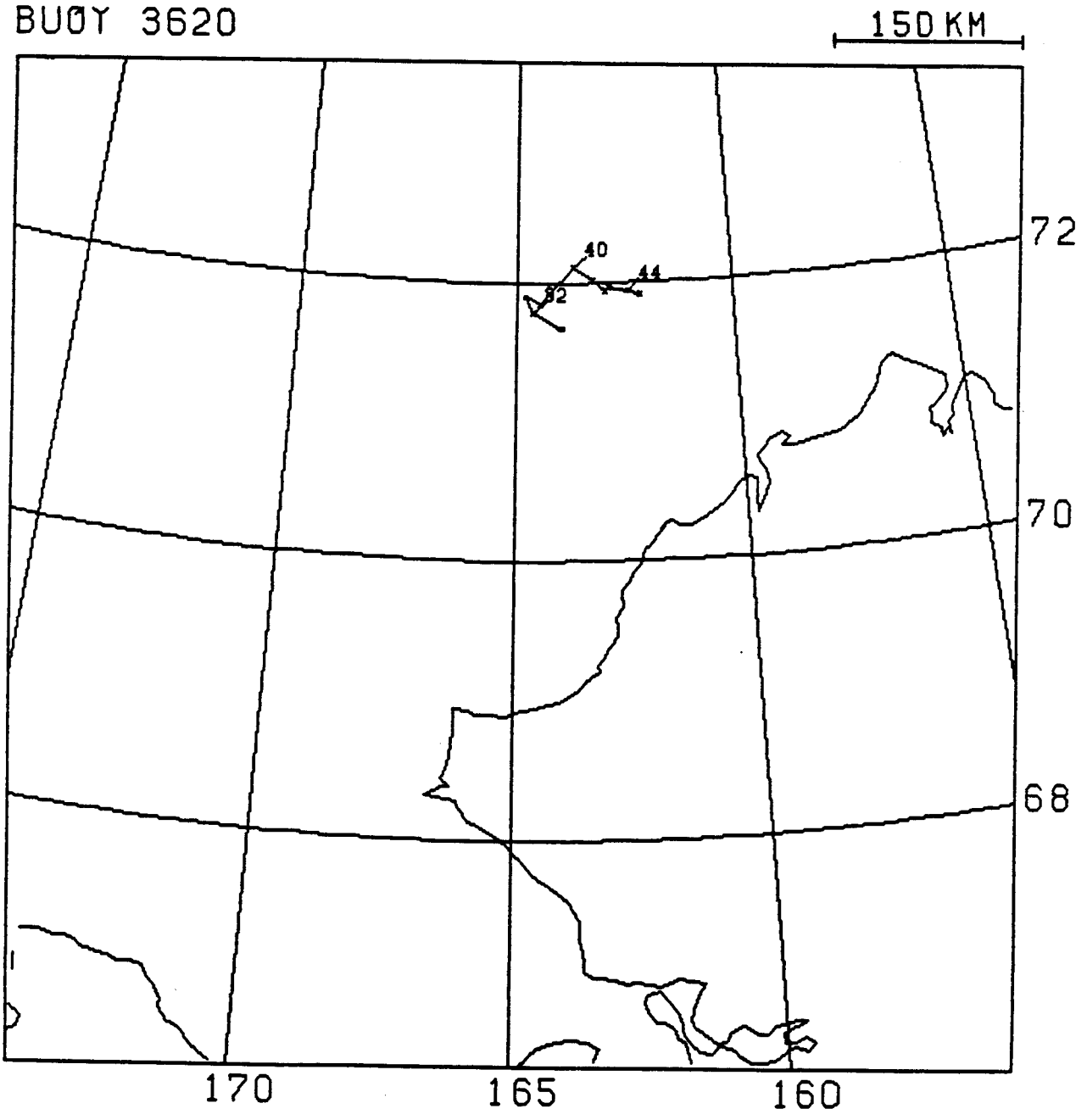

Figure 1. Trajectory for Buoy Number 3620

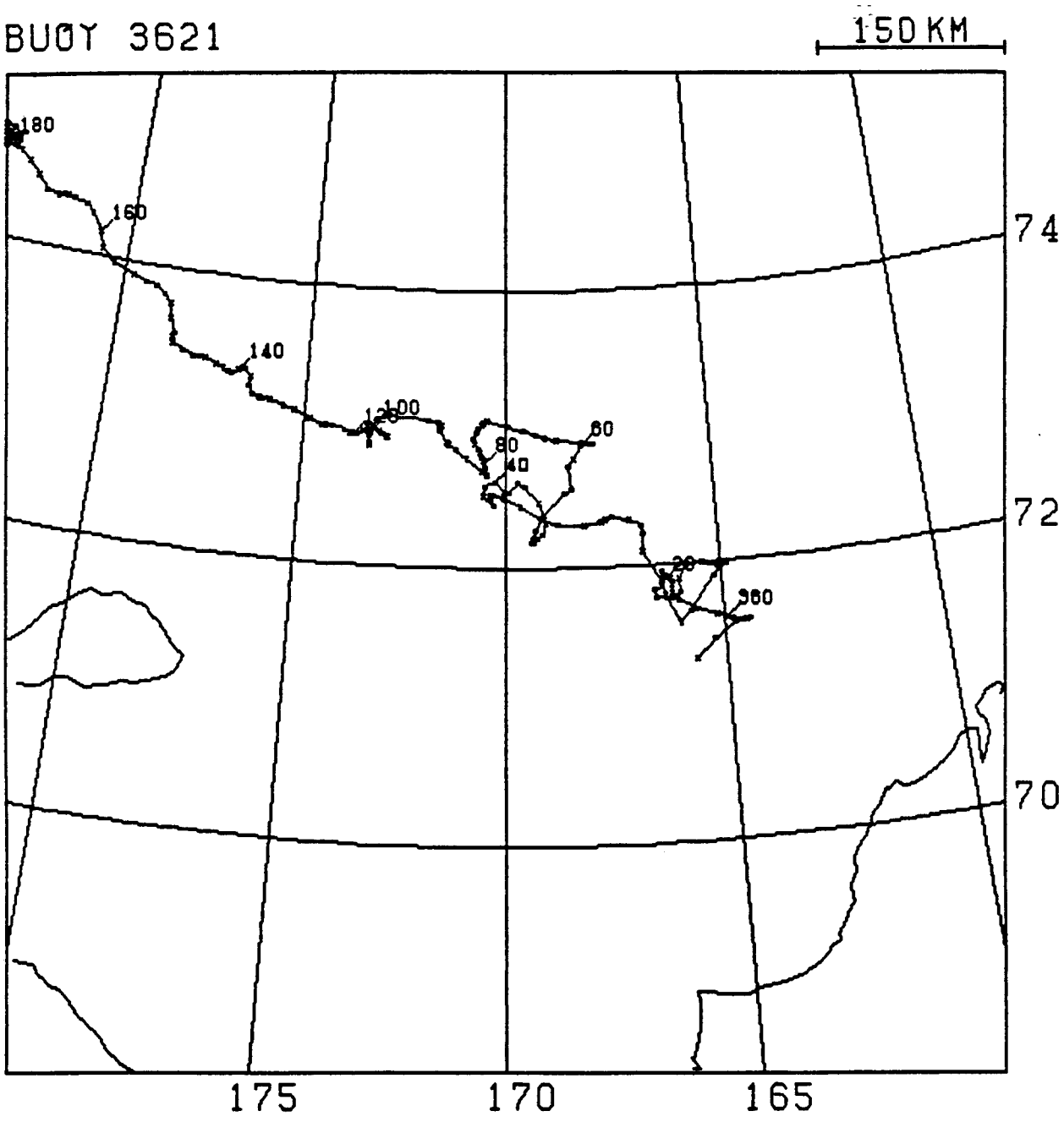

Figure 2. Trajectory for Buoy Number 3621

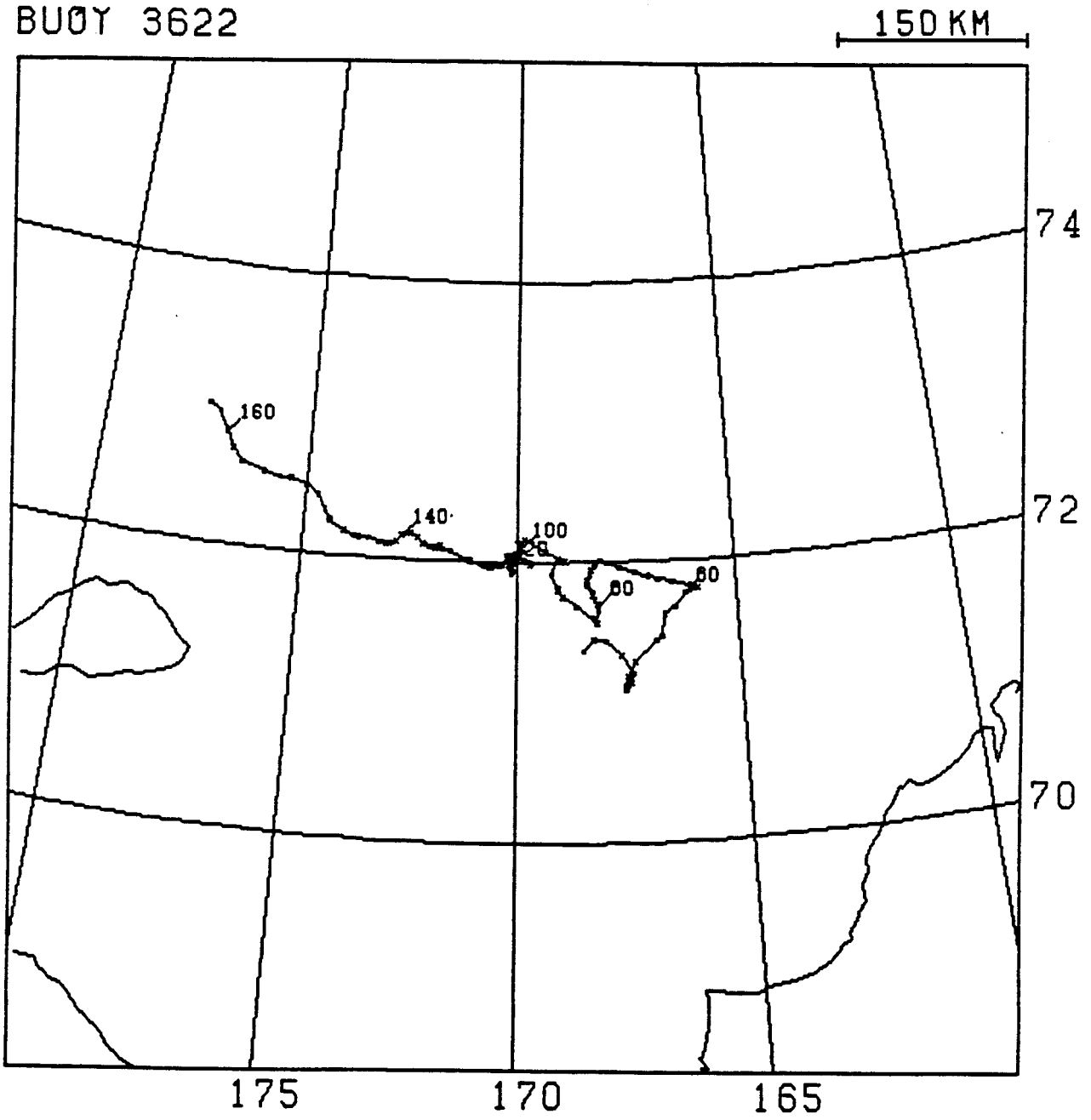

Figure 3. Trajectory for Buoy Number 3622

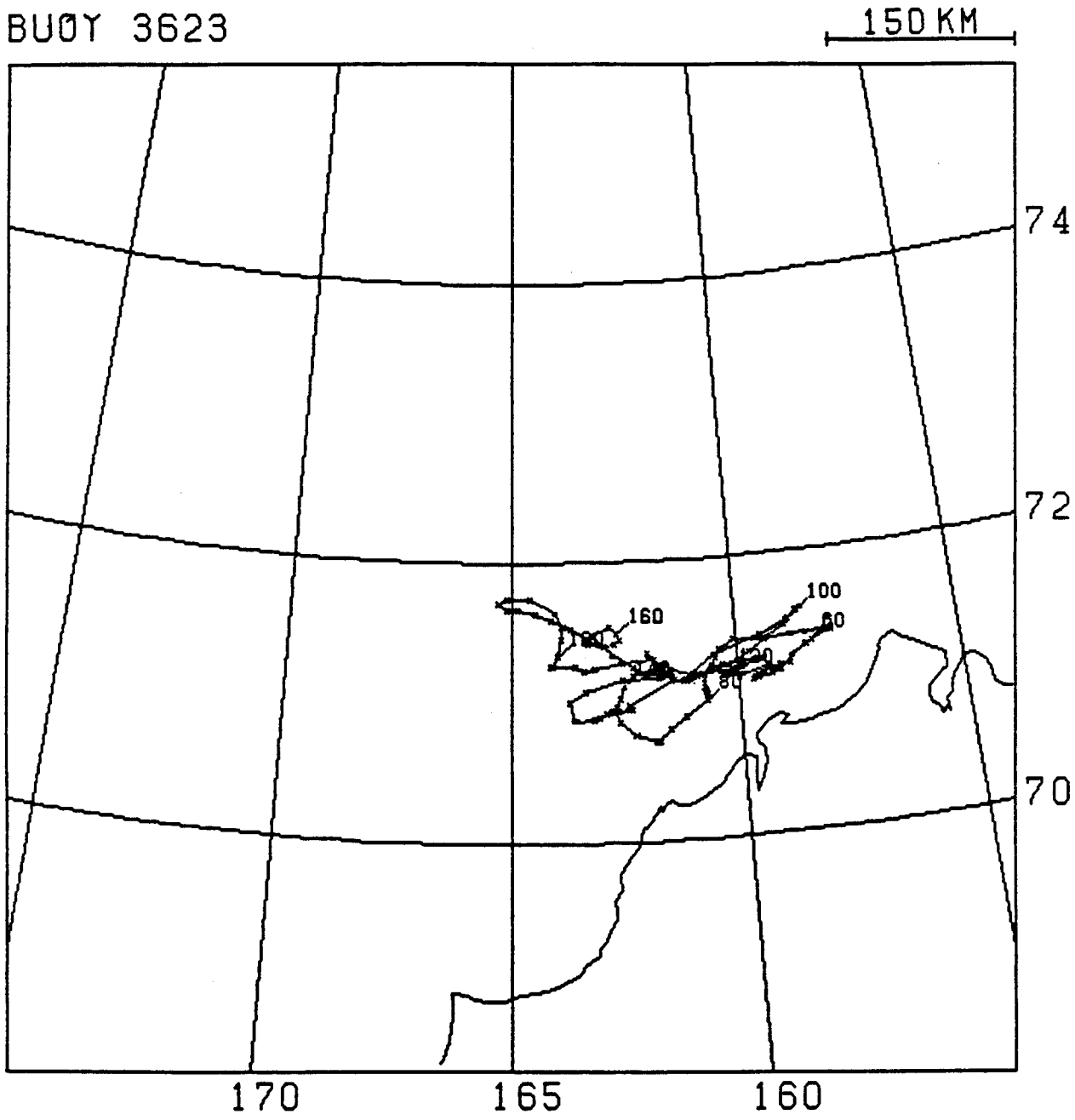

Figure 4. Trajectory for Buoy Number 3623

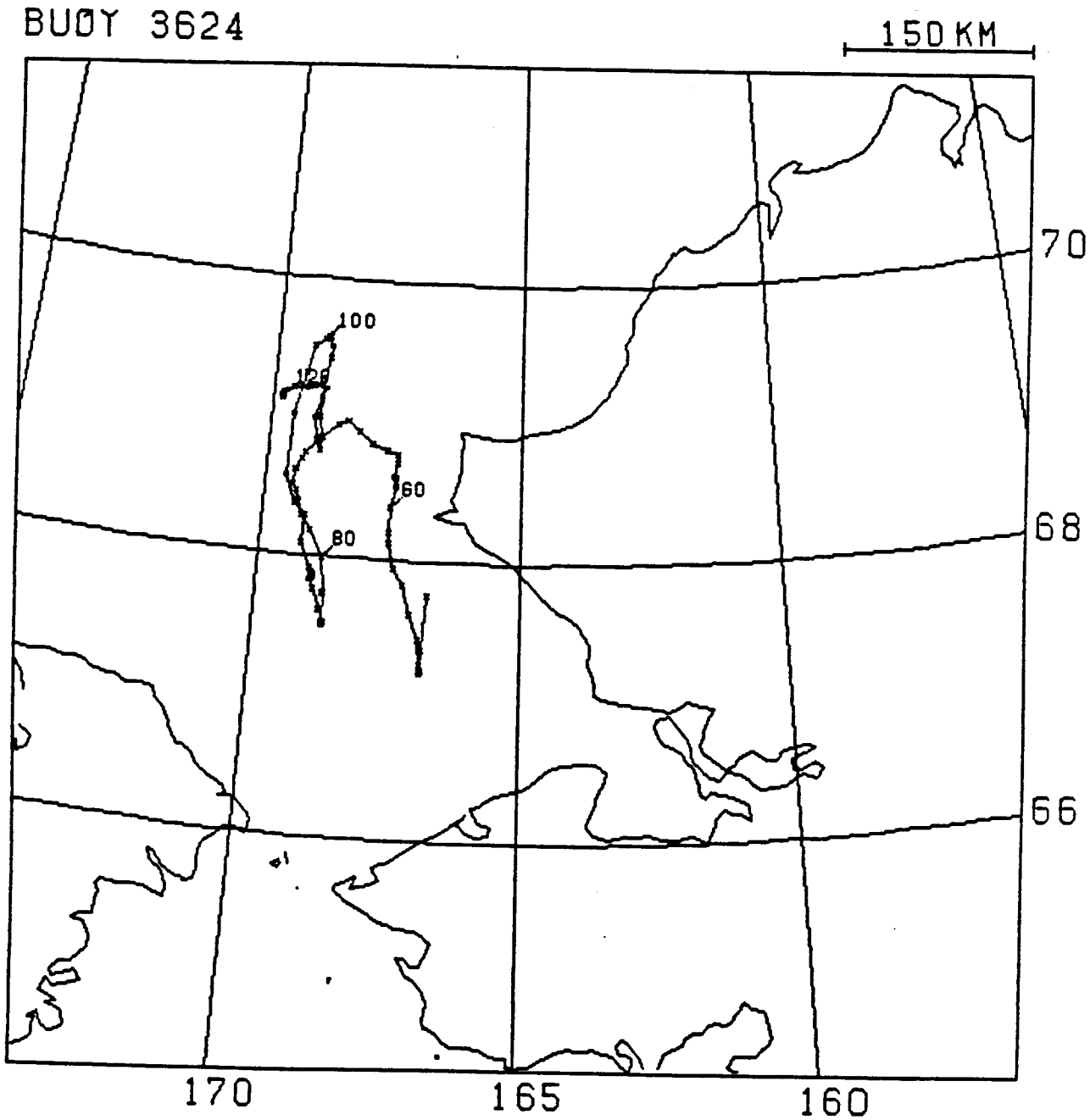

Figure 5. Trajectory for Buoy Number 3624

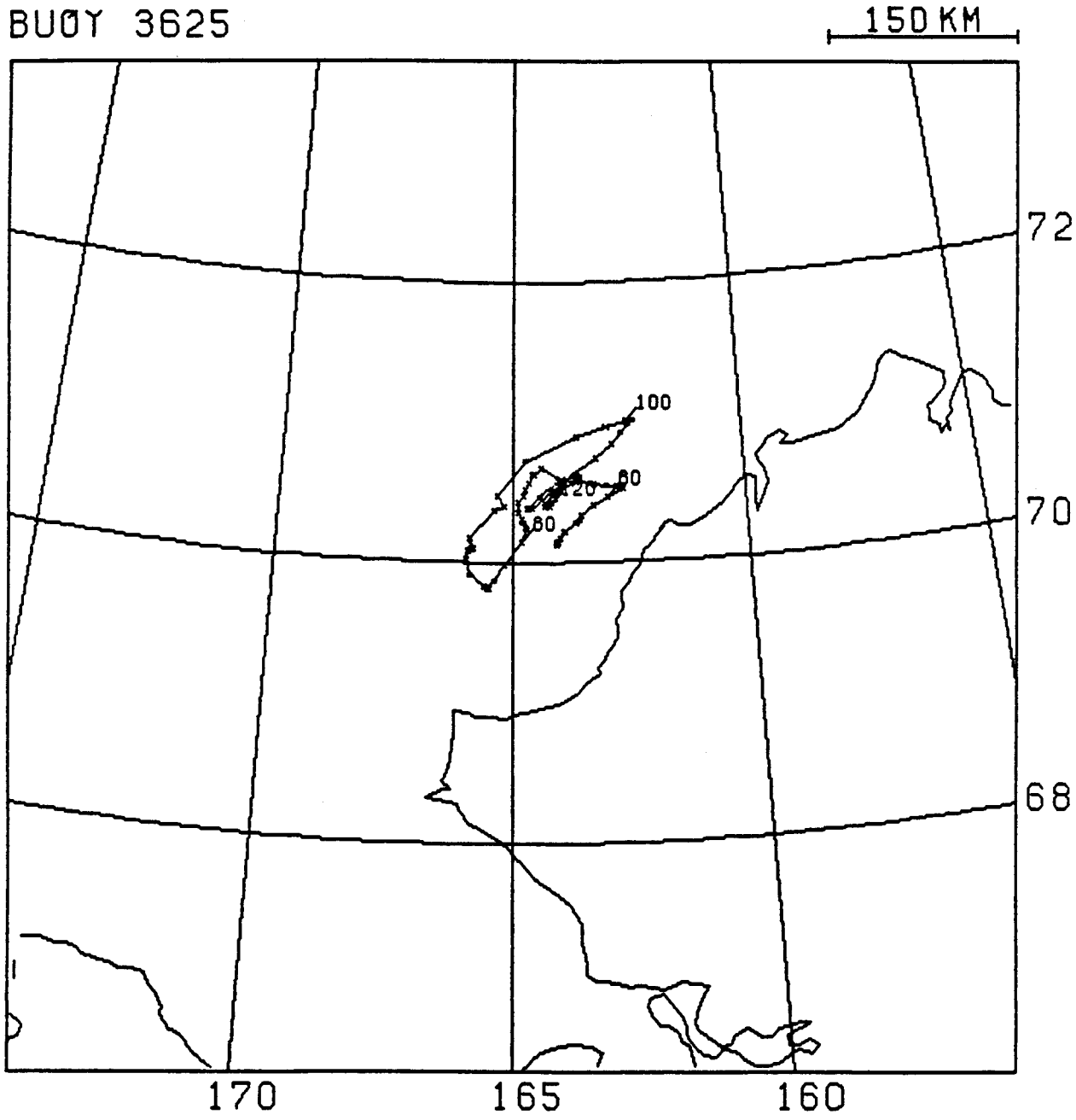

Figure 6. Trajectory for Buoy Number 3625

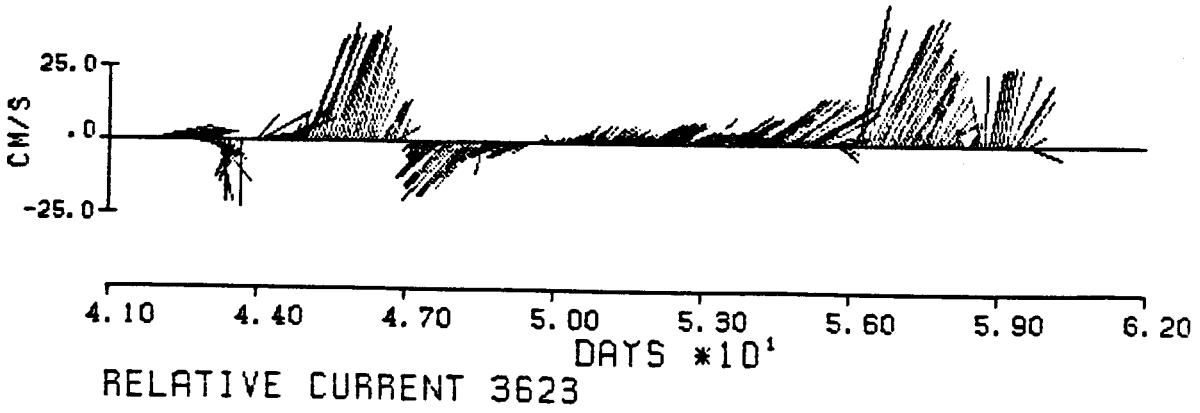

Figure 7. Relative Current Measurements for Buoy Number 3623

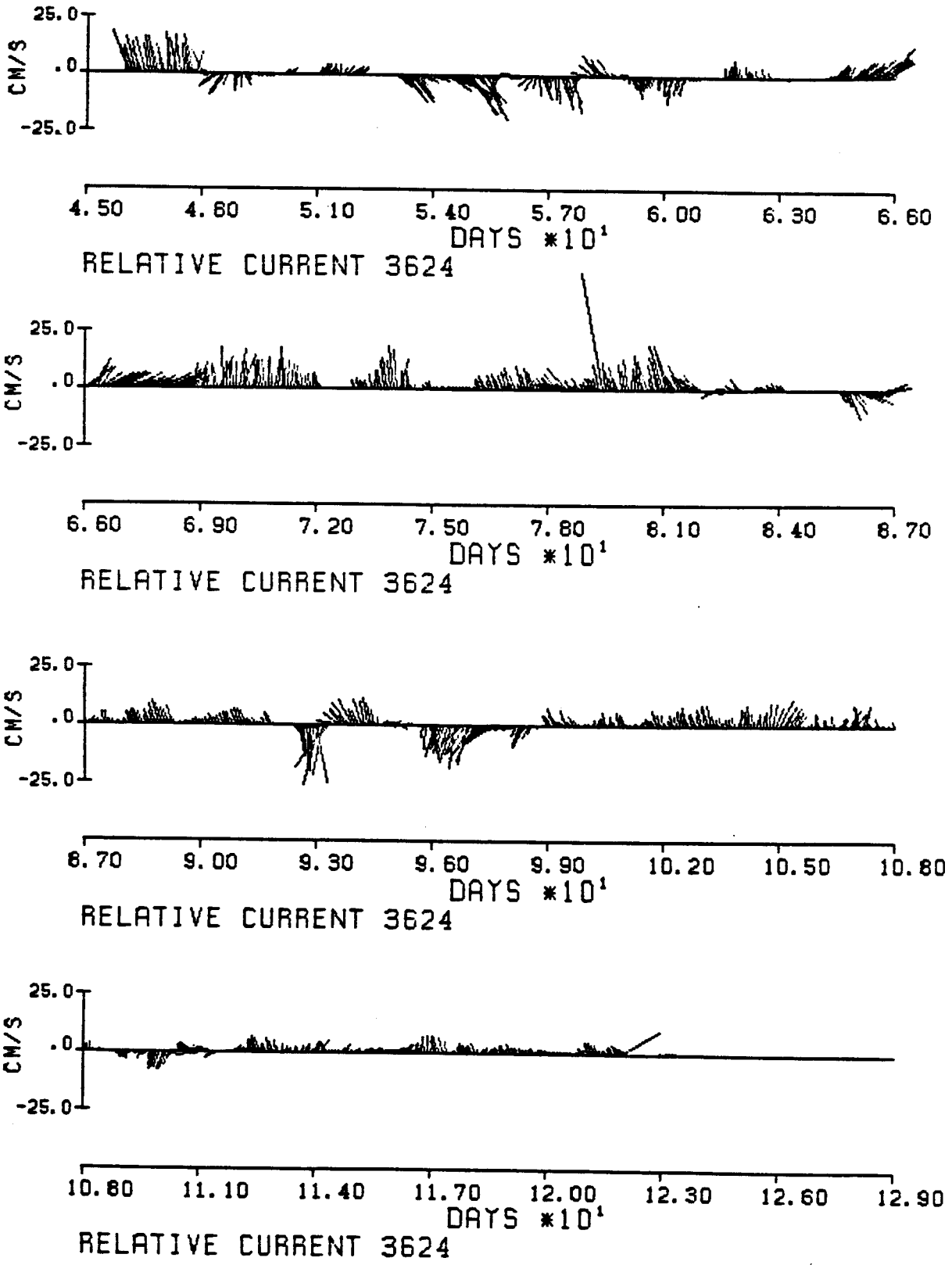

Figure 8. Relative Current Measurements for Buoy Number 3624

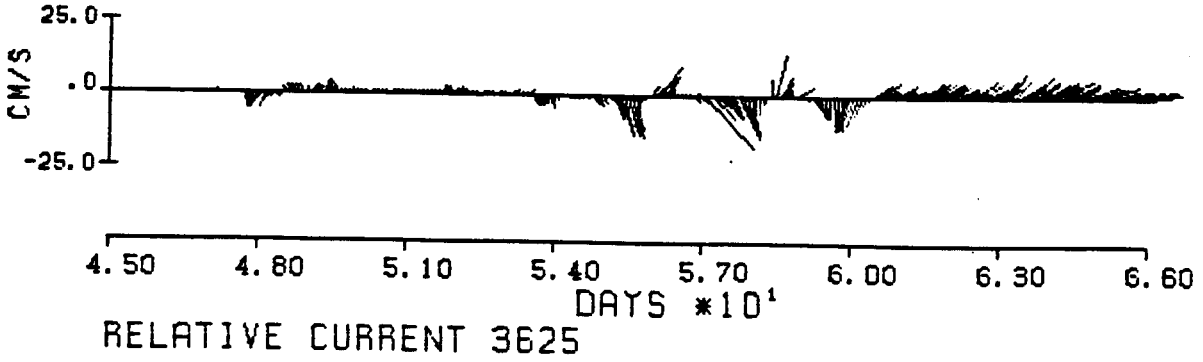

Figure 9. Relative Current Measurements for Buoy Number 3625

CONCLUSIONS

This narrative report briefly discusses the Chukchi Sea ice motions and ocean currents observed by a set of Argos buoys during the winter of 1981-82. Some of the buoys were equipped with current meters suspended 10 meters below the ice to determine ocean currents and also with barometers to determine atmospheric barometric pressure. These instruments were added so we could gain some understanding of the forces that drive the ice motion. It is essential in future experiments to include current meters in order to gain this understanding.

The buoy trajectories and current velocity data are presented in the figures in this report. The driving forces are not evaluated here.

During this experiment, the ice in the central Chukchi Sea drifted toward the west and northwest. The ice within about 200 km of the northwest coast of Alaska, on the other hand, tended to drift alongshore. It drifted back and forth, moving up to 200 km with each excursion.

At a depth of about 10 meters, the ocean currents relative to the ice did not show any strong correlations that would indicate that currents were driving the ice motion. The relative currents offshore Wainwright and Barrow differed from those offshore of Pt. Hope and Icy Cape, which were similar.

The results presented here do not attempt to explain what caused the ice motions, only to report what was observed. A cursory look at the relationship between ice velocity and ocean current showed little correlation, a result that appears to contradict conclusions of other investigators who have studied the breakout of ice through the Bering Strait. Although a more thorough study of the data should be made, the best understanding will come from using an ice dynamics model to estimate the forces exerted on the ice by the current and wind and by the internal ice stress.

REFERENCES CITED

Thomas, D. R., and Pritchard, R. S. (1981) "Norton Sound and Bering Sea Ice Motion; 1981," Flow Research Report No. 209, Flow Research Company, Kent, Washington.

Thomas, D. R., and Pritchard, R. S. (1982) "The Transport and Behavior of Oil Spilled In and Under Sea Ice," Annual Report to Outer Continental Shelf Environmental Assessment Program on Research Unit 567, National Oceanic and Atmospheric Administration, Boulder, Colorado; also published as Flow Research Report No. 240, Flow Research Company, Kent, Washington.

Reimer, R. W., Pritchard, R. S., and Coon, M. D. (1979) "Beaufort and Chukchi Sea Ice Motion - Part 2. Onset of Large Scale Chukchi Sea Ice Breakout," Flow Research Report No. 133, Flow Research Company, Kent, Washington.

ANCHOR ICE AND BOTTOM-FREEZING IN HIGH-LATITUDE MARINE SEDIMENTARY ENVIRONMENTS: OBSERVATIONS FROM THE ALASKAN BEAUFORT SEA

by

Erk Reimnitz, E. W. Kempema, and P. W. Barnes

U.S. Geological Survey
Menlo Park, California 94025

Final Report
Outer Continental Shelf Environmental Assessment Program
Research Unit 205

1986

This report has also been published as U.S. Geological Survey Open-File Report 86-298.

ACKNOWLEDGMENTS

This study was funded in part by the Minerals Management Service, Department of the Interior, through interagency agreement with the National Oceanic and Atmospheric Administration, Department of Commerce, as part of the Alaska Outer Continental Shelf Environmental Assessment Program.

We thank D. A. Cacchione for his thoughtful review of the manuscript.

TABLE OF CONTENTS

Page

INTRODUCTION

As early as 1705 sailors observed that rivers sometimes begin to freeze from the bottom (Barnes, 1928; Piotrovich, 1956). Anchor ice has been observed also in lakes and the sea (Zubov, 1945; Dayton, et al., 1969; Foulds and Wigle, 1977; Martin, 1981; Tsang, 1982). The growth of anchor ice implies interactions between ice and the substrate, and a marked change in the sedimentary environment. However, while the literature contains numerous observations that imply sediment transport, no studies have been conducted on the effects of anchor ice growth on sediment dynamics and bedforms.

Underwater ice is the general term for ice formed in the supercooled water column. It exists in 2 forms: frazil ice and anchor ice, also called ground ice or bottom ice. Frazil ice consists of disk-shaped crystals 1-4 mm in diameter and 1-100 microns thick, that form in turbulent, slightly supercooled water (Kivisild, 1970). Frazil crystals during periods of supercooling are sticky, adhering to each other and to foreign objects (Martin, 1981). When turbulence carries frazil ice to submerged, supercooled objects or the bottom, the frazil therefore may adhere to the subtrate, forming anchor ice (Piotrovich, 1956; Benson and Osterkamp, 1974; Tsang, 1982; Osterkamp and Gosink, 1982). Once anchor ice is formed, it may grow rapidly by free growth in the supercooled water or by trapping other frazil crystals from the water column (Osterkamp and Gosink, 1982; Tsang, 1982). Since the substrate also has to be supercooled, an ice-bonded crust should form in sediment saturated with water of the same or lower salinity than the water column.

The most convincing observations on actual sediment transport by anchor ice have been made in the Niagara River. Here masses of "muddy colored ice filled with bed material" rise to the surface following a night of anchor ice growth. Also, traps placed on the bottom collect masses of spongy ice with sediment. Furthermore, settling basins near water intakes collect up to boulder-size material during winters, while almost no sediment is moved during summers (Tsang, 1982). Osterkamp and Gosink (1982), in a study of interior Alaskan streams, describe how slabs of porous ice accreted on the bed are picked up with the attached sediment by turbulent flow and are moved slowly and intermittently downstream. The above observations imply that much more sediment is transported in a flow than that seen on the surface. Benson and Osterkamp (1974) discuss the possibility of sediment transport into northern seas by anchor ice.

The mechanism of anchor ice growth whereby "sticky" frazil crystals attach to bed material implies grain transport on a microscopic scale as well. The bed material has to be coarse, with individual clasts heavy enough to counteract the buoyancy or drag resistance of the ice buildup (Arden and Wigle, 1972). Particles smaller than fine sand are lifted off the bottom under the buoyancy of ice flocs or even individual frazil crystals, and thence are carried along with the flow. For this reason, anchor ice has only been observed on sand and coarser substrate, but almost never on fine sand, silt, or clay (Wigle, 1970; Arden and Wigle, 1972; Tsang, 1982). Frazil crystals have

also been noted for their scavenging of algae from the water column (Weeks and Ackley, 1982). This action removes fine suspended matter from the water (Altberg, 1938), so that "the first run of frazil has a remarkable cleansing effect in the water" (Barnes, 1928). Coarse organic matter and organisms also attract the growth of anchor ice. In the 18th century, Elbe River fishermen noted that willow baskets used as eel traps were commonly covered by ice when raised to the surface (Barnes, 1928). Dayton, et al. (1969) report anchor ice in the Antarctic to 33 m depth. Above this depth benthic organisms are lifted off the bottom and incorporated into the surface ice canopy when the buoyancy of growing anchor ice exceeds their weight or strength. The result is a reduction of certain benthic organisms above the 33 m isobath.

These observations of Dayton, et al. (1969) represent the best documented case of anchor ice in the sea. Sadler and Serson (1981) describe the formation of a narrow fringe of anchor ice near beaches in the Canadian Arctic, and large masses of anchor ice have been reported growing off Newfoundland to depths of 20 m (Barnes, 1928). Besides these observations we only find statements that anchor ice is well known, widespread, and sailors see it rising to the surface.

In this report we describe miscellaneous observations relevant to anchor ice in the Alaskan Beaufort Sea, including direct diving observations. We also discuss the conditions, timing, and probable extent of the phenomenon, and lastly we emphasize anchor ice as a potentially important geologic agent.

REGIONAL SETTING

The open shelf of the Alaskan Beaufort Sea, in the area of our observations (fig. 1) is covered by a thin layer of muddy sand to mud, has very little relief, and is shallower than 20 m for 10 to 50 km from land. The coast is fringed by island chains up to 15 km from land, protecting 1- to 6-m deep lagoons from pack-ice intrusion. Total ice cover exists for more than 9 months of the year, and even during the navigation season heavy pack ice concentrations normally remain over much of the shelf. River discharge begins in early June by flowing out across the extensive fast ice. By mid September the North Slope drainage basins begin to freeze, effectively eliminating river-water discharge to the sea, and a new sea ice cover begins to grow by late September. At this time bottom-water temperatures below the 10 to 15-m thick mixed layer are only slightly above their freezing points (Hufford, 1974). In winter the water column typically is at its freezing point down to a depth of 40 m (Aagaard, 1984). Much of the inner shelf is underlain by ice-bonded sediments at shallow depths below the seafloor (Neave and Sellman, 1984; Morack and Rogers, 1984) Along a transect from Prudhoe Bay northeastward to 12 m depth seaward of Reindeer Island (fig. 1) winter seafloor temperatures are at the freezing point for the salinity of interstitial waters, and seasonal freezing is assumed to occur (Sellman and Chamberlain, 1979). Widespread overconsolidation of surface sediment could be attributed to seasonal freeze-thaw (Lee et al., 1985), but general ice-bonding of the seafloor is not documented. For more details of the regional setting the reader is referred to Norton and Sackinger (1981).

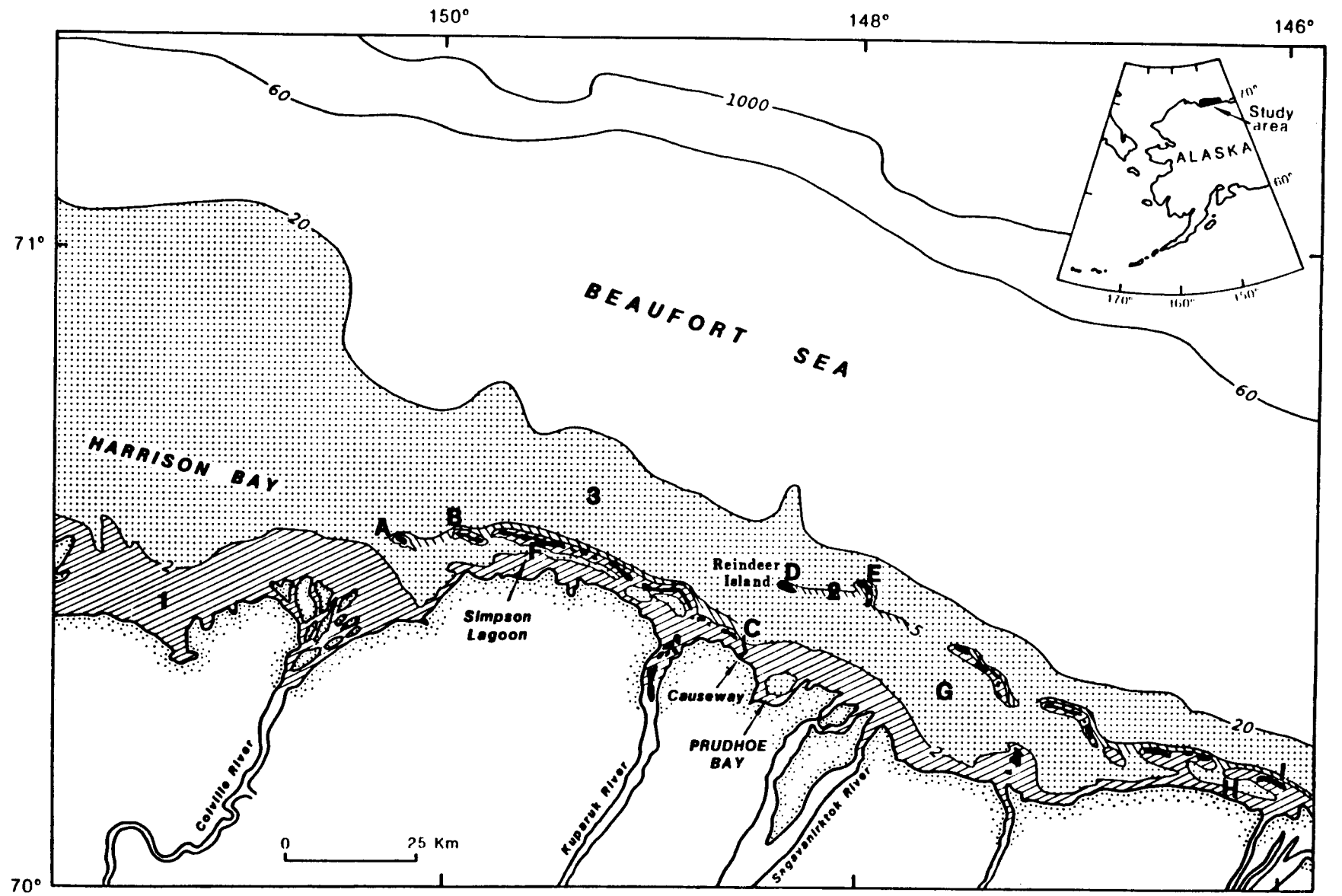

Figure 1. Map of central Beaufort Sea shelf with lettered sites where evidence of anchor ice or bottom freezing was observed: (A) Thetis Island, (B) Spy Island, (C) West Dock, (D) Reindeer Island, (E) Cross Island, (F) Simpson Lagoon, (G) Stefansson Lagoon, (H) Point Thomson, and (I) Flaxman Island. Three regions with different likelihoods of seasonal bottom freezing are delineated: (1) certain at lower than 2 m, (2) very likely on exposed shorefaces to 5-m depth, and (3) possible to 20-m depth.

Based on our observations over the last 15 years, the onset of freeze-up and the formation of a new ice canopy are commonly initiated by one or more storms with 10 m/s or stronger easterly winds and freezing air temperatures. During this period night temperatures may drop to -10°C, and increasing amounts of new ice are seen daily in sheltered areas between ice floes and on brackish-water plumes in extensive shallows near rivers. Storms lasting several days cause a number of important changes. We have observed that a cold 3 to 4 day storm generates inner-shelf currents of 50 to 100 cm/s, mixes waters laterally and vertically to the thermocline near 15 to 20 m depth on the mid-shelf, replaces brackish waters in bays and lagoons with higher salinity shelf waters, generates brash ice from the impacts and grinding action in fields of multi-year ice, and extensively rearranges the sea-ice distribution. Most important for the formation of underwater ice is the fact that such a cold storm cools the ocean, and results in the formation of large amounts of frazil ice aligned on the sea surface in streaks parallel to the wind, a sure sign that the surface layer of the ocean now is supercooled. Cooling of surface waters is enhanced by wave- and ice-induced turbulence associated with the storm. In the calm following storms this frazil ice is found as a surface layer of grease ice with reported thicknesses of up to 4 m (Collinson, 1889), depending on how the coast, island chains, and grounded ice-fields are oriented with respect the driving storm winds. Swell can travel through the grease-ice layer for a few km.

INDIRECT EVIDENCE FOR ANCHOR ICE IN THE BEAUFORT SEA

From the beginning of our Beaufort Sea studies in 1970 we were aware of the possible presence of anchor ice (Reimnitz and Barnes, 1974). While routine marine geological survey techniques may not reveal the phenomenon, our work has also included hundreds of research dives in diverse settings and seasons, as well as years of small boat and skiff operations in the nearshore environment during freezeup. Our knowledge also includes observations from increasing numbers of dives made under the ice canopy by consulting firm personnel and researchers.

Prior to 1982 we had no direct evidence for anchor ice in the Beaufort Sea, although indirect evidence suggested its presence. (Reimnitz and Dunton, 1979). One type of indirect evidence is the large amounts of fine sediment that are incorporated into the seasonal fast-ice canopy (Barnes, et al., 1982; Osterkamp and Gosink, 1984). The concentrations of fine sediments over extensive regions in this ice are at times an order of magnitude larger than concentrations of suspended matter seen in the open-water season (Barnes, et al., 1982). Barnes, et al. (1982) attribute these high sediment concentrations to scavenging of sediment particles from the water column by frazil ice. The sediment at the sea surface could also be attributed to the buoyant action of frazil or anchor ice adhering to sediment particles on the seafloor during fall storms (Reimnitz and Dunton, 1979), although Barnes et al. (1982) reasoned this is unlikely. Spotty occurrences of organic matter, coarse sediments, and clam shells, often with attached benthic organisms such as kelp (i.e. Reimnitz and Barnes, 1974), are commonly seen in the smooth ice canopy (fig. 2), or in the layer of soft ice below the solid ice canopy. Such materials are never seen on the sea surface in open water, and therefore their isolated inclusion in the ice canopy requires suspension by anchor ice. For example,

Figure 2. Mass of coarse-grained sediment entrained in new, thin ice cover on seaward side of Flaxman Island (fig. 1-I). Masses such as these are probably carried to the water surface by the buoyant action of anchor ice acting on bottom sediments.

incidental collection from 500 m^2 of soft ice under a lagoonal ice canopy produced a handful of kelp and other benthic organisms, some attached to pebbles (fig. 3, from Dunton, written communication, 1980). These materials match the unique local substrate.

Ice growth on objects in the water column, both below the ice canopy and in open water during fall storms, has been variously observed (i.e. Reimnitz and Dunton, 1979). For example, fish nets of certain materials are carried to the surface when the buoyancy of ice growing on webbing exceeds the weight of lead lines (Jim Helmericks, oral communication, 1979). Such ice growth has been seen on mooring lines and oceanographic equipment (fig. 4) in the quiet water column under an ice cover.

During or after fall storms there are various indicators that either the bottom is frozen or that anchor ice exists. An example are slabs of sand with vertical edges littering a gravel beach (fig. 5A and B). We commonly see 2- to 4-cm flocs of sediment-laden ice rise to the clean sea-surface when anchoring a small boat in 2 m water depth. These flocs apparently are released from the bottom by turbulent propwash when backing the vessel. In several instances, when anchored 150 m from a

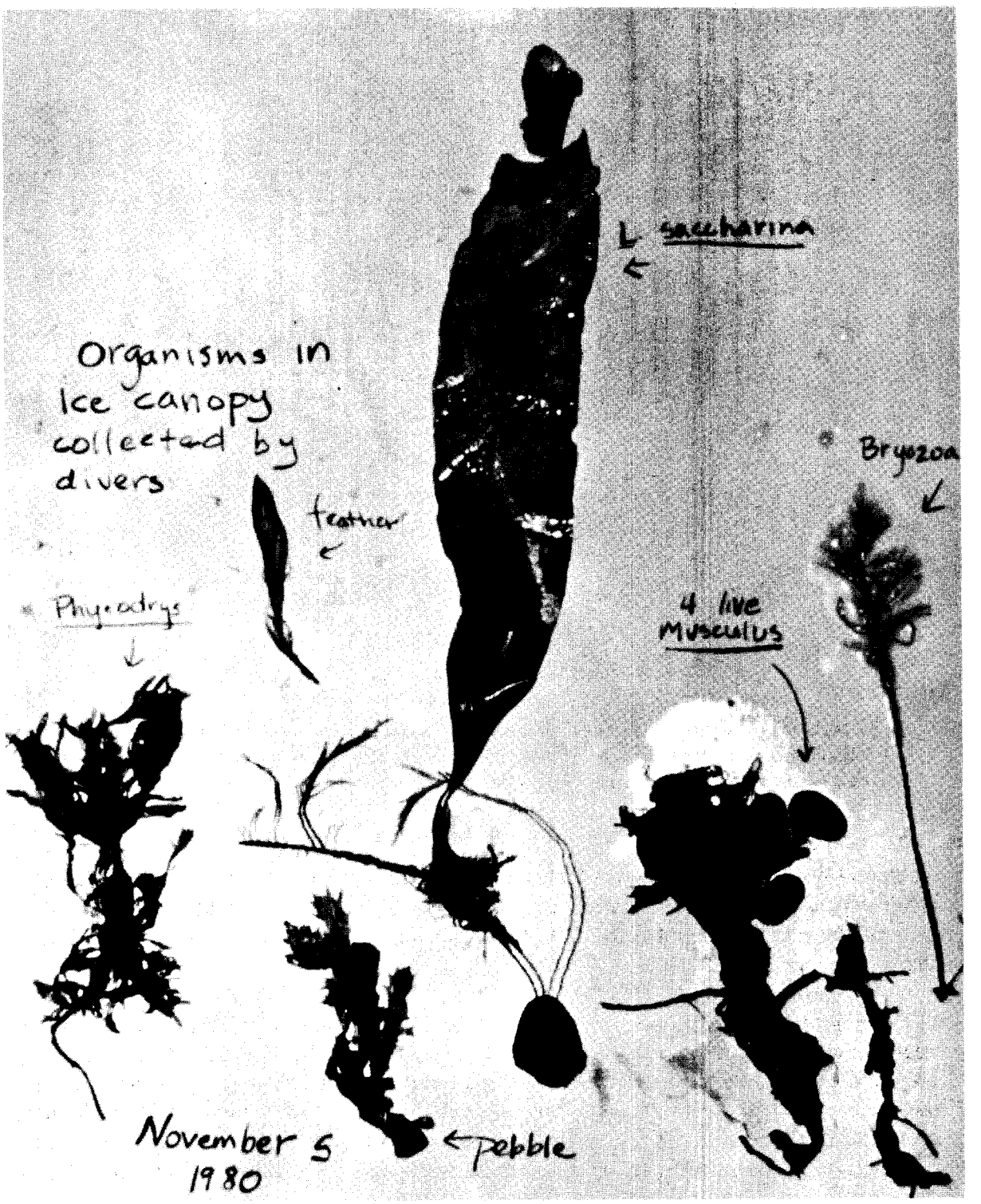

Figure 3. Example of different organic materials found in the soft ice under the solid ice canopy in Stefansson Sound. These materials are never found floating on the water surface in the summer, and are believed to be incorporated into the ice canopy by the action of anchor ice (Photograph by K.H. Dunton).

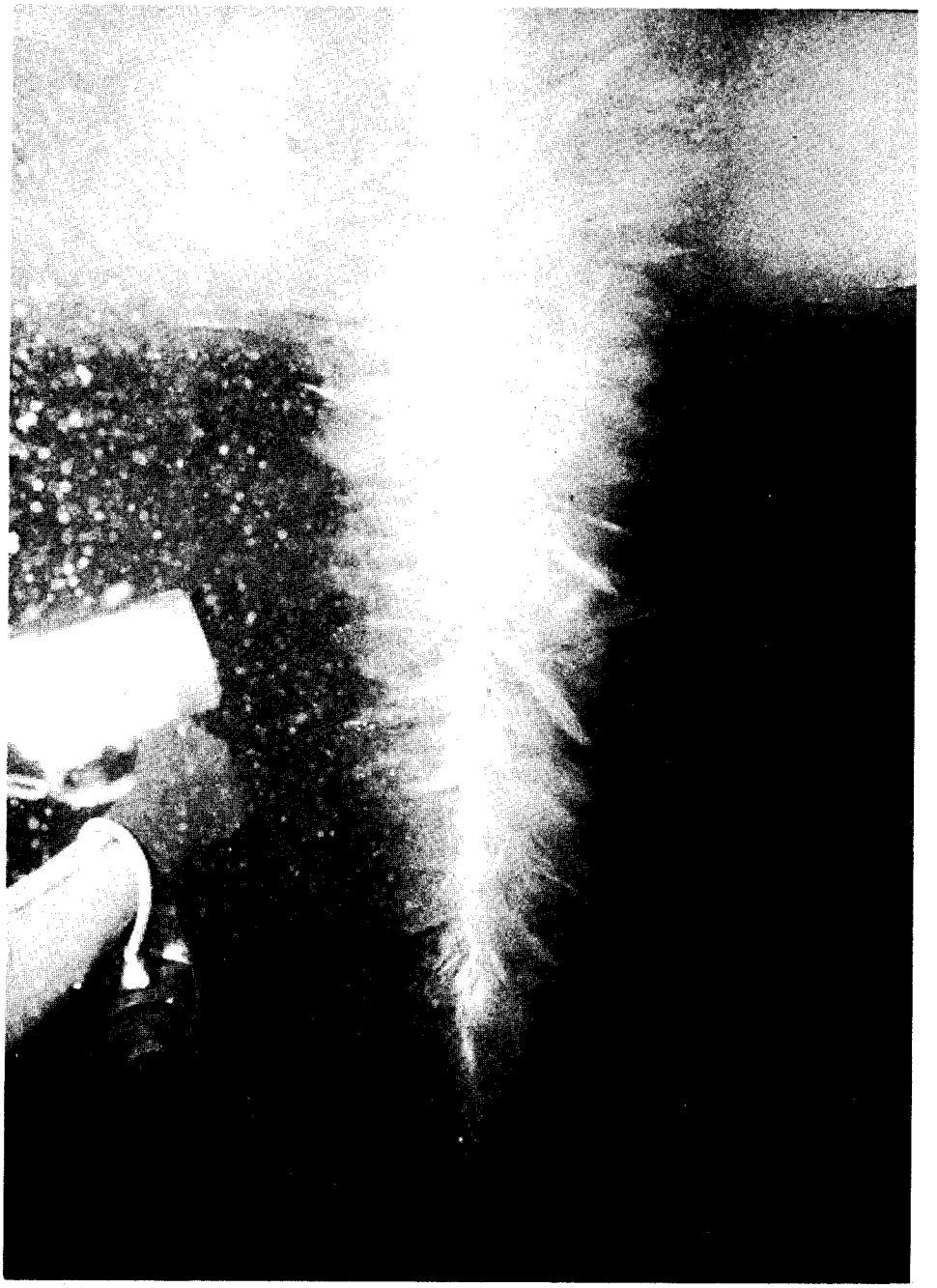

Figure 4. Anchor ice growth below ice canopy on instrument mooring ice in Stefansson Sound (K.H. Dunton, Harding and Lawson Assoc.).

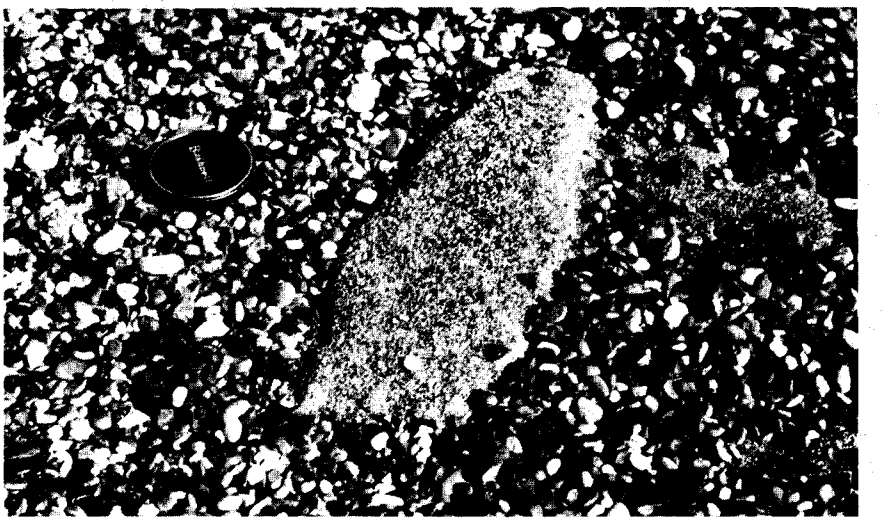

Figure 5. Plaques of sand, tossed as a frozen slab onto beach during fall storm. (A) Plaques on beach face during a fall storm (B) Sand plaque on gravel beach during the summer, after the ice holding the plaque together has melted. Such evidence for seafloor freezing is common on seaward facing beaches.

protecting barrier island at water depths of 1.5 to 2 m during freezing storms, we observed such sediment-laden spongy ice drift past the vessel. At Thetis Island (fig. 1-A) on 9-21-1980, wind-parallel streaks of slush extended windward to within 10 m of the lee shore. These streaks contained many ice flocs carrying sand and coarser material, which most likely had an anchor ice origin. By jabbing the seabed we determined that it was ice-bonded. At this same time, near the beach at a water depth of 0.8 m we used a shovel to retrieve a slab of ice-bonded sand. On the same day in Simpson Lagoon (fig. 1-F) we repeatedly encountered hard bottom at a water depth of 1.5 m, where only unconsolidated sediment is normally found. This hard bottom is evidence for ice-bonding of sediments. A Beaufort Sea tugboat operator related that during a fall storm two anchors bounced along the seafloor without digging in at a normally good anchor site (Jim Adams, oral communication, 1984). He believes this may have been due to anchor ice and frozen seafloor.

DIVER OBSERVATIONS OF ANCHOR ICE AND ICE-BONDED SEDIMENTS

Direct evidence for anchor ice was obtained from two dives made after fall storms. The dives were prompted after observing rising ice while wading in waist-deep, open water seaward of Cross Island (fig. 1-E), where slabs of frozen sand had been thrown onto the beach face by waves. During the 5 days prior to the first dive (10-5-1982), daily minimum temperatures of -8 to -10°C and maximum wind velocities of 21 m/s were recorded along the Beaufort Sea coast (U.S. Department of Commerce, NOAA, 1982). New ice covered large areas of the inner shelf during this time, indicating surface water temperatures at the freezing point.

The first dive, a shore-normal, 130-m-long traverse from the beach to 4.5 m depth, was made off Reindeer Island (fig. 1-D). Turbid waters obscured the seafloor viewed from above even where the depth was only 0.5 m. Open water prevailed on the inner 50 m, and a 20-cm thick layer of weakly sintered slush ice covered the outer part of the traverse. About 90 m from shore the traverse crossed a 2-m-high, shore-parallel sand bar. Bottom sediments ranged from gravelly sand nearshore to sorted fine sand offshore. At the time of the traverse near-bottom salinity was measured at 36.8 ppt, and the temperature was -2°C.

From the beach to 2-m depth, about 30 m from shore, the seafloor was partially to totally ice-bonded. At less than 1-m depth, 5-10 cm high, ill-defined 1-m or larger slabs of rippled gravelly sand, elongated parallel to the beach, gave the bottom an eroded appearance. At depths greater than 1 m irregular pillow-shaped masses of ice and ice-bonded sediments 10 to 40 cm across and 5 to 8 cm high rose above a rippled sand and gravel bottom (fig. 6). These pillows had an external crust of randomly oriented ice platelets up to 1 cm in diameter, with sediment grains trapped in the interstices between the ice platelets. With increasing depth below the outer crust the pillows were increasingly firm and dense, and their cores could be extracted from the surrounding sediment intact. Figure 7 shows several of these cores that were extracted from the seafloor and carried up to the surface. The anchor ice pillows were largest and best-developed at 3 to 4 m water depth on either side of the offshore bar, and were absent on the bar crest. Pillows occurred singly, or in patches up to four meters

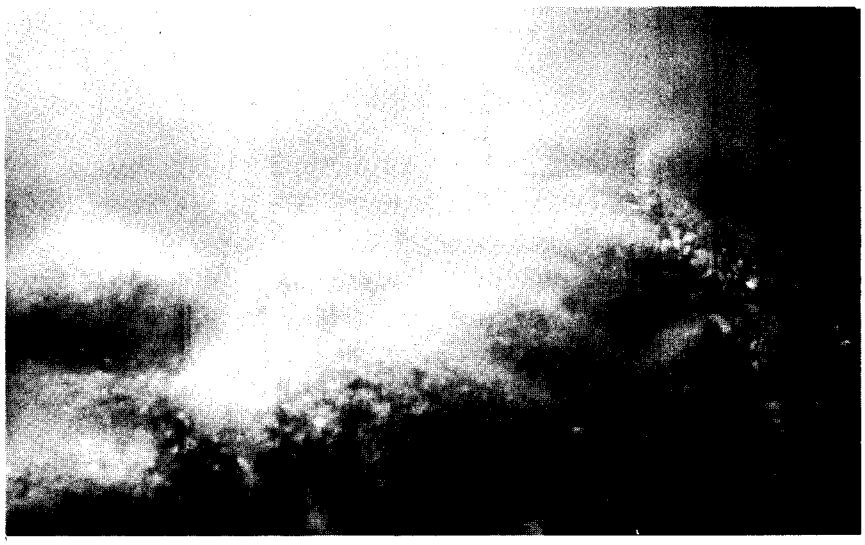

Figure 6. Fuzzy-looking anchor ice attached to gravel bottom at 1.5 m water depth off Reindeer Island (fig. 1-D.). Width of scene is about 1 m.

Figure 7. Ice-bonded sediment cores of anchor-ice pillows collected off Reindeer Island (fig. 1-D). Cleat is 30 cm long.

Figure 8. Anchor-ice pillows at 4-m depth, 130 m seaward from Reindeer Island. Individual pillows are 0.3 to 0.5 m in diameter, with a massive core of ice-bonded sand below a rind of delicate ice-crystals.

across, with individual pillows in close contact, but retaining well-defined boundaries (fig. 8). A rippled, thawed sand bottom surrounded the ice pillows in these deeper regions of the traverse. But the pillows were not only surficial features. To raise one off the bottom, we had to probe into the thawed sand to reach underneath an ice-bonded pillow-root, 5-10 cm below the seafloor. Such massive cores of ice pillows were difficult to break by hand, producing angular blocks of ice-bonded sand. Besides the large ice pillows we saw numerous 4-5 cm wide, 3-cm high balls of porous ice resting on the seafloor. When disturbed, these fragile balls of ice rose to the sea surface with some incorporated sediment. We did not detect any nuclei of ice-bonded sediment for these ice flocs.

None of the large, massive ice pillows dislodged were sufficiently buoyant to ascend to the surface. The massive cores of ice rich sand carried to the surface (fig. 7) contained 20% of excess ice. A 100 kHz side-scan sonar traverse recorded along the diving traverse provided no clues of the existence of anchor ice.

On the next day, anchor ice and ice-bonded seafloor were observed during a dive made near a gravel causeway at water depths between 1 and 2 m (fig 1-C). The weather was calm and sheets of fresh ice covered the sea surface. The underwater visibility was 0.75 m. Along the 175-m traverse the bottom sediments ranged from solidly ice-bonded sandy gravel, to lightly bonded rippled muddy sand, to soft mud in 5- to 10-m wide depressions riddled with fragile ice platelets. The surfaces of mud-filled basins were marked by faint geometric patterns. Running a gloved hand through

such soft mud-and-ice mixtures gave a distinct crunching sensation. Patches of ice-bonded muddy sand could be broken and disturbed under strong pressure by hand, but in the sandy gravel even an entrenching tool was useless to dislodge a single clast protruding above the bottom.

Also seen on this diving traverse were small, scattered accumulations of ice platelets with traces of entrapped sediment. These accumulations had nuclei of fibrous organic matter, kelp fragments, and gravel clasts, but wooden twigs apparently did not attract ice growth. The most remarkable growth of anchor ice was seen on trash, such as a rubber tire and a heap of steel banding. Accumulations of randomly oriented, thin ice platelets constituted a very open framework 40 cm across, appearing similar to an irregular bush with a structure of branches. The lightest water turbulence generated by our hands broke apart these large ice aggregates and sent the components rising to the surface.

DISCUSSION AND CONCLUSION

Diving observations suggest that anchor ice and bottom freezing are important for sediment dynamics. For future studies of how seafloor sediments are entrained into and rafted by ice, the generally accepted definition for anchor ice quoted initially is imprecise, as already pointed out by Tsurikov (1966) and Dunbar (1967). For a clear distinction from other forms of ice that may be stuck on the bottom and in the process may incorporate sediments, we suggest the following definition for anchor ice: "Ice accreted on a substrate submerged in either quiet or turbulent supercooled water, and remaining attached to the substrate." When dislodged, the ice generally transports some components of the substrate. The sediment-enriched base of anchor ice may not be distinguishable from underlying pre-anchor-ice sediments, which became ice bonded. However, the present definition excludes simply ice-bonded sediment from ice and sediment that accreted during an event, but future work may justify combining the two.

The different heat sinks for the formation of underwater ice may need to be distinguished for future studies of related sediment dynamics. Thus, the anchor ice forming in quiet conditions under an ice canopy in the Antarctic discussed by Dayton, et al. (1969) or shown in figure 4, and that forming where different water masses interact (i.e. Sadler and Serson, 1981), will have a different impact on the sedimentary regime than the anchor ice we find forming in the Beaufort Sea during turbulent open-water conditions, where the immediate heat sink is the atmosphere. Because of the hostile environment during the latter condition, this will be the most difficult to study.

Our sketchy observations from the shallow Beaufort Sea suggest ice-bonded sediments and anchor ice are widespread, if not ubiquitous, in years when the freeze-up is initiated by 12 m/s or stronger winds. Applying our understanding of why the bottom may become ice bonded and how anchor ice forms to the environment within the area shown in figure 1 allows regional extrapolation from our spotty observations. Wind-driven currents during fall storms, when freshwater input from rivers has terminated, homogenize the waters of the inner shelf. With these waters supercooled, subtle

differences in salinities of interstitial waters in bottom sediments result in different seafloor freezing points and thereby influence the occurrence of ice-bonded sediments. Bottom sediments in Harrison Bay and Simpson Lagoon (fig. 1), infiltrated by river water during summer, have higher freezing points than bottom sediments seaward of the barrier islands, where sea-water salinities are higher. In general, ice bonding apparently extends to 2 m depth, but in embayments influenced by fresh water we expect bottom-freezing and perhaps anchor ice formation to begin sooner, and to extend seaward beyond the 2-m isobath (fig. 1). Conditions off exposed beaches, such as off Reindeer Island, are different. We observed patchy anchor ice and ice-bonded sand out to 150 m from shore, where the traverse terminated. But during the preceding storm we observed waves breaking as far seaward as 500 m from shore (4-6 m depth on shoals). Within this 500-m-wide surf zone, high turbulence and entrainment of cold air bubbles enhances the heat transfer from the water and seafloor to the atmosphere. We believe that anchor ice and ice-bonded sediments existed throughout this zone at least in patches, but possibly as a continuous sheet (fig. 1). The externally fragile crystal lattice of ice pillows obviously was a product of post-storm ice growth, as was the buildup of rippled, loose sand around the pillows. Flume studies show that such crystal lattice structures can grow by accretion of frazil ice onto an ice-bonded sediment core (Kempema, 1986).

We have no observational basis for extending the occurrence of anchor ice seaward across the shelf beyond the 5-m isobath. However, large amounts of storm-produced anchor-ice form to at least 15 m depth at Molodeshnaya in the Antarctic (Cherepanov and Kozlovskiy, 1972). This anchor ice forms before an ice cover, when the water column is well mixed by fall winds. The conditions therefore seem similar to those in the Beaufort Sea, except that here waters shallower than 15 m are vastly more extensive. One may argue that increased pressure lowers the freezing point and therefore water depth will limit the seaward extent of storm-generated anchor ice. However, such ice forms under strong, cold offshore winds to 17-m depth in Lake Ontario (Foulds and Wigle, 1977). We suggest that in the Beaufort Sea the thickness of the mixed layer, all being supercooled to the same degree, should determine the seaward extent of anchor ice formation. This layer is about 15 m at the end of the summer, and should deepen during storms. We therefore map the probable extent of anchor ice to 20 m in figure 1.

Cherepanov and Kozlovskiy (1972) report that anchor is particularly common on banks and shoals. This observation is supported by the work of Untersteiner and Sommerfeld (1964), who speculate that downward protuberances in the ice canopy are flow obstacles which act as nucleating surfaces for anchor ice. We suspect that the upward protuberances on the middle Beaufort Sea shelf in the form of 5-10 m high shoals should also focus the growth of anchor ice.

The strong bond between anchor ice and substrate holds only during and shortly after formation (Tsang, 1982), as long as the water is supercooled. The growth of a surface ice sheet eliminates the atmosphere as heat sink, and results in a rise of water temperature from the heat released by further ice growth. The sub-bottom-heat conducted upward from the geothermal temperature gradient (fig. 9) probably weakens the

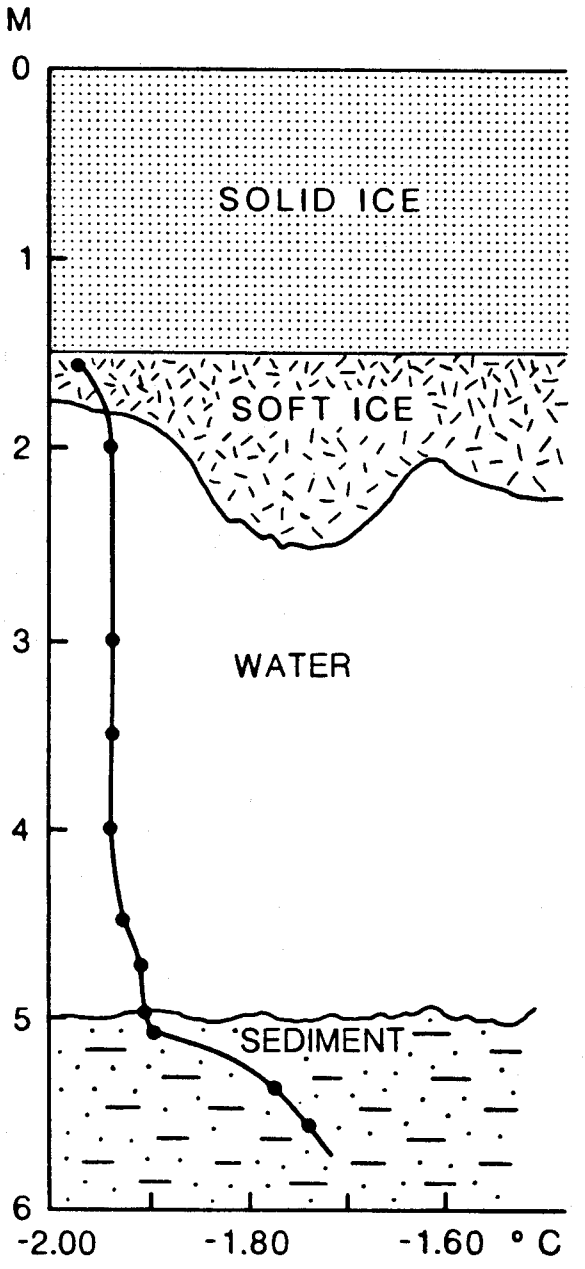

Figure 9. Depth/temperature curve measured in Stefansson Sound on March 6th, 1979. (From T. Osterkamp, written commun., 1979).

strong bond between substrate and anchor ice (Tsang, 1982), to where its buoyancy may carry it to the surface. This porous anchor ice containing some components of the substrate then becomes part of the seasonal ice canopy. Cherepanov and Kozlovskiy (1972) describe the resulting under-ice deposits, which to us seem similar to the billows of soft ice with included sediment observed in different years under the Beaufort Sea ice canopy (fig. 10) (Reimnitz and Dunton, 1979). The disruption of the bond from conduction of sub-bottom heat also explains why storm-generated anchor ice is not observed in winter diving.

Figure 10. Photograph of highly irregular base of soft-ice layer in Stefansson Sound, where depth/temperature profile of figure 9 was measured. Both the relief and large ice crystals are best explained by an anchor-ice origin. This ice offers little resistance to a diver's arm until the congelation ice base, 0.5 to 2 m above is felt. In the background the field of view is 2 to 3 m wide.

The short-lived nature of storm-generated anchor ice makes study of related sediment transport and bedform dynamics extremely difficult. The huge amounts of sediment held by the immobile winter ice canopy in some years (Barnes, et al., 1982) reflect only what rose to the surface once the storm died down. Sediment movement with anchor during the storm near the seabed is probably more important for overall sediment transport than that rafted on the sea surface. The frozen sand slabs we see cast by waves onto beaches probably are moving along the bottom during storms, similar to the ice/sediment masses observed moving along stream beds (Arden and Wigle, 1972; Osterkamp and Gosink, 1982). We commonly observe wind-driven surface currents of 100 cm/s in the shallow Beaufort Sea. When wave orbital motion is superimposed on such flow, bedload transport of sediment with ice may be significant. But there is a total lack information on the extent and strength of sea-bed ice bonding, which may resist transport during storms. There also is a total lack of information on the kinds of internal sedimentary structures produced by anchor ice accretion and by ice bonding of surface sediments.

The ice pillows observed off Reindeer Island may result from post-storm ice nucleation on angular slabs of ice-bonded sand produced during the preceeding storm. Transport of slabs from bar crests to the troughs would explain the observed scarcity of ice pillows on the shore-parallel bar and abundance in adjacent troughs. Lastly, our observations of wide-spread ice bonding in shallow regions supports the theory of Sellmann and Chamberlain (1979) that cyclic freeze-thaw may be a cause for dewatering and widespread overconsolidation of surface sediments in the Beaufort Sea.

We believe that the influence of anchor ice and ice bonding of surface sediments during fall storms may be one of the most important phenomena for the sedimentary regime of shallow arctic seas. Twenty five percent of the world's continental shelves are seasonally ice covered, and might be affected by the phenomenon. Anchor ice forms in Eurasia as far south as the Sea of Azov (46°N) (Zubov, 1945), and should be equally widespread in North American seas. The lack of knowledge about anchor ice and frozen seabed thus remains an important gap in our understanding of high-latitude sedimentary environments.

REFERENCES CITED

Aagaard, Knut, 1984, The Beaufort Undercurrent, in: Barnes, P.W., Schell, D.M., and Reimnitz, Erk, The Alaskan Beaufort Sea: Ecosystems and Environments: Orlando, Florida, Academic Press, p.47-72.

Altberg, V. IA., 1938, On centers or nuclei of water crystallization: Meteorologiia i Gidrologiia, Bull., no. 3, p.3-12. CRREL Draft Translation 294, January 1972, Hanover, NH.

Arden, R.S. and Wigle, T.S., 1972, Dynamics of ice formation in the upper Niagra River, *in* International Symposium on the Role of Snow and Ice in Hydrology, Banff, Alberta: UNESCO-WMO-IHAS, v.2, p1296-1313.

Barnes, H.T., 1928, Ice engineering: Montreal, Renouf Publishing Company.

Barnes, P.W., Reimnitz, Erk, and Fox, Dennis, 1982, Ice rafting of fine grained sediment, a sorting and transport mechanism, Beaufort Sea, Alaska: Journal of Sedimentary Petrology, v.52, no. 2, p.493-502.

Benson, C.S. and Osterkamp, T.E., 1974, Underwater ice formation in rivers as a vehicle for sediment transport, *in* Oceanography of the Bering Sea: Institute of Marine Science, University of Alaska, Fairbanks, p.401-402.

Cherepanov, N.V. and Kozlovskiy, A.M., 1972, Underwater ice in the coastal waters of Antarctica: Soviet Antarctic Expedition Information Bulletin 84, v.8, no.6, p.335-338.

Collinson, Richard, 1889, Journal of the H.M.S. Enterprise, 1850-1855; Sampson, low, Marston, Searle, and Rivington, Ltd., London, 531p.

Dayton, P.K., Robilliard, G.A., and DeVries, A.L., 1969, Anchor ice formation in McMurdo Sound, Antarctica, and its biological effects: Science, v. 163, p. 273-274.

Dunbar, Moria, 1967, International ice nomenclature: Oceanology, Academy of Sciences of the USSR, v.7, no.1 ,p.879-882.

Foulds, D.M. and Wigle, T.E., 1977, Frazil- the invisible strangler: Journal AWWA, April 1977, p. 196-199.

Hufford, G.L., Fortier, S.H., Wolfe, D.E., Daster, J.F., and Noble, D.L., 1974, Physical oceanography of the western Beaufort Sea, *in* An Ecological Survey in the Beaufort Sea, Dept. of Trans., Coast Gaurd Oceanographic Report No. CG373-64:, p.1-173.

Kempema, E.W., (1986), Flume Studies and Field Observations of the Interaction of Frazil Ice and Anchor Ice With Sand-Sized Sediments, San Jose State University, unpublished thesis, 85p.

Kivisild, H.R., 1970, River and lake ice terminology, *in* Proceedings of IAHR Symposium on Ice and Its Action on Hydraulic Structures, Iceland, Paper 1.0.

Lee, H.J., Winters, W.J., and Chamberlain, E.J., 1985, Geotechnical properties and freeze/thaw consolidation behavior of sediment from the Beaufort Sea, Alaska; U.S. Geological Survey Open-File Report 85-612, 83p.

Martin, Seelye, 1981, Frazil ice in rivers and oceans, *in* Ann. Rev. Fluid Mech.: Annual Reviews Inc., v.13, p.379-397.

Morack, J.L and Rogers, J.C., 1984, Acoustic velocities of nearshore materials in the Alaskan Beaufort and Chukchi Seas, *in* Barnes, P.W., Schell, D.M., and Reimnitz, Erk, The Alaskan Beaufort Sea: Ecosystems and Environments: Academic Press, Orlando, FL, p.259-274 .

Neave, K.G. and Sellman, P.V., 1984, Determining distribution patterns of ice-bonded permafrost in the U.S. Beaufort Sea from seismic data, *in* Barnes, P.W., Schell, D.M., and Reimnitz, Erk, The Alaskan Beaufort Sea: Ecosystems and Environments: Academic Press, Orlando, FL, p.237-258 .

Norton, D.W. and Sackinger, W.M. (editors), 1981, Beaufort Sea (Sale 71) Synthesis Report, Chena Hot Springs, Alaska, April 21- 23 1981: U.S. Department of Commerce, National Oceanic and Atmospheric Administration, Juneau, AK, p.165 .

Osterkamp, T. E. and Gosink, J. P., 1982, Frazil ice formation and ice cover development in interior Alaska streams: Cold Regions Science and Technology, v.8, p.43-86.

Osterkamp, T.E. and Gosink, J.P., 1984, Observations and analysis of sediment laden sea ice, *in* The Alaska Beaufort Sea: Ecosystem and Environment: Academic Press, San Francisco, CA, p.73-94.

Piotrovich, V.V., 1956, Formation of depth-ice: Translated from Priroda, Translated by E.R. Hope, Directorate of Scientific Information Survice, DRB Canada, November 1956., v.9, no.94-95, p.1-4.

Reimnitz, Erk and Barnes, P.W., 1974, Sea ice as a geologic agent on the Beaufort Sea shelf of Alaska, *in* Reed, J.C., and Sater, J.E. (editors), The Coast and Shelf of the Beaufort Sea: The Arctic Institute of North America, Arlington, VA, p.251-301.

Reimnitz, Erk and Dunton, Kenneth, 1979, Diving observations of the soft ice layer under the fast ice at DS-11 in the Stefansson Sound Boulder Patch, *in* Environmental Assessment of the Alaskan Continental Shelf, Principal Investigators' Annual Reports, March 1979, National Oceanic and Atmospheric Administration, v.IX, p.210-230.

Sadler, H.E. and Serson, H.V., 1981, Fresh water anchor ice along an arctic beach: Arctic, v.34, no.1, p.62-63.

Sellman, P.V. and Chamberlain, E.J., 1979, Permafrost beneath the Beaufort Sea near Prudhoe Bay, Alaska, *in* Proceedings of the 11th Annual Offshore Technology Conference, Houston, TX, 30 April - 3 May 1979: p.1481-1493.

Tsang, Gee, 1982, Frazil and anchor ice: a monograph: NRC Subcommittee on hydraulics of ice covered rivers, Ottawa, Ontario, Canada, p.90.

Tsurikov, V.L., 1966, The problem of international ice nomenclature: Oceanology, Academy of Sciences of the USSR, v.6, no.1, p.305-311.

Untersteiner, N. and Sommerfeld, R., 1964, Supercooled water and the bottom topography of floating ice: JGR v.69, no.6, p.1057-1062.

U.S. Department of Commerce/NOAA, 1982, Local climatological data, monthly summary, October 1982 Barter Island, Alaska: NOAA, Asheville, NC, National Climatic Center.

U.S. Department of Commerce/NOAA, 1982, Local climatological data, monthly summary, October 1982, Barrow, Alaska: NOAA, Asheville, NC, National Climatic Center.

Weeks, W.F. and Ackley, S.F., 1982, The growth, structure, and properties of sea ice; CRREL Monograph 82-1: Cold Regions Research and Engineering Laboratory, Hanover, NH, p.130.

Wigle, T.E., 1970, Investigations into frazil, bottom ice and surface ice formation in the Niagra River, *in* Proceedings of the Symposium on Ice and Its Action on Hydraulic Structures, Reykjavik, Iceland.: International Association for Hydraulic Research, Paper no. 2.8, 16p..

World Meteorological Organization, 1970, WMO Sea-Ice Nomenclature, Codes, and Illustrated Glossary, Report 259, TP145, Geneva, 147p.

Zubov, N. N., 1945, Arctic Sea Ice, Translated by Naval Oceanographic Office and American Meteorological Society under contract to Air Force Cambridge Research Center, 1963, U.S. Naval Electronics Laboratory, San Diego, CA, p.491.

FLUME STUDIES AND FIELD OBSERVATIONS OF THE INTERACTION OF FRAZIL ICE AND ANCHOR ICE WITH SEDIMENT

by

E. W. Kempema, Erk Reimnitz, and R. E. Hunter

U.S. Geological Survey
Menlo Park, California 94025

Final Report
Outer Continental Shelf Environmental Assessment Program
Research Unit 205

1986

This report has also been published as U.S. Geological Survey Open-File Report 86-515.

ACKNOWLEDGMENTS

This study was funded in part by the Minerals Management Service, Department of the Interior, through interagency agreement with the National Oceanic and Atmospheric Administration, Department of Commerce, as part of the Alaska Outer Continental Shelf Environmental Assessment Program.

We thank Dave Andersen for his thoughtful review of this manuscript.

ABSTRACT

Frazil ice and anchor ice are types of ice that form in turbulent, supercooled water. Frazil and anchor ice phenomena have received a relatively large amount of study in recent years because of the problems they pose to man-made hydraulic structures. In the course of these studies, there have been many observations of interactions of frazil and anchor ice with sediment, but the relationship has never been viewed from a geologic standpoint.

This is a report of flume experiments undertaken to observe the interactions of frazil and anchor with sand-sized sediment both in suspension and as bed material in fresh and salt water. Observations of frazil and anchor ice from the Alaskan Beaufort Sea also are presented. In the flume, anchor ice resembling that seen in natural settings formed over ice-bonded sediment.

In fresh-water flume experiments, frazil ice formed flocs up to 8 cm in diameter that tended to roll along the bottom and collect bed sediment. These flocs often came to rest in the lee of bedforms, forming anchor ice that was buried as the bedform advanced. As the anchor ice was buried, it was compressed into an ice-bonded sediment-rich block. Anchor ice buried by migrating bedforms disrupts normal ripple cross-bedding and may produce unique sedimentary structures.

Salt-water frazil-ice flocs were smaller, picked up less bed sediment, and formed less anchor ice than their fresh-water counterparts. In salt water, anchor ice most readily formed on blocks of ice-bonded sediment.

A calculation based upon the buoyancy of ice in fresh water shows that floating ice masses can move sediment concentrations of up to 122 g/l. Sediment concentrations of this magnitude have not been observed in either flume or natural settings, but very few measurements have been made. The maximum sediment concentration measured in this study was 88 g/l. These high theoretical and measured sediment concentrations suggest that frazil and anchor ice are important sediment transport agents in rivers and oceans.

TABLE OF CONTENTS

INTRODUCTION

Frazil and anchor ice commonly form in turbulent water bodies exposed to subfreezing air temperatures. Frazil ice is defined as "fine spicules, plates, or discoids of ice suspended in water" (Kivisild, 1970). It usually occurs as small discs 1 to 4 mm in diameter and 1 to 100 μm thick. The World Meteorological Organization (1970) defines anchor ice as "submerged ice attached or anchored to the bottom, irrespective of the nature of its formation." In this report the term will be used to describe accumulations of sticky or sediment-laden frazil ice masses that are either attached to or resting on the bottom (fig. 1).

There is a long history of published observations on the formation of frazil and anchor ice. Benedicks and Sederholm (1943) summarized observations from as early as 1708, and Barnes (1928) reported observations dating to 1788. However, detailed studies of frazil and anchor ice formation and processes began only in the last 50 years and intensified in the last 20 with the construction of engineering projects in high-latitude rivers. Frazil and anchor ice production can cause many engineering problems, including flooding caused by frazil ice jams and anchor ice accumulations, interference with hydroelectric facilities, blockage of water supply intakes, interference with shipping, and damage to hydraulic structures (Carstens, 1966; Osterkamp, 1978). To date most studies have dealt with the engineering properties of frazil and anchor ice, and have been aimed at understanding the meteorological and hydraulic conditions necessary for frazil and anchor-ice formation. Osterkamp (1978), Martin (1981), and Tsang (1982) presented reviews of the state of present knowledge on frazil and anchor ice.

Although there is a large body of literature that covers the theoretical aspects of frazil and anchor ice formation, little work has been done on the interaction of frazil and anchor ice with sediment. Most of the literature on frazil/anchor ice/sediment interaction is of an observational nature. The purpose of this study is to examine frazil/anchor ice/sediment interactions from a geological viewpoint, and specifically to address the following questions: (1) How does the presence of frazil ice in the water column affect sediment transport? (2) What products of the interaction of frazil and anchor ice with bottom sediment might be preserved in the sedimentary record?

To study these questions, experiments were conducted in a small flume under controlled conditions. A number of variables were investigated, including cooling rate, current speed, and salinity. In addition, field observations of anchor ice from the Beaufort Sea are presented, and results of the flume studies are compared to the field observations.

FRAZIL ICE AND ANCHOR ICE FORMATION

In fresh water, frazil ice forms in turbulent water that has become supercooled by exposure to air at sub-freezing temperatures. Turbulence, caused by currents or wind-generated waves, inhibits the formation of a surface ice cover and allows supercooling of the water column to some depth. This supercooling is generally on the order of 0.05 to 0.10°C (Schaefer, 1950; Wigle, 1970; Arden and Wigle, 1972). Water cannot spontaneously freeze at this slight degree of supercooling, and it is necessary to seed the water column to initiate formation of frazil ice. Osterkamp (1978) reviewed the various mechanisms proposed to initiate formation of frazil ice and concluded that the most likely is some form of mass exchange process at the water surface. In this model, ice particles in the air from a variety of sources such as sleet, snow, or frozen spray fall into the water and act as seed crystals to initiate the growth of frazil ice. Another possible source of seed crystals is cold dust particles that fall into the water. Upon entering the water, these dust particles could absorb enough heat to freeze a thin layer of surrounding water (Tsang, 1982). Once the original seed crystal has entered the water, it grows rapidly and is broken up by turbulence and collisions in the flow. The pieces broken from the seed crystal act as secondary nuclei, allowing the growth of more frazil crystals. Pieces of ice also are broken from these new frazil crystals to act as more nuclei, so that in a short time period many nuclei are made, and a large amount of frazil ice can be produced.

Figure 2 is an idealized curve of temperature change in a water body as it is cooled and frazil ice is produced. This curve shows water temperature dropping with time through T_f, the freezing point of the water at a given salinity. Once the temperature drops below T_f the water is supercooled. At temperature T_n, the supercooled water is seeded with ice crystals, frazil production begins, and the slope of the time-temperature curve decreases. Frazil-ice growth is slow at first because there are few seed crystals, and the latent heat of fusion released by ice formation is too small to overcome heat loss through the free water surface, so the temperature continues to drop. However, as more ice nuclei are produced through the process of secondary nucleation, the rate of frazil production increases until the latent heat of fusion produced by ice growth becomes equal to the rate of heat loss to the air. At this point, the water reaches its lowest temperature, T_m. After this, the increased latent heat released by frazil production is absorbed by the water, raising its temperature to an equilibrium temperature, T_e. The period of greatest frazil production occurs when the water temperature is between T_m and T_e. As the water temperature approaches T_e the rate of frazil production decreases, and the rate of heat loss at the water surface becomes equal to the rate of latent heat liberation associated with frazil production. T_r is the residual temperature, defined as the difference between T_f and T_e. Tsang (1982) noted that T_r is dependent upon hydrometeorological conditions. As long as there is a residual temperature frazil ice will continue to be produced. Tsang (1982) also pointed out that the values of T_n, T_m, T_e, and T_r in natural water bodies have not been well

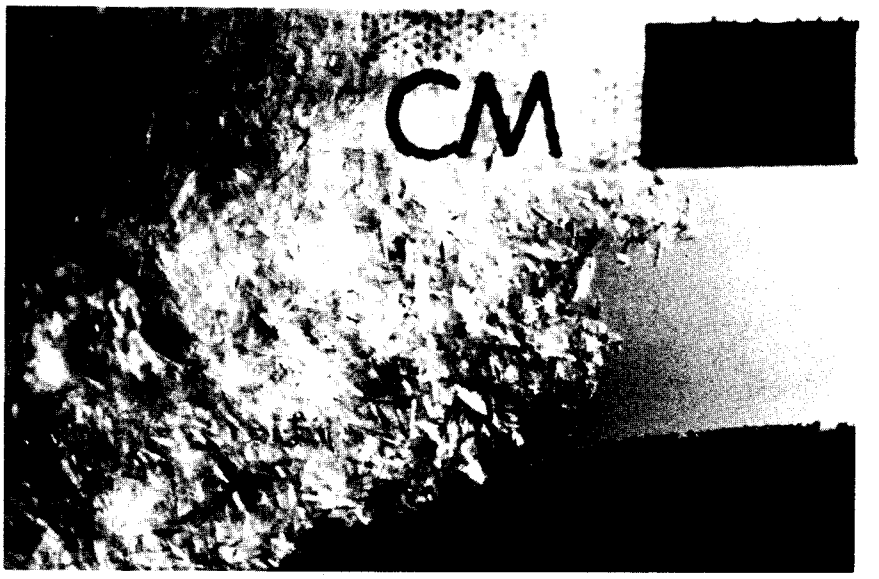

Figure 1. Photograph of an anchor ice mass composed of an agglomeration of individual frazil ice crystals. Individual disc-shaped frazil crystals are visible on the right side of the mass. The anchor ice is attached to an obstruction out of view to the left; current is from the right. The black rectangle in the upper right is 1 cm long. Flume experiment 43.

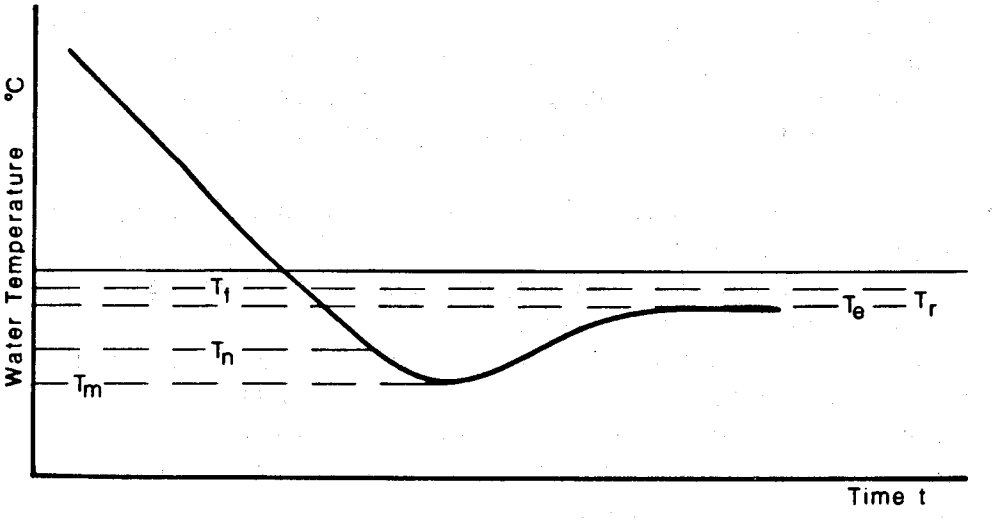

Figure 2. Idealized curve showing supercooling of a water body leading to the formation of frazil ice. T_n: nucleation temperature, point where frazil ice crystals first appear in the water; T_m: temperature minimum; T_e: equilibrium temperature, temperature at which heat lost to the atmosphere is equal to heat released by the growing ice; T_f: freezing point of the water, this may be below 0^oC because of impurities in the water; and T_r: residual temperature, the difference between T_e and T_f. This small residual temperature is the driving force for producing most frazil ice in natural systems. Modified from Tsang and Hanley (1985).

documented, but available data suggests that they are on the order of hundredths of a degree below T_f.

The method described above of supercooling turbulent water by heat exchange with the atmosphere is the only known method of producing frazil ice in fresh water. In the ocean, however, there are at least four methods of supercooling water that can lead to frazil-ice production (Martin, 1981): (1) in open water regions, supercooling and frazil ice can occur where heat is lost to the atmosphere (as already described for fresh water); (2) at the interface between 2 fluid layers, each at its freezing point and with different salinities, frazil ice grows in the less saline water as heat is lost to the more saline water; (3) frazil ice may occur where cold brine formed by development of a surface ice cover sinks and cools less saline water; and (4) adjacent to ice shelves frazil may form by direct cooling of seawater from cold ice or by raising a parcel of water from the bottom of the shelf to the water surface. The freezing point of the water parcel is depressed because of pressure at depth; as the water rises, pressure is reduced and the freezing point rises, allowing frazil ice to form. The only type of salt-water frazil growth considered in this paper is that produced by supercooling of the water through heat loss to the free-air surface.

Frazil ice in supercooled water is 'sticky', exhibiting strong cohesive tendencies between individual ice crystals and between ice crystals and materials on the bottom (Carstens, 1966). Once frazil-ice crystals form, they agglomerate to each other and form buoyant flocs 3 to 10 cm in diameter that rise to the water surface. Flocs evolve into frazil-ice pans when exposed to frigid air. Frazil pans can range from 2 to 10 m in diameter and exceed 1 m in thickness (Osterkamp and Gosink, 1983). The accumulation of frazil ice pans against an obstruction and subsequent freezing of the water between pans can lead to the formation of a solid ice cover. The present study is concerned only with the stages from frazil ice through floc formation.

When a frazil crystal sticks to the bottom, or to a submerged object, it becomes anchor ice (Benson and Osterkamp, 1974). Before frazil crystals can stick to the bottom, the bottom must be cooled to a temperature below the freezing point of the surrounding water (Piotrovich, 1956). The bottom loses most of its heat to the overlying water, so to reduce the temperature of bottom materials to below the freezing point the water must be supercooled. Once formed, an anchor-ice mass can grow by accretion of frazil crystals or by accelerated growth of crystals already making up the mass (Piotrovich, 1956). Accelerated growth of the anchor-ice crystals occurs because the crystals are exposed to a continuous flow of supercooled water. Osterkamp and Gosink (1983) reported that the growth rate of anchor ice may increase by an order of magnitude over the growth rate of frazil-ice crystals in the flow. These two processes also can act simultaneously. Tsang (1982) pointed out that, while important, stickiness of anchor ice is not necessary for growth by frazil accretion. The rough surface of the anchor ice can easily trap frazil crystals from the water column, adding to the volume of the anchor-ice mass.

Anchor ice can grow to large sizes, and it can affect the hydrologic regime of rivers. Tsang (1982) quoted sources that document anchor ice thicknesses of up to 1 m in the Neva River and up to 0.5 m in the Niagara River. Wigle (1970) and Arden and Wigle (1972) reported that anchor ice forms in all reaches of the upper Niagara River, and that the formation of anchor ice on clear, cold nights can reduce the river flow by 20 to 30 percent. Osterkamp and Gosink (1983) observed that anchor ice modifies the hydraulic conditions in streams and can be responsible for substantial reworking of bottom sediments.

PREVIOUS STUDIES

Observations of frazil and anchor ice have been published for at least 275 years (Benedicks and Sederholm, 1943), but the modern study of frazil ice can be considered to start with the work of Barnes (1928). A large body of literature has been published since that time, but the majority of this work deals with the dynamics of frazil ice formation, and it does not deal specifically with the interactions of frazil ice with bottom materials. However, several workers have recorded observations of frazil and anchor ice interacting with sediment.

Anchor-ice growth is initiated when frazil-ice crystals in supercooled water become attached to bottom materials (Piotrovich, 1956; Michel, 1972). Frazil-ice crystals become anchor ice when they become attached to the bottom or when they collide with and stick to an obstruction (Michel, 1972; Osterkamp and Gosink, 1983). Benedicks and Sederholm (1943) and Michel (1972) have suggested that frazil-ice crystals preferentially stick to and grow on substances with a crystalline structure similar to that of ice, but this theory has never been proven. Anchor ice most often grows on bottoms composed of coarse materials, because the coarse materials overcome the buoyancy of the attached ice (Wigle, 1970; Arden and Wigle, 1972). Coarse materials also project into the flow, and are thus cooled to subfreezing temperatures by the supercooled water more readily than smooth, fine-grained materials, making it easier for frazil crystals to stick to them (Michel, 1972).

Frazil and anchor ice have been studied mostly in fresh-water settings. One common observation in rivers is that sediment-laden anchor ice often rises to the surface on mornings following cold, clear nights (Barnes, 1928; Wigle, 1970; Arden and Wigle, 1972; Michel, 1972; Foulds and Wigle, 1977). This released anchor ice has the potential to carry sediments long distances downstream, and in some cases may carry sediment to the sea, where it may be incorporated into the seasonal ice cover (Benson and Osterkamp, 1974). Not all anchor ice rises to the surface. Osterkamp and Gosink (1983) observed sheets of anchor ice tens of centimeters in diameter and 10 to 20 mm thick moving along the bottom of Alaskan streams. This anchor ice had incorporated sediment, and when sheets came to rest on top of other anchor-ice masses, an anchor-

ice mass with sediment distributed throughout its thickness formed. Materials that are carried by anchor ice include boulders of up to 30 kg (Martin, 1981), sand and gravel (Arden and Wigle, 1972), and mud and vegetable material (Barnes, 1928). The importance of anchor ice as an agent of sediment transport in rivers is not known, but Tsang (1982) noted that the Niagara River transports little sediment during the summer, but a considerable quantity of large stones is found upstream of a large hydraulic structure each spring. Tsang (1982) said that only anchor ice can account for the movement and deposition of these large stones.

There are fewer observations of anchor ice in salt water than in fresh water. Zubov (1943) listed a variety of objects that were lifted off the bottom by anchor ice in Russian waters, including a tool box, sediment, and 40-cm-long rods that had been driven into the bottom until only 4 cm protruded from the sediment. He also noted that anchor ice can stay attached to the bottom for long periods of time. In some cases anchor ice persists long enough for organisms to become established on its top surface.

Dayton et al. (1969) reported on the formation of frazil and anchor ice in McMurdo Sound, Antarctica. They observed "masses of platelets frozen to the bottom" in depths of up to 33 m. The anchor ice apparently controls benthic biological and sediment zonation. Below the depth of anchor ice formation there is an abrupt increase in the number of sponges, and sediment is enriched in sponge spicules compared to sediment at shallower depths where anchor ice forms. Dayton et al. (1969) also noted that anchor ice can form rapidly, trapping motile benthic organisms. When this anchor ice is released from the bottom it can carry these organisms and sediment to the underside of the floating ice cover (Curtsinger, 1986). The anchor ice can lift large portions of the bottom, weighing up to 25 kg.

In addition to forming anchor ice, frazil ice may also interact with sediment in suspension and on the bottom. Barnes (1928) and Altberg (1938) observed that frazil ice will remove suspended sediment particles from rivers, so that "...The first run of frazil has a remarkable cleansing effect on the water" (Barnes, 1928). Arden and Wigle (1972) also observed frazil ice interacting with bottom sediments. In the Niagara River, flocs of frazil ice would strike sandy portions of the river and pick up bottom material before they were carried back into suspension.

Barnes et al. (1982), in their study of sediment-laden sea ice in the Alaskan Beaufort Sea, suggested that frazil-ice formation is responsible for the widespread occurrence of finely disseminated silt and clay found in the sea-ice cover. The frazil ice forms during fall storms associated with freezeup. Sediment concentrations measured in the ice ranged up to 1600 mg/l, 1 to 2 orders of magnitude greater than sediment concentrations normally found in coastal waters.

Osterkamp and Gosink (1984) also studied sediment-laden ice in the Beaufort Sea. They measured sediment concentrations in the ice of up to 1290 mg/l. They

proposed 9 different methods of incorporating sediment into the ice cover. Seven of these call for some type of frazil or anchor-ice process to incorporate sediment into the ice cover. The proposed methods are untested, however, and Osterkamp and Gosink (1984) presented no observations (other than the observed sediment in the ice cover) to support any of their methods of sediment entrainment.

The above synopses illustrate a number of facts known about frazil and anchor ice and their interactions with sediment: (1) frazil and anchor ice are capable of moving clasts as large as boulders weighing at least 30 kg; (2) anchor ice seems to form preferentially on rocky bottoms; (3) anchor ice may form preferentially on certain materials; (4) frazil ice has the ability to clear the water of suspended particulate matter; (5) frazil and anchor ice form most often on clear, cold nights; (6) the growth of large masses of anchor ice changes the hydrologic regime of rivers, and may reduce flow as much as 30 percent. The synopses also illustrate how little is known about the details of frazil and anchor ice interactions with sediment. It is clear that these forms of ice do interact with materials in suspension and lying on the bottom, but there is no detailed information on how these processes operate or on the overall geologic significance of frazil and anchor ice.

FIELD OBSERVATIONS

Field observations of frazil and anchor ice in salt water were made in the Alaskan Beaufort Sea near Prudhoe Bay (fig. 3) during the fall freezeup in 1982. This area is characterized by an almost complete ice cover for about 9 months of the year, with a 2- to 3-month open-water season with fetch typically limited by ice. Astrological tides in the area are less than 15 cm, but strong westerly winds can drive up the water level as much as 3.4 m (Reimnitz and Maurer, 1979). Reimnitz and Barnes (1974) and Barnes and Reimnitz (1974) described the setting of this area in detail.

As part of the field observations, two diving traverses were made. Each of these traverses was about 150 m long, and each was made in water depths of 0 to 4 m. The traverses were located on the seaward side of Reindeer Island and on the east side of the West Dock (fig. 3). Observations of anchor ice and seafloor sediment types were made along the traverses. Observations of frazil ice between the West Dock and Reindeer Island were made at the same time.

For 6 days preceding the diving observations off Reindeer Island on October 5, 1982, there were continuous winds of up to 12.5 m/s (25 knots). The air temperature never rose above 0°C during this period, and frazil ice was observed forming windrows parallel to the wind on the sea surface. At the time the dives were made, the wind had died down but the air temperature remained below freezing, and much of the sea surface was covered with a grease ice layer composed of frazil ice crystals. As a

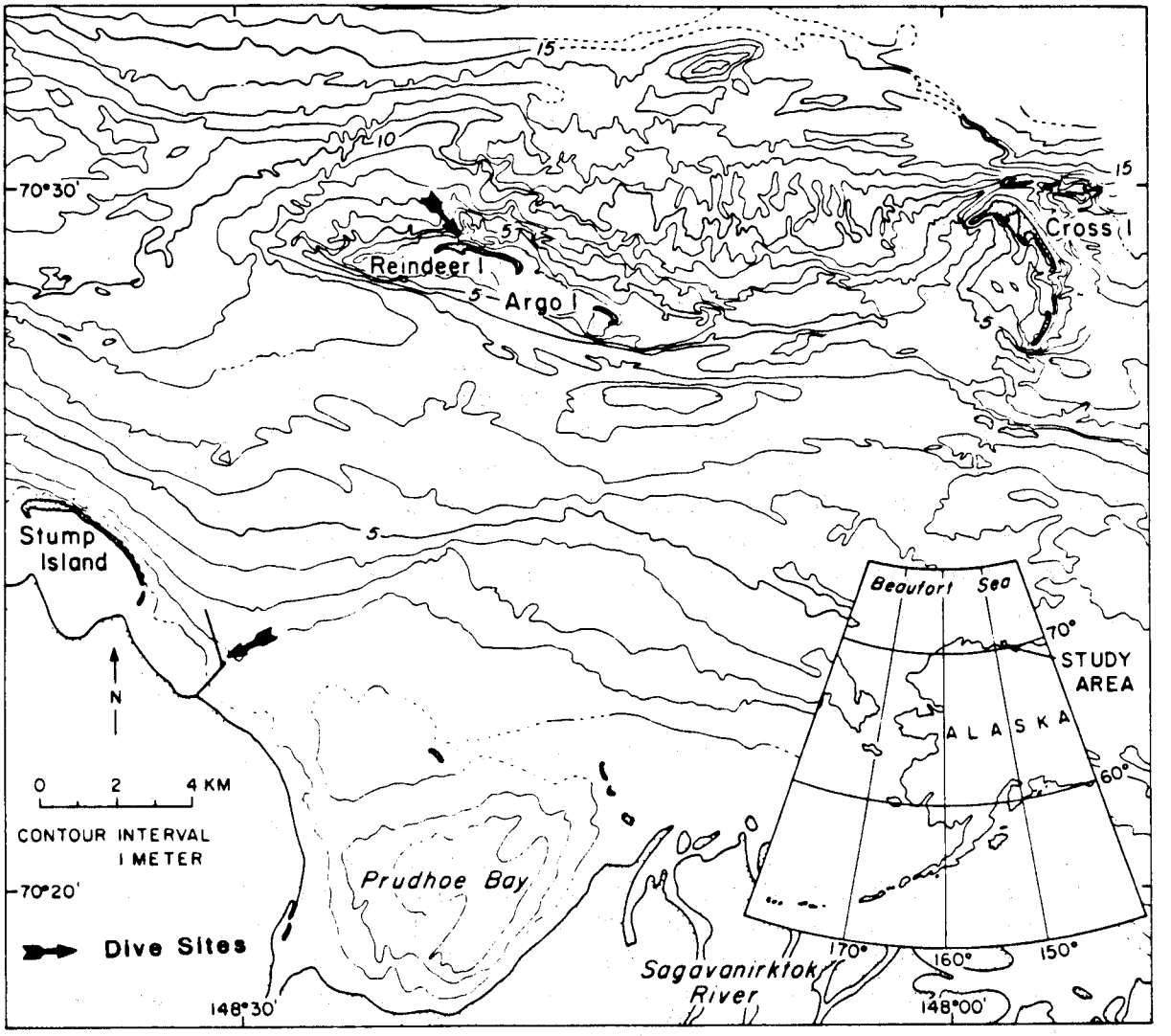

Figure 3. Beaufort Sea dive sites where anchor ice was observed in October 1982.

result of this ice cover, sea conditions were calm for diving operations.

The 130-m-long dive traverse extended from the seaward-facing beach to a water depth of 4 m. One 2-m-high bar, approximately 90 m from shore, was traversed. For a distance of 10 m out from the shoreline the gravel and coarse sand bottom was ice bonded. The ice-bonded sediment formed slabs that were up to 40 cm in diameter and 10 to 15 cm thick. Several of these slabs were collected and subsequently melted down. After melting and settling, approximately 20% excess water by volume was standing on top of the sediment. In addition to being ice bonded, some of the area within 10 m of the shoreline was covered by clumps of anchor ice up to 30 cm in diameter (fig. 4). Seaward of 10 m the bottom consisted of clean, medium, rippled sand with widely scattered pebbles. Clumps of anchor ice, with a surface of delicately intertwined ice crystals and a core of ice-bonded sediment, were observed on the sand bottom (fig. 5). These clumps of anchor ice were roughly circular in plan view, and ranged from 3 cm to 1 m in diameter. The largest clumps were about 30 cm high. In some areas, several of these clumps rested next to each other, creating anchor-ice masses that covered areas up to 3 by 4 m. The anchor ice commonly contained sediment grains resting in the interstices between ice crystals. When the crystals were disturbed they readily broke up and floated away, and the cores of the anchor-ice clumps were exposed. These cores were ice-bonded sediment, and although composed of sand-sized material they were similar to the ice-bonded gravel slabs seen closer to the beach, with the exception that they projected above the level of the surrounding sea floor.

The smallest anchor-ice clumps were observed nearest to the beach, and size increased to a maximum offshore in the trough and on the outer side of the bar. There was less anchor ice on the crest of the bar than in the deeper water on either side. The anchor ice tended to sit in small depressions on the rippled bottom (fig. 5). At the seaward end of the traverse the water surface was covered with a layer of grease ice up to 20 cm thick. This layer had up to 10 cm of relief and did not appear to have any incorporated sediment.

The weather conditions for the dive at the West Dock on the following day were similar to those at Reindeer Island. This dive was made near a gravel causeway at a distance of about 1400 m from shore and consisted of a 150-m traverse in water depths of less than 2 m. Visibility was 50 to 75 cm during the dive, so only a narrow strip of seafloor was observed. Bottom sediment along the traverse consisted of gravel, sand, and mud. Ice bonding of sediment was observed in all of these materials. The distribution of gravel was patchy, and it was all strongly cemented by ice, making it impossible to drive a spade into the bottom and difficult to dislodge even a single clast. The sand along the traverse was rippled and frozen to a depth of several centimeters. The ripples had wavelengths of 20 cm and heights of 5 cm. There was no observed difference in depth of ice bonding from the ripple crest to the ripple trough, although changes of a centimeter or less could have been missed. Ice bonding was minimal in the mud, occurring as a layer less than 1 cm thick that extended downward

Figure 4. Anchor ice resting on frozen, ice-bonded sand and gravel bottom in 1-m-deep water on the seaward side of Reindeer Island (fig. 3). Center of photograph is about 75 cm across.

Figure 5. Anchor ice in 4-m-deep water off Reindeer Island (fig. 3) in October 1982. The anchor ice masses were composed of a sediment-rich, ice-bonded core surrounded by a halo of delicately intertwined ice crystals. The masses were resting on unfrozen, clean, rippled, sand bottom. Individual ball-shaped anchor ice masses were about 40 cm in diameter.

into the sediment from the sediment/water interface. We estimated that 60 to 75 percent of the bottom was ice bonded along this traverse; but no anchor-ice clumps with free ice crystals similar to those seen at Reindeer Island were observed on the sediments. However, several pieces of trash, including a tire, steel banding, and organic debris were seen along the traverse. All of these materials had anchor ice composed of frazil ice crystals attached to them. Several twigs also were seen along the traverse, these were conspicuous because they lacked a covering of anchor ice. In some cases, the anchor ice formed a halo with a radius of 10 cm around an object. This anchor ice was so poorly attached to its substrate that the slightest touch would release it from the substrate and it would rise to the water surface. The anchor ice growing on debris was similar in appearance to the anchor ice observed resting on the bottom near Reindeer Island; the only apparent difference was the type of substrate.

LABORATORY EXPERIMENTS

Methods

Laboratory work consisted of 39 flume experiments made in a small race-track flume at the U.S. Geological Survey facility in Palo Alto, California. Flume experiments were made under a variety of conditions, and variables including cooling rates, currents speeds, and water salinity were changed to learn how they might affect frazil/anchor ice/sediment interactions. In addition, four special flume experiments, with non-routine variables, were made. These non-routine variables included injecting supercooled air into the water; seeding the supercooled water with dry ice (Shaefer, 1950); cooling the underside of the flume with dry ice to simulate cooling of bed sediment from permafrost at depth; and sprinkling cold sand into the water during the period of frazil formation.

Making Frazil and Anchor Ice

Frazil and anchor ice were made in a race-track flume similar in shape to the one used by Carstens (1966). The flume was constructed of aluminum with plexiglas windows built into one straight segment (fig. 6). The flume was 1.2 m long, 75 cm wide, and 32 cm deep. The channel width was 21 cm. During use, the flume was filled with a level layer of sand 4 cm thick overlain by 17 cm of water. The volume of water in the flume during an experiment was about 110 liters. The aluminum sides of the flume were insulated with 1.5 cm of closed-cell foam, and the bottom was insulated with 5 cm of foam, so water was cooled predominantly from the surface.

Currents in the flume were produced with a plastic propeller from a model boat. This propeller was positioned in the back straight section of the flume, and was connected to a variable speed electric motor by means of a flexible steel drive shaft. With

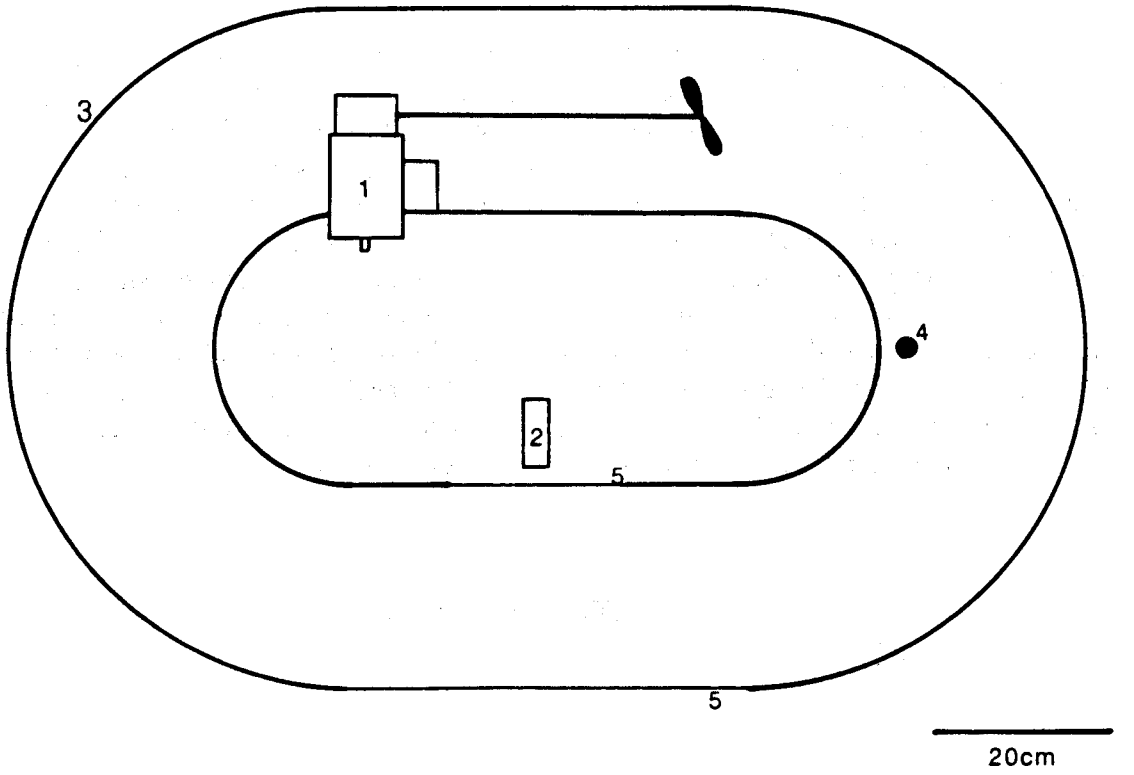

Figure 6. Plan view of flume showing: (1) variable speed electric motor attached to propeller, (2) light, (3) 1.5-cm-thick insulation, (4) thermistor, and (5) plexiglas windows.

this system, current speed in the flume could be varied between 30 and 70 cm/s. The shape of the flume and the rotary motion of the propeller resulted in non-uniform flow, and the reported current speeds are averages. Current speeds were determined by timing neutral-density disks as they traveled around the flume. For making the current speed calculations, it was assumed that the average path a disk took around the flume was equal to the path length measured along the centerline of the flume channel. All current speed calculations were carried out at room temperature and with no sand in the flume. The presence of sand on the floor of the flume probably would result in slightly lower current velocities.

For an experiment the flume was pushed into a 4X4 m walk-in freezer that maintained an air temperature of -17°C +/- 1°C. Fans in the freezer produced slight air movement at the water surface in the flume. To increase cooling during some experiments a 30-cm-diameter fan was placed so that it blew a steady stream of cold air across the water surface at a speed of 4 m/s. Air temperature was measured to +/- 0.25°C with a standard laboratory thermometer several times during each flume experiment. Water temperature was measured with a thermistor accurate to 0.004°C. This thermistor was inserted to a water depth of 9 cm at a turn in the flume (fig. 6). Care had to be taken during the period of frazil formation to assure that no frazil stuck to

the thermistor, because this resulted in anomalously high temperature readings. To avoid this problem the thermistor probe was mechanically cleaned during periods of active frazil formation, or the probe was coated with silicone grease before the start of the experiment to retard the adhesion of frazil. Resistance readings from the thermistor and time were recorded on a manually triggered printer. Time and resistance readings were recorded at 10 to 20 second intervals during periods of frazil formation; at other times these readings were taken at 1 to 5 minute intervals. At the end of the experiment these readings were converted to time and temperature and plotted in graphical form.

For fresh-water experiments, tap water was used to fill the flume. For salt-water experiments 'Forty Fathoms', a commercially available aquarium salt, was used to make a saline solution. 'Forty Fathoms' was also used by Tsang and Hanley (1985) in their study of frazil formation in saline waters, and they found no significant differences in experimental results when comparing the artificial sea water with natural Atlantic Sea water. In the present group of experiments, the water salinities were about 0 parts per thousand (ppt), 29 ppt, and 36 ppt. For the saline water experiments, the salinity was determined by the method outlined by Lewis (1980).

It is important to seed the supercooled water to initiate the growth of frazil ice. In carefully controlled laboratory experiments it is relatively simple to get supercooling of at least several degrees centigrade (see, for example, Hanley and Tsang, 1984). In the present experiments, artificial seeding was not necessary. There apparently were enough ice crystals in the air that fell into the water to initiate frazil growth. The degree of maximum supercooling seen in these experiments is close to that seen in natural settings.

Flume Sediment

Two different sands were used as bed material in the flume experiments. For most experiments a clean, well-sorted, quartz-rich beach sand with a mean grain size of 2.0 phi was used. In three experiments a poorly-sorted sand with mean grain size of 2.5 phi was used. This sand was very dirty, and the silt and clay that went into suspension made the water opaque. This made viewing frazil and anchor-ice formation impossible, so the use of this sediment was discontinued.

At all current speeds used in the flume, the sand moved as both bed load and suspended load. Well-developed ripples up to 7 cm high formed in the straight segments of the flume when current speeds were below 60 cm/s. At current speeds above 60 cm/s these ripples were destroyed, and the sand assumed a flat bed configuration. Because flow in the flume was not uniform, several dead spots or depositional areas formed, especially along the inside turns of the flume and along the back straight segment just upstream of the propeller. In a similar fashion, the areas along the outsides of the turns and directly down stream from the propeller were areas of scouring and non-deposition. However, the area along the window generally maintained a cover of at least 2 cm of sediment throughout any given experiment, and it contained no regions of consistent scour or deposition. Flow conditions in the area of the window

appeared uniform across the entire width of the channel; migrating bedforms usually reached from one wall of the channel to the other.

During several experiments, cobbles up to 12 cm in diameter were added to the flume to learn how they interact with frazil and anchor ice. Some of these cobbles had algae up to 20 cm long attached to them. For some salt-water experiments, ice-bonded sand blocks with a volume of about 250 ml were placed on the flume floor. These sand blocks were similar to the blocks of ice-bonded sediment observed in the Beaufort Sea. To determine if frazil ice and anchor ice preferentially adhere to certain materials, several mineral specimens and other materials were suspended on aluminum or plexiglas rods in the flow during frazil production. A list of these specimens is given in Table 1.

To determine whether sedimentary structures are produced by anchor and frazil ice, specific observations were made of ice/sediment interactions. In addition, cores were collected where anchor ice had been buried by migrating ripples. These cores were allowed to freeze and then were sawn into slabs and X-rayed. Unfortunately, the open packing of sediment and ice precluded preservation of sedimentary structures while sampling, and little can be documented from this part of the study.

Table 1. List of mineral specimens that were placed on a frame in the flume to determine if frazil ice preferentially stuck to specific minerals. In addition, fresh water algae and Macrocystis spp. were used in fresh and salt water experiments, respectively, to determine how frazil ice interacts with aquatic plant material.

ROW 1	ROW 2	ROW 3
staurolite	chert	copper
brass	flourite	chiastolite
plastic drifter	galena	epidote
quartz	garnet	black limestone
	gypsum	white limestone
	hornblende	kyanite
	specular hematite	lepidolite
	albite	magnetite

Measuring Sediment Concentrations

One of the goals of the study was to monitor suspended sediment concentrations during the experiments. Suspended sediment samples were collected by lowering a 300-ml sample bottle through the water column at a constant rate so that it reached the bottom just as it filled with water (Rudolfo, 1970). Two samples were collected on most runs: one just before frazil production began and another during the period of maximum frazil production. These two samples usually were collected within 3 minutes of each other. After collection the samples were processed by measuring the

volume of water to the nearest milliliter and then filtering the water through a pre-weighed 3 μm Millipore filter. The filters were then dried overnight at 50°C, weighed to the nearest 0.1 mg, and the sediment concentrations were calculated.

When possible, samples of frazil and anchor ice were collected to determine sediment concentrations. Ice samples were collected with a small strainer, and as much water as possible was shaken out of the ice before it was transferred to a beaker for melting. After the ice had melted the sample was processed in the same way as the suspended-sediment samples.

Results

Table 2 summarizes the data collected in the 39 flume experiments, including salinity, freezing point (T_f) for the salt water experiments calculated from the equation of Millero (1977), current speed, cooling rate, T_m, T_e, T_e-T_m, and whether or not anchor ice formed. Figure 7 is a typical plot of time versus temperature for an experiment with fresh water (Experiment 53). The curve is similar to the curve presented by Tsang and Hanley (1985) and shown in figure 2. A minimum temperature of -0.112°C was reached after about 6 minutes of supercooling. After reaching T_m, the temperature rose sharply, leveled off, and then slowly approached T_e. During this period a large amount of frazil ice formed. The time of approximately 30 minutes required for supercooling, frazil formation, and warming is within the range given by Tsang (1982) as typical for flume experiments.

The values of T_m, T_e, and T_e-T_m are easy to determine for the flume experiments, but it is difficult to relate these values to the amount of supercooling (T_f-T_m) or to the difference between the freezing point and the equilibrium temperature (T_f-T_e). In

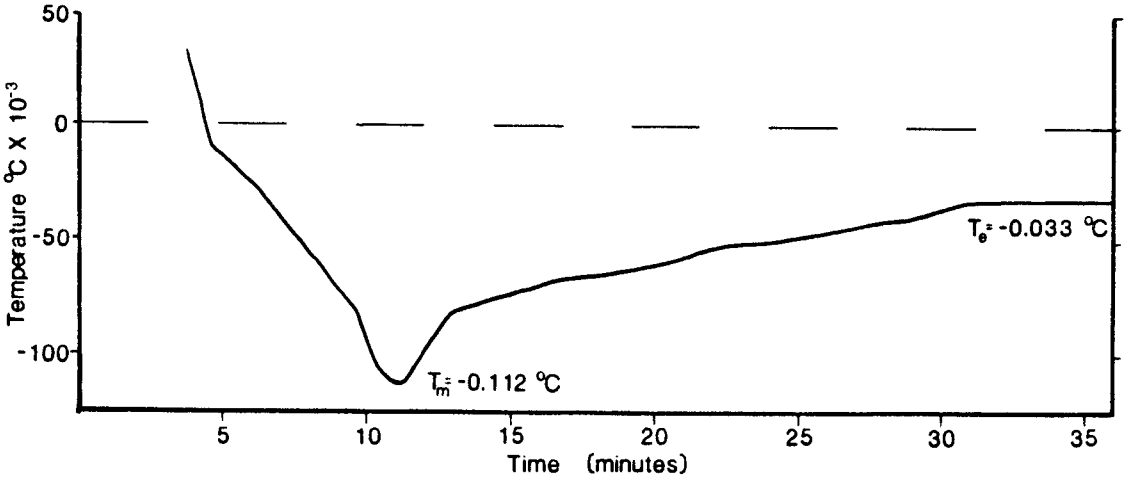

Figure 7. Cooling curve for typical flume experiment (Experiment 53, with fresh water). This curve closely approximates the theoretical curve shown in Figure 2.

Table 2. List of measurements made during different flume experiments.

Experiment Number	Salinity (ppt)	T_f (^oC)	Current Speed (cm/s)	Cooling Rate ($X10^{-4}$ cm/s)	T_m (^oC)	T_e (^oC)	T_e-T_m (^oC)	Anchor Ice Formation
16	**	**	50	6.7	-0.076	-0.011	0.065	no
17	**	**	*	5.8	-0.062	-0.021	0.041	yes
18	**	**	*	6.1	-0.066	-0.014	0.052	yes
19	**	**	*	6.2	-0.066	-0.017	0.049	yes
20	**	**	*	6.5	-0.077	-0.010	0.067	yes
21	**	**	40	4.4	-0.066	-0.017	0.049	yes
22	**	**	70	4.7	-0.059	-0.017	0.042	yes
23	**	**	43	5.6	-0.076	-0.017	0.059	yes
24	**	**	70	4.6	-0.066	-0.027	0.039	yes
25	**	**	43	6.8	-0.079	-0.021	0.058	yes
26	**	**	70	7.8	-0.069	-0.021	0.048	yes
27	**	**	60	10.0	-0.134	-0.028	0.106	yes
28	**	**	60	4.6	-0.048	-0.045	0.003	yes
29	**	**	40	4.6	-0.131	-0.031	0.100	yes
30	**	**	60	4.5	-0.083	-0.035	0.048	no
31	**	**	43	8.5	-0.100	-0.035	0.065	yes
32	**	**	60	3.2	-0.069	-0.028	0.041	yes
33	**	**	43	5.0	-0.097	-0.021	0.076	yes
34	**	**	43	4.2	-0.097	-0.031	0.066	yes
35	**	**	57	5.0	-0.097	-0.021	0.076	yes
36	**	**	70	10.0	-0.107	-0.017	0.090	yes
37	**	**	57	#	-0.068	-0.016	0.052	yes
38	29.14	-1.590	57	#	-1.731	-1.627	0.104	no
39	29.14	-1.590	57	#	-1.718	-1.623	0.095	no
40	29.38	-1.603	40	6.1	-1.703	-1.643	0.060	yes
41	29.38	-1.603	*	#	-1.677	-1.642	0.035	yes
42	**	**	57	#	-0.107	-0.042	0.065	yes
43	36.14	-1.988	70	8.4	-2.176	-2.083	0.093	no
44	36.14	-1.988	70	4.3	-2.139	-2.073	0.066	no
45	36.14	-1.988	57	8.9	-2.142	-2.080	0.062	no
46	36.14	-1.988	57	#	#	#	#	yes
47	36.38	-2.002	40	7.6	-2.167	-2.083	0.084	yes
48	36.38	-2.002	57	3.2	-2.139	-2.067	0.072	no
49	36.95	-2.030	43	6.1	-2.197	-2.098	0.099	yes
50	36.95	-2.030	*	5.9	-2.225	-2.092	0.133	yes
51	36.95	-2.030	57	3.3	-2.126	-2.089	0.037	yes
52	36.95	-2.030	43	3.7	-2.176	-2.142	0.034	yes
53	**	**	57	6.1	-0.112	-0.033	0.079	yes
54	**	**	40	8.2	-0.088	-0.033	0.055	yes

*Current speeds were varied in this experiment.
**Fresh water experiment, salinity and T_f not calculated.
#Value not calculated because of lack of data.

fresh-water experiments, the amount of dissolved salts in the water was not measured, so calculation of T_f is impossible. For salt-water experiments, T_f is calculated using the equation of Millero (1977). Knowing this value allows calculation of T_f-T_m. However, as frazil ice forms, salt is rejected, increasing the concentration of dissolved salts in the remaining water and lowering T_f. Because only the initial salinity was measured, it is impossible to determine T_f-T_e. Even with these limitations, the amount of supercooling can be estimated from the value of T_e-T_m, because T_e is within hundredths of a degree of T_f (Tsang, 1982). Assuming that T_e-T_m is a close approximation of T_f-T_m, the maximum amount of supercooling occurred during a salt water experiment (#50) and has a value of ˜0.133°C. This value is about twice as high as values of supercooling reported for natural systems. The values of T_e-T_m range from ˜0.003 to ˜0.133°C (Table 2). Most values are less than 0.100°C, within the reported range of supercooling in natural systems.

Cooling rate was varied between experiments by controlling the rate of air flow across the water's surface. In different experiments, the cooling rate varied by a factor of 3, from 3.2 to $10X10^{-4}$°C/s. A plot of cooling rate versus T_e-T_m (fig. 8) shows a weak trend toward increased supercooling as the cooling rate increases. The best-fit regression lines generated from the fresh and salt water data suggest that T_e-T_m is greater for salt-water experiments than for fresh-water experiments at the same cooling rate. However, the low correlation coefficients of r=0.42 for salt-water experiments and r=0.46 for fresh-water experiments indicate large amount of scatter in the data

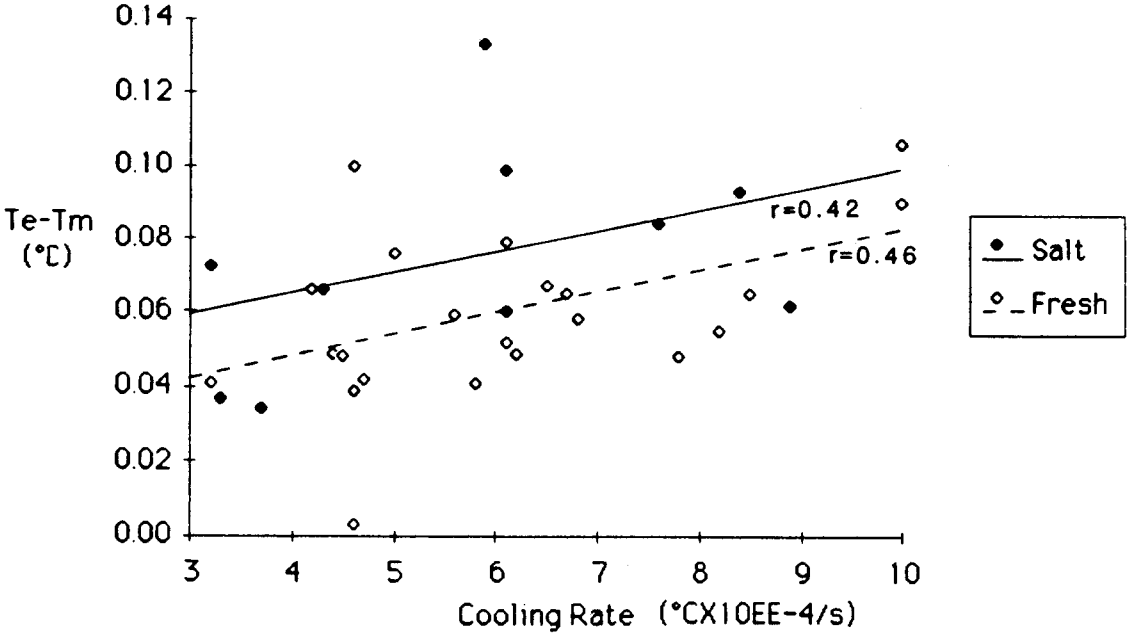

Figure 8. Graph of T_e-T_m versus cooling rate. T_e-T_m is a close approximation of the degree of supercooling. This graph shows that for a given cooling rate salt water generally reaches a greater degree of supercooling than fresh water.

sets. The only visual difference observed in frazil and anchor-ice formation at different cooling rates was the formation of hexagonally-shaped frazil crystals in Experiment 43. This experiment had one of the highest cooling rates of any of the salt-water experiments (Table 2); there may be a relationship between the high cooling rate and the shape of frazil crystals in salt water.

A graph of current speed versus T_e-T_m shows no apparent correlation (fig. 9). However, current speed does affect the formation of anchor ice on bottom sediment: anchor ice is more likely to form at lower current speeds. At the highest current speeds used in this study, the sand bottom was an upper flow regime plane bed, providing no shelter for anchor ice to settle. Even at the highest current speeds, anchor ice formed on objects suspended in the flow.

Formation and Characteristics of Frazil and Anchor Ice

Fresh Water. Frazil ice formed in all of the flume experiments. The main form of frazil crystals in fresh water was a thin disc 1 to 5 mm in diameter. Small amounts of needles up to 5 mm long also formed sometimes. These frazil crystals readily agglomerated into flocs up to 8 cm in diameter and roughly spherical in shape, stuck to objects projecting into the flow, and picked up sediment from the flume floor. Individual crystals in the frazil-ice flocs were randomly oriented, and there were relatively large voids between the crystals making up the floc. Sediment in the flocs appeared to

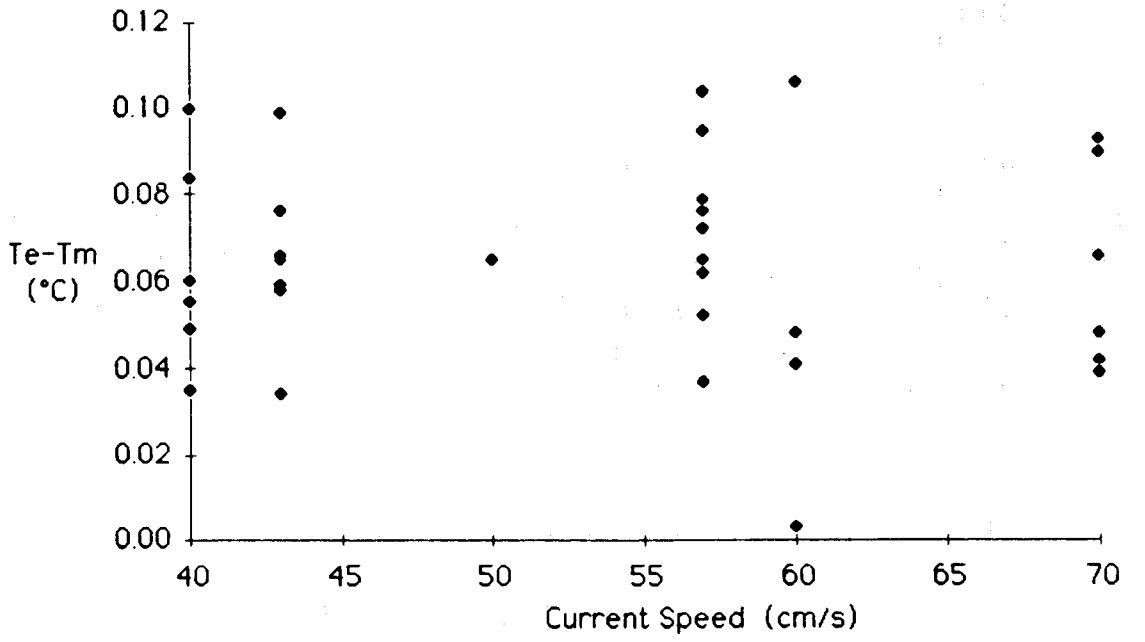

Figure 9. Graph of T_e-T_m versus current speed. This plot shows that there is no clear correlation between current speed (and turbulence) and the amount of supercooling reached in the flume.

be trapped in these voids between ice crystals. In many experiments, frazil flocs collected enough sediment to become negatively buoyant and settled to the bottom, usually in the lee of a ripple. Although not strictly within the WMO definition because it is not 'attached' or 'anchored' to the sandy bottom, this type of dirty ice resting on the bottom is here classed as anchor ice. Table 2 lists the experiments in which anchor ice was observed to form. Although anchor ice was common, the majority of frazil ice flocs remained buoyant and floated to the water surface where they soon congealed into a solid ice cover.

Salt Water. In salt-water experiments, frazil ice usually occurred as thin discs 1 to 3 mm in diameter. Figure 1 shows a salt-water anchor-ice mass composed of frazil ice. The disc shape of the frazil crystals is clearly visible. In Experiment 43 a few hexagonally-shaped crystals were observed along with the more common disc-shaped crystals. Salt-water frazil-ice flocs were much smaller than fresh-water flocs. Individual frazil crystals in salt-water flocs were aligned with their flat surfaces in contact with each other, forming tabular bodies like jumbled piles of cards that were up to 1 cm across. Frazil crystals commonly protruded from the plane of the the main tabular body, giving the aggregates a dendritic appearance. These flocs did not accumulate much sediment, and relatively little anchor ice formed on the bottom. However, anchor ice formed readily on objects suspended in the flow, particularly on the mineral specimens mounted on the plexiglas supports (fig. 10). Unlike the fresh-water frazil ice, salt-water frazil ice stayed in suspension as long as current speeds were high enough for turbulence to overcome the buoyancy of the small aggregates. When the flow was stopped, the frazil crystals rose to the surface, but they did not freeze together into a solid mass. Even after periods of up to 1 hour, when the current was turned back on the frazil crystals disaggregated and were carried back into suspension. The frazil-ice concentrations in the water column were often high enough to obscure vision across the 21-cm width of the flume. This is a sharp contrast to fresh-water frazil crystals, which agglomerated into flocs soon after forming and rose to the water surface where they congealed into a solid mass.

Interaction of Frazil and Anchor Ice with Sediment

Two different sediment types were used in the flume experiments: a clean beach sand with a mean grain size of 2 phi and a muddy sand with mean grain size of 2.5 phi. The latter was used only in Experiments 16, 51, and 52, because it released so much clay into suspension that visual observations were not possible. Contrary to previously published observations (Barnes, 1928; Altberg, 1936), there was no noticeable improvement in water clarity after frazil ice had formed. Apparently the frazil ice did not remove much of the fine-grained sediment from suspension.

Two different methods of frazil ice interaction with sediment are considered: (1) interaction with suspended particles, and (2) interaction with bottom sediment.

Interaction with Suspended Sediment. To study the effects of frazil ice formation on suspended-sediment transport, aliquots of water/sediment/frazil masses were collected before and during periods of active frazil formation and the suspended sediment

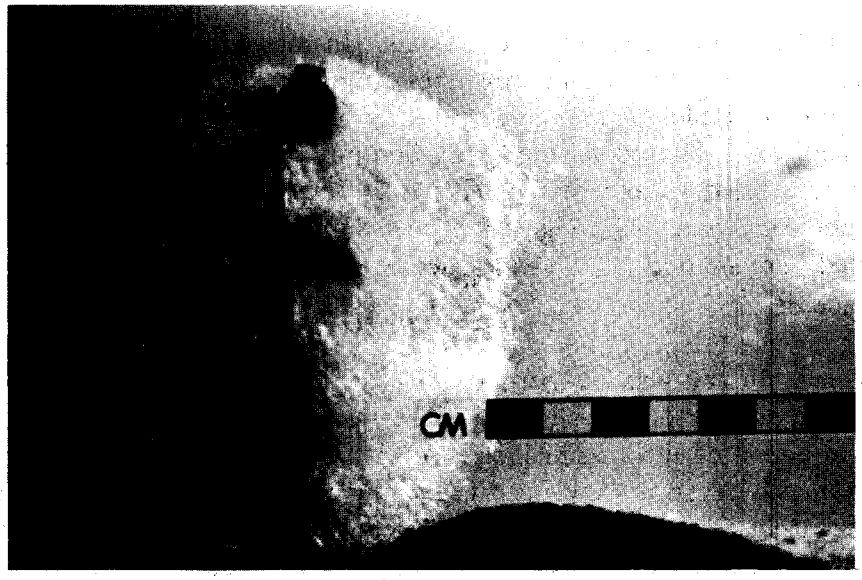

Figure 10. Anchor ice on mineral specimens and plexiglas frame in Experiment 43 (salt water). This anchor ice mass grew by trapping frazil ice crystals out of suspension. Current is from the right.

concentrations were determined. Large flocs of frazil ice and anchor ice also were collected to determine their sediment concentration. Table 3 shows the concentration of suspended sediment in the water before and during the periods of active frazil formation.

Table 3 and Figure 11 show a general increase in sediment concentration with increasing current speed, regardless of whether or not frazil ice was present. The low correlation coefficients of r=0.32 for before the period of frazil formation and r=0.54 for during the period of frazil formation show that there was substantial scatter of sediment concentration as a function of current speed. Suspended sediment concentrations ranged from 0.037 g/l at a current speed of 40 cm/s to 2.3 g/l at a current speed of 60 cm/s. At any given current speed, there tends to be more sediment in suspension before frazil ice starts forming compared to the sediment concentration at the period of maximum frazil-ice formation. In several experiments, we had the impression, based on visual observations, that suspended sediment concentrations decreased even more after T_e was reached.

Table 4 shows the amount of sediment trapped in frazil- and anchor-ice masses. These ice masses were collected after T_e was reached. Sediment concentrations in these masses range from 0.10 to 88.30 g/l. Generally, the sediment concentrations in the ice are much greater than the highest measured value of suspended sediment in the water.

Table 3. Suspended sediment concentration in water before and during periods of frazil-ice formation.

Experiment Number	Current Speed (cm/s)	Sediment Conc. (g/l)		Water Salinity
		Before Frazil Formation	During Frazil Formation	(ppt)
30	60	2.300	#	fresh*
33	43	0.800	0.500	fresh*
34	43	0.400	#	fresh*
35**	57	0.300	#	fresh*
35**	57	0.350	0.21	fresh*
36	70	0.360	0.180	fresh*
37	57	0.580	0.350	fresh*
38	57	0.470	0.320	29.14
39	57	0.471	0.388	29.14
40	40	0.037	#	29.38
41	57	#	0.126	29.38
42	57	0.133	0.130	fresh*
43	70	0.745	1.460	36.14
44	70	#	1.065	36.14
45	57	1.500	0.103	36.14
46	57	1.060	0.191	36.14
48	57	0.659	0.103	36.38
49	42	0.047	0.083	36.95
51	57	0.235	0.163	36.95
52	42	0.121	0.127	36.95

*Salinity was not determined in fresh-water experiments.
**2 samples were collected before frazil ice began forming.
#No sample was collected during this experiment.

Interaction with Bed Sediment. Anchor ice in the flume formed by two different methods: frazil flocs became attached to cobbles or mineral specimens projecting into the flow, or frazil ice accumulated enough sediment to become negatively buoyant and settle to the bottom in the lee of a ripple.

Frazil ice readily stuck to any flow obstruction in fresh water. Once the original frazil stuck to an object, the resulting anchor ice grew rapidly by addition of more frazil crystals. The fastest anchor ice growth occurred on the up-current side of objects.

Anchor ice formation caused by sediment-laden frazil flocs settling in the lee of ripples occurred most often in fresh water. The flocs forming anchor ice in fresh water ranged from a few millimeters to 8 cm in diameter. These flocs were carried over the ripple crest, got caught in an eddy, and were carried up-current and deposited in the lee of a ripple. As flocs were carried up-current by the eddies, they sometimes gouged faint striations on the lee side of the ripple. These striations were up to 8 cm long parallel to the current direction, 0.5 cm wide, and less than 0.5 cm deep.

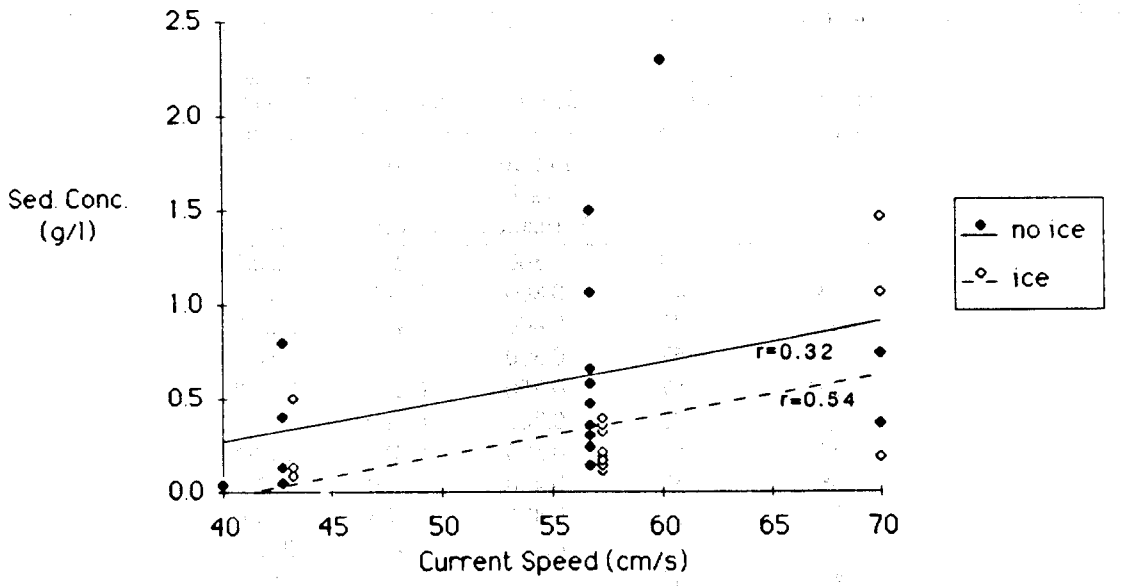

Figure 11. Graph of suspended sediment concentration versus current speed. At similar current speeds there generally are higher concentrations of suspended sediment in the water before the frazil ice starts forming than after.

When frazil flocs came to rest in the lee of migrating ripples, the resulting anchor ice commonly was buried by the advancing bedform. This burial occurred as sand avalanched down the slip face of the ripple (fig. 12). The normal motion of the avalanching sand was disrupted when it hit the the anchor ice. As the avalanching grains encountered anchor ice, they filled voids in the porous structure and cascaded down the outside of the anchor ice mass. The anchor ice was compressed by the weight of the sand, forming a compact mass of ice and ice-bonded sediment. This buried anchor ice sometimes acted as a surface for continued ice growth by frazil-crystal accretion above the sediment surface. The weight of the sediment on the buried anchor ice held the cleaner anchor ice above the sediment/water interface down, so the ice above the sediment had very little sediment incorporated into its structure. If the ripple continued to migrate past the buried anchor ice, the anchor ice was excavated on the stoss side as a single block of ice-bonded sediment. This ice-bonded sediment block acted as a single large grain in the flow. If currents were strong, they scoured depressions around the ice-bonded sediment block similar to scour depressions seen around pebbles in streams. If frazil ice was still in suspension when the ice-bonded sediment block was excavated, it would become attached to the anchor ice mass.

In the salt-water experiments, frazil ice normally did not stick to cobbles or other smooth obstructions in the flow. It did, however, stick readily to mineral specimens mounted on plexiglas bars in the flow. The first frazil usually was trapped at the intersection of the mineral specimen and the plexiglas bar. A rough surface texture

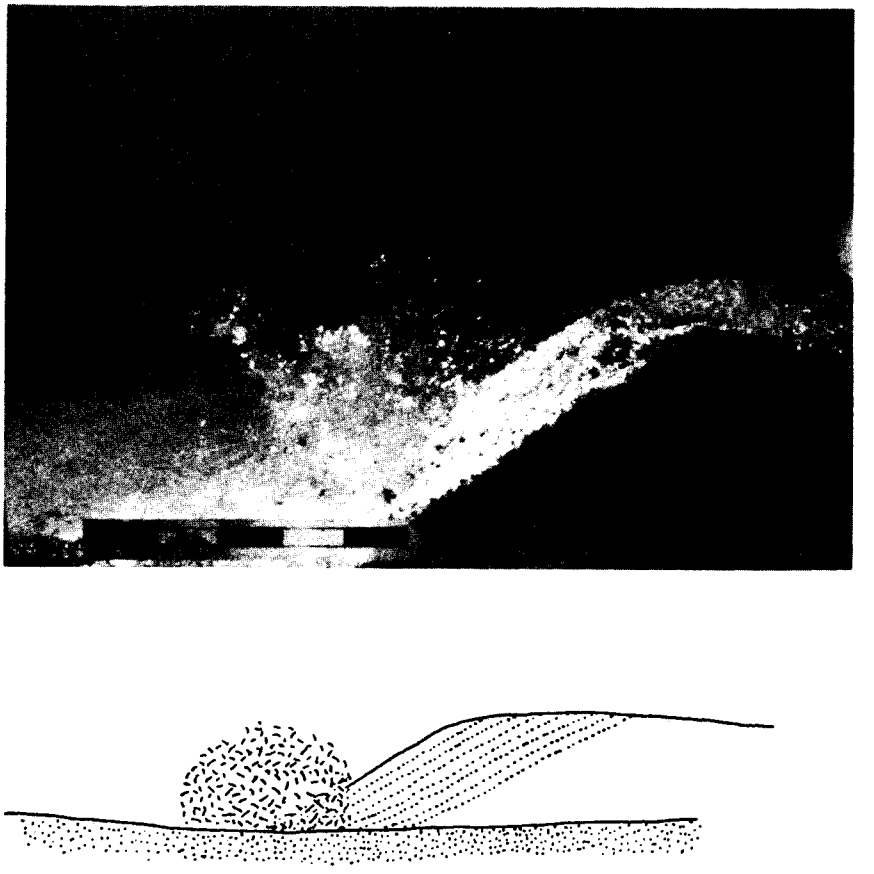

Figure 12. A) Anchor-ice mass composed of frazil ice crystals lying in the lee of a 3.5-cm-high ripple (Experiment 29). B) Such masses disrupt normal avalanching and generation of cross bedding in the lee of ripples.

apparently is necessary to trap frazil crystals in salt water. Once the first ice crystals were trapped, the anchor-ice mass grew rapidly by scavenging frazil crystals from the water column. Anchor ice rarely formed in the lee of ripples in salt water experiments, and in those cases where it did form it was less than 1 cm in diameter.

Since little anchor ice formed in the lee of ripples in salt water, three different approaches were used to simulate the ice-bonded sediment seen in diving traverses. First, in some experiments a 250-ml block of ice-bonded sediment was placed on the floor of the flume. Second, in some experiments a plastic bag filled with sand saturated with brackish (~14 ppt) water was placed on the floor of the flume (fig. 13). This bag was cut open when the water temperature approached T_m, exposing the sand within. The brackish water had a higher freezing point than the overlying water, so the sand inside the bag was ice bonded when the bag was removed. Finally, in some experiments 100 ml of brackish water was injected directly into bottom sediment

Table 4. Sediment concentrations in frazil and anchor ice samples.

Experiment Number	Current Speed (cm/s)	Sediment Conc. (g/l)	Sample Type	Water Salinity (ppt)
24	70	17.60	frazil/anchor ice	fresh*
26	70	42.80	frazil/anchor ice	fresh*
27	60	9.50	frazil ice	fresh*
29	43	0.94	frazil ice	fresh*
30	60	20.20	frazil ice	fresh*
37	57	3.70	frazil ice	fresh*
37	57	37.00	anchor ice	fresh*
38	57	0.02	frazil ice	29.14
39	57	0.10	frazil ice	29.14
39**	57	1.04	anchor ice	29.14
39**	70	3.39	anchor ice	29.14*
52**	42	88.30	anchor ice	36.95
52**	42	13.50	anchor ice	36.95
53	53	4.74	anchor ice	fresh*
54	42	31.25	anchor ice	fresh*

*Salinity was not determined in fresh-water experiments.
**Two anchor ice samples collected in this experiment.

before supercooling began. This was not a satisfactory method for producing ice-bonded sediment; in most cases the sediment with brackish water was either transported away or buried before frazil ice was produced.

Anchor ice formed on all ice-bonded sediment at low current speeds. At higher current speeds, there was not enough adhesion between frazil crystals and the ice-bonded sediment to form anchor ice. Of the 3 methods used to artificially produce ice-bonded sediment, the first approach was best at collecting anchor ice, probably because the block projected up into the supercooled flow. Often the anchor-ice masses that formed around the block were very similar to those observed along the diving traverses (fig. 14). In salt-water experiments, anchor ice formed more readily on ice-bonded sediment than on any other material used.

At the end of several experiments, in both fresh and salt water, the sediment incorporated into frazil and anchor ice was observed to rain out of the ice when the flow was stopped. If enough sediment dropped from an anchor-ice mass, it became positively buoyant and rose to the water surface. This indicates that most of the sediment in frazil and anchor ice is trapped in spaces between ice crystals, rather than

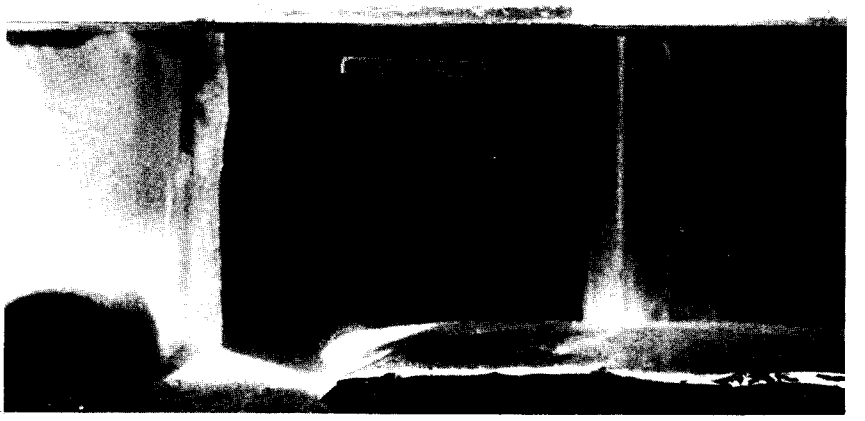

Figure 13. View of flume showing bag containing sand and brackish water (left) and a man-made block of ice-bonded sediment (right) used as a nucleus for growth of anchor ice.

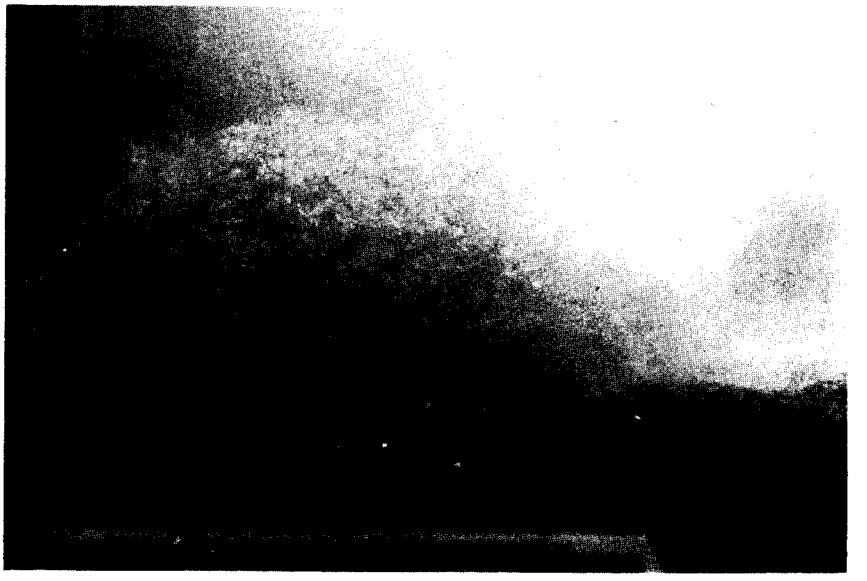

Figure 14. Salt-water anchor ice growing from the block of ice-bonded sediment shown in Figure 13. This anchor ice mass has a morphology that is very similar to the anchor ice masses observed on the diving traverses in the Beaufort Sea (figs. 5 and 6).

adhering to or being incorporated within the ice crystals.

Mineral Specimens, Frazil Ice, and Anchor Ice

Attempts were made to ascertain if anchor ice forms preferentially on certain materials. For this purpose samples of different materials, mostly mineral specimens (Table 1), were supported in the flow, either on metal rods or a plexiglas frame. In addition to the listed materials, in two fresh-water experiments a cobble with attached algae was placed in the flow, and in 2 salt-water experiments fronds of *Macrocystis* spp. (Giant Perennial Kelp) were placed in the flow to learn how frazil and anchor ice interact with aquatic plant material.

All samples except the *Macrocystis* collected anchor ice without notable selectivity. Anchor ice started growing first on samples closest to the water surface and on samples with rough surface textures. Usually the first frazil crystals were caught on rough minerals or at the intersection of a mineral sample and its support. After the first ice crystals were trapped, the anchor-ice mass grew quickly by addition of frazil-ice particles, until it filled all space between sample supports, and then continued to grow in an upstream direction. Figure 10 shows the mineral specimens and their support covered with a mass of anchor ice from salt water Experiment 43. Here the anchor-ice mass is about 5 cm thick up-current from the mineral specimens, it extends from one side of the flume to the other, and it is largest near the water surface. This is because the buoyant frazil-ice crystals are concentrated near the water surface.

Once anchor ice began forming on the mineral specimens and their supports, it trapped essentially all of the frazil. Anchor ice formed similarly on the mineral specimens in fresh and salt water. Regardless of water salinity, large masses of anchor ice formed on the minerals, materials, and their supports, except for the *Macrocystis*. Conversely, the fresh-water algae collected a great deal of anchor ice.

The above tests suggest that surface texture of an object probably is more important than composition or crystal structure for collecting anchor ice. Irregularly shaped objects with rough surfaces are best at accumulating anchor ice. The bond between anchor ice and the specimens in the flow was weak; when the supporting frame was disturbed or removed from the water the anchor ice broke free and was carried away by currents.

Special Runs

Cooling through the Flume Floor. In Experiment 37 an 11X18 cm area of the flume floor was cooled with dry ice to simulate cooling by permafrost. The dry ice was placed in contact with the aluminum floor of the tank. The sediment cover in the area underlain by dry ice was approximately 3 cm thick. The experiment was conducted in fresh water at a current speed of 57 cm/s. T_m, T_e, and T_e-T_m for this experiment were typical for fresh-water experiments (Table 2). No anchor ice or ice-bonded

sediment formed over the dry ice during the experiment, but several flocs of anchor ice did collect upstream in the lee of a migrating ripple. It appears that the sediment cover was thick enough to insulate the sediment at the sediment-water interface, so that the dry ice exerted no influence.

Addition of Dry Ice to Supercooled Water. Shaefer (1950) proposed seeding supercooled water with dry ice to initiate formation of a surface ice cover and reduce supercooling. The formation of a solid ice cover inhibits the formation of frazil ice (Shaefer, 1950). In Experiment 28 the water was seeded with approximately 200 g of pea-sized dry ice at the first appearance of frazil ice. A large amount of frazil ice formed as soon as the dry ice was added, but there was almost no reduction in water temperature (Table 2). Although the water temperature remained low, frazil ice that formed was not sticky, and no sediment-laden anchor-ice flocs formed. After the dry ice had sublimed, the water temperature began dropping until it eventually reached a temperature below the initial supercooling. High turbulence in the flume inhibited the formation of a solid ice cover even with the addition of dry ice.

Addition of Chilled Sand to Supercooled Water. During Experiment 34 (Table 2) approximately 80 g of dry sand at a temperature of -18°C was added to fresh water in the flume over a 10 minute period during frazil-ice formation. The purpose of adding cold sand was to simulate sediment blowing into a water body from surrounding land. The sand was sprinkled into the flow, and it was carried at least some distance down current before settling to the bottom. Sediment-laden anchor ice flocs formed during this experiment, but not in significantly greater quantity than in those experiments where no chilled sand was added to the flow. There was no correlation observed between the addition of sand and the formation of sediment-laden frazil or anchor ice.

In some cases, when the cold sand grains fell into the water a sheath of ice instantly formed around them. This ice increased the buoyancy of sand grains and kept them in suspension. Ice that formed around the sand grains was not frazil ice, but rather a solid coating of ice that conformed to the shape of the sand grain. This ice apparently formed because the sand grains were below the freezing point of the water.

Bubbling Cold Air into the Flume. Carstens (1966) suggested that bubbling air into a supercooled water column would supply the necessary turbulence to 'freeze out' any supercooling. To test this hypothesis, in Experiment 22 compressed air at -14°C was bubbled into the flume through a scuba regulator. The addition of compressed air did 'freeze out' the supercooling (Table 2), but in the process a large amount of sticky frazil and sediment-laden anchor ice was made. This is exactly what Carstens (1966) was trying to prevent. Apparently, introducing cold air directly into the water resulted in increased heat transfer from the water to the air, producing large amounts of frazil and anchor ice. Perhaps if warm air were bubbled into the supercooled water it would 'freeze out' the supercooling while not supplying another heat sink to increase the production of frazil ice.

DISCUSSION

Comparison of Frazil and Anchor Ice in Fresh and Salt Water

Several differences were observed between frazil- and anchor-ice formed in fresh and salt water. These differences include the morphology of the frazil flocs, freezing of the floating frazil into a solid ice cover, and the formation of anchor-ice masses. The size and shape of individual frazil-ice crystals, however, appear to be identical, regardless of salinity.

Most frazil crystals in the flume were in the shape of small, thin discs. In one salt-water experiment, hexagonally-shaped crystals were seen in addition to the more common discs and in several fresh-water experiments a few needle-shaped frazil crystals were observed. The disc-shape is apparently the most common form of frazil ice in both fresh and salt water, and has been reported by many authors. Martin and Kauffman (1981) saw disc-shaped frazil ice in a wave tank with salinities of 35.5 ppt. However, Hanley and Tsang (1984) reported that they never saw frazil-ice discs in their salt-water experiments. Instead, salt-water frazil ice formed whitish, waxlike crystals that "...grew three dimensionally by producing thin fingers and plates in different directions...". As Hanley and Tsang (1984) noted, systematic studies are needed to shed more light on the parameters that affect the frazil-ice crystal form.

Figure 8 suggests that, for a given cooling rate, salt water will reach a slightly greater degree of supercooling than fresh water, assuming that the value T_c-T_m is a close estimate of supercooling. However, the large amount of scatter at any given cooling rate makes the data somewhat ambiguous, and the effects of salinity on supercooling may be negligible.

The major differences observed between frazil and anchor ice formation in fresh and salt water are the ways in which flocs grow and react with bottom sediment. Relatively large flocs formed in fresh water. These large flocs either rose to the surface soon after forming or rolled along the bottom and collected large amounts of sediment. If a floc collected enough sediment, it settled into the lee of a bedform, forming anchor ice (fig. 12). No large frazil-ice flocs formed in salt water. Instead, small aggregates of two or more crystals formed. These aggregates appeared to be very similar in form to the three-dimensional crystals described by Hanley and Tsang (1984). Much less anchor ice formed on bottom sediment in the salt-water experiments than in the fresh-water experiments.

In fresh water, frazil-ice flocs rose to the surface shortly after forming and froze into a solid ice cover from the surface downward. Salt-water frazil ice tended to stay in suspension for long periods after it formed. Salt-water frazil probably stays in suspension more readily than fresh water frazil because it is easier to overcome the

buoyant forces on single crystals or small aggregates than it is to overcome the buoyancy of the large fresh-water frazil-ice flocs. Hanley and Tsang (1984) also noticed that salt-water frazil ice is much less likely to form large flocs or a solid ice cover than fresh-water frazil ice.

The amount of frazil ice that formed on the mineral specimens suspended in the flow was uniform, regardless of water salinity. Whenever the mineral specimens were placed in the flume they collected large masses of anchor ice, thereby nearly eliminating the frazil ice in the flow. The *Macrocystis* in salt water did not support any anchor ice growth, whereas the algae used in the fresh-water experiments collected large amounts of anchor ice. This suggests that anchor ice sticks more readily to aquatic plant material in fresh water than in salt water, although the ability of frazil ice to stick to plant material may be more a function of the particular plant material than the salinity of the water that the frazil ice formed in.

Many of the observed differences in fresh and salt water may be a function of whether different types of frazil are sticky. Carstens (1966) noted that fresh-water frazil is sticky or 'active' in supercooled water. This stickiness makes the formation of anchor ice much more likely and probably contributes to the growth of the large frazil-ice flocs in fresh water. In water that is not supercooled, frazil ice is 'passive' and has much less tendency to stick to submerged objects. The little work that has been done on salt-water frazil- and anchor-ice formation suggests that, even in supercooled water, salt-water frazil ice is not sticky (Hanley and Tsang, 1984). This lack of stickiness is explained by salt rejection from the ice as a frazil-ice crystal forms. This salt forms a thin layer of water with higher salinity and correspondingly lower freezing point around the frazil crystal, which in turn inhibits continued frazil ice growth and apparently also reduces the stickiness of the frazil crystal (Hanley and Tsang, 1984).

The apparent lack of stickiness of salt-water frazil ice could explain why no large flocs formed in the salt-water experiments and why less anchor ice formed. Salt rejection also may have inhibited the formation of a solid ice cover in the floating salt-water frazil ice. The conclusion that salt-water frazil ice is not sticky is the result of flume studies, and these studies may not accurately duplicate natural systems, because in a small flume there is a relativly large change in the water salinity as ice is formed. These large salinity changes don't occur in the ocean, where the ratio of frazil ice to water is much lower. It is possible that frazil ice in natural salt-water environments is sticky, in fact this is suggested by the formation of anchor ice in marine environments in both the Arctic and Antarctic. More studies of naturally occurring marine frazil and anchor ice are necessary to determine whether or not it really is sticky.

Frazil Ice, Anchor Ice, and Sediment Transport

One possible explanation for the observed reduction in suspended sediment concentration during periods of frazil formation (Table 3 and fig. 11) is that sticky frazil ice crystals in supercooled water scavenged sediment particles out of suspension, as

suggested by Osterkamp and Gosink (1984). Frazil ice tends to form flocs that are not uniformly distributed through the water column, and the sampling method used to measure suspended sediment concentration excluded large, sediment-rich flocs. Thus, although the amount of sediment in suspension may have been less, the total load carried in suspension and by frazil ice may have been equal to or greater than the amount carried in suspension before frazil ice formed. Another possible reason for a reduction in suspended sediment concentration during frazil formation is decreased turbulence in the water caused by the presence of frazil ice (Tsang, 1982). This decreased turbulence reduces the capacity of the flow. From the present experiments no conclusions can be drawn about which process led to the observed reduction in suspended sediment concentration during periods of frazil formation.

The high sediment concentrations measured in frazil ice compared to those in water (Tables 3 and 4) tend to support the idea that suspended sediment is scavenged by frazil ice. However, some of the sediment seen in the frazil ice clearly was incorporated into flocs as they bounced and rolled along the bottom. The same processes of flocs rolling along the bottom and picking up sediment have been described in rivers by Arden and Wigle (1972) and Osterkamp and Gosink (1974). Thus, there is some question wether scavenging occurs by the sticky action of the frazil ice, or wether it occurs by trapping of sediment particles at the interstices between ice crystals in flocs. More work is needed to determine if sediment inclusions in frazil ice occur within an individual ice crystal or just at the interstices between ice crystals. If sediment is trapped at the interstices between frazil-ice crystals, it is possible that 'stickiness' plays no part in sediment transport by ice.

The buoyant force of frazil and anchor ice has the potential to lift large amounts of sediment from the bottom and carry it away with the flow. The maximum amount of sediment a block of ice can carry is limited to the amount that brings the combined mass of the ice/sediment conglomeration to the mass of an equal volume of the surrounding water, that is

$$\rho_w V_{i+s} = \rho_s V_s + \rho_i V_i \qquad (1)$$

where ρ_w is the density of water (for these calculations, assumed to be pure water at 1.0 g/cm^3); ρ_s is the density of sedimentary particles (2.65 g/cm^3); ρ_i is the density of ice (0.92 g/cm^3); V_{i+s} is the volume of ice plus sediment in the neutrally-buoyant mass; V_s is the volume of sediment in the mass; and V_i is the volume of ice in the mass. V_{i+s} is composed of fractional volumes of sediment (f_s) and ice (f_i) such that

$$V_s = f_s V_{i+s} \qquad (2)$$

and

$$V_i = V_{i+s} - f_s V_{i+s} \qquad (3)$$

or

$$V_i = V_{i+s}(1-f_s). \tag{4}$$

Substituting the terms for V_s and V_i from equations (2) and (4) into equation (1) gives

$$\rho_w V_{i+s} = \rho_s f_s V_{i+s} + \rho_i V_{i+s} (1-f_s). \tag{5}$$

Both sides of the equation can be divided by the term 'V_{i+s}', leaving

$$\rho_w = \rho_s f_s + \rho_i - \rho_i f_s. \tag{6}$$

Substituting the numeric values of ρ_w, ρ_i and ρ_s into equation (6) leaves

$$1 = 2.65 f_s + 0.92 - 0.92 f_s. \tag{7}$$

Solving equation (7) for f_s yields

$$f_s = 4.6\% \tag{8}.$$

Thus, the volume of sediment in a neutrally buoyant ice/sediment block in fresh water is 4.6 percent of the total volume of the block. This value can be translated to the more common measure of weight of sediment per unit volume by considering a neutrally buoyant block that has a volume of 1 liter. The weight of this block would be 1000 g. The weight of sediment in the block will be equal to the volume of sediment times its density, or

$$\begin{aligned} V_s p_s &= 0.046(1000\ cm^3)(2.65\ g/cm^3) \\ &= 122\ g \end{aligned} \tag{9}$$

so the maximum sediment concentration that can be carried by a neutrally buoyant ice-sediment mass in fresh water is 122 g/l.

This value considers only the buoyant force of the ice, and does not account for increased surface area and current drag, which would add to the transport capacity of a turbulent flow. Also, salt water, with its greater density, is able to buoy up slightly more sediment per unit volume of ice.

Nearly all published values of sediment concentrations in naturally occurring frazil ice come from the Alaskan Beaufort Sea. Barnes et al. (1982) sampled sediment-laden fast ice and found maximum sediment concentrations of about 1.6 g/l. During a different year in the same area, Osterkamp and Gosink (1984) found maximum sediment concentrations of 1.3 g/l. In both of these studies, the frazil ice was sampled

after a solid ice cover had formed by freezing of the interstitial water of floating frazil ice. Martin and Kauffman (1981) found that, in a floating frazil-ice mass, the maximum concentration of frazil ice is about 44 percent of the total volume. The remaining volume is water filling the voids between frazil crystals. If one assumes that all of the sediment measured by Barnes et al. (1982) and Osterkamp and Gosink (1984) was trapped in the frazil ice and none in the interstitial water, the sediment concentration in the frazil ice is calculated to be around 3 g/l. This value is about 2 orders of magnitude below the theoretical limit of 122 g/l.

In the flume, sediment concentrations in the frazil ice measured as high as 20.2 g/l, although most of the values fell below 3.7 g/l (Table 4). These lower values are in the same range as those seen in natural settings. Table 4 also lists the values of sediment concentrations in anchor ice. These values also fall well below the calculated maximum sediment concentration that an ice mass can carry, so the buoyancy of the ice should have lifted the anchor ice off the bottom. However, only the upper portion of anchor ice masses were collected to prevent contamination by bottom sediment. As discussed earlier, the excluded bottom portion of anchor ice commonly was buried by advancing ripples, so the listed values of sediment in the anchor ice probably are too low. Some water is retained in the interstitial spaces of ice samples that were collected to determine sediment concentrations (Tsang, 1982). This water results in slightly low values for the amount of sediment actually carried by frazil and anchor ice.

The literature contains numerous examples of anchor ice with large (but unmeasured) amounts of entrained sediment being released from the bottom and carried away by currents (Zubov, 1943; Dayton et al, 1969; Wigle, 1970; Arden and Wigle, 1972; Gilfilian et al., 1972; Osterkamp and Gosink, 1974; Martin, 1981, Tsang, 1982). Anchor ice is released from the bottom when the water is no longer supercooled and geothermal heat warms the bottom side of the anchor ice. In rivers, this sediment-laden anchor ice commonly rises to the surface and is carried downstream by currents (Arden and Wigle, 1973; Wigle, 1970). These anchor-ice masses can move boulders weighing up to 30 kg (Martin, 1981). Apparently not all of the released anchor ice rises to the surface. Gilfilian et al. (1972) and Osterkamp and Gosink (1983) reported that anchor ice sometimes is seen traveling just below the base of a solid ice cover or bouncing along the bottom in streams. As noted by Martin (1981), anchor ice and frazil ice increase the competence of streams, and observations by other workers and this study suggest that they also can increase stream capacity. Unfortunately, there are no published values for the amount of sediment transported by frazil or anchor ice in streams and rivers, or any estimates of the amount of sediment moved by ice compared to the total annual sediment load of a river. Both of these questions deserve further study, first to see if sediment concentrations in ice in natural systems approach the theoretical maximum of 122 g/l, and also to determine the significance of frazil and anchor ice as sediment transport agents.

Observations of Anchor Ice

Although there are numerous published observations of anchor ice resting on bottom sediment, or picking up and moving bottom sediment, there is little information on how anchor ice could affect primary sedimentary structures. If evidence of anchor ice is preserved in the sedimentary record, it could be an important paleo-environmental indicator. Reineck and Singh (1980) reported that ice-crystal imprints can be observed in bedding planes in both modern and ancient sediment. These imprints were thought to form mainly under subaerial conditions, but the present findings suggest that they also can form in subaqueous environments.

The flume experiments show that anchor ice can be deposited in the lee of migrating bedforms and become buried (fig. 12). Burial of anchor ice masses results in disruption of normal avalanching on the slip face and disrupts ripple cross-bedding. Unstable sediment precluded determining whether any sedimentary structures were formed by these processes. At the very least, melting of buried anchor ice masses should result in collapse and disruption of any structures in overlying sediment, in addition to any localized disruption of cross-bedding caused by sediment avalanching onto the anchor ice mass. Such disruption features might be hard to distinguish from features caused by other processes like bioturbation or ice gouging. It also is probable that the faint striations caused by frazil ice flocs sweeping up the back side of ripples could be preserved under favorable conditions. However, it would be difficult to distinguish these striations from similar marks formed by other tools.

Anchor ice masses buried by advancing ripples are infiltrated by large amounts of sediment and then compacted. If ripples migrate past the buried anchor ice mass, the sediment-rich block is excavated and exposed to overlying water once again. This is one possible mode of formation of the sediment-rich cores seen in anchor ice clumps on the diving traverse off Reindeer Island and shown in figures 4 and 5. This process also would explain the 20 percent excess water by volume found when the cores were melted and the sediment was allowed to settle. When similar ice-bonded sediment blocks were placed in the flume in salt-water experiments, they collected halos of delicate crystals that are similar to the anchor ice clumps seen along the diving traverse (fig. 14).

Reimnitz et al. (1986) present another hypothesis to explain the presence of the sediment-rich ice bonded cores seen in the anchor ice masses off Reindeer Island, and also to explain the ice-bonded sediment seen during the diving traverses off the West Dock and Reindeer Island. In the summer, ice melt and river discharge reduce the salinity of nearshore water, and of interstitial water in nearshore sediment. During freezeup, water output from rivers is low, and water of higher salinity moves from offshore into shallow-water areas. This higher-salinity water has a lower freezing point than the interstitial water. During storms, the high-salinity water is cooled to below the freezing point of the less saline interstitial water, and it supplies a heat sink for freezing of the interstitial water. This theory explains the large areas of frozen

sediment seen near the beach off Reindeer Island and the West Dock, but it does not adequately explain the presence of sediment-rich ice-bonded blocks surrounded by unbonded sediment like those observed in deeper water off Reindeer Island. This method of formation also does not account for the excess water observed in the cores after melting. One possible method of producing blocks from a large area of ice-bonded sediment is to break up the large area of ice-bonded sediment by wave and pack-ice activity during storms and transport the smaller blocks to quiet spots in troughs between offshore bars. In the dying stages of a storm, frazil ice crystals could be plated onto the ice-bonded sediment core, forming the open, delicate crystal structure observed in the anchor ice clumps off Reindeer Island.

There is no information on how long anchor ice lasts in the Beaufort Sea. Prior to 1982, we had never observed anchor ice in the Beaufort Sea, although we have made over 100 research dives in a variety of settings and seasons. In addition, we have talked to other researchers and consultants who have made numerous winter dives in the Beaufort Sea, but have not observed anchor ice. However, none of these winter dives were made earlier than middle to late November, and any anchor ice that had formed could have already disappeared. Observations from the Antarctic, in McMurdo Sound (Dayton et al., 1969) suggest that anchor ice has a short life span of only two weeks. Similarly, in the Niagara River anchor ice usually rises to the surface a few hours after it forms (Arden and Wigle, 1972). The release of anchor ice from the bottom is caused by a rise in the surrounding water temperature. Anchor ice in the Beaufort Sea probably lasts no longer than that in McMurdo Sound, but observations will have to be made in the period immediately following freezeup to determine its actual life span. It is important to note that the absence of anchor ice in late winter does not necessarily mean that no anchor ice formed during the freezeup.

Both of the above methods may play a part in forming the sediment-rich cores of the anchor-ice masses observed off Reindeer Island, and careful study is needed to determine the exact nature of formation of both the sediment-rich core and the delicate outer crystal array. Unfortunately, gathering information on the mode of formation of anchor ice is difficult because it involves working in a very harsh environment.

Regardless of the method of formation of the ice-bonded sediment and anchor ice seen in the Alaskan Beaufort Sea, these sediment-rich ice blocks obviously are moved by waves and currents. It is common to see such blocks thrown up onto beaches by storms during freezeup, and often in the summer plaques of fine-grained sediment in a coarser grained matrix are found on seaward-facing beaches (fig. 15). These ice-bonded blocks and sand plaques in a coarse matrix are evidence that ice-bonded sediment is transported onto beaches during freezeup. It also is possible that such material is transported offshore, especially if the ice-bonded blocks contain enough ice to significantly increase their buoyancy. This could be an important sediment transport mechanism in shallow-water shelf areas where anchor ice forms.

Anchor-ice formation and ice-bonding of sediment affects the sedimentary regime in rivers and oceans by armoring the bottom. Armoring of the bottom reduces the ability of waves and currents to move sediment, but the effects of armoring the bottom

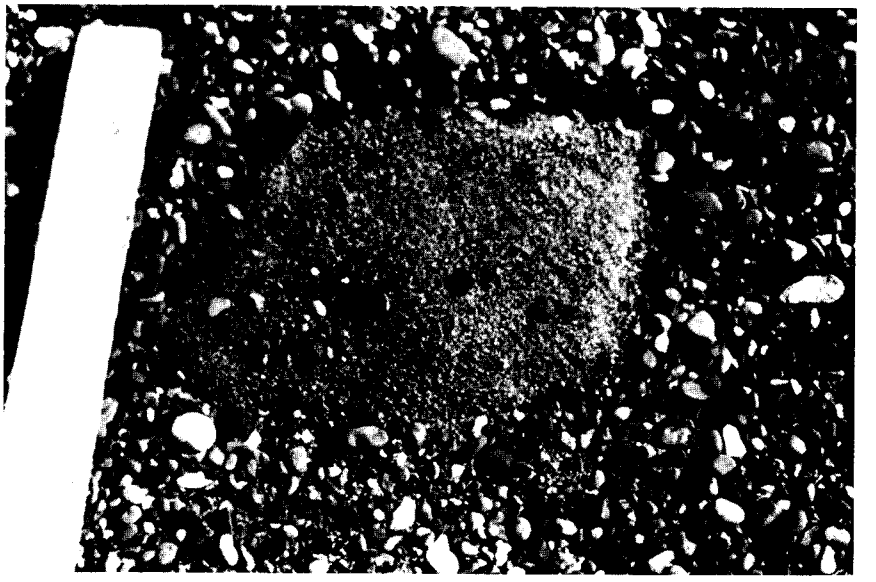

Figure 15. A small plaque of sand in a gravel matrix on a seaward-facing barrier-island beach in the Beaufort Sea. This plaque was transported and deposited as anchor ice during a fall storm. Such plaques are common on seaward-facing beaches. Wood in left corner is 5 cm across.

during a dynamic event are only a matter of speculation. Anchor ice can form along the entire length of the Niagara River, regardless of water depth or velocity (Arden and Wigle, 1972). In this situation, the presence of anchor ice may result in a significant reduction in suspended sediment load. However, this reduction in suspended sediment load would last only a few hours, since the anchor ice usually forms at night and is released from the bottom on the following day (Arden and Wigle, 1972). Along the West Dock diving traverse in the Beaufort Sea, up to 75 percent of the bottom was ice bonded. On the Reindeer Island traverse there was considerably less ice bonding. This ice bonding occurred during a major fall storm, a period of major sediment reworking on the shelf. The presence of ice bonding and anchor ice might have played a major role in armoring the bottom from storm waves at this time, but the distribution of anchor ice and ice bonding is not known so it is impossible to evaluate its significance.

In addition to armoring the bottom, the formation of anchor ice can reduce the amount of water carried by rivers, as discussed earlier. This flow reduction should result in a net reduction of suspended sediment transport. However, these losses may be balanced by possible increased sediment transport caused by frazil ice and anchor ice lifting and carrying bottom sediment because of their buoyant forces. Thus, the net result of frazil and anchor ice formation on sediment transport in rivers and oceans is unknown, and systematic studies of the interactions of sediment with frazil and anchor ice in both fresh and saline water are needed.

CONCLUSIONS

The field observations and flume studies presented in this report indicate that frazil and anchor ice are important geologic agents. The main findings of this report include:

(1) Anchor ice and ice-bonded sediment form on the shallow shelf of the Alaskan Beaufort Sea during cold storms associated with freezeup. Anchor ice consists of mounds of delicate ice crystals attached to ice-bonded sand and gravel seafloor, tires, and steel banding. The regional extent of anchor ice and ice bonding is not known, but along the diving traverses up to 75 percent of the sea floor was ice bonded. Ice bonding was observed in gravel, sand and mud substrates, with an apparent inverse correlation between sediment grain size and depth of ice bonding.

(2) Flume experiments show that frazil ice forms readily in both fresh and salt water. Frazil ice crystals have the same morphology in fresh and salt water, usually forming thin discs up to 5 mm in diameter. However, the morphology of frazil-ice flocs and the way frazil ice interacts with sediment varies with salinity. Fresh-water frazil flocs are larger and more cohesive than salt-water flocs, and individual ice crystals have a random orientation. Salt-water flocs are tabular masses with the flat sides of individual crystals in contact with each other. Dendritic arms, composed of individual frazil crystals, sometimes grow out from the main tabular body. Frazil-ice flocs in fresh water are more likely to collect sediment than salt-water flocs, and they freeze into a solid ice cover more rapidly.

(3) In the flume, anchor ice forms more readily in fresh water than in salt water. Anchor ice forms from frazil ice, either when frazil flocs stick to the up-current side of projections in the flow or when frazil-ice flocs come to rest in the lee of ripples.

(4) Anchor ice forming in the lee of ripples commonly is buried by migrating bedforms. As the anchor ice is buried, it is compressed and sediment is incorporated into its structure, forming an ice-bonded sediment block similar to those seen in the Beaufort Sea. These ice-bonded sediments may be the site of later anchor-ice growth by accretion of frazil ice. When ice-bonded sediment blocks were placed in the flume during salt-water experiments, they formed anchor-ice masses that were very similar in appearance to the anchor ice seen in the Beaufort Sea.

(5) Burial of anchor ice results in disruption of normal ripple cross-bedding and may result in unique primary sedimentary structures. The form of any sedimentary structures produced by frazil and anchor ice was not determined in this study.

(6) Experiments performed to test if anchor ice forms preferentially on specific materials show that a rough surface texture is more important than material type for initial formation of anchor ice. Anchor ice forms on all of the materials tested except for *Macrocystis* spp., a marine alga.

(7) Analysis of flume data suggests that the suspended sediment load decreases during periods of frazil formation. However, the scatter in the data makes this conclusion somewhat tentative. More measurements of suspended sediment concentrations before and during frazil ice formation should be gathered from natural settings.

(8) Frazil ice and anchor ice are able to lift bed sediment with their buoyancy. Calculations show that ice is able to lift up to 122 g of sediment per liter of ice/sediment mixture by buoyant force alone. Sediment concentrations of this magnitude have never been observed, but there are very few measurements of sediment concentrations in frazil and anchor ice. The sediment carried by frazil and anchor ice offsets the reduction in suspended sediment in the water column. Thus, the net effect of frazil and anchor ice on sediment transport is unknown, but the scanty data suggest that frazil and anchor ice increase the capacity and competence of streams and ocean currents.

Many questions remain about frazil and anchor ice as geologic agents. These questions may be difficult to resolve with flume studies, because the short periods of supercooling and the small amounts of water, sediment, and ice in flumes make extrapolation of flume results to larger natural systems difficult. Problems that need to be examined in more detail include: (1) What is the geographic extent of anchor ice and ice bonding in the sea, and what are the life spans of these phenomena? (2) How important is sediment transport by frazil and anchor ice in natural environments? To study this question, sediment budgets of fluvial and marine systems where frazil and anchor ice form should be determined, and the amount of sediment moved by ice should be compared to the total sediment load. (3) Does frazil ice in natural settings carry anywhere near the calculated amount of 122 g/l of sediment? Samples of sediment-laden frazil and anchor ice should be collected from a number of river and marine settings to get a better understanding of how much sediment these types of ice actually carry. (4) What causes the differences observed in fresh- and salt-water frazil and anchor ice? If these differences are caused by salinity, is there some critical value at which the behavior of the ice changes? (5) Are unique sedimentary structures formed by frazil and anchor ice? The present study suggests that sedimentary structures are formed, but these structures have not been described. If unique sedimetary structures are formed by frazil and anchor ice, they would be important paleoenvironmental indicators.

Frazil and anchor ice can form wherever there is turbulent, supercooled water. The surface waters of 48 percent of the rivers and lakes in the Northern Hemisphere freeze annually (Encyclopedia Britannica, 1981), and 25 percent of the world's continental shelf areas less than 200 m deep have an ice cover for part of each year

(Barnes and Reimnitz, 1974). Under suitable conditions frazil ice and anchor ice can form in any of these waters. Thus, the area of subaqueous sediment potentially affected by frazil and anchor ice is very large. Until now, the role of anchor ice and frazil ice as geologic agents has received little attention, probably because of the difficult weather conditions that must be worked under to study these phenomena. More work is needed to define the extent of their influence.

REFERENCES CITED

Altberg, V. IA., 1938, On centers or nuclei of water crystallization: Bulletin Meteorologiia i Gidrologiia, no. 3, p. 3-12. U.S. Army Corps of Engineers, Cold Regions Research and Engineering Laboratory Draft Translation 294, January 1972, Hanover, NH.

Arden, R.S. and Wigle, T.S., 1972, Dynamics of ice formation in the upper Niagara River, *in* International Symposium on the Role of Snow and Ice in Hydrology: Banff, Alberta, United Nations Educational, Scientific and Cultural Organization/World Meteorological Association/International Association of Hydrological Sciences, v. 2, p. 1296-1313.

Barnes, H.T., 1928, Ice Engineering: Montreal, Renouf Publishing Company.

Barnes, P.W., and Reimnitz, Erk, 1974, Sedimentary processes on arctic shelves off the northern coast of Alaska, *in* Reed, J.C., and Sater, J.E., eds., The Coast and Shelf of the Beaufort Sea; Proceedings of the Arctic Institute of North America Symposium on Beaufort Sea Coast and Shelf Research: Arlington, VA, p. 439-476.

Barnes, P.W., Reimnitz, Erk, and Fox, Dennis, 1982, Ice rafting of fine grained sediment, a sorting and transport mechanism, Beaufort Sea, Alaska: Journal of Sedimentary Petrology, v. 52, p. 493-502.

Benedicks, Carl and Sederholm, Per, 1943, Regarding the formation of anchor (ground) ice: Arkiv for Matematik, Astronomi, och Fysik, v. 29, no. 22, p. 1-7.

Benson, C.S. and Osterkamp, T.E., 1974, Underwater ice formation in rivers as a vehicle for sediment transport, *in* Oceanography of the Bering Sea: Institute of Marine Science, University of Alaska, Fairbanks, p. 401-402.

Carstens, Torkild, 1966, Experiments with supercooling and ice formation in supercooled water: Geofysiske Publikasjoner, v. XXVI, no. 9, p. 1-18.

Curtsinger, Bill, 1986, Under Antarctic ice: National Geographic, v. 169, no. 4, p. 497-511.

Dayton, P.K., Robilliard, G.A., and DeVries, A.L., 1969, Anchor ice formation in McMurdo Sound, Antarctica, and its biological effects: Science, v. 163, p. 273-274.

Encyclopedia Britannica, 1981, Ice in rivers and lakes: Encyclopedia Britannica, Inc., Chicago, v. 9, p. 165-170.

Foulds, D.M. and Wigle, T.E., 1977, Frazil- the invisible strangler: Journal American Water Works Association, v. April, p. 196-199,

Gilfilian, R.E., Kline, W.L., Osterkamp, T.E., and Benson, C.S., 1972, Ice formation in a small Alaskan stream, *in* The Roll of Snow and Ice in Hydrology, Proceedings of the Banff Symposia, Sept. 1972, United Nations Educational, Scientific and Cultural Organization/World Meteorological Association/International Association of Hydrological Sciences, p. 505-513.

Hanley, T. O'D. and Tsang, Gee, 1984, Formation and properties of frazil in saline water: Cold Regions Science and Technology, v. 8, , p. 209-221.

Kivisild, H.R., 1970, River and lake ice terminology, *in* Proceedings of International Association for Hydraulic Research Symposium on Ice and Its Action on Hydraulic Structures, Iceland, Paper 1.0, 14 p.

Lewis, E.L., 1980, The practical salinity scale, 1978, and its antecedents: IEEE Journal of Ocean Engineering, v. OE5, no. 1, p. 3-16.

Martin, Seelye, 1981, Frazil ice in rivers and oceans: Annual Review of Fluid Mechanics, v. 13, p. 379-397.

Martin, Seelye and Kauffman, Peter, 1981, A field and laboratory study of wave damping by grease ice: Journal of Glaciology, v. 27, no. 96, p. 283-313.

Michel, Bernard, 1972, Properties and processes of river and lake ice, *in* The Role of Ice and Snow in Hydrology: International Association for Scientific Hydrology Publication No. 107, v. 1, p. 454-481.

Millero, F.J., 1977, Freezing point of seawater, *in* Eighth report of the joint panel on oceanographic tables and standards, Woods Hole, United States of America, 23-25 May 1977: United Nations Educational, Scientific and Cultural Organization, technical papers in marine science #28, p. 29-35.

Osterkamp, T.E., 1978, Frazil ice formation: a review: Journal of the Hydraulics Division, American Society of Civil Engineers, v. 104, no. HY9, p. 1239-1255.

Osterkamp, T.E. and Gosink, J.P., 1983, Frazil ice formation and ice cover development in interior Alaska streams: Cold Regions Science and Technology, v. 8, p. 43-56.

Osterkamp, T.E. and Gosink, J.P., 1984, Observations and analysis of sediment laden sea ice, *in* The Alaska Beaufort Sea: Ecosystem and Environment: Academic Press, San Francisco, CA, p. 73-94.

Piotrovich, P.P., 1956, Formation of depth-ice: Priroda, v. 9, p. 94-95.

Reimnitz, Erk, and Barnes, P.W., 1974, Sea ice as a geologic agent on the Beaufort Sea shelf of Alaska, *in* Reed, J.C., and Sater, J.E., eds., The Coast and Shelf of the Beaufort Sea; Proceedings of the Arctic Institute of North America Symposium on Beaufort Sea Coast and Shelf Research: Arlington, VA, p. 301-353.

Reimnitz, Erk, and Maurer, D.K., 1979, Effects of storm surges on the Beaufort Sea coast, Northern Alaska: Arctic, v. 32, p. 329-344.

Reimnitz, Erk, Kempema, E.W., and Barnes, P.W., (1986), Anchor ice and bottom freezing in high-latitude marine sedimentary environments: observations from the Alaskan Beaufort Sea: U.S. Geological Survey Open-File Report 86-298, 17 p.

Reineck, H.E. and Singh, I.B., 1980, Depositional sedimentary environments: Berlin, Springer-Verlag, 549 p.

Rudolfo, K.S., 1970, Annual suspended sediment supplied to the California continental borderland by the southern California watershed: Journal of Sedimentary Petrology, v. 40, p. 666-671.

Schaefer, V.J., 1950, The formation of frazil and anchor ice in cold water: Transactions, American Geophysical Union, v. 31, p. 885-893.

Tsang, Gee, 1982, Frazil and anchor ice: a monograph: National Research Council Subcommittee on Hydraulics of Ice Covered Rivers, Ottawa, Ontario, Canada, 90 p.

Tsang, Gee and Hanley, T. O'D., 1985, Frazil formation in water of different salinities and supercoolings: Journal of Glaciology, v. 31, p. 74-85.

Wigle, T.E., 1970, Investigations into frazil, bottom ice, and surface ice formation in the Niagara River, *in* Proceedings of the Symposium on Ice and Its Action on Hydraulic Structures: Reykjavik, Iceland, International Association for Hydraulic Research, Paper no. 2.8, 16 p.

World Meteorological Organization, 1970, WMO Sea-Ice Nomenclature, Codes, and Illustrated Glossary, Report 259, TP.145, Geneva, 147 p.

Zubov, N.N., 1943, Arctic Ice: Translated by Naval Oceanographic Office and American Meteorological Society under contract to Air Force Cambridge Research Center, 1963, U.S. Naval Electronics Laboratory, San Diego, CA, 491 p.

FIELD OBSERVATIONS ON SLUSH ICE GENERATED DURING FREEZEUP IN ARCTIC COASTAL WATERS

by

Erk Reimnitz and E. W. Kempema

U.S. Geological Survey
Menlo Park, California 94025

Final Report
Outer Continental Shelf Environmental Assessment Program
Research Unit 205

1986

ACKNOWLEDGMENTS

This study was funded in part by the Minerals Management Service, Department of the Interior, through interagency agreement with the National Oceanic and Atmospheric Administration, Department of Commerce, as part of the Alaska Outer Continental Shelf Environmental Assessment Program. Without this long term support and encouragement of our field program, the observations incorporated into this study could not have been made.

Moira Dunbar pointed out problems with our usage of ice terminology, and George Moore's critical review greatly improved the paper. We thank them for their help. We are very grateful to Ken Dunton, who freely shared with us logistics for winter field operations and his own numerous independent observations. Finally, we thank Peter Barnes for many discussions of the topic.

ABSTRACT

In some years, large volumes of slush ice charged with sediment are generated from frazil ice in the shallow Beaufort Sea during strong storms at the time of freezeup. Such events terminate the navigation season, and because of accompanying hostile conditions, very little is known about the processes acting. The water-saturated slush ice, which may reach a thickness of 4 m, exists for only a few days before freezing from the surface downward arrests further wave motion or pancake ice forms. Movement of small vessels and divers in the slush ice is accomplished only in phase with passing waves, producing compression and rarefaction, and internal pressure pulses. Where in contact with the seafloor, the agitated slush ice moves cobble-size material, generates large sediment ripples, and may possibly produce a benchlike feature occasionally observed on the Arctic shoreface. Processes charging the slush ice with as much as 1000 m^3/km^2 of sediment remain uncertain, but our field observations rule out previously proposed filtration from turbid waters as a likely mechanism. Sedimentary particles apparently are only trapped in the interstices of the slush ice rather than being held by adhesion, since wave-related internal pressure oscillations result in downward particle movement and cleansing of the slush ice. This loss of sediment explains the typical downward increase in sediment concentration in that part of the fast ice canopy composed largely of frazil ice. The congealing slush ice in coastal water does not become fast ice until grounded ridges are formed in the stamukhi zone, one to two months after freezeup begins. During this period of new-ice mobility, long-range sediment transport occurs. The sediment load held by the fast ice canopy in the area between the Colville and Sagavanirktok River deltas in the winter of 1978-79 was 16 times larger than the yearly river input to the same area. This sediment most likely was rafted from Canada, more than 400 km to the east, during a brief time period in the previous fall. Ocean turbulence is greatly reduced while the congealing slush ice drifts about. Therefore, new ice then forming in intervening open-water areas is clean. These events explain the patchy appearance of the fast ice after the summer snowmelt. More work on the important phenomena reported here is needed to close a major gap in the knowledge of the Arctic marine environment.

TABLE OF CONTENTS

INTRODUCTION

The short period when a new ice canopy forms may be geologically the most important time of the year in arctic seas. At this time processes are intensely dynamic, and the ice cover that forms influences the environment most of the following year. Freezing fall storms remove heat from the water and in a very short time may generate large amounts of frazil ice that rises and is incorporated into the new ice canopy, thereby speeding up its formation. The ice canopy initially is a slush composed of ice grains and water. This slush often contains entrained sediment, and in glossaries is called grease ice, ice gruel, frazil slush, sludge, slob, lolly ice, cream ice, new ice, and shuga (for example, U.S. Navy Hydrologic Office, 1952; World Meteorological Organization, 1970; Bates and Jackson, 1980). The distinctions (if any) between all these terms are subtle and appear unclear to us. In our own work we therefore initially followed the recent usage by Martin and Kaufmann (1981), where the term grease ice was applied to accumulations of granular, water-saturated ice of any thickness. A reviewer, however, pointed out that the usage intended for the term was for the soupy layer formed from the first frazil ice rising to the surface and giving the sea a greasy or matte appearance. Since there is no satisfactory, generally accepted term among those listed above we here use the descriptive phrase "slush ice" to denote a water-saturated, internally mobile surface layer of granular (not restricted to frazil) ice that may vary in thickness from a few centimeters to several meters. The thicker accumulations described later clearly are not greasy.

Marine research traditionally is done either in the summer open-water season with standard oceanographic techniques or from the winter ice canopy once it is firmly established. For this reason, almost nothing is known about processes that occur during the transition period from the navigation season to that of winter ice travel. During the past 15 years of arctic marine research, we have witnessed this transition several times, at first involuntarily and later deliberately. Such experiences led us to read accounts by early explorers in search of descriptions of the unique properties and behavior of slush ice. In this report we repeat some of those observations on how the sea virtually turns to "applesauce" and document some of our own reconnaissance observations made during freezeup. We believe that huge volumes of sediment move during such sporadic events, and that the bottom is reshaped by slush ice in very shallow water. Because processes during the period are important geologically, we review here sparse information that may shed light on them, but this work can be considered no more than a small step toward the basic knowledge on the topic needed for the rapid offshore development in the Arctic.

BACKGROUND INFORMATION

During an open-water storm with freezing air temperatures, frazil-ice crystals 1 to 5 mm in diameter may form throughout the upper mixed layer of the turbulent, slightly supercooled sea (Martin, 1981). On the surface, the frazil ice, sometimes mixed with snow, is aligned in long wind-parallel plumes (fig. 1) marking secondary (Langmuir) circulation patterns (Martin and Kauffman, 1981). The equivalent of as much as 2 m of ice can be produced at a site within a 20-hour period, as long as enough open water remains between plumes for heat transfer to the atmosphere (Weeks and Ackley, 1982). Frazil ice under the influence of strong winds moves across polynyas, and at the downwind end of these may be swept underneath solid ice sheets in accumulations more than 4 m thick (Bauer and Martin, 1983). When the wind subsides, all frazil ice, sometimes along with dislodged anchor ice, rises to the surface where it may mix with snow and form a layer of slush ice. Surface circulation may drive this slush ice into lagoons, embayments, and against flow obstacles (fig. 2), where thicknesses of 4

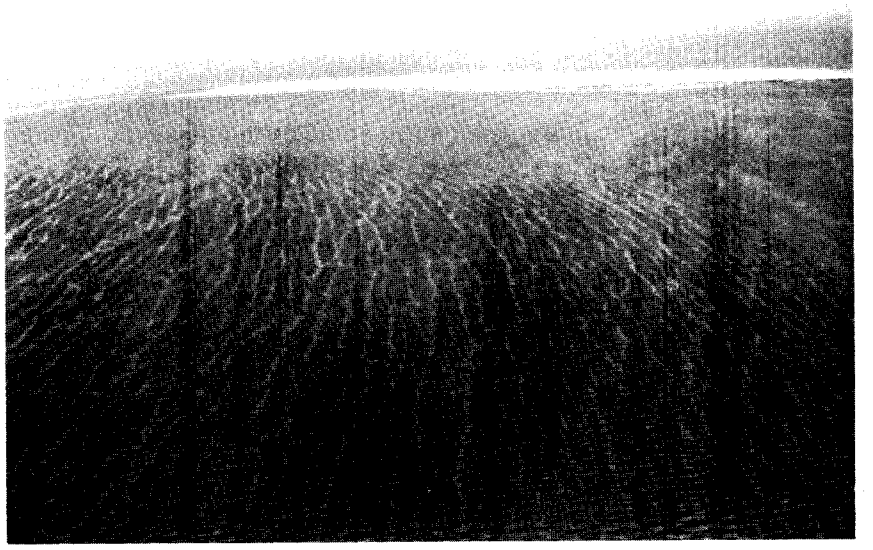

Figure 1. Wind-parallel streaks of newly forming slush ice marking secondary circulation patterns within a 2-m-deep lagoon.

Figure 2. Accumulation of slush ice herded by wind and waves against a snow-covered beach. The white bands in the ice, oblique to the beach, mark advancing wave fronts where slush ice is compressed and the ice surface dry.

m and greater have been reported (Collinson, 1889; Morecki, 1965; Reimnitz and Dunton, 1979). The only study of the physical properties of the slush ice in a wave field is that by Martin and Kauffman (1981), who conducted experiments in a tank. They found that waves in the tank are damped within 4 to 6 wavelengths of travel through the slush ice. The slush ice is a non-Newtonian fluid, behaving as a solid at low shear rates, where sintering between ice crystals becomes effective and as a fluid at high shear rates.

When large volumes of frazil ice are produced on the shallow Beaufort Sea shelf by freezeup storms, the resulting slush ice is enriched with fine-grained sediments by unknown mechanisms (Barnes et al., 1982; Osterkamp and Gosink, 1984). Osterkamp and Gosink (1984) discussed nine possible mechanisms that might result in the observed high sediment loads carried by ice over that of open-water suspended-sediment loads. Our field observations shed some light on several of the proposed mechanisms. Whatever the sedimentary particle-entrainment mechanism, sediment is later exposed by summer melting of snow and upper-ice layers and consequently reveals the extent of slush ice during the previous fall. This is shown in Figure 3, a computer-enhanced Landsat image. Melting of the seasonal fast-ice canopy was aided by reduced albedo resulting from sediment inclusions, which have highest concentrations in shallow coastal waters. The water beneath this turbid ice canopy is in total darkness even on sunny spring days, thereby restricting primary biological productivity to a few summer months (Dunton et al., 1982).

SLUSH ICE OBSERVATIONS

Sailing-Ship Observations

An older glossary of ice terminology (U.S. Navy Hydrographic Office, 1952) listed "slob" as a dense form of sludge, originally defined as being so dense as to impede the progress of sealing vessels. The scientific literature has not previously discussed the properties and behavior of slush ice in nature, as far as we know. An informative encounter with such slush ice, however, is described in the journal of *H.M.S. Enterprise* (Collinson, 1889, p. 239). In late September 1852, the *Enterprise* sailed toward Cambridge Bay in the Canadian Arctic. During the night of September 24, the temperature fell to -11 °C with the onset of a northerly gale that lasted through the 27th. Collinson feared the bay would get choked with "bay ice." The vessel ran aground on the 28th, surrounded by water depths of 3 to 5 m, while the gale was subsiding. The wind was still strong when Collinson recounted: "the sludge was so thick that we had great difficulty in laying out our stream anchor" (a light bow anchor). The ship's sailing cutters were used to transfer winter stores and gear to shore. On the 29th, "the sludge rendered the communication with the shore very precarious, the boats sometimes being within half a cable's length of the ship, and not getting on board for an hour. The cutter in one instance remained stationary half an hour, although there was as much wind as the mast would stand." After four days (October 2), the ice was firm enough to walk to shore. On October 3, "the sludge about the ship was 10 to 12 ft [3-4 m] deep; and such was its consistency that immediately after a block of ice was cut out and removed, the hole filled, and having exactly the same appearance as the firm ice, many of the men fell in." In May of the following year, the ice thickness was 8 ft 2 in [2.5 m] around the vessel.

A quite similar experience is told in "Captain Bob Bartlett's briny boast: Shipwrecked fourteen times" (Bartlett, 1927). In early March, the sailing ship *Leopard* was on a seal hunt in foul weather with slush ice forming along the rocky Labrador coast. "This ice had formed a sludge, fathoms deep, so that we couldn't even use our hand lead." At midnight, "it began to

Fig. 3. Landsat image of July 15, 1979, computer-enhanced to show the sediment layer on the ice surface, and thereby the extent of sediment-laden slush ice during October 1978. The ice between the Colville and the Sagavanirktok Rivers is estimated to carry 16 times more sediment at this time than the yearly input by these two large rivers. Image produced by William Acevedo, U.S.G.S.

snow a perfect smother. You couldn't see your hand before your face." Shortly thereafter, they shipwrecked on a rock. "I set them to work right away ripping off sheathing, oars, spars, and other spare timber. These they laid on the slush ice, forming a sort of roadway over to the other wreck. It sounds simple enough, but the ice was just wet slush, a sort of snowy quicksand with water all through it."

Recent Observations

Several sets of observations that we made in the Alaskan Beaufort Sea shed additional light on the extremely viscous nature and strange behavior of the slush ice and therefore are described in some detail. These observations were made in the fall of 1982, when we extended field studies to include freezeup.

The R/V Karluk. On September 30, the air temperature was about -5 °C, the wind was blowing from the northeast at 15 m/s, and frazil ice was forming in coastal waters near Prudhoe Bay. The West Dock, a 4-km-long gravel causeway at nearly right angle to the wind direction, was trapping frazil ice on its east side, particularly in bights between moored barges. In one such place, steep waves of 1.2 to 1.5 m height and 3.5 s period were subdued as they traveled through a 120-m wide accumulation of slush ice, where the water depth was nearly 3 m. Because the sea was too rough for any kind of oceanographic work, we chose the area with slush ice for a diving investigation. From shore we observed that the waves propagated through the slush ice all the way to the beach, giving us the false impression that the slush ice had the consistency of pea soup and would be suitable for diving. Sailing the 12-m *Karluk* downwind into the calm part of the slush ice, with a steep following sea and whitecaps, the wave motion of the boat gradually decreased. In order to anchor the vessel at a point about 60 m into the slush ice, she first had to be turned 180° to point into the wind. Now the unique characteristics of the slush ice became apparent. At half-power ahead and hard-right rudder, the vessel neither advanced or turned. Only after several minutes, a slight heading change was noted, and we realized that minute cyclic heading changes occurred in phase with passing waves. Eventually, when the boat was properly positioned, the anchor and chain were lowered, but they initially came to rest on the very surface of the slush ice. About eight waves passed before the anchor broke through the bottom of the slush ice. The cyclic settling rate again made cyclic strength changes of the slush ice very apparent: settling of the anchor occurred between passing wave fronts, which were marked by dry-appearing white patches or bands (fig. 4).

A Grease-Ice Dive. The scuba-diving operation held similar surprises. Jumping fully equipped feet-first from a height of 1 m from the boat, our fall was first arrested about waist-deep into the slush ice, and we then settled with each passing wave. Unable to extract our arms from the dense slush ice, or to rotate around a vertical axis, we needed assistance from the deck to keep our heads above ice. Wave motion of the slush ice produced pronounced cyclic pressure pulses on our chests. These pressure pulses expelled the air from the dry suit around our face seals until all excess buoyancy was lost. Only with the aid of a heavy weighted line were we able to force our way down and back up through the 75-cm thick slush ice. The lower part of the layer was distinctly more fluid than the upper part. Figure 5 shows a diver resting on the viscous slush ice agitated by surface waves. Lying thus on the surface felt rather similar to resting on a waterbed.

A small pressure-sensitive transducer coupled to a recorder was used to measure the surface-wave amplitude and related pressure fluctuations within the slush ice. For the latter

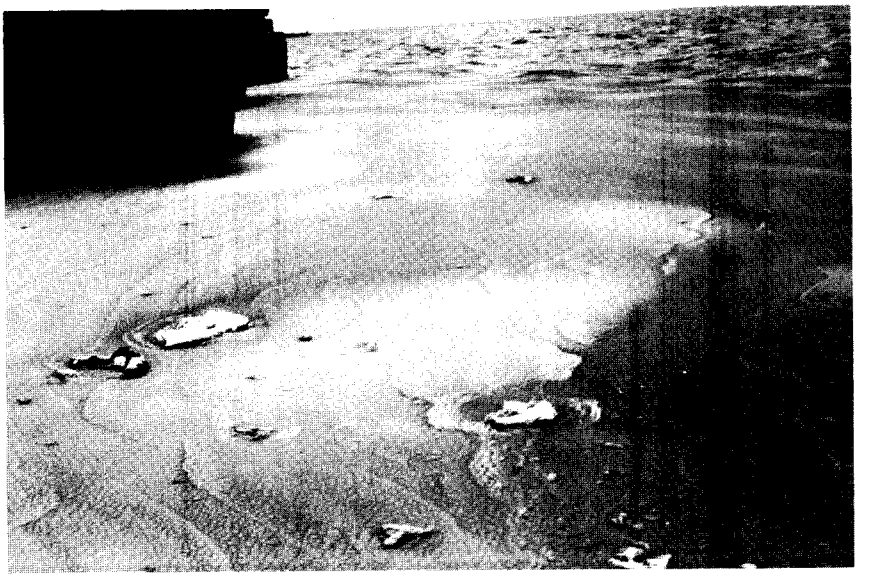

Figure 4. Accumulation of slush ice driven by wind into a bight between two barges along the Prudhoe Bay West Dock. While the passage of waves makes the slush ice appear fluid, both the R/V Karluk *and divers had difficulty maneuvering within it. The white patches of dry-appearing slush ice mark pressure pulses traveling in phase with advancing surface waves.*

Figure 5. Fully equipped diver supported by the wave-agitated slush ice. Lying on this slush ice felt similar to lying on a (cold) waterbed.

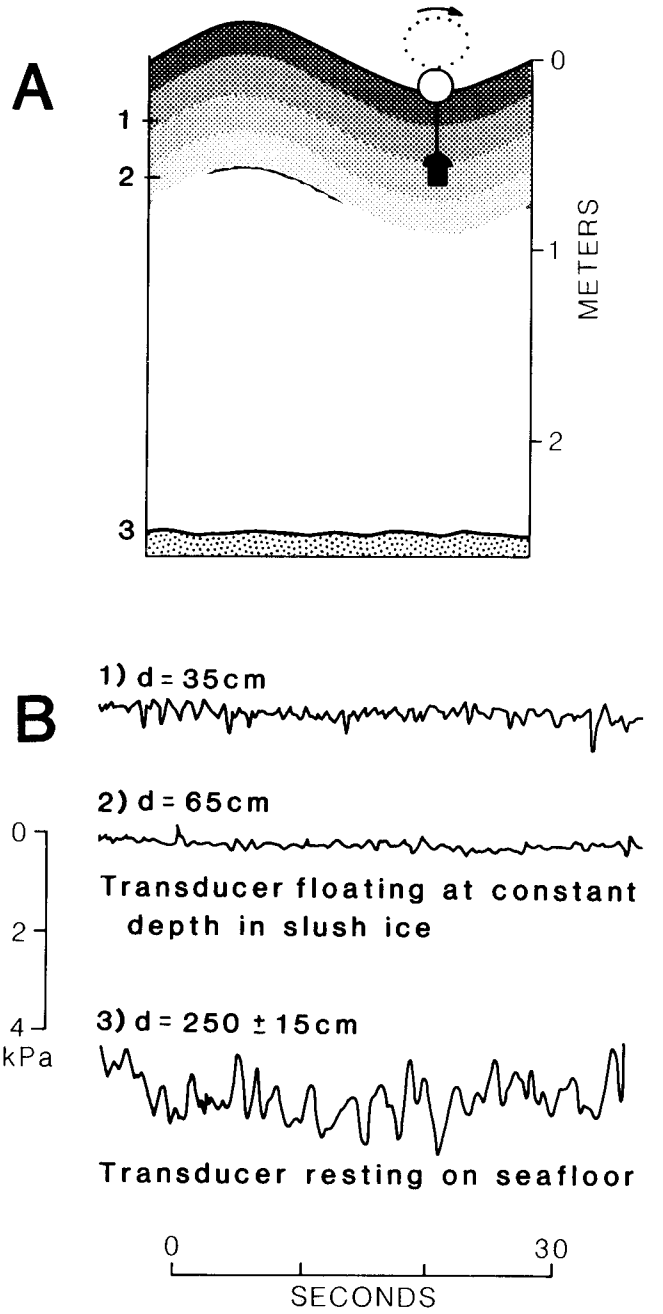

Figure 6. A) Schematic view of pressure transducer suspended in slush ice layer, and the three points at which pressure oscillations were measured sequentially within a half-hour period. B) Traces of pressure oscillations recorded at points 1, 2, and 3. The bottom trace represents the surface-wave amplitude.

measurements the transducer was held first at 35 cm and 5 minutes later at 65 cm depth within the slurry by hanging from a buoy that was allowed to freely follow the waves orbital motion. This is shown schematically in figure 6A. To measure the amplitude of surface waves shortly thereafter, the transducer was simply laid on the bottom at 2.5-m depth. The three traces of pressure fluctuations thus recorded are shown in figure 6B. The irregular surface-wave pattern is a result of refraction and reflection interference from large nearby obstacles. At 65-cm depth, in the lower more fluid part of the slush-ice layer, the pressure pulses have less amplitude than at 35-cm depth.

Throughout the 5-hour period anchored at the site we observed a slow but constant shoreward flux of individual ice pieces 10-cm to 30-cm-across incorporated into the slurry and floating on its surface.

Miscellaneous Observations off Cross Island. On October 4, a small swell from the northwest with a 2-s period was driving frazil ice into a small bight on the seaward side of Cross Island (fig. 3). The belt of slush ice accumulating at this site was 100 m wide. During a preceding time of slightly higher sea level, the wave train apparently had shoved such slush ice onto the beach, forming a layer of well-drained granular material. Right along the water's edge this deposit was terminated by a 50-cm-high vertical scarp against which the slush-ice waves were lapping without breaking (fig. 7). Wading seaward from the scarp, the force of the wave-agitated slush ice became noticeable and increased with water depth, until at 10-m distance and 95-cm depth, the excursions of the slush ice with passing waves caused our feet to slide across

Figure 7.- View of the Cross Island study site, where wave-agitated slush-ice in bottom contact to 95-cm depth was generating 50- to 75-cm-long ripples in coarse sand, and cobbles were rolling to and fro.

the bottom. At this point, the slush ice was in contact with the seafloor. We felt 20-cm-high sharp-crested ripples with an estimated wavelength of 50 to 80 cm in coarse sand. When we shifted weight to one foot, firmly implanting it in the sand, our ankles were struck by fist-size cobbles rolling to and fro.

A 24-hr experiment was begun at about 1-m depth to investigate the behavior of sediment within the framework of larger ice crystals where the mixture was subjected to oscillating pressure pulses. For this purpose, we mixed slush ice with medium-grained sand from the site and put the seawater-saturated slush into three 75-cm-long, 10-cm-diameter clear plastic bags. The bags were inserted vertically into the slush ice, and their lips nailed to a 1-m-long "two-by-four" board floating on the slush. The board in turn was secured to a buoy with an anchor rated at over 1-ton horizontal holding power in sand. Measured over a 3-minute period, the array was oscillating an average of 35 cm with each wave, with a maximum displacement of 75 cm. The maximum wave amplitude measured during that time was 25 cm. Upon returning to the experiment site on the next day, we found that the anchor had been moved 8 m obliquely onshore into 30-cm water depth. Only one of the bags remained intact. All sand had settled to the bottom in this bag, leaving the slush ice entirely clean except for several remaining fine pieces of organic matter.

At the experiment site, a flexible 20 x 25-cm hot-water bottle fitted with a sight-glass was suspended vertically in the slush ice, with the sight-glass protruding above the surface. This crude manometer was allowed to oscillate freely with passing waves, while the fluid level in the sight- glass was monitored during the passage of 20 waves. The amplitude of the pressure pulses thus measured ranged up to 1 kPa (about 11 cm of water column), and thus were similar to those recorded in figure 6. The ice content in the slush surrounding this bottle measured 62% by volume.

General Observations. Beaufort Sea aerial observations between longitude 147° and 151°W during and after numerous freezeups give us the following general impressions of the fate of slush ice, and of how the winter ice canopy is initially established.

Large volumes of slush ice are produced only in those years in which the navigation season is terminated by freezing winds with velocities of at least 10 m/s and temperatures of -10°C or colder. Such combinations usually occur with east to northeast wind directions, an important factor to consider when speculating on the sources and dispersal of sediment incorporated within the ice. This typical wind direction also determines the most efficient trapping orientations for flow obstacles, such as lines of grounded ice (fig. 3) or islands. We believe that the largest amounts of sediment are incorporated into the slush ice in years when the pack is 50 km or more from the coast, resulting in a long fetch.

The period in which there is 50% or more of open water for the generation of frazil ice on the inner shelf may last from just a few days to nearly a month. It generally starts in the last week of September, but has been known to start and terminate as early as the first week of September (Stefansson, 1921). Freezeup can also be delayed until the second half of October. Judging by the volume of soft ice with sediment seen under the winter ice-canopy by divers in about 6 years of records, and by the amount and extent of sediment found in the seasonal ice canopy in 15 years, we believe that during the past 15 years the fall of 1978 produced the most slush ice with sediment (fig. 3). This freezeup, apparently lasting only for a several-day period around October 6 to 8 (Reimnitz and Dunton, 1979), was also of the shortest duration.

Freezeup in the fall of 1982, in which the above described experiments were conducted and our first direct observations on anchor ice were made (Reimnitz et al., 1986), was spread out over a period of a month. The first threat of freezeup, restricting our research operations to the close vicinity of Prudhoe Bay, was seen on September 18. A lack of open water and rapid thickening of new ice eventually forced us to haul out the boat on October 7. However, on October 19 and 20, a 25 m/s storm from the southwest broke up and drove off the new 20-cm-thick ice. The storm also broke the moorings on Arctic Marine Freighters' fleet of tugs and barges that had long ago been winterized, and drifted much of this equipment 175 km eastward to the vicinity of Barter Island during a two-day period. Here the equipment was secured, while the new ice that had been displaced along with the barges kept on moving eastward. Because of a small offshore component in the wind direction, a zone of the inner shelf 20 to 30 km wide, including many of the lagoons was swept clean of first-year ice (Kenneth Vaudrey and Steven Amstrup, oral commun., 1982). On the second day of the storm, notable frazil ice was generated. This event demonstrates how mobile the new ice canopy can be under certain conditions, and also the minimum distances over which the sediment load in the ice canopy can be transported before the true fast ice has been established.

Some open-water seasons end without climactic events, and therefore without the production of large volumes of frazil ice. The summer of 1985 was such a season. We extended our field work to include freezeup, but neither large amounts of slush ice nor anchor ice were generated. Such freezeup conditions lead to the growth of a clean fast-ice canopy without a significant amount of sediment. As a result, light easily penetrates through the ice canopy. In such winters, the water turbidity under the ice cover also is low. An extreme case was the winter from 1970 to 1971, when the horizontal visibility in the water beneath the ice canopy near Prudhoe Bay in May measured over 60 m (Thomas Scanland, Marine Advisors, written commun., 1971). The 1978 freezeup (fig. 8), on the other hand, locally resulted in 4-m-thick masses of slush ice with large sediment loads (Reimnitz and Dunton, 1979) and led to almost total elimination of sunlight below the ice (Dunton et al., 1982). Within one month after freezeup, large amounts of suspended matter slowly released from the slush ice reduced visibility in the water to 1 to 2 m, but sediment fallout from disturbing the slush temporarily reduced visibility to 0.5 m.

During the climax of frazil-ice production, waves are propagated for several kilometers through fields of slush ice, depending on the thickness of the layer. From wave tank studies (Martin and Kaufman, 1981) and our field observations, the slush ice thins in a windward direction toward open water. Even short steep storm waves propagated into slush ice do not break over the fringes of the slush fields, but are gradually subdued over the distance traveled (fig. 9). The slush ice, whether in large fields, in patches, or in wind-parallel streaks, moves with the wind-driven surface water, except where it is piled up against stationary ice or land. Waves may agitate the slush ice for several days before it congeals. Our observations indicate that pancake-ice formation is relatively uncommon in the Alaskan Beaufort Sea. With continuing cold after a storm subsides, the slush ice congeals from the surface down. Once congealed, this somewhat turbid ice canopy usually is broken again under shearing or tensional forces. Tensional forces acting on a congealed slush ice sometimes result in the formation of elongate floes with geometric shapes (fig. 10). The resulting floes of a large variety of shapes and sizes subsequently may be extensively rearranged. As discussed earlier, the rearrangement may displace such new ice floes over distances of hundreds of kilometers before a continuous ice canopy forms. Because the sea, cluttered by new ice floes, is no longer agitated by storm waves during this period, suspended matter settles out of the water, and the new ice growing in the spaces between the floes may be entirely clean and transparent.

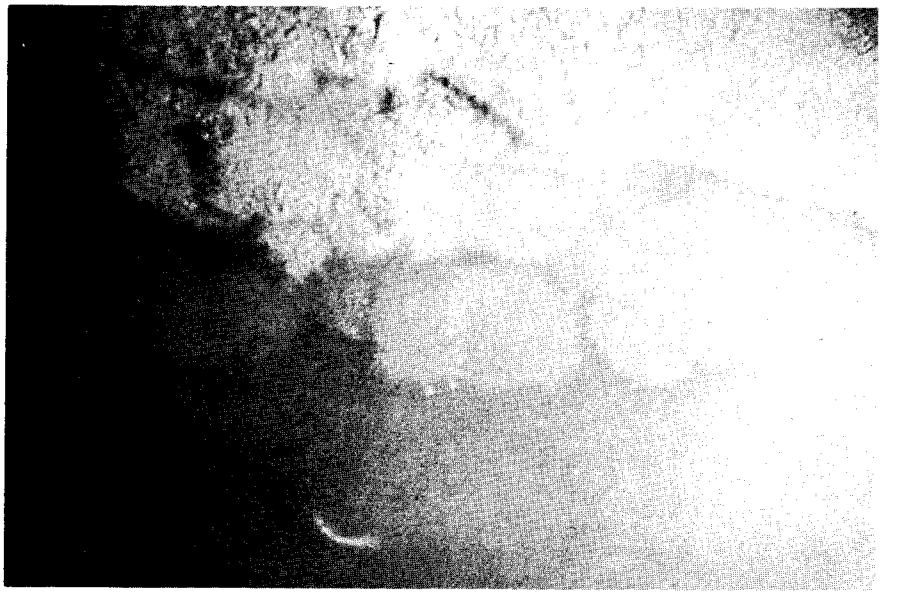

Figure 8. Bottom view of soft, sediment-laden slush ice in March 1979. Any disturbance by divers resulted in a rain of sediment into the water. The field of view in the background is 2-3 m.

Figure 9. Storm-whipped waves traveling from open water in the background into 15-cm-thick slush ice without breaking over the windward edge.

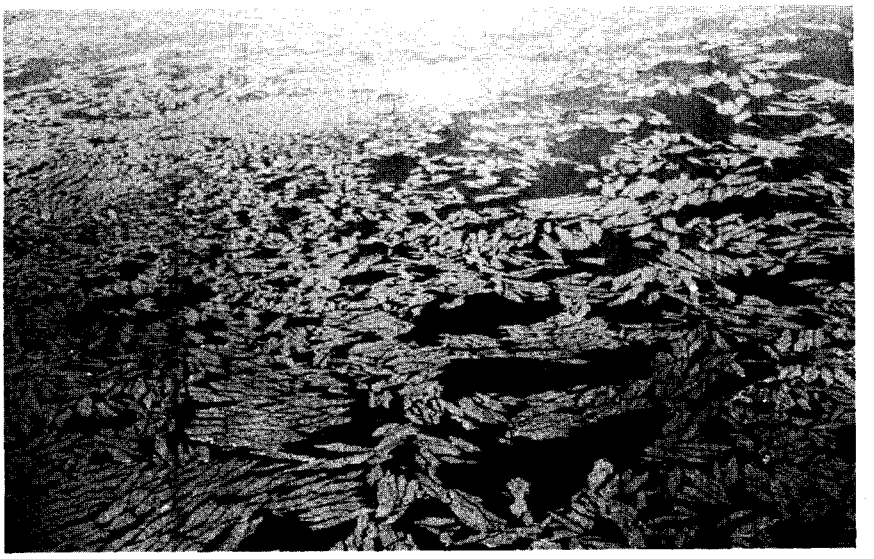

Figure 10.- Congealed slush ice breaking up under tension. The breakage pattern suggests that the ice is anisotropic, possibly due to ice-crystal orientation caused by waves passing through slush ice. The estimated sliver length is 8m.

Within a month or two after freezeup, a zone of grounded pressure and shear ridges on the midshelf, called the stamukhi zone, is established, thereby stabilizing the fast-ice canopy on the inner shelf (Reimnitz et al., 1977). After this, major ice movement over the inner shelf is rare. During years in which this new ice is composed largely of slush ice containing sediment, pressure ridges are constructed of brown ice, which is very conspicuous in the following navigation season.

DISCUSSION

The field observations serve to illuminate one aspect of sea ice that has been largely ignored where geologic processes are concerned. As far as we know, almost no work has been done on sediment dynamics related to slush ice, nor on its behavior and effects in a wave train.

Where frazil-ice crystals are concentrated by wind and waves against a beachface, they are compacted into a highly viscous slush. While further agitated by waves, this viscous ice blanket provides for littoral processes different from any studied so far. At the Cross Island site, cobbles were moving with each small passing wave in a zone at least 10 m wide out to a depth of 95 cm. The observed 50- to 80-cm wave length of sediment ripples matches the average orbital diameter measured at that site. These two facts indicate that the slush ice actively shaped the bottom during the two days of the experiment. A very gently sloping, smooth shoreface 10 to 30 m wide, extending out to the 2- or 3-m isobath, characterizes the seaward side of nearby Reindeer Island in some years (Reimnitz and Barnes, 1974; Reimnitz and Kempema, 1982, Reimnitz et al., 1986). In other years that same shoreface is marked by a well-defined, narrow trough directly adjacent to the beach and paralleling it for several kilometers (Reimnitz and Kempema, 1982, fig. 2). A possible explanation for the occasionally very flat shoreface off Arctic beaches is the abrasive action of slush ice worked by a wave train.

The 2 to 3-m depth of the sharply defined outer edge of the shoreface then could record the thickness of the slush ice during the previous freezeup. A wave-agitated slush ice may also lead to sediment sorting. Thus, a strip of pea-size gravel was noted forming on the beach face at Barrow, Alaska, during a storm when the surf zone turned into a rolling slush of frazil ice (Sackinger, oral commun., 1985).

Our observations do not suggest any new mechanisms for sediment enrichment of frazil ice in the sea, besides those that were proposed by Osterkamp and Gosink (1984), but two of the methods they proposed clearly can be eliminated from consideration. First, turbid water carried by waves overtopping the slush ice was suggested to percolate down through the ice, which in turn filters out the particulate matter (Osterkamp and Gosink, 1984). Waves do not break over slush ice, but they can propagate through the ice for kilometers. Second, currents were suggested to flow past slush ice, to result in a pressure differential through slush, which in turn leads to percolation of turbid water through the slush and filtration of particulate matter (Osterkamp and Gosink, 1984). In the sea, unlike rivers, the surficial slush ice normally moves with the surface water. The proposed mechanism therefore could operate only in very special settings of limited aerial extent.

In tank experiments, waves seem to travel only several wavelengths into the slush ice, beyond which a "dead zone" with no motion is established (Martin and Kaufman, 1981). We believe that this dead zone is an artifact of slush ice confinement in a tank and does not apply to the open spaces of the sea. Here waves are propagated for at least several kilometers through an ice slush as thin as that observed in wave tanks. Studies of slush ice generated in a wave tank indicate an imbrication of individual crystals at right angles to the wave orthogonals (Martin and Kaufman, 1981). W.F. Weeks (oral commun., 1986) also saw indications of crystal alignment in nature. The breakage pattern in congealed slush ice into elongated slivers (fig. 10) suggests that the ice is indeed anisotropic, perhaps from wave-reworking resulting in preferred crystal orientation.

Any disturbance of the slush ice, such as from wave action, has a cleansing effect. This was demonstrated by the Cross Island experiment, in which downward particle movement under the force of gravity probably was aided by oscillatory flow of interstitial water. Purging of sediment was also observed in winter diving, when we thrust our arms into the slush ice overhead (Reimnitz and Dunton, 1979). From this we infer that individual frazil crystals in a slush are not sticky, even if they originally acted as scavengers adhering to sedimentary particles (Osterkamp and Gosink, 1984). The property of the slush ice to release sediment on agitation supports the suggestion by Osterkamp and Gosink (1984) that sedimentary particles reside mainly in interstitial water, rather than within ice crystals. Cores taken from sediment-laden ice in winter reveal a characteristic downward increase in concentrations of finely disseminated sedimentary particles in that part of the ice canopy that originated from frazil ice accumulations. The origin of the turbid ice has been ascribed to processes at time of freezeup, but the downward increase in sediment concentration was uncertain (Barnes et al., 1982; Osterkamp and Gosink, 1984). The downward mobility of particles in agitated slush ice demonstrated by our field observations provides a satisfactory explanation for the downward gradient in sediment concentration. Where the slush ice layer is less than 2 m thick, clear columnar ice grows below later in the season. A sharp boundary between upper turbid ice and lower clear ice has commonly been noted in late-winter ice cores.

The self-cleansing property of fresh slush ice, coupled with the evidence ruling out subsequent processes of sediment enrichment, indicate that the enrichment occurs by the scavenging action of frazil ice or flocs in the water column or on the bottom (Osterkamp and Gosink, 1984; Kempema et al., 1986). Particles as large as coarse sand have been observed within actively forming slush ice in 2 m water depths (Reimnitz et al., 1986). The occurrence of frazil ice and flocs on the Beaufort Sea shelf probably is restricted to the upper 20 m of the water column, the approximate thickness of the mixed layer (Reimnitz et al., 1986). Thus the sediment scavenging action on the seafloor is restricted to the shelf surface landward of the stamukhi zone. Whatever the precise mechanism of particle scavenging may be, the frazil ice must remain undisturbed after rising to the surface in order to retain the original sediment load. Such optimum conditions for achieving maximum sediment concentrations in the fast ice probably are rarely met, since wave and other processes continue to agitate the slush layer for several days before congelation arrests the sediment.

The 1978 freezeup may have provided nearly optimum conditions for sediment retention by slush ice. The regional extent of the slush-ice cover for that season, as delineated by a surface sediment cover, is shown in figure 3. At the time of the Landsat image, the surface sediment layer was between 0.1 cm and 1 cm thick near Prudhoe Bay, and the sediment load on top of the ice was estimated at 1000 m^3/km^2 (Northern Technical Services, 1981). But this estimate considers only the sediment concentrated on the ice in mid July by surficial melting, and excludes that still held within the remaining ice. The total sediment load carried by the ice prior to melting therefore probably was higher. We applied the above sediment load to the total area of discolored ice between the Colville and Sagavanirktok Rivers in figure 3, to calculate a total sediment load carried by ice. Comparing the results to the sediment supplied by rivers yearly to the same area from Reimnitz et al. (1985), we find the sediment load on the ice 16 times larger. This comparison implies that the processes leading to the formation of slush ice are erosive.

During the following summer we observed that most of the sediment-laden ice still seen intact in figure 3 melted locally and discharged its load to the water column before breakup allowed long-distance ice excursions. Sediment-rafting during the decay of first-year ice therefore is insignificant in the overall transport regime (Reimnitz and Barnes, 1974). As shown earlier, rafting during the dynamic period of incipient ice growth can cover long distances. Frazil ice with entrained sediment within the fast ice may have originated far away. Reimnitz and Dunton (1979) showed that most of the slush ice incorporated in the winter ice canopy in figure 3 must have formed during the first few days of October 1978. From October 5 through October 9, wind from the east was gusting to 20 m/s at Barter Island, and averaged 12.5 m/s. From spot measurements of currents, local tracking of ice floes, and many years of summer field observations, surface currents of 1 m/s (2 knots) are common on the inner shelf under such wind conditions. Assuming a westward drift rate of 1 m/s for 5 days, all of the slush ice and sediment seen in figure 3 had traveled 430 km before coming to rest within the study area. The sediment seen discharged by melting ice in the study area therefore may have had its origin in Canada.

SUMMARY AND CONCLUSIONS

Large volumes of slush ice generated over several-day periods during strong fall storms at freezeup may reach thicknesses of 4 m in coastal waters of the Arctic. Waves propagate through the slush ice for kilometers, resulting in internal pressure oscillations associated with compression and rarefaction. The compacted slush ice may be nearly impenetrable for small vessels and divers, allowing progress only in small increments, in phase with advancing waves. Where slush ice is in contact with the bottom, large ripples develop and cobbles roll to and fro. Flat ramparts seen on the arctic shoreface in some years also may possibly result from the abrasive action of the slush ice layer.

The slush ice may carry up to 1000 m^3/km^2 of mainly fine grained sediment. This sediment probably is entrained by individual frazil-ice crystals or flocs scavenging from the bottom or the water column during storms and subsequently rising to form a slush-ice layer up to 4 m thick. Contrary to theory, post-frazil-ice filtration processes do not seem to add sediment to the slush ice. The sediment particles reside in the interstices of slush ice. Any disturbance of the layer, such as the passage of surface waves, results in a downward migration of individual particles in the water-filled interstices and a rain of particles from the slush ice. Downward particle migration and particle loss from the bottom of the slush ice explains the characteristic downward increase in sediment concentration in the winter ice canopy, and the sharp contact between upper turbid ice and lower clean ice. Downward migration of sediment particles in slush ice indicates that individual frazil crystals at this stage are not adhesive.

Slush ice in coastal regions does not become fast ice until formation of grounded ridges in the stamukhi zone, 1 to 2 months after freezeup begins. During this period of new ice mobility, long-range sediment transport occurs. The sediment load of 1000 m^3/km^2 held by the fast ice off Prudhoe Bay in the winter of 1978-79 probably had its source on the Canadian shelf surface, at least 400 km to the east. Ocean turbulence is greatly reduced while the congealing slush ice drifts about; therefore, new ice forming on open spaces is clean. This series of events explains the patchy appearance of the fast ice after the summer snowmelt.

The processes related to the formation and movement of slush ice are not only important for the sedimentary environment. Major slush-ice production during the fall affects the overall marine environment in the fast-ice zone for the following 9 months. Sediment incorporated into the slush ice leads to a strong reduction of fast-ice albedo, and therefore increases the summer melting rate. Sediment entrainment also affects the strength of the ice, and could be very important for dispersal of future pollutants. Water below turbid ice also is very turbid from sediment settling out. Most important of all are the effects on life below the ice canopy. A heavy load of sediment in slush ice results in almost total elimination of sunlight to primary producers below the ice and therefore affects the entire food web for a long period of time. Full-scale slush-ice production in the Alaskan Beaufort Sea is restricted to a short period of time, and does not even occur each fall. Similar processes may be occurring each year, and for longer periods of time, in perennial polynyas of the Canadian Arctic (Dunbar, 1986) and recurring polynyas in the Chukchi and Bering Seas. Our lack of full understanding of the important phenomena reported here represents a major gap in the knowledge of the Arctic marine environment.

REFERENCES CITED

Barnes, P.W., Reimnitz, Erk, and Fox, Dennis, 1982, Ice rafting of fine grained sediment, a sorting and transport mechanism, Beaufort Sea, Alaska: Journal of Sedimentary Petrology, v. 52, no. 2: 493-502.

Bartlett, Bob, 1927, Captain Bob Bartlett's briny boast: shipwrecked 14 times: Literary Digest, July 9, 1927. 42-44.

Bates, R.L., and Jackson, J.A., (editors), 1980, Glossary of Geology: American Geological Institute, Falls Church, VA. 749 pp.

Bauer, Jane, and Martin, Seelye, 1983, A model of grease ice growth in small leads: Journal of Geophysical Research. 88, C5: 2917-2925.

Collinson, Richard, 1889, Journal of the H.M.S. Enterprise, 1850-55: Sampson Low, Marston, Searle, and Rivington, Ltd., London. 531 pp.

Dunbar, M.J., 1986, Arctic marine ecosystems, Oceanus. 29, 1: 36-40.

Dunton, K.H., Reimnitz, Erk, and Schonberg, Susan, 1982, An arctic kelp community in the Alaskan Beaufort Sea: Arctic. 35, 4: 465-484.

Kempema, E.W., Reimnitz, Erk, and Hunter, R.E., (in press), Flume studies and field observations of the interaction of frazil ice and anchor ice with sediment: U.S. Geological Survey Open-File Report 86-515. 49 pp.

Martin, Seelye, 1981, Frazil ice in rivers and oceans: Annual Reviews of Fluid Mechanics. 13: 379-397.

Martin, Seelye, and Kauffman, Peter, 1981, A field and laboratory study of wave damping by grease ice: Journal of Glaciology. 27, 96: 283-313.

Morecki, V.N., 1965, Underwater sea ice: Problemy Arktiki i Antarktiki, no. 19, p. 32-38. Translated by E.R. Hope, Directorate of Scientific Information Services, DRB Canada, April 1968. Paper T 497 R. Available from CFSTI, Springfield, VA 22151

Northern Technical Services, 1981, Beaufort Sea drilling effluent disposal study. Prepared for a 19-company consortium under the direction of Sohio Alaska Petroleum Company, Anchorage, Alaska. 329 pp.

Osterkamp, T.E., and Gosink, J.P., 1984, Observations and analysis of sediment-laden sea ice. *In* Barnes, P.W., Schell, D.M., and Reimnitz, Erk (editors): The Alaska Beaufort Sea: Ecosystem and Environment. Academic Press, San Diego. 73-94.

Reimnitz, Erk, and Barnes, P.W., 1974, Sea ice as a geologic agent on the Beaufort Sea shelf of Alaska. *In*: Reed, J.C., and Sater, J.E. (editors). The Coast and Shelf of the Beaufort Sea. The Arctic Institute of North America, Arlington, VA. 301-351.

Reimnitz, Erk, Toimil, L.J., and Barnes, P.W., 1977, Arctic continental shelf morphology related to sea-ice zonation, Beaufort Sea, Alaska. Marine Geology. 28: 179-210.

Reimnitz, Erk, and Dunton, K.H., 1979, Diving observations of the soft ice layer under the fast ice at DS-19 in the Stefansson Sound Boulder Patch. *In* Environmental Assessment of the Alaskan Continental Shelf: Principal Investigator's Annual Reports, March 1979. National Oceanic and Atmospheric Administration. 9: 210-230.

Reimnitz, Erk, and Kempema, E.W., 1982, Dynamic ice-wallow relief of northern Alaska's nearshore -- a dynamic bedform. Journal of Sedimentary Petrology. 52, 2: 451-462.

Reimnitz, Erk, Graves, S.M., and Barnes, P.W., 1985, Beaufort Sea coastal erosion, shoreline evolution, and sediment flux, *in* U.S. Geological Survey Open-File Report 85-380, 74 p.

Reimnitz, Erk, Kempema, E.W., and Barnes, P.W., 1986, Anchor ice and bottom-freezing in high-latitude marine sedimentary environments: Observations from the Alaskan Beaufort Sea. U.S. Geological Survey Open-File Report 86-298. 21 pp.

Stefansson, Vilhjalmur, 1921, The Friendly Arctic. The MacMillan Company, New York. 784 pp.

U.S. Navy Hydrographic Office, 1952, A functional glossary of ice terminology; U.S. Navy H.O. Publication No. 609, Washington, D.C., 88 pp.

Weeks, W.F. and Ackley, S.F., 1982, The growth, structure, and properties of sea ice; CRREL Monograph 82-1. U.S. Army Cold Regions Research and Engineering Laboratory, Hanover, NH. 130 pp.

World Meteorological Organization, 1970, WMO Sea-Ice Nomenclature, Codes, and Illustrated Glossary, Report 259, TP.145, Geneva. 147 pp.

MECHANICAL PROPERTIES OF SEA ICE AND SEA ICE DEFORMATION IN THE NEARSHORE ZONE

by

Lewis H. Shapiro, Peter W. Barnes, Arnold Hanson, Earl R. Hoskins,
Jerome B. Johnson, and Ronald C. Metzner

Geophysical Institute
University of Alaska Fairbanks
Fairbanks, Alaska 99775-0800

Final Report
Outer Continental Shelf Environmental Assessment Program
Research Unit 265

December 1987

ACKNOWLEDGMENTS

This program was funded primarily by the Minerals Management Service, Department of the Interior, through an Interagency Agreement with the National Oceanic and Atmospheric Administration, Department of Commerce, as part of the Alaska Outer Continental Shelf Environmental Assessment Program. Additional funding support for the study titled "Vibration of Sea Ice Sheets" came from the National Science Foundation. The Alaska Sea Grant Program contributed funds for analysis of the radar data which were used in several studies. Timely support from several industry groups was important for the conduct of the experimental program on the mechanical properties of sea ice. Finally, additional funds from the State of Alaska were used for preparation of reports.

ABSTRACT

The primary objectives of this program were (1) to develop and test procedures and hardware required for in situ measurement of the strength and other mechanical properties of sea ice, (2) to use the appropriate procedures to determine the deformational behavior of ice, and (3) to combine the experimental results with existing data for use as background in a search for an appropriate stress-strain law and failure criterion for sea ice. In addition, to take advantage of the extended field season required for meeting the objectives and the presence of a radar system in the field area, a series of studies of fast ice deformation in the nearshore area was conducted. The subjects under this part of the program included ice-push, ice sheet vibration as an indicator of rising stress levels, ice gouges, and other topics. The program results are described in the 10 technical subsections (i.e., 2.2–2.5 and 3.1–3.6) of this report.

TABLE OF CONTENTS

TABLE OF CONTENTS (continued)

LIST OF FIGURES

LIST OF FIGURES (continued)

LIST OF FIGURES (continued)

LIST OF FIGURES (continued)

LIST OF TABLES

1.
EXECUTIVE SUMMARY

This report describes the results of studies in two general subject areas: (1) strength and mechanical properties of sea ice, and (2) ice deformation in the nearshore area. During the course of the program, numerous studies were done consistent with the two basic themes. The number of these studies is large enough that it is not feasible to include complete reports on all of them here; in fact, most have been described in reports or publications in the open literature. However, all are summarized (or noted in passing) and references are provided to the earlier work. Material which was not covered completely in previous reports and publications is, of course, treated fully here. Thus, this report provides a complete record of the program.

The primary objectives of this program were to (1) develop and test procedures and hardware required for in situ measurement of the strength and other mechanical properties of sea ice, (2) use the appropriate procedures to determine some aspects of the deformational behavior of ice and, (3) combine the experimental results with existing data for use in a search for an appropriate stress-strain law and failure criterion for sea ice. In addition, in order to take advantage of the extended field season required for the objectives above and the presence of a radar system in the field area near Barrow, Alaska, several aspects of fast ice deformation in the nearshore area were studied while the the work of the first project was in progress. Projects under this part of the program included studies of ice-push and ice-override, ice sheet vibration as an indicator of rising stress levels, nearshore ice motion patterns, correlation of ice movement with sea-bed ice gouges and other subjects. The results of all aspects of the program are described in the ten technical sub-sections of this report.

The rationale for the study and its relevance to problems of offshore development follow from the premise that any permanent or semi-permanent offshore structure off the Chukchi, Beaufort or (most of) the Bering Sea coast of Alaska must contend with problems related to the presence of sea ice. A broad range of potential problem areas were examined in this project. The purpose was to help define some of the properties and processes in the ice cover which needed to be considered in both the design and the evaluation of structures for offshore exploration and development.

The major results of the program are:

(1) Procedures and hardware for tests in uniaxial and biaxial compression, direct shear and indirect tension were developed and tested. In all cases, flatjacks were used to apply loads to samples in situ in the ice sheet. The samples were intermediate in size between small-scale laboratory samples and the full thickness of the ice sheet.

(2) An extensive series of uniaxial compression tests was conducted which yielded data on strength vs. stress rate and stress vs. time-to- minimum strain rate in constant stress tests. The data provide useful values and, in addition, they define strength ranges which are important elements in the stress-strain law and failure criterion developed to interpret the data.

(3) The stress-strain law under study is based on the model of a 4-parameter viscoelastic fluid constrained by the distortional strain energy yield criterion. Both linear and non-linear viscoelastic models have been considered, and the similarity of the trends predicted by the theory are evident in the data. However, further refinements are required in order for the results to agree quantitively.

(4) Two series of tests were conducted to examine the effect of grain size and c-axis orientation on the uniaxial compressive strength of sea ice. In the first series, the results were in general agreement with the results of small-scale laboratory

tests; the strength varied with loading direction relative to the dominant c-axis orientation direction. However, the second series, which was done on ice which clearly had a well-developed c-axis fabric, showed no variation of strength with direction. We interpret this to indicate that there may be a sharp limit to the intensity of c-axis orientation required for the ice to become mechanically anisotropic for loading in the plane of the ice sheet.

(5) A short series of tests were done to compare the uniaxial compressive strength of first year and multiyear ice over a range of loading rates. The results showed no significant differences over the range of loading rates used.

(6) There were opportunities to study several ice-push and ice-override events in the field, including the first documented case of complete override of a barrier island during an ice-push event. A model of the deformation pattern in the plane of the fast ice sheet during an ice-push event was developed, based upon observations made during the project. In the winter, when the fast ice is firmly in contact with (and possibly frozen to) the beach, ice-push events originate with fracture of the ice sheet in a pattern which resembles the shear lines in a plastic medium compressed between rough plates. This pattern apparently serves to concentrate the distributed stress from the pack ice-fast ice boundary to a smaller reach along the beach. Subsequently, the fast ice sheet can advance as series of segments bounded by fractures at high angles to the beach, which appear to originate at the shoreline and extend offshore in response to the motion. Ice-push events during breakup, when the ice is not frozen to the beach, do not display the initial pattern of shear fracturing. Instead, the ice sheet simply advances by the mechanism of segmenting along fractures at high angles to the beach.

(7) Several instances of "long" period vibration of the fast ice sheet as an indicator (leading by periods of hours) of rising stress level were observed during the project. Based upon these, a theoretical study was conducted of wave propagation in

an ice covered sea. The purpose of the study was to evaluate a model of the relationship between the vibrations and the rising stress level, in order to determine whether the association could be useful as a warning of impending stress increase or motion of the ice sheet. The study suggests that the model is reasonable. In addition, some results were obtained which suggest guidelines for the safe transit of vehicles over ice or, conversely, for the use of over-ice vehicles in ice breaking.

(8) Side-scan sonar surveys of the sea floor were done in two consecutive summers within the field-of-view of the radar system near Barrow. The purpose was to attempt to correlate the pattern of gouges in the sea floor with movement of the ice as monitored by the radar. The results showed that the dominant ice gouge direction was at a high angle to the isobaths (and the shoreline) in the area. This is different from the pattern along the Beaufort Sea coast where the gouges tend to be parallel to the isobaths (and the shore). The history of the ice cover in the area was determined from the radar data for the years prior to and between the side-scan sonar surveys and was used to interpret the gouge pattern. The results suggest that the prominent gouge orientations in the area normally occupied by fast ice were formed by the drag of keels during ice-push events, while the majority of the gouges reflect incision during ridging.

(9) The imagery from the sea ice radar system was evaluated and used to describe some of the processes and patterns of sea ice drift in the nearshore area. In addition, ice conditions through a "typical" ice year in the Barrow area were defined. The results of this work, while specific to the area, are used to point out the potential utility of data of this type for any area where development in the nearshore zone is anticipated.

(10) A short series of experiments were done to determine the coefficients of static and kinetic friction between sea ice and unfrozen beach gravel. The experiments involved dragging large blocks of ice (i.e., 10,000 to 12,000 kg) up the

beach slope with a bulldozer and monitoring the forces required. The results of 36 separate movements of the blocks gave values for the coefficients of static and kinetic friction of 0.50 and 0.39, respectively. These values should be applicable to calculations of the forces required to drive an ice sheet on shore during an ice push event.

Other completed work summarized in the report includes (1) the results of preliminary measurements of the fracture toughness of sea ice, (2) the design of a new strain transducer for laboratory studies of ice strength, and (3) the description of a series of interviews with older residents of arctic Alaska regarding historical occurrences of unusual or extreme events in the fast ice cover along the Beaufort Sea coast.

2.
MECHANICAL PROPERTIES OF SEA ICE

2.1 INTRODUCTION

The problem of translating the results of laboratory tests of the mechanical properties of natural materials into field application is well known in both soil and rock mechanics, and is no less acute for the case of sea ice. In its natural state, sea ice occurs as an ice sheet which, in the offshore areas of Alaska, may freeze to a thickness of about 2 m through a winter. Within this vertical distance grain sizes range from dimensions of a few millimeters at the surface to several centimeters at the base. Often there is a tendency for strong preferred orientation of the grains by alignment of c-axes in the horizontal plane (Weeks and Gow, 1978; Weeks and Assur, 1967). Superimposed over this fabric are both horizontal and vertical variations in salinity of the ice, and a temperature gradient reflecting temperature differences which may be in excess of 40 °C between the top and bottom of an ice sheet at various times during the winter.

Prior to the start of this project, the determination of the mechanical properties of sea ice sheets under in-plane loading (as opposed to bending under vertical loads) was approached from two directions. The first was through small-scale laboratory or field tests involving large numbers of samples. The best example is the work of Peyton (1966) in which the properties of an ice sheet were deduced by integrating the results of tests on samples collected at different depths in an ice sheet. The second approach was to test the full thickness of an ice sheet in crushing (Croasdale, 1974; Croasdale et al., 1977). Obviously, the number of tests of this type which could be done is limited, and not all properties or ice types of interest could be tested. The objective of this project was to develop a series of tests through which the strength and other mechanical properties of sea ice could be determined for samples

which were large relative to those normally used in laboratory testing programs. The samples were to be loaded parallel to the surface of the ice sheet (as opposed to vertical loading as in tests of bearing strength), and the tests were to be done in the field under ambient conditions in a manner which minimized the disturbance to the samples. Thus, the tests were required to be relatively easy to set-up and run. Once the test procedures were developed, a program of measurements was to be conducted to determine the strength and viscoelastic properties of the ice.

During the course of the program we developed procedures for doing uniaxial and biaxial compression tests, direct shear tests and indirect tension (Brazil) tests. This involved experiments to evaluate (1) the loading system, (2) strain measuring devices, (3) the accuracy of temperature and salinity measurements, and (4) the extent to which the samples represented the ambient conditions in the ice sheet. The nature of the tests required that these experiments all be done as part of the field program. Then, an extensive series of uniaxial compression tests was done in the field to attempt to define the strength and deformational properties of sea ice in this loading mode. Some experiments were also done in biaxial compression over a small range of confining pressures. Late in the program a series of fracture toughness measurements on small beams of sea ice were made in the laboratory, and development work was done on an inexpensive strain gauge for use in testing small-scale samples of sea ice in uniaxial compression. It was anticipated that this gauge would be used in a series of tests to be done in the field using small samples collected from the site at which the tests on the large samples were being conducted. Unfortunately, the experimental phase of the project was terminated before this could be done.

Along with the testing program, we undertook a review of previous work on the strength and mechanical properties of sea ice [most notably, the extensive series of tests done by Peyton (1969)]. The objective was to combine these results with those

of the field testing program to develop a stress-strain law and failure criterion for sea ice.

All of the experimental work done in the field is described in Section 2.2 including the equipment and procedures for the different types of field tests and the results of experimental measurements of the strength of sea ice in uniaxial compression at constant stress and constant stress rates. A discussion of the progress made toward the development of a stress-strain law and failure criterion for sea ice is then given in Section 2.3. Finally, the results of the laboratory measurements of the fracture toughness of sea ice and the work the strain transducer are described in Sections 2.3 and 2.4, respectively.

2.2 FIELD EXPERIMENTS ON THE MECHANICAL PROPERTIES OF SEA ICE

by

Lewis H. Shapiro, Ronald C. Metzner, and Earl R. Hoskins*

ABSTRACT

The purpose of these experiments was to develop procedures for conducting field tests of the mechanical properties of sea ice. Stresses were to be applied in the plane of the ice sheet and the samples were to be large in comparison to those normally used in laboratory tests. Following this, tests were to be done to determine aspects of the deformational behavior of sea ice for comparison with the results of laboratory tests and for use in the development of a stress-strain law and failure criterion for sea ice in uniaxial compression.

Procedures for tests in uniaxial compression, direct shear and indirect tension were devised and a procedure for testing in biaxial compression was under development when field work for the project was terminated. In all the tests, the stresses were provided by flatjacks loaded by high-pressure gas through a pressure regulator. The system permits tests in both constant stress rate and constant stress to be conducted. Deformation was monitored by linear potentiometers mounted on pegs frozen into the surface of the samples.

Uniaxial compression tests were conducted on samples with dimensions of 30 x 30 x 60 cm at constant stress rates from about 0.4 to 4 x 10^4 kPa/sec and in several temperature ranges. The results follow the same trend of increasing strength with loading rate as is found in constant strain rate tests. Based upon the peak strengths reached in tests of both types, the results suggest that there is no marked difference in strength between the samples tested in this program and the smaller samples usually used in laboratory testing programs.

---

*Department of Geophysics, Texas A & M University.

The results of uniaxial compression tests at constant stress define a "transition" stress, below which there is a rapid increase in the time which a sample can sustain the applied stress without failure.

The trends in the results of tests to evaluate the effects of grain size and c-axis orientation on the uniaxial compressive strength of sea ice generally agree with the results of small-scale laboratory tests. However, the data acquired in this program suggest that it is possible for ice which shows an apparently strong c-axis orientation in thin section to be mechanically isotropic. This implies that there is a sharp limit to the intensity of c-axis orientation that is required in order for the ice to be mechanically anisotropic.

A short series of uniaxial compression tests was done to compare the strengths of first year and multiyear sea ice. The results indicate that there is little difference in strength over the range of temperatures and stress rates used in the experiments.

2.2.1 INTRODUCTION

The same basic approach was used in all of the tests done in the field for this program. The loading devices were flatjacks which were expanded under internal pressure to provide a known force. In some tests, the geometry of the resulting stress field was controlled by creating internal boundaries in the ice sheet using chain saw cuts as free surfaces; these cuts defined the geometry of the samples. In other tests, samples were removed from the ice sheet, shaped according to the type of test, replaced and then loaded. In either case, the ice sheet served as the loading frame.

The tests were done by controlling the load or loading rate on the sample, rather than the rate of deformation. This was a necessary choice, because the equipment required to load large samples under controlled rates of deformation (large hydraulic rams, pumps, an elaborate strain measuring system, automatic controls, etc.), and the personnel to operate that equipment, were too costly. Various

loading paths were used in experiments to develop the test procedures. Constant loading rates or constant loads were used in the experiments to provide data to determine the strength and mechanical properties of the ice.

Sensors of various types were used to monitor displacements from which strains were calculated. Temperature and salinity measurements were made by conventional methods, although some preliminary work was required to determine the effect of the process of setting up the experiments on these parameters.

This section is devoted primarily to descriptions of the loading system and strain measurement procedures. The reader is referred to Shapiro et al. (1979) for a more complete discussion.

2.2.2 LOADING SYSTEM

2.2.2.1 Flatjacks

In all the experiments, the loads were introduced into the ice sheet by flatjacks. These are simple devices which are inexpensive to construct, consisting only of an envelope of thin, sheet metal (or other suitable material) welded together along the edges. One or two nipples are installed along the edges of the envelopes. A fluid under pressure is introduced through one nipple to expand the flatjack and transmit a force to the surrounding ice. A pressure transducer can be attached to the other nipple to monitor the pressure in the flatjack. The envelope can be constructed in any suitable size and shape, depending upon the experiment to be done. During this program, experiments were done using square, rectangular and triangular flatjacks of various sizes. In addition, for the indirect tension test, the flatjacks were curved to provide a load over part of a cylindrical surface. In all cases, the flatjacks were thin enough to be inserted into a chain saw cut in the ice.

Loading is done by introducing a fluid under pressure into the envelope. The properties of the fluid are not important, although, of course, it must not freeze. The bulk of the experiments done on this program were loaded by high pressure nitrogen

gas through a pressure regulator, although a few tests were done with hydraulic oil loaded through a hand-operated hydraulic pump.

2.2.2.2 Load Transmission and Flatjack Efficiency

When under internal pressure, the flatjacks tend to expand, transmitting a force to the surrounding ice. If the expansion were uniform, and if the contact area between the flatjack and the ice remained constant, then the total force transmitted would simply be the product of the internal pressure and the flatjack area. However, the expansion of the flatjacks is not uniform because the edge welds prevent expansion near the margins of the envelope. Thus, the force transmitted is not the simple product described above. Instead, it depends upon the ratio of the flatjack area to the edge length (Deklotz and Boison, 1970; Pratt et al., 1974), so that it is necessary to calibrate flatjacks of different sizes and shapes.

Calibration experiments were done only for the 30 x 30 cm flatjacks used in the uniaxial compression testing program (Section 2.2.4) for which a knowledge of the stress magnitudes was required. No calibrations were done for flatjacks used in the experiments for developing techniques only.

Two separate calibration experiments were done. The first was described in Shapiro et al. (1979) and is illustrated in Figure 2.2-1. A block of ice 30 x 32 x 60 cm was prepared as if for a uniaxial test (described in Section 2.2.4.1) with a double layer of polyethylene sheeting at its base and a 30 x 30 cm steel flatjack at each end. A 35 x 35 cm flatjack made of thin, sheet copper was installed in a chain saw cut parallel to, and midway between, the steel flatjacks, with its top edge at the surface of the ice. Chain saw cuts were then made to define the sides of the block as shown in the figure, forming two blocks, 30 x 30 x 32 cm which separated the copper flatjack from the steel flatjacks. The copper flatjack was then expanded slightly with hydraulic oil, sealed, and the pressure allowed to relax back to near zero. In this

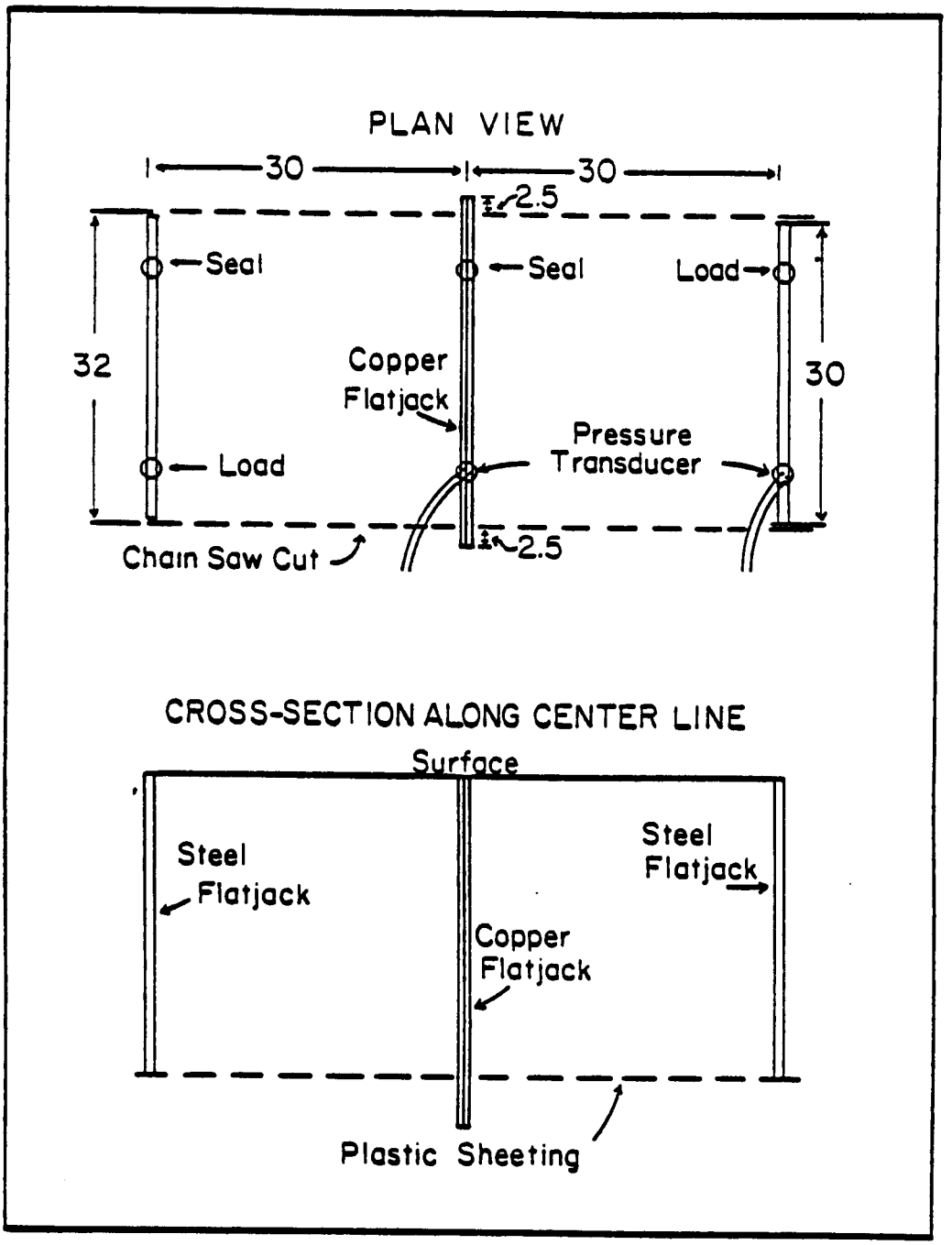

Figure 2.2-1 Plan view and cross-section of set-up for flatjack calibration experiment using copper flatjack. The dimensions are in cm.

configuration, the full surface area of the steel flatjacks, and most of the surface area of the copper flatjack, were in contact with the test block, while most of the edge of the copper flatjack (with the exception of the edge at the surface) was outside the test block, but confined in the surrounding ice. In its expanded condition, the copper flatjack then acted as a pressure sensor to the load transmitted through the ice from the steel flatjacks.

The steel flatjacks were loaded at rates of about 14 kPa/sec (2 psi/sec) and the internal pressure of the copper flatjack was recorded. The results are shown in Figure 2.2-2; the data points were acquired at 10 second intervals.

At the peak load the pressure in the steel flatjacks was held constant for about 1 minute, during which time the pressure in the copper flatjack drifted down. The drift may have been in response to the gradual closure of the copper flatjack as the fluid was squeezed toward the margins outside of the loaded surface. This was indicated by the formation of tension fractures at the tips of the copper flatjack.

The efficiency "e" of the steel flatjacks can be calculated from the equation

$$eP_s A_s = P_c A_c$$

where P_s and P_s are the internal pressures of the steel and copper flatjacks, A_s is the area of the steel flatjacks (30 x 30 cm) and A_c is the area of the copper flatjack which is in contact with the test block (30 x 32 cm). Over the linear portions of the loading segments of the curves in Figure 2.2-2 the slopes average 0.63. Thus, using $P_c = 0.63P_s$, the efficiency "e" is found to be 67% for the range of pressures from about 0.2 MPa (30 psi) to 1.38 MPa (200 psi). This is in agreement with the efficiency determined by Deklotz and Boisen (1970) for flatjacks of this size.

The nature of the experimental set-up required that the calibration be done at relatively low stresses. This was necessary to assure that the fluid was not squeezed entirely out of the part of the copper flatjack which was in contact with the test block. If this occurred, the copper flatjack would no longer serve as a pressure sensor.

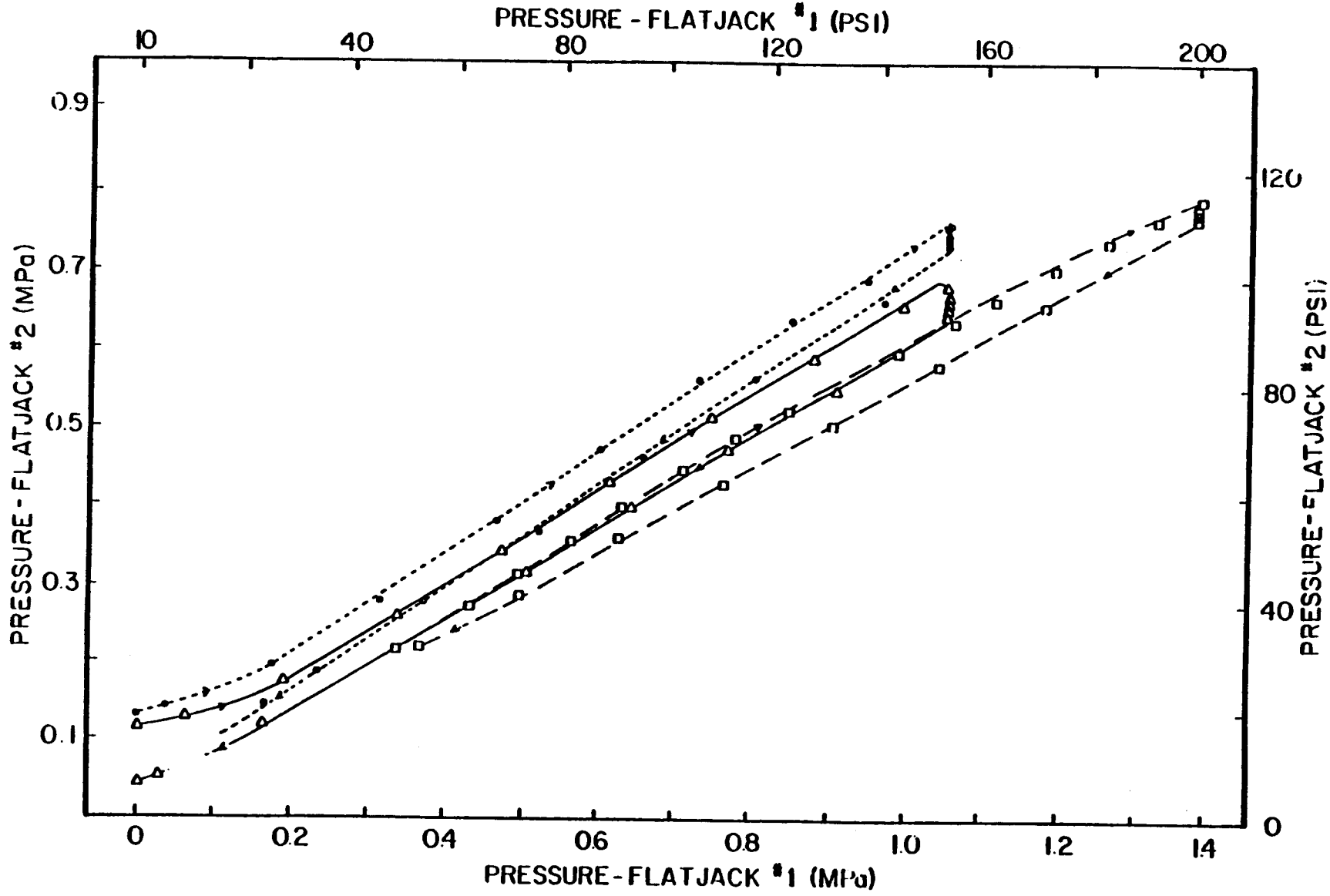

Figure 2.2-2 Results of calibration experiment. Flatjack #1 is the steel flatjack pair and flatjack #2 is the copper flatjack.

In order to extend the calibration to the higher loads reached in tests taken to failure of the ice, a second experiment was done using different equipment. The arrangement is shown in Figure 2.2-3. A load cell with a capacity of 1.03 GN (150,000 lbs) was placed in contact with the flatjack at one end of a uniaxial compression sample, through a spherical seat and a rigid plate with dimensions of 30 x 30 cm. The other end of the load cell was fixed to a reaction plate. The entire apparatus was enclosed in an aluminum box for ease of handling and emplacement.

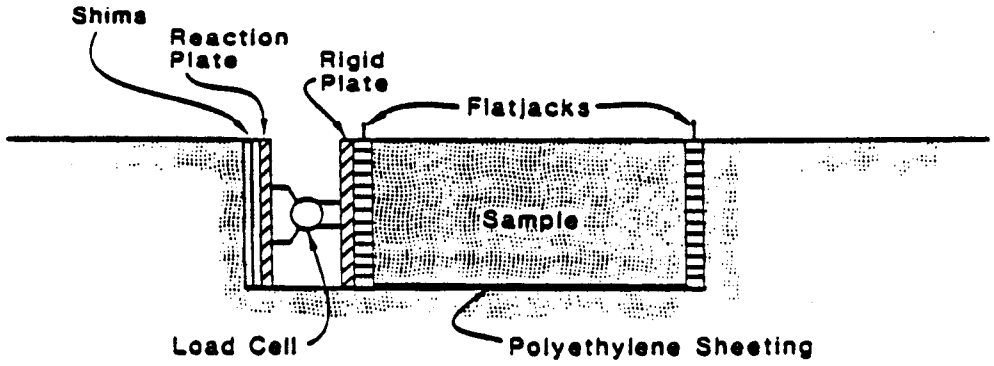

Figure 2.2-3 Cross-sectional view of the set-up for the second flatjack calibration experiment.

Once in position, the box was pressed close against the flatjack by shims driven between the reaction plate and the ice, so that the pressure exerted by the flatjack could be sensed by the load cell. The output from the load cell and the pressure transducer on the flatjacks was recorded on an X-Y recorder. The ratio between these values was the required measure of flatjack efficiency.

Experiments were done at several loading rates and the curves were generally repeatable. For flatjack pressures above about 1.38 MPa (200 psi), the output stress of the flatjacks was found to be represented by the equations

Output stress = 0.875 (flatjack pressure) - 0.24

in units of MPa, or

Output stress = 0.875 (flatjack pressure) - 35

in psi. For lower flatjack pressures the curves were similar to those determined in the first experiment. The slopes of the curves between 0.35 MPa (50psi) and 1.38 MPa (200 psi) give an efficiency of approximately 70%, compared to the 67% determined for this range of flatjack pressures in the first experiment.

The uniaxial compression test set-up requires that a double layer of polyethylene sheeting be installed at the base of the sample to reduce the shear stress between the sample and the ice sheet. This stress component was measured during the second calibration experiment by loading the flatjacks separately and attributing the difference in efficiency between the two flatjacks to the shear stress transmitted across the base of the sample. The result was about 2% of the flatjack pressure, so that the shear stress can be considered to be negligible.

2.2.2.3 Load Control

In all the experiments to determine ice properties, loading was done with high-pressure nitrogen gas from a pressurized gas bottle (initial pressure about 14 MPa or 2000 psi) controlled by a pressure regulator. Flatjacks at both ends of a test sample were loaded simultaneously and at the same rate. The load was controlled by monitoring the pressure at the gas bottle while the pressure in the flatjacks, which was used for stress calculation, was monitored by a pressure transducer mounted on the flatjacks. Comparison of the pressures measured at both sites indicated that the pressure drop in the line between them was always less than 1%.

In creep tests (which are run at relatively low constant loads), the pressure regulators proved capable of maintaining the desired pressures to within about 5% of the selected value for up to 12 hours. Thus, long-term tests could be run without the continuous presence of the experimenter

Creep-rupture tests (which require that a constant load be held until failure of the sample) were run using two different methods of load control depending upon the

anticipated time to the inflection point in the strain-time curve. In creep-rupture tests at low loads, the time required to apply the load is negligible compared to the time to the minimum strain rate, so that the load was applied by a hand-operated pressure regulator. At higher loads, the loading time can be significant with respect to the time to the minimum strain rate, so that it must be applied rapidly. For tests at high loads, a gas bottle was used as an accumulator and loaded to the desired test pressure. Then, the gas was released rapidly through a ball valve, so that the only limitation on the rate of loading was the rate at which the gas could flow into the flatjacks under the bottle pressure. A valving system was used to maintain the load through the pressure regulator after the desired test pressure was reached.

Most of the constant loading rate tests were also controlled by a pressure regulator. In this case it was operated by hand to control the rate of application of the load; the operator simply watched the time and pressure indicators and adjusted the pressure regulator so that the pressure followed a selected path with time. Loading rates that were accurate and repeatable to within a few percent were easily achieved in this manner, although the actual stress rates varied because of variations in sample size. The problem is discussed in Section 2.2.4.2.

Constant loading rate tests at rates greater than 20 MPA/sec (about 3000 psi/sec) were also run by using a ball valve to release the gas directly from a bottle at high pressure into the flatjacks

Flatjacks provide a relatively inexpensive and efficient tool for introducing controlled stresses into an ice sheet. The details of their installation for specific tests are given in the appropriate sections below.

2.2.3 DEFORMATION MEASUREMENTS

Strain measurements presented particular problems in this program because only the surface of the ice sheet was exposed for the installation of strain measuring

equipment. Restricting measurements to only one surface does not permit corrections to be made for bending of the sample due to misalignment of the loading surfaces. In the early stages of the field program, we attempted to overcome this problem by measuring strain using wire strain gages embedded in cylinders of ice to form "strain cells." The gages (either 2.5 cm or 1.25 cm long) were waterproofed and sealed with epoxy. They were then frozen into the centers of small cylinders prepared from fine chips of sea ice frozen together with water with a salinity of 6 parts per thousand. The cylinders (diameter 5 cm and length 10 cm) were then frozen into holes drilled in the ice samples with the strain gages oriented parallel to the sample axes to measure axial strain, or normal to the axis for measurement of lateral or vertical strain. The cylinders acted as inclusions of a relatively homogeneous material with properties similar to those of the surrounding normal sea ice. They deformed along with the sample when the load was applied. However, strain gages in the cylinders were in contact with many small, randomly oriented grains, so that the measured strain was not dominated by the deformation of a few large grains.

The strain gages prepared in this manner responded instantly to changes in load and generally provided repeatable results for small strains. However, the time required for preparation and installation of the gages made them impractical for use in a program involving a large number of tests. The technique could be useful in programs in which only a limited number of measurements are to be made, or when it is necessary to monitor the strain variation through the entire thickness of a sample or an ice sheet

An alternative method of monitoring strain was developed for use in the uniaxial compression testing program, because the data were needed for identifying the inflection point in creep-rupture tests. The method involved the use of linear potentiometers (LP's) attached to pegs frozen into the surface of the sample, so that, as explained above, the measurements could not be corrected for bending.

The depth to which the pegs can be sunk varies with the sample size because, if sunk too deeply, the pegs tend to reinforce the strength of the ice by restricting vertical expansion of the sample during loading. For the 30-cm-thick samples used in the uniaxial testing program, experiments showed that the pegs had no effect on the strength if they were sunk to depths of 12 cm or less. Observations of samples during and after testing showed that no identifiable patterns of fractures were associated with the pegs.

The arrangement of the LP's for uniaxial tests (described in Section 2.2.4.1) is shown in Figure 2.2-4. The slide bars of the LP's were held firmly to a flat plate by springs, which left them free to rotate if the pegs rotated outward as the sample surface expanded vertically. The LP's were calibrated for displacements of 1 part in 10^{-5}, so that over the gauge length of 20 cm, strains on the order of 10^{-6} could be measured.

The geometric relations used in calculating the strain from displacement measurements are shown in Figure 2.2-5. The strain δ_d is calculated from the equation

$$\delta_d = \delta_l - [(a-d)/(b-a)](\delta_u - \delta_l)$$

where a and b are the heights from the ice surface of the lower and upper LP's respectively (5 and 20 cm in Figure 2.2-4), d is the depth at which the strain is calculated and δ_l and δ_u are the displacements of the lower and upper LP's. Note that this equation is derived on the assumption that the LP's remain horizontal during deformation. However, it can be shown that for small strains, only a minor correction is required to correct for peg rotation out of vertical as the surface of the sample bends upward. For simplicity, the correction was neglected.

The strain measuring system shown in Figure 2.2-4 proved to be easy to set up in the field, and the instrumentation was sufficiently rugged to withstand repeated use.

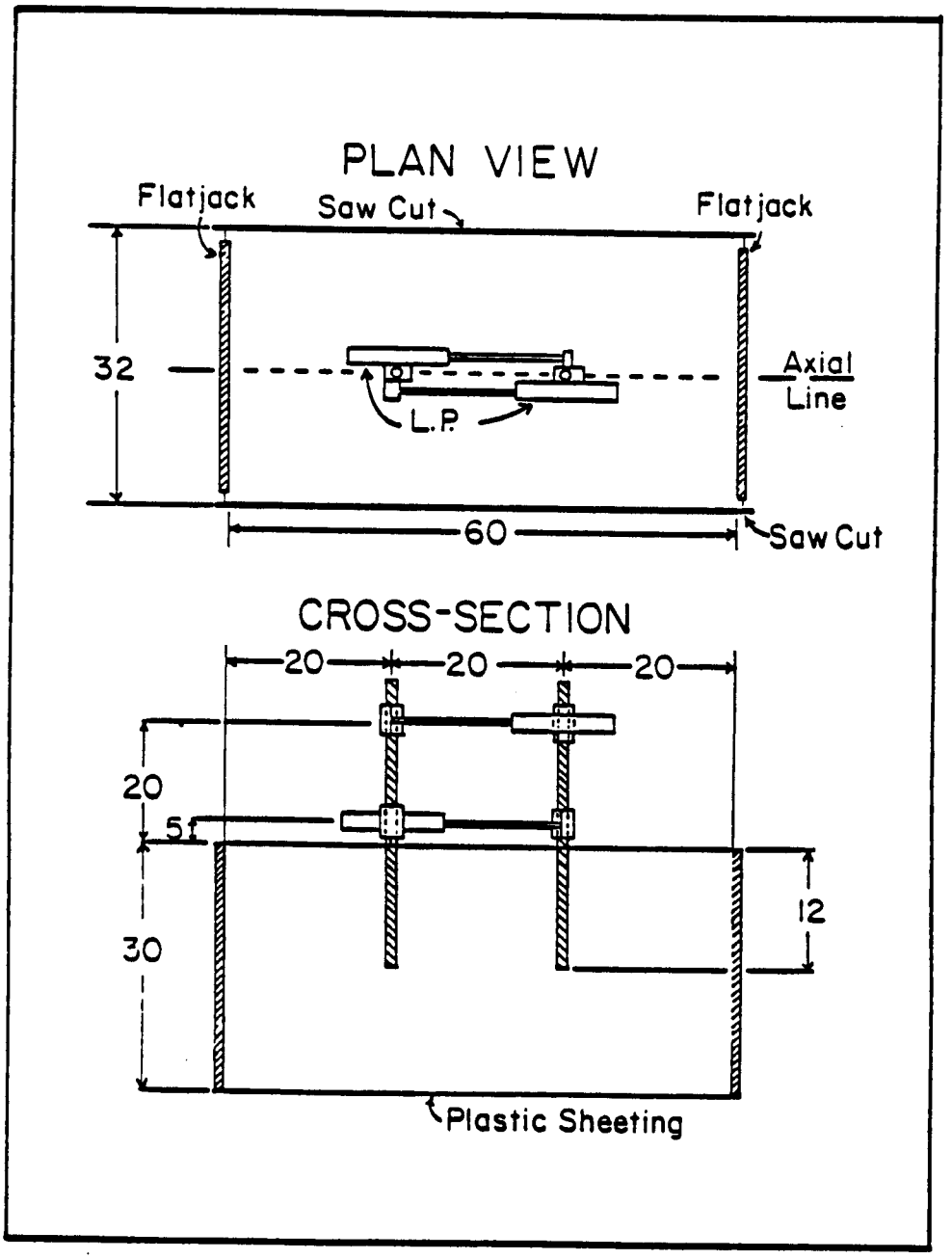

Figure 2.2-4 Set-up for a uniaxial compression test illustrating the placement of linear potentiometers on pegs frozen into the sample. Dimensions are in cm.

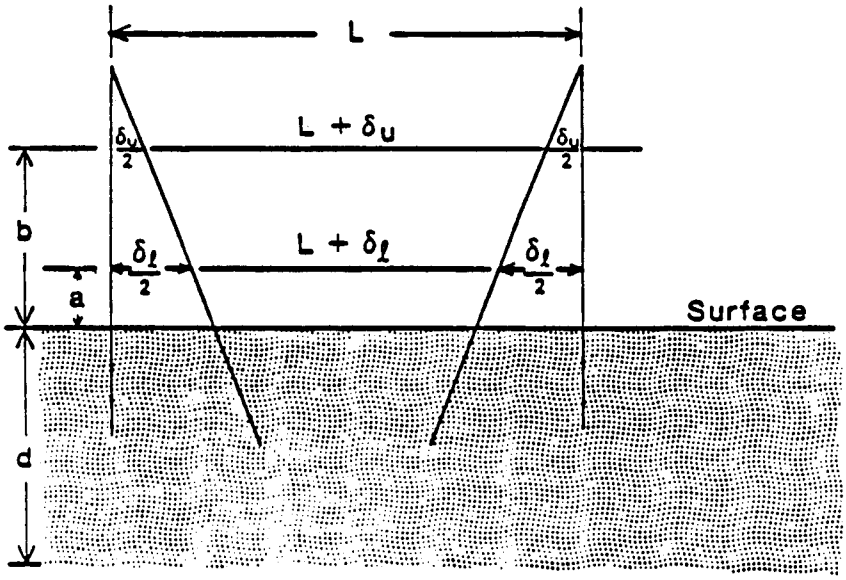

Figure 2.2-5 Geometric relationships between the pegs and linear potentiometers used for strain calculations. a and b are the heights of the lower and upper LP's respectively in Figure 2.2-4, and d is the depth at which the strain is calculated.

2.2.4 UNIAXIAL COMPRESSION TESTS

2.2.4.1 Sample Preparation

Uniaxial compression test procedures were developed using specimens in two geometries: triangular prisms and rectangular prisms. In the former, triangular flatjacks are installed in the ice as shown in Figure 2.2-6. After freezing, chain saw cuts are made connecting the ends of the flatjacks and dipping into the ice sheet parallel to the edges of the jacks. This isolates a triangular prism of ice which is attached to the ice sheet only through the flatjacks at the ends of the sample. The test is relatively easy to set up using flatjacks of any size. However, it can be difficult to control the angle of the chain saw cuts to assure that the test specimen has smooth, straight sides. In addition, there are uncertainties in

interpreting the results of the tests, because of the unusual geometry of the samples in relation to the ice fabric.

All of the data reported in the next section were done using test specimens in the form of rectangular prisms with dimensions of 30 x 32 x 60 cm. Most were collected from the surface of the ice sheet. Therefore, they included the slush layer, with a maximum thickness of 10-15 cm, consisting of fine-grained ice with random c-axis orientation. Most of the remainder of the samples was ice of the transition zone between the slush layer and the columnar ice zone below. In general, the ice in the transition zone shows a tendency to increase in grain size with depth and to take on the preferred orientation (if present) of the c-axes of the crystals of the columnar zone. In a few cases, the ice at the base of the samples (30 cm depth) might properly have been classified as part of the columnar zone, but the bulk of any particular sample was always in the slush layer and transition zone. For consistency, samples were always oriented along the dominant direction of c-axis orientation in the columnar zone.

The completed test set up is shown in Figure 2.2-7. To prepare it, samples about 40 cm wide were cut from the surface of the ice sheet and trimmed to a thickness of 30 cm and a length of 60 cm. Cutting was done with a chain saw and various methods were used to assure that the sample ends were parallel and at a right-angle to the base of the sample. This could not be done to the degree that would be expected in laboratory tests. However, the results of experiments done under similar conditions were generally repeatable, indicating that variations between samples were relatively minor.

After a sample was removed from the ice sheet, the bottom of the hole from which it was taken was filled with fresh water leaving a depth of 30 cm. When the water was frozen, a double layer of plastic sheeting was placed at the bottom of the hole and the test block was replaced. The plastic sheeting provided a low friction

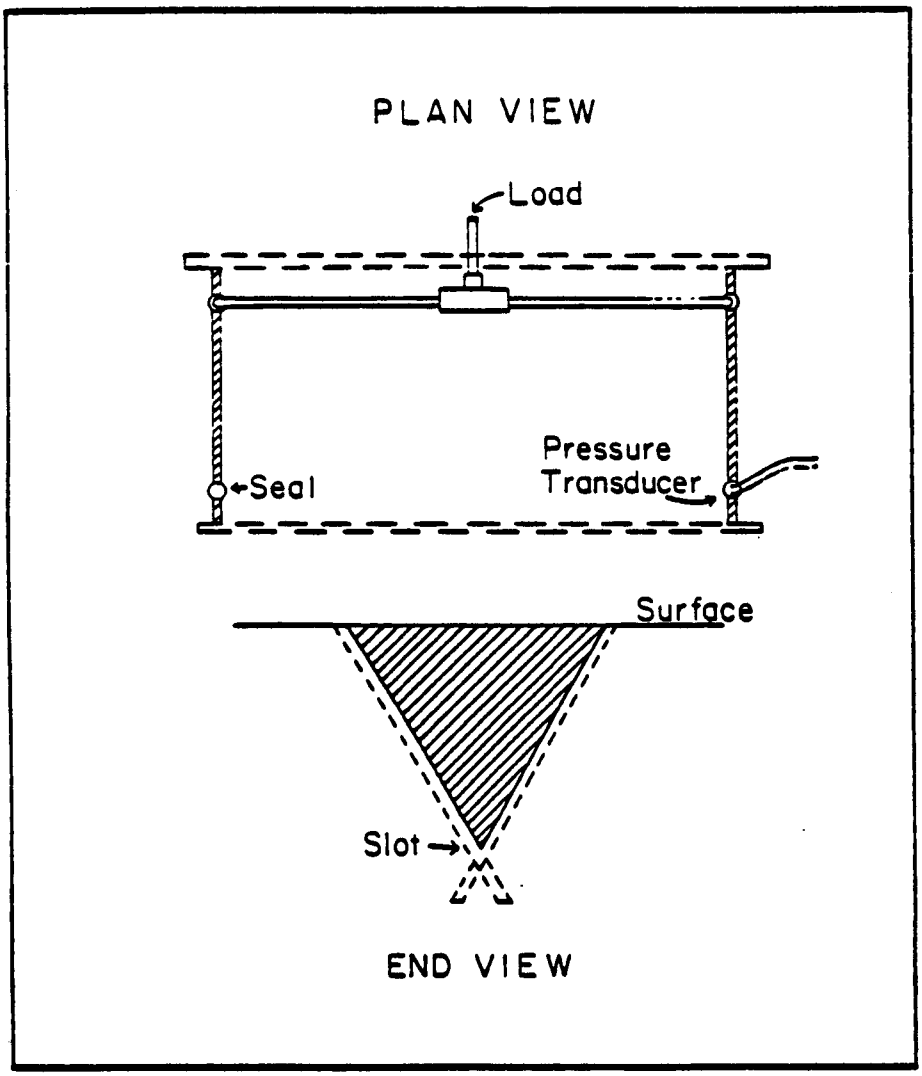

Figure 2.2-6 Plan and end views of uniaxial compression test set-up using triangular flatjacks.

boundary at the base of the test block, across which only minimal shear stress could be transmitted (see discussion of calibration in Section 2.2.2.2). Flatjacks (30 x 30 cm) were placed at the ends of the sample and fresh water was added to fill the void spaces around the test block and flatjacks. Pegs for attachment of LP's for strain measurement were then installed. The samples were then left for a minimum of several days to come to temperature equilibrium with the ice sheet (Shapiro and Hoskins, 1975) so that testing was done at the ambient temperature gradient.

2.2.4.2 Test Procedures

In order to conduct a test, the sides of the sample were cut loose from the surrounding ice sheet by removing thin slabs of ice with a chain saw. An allowance of about 1 cm was made on each side of the sample to provide clearance so that the flatjacks were not damaged by the chain saw during cutting. Thus, the final sample width was approximately 32 cm (the actual width of each sample was measured so that the cross-sectional area could be used for calculating the stress). Prepared in this manner, the sample was isolated from the ice sheet along the sides, free at the upper surface, and rested on a base across which friction was low. In most tests the flatjacks were also wrapped with double layers of plastic sheeting to reduce friction on the sample ends. On loading, the degree to which uniaxial compression was approximated depended upon the ease with which the sample could expand upward, particularly at the sample ends. Vertical expansion always occurred (except in tests at high rates of loading), but we were not able to measure it.

As noted in Section 2.2.2.3, the loading system was capable of controlling the rate of increase of internal flatjack pressure so that the curves of flatjack pressure vs. time were virtually identical for different tests at the same rates. However, the actual stress rates varied, because of the need to account for variations in width between samples for stress calculations. As an example, tests at a loading rate of 6.9

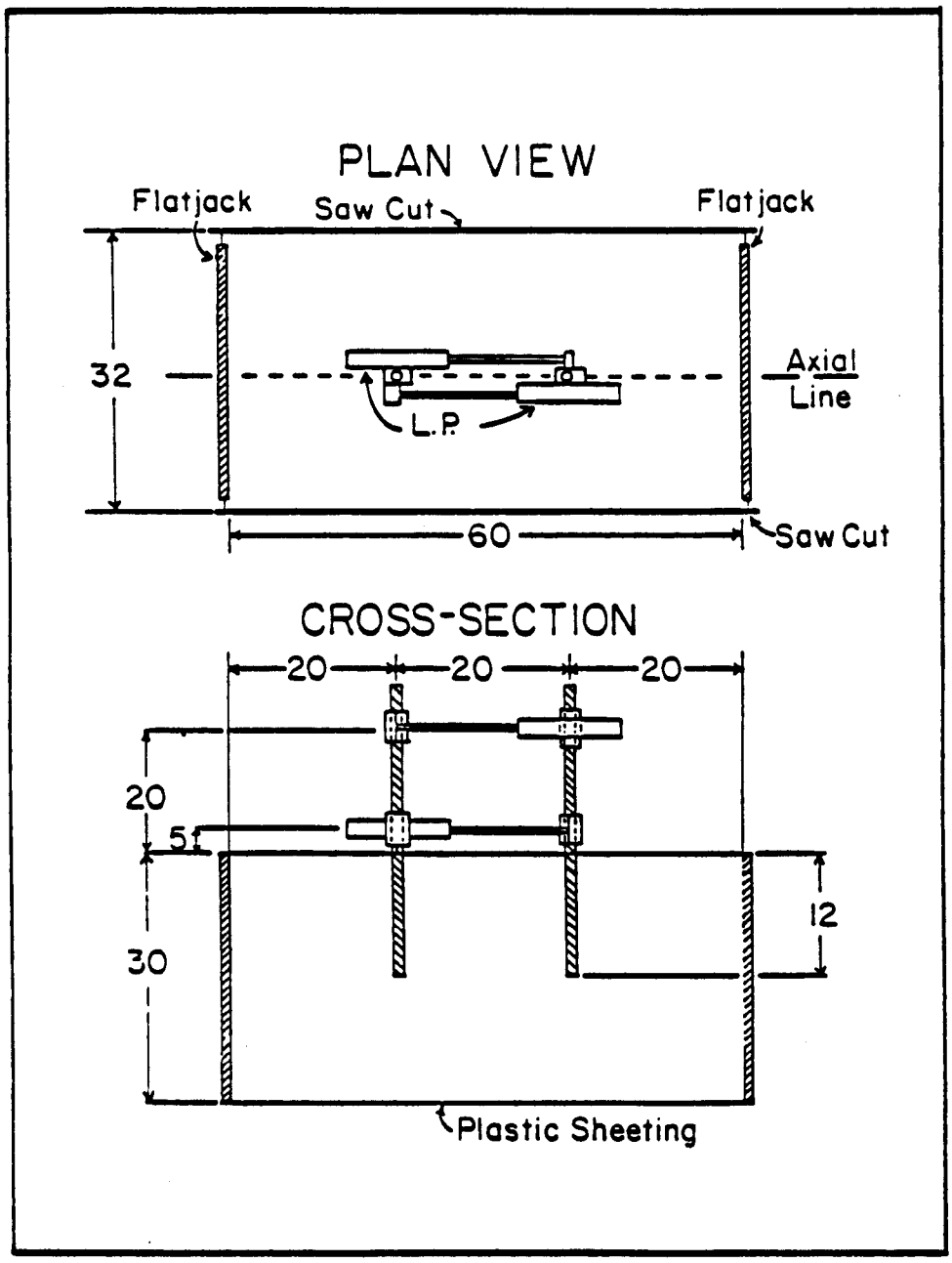

Figure 2.2-7 Set-up for a uniaxial compression test using a 30 x 30 x 60 cm test sample (same as Figure 2.2-4).

kPa/sec (1 psi/sec) for flatjack pressure gave actual stress rates from about 4.9 to 5.3 kPa/sec.

The combined use of flatjacks to apply load and the ice sheet as a loading frame gives the effect of a "soft" testing machine, so that samples tend to fail explosively. However, it is not the release of strain energy stored in the ice sheet or the samples which causes failure in this manner. Instead, it results from the fact that as failure is approached the sample weakens and loses the capability to resist load. The deformation rate then increases rapidly, reducing the constraint on the flatjacks. This permits the flatjacks to expand rapidly with an accompanying stress drop. The operator must then increase the rate of gas flow in order to keep the stress-rate constant up to the point of failure. It was usual for the operator to have no more than one or two seconds of warning that the sample was about to fail. If it was not possible to stop the flow of gas and release the internal flatjack pressure within that time, the flatjacks would expand rapidly and fail explosively, shattering the sample. Thus, examination of samples for indications of the failure mechanisms was generally not possible, other than in a few cases in which pressure was released quickly enough to save the sample. However, in tests at very high loading rates the samples generally failed along a few (or one) long cracks which traversed the sample, with only minor shattering at the sample ends. Observations of failure mechanisms are given in Section 2.2.4.6.2.

2.2.4.3 Temperature and Salinity Measurements

The large number of tests run made it impractical to measure the temperature profile of each sample at the time it was tested. Instead, a thermister string (with thermisters at the surface and at depths of 10, 20 and 30 cm) was installed at a central location within the test area. The ice surface at its location was regularly

cleared of snow to simulate test conditions. The readings from these thermisters at the time a test was run were averaged to give the test temperature.

Salinities were determined by collecting a column of ice 5 x 5 x 30 cm deep adjacent to each sample at the completion of a test. Each column was cut into 5 cm cubes and the salinity was determined for each cube. The results were then averaged to give an average salinity for the sample. The validity of the method was checked by dividing one sample block into columns as described above, and determining the range of salinities of these. The result showed that the salinity variation between the columns within the single test sample was greater than that between the representative columns for the individual test blocks through the entire field season, indicating that the method was appropriate.

2.2.4.4 Acoustic Emissions

We conducted a short pilot program of monitoring rates of acoustic emissions indicating sample cracking. The intent was to use simple, available equipment for a feasibility study to determine whether usable data on fracture rates could be obtained during field testing. If so, the tests were to regularly include such measurements to provide additional data for interpretation of failure mechanisms. The results were promising, but the project was terminated before the equipment could be upgraded to provide data of the required quality.

For the pilot program, no attempt was made to determine the sensitivity of the equipment to small cracking events. However, the system certainly recorded events which were inaudible to an observer standing near the test samples.

The data were taken by freezing a piezoelectric crystal to the surface of a test sample, and recording its output on a strip chart recorder. An event counter would have been more desirable for the purpose, but we were unable to acquire one because of budget limitations. The strip chart recorder was adequate for discriminating

individual events at low rates of cracking. Each event was recorded as a peak on the output chart. However, the rate at which the pen recovered toward zero after each event was slow compared to the time between events, so that it seldom reached the zero line before the next event occurred. As a result, the pen migrated across the chart and eventually became pinned (usually at 50 to 60% of peak load) so that individual events could no longer be discriminated.

The results suggest that, given proper recording equipment, measuring acoustic emission rates on samples in the field is no more difficult than doing so in the laboratory (as described, for example, by St. Lawrence and Cole, 1982).

2.2.4.5 Results of Experiments in Uniaxial Compression

The results of all experiments in uniaxial compression on rectangular prisms are presented in Tables 2.2-1 to 10. Samples were first year ice, except for those listed in Table 2.2-5. The reported values of strength or applied stress were calculated from the measured flatjack pressures using the equation

$$\sigma_c = (P \times A_f)/(A_s)$$

where P is the output stress of the flatjack as determined from the calibration equation (Section 2.2.2.1), A_f is the area of the flatjack and A_s is the cross-sectional area of the sample. Stress rates were calculated as the strength divided by the time-to-failure. The values should be close to the true loading rates because, as noted in Section 2.2.2.4, loading curves were generally linear and repeatable. The methods of measuring the average temperature and salinity for each sample were given in Section 2.2.4.3. The average brine volume (v_{ave}) was calculated from the equation

$$v_{ave} = S_{ave}\,(0.532 - 49.15/T_{ave})$$

where S_{ave} and T_{ave} are the average salinity and temperature.

Note that the time measurements in the tables are given in different degrees of precision for different tests. The variation reflects the fact that different methods were used, depending upon the expected duration of a particular test.

Procedures used in setting up individual tests varied through the first year of the program as new materials or methods were introduced. These are described in the keys to the column labeled "Set-up" in Tables 2.2-1 to 3; the key is given at the end of Table 2.2-3. In subsequent field seasons all tests were done with the set-ups described in either note 4 or 6 of the key.

The comments in the tables record particular features of some of the tests. As an example, after some creep tests, the sample was allowed to relax for some time, and then loaded as a constant loading rate test. The purpose was to attempt to evaluate the effect of possible strain softening (or hardening) during creep. However, the results were in consistent. Similarly, if one flatjack on a sample failed (by splitting along one edge) before the sample failed, the test was usually completed with the one remaining flatjack. The results of these tests are presented here for the sake of completeness; none are used in the discussion of the results (Section 2.2.5.6).

The presence of thin silt layers (which were of various thicknesses, depths and lateral extent) in the samples is also noted in the comments. These were always associated with layers of fine-grained ice which served to break the smooth downward transition from slush ice to columnar ice. The presence of silt layers had the apparent effect of increasing the strength of the samples by up to (about) 20% over silt-free samples tested under the same conditions. There are not enough examples to permit any relationships to be established between the distribution and thickness of the silt layers and the specific increase in strength. Hence, the data are not included in the discussion in Section 2.2.5.6.

TABLE 2.2-1

RESULTS OF CONSTANT LOADING-RATE TESTS IN UNIAXIAL COMPRESSION - 1978

Sample Number	Peak Stress (MPa)	Time to Peak Stress (sec.)	Stress Rate (kPa/sec.)	Average Temp. (-°C)	Average Brine Volume $\sqrt{v}$ (ppt)	Set-up (see key after Table 2.2-3)	Comments
1	3.90	25.0	156	14.9	5.13	1	
2	2.17	1.4	1550	6.5	7.50	1	
8	2.22	420	5.29	9.8	6.37	1	Silt 8-12 cm
10	3.56	65.0	54.8	9.6	6.26	1	
15	2.07	390	5.31	11.5	5.74	1	
16	3.95	2.5	1580			1	
17	3.68	3.0	1230			1	
18	2.95	575	5.13	11.5	5.92	1	Break in loading curve at 2.46 MPa, 480 sec.
20	3.56	2.6	1370	10.3	5.92	1	
21	3.68	6.8	540	10.3	6.02	1	
22	3.68	82.5	44.5	10.0	5.73	1	
23	3.04	116	26.2	10.3	6.05	1	
24	3.40	21.8	156	10.3	6.01	1	
25	1.70	4200	0.41			1	
26	3.65	6.4	570	11.5	5.71	1	
27	3.40	24.8	137	10.3	5.94	1	
28	3.95	1.0	3950			1	
29	3.00	0.072	4.17×10^4	13.2	5.26	1	
30	3.10	0.4	7760	12.4	5.68	1	
31	4.21	7.5	562	11.5	5.66	1	
32	4.29	0.48	8930	13.2	5.29	1	
33	3.79	0.11	3.45×10^4	13.1	5.46	1	
34	3.45	0.15	2.30×10^4	14.0	5.29	1	

TABLE 2.2-1 (Cont'd)

Sample Number	Peak Stress (MPA)	Time to Peak Stress (sec.)	Stress Rate (kPa/sec.)	Average Temp. (-°C)	Average Brine Volume $\sqrt{v}$ (ppt)	Set-up (see key after Table 2.2-3)	Comments
36	4.01	20	201	19.8	4.49	2	2nd loading after rupture of one flatjack at low stress
37	3.00	578	5.19	19.8	4.51	2	
39	5.07	0.18	2.82×10^4	19.4	4.44	2	
40	3.95	0.14	2.82×10^4	19.4	4.42	2	
43	4.62	0.16	2.89×10^4	12.7	5.30	6	
47	3.58	677	5.29	14.3	5.39	6	Previous creep test at 0.61 MPa for 24 hrs.
48	2.33	5476	0.43			6	Previous creep test at 0.62 MPa for 18 hrs.
50	4.66	1.50	31.1	18.8	4.71	6	Previous creep test at 0.81MPa for 20 hrs.
55	1.92	387	4.97	7.4	6.96	6	
61	2.59	514	5.04	18.4	4.55	6	
62	1.72	360	4.91	6.5	7.31	4	[1]Rotated 90°
63	1.83	374	4.89	7.1	7.17	4	
64	2.59	102	25.4	6.5	7.31	4	[1]Rotated 90°
65	1.87	385	4.85	7.0	7.13	4	
68	1.94	405	4.78	10.5	6.15	6	[2]Composite block, lower halves
69	2.24	463	4.84	9.9	6.24	6	[2]Composite block, upper halves

TABLE 2.2-1 (Cont'd)

Sample Number	Peak Stress (MPa)	Time to Peak Stress (sec.)	Stress Rate (kPa/sec.)	Average Temp. (-°C)	Average Brine Volume $\sqrt{v}$ (ppt)	Set-up (see key after Table 2.2-3)	Comments
70	2.45	489	5.01	9.8	6.20	6	[2]Composite block, upper halves
71	1.87	385	4.85	9.9	6.24	6	[2]Composite block, lower halves
77	1.41	3333	0.422	9.5	6.20	6	
79	1.90	390	4.86	8.8	6.38	6	
86	2.32	463	5.00	8.4	6.58	5	Silt zone 7.5-23 cm
87	1.87	376	4.97	8.3	6.55	5	
88	1.85	373	4.97	8.1	6.48	5	
90	1.88	385	4.89	8.3	6.58	6	
91	2.54	48.8	52.0	7.9	6.77	6	
93	2.07	418	4.95	8.1	6.95	6	
94	2.11	424	4.98	8.3	6.76	6	Silt zone 5-20 cm
95	1.90	384	4.96	8.1	6.41	6	
98	1.81	372	4.86	7.0	7.23	6	Tested 3 min. after unloading constant load test at 0.33 MPa for 55,800 sec.; minimum strain rate at 39,900 sec.

TABLE 2.2-1 (Cont'd)

Sample Number	Peak Stress (MPa)	Time to Peak Stress (sec.)	Stress Rate (kPa/sec.)	Average Temp. (-°C)	Average Brine Volume $\sqrt{v}$ (ppt)	Set-up (see key after Table 2.2-3)	Comments
103	2.36	48.0	49.1	5.9	7.43	6	
104	2.12	15.3	138	5.9	7.74	6	
108	1.86	378	4.93	5.6	7.72	6	Previous creep-rupture test at 0.33 MPa for 58,800 sec.; minimum strain-rate at 40,200 sec.
109	2.47	15.0	165	6.0	7.69	6	
110	2.90	5.0	579	7.7	6.42	6	Thin silt band at 15 cm
111	2.56	3.5	733	7.0	6.90	6	
112	2.27	85.0	26.7	7.0	7.05	6	
113	2.32	1.5	1540	6.9	7.15	6	
114	2.01	1.5	1340			6	
115	2.73	1.4	1950			6	
116	2.34	1.4	1670			6	Silt band 10-20 cm
117	2.23	4.5	495	7.2	6.93	6	
118-1	2.52	500	5.03			6	1st loading, one flatjack failed
118-2	3.89	85.0	45.8			6	2nd loading, with one remaining flatjack
119	4.54	109	41.7			6	

1. Sample rotated 90° about long axis.
2. Composite samples prepared by freezing together the top 15 cm (slush ice zone) and the bottom 15 cm (transition zone) of two samples to form composite samples of both zones.

TABLE 2.2-2

RESULTS OF CREEP-RUPTURE TESTS IN UNIAXIAL COMPRESSION - 1978.

Sample Number	Stress (MPa)	Time to Min. Strain rate (sec)	Time to Rupture (sec)	Strain at Minimum Strain rate	Minimum Strain rate	Average Temp (-°C)	Average Brine Vol. $\sqrt{v}$ (ppt)	Set-up (see key after Table 2.2-3)	Comments
5	1.11		590			10.4	5.76	1	
9	1.66		40			9.8	6.34	1	
11	3.34		3.8			9.6	6.32	1	Silt 5-15 cm
14	3.01		10			11.5	5.72	1	
19	1.90		70			11.5	5.85	1	
35	1.45		900			10.0		2	
38	1.45		820			17.3	4.79	2	
42	2.34	20	230	1.6×10^{-3}	3.2×10^{-5}	18.4		6	
44	2.94		55			18.5		6	
46	0.89	3070	>18,000	3.9×10^{-3}	8.4×10^{-7}	16.0	4.96	6	
49	2.34		1080			18.4	4.60	6	
51	2.99	20	170	1.4×10^{-3}	1.6×10^{-5}	20.5	4.43	6	Silt 10-22 cm, previous creep test, 0.2 MPa for 58,900 sec.
52	1.23	410	1085	2.0×10^{-3}	3.7×10^{-6}	20.0	4.49	6	
53	1.17		6960			20.0	4.52	3	
58	1.55	264	735	3.4×10^{-3}	1.3×10^{-5}	16.0	4.92	6	
59	2.34	50	400	2.2×10^{-3}	1.6×10^{-5}	18.9	4.41	6	Silt 10-22 cm, previous creep test, 0.66 MPa for 27,000 sec.

TABLE 2.2-2 (Cont'd)

Sample Number	Stress (MPa)	Time to Min. Strain rate (sec)	Time to Rupture (sec)	Strain at Minimum Strain rate	Minimum Strain rate	Average Temp (-°C)	Average Brine Vol. V_v (ppt)	Set-up (see key after Table 2.2-3)	Comments
60	2.62	10	100	1.1×10^{-3}	4.1×10^{-5}	18.0	4.73	6	
66	1.72		86			7.6	6.76	6	
67	1.72	13	53	1.8×10^{-3}	1.1×10^{-4}	7.3	6.73	6	
72	1.45	20	140	1.8×10^{-3}	3.1×10^{-5}	7.1	7.26	6	
73	1.45	10	130	9.2×10^{-4}	4.3×10^{-5}	7.2	6.95	6	
76	1.40	30	245	1.5×10^{-3}	7.4×10^{-6}	9.1	6.47	6	
78	1.61	50	175	2.1×10^{-3}	2.6×10^{-5}	8.8	6.35	6	
81	1.17	440	1240	5.5×10^{-3}	1.7×10^{-5}	11.1	6.00	6	
82	1.19		683			10.8	6.18	6	
83	1.33	130	>305	4.2×10^{-3}	4.2×10^{-5}	7.5	6.90	6	
92	1.04	260	716	4.5×10^{-3}	1.7×10^{-5}	7.3	7.16	6	Silt, 10-20 cm
96	2.01	10	37	$1.2\,10^{-3}$	5.0×10^{-5}	5.5	7.78	6	Silt, 5-17 cm
97	1.62	46	174	1.8×10^{-3}	2.8×10^{-6}	7.0	7.37	6	
98	0.33	34900	>55800	8.5×10^{-4}	8.1×10^{-9}	7.0	7.25	6	
99	0.85	480	3127	2.7×10^{-3}	3.3×10^{-7}	6.9	7.14	6	
100	1.87	15	49	1.4×10^{-3}	9.6×10^{-5}	6.5	7.36		
108	0.33	40200	>58800	4.1×10^{-4}	1.7×10^{-8}	6.5	7.74	6	

TABLE 2.2-3

RESULTS OF CREEP TESTS IN UNIAXIAL COMPRESSION - 1978.

Sample Number	Stress (MPa)	Strain rate (sec^{-1})	Test Duration (sec)	Average Temp (-°C)	Average Brine Volume $\sqrt{v}$ (ppt)	Set-up (see key below)	Comments
3	0.41		66,600	13.6	5.5	1	
41	0.67	9.06×10^{-8}	63,000	10.0		6	
47	0.48	9.69×10^{-9}	81,900	14.3	5.39	6	
48	0.49	1.11×10^{-8}	60,320	18.5		6	
50	0.67	1.64×10^{-8}	64,800	18.1	4.71	6	
51	0.22	5.99×10^{-9}	58,900	19.0	4.43	6	Silt zone 10-18 cm
53	0.12		40,000	19.9	4.50		
54	0.33		36,000	18.0		6	
57	0.43	5.25×10^{-8}	90,600	13.0	5.30	6	
59	0.66		27,000	18.9	4.40	6	
74	0.10	6.56×10^{-9}	127,800	10.9	6.17	6	
75	0.28	1.42×10^{-8}	91,100	9.2	6.38	6	
80	0.67	2.35×10^{-7}	37,000	10.7	6.12	6	

Set-up Key:
1. No plastic sheeting on flatjacks; wooden pegs, 1.3 cm diameter, 20 cm deep.
2. Plastic sheeting on flatjacks; wooden pegs 10 cm deep.
3. Plastic sheeting on flatjacks; aluminum pegs 1.3 cm diameter, 20 cm deep.
4. Plastic sheeting on flatjacks; no pegs.
5. No plastic sheeting on flatjacks; aluminum pegs 12 cm deep.
6. Plastic sheeting on flatjacks; aluminum pegs 12 cm deep.

TABLE 2.2-4
RESULTS OF CONSTANT LOADING-RATE TESTS
IN UNIAXIAL COMPRESSION - 1979.

Sample Number	Peak stress (MPa)	Time to peak stress (sec)	Average stress rate (kPa/sec)	Average temp. (-°C)	Average Brine Volume $\sqrt{v}$ (ppt)	Comments
1	3.28	645	5.08	23.9	3.69	
2	3.72	711	5.24	23.8	3.86	
3	5.45	0.9	6060	20.8	3.96	1 Flatjack
5	5.69	1.3	4380	20.4	3.78	
6	3.34	671	4.98	18.0	4.21	Previous creep-rupture test at 0.90 MPa, minimum strain-rate at 14,640 sec.
7	5.40	22.8	237	19.3	3.86	
8	6.05	24.0	252	18.9	3.97	Previous creep test at 0.96 MPa for 75,300 sec.
9	5.89	0.33	17800	18.5	4.12	
10	6.26	1.73	3620	19.0		
11	4.67	99	47.2	17.9	4.32	
12	4.56	96	47.5	18.5	4.18	
15	6.18	25	251.0	18.3	4.22	Previous creep test at 0.62 MPa for 47,800 sec.
16	3.24	600	5.4	17.9	4.30	Previous creep test at 0.68 MPa for 51,300 sec.
28	6.68	0.48	13900	16.1	4.38	
30	4.63	84	55.2	15.9	4.56	
35	6.21	24	259	18.4	3.98	
36	3.51	664	5.29	18.4	3.98	
42	4.46	19	235	12.3	4.77	

TABLE 2.2-4 (Cont'd)

Sample Number	Peak stress (MPa)	Time to peak stress (sec)	Average stress rate (kPa/sec)	Average temp. (-°C)	Average Brine Volume $\sqrt{v}$ (ppt)	Comments
43	2.87	550	5.22	11.8	4.82	
44	4.21	15	274	12.5	4.78	
46	2.61	495	5.28	6.0	6.82	
47	3.16	61	51.9	5.5	6.99	
48	2.11	420	5.02	4.8	7.40	
50	1.74	4350	0.40	6.0	6.74	Previous creep test at .36 MPa for 28,000 sec.
60	3.92	72	54.4	5.9	6.76	Low (?); -gas ran out during test
61	4.20	16	262	3.8	8.76	
62	4.27	17	251	3.3	9.31	
63	2.25	0.15	15000	2.7	10.02	Low; peak stress not recorded
64	3.98	0.40	9950	3.0	9.50	
65	4.37	0.40	10900	2.5	10.15	
68	1.76	3960	0.44	3.6	8.62	

TABLE 2.2-5

RESULTS OF CONSTANT LOADING-RATE TESTS IN COMPRESSION - 1979, MULTI-YEAR* ICE.

Sample Number MY-	Peak stress (MPa)	Time to peak stress (sec)	Average stress rate (kPa/sec)	Average Temp. (-°C)	Comments
1	4.76	95	50.1	20.0	
2	2.72	518	5.24	14.0	
3	1.94	4518	0.43	11.2	
4	2.68	503	5.32	13.8	
5	4.26	15	284	3.3	
7	5.65	0.75	7540	2.0	
8	3.63	69	52.6	5.7	
9	2.41	478	5.03	5.9	
10	2.28	456	5.00	5.5	
11	3.69	66	55.9	5.3	
12	4.87	0.59	8250	3.0	
13	1.50	3510	0.43	3.0	
14	4.37	16	273	3.0	
15	1.67	3990	0.42	3.4	

*Salinity <0.2 ppt for all samples.

TABLE 2.2-6
RESULTS OF CREEP-RUPTURE TESTS IN UNIAXIAL COMPRESSION - 1979

Sample Number	Stress (MPa)	Time to min. strain rate (sec.)	Time to rupture (sec.)	Strain at min. strain rate	Minimum strain rate (sec^{-1})	Average Temp. (°C)	Average Brine Volume $\sqrt{v}$ (ppt)	Comments
4	1.19	5770	>14460	5.7×10^{-3}	6.23×10^{-7}	16.2	4.35	
6	0.90	14640		2.2×10^{-3}	9.11×10^{-8}	16.8	4.06	
37	1.48	840	>5007	2.4×10^{-3}	2.18×10^{-6}	15.8	4.42	
38	2.04	220	878	2.9×10^{-5}	1.18×10^{-5}	16.6	4.28	
39	2.59	135	340	2.6×10^{-3}	1.35×10^{-5}	19.0	4.11	
41	1.79		2384			14.3	4.57	

TABLE 2.2-7
RESULTS OF CREEP TESTS IN UNIAXIAL COMPRESSION - 1979

Sample Number	Stress (MPa)	Strain rate (sec^{-1})	Test Duration (sec.)	Averager Temp. (-°C)	Average Brine Volume $\sqrt{v}$ (ppt)
8	0.96	4.12×10^{-8}	75,300	17.6	4.09
14	0.86	1.67×10^{-8}	202,200	17.6	4.04
15	0.62	2.41×10^{-8}	47,800	17.8	4.22
16	0.68	2.12×10^{-8}	51,300	18.0	4.30
45	0.53	6.78×10^{-9}	147,100	13.9	4.72

TABLE 2.2-8
RESULTS OF CONSTANT LOADING, RATE TESTS IN UNIAXIAL COMPRESSION - 1979; VARIATION WITH DEPTH AND ORIENTATION

[1]Loading Direction (deg)	[2]Column Number	Depth range (cm)	Peak stress (MPa)	Time to peak stress (sec)	Average stress rate (kPa/sec)	[3]Average Brine Volume $\sqrt{v}$ (ppt)
0°	1	0-30	3.45	65	53.0	9.36
		30-60	3.97	76	52.3	9.26
		60-90	4.05	76	53.3	9.16
0°	2	0-30	3.54	67	52.8	9.36
		30-60	4.06	81	50.1	9.26
		60-90	4.46	83	53.7	9.16
0°	3	15-45	3.36	65	51.7	9.19
		45-75	4.49	86	52.2	9.20
		75-105				
0°	4	15-45	3.41	63	54.2	9.19
		45-75	4.07	78	52.2	9.20
		75-105	4.40	83	53.0	9.32
45°	1	0-30	2.66	49	54.3	9.36
		30-60	1.81	37	49.0	9.26
		60-90	2.08	41	50.8	9.16
45°	2	0-30	2.29	45	50.9	9.36
		30-60	2.34	47	49.9	9.26
		60-90	2.09	42	49.7	9.16
45°	3	15-45	1.99	40	49.6	9.19
		45-75	1.97	40	49.1	9.20
		75-105	2.00	40	50.0	9.32
45°	4	15-45	1.99	41	48.6	9.19
		45-75	2.10	45	46.7	9.20
		75-105	2.22	44	50.5	9.32
90°	1	0-30	2.91	56	52.0	9.36
		30-60	3.90	75	51.9	9.26
		60-90	4.39	81	54.1	9.16
90°	2	0-30	3.42	64	53.4	9.26
		30-60	3.57	72	49.6	9.26
		60-90	4.36	76	57.4	9.16
90°	3	15-45	3.84	70	54.9	9.19
		45-75	3.78	77	49.1	9.20
		75-105	4.35	81	53.7	9.32
90°	4	15-45	4.00	73	54.8	9.19
		45-75	4.12	74	55.6	9.20
		75-105	4.48	81	55.3	9.32

[1]Angle between average c-axis orientation and direction of load application.
[2]See Figure for sampling scheme.
[3]Average temperature -3°C for all tests.

TABLE 2.2-9
RESULTS OF CONSTANT LOADING RATE TESTS IN
UNIAXIAL COMPRESSION- 1980

Sample Number	Peak stress (MPa)	Time to peak stress (sec.)	Average stress rate (kPa/sec.)	Average Temp (-°C)	Average Volume Brine $\sqrt{v}$ (ppt)	Sample type (see note below)	Comments
1	2.23	479	4.66	12.3	4.8	1	
2	2.52	505	4.99	12.4	4.8	1	
3	3.12	12.4	251	4.8	8.6	2	1 flatjack
4	2.31	476	4.86	8.8	5.6	1	
5	2.06	9.0	229	4.7	8.6	2	Peak stress low, sample cracked across one corner.
6	1.87	3.3	568	4.7	8.6	2	
7	2.47	5.2	476	4.7	8.6	2	1 flatjack
9	2.15	427	5.02	13.1	4.6	3	
10	2.13	415	5.14	13.1	4.6	3	
11	2.63	54.2	48.5	8.4	5.6	3	
12	2.51	56.8	44.3	8.4	5.6	3	
13	1.73	380	4.56	8.7	5.5	3	
15	1.84	3.75	4.90	8.7	5.5	3	
16	12.9	3480	0.37	3.7	9.7	2	1 flatjack
17	1.22	3387	0.36	3.7	9.7	2	
18	2.38	48	49.5	4.9	8.5	2	
19	2.31	46	50.2	4.9	8.5	2	
20	3.07	9.8	314	5.2	7.0	4	Load cell operated during test
22	1.84	370	4.97	5.0	8.4	2	
23	2.17	425	5.11	4.9	8.5	2	

TABLE 2.2-9 (Cont'd)

Sample Number	Peak stress (MPa)	Time to peak stress (sec.)	Average stress rate (kPa/sec)	Average Temp. (-°C)	Average Volume Brine V_v (ppt)	Sample type (see note below)	Comments
24	2.58	50.4	51.2	5.2	8.2	2	
25	1.85	38.5	48.0	4.9	8.5	2	
28	1.04	3043	0.34	9.0	5.4	4	
29	1.45	3460	0.42	9.0	5.4	4	
30	2.16	410	5.26	8.8	5.5	4	
31	2.14	414	5.18	8.6	5.5	4	
32	3.19	59.4	53.7	8.4	5.6	4	
33	3.04	56.8	53.6	8.4	5.6	4	
34	1.66	330	5.02	5.3	6.9	4	
35	1.90	356	5.34	5.0	7.1	4	

Sample types
1. Silty, fine-grained, 0-30 cm depth, random c-axis orientation.
2. Clean, fine-grained, 0-30 cm depth, random c-axis orientation.
3. Columnar ice from 25-55 cm depth, weak orientation (see Table 3B).
4. Same as 3, with flatjacks backed by aluminum plates 30 cm deep by 60 cm wide.

TABLE 2.2-10
RESULTS OF CONSTANT LOADING RATE TESTS
IN UNIAXIAL COMPRESSION - 1980;
VARIATION WITH DEPTH AND ORIENTATION

[1]Loading Direction	Depth range (cm)	Sample Number	Peak stress (MPa)	Time to Peak stress (sec.)	Average stress (kPa/sec.)	Average Temp. (-°C)	Average Brine Vol. (√v ppt)
0°	25-55	26	2.46	58.2	42.3	7.8	5.8
		27	2.84	61.0	46.6	7.8	5.8
0°	40-70	38	2.67	56.3	47.5	9.3	5.3
		39	2.78	58.0	48.0	9.3	5.3
0°	55-85	36	2.63	56.8	46.3	9.1	5.2
		37	2.79	60.0	46.5	9.1	5.2
0°	70-100	14	2.50	52.2	48.0	9.4	4.9
		40	2.52	55.8	45.2	9.3	4.9
0°	85-115	43	2.84	60.0	47.4	8.8	4.8
		44	2.48	57.4	43.2	9.0	4.8
45°	25-55	41	2.95	61.0	48.4	8.9	5.4
		42	2.65	63.0	42.0	8.7	5.5
45°	40-70	65	2.75	59.0	46.4	9.3	5.3
		66	2.56	52.6	48.7	9.3	5.3
		75	2.16	44.0	49.1	3.7	8.1
		76	1.97	41.4	47.5	3.7	8.1
45°	55-85	67	2.73	56.8	48.1	8.9	5.3
		68	2.47	52.8	46.7	8.9	5.3
45°	70-100	63	3.12	63.6	49.0	8.9	5.0
		64	2.66	59.0	45.1	8.9	5.0

TABLE 2.2-10 (Cont'd)

‡Loading Direction	Depth range (cm)	Sample Number	Peak stress (MPa)	Time to Peak stress (sec.)	Average stress rate (kPa/sec.)	Average Temp. (-°C)	Average Brine Vol. (√v ppt)
45°	85-115	45	2.48	53.8	46.0	8.7	4.8
		46	2.49	54.5	45.6	8.6	4.9
90°	25-55	59	2.39	52.0	45.9	7.7	5.8
		60	2.47	52.5	47.0	7.7	5.8
90°	40-70	56	2.63	56.4	46.6	9.3	5.3
		58	2.63	57.2	45.9	9.3	5.3
		77	2.02	43.6	46.2	3.6	8.3
		78	2.16	46.8	46.2	3.7	8.1
90°	55-85	61	2.68	58.6	45.8	8.9	5.3
		62	2.81	60.8	46.2	8.9	5.3
90°	70-100	55	2.84	59.0	48.2	9.3	4.9
		57	2.74	58.6	46.7	8.4	5.1
90°	85-115	69	2.79	61.0	45.8	8.6	4.9
		74	2.54	56.8	44.7	8.5	4.9

2.2.4.6 Discussion of Results of Uniaxial Compression Tests

2.2.4.6.1 *Introduction*

The purpose of this section is to present and describe the results of the experiments listed in the tables in the preceding section. The interpretations are given strictly in terms of the data and the relevant background material. More general interpretations in terms of the results of the theoretical study are given in the appropriate subsections of Section 2.3.

Because the program was done entirely in the field under ambient conditions, it was obviously not possible to control the temperature or the sample properties. This leads to some difficulty in organizing the data because the range of variables examined is limited to some extent. This is because it was generally not possible to run large numbers of tests at the same temperatures. In general, tests were selected depending upon the ice temperature on a particular day and the number and types of tests already done at that temperature. The intent was to assemble the most complete data set possible within a given temperature range. However, there was no certainty that temperatures in a particular range would occur often enough to permit an acceptable data set to be obtained. In addition, it was necessary to duplicate (or triplicate) some tests in order to establish repeatability so that variations in sample properties and set-up could be accounted for. This further reduced the range of variables which could be covered with the available samples. For these reasons, the results have been grouped into temperature ranges, which are kept as small as possible while providing a reasonable sample size. This introduces some scatter into the data, but the trends are still apparent.

In the following sections data bearing on four aspects of sea ice properties in uniaxial compression are described. These are (1) the relationship between strength and stress rate in different temperature ranges, (2) the "long" term strength of sea

ice, (3) the effect of grain size and c-axis orientation on sea ice strength and (4) comparison of the strength of first year and multiyear ice in uniaxial compression.

2.2.4.6.2 *Strength vs. Stress Rate*

The results of measurements of strength vs. stress rate in three temperature ranges are shown in Figure 2.2-8. The data show the anticipated increase of strength with stress rate (although the scatter is large) as well as the increase in strength with decreasing temperature. Peak strengths varied from 2.7 MPa for the temperature range from -5.5° to -7.5°C, to about 4.5 MPa for -10° to -14°C to about 6.2 MPa for temperatures between -17° and -22°C.

The strength of 4.5 MPa for the temperature range of -10° to -14°C can be compared to the peak strengths reached in Wang's (1979) laboratory tests of the uniaxial compressive strength of small-scale cylindrical (7.5 x 15 cm) samples of natural sea ice at constant strain rates and a temperature of -10°C. For fine-grained (<2 mm) ice, the peak strength was about 7.2 MPa, while for slightly larger grain sizes (2-3 mm) the peak decreased to about 5.9 MPa. However, for unoriented columnar ice, Wang found peak strengths of 4.8 and 3.8 MPa for grain sizes of 10 and 15 mm, respectively, which are similar to the value of 4.5 MPa reported above. It is difficult to draw a conclusion from this, other than to speculate on the possibility that the strengths reported here may reflect the strength of the ice in the transition zone of the samples rather than the fine-grained slush ice near the surface.

In experimental programs in which samples are failed at high rates of deformation, the strength of the ice often appears to decrease at strain rates in excess of (about) 10^{-3}/sec (the question is discussed more fully in Section 2.3.6). No such decrease in strength is evident in the data in Figure 2.2-8, which raises the question of whether the stress rates were high enough to reach the peak if, in fact, it is real. There is no stress-strain law with which to accurately calculate the strain rate.

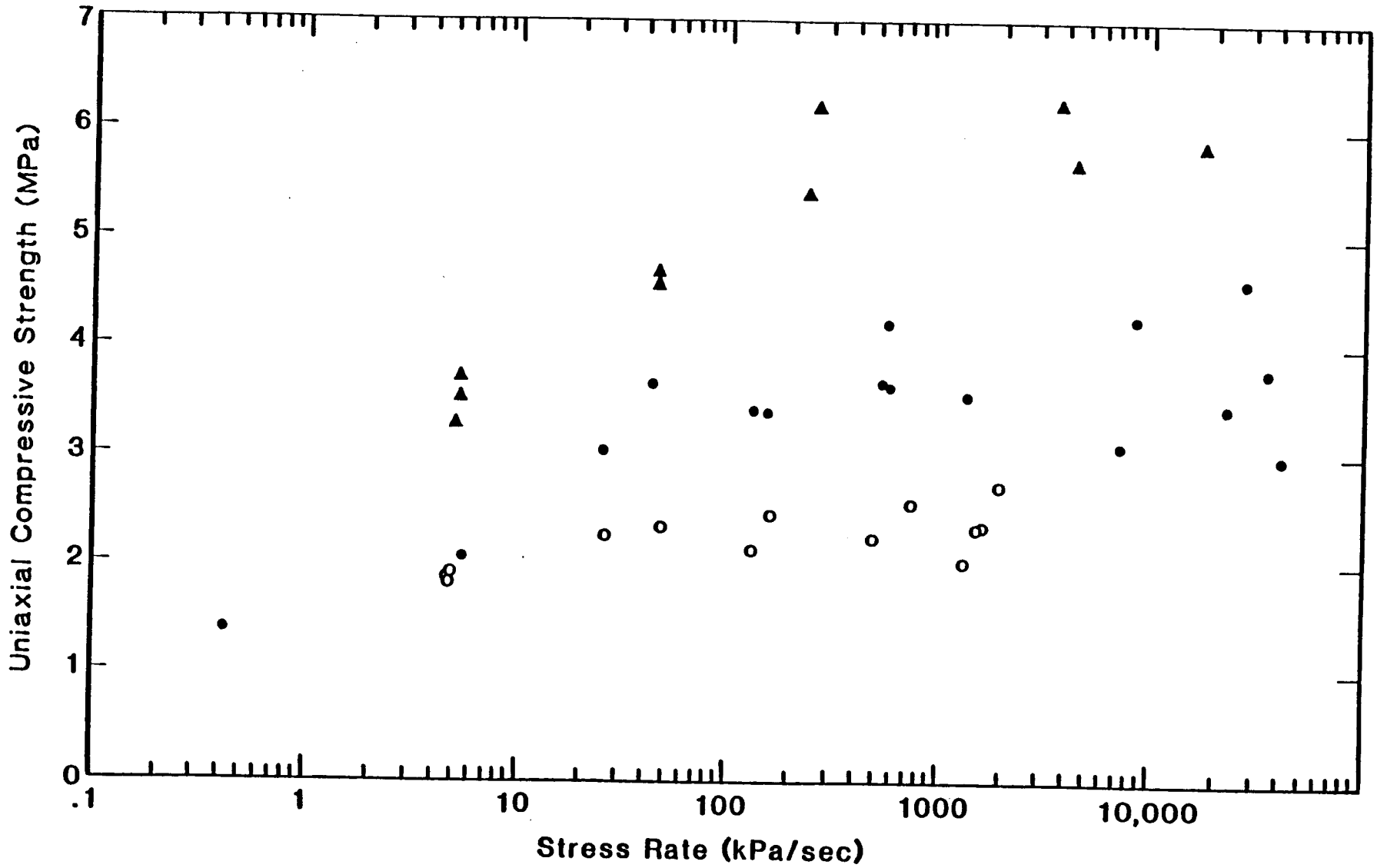

Figure 2.2-8 Plots of uniaxial compressive strength vs. stress rate for three temperature ranges (-17° to -22°C - solid triangles; -10° to -14°C - solid circles; -5.5° to -7.5°C - open circles).

However, a lower limit to the strain rate can be calculated if it is assumed that the ice deformed as a linear elastic solid at the higher stress rates. In that case, the strain rate is related to the stress rate through the derivative of the one-dimensional Hooke's law,

$$\dot{\varepsilon}(t) = \dot{\sigma}(t)/E$$

where E is Young's modulus. At the higher rates used in this project (say, $\dot{\sigma} = 10^4$ kPa/sec), for a modulus of 9 GPa, the strain rate would have been on the order of 10^{-3}/sec. This suggests that the data at the highest rates are probably close to the peak and do not contribute to the resolution of the problem.

The variation in failure mechanism over the range of stress rates shown followed the same pattern for all three data sets. At the lower rates, the ice failed by the pervasive formation of small, stable cracks which progressively weakened the sample until it could no longer sustain the load. Samples that were unloaded before they failed explosively were milky-white, due to the distribution of small cracks. At the higher rates, the failure always occurred by brittle fracture. In some cases the fractures were through-going extension cracks aligned parallel to the sample axes. In others, a single vertical shear crack extended across the sample at about 30° to the axis. In either case, the ice between the main fractures was still clear, with no small fractures such as were present in samples which were tested at lower rates.

2.2.4.6.3 *Long-term Strength*

Gold (1979) presented data for the time-to-failure of fresh water polycrystalline ice in constant stress in which, for stresses above some "transition" range, the samples passed through the inflection point between secondary and tertiary creep in a relatively short time. Once in tertiary creep the strain rate accelerated until

failure occurred. However, the length of time the sample could sustain a stress without passing to tertiary creep increased rapidly for stresses below the transition. This suggested the possibility that the ice might have a "fundamental" strength; that is, an upper limit of the range of stresses which the ice could sustain "indefinitely" without failing. More recently, Jacka (1984) showed that even at low constant stresses, the inflection point is ultimately reached, and ice passes into tertiary creep.

A knowledge of the stress range over which the transition occurs could be useful for engineering applications. It is not an indicator of a fundamental strength in the sense defined above. However, it does define a stress below which the ice can be expected to sustain a load for a relatively long time. In addition, the transition is of interest for the theory described in Section 2.3.

Data relevant to the question of transition stress are shown in Figures 2.2-9 and 10. The data in Figure 2.2-9 show the time-to-minimum strain rate and time-to-rupture for tests at constant stress in a relatively low temperature range. In addition, the time-to-failure for several tests at constant stress rates, and the total times of constant stress tests which did not reach the inflection point at the minimum strain rate are also shown. The data show that linear projections of curves of time-to-failure (for both the constant stress and constant stress rate tests) or time-to-minimum strain rate must pass through shorter times than those for which the samples were able to maintain lower stresses without reaching a minimum strain rate. Thus, the stress vs. time-to- minimum strain rate curve must flatten as indicated on the figure, defining the "transition" stress. For the data shown, the transition stress is approximately 1 MPa, and the data indicate that it is sharply defined.

A similar data set at a higher temperature range is shown in Figure 2.2-10. In this figure, the minimum strain rate was reached in even the longest tests, although

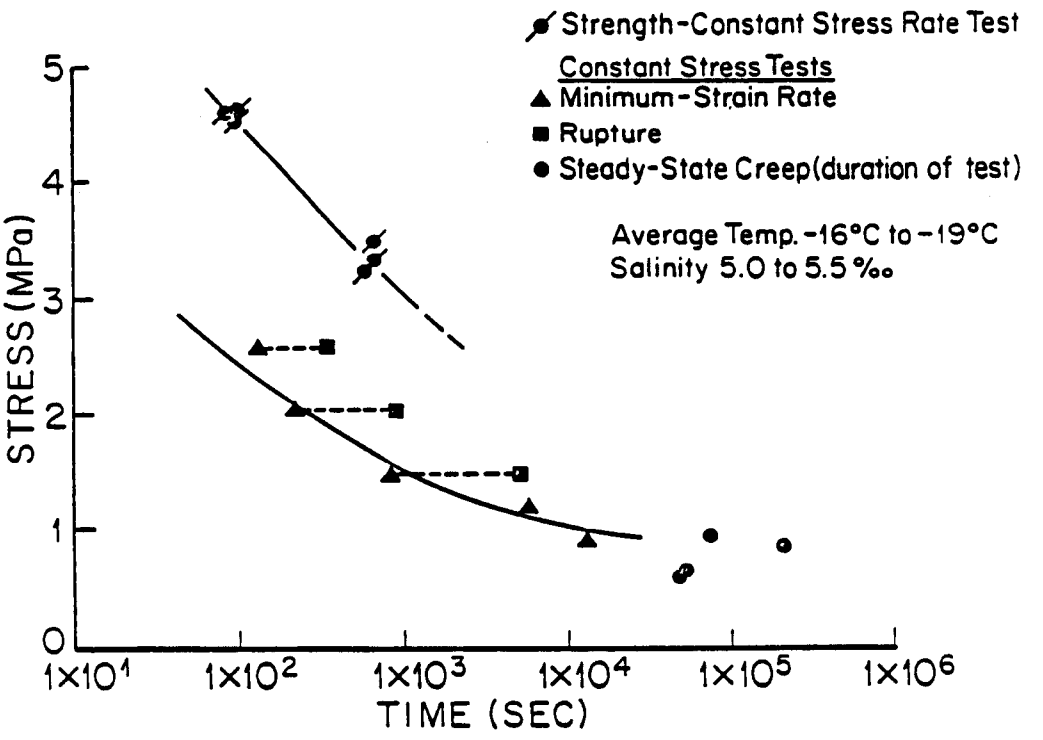

Figure 2.2-9 Uniaxial compressive strength vs. time-to-failure for constant stress rate tests and time-to-minimum strain rate and time-to-rupture at constant stress in the temperature range -10° to -19°C.

it was not possible to hold the loads on the samples until rupture. The curves through the data points are estimates (their shapes reflect the results discussed in Section 2.3.4). The transition is less well defined in this figure, because the slope of the stress vs. minimum strain rate curve is low compared to that in Figure 2.2-9. However, a value of 0.5 MPa might be a reasonable estimate.

In general, samples which ruptured at constant stress failed by the pervasive growth of small cracks, which gave the ice a whitish color. Few cracks were ever observed to form in samples tested at stresses below the transition stress.

It is of interest to note that for constant stress tests, the time- to-rupture is usually between a factor of 3 and 10 greater than the time-to-minimum strain rate, with a tendency to increase at lower stresses. Similar data for ice in bending would

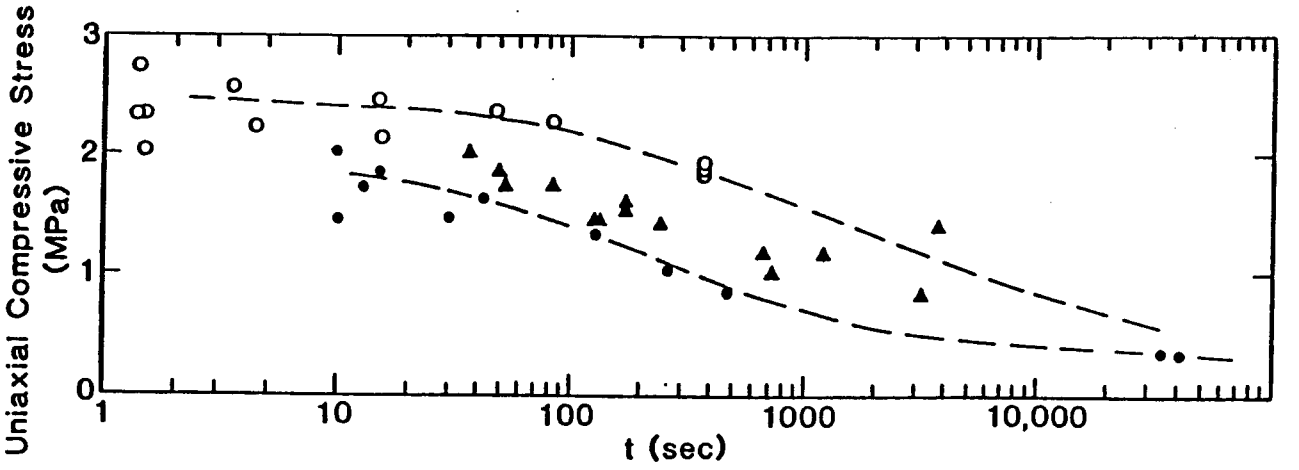

Figure 2.2-10 Uniaxial compressive strength vs. time-to-failure for constant stress rate tests (open circles), and time-to-minimum strain rate (solid circles) and time-to-rupture (solid triangles) for constant stress tests. Temperature range -5.5° to -7.5°C. Curves are estimated based on the results in Section 2.3.4.

have application to the problem of the length of time for which an ice sheet can be expected to safely bear a load.

2.2.4.6.4 *Effect of Grain Size and C-Axis Orientation on Strength*

Peyton (1966) and Wang (1979) both demonstrated the effect of strong alignment of crystallographic c-axes of crystals in an ice sheet on the strength of the ice loaded in various orientations. In this study, similar measurements were made to include the effect of depth (and therefore increasing grain size). To accomplish this, samples were collected in 30-cm increments of depth down to 105 cm in the ice sheet (Figure 2.2-11). These were oriented so that loading could be done at 0°, 45° and 90° to the dominant c-axis direction on two samples collected for each orientation and depth interval. The study was first done in 1979 and was repeated in 1980 in an effort to collect data over a different temperature range. The results of the 1979 program are shown in Figure 2.2-12. Loading was done at a stress rate of about 52 kPa/sec (7.5 psi/sec) which was similar to that used by Peyton (1966) in his work on

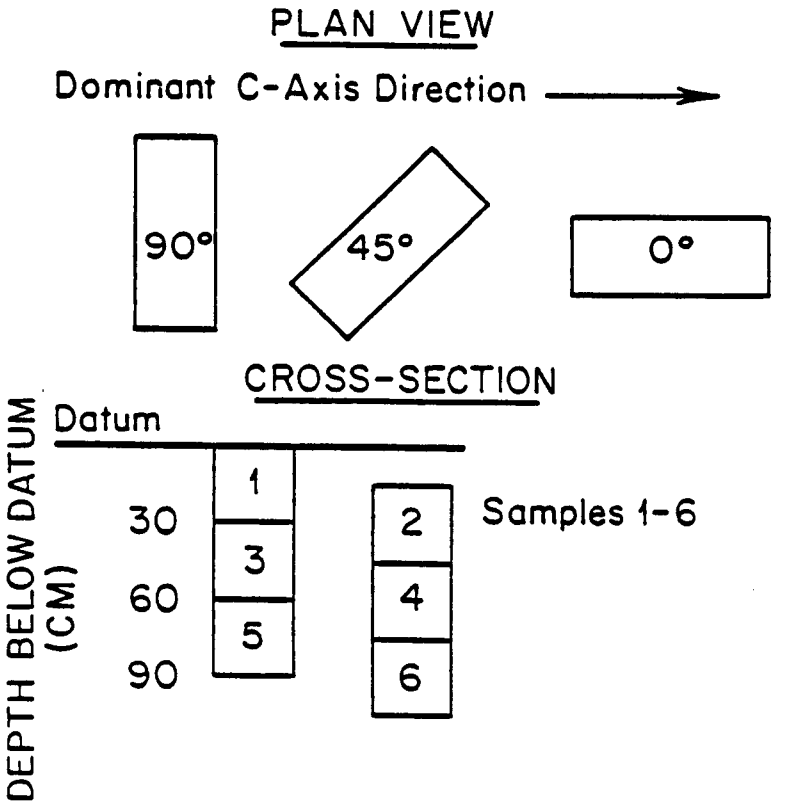

Figure 2.2-11 Arrangement of samples collected for evaluation of uniaxial compressive strength vs. grain size and c-axis orientation.

ice strength as a function of grain size and c-axis orientation. Average sample temperatures during testing were -3°C (+/- 0.5°C).

The results of the 1979 study agree with those of Wang (1979) with respect to the increase of strength with depth for the 0° and 90° orientations. However, they contrast with the results of both Wang (1979) and Peyton (1966) which show that the strength in the 0° direction is greater than that in the 90° direction. There may be no discrepancy with respect to Wang's results because, at the loading rate used in this program, the sample strain rates would probably have been in the range of 10^{-6}/sec to 10^{-5}/sec. At those rates, the difference between the strength in the 0° and 90° directions in Wang's (1979) data are small and possibly within the scatter of the results in Figure 2.2-12.

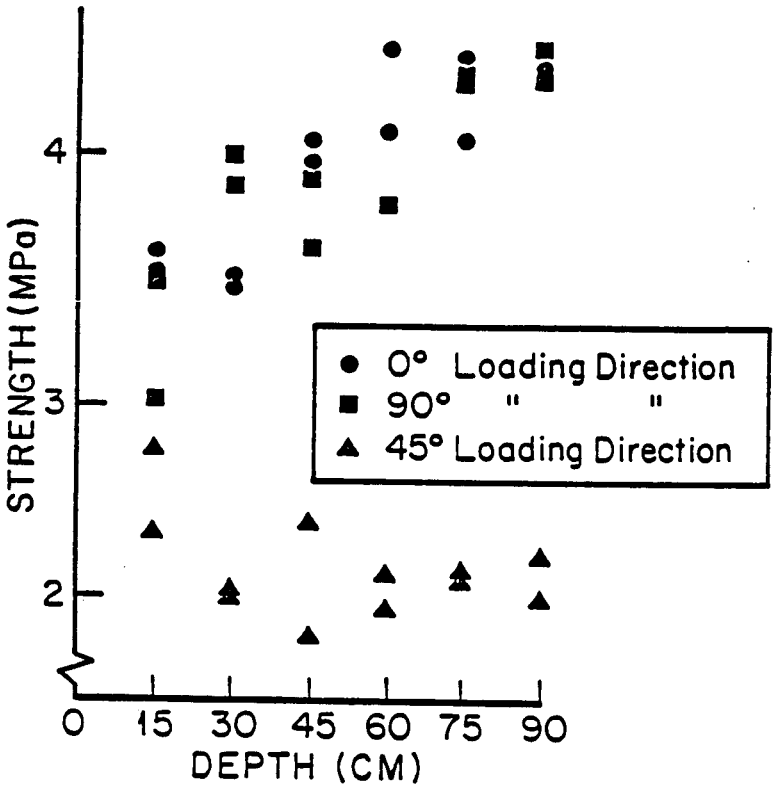

Figure 2.2-12 Results of the 1979 series of tests of uniaxial compressive strength vs. grain size and c-axis orientation.

It is likely that the discrepancy is real with respect to the data in Peyton (1966) but, if so, the same discrepancy exists between Wang's and Peyton's results. In this case, the lack of agreement may be due to the differences in the volume of the samples used in the three studies.

Peyton's tests were done on samples about 3.5 cm in diameter by 7 cm long. For depths greater than about 30 to 60 cm in an ice sheet (particularly when the c-axes are strongly oriented), samples of this size are probably closer to single crystals of ice than to polycrystalline ice. For the 90° orientation, the brine planes in the ice were aligned parallel to the sample axis. Thus, when loaded in uniaxial compression, the brine planes were properly oriented to nucleate extension fractures which, in a large sample might have been trapped at the grain boundaries and stablilized. However,

for Peyton's small samples their size would have been significant compared to the length of the sample, leading to weakening and premature fracture. In contrast, the samples used by Wang (approximately, 7.5 x 15 cm) and in this study, were large enough that the grain sizes were insignificant in comparison to the sample volumes. Thus, small cracks parallel to the brine planes would have stabilized, increasing the stress required to cause failure.

Note that for the 45° direction the strength decreased with depth initially, and then remained constant (within the scatter) despite the increase in grain size with increasing depth. An interpretation is suggested by the observation that, with the exception of samples including the slush ice layer, failure in samples with this orientation always occurred by shear fracture at 45° to the sample axis. Thus, the fracture plane was always parallel to the orientation of the brine planes and in the plane of maximum shear stress. This implies that once the orientation was sufficiently strong for sliding to occur easily in the direction of orientation of the brine planes, further intensification of the orientation had little effect on the strength.

The results of the test series in 1980, in which the same test program was repeated at average sample temperatures of -7 to -9°C are shown in Figure 2.2-13. These data indicate little or no variation in strength with depth or loading direction relative to c-axis orientation. The results of additional tests at -3°C, which were run to check the results of the first series, also indicate no difference in strength between the 45° and 90° directions (Figure 2.2-13). The apparent reason for the absence of any particular orientation effect in these results is that the orientation was simply not developed strongly enough. There is no question that the ice tested in 1980 should be classified as "oriented," because an average c-axis orientation could easily be identified in thin sections of the ice. However, thin section analysis showed that in 1979, the ice at a depth of 32 cm had a maximum angular spread between c-axes of

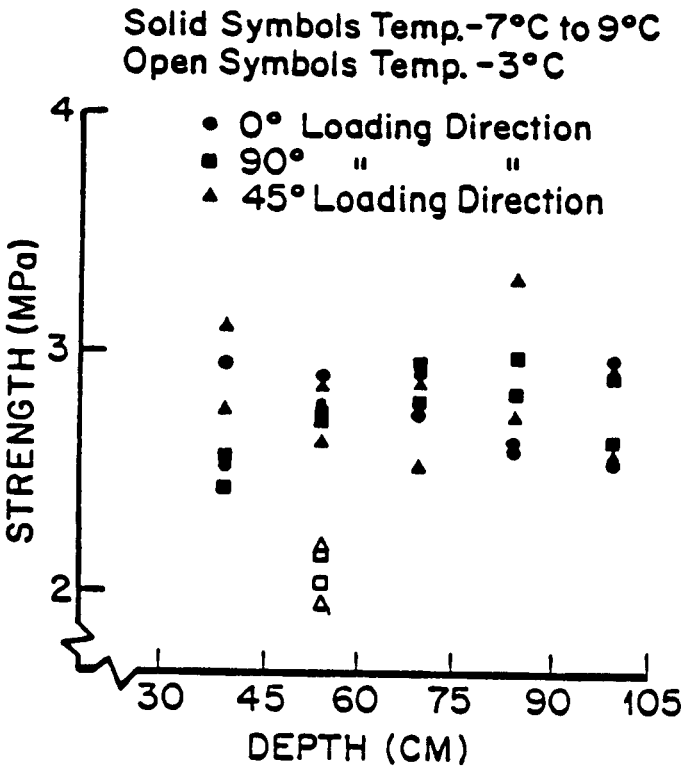

Figure 2.2-13 Results of the 1980 series of tests of uniaxial compressive strength vs. grain size and c-axis orientation.

about 30°, decreasing to 15° at 1 m. In contrast, in 1980, the angular spread was up to 66° at a depth of 75 cm. This large variation was apparently sufficient to neutralize the effect of the average c-axis orientation, with the result that the ice in 1980 was essentially isotropic for loading in the horizontal plane. This result indicates that there is some limit in the degree of orientation (i.e., some maximum permissible spread of c-axis orientation) which is required before the ice will exhibit mechanical anisotropy for loading in a horizontal plane. The fact that an average c-axis orientation can easily be identified in a sample does not assure that such a mechanical anisotropy exists.

2.2.4.6.5 *Comparison of the Strength of First Year and Multiyear Ice*

A series of tests was run to provide a comparison between the strength of first year and multiyear sea ice in uniaxial compression at the same temperatures and loading rates. The samples of multiyear ice were collected from a floe frozen into the landfast ice sheet near the test site. Average ice temperatures ranged from -2° to -6°C during the test program. Tests at each stress rate were run consecutively, alternating between the two ice types. The results are shown in Figure 2.2-14 and indicate that there is little difference in strength between the two ice types, except possibly at the highest rate at which tests were conducted. This suggests that the strength of multiyear ice may be greater than that of first year ice in the brittle range, but there is little difference over the remainder of the range of loading rates used.

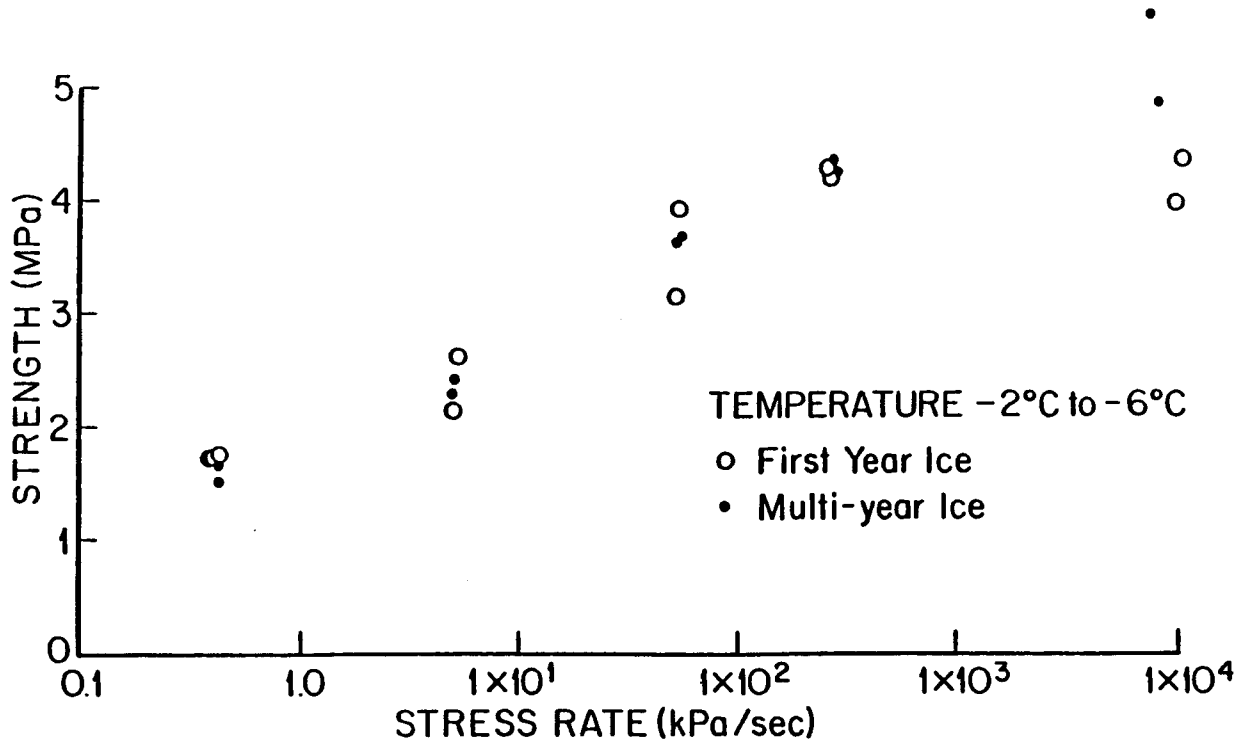

Figure 2.2-14 Uniaxial compressive strength of first year and multiyear ice vs. stress rate.

2.2.5 DIRECT SHEAR TESTS

A direct shear test (which is similar to a standard "shear box" test) was designed, and several preliminary experiments were run. The values are not reported here because the flatjacks used for loading were not calibrated. However, the test results were repeatable, and the procedure could form the basis for a test program to evaluate the shear strength of sea ice. Details were described in Shapiro et al. (1979) and are only summarized here.

The configuration of the test is shown in Figure 2.2-15. The sample is defined by the relief slots which are cut to the depth "a" with a chain saw. The test is done by loading the flatjack until failure occurs along the plane at the base of the block. The shear strength is then calculated assuming that the stress is uniformly distributed on the failure plane, as is done in the case with shear box experiments. Thus, if the dimensions of the flatjacks are a and b, and the (calibrated) flatjack pressure at failure is P, then the total force is Pab. This is assumed to be equal to τ bc, where τ is the shear strength, and b and c are the dimensions of the block in the plane of the ice sheet as outlined by the relief slots. In the tests done during the program, b and c were equal, so that $\tau = (a/c)P$. Experiments were done with the ratios a/b and a/c equal to both 1/2 and 1/3, which gave similar values of τ.

The geometry of the stress distribution in the test block was studied using a 2-dimensional plane stress, finite element analysis. The results were compared to similar calculations for the geometry of a punch test (Figure 2.2-16) which is often used to determine the shear strength of materials. The calculations indicate that the first crack to form in the shear test would likely be a tension crack propagating downward under the flatjack into the ice sheet. Subsequently, the stress configuration near the flatjack closely resembles that of the punch test as shown in Figure 2.2-16. The vertical crack can be simulated at the time the test is set up by deepening the chain saw cut made to receive the flatjack and installing a piece of

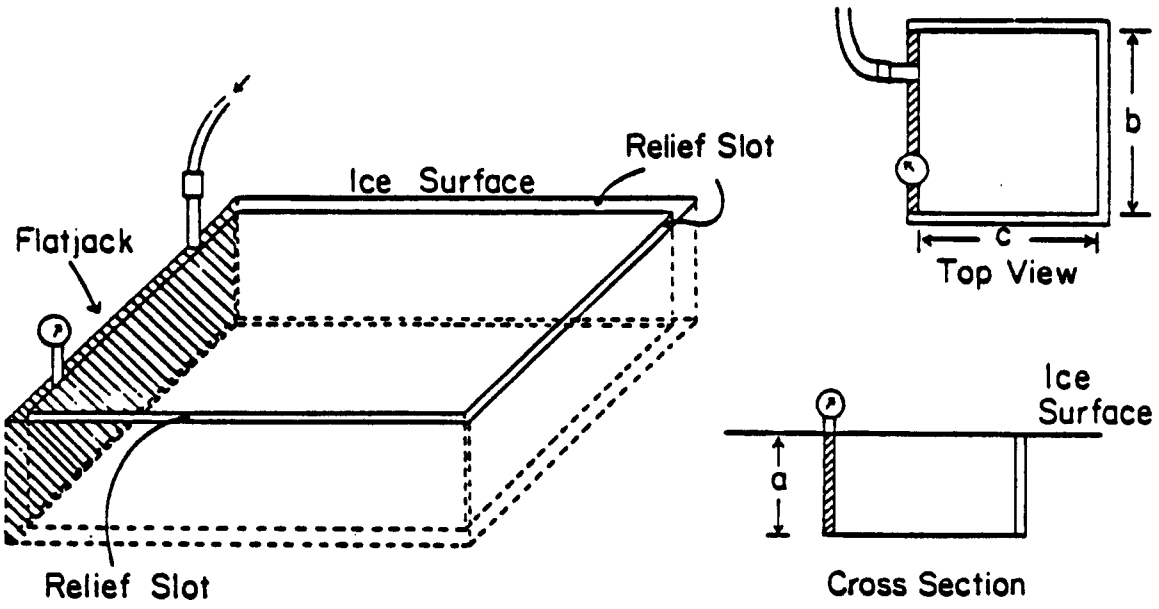

Figure 2.2-15 Set-up for direct shear test.

stiff cardboard wrapped in polyethylene sheeting in the slot below the flatjack. This would provide a low tensile strength bond, assuring that the first crack will propagate downward.

Examination of the fracture zones which formed on the shear plane as a result of the tests, shows that the zones were generally thin, involving only the lower 20% of the thickness of the blocks. Within the zone, the ice tended to shatter into flat plates about 1 cm thick, with linear dimensions of several centimeters. The failure plane in the ice sheet typically showed irregular "step" asperities oriented transverse to the direction of motion of the failed block, with the riser of the step facing the loading direction. Flat cracks extended down into the ice from the base of each step, as evidenced by the distinct gray color of the ice in these areas. The failure mode was similar to that in the fracture zone of rocks which fail in shear by brittle fracture in uniaxial compression. The mechanism clearly indicates failure under the influence of a shear stress parallel to the failure plane.

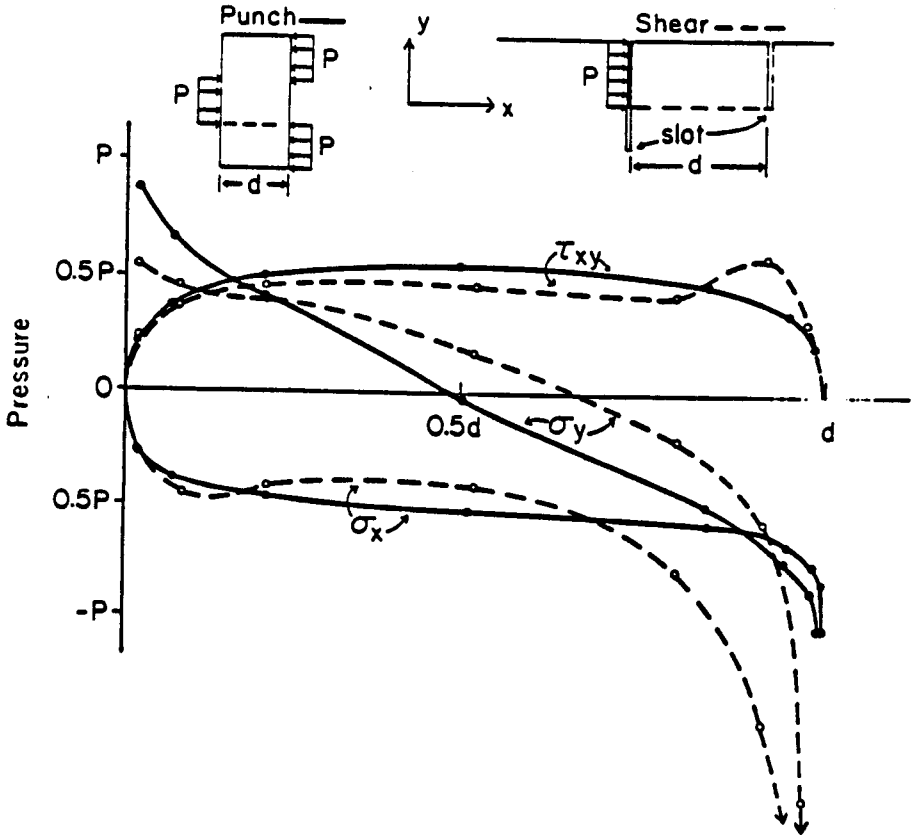

Figure 2.2-16 Results of finite element analysis of punch test (solid line) and direct shear test (dashed line). Calculations refer to a surface just below the dashed lines on the diagrams. The slot below the flatjack represents either the first crack or the prepared "crack" described in the text.

It should be noted that attempts to conduct direct shear tests using square flatjacks and blocks with dimensions a = b = c invariably resulted in tensile failure across the base of the specimen. Thus, cubical blocks simulate the bending of a thick cantilever beam under a uniformly distributed load. However, tests in which the width of the flatjack was at least twice the depth always failed in shear.

Finally, note that the test described above can be used to determine the shear strength of the ice in any direction. This would involve quarrying samples from the ice sheet, rotating them into the desired orientation, and then freezing them into holes prepared in the surface of the ice sheet. A sample need only be large enough that the set-up shown in Figure 2.2-15 can be made on its surface.

2.2.6 INDIRECT TENSION (BRAZIL) TEST

A procedure for running indirect tension tests in situ in the ice sheet was also tried (Shapiro et al., 1979). Only two tests were required to duplicate failure patterns obtained in the laboratory. In the first of these, a circle with a diameter of 59 cm was outlined on the ice surface and two 15-x 60-cm flatjacks were installed on the opposite ends of one of its diameters; the 15-cm edges of the flatjacks were at the surface of the ice sheet. A chain saw cut 75 cm deep was made along the circumference of the circle, and the flatjacks were then loaded until failure occurred. The cylinder failed with a single crack along the diameter and minor secondary cracks near the flatjacks. This is the typical mode of failure in laboratory tests of this type when the cylinders are loaded by line loads on opposite ends of a diameter.

Curved flatjacks were used in the second test, in order to provide a load over 15° arcs of the test specimen as discussed by Jaeger and Cook (1976). The purpose of loading over the arc is to eliminate the secondary cracking near the points of application of the line load, and assure that failure occurs along a single fracture which originates near the center of the sample. The sample used for this test was another cylinder of the same size as in the first test (diameter 59 cm, depth 75 cm). The flatjacks were prepared by flattening two 46 cm lengths of 7.6 cm diameter copper tubing, and then bending them to the curvature of the test specimen. The ends of the flatjacks were sealed by silver soldering, with inlets for loading installed at one end. The test was set up and run as described above, but in this case failure occurred along a single crack with no secondary cracking near the flatjacks. Further, when the sample was cut normal to the crack with a chain saw, it separated into two blocks along the crack. There was no evidence of splaying of the crack with depth in the ice sheet, which indicates that plane strain conditions were achieved over a sufficient length of the sample to provide an adequate test.

The results show that large-scale, in situ indirect tension tests are relatively easy to set up and run and failure mechanisms duplicate those which typically occur in laboratory tests. Thus, there should be no difficulty in conducting a larger program of tests of this type if the results were needed.

2.2.7 BIAXIAL COMPRESSION TESTS

Experiments were done to develop a biaxial compression test using rectangular prisms of sea ice of the same dimensions as those used in the uniaxial compression tests (Shapiro et al., 1979). The tests differ only by the addition of a confining pressure applied through 30-x 60-cm flatjacks installed along the sides of the samples. The confining pressure was controlled by a loading system which was separate from that used to apply the loads to the ends of the sample.

The tests were done by loading both pairs of flatjacks simultaneously, until the selected confining pressure was reached. Then, the pressure in the confining pressure flatjacks was held constant, while the pressure in the flatjacks at the ends of the sample was increased at a constant rate until failure occurred.

The results of the experiments indicate that this test is likely to be useful only when the ice temperature is low and the loading rate of the axial flatjacks is less than 0.35 MPa/sec (50 psi/sec). The limitations are due to the increase in the strength of the samples with application of confining pressure. This allows the pressure in the axial flatjacks to become so large that the ice sheet (the "loading frame"), which is not under confining pressure, is not sufficiently strong to resist the expansion of the flatjacks under internal pressure. As a result, the axial flatjacks fail along the edge weld at the ice surface as the flatjack overexpands.

Additional work in progress when the field program was terminated was directed at testing the use of aluminum or steel plates installed behind the axial flatjacks to spread the load and reduce the stress applied to the ice sheet by the

reaction pressure. A few experiments run under these conditions suggested that the approach might lead to an increase in the range of pressures over which tests could be done.

Since the procedure was never developed to the point of running a series of tests to obtain numerical values of the strength, the flatjacks used to apply the confining pressure were not calibrated. For the limited data obtained, the results suggest that the increase in peak axial stress with increase in confining pressure is strongly dependent on both the temperature and the rate of loading. In addition, it was never possible to bring a sample to failure by the development of through-going cracks, although a few tests were done at rates which, for uniaxial compression, would have caused failure by that mechanism. Instead, cracking was always pervasive, turning the sample milky-white, as occurred in uniaxial compression tests at low loading rates (Section 2.2.4.6.2).

The procedure as described above could be used for conducting creep tests at low flatjack pressures, but further development is required if the test is to be used to establish the strength at higher rates of loading and confining pressures.

2.2.8 SUMMARY AND DISCUSSION

The physical properties of sea ice, and its mode of occurrence in nature require that at least some determinations of the mechanical properties of the ice must be conducted in situ in order to supplement laboratory results. In situ tests involving vertical loading of an ice sheet (or of beams isolated within an ice sheet) had been done previously, but the problem of testing under in-plane loading had received little attention prior to this program. Therefore, one task was to investigate methods through which the properties of sea ice could be determined on relatively large samples under conditions of in-plane loading, and with minimal disturbance to the samples being tested.

Flatjacks proved to be ideal devices for introducing controlled stress fields into an ice sheet. They are relatively simple and inexpensive to construct in any shape, and can be adapted to a variety of test types. Loading by high pressure gas controlled by a pressure regulator proved to be satisfactory for tests at both constant load and constant loading rate. For the latter, rates ranging from less than 1 kPa/sec to greater than 10^4 kPa/sec were achieved.

Deformation measurements can be made using a variety of equipment but are limited by the fact that, in the tests described here, only the face of the sample at the ice surface can be instrumented. The result is that as the sample surface bulges upward in response to the in-plane shortening, the measured strain on the single exposed face ceases to be representative of the true shortening. The method of attaching displacement measuring devices to pegs in the ice overcomes this difficulty to some extent, but introduces the question of whether the pegs affect the deformation characteristics of the ice. The results presented here suggest that it is possible to determine the conditions under which this does not occur. However, it would still be desirable to verify the validity of the strain determinations by other methods.

During the program, procedures for conducting tests in uniaxial compression (triangular and prismatic specimens), direct shear and indirect tension were designed and tested with satisfactory results. A biaxial compression test was also tried. It is adequate for creep tests or for measurements of strength at low confining pressures (i.e., less than about 20% of the peak axial stress), but requires further work if it is to be extended to higher confining pressure.

The data on uniaxial compressive strength as a function of loading rate follows the same trend of increasing strength with increasing rate as established for constant deformation rate tests. There is no stress- strain law available with which to correlate between test types. However, estimates suggest that the data presented

here are comparable to those obtained by Wang (1979) on smaller samples, implying that there is no marked decrease in strength with increasing sample dimensions for samples in which the c-axes are not strongly oriented.

The results of tests at constant stress verify that some transition stress range exists for sea ice, below which the time that the ice can sustain a load increases rapidly. The transition is defined by plots of stress vs. time-to-minimum strain rate (the onset of the tertiary creep stage leading to rupture) for a series of tests. The data indicate that the transition is sharp at low temperatures but becomes more gradual as the temperature increases. The recognition of the transition range may have engineering applications by defining the upper limit of the stress which the ice can sustain for a relatively long time. In addition, while any sample under load must eventually fail, the data indicate that the time between the inflection point and rupture of the sample is from 3 to 10 times as great as the time-to-minimum strain rate. This may provide a basis for deriving safety factors for loads on ice sheets.

A series of determinations of sea ice strength as a function of depth in the ice sheet (or, alternatively, grain size) and c-axis orientation follows trends indicating strong mechanical anisotropy of the ice. The tests were done on strongly oriented ice, and the trends are similar to those derived in laboratory measurements. However, the results of a second series of tests raise the question of the intensity of c-axis orientation which is required in order for the anisotropic effects to become important. In that series, the intensity of c-axis orientation of the ice was weaker than that in the first series, but still strong enough to be easily recognized. The results showed that the ice was essentially mechanically isotropic for loading in the plane of the ice sheet, implying that there is a relatively sharp transition from isotropy to anisotropy as the intensity of c-axis orientation increases.

Finally, a short series of measurements was done to compare the strengths of first year and multi-year ice. The results showed no significant differences over the range of loading rates and temperatures used in the experiments.

2.2.9 REFERENCES CITED

Croasdale, K. R. (1974) Crushing strength of Arctic Ice; *in* Coast and Shelf of the Beaufort Sea, Proceedings of a Symposium on Beaufort Sea Coast and Shelf Research, J. C. Reed and J. E. Slater, eds., Arlington, Virginia, Arctic Institute of North America, PP. 377-399.

Groasdale, K. R., Morgenstern, N. R. and Nuttall, J. B. (1977) Indentation tests to investigate ice pressures on vertical piers; Jour. Glac., v. 19, no. 81, pp. 301-312.

Deklotz, E. J. and Boisen, B. P. (1970) Development of Equipment for determining deformation modulus on in situ stress by means of large flatjacks; *in* Determination of the In Situ Modulus of Deformation of Rocks, ASTM STP 477, pp. 117-125.

Gold, L. W. (1979) The process of failure of columnar-grained ice; Phil. Mag., v. 26, no. 2, pp. 311-328.

Jacka, T. H. (1984) The time and strain required for development of minimum strain rates in ice; Cold Regions Sci. and Tech. v. 8, pp. 261-268.

Jaeger, J. C. and Cook, N. G. W. (1976) Fundamentals of Rock Mechanics, 2nd ed., Halsted Press, New York, pp. 585.

Peyton, H. R. (1966) Sea ice strength; Geophysical Inst. U. of Alaska-Fairbanks Report UAG R-182, pp. 273.

Pratt, H. R., Black, A. D., Brown, W. S. and Brace, W. F. (1974) A new technique for determining the deformation frictional characteristics of in situ rock; *in* Field Testing and Instrumentation of Rock; ASTM STP 554, pp. 3-19.

Shapiro, L.H. and Hoskins, E. R. (1975) The use of flatjacks for the in situ determination of the mechanical properties of sea ice; Proc. 3rd Conf. on Port and Ocean Eng. under Arctic Conditions, Fairbanks, Alaska, pp. 427-436.

Shapiro, L. H., Hoskins, E. R., Nelson, R. D. and Metzner, R. C. (1979) Flatjack methods of in situ measurement of the mechanical properties of sea ice; Trans., A.S.M.E., Jour. Energy Resources Tech., v. 101, pp. 1996-2002.

St. Lawrence, W. F. and Cole, D. M. (1982) Acoustic emissions from polycrystalline ice; Cold Regions Sci. and Tech. v. 5, pp. 183-199.

Wang, Y. S., 1979, Crystallographic studies and strength tests of field ice in the Alaskan Beaufort Sea; Proc. 5th Conf. on Port and Ocean Eng. under Arctic Conditions, Trondheim, Norway, pp. 651-655.

Weeks, W. F. and Assur, A. (1967) The mechanical properties of sea ice; USA CRREL Cold Regions Science and Engineering, Part II, Section C, pp. 80.

Weeks, W. F. and Gow, A. J. (1978) Preferred crystal orientations in the fast ice along the margins of the Arctic Ocean; USA CRREL Report 78-13.

2.3 A STRESS-STRAIN LAW AND FAILURE CRITERION FOR SEA ICE

by

Lewis H. Shapiro

ABSTRACT

The objective of this section is to describe the deformational behavior of the spring-dashpot model of a 4-parameter viscoelastic fluid constrained to fail according to the distortional strain energy density criterion. The results predict upper and lower strength limits for the model, and permit curves to be derived which show the relationships between the results of hypothetical tests on the models at different loading paths and rates. Comparison of the analytical results to experimental data for sea ice and polycrystalline fresh ice shows that the trends of the curves are similar and that the strength limits may correspond to transitions in deformation mechanisms. This suggests that the combination of a more realistic non-linear model with the failure criterion could provide an accurate description of the stress-strain relations and failure of ice under a range of loading conditions.

2.3.1 INTRODUCTION

A program of evaluation of previous work on the strength and mechanical properties of sea ice was conducted along with the experimental work described in the last section of this report. The objective was to identify and characterize the deformational behavior of sea ice, with the intent of using the results to indicate a possible form of a stress-strain law and failure criteria for sea ice. Since most of the available data are for loading in uniaxial compression (as are the results reported in Section 2.2.4.5), the law was to be restricted to deformation in that loading mode. However, examination of the published data for tests in other loading modes suggests that the results may be applicable to some of these as well.

It is well known from experimental work that, for uniaxial compression tests, most types of ice follow the same basic patterns of response to load. In general, the strength and rate of deformation are non-linearly related to the load (in constant load tests) or to the rate of loading (in constant load rate or constant deformation rate tests). This is certainly true for sea ice, as shown by the data in the last section and by the review of the literature. In addition, as has been previously noted (see, for example, Mellor, 1980), the stress-strain curves for ice are qualitatively similar to curves calculated for the response to load of the model of a linear 4-parameter viscoelastic fluid (4-PF). This suggested that the stress-strain law for a 4-PF with non-linear elements might provide realistic curves to match the data. Accordingly, a series of stress-strain calculations were done for such a 4-PF model, and the work was extended to consider the case where the model is constrained to fail under the distortional strain energy criterion (DSEC). The results qualitatively predict the relationships between tests along different loading paths and also provide a basis for explaining many of the results of experimental programs. In addition, they lead to suggestions for further experimental work.

The stress-strain law for the 4-PF model with non-linear elements is cumbersome and requires numerical values of the parameters for calculation of the curves, so that it is difficult to generalize the results. In order to permit generalizations to be made, and to examine the details of the behavior of the combined 4-PF and DSEC model, it is preferable to use the model with linear elements for which most-of the derivations can be done in closed form. The presentation and discussion of the results of that work in terms of available data is the subject of this report.

The remainder of this section is divided into five subsections. The characteristics and justification for the use of the 4-PF model and the DSEC are described in Sections 2.3.2 and 2.3.3, respectively. They are then combined in Section 2.3.4

and the conditions for yield of the model under different loading programs are derived without reference to experimental results. There are two reasons for this approach. First, as noted above, the stress-strain laws for the elements in the model are taken to be linear. This permits most of the derivations and proofs to be done in closed form rather than numerically, which is convenient for qualitative comparison between the deformation of the model and the available data. However, the results of this analysis cannot be applied quantitatively to the non-linear behavior of sea ice. The results of calculations based on the non-linear model are shown for comparison, to illustrate that the trends of the relationships are independent of the form of the laws. However, the results of this section are intended to be interpreted qualitatively.

The second reason is to emphasize the fact that the model is simply a mathematical device which may (or may not) represent the response to load of a real material over some range of conditions. In effect, it is a mathematical entity which is independent of any data set. Its utility for describing the deformational behavior of a real material depends upon the extent to which the calculated deformation of the model and the actual data agree. There is no *a priori* reason to expect these to agree over any, or all, of the possible ranges of the variables; the degree to which they correspond is a matter to be determined from examination of the data. The model responses are discussed in terms of imaginary experiments on some ideal material which the model represents. This is done so that uncertainties which arise in experimental programs can be included in the interpretation of the calculated results.

The results of the calculations are compared to the data on different ice types in Section 2.3.5. This section relies heavily on the data for sea ice presented in Sections 2.2.4.5 and 2.2.4.6, and on data from Hawkes and Mellor (1972), Mellor and Cole (1982), and Jacka (1984) on polycrystalline fresh ice.

The summary, conclusions, and suggestions for further work are given in Section 2.3.6, which is followed by an appendix (Section 2.3.8) where the details of the derivations appear.

In the equations which follow, the symbols σ for stress and ε for strain are assumed to be functions of time. They are written as shown in the interest of brevity. A dot over a time-dependent variable indicates the time derivative, and a zero subscript always defines a constant value (i.e. ε_0 is a constant strain rate; σ_0 is a constant stress). The "constants" used in the model are constant with respect to stress and strain, but would be expected to vary with the temperature and physical properties of the medium they represent. That variability is not considered here.

2.3.2 DESCRIPTION OF THE 4-PARAMETER FLUID MODEL

The justification for the use of the 4-PF model follows from the assumption (commonly used in the analysis of deformation experiments on ice and other materials) that the total deformation includes elements of instantaneous elastic response to the applied load followed by both time-dependent elastic and plastic behavior. Thus, the total strain is often represented by the equation

$$(1) \qquad \varepsilon_T = \varepsilon_E + \varepsilon_V + \varepsilon_D$$

where ε_T, ε_E, ε_V and ε_D are the total strain, "instantaneous" elastic strain, time-dependent elastic strain and time-dependent plastic strain, respectively. Equation (1) represents the response to load of the spring- dashpot model of a 4-PF (shown with linear elements in Figure 2.3-1) consisting of Voigt and Maxwell models connected in series. This is the simplest of the spring-dashpot models that contains all of the elements of a creep curve. The spring of the Maxwell model gives the "instantaneous" elastic response to an applied load while the viscous creep of the dashpot of the Maxwell model at constant stress represents the summation of the contributions of the mechanisms which produce time-dependent permanent

deformation in actual materials. The Voigt model provides a time-dependent elastic response which, in a creep curve, gives the decrease in strain rate with time through the primary creep stage and the time-dependent recovery of strain in the recovery stage following release of the load. Sinha (1979) suggested that grain boundary sliding is the mechanism which is responsible for this behavior. The use of the Voigt model here is justified by Hart et al. (1975) based upon experimental data from metals. They argued that the data require that the stress-strain relationship for delayed (time-dependent) elasticity is of the form

$$\dot{\varepsilon} = f[\sigma - M\varepsilon] \tag{2}$$

where $\dot{\varepsilon}$ is the strain rate and σ is the applied stress. The parameter M is defined as the "saturation" modulus and is found from the equation

$$M = \sigma_o/\varepsilon_M$$

when $\dot{\varepsilon}$ goes to zero and the strain reaches its maximum value ε_M at the transition from primary to steady state creep in a test at constant stress. Equation (2) is simply the form of the stress-strain law for a Voigt model (Flugge, 1967) in which M corresponds to the modulus of the spring k_2 in the 4-PF model (Figure 2.3-1).

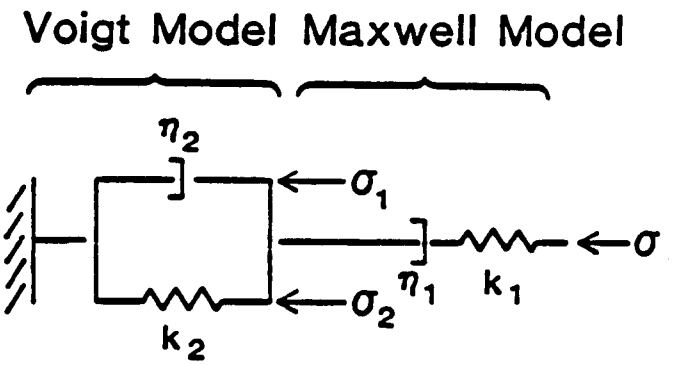

Figure 2.3-1 Spring-dashpot model of a 4-parameter linear viscoelastic fluid. k_1 and k_2 are spring constants, η_1 and η_2 are the Newtonian viscosities of the dashpots. σ_1 and σ_2 show the partitioning of the applied stress σ across the arms of the Voigt model, such that $\sigma = \sigma_1 + \sigma_2$ (see text).

Equilibrium of the stresses across the Voigt model (Figure 2.3-1) requires that

$$\sigma = \sigma_1 + \sigma_2$$

so that, for the linear case, the strain and strain rate are

$$\varepsilon_V = \sigma_1/k_2$$

and

$$\dot{\varepsilon}_V = \sigma_1/\eta_2,$$

where η_2 is the coefficient of Newtonian viscosity. Thus, the stresses, strain and strain rate of the Voigt model are related by the equilibrium condition at any stage in the loading path.

An important limitation on the ability of the 4-PF model to predict the response of actual materials follows from the form of equation (1) in which the contributions of the mechanisms which produce each of the types of response to load described above are added linearly. This is equivalent to the assumption that the elements do not influence each other in the sense that, for example, the magnitude of deformation due to time-dependent plastic flow mechanisms does not lead to changes in the values of the parameters which govern other types of deformation. It seems likely that this assumption must fail at some point in the deformation process, but the subject has not been investigated.

The parameters of the linear form of the 4-PF model have been determined for polycrystalline fresh ice from creep tests in tension (Jellenick and Brill, 1956) and in uniaxial and biaxial compression (Lindgrin, 1970), and for young sea ice in compression and bending (Tabata, 1958). Nevel (1976) used this stress-strain law in a theory of the creep of floating ice sheets. Stress-strain laws which are similar to the 3- or 4-parameter viscoelastic model have been applied to ice by Maser (1972) and Sinha (1978). The general application of these types of laws to ice has been discussed by Mellor (1980).

Note that there is no requirement that the elements of the model in Figure 2.3-1 be linear; non-linear elements (both springs and dashpots) have been used by different authors to describe the deformation of different materials. Hutter (1980) pointed out that only the hyperbolic sine law for steady-state creep is based on a theory of material behavior, the rate process theory [Glasstone et al., (1941); Krausz and Eyring, (1975)]. Commonly, the hyperbolic sine law is used for the dashpot of the Maxwell model in Figure 2.3-1, as in the non-linear stress-strain rate law for creep

$$\dot{\varepsilon} = A (\sinh \phi\sigma)^n.$$

However, it has also been used for the dashpot of the Voigt model in the application of the stress-strain law of a 3-parameter viscoelastic solid to polymers, rubber and textiles (Krausz and Eyring, 1975, and references cited therein). The non-linear law considered earlier in this project (and described in the appendix) involved the use of the hyperbolic sine law for both dashpots. Other workers have used other combinations of linear and non-linear elements. This is permissible, provided that the contributions of the model elements add as shown in equation (1).

For any stress-strain relations of the individual elements, the 4-PF model yields a differential equation which can be integrated for any loading path. The discussion here will be restricted to the paths commonly used in experimental programs; constant stress (CS), constant stress rate (CSR) and constant strain rate (CDR). The curves from the integrated equations for these paths for the linear model are shown in the appendix. They are qualitatively similar to experimental curves for ice up to the point of failure (see, for example, the discussion in Mellor, 1980).

The parameters of an ideal linear material represented by a 4-PF model can be determined from the results of a single creep test. More creep tests would be required in order to determine the form of the stress-strain law for the dashpot of the Maxwell model of an ideal non-linear material. Given that law, the form of the laws

for the elements of the Voigt model can be found. However, these determinations assume that the material is in steady state creep, as required by the definition of the "saturation" modulus. As discussed in Section 2.3.5.2, this condition is probably never reached in experiments on ice. Thus, there is a question as to the significance of the parameters reported in the references cited above. The point is discussed in Section 2.3.5.4.

2.3.3 DESCRIPTION OF THE DISTORTIONAL STRAIN ENERGY DENSITY YIELD CRITERION

Reiner and Weissenberg (1939) suggested the idea of applying the DSEC to spring-dashpot models, and Reiner (1960) demonstrated the results for the 3-parameter linear viscoelastic solid. The extension to the 4-parameter model follows directly. Day (1975) has given a general proof that the application of the DSEC to models of this type is valid without restriction to elements with linear stress-strain laws, provided that the model elements do not influence each other, in the sense described above.

The DSEC is based upon Von Mises' criterion expressed in terms of the strain rather than the stress (Reiner, 1960). The work done by the applied stress in deforming the dashpots of the model is assumed to be dissipated through internal friction, while that done on the springs is stored as distortional elastic strain energy. Yield is assumed to occur when the stored distortional strain energy reaches the resilience, "R", the energy (per unit volume) required to deform an elastic body to its elastic limit.

Note that while Von Mises' criterion was derived to predict yield (the onset of flow) of plastic materials, it has also been used as a fracture criterion for ice, rock, and other materials (as in Section 3.1). For the remainder of this work, the general term "failure" is used in place of "yield" since, as shown below, the DSEC

appears to apply to experimental results over the range from ductile to true brittle behavior.

Von Mises criterion is expressed by the equation

$$J_2 = K^2,$$

where J_2 is the second invariant of the stress deviator tensor and K is the shear strength of the material represented by the model. Assuming the material to be elastically isotropic, for uniaxial loading at a stress σ, following Mendelson (1968)

$$J_2 = (1/3)\,\sigma^2$$

and the distortional strain energy is

$$U_d = (1/6G)\,\sigma^2 = (1/2G)\,J_2$$

where G is the shear modulus. Then, from Reiner (1960) the distortional strain energy of the 4-parameter model is simply the sum of the strain energies stored in the two springs. Failure occurs when

$$U_d = R = k_1(\varepsilon_E)^2 + k_2(\varepsilon_V)^2 \tag{3}$$

in which k_1 and k_2 are the spring constants (Figure 2.3-1).

Note that this relationship applies regardless of the functional form of the stress-strain laws of the elements of the model, or the loading path. It simply expresses the required relationship between the spring modulii and the stored elastic energy at the instant of failure. In this sense, the DSEC differs from some other failure criteria in that it is written in terms of the material parameters rather than the instantaneous state of stress, strain or strain rate, or their histories. It is this aspect of the criterion which provides flexibility in application to different loading paths and has the potential to predict the strength of the model from its properties alone, independently of the the loading paths. However, the influence of deformation history is accounted for in the calculation of the failure stress in any particular case, as shown in Section 2.3.4.

In using the model to represent a real material, the model parameters are determined from experiments in which no permanent deformation of the sample (i.e., fracturing or re-crystallization) occurs. This introduces a question as to the meaning of the term "failure" as it applies to the model. In general, failure can be viewed as a process, rather than an event, in the sense that a critical stress at which failure occurs is not reached throughout the entire test specimen at the same instant. Instead, the sample breaks down over a finite time interval as the stress is redistributed after each successive failure of a relatively small volume within which the critical state has been reached. The time required for the process to run its course varies from almost instantaneous for the case of brittle fracture at high loading rates, to much longer times for lower loading rates or low magnitudes of constant stress. In any case, the breakdown of the sample is accompanied by changes in the material constants, such as the decrease in Young's modulus which results from an increase in the number and lengths of cracks in a sample. Similarly, re-crystallization during creep at low stresses produces an essentially new material. Now, assume that an accurate stress-strain law is written for some material based upon its properties in the initial state, and the law is used to calculate the response of the material for a particular loading path. The experimental curve for such a material loaded to "failure" along that loading path would initially follow the calculated curve. However, as the material parameters of the sample change by crack growth or re-crystallization as failure is approached (depending upon the loading path, as discussed below) the experimental curve would tend to deviate from the calculated curve. The separation of the two curves would occur when the material parameters had changed sufficiently that the material no longer followed the calculated curve. Subsequently, the test is, in effect, being conducted on a "new" material, in the sense that its properties are not the same as those at the start of the test. In an actual experiment, the identification of the point where the curves

separate would depend upon the precision with which the test parameters could be monitored.

The sense in which the discussion above is meant is well illustrated by the inflection point at the minimum strain rate of a CS test. Since the stress (and other test conditions) are held constant through the test, the change in response of the sample to the load as it passes from the secondary to tertiary creep stages can best be explained as resulting from changes in the values of the material parameters. The changes may occur gradually through the test, but only become apparent when they are cumulatively great enough to cause the curve to deviate from its projected path.

The suggestion is that the point of separation of the experimental and theoretical curves in CS tests is predicted by a failure criterion based upon the initial parameters. This raises the question of whether the comparable point in CSR or CDR tests is close to or at the peak stress which might ultimately be reached in the test. There is presently no firm basis for answering this question in the absence of experimental data. The best that can be done is to compare the theory to the data, as is done in Section 2.3.5.

The reader who is familiar with the literature on the deformation of ice in uniaxial compression will undoubtedly recognize the similarities to the behavior of the model as they arise in the following sections. However, for purposes of discussion, it is simpler to describe these relationships first in terms of the idealized model. Then, the results can be compared to the data for the real material. This approach has the added advantage of emphasizing the fact that the model is a mathematical device which may or may not represent the behavior of a real material over some range of conditions. The degree to which the response to applied load of the model and the real material correspond is a matter to be determined.

2.3.4 APPLICATION OF THE DSEC TO THE 4-PF MODEL

2.3.4.1 Upper and Lower Strength Limits

An immediate result of the application of the DSEC to the 4-PF model is to set upper and lower bounds on the strength of the model. Further, these limits are independent of the loading path and the functional forms of the stress-strain laws for the viscous elements of the model. The upper limit can be found in terms of the strain in the springs by rewriting equation (3) in the form of the ellipse

$$(k_1/R)(\varepsilon_E)^2 + (k_2/R)(\varepsilon_V)^2 = 1$$

in which k_1/R and k_2/R are the major and minor axes respectively. Note that this assumes that $k_1 > k_2$, which seems to be justified based upon the determinations of the parameters noted above. Stable combinations of the elastic strains plot within the ellipse while failure occurs for combinations of the elastic strain of the two spring elements which plot along the ellipse. Failure at the point of intersection of the ellipse and the ε_E-axis corresponds to the case when all of the strain energy required to cause failure is stored in the lead spring of the model. Since the spring of the Voigt element extends as a function of time, it follows that failure under this loading condition occurs instantly on application of the load, before any strain can accumulate in the Voigt model. The stress required to cause failure under this condition is simply

$$\sigma_u = k_1 \varepsilon_u \tag{4}$$

where $\varepsilon_u = \varepsilon_E$ when the strength $\sigma_c = \sigma_u$ as time t goes to zero in the limit.

Failure at the intersection of the ellipse and the ε_V-axis (i.e. $\varepsilon_E = 0$) requires that the applied stress and the modulus of the spring of the Voigt model be infinitesimally small. This is because any applied stress of finite magnitude must cause some strain in the spring of the Maxwell model. Thus, if the spring moduli are finite, there must be some lower limit to the stress which can cause failure.

The stresses at both the upper and lower limits can be found by rewriting equation (3) in terms of the stresses across the springs at failure, using Hooke's law for each of the springs, to give

(5) $$U_d = R = (1/k_1)\,\sigma^2 + (1/k_2)(\sigma_2)^2$$

or

$$(1/k_1R)\,\sigma^2 + (1/k_2R)(\sigma_2)^2 = 1.$$

As above this is also the equation of an ellipse with k_1R and k_2R as the major and minor axes respectively (Figure 2.3-2). Equilibrium of the stresses across the elements of the Voigt model requires that σ_2 be less than or equal to σ. Therefore, the stresses at failure must lie on the ellipse and to the right of the 45° line in Figure 2.3-2. Stable combinations of stresses plot inside the ellipse.

The intersection of the failure ellipse with the σ-axis gives σ_u as defined in equation (4) or, from equation (5), with $\sigma_2 = 0$,

(6) $$\sigma_u = (k_1R)^{1/2}.$$

Note that this represents an upper limit to the strength only in the sense that it is the largest stress that the model can sustain for a finite length of time and can therefore be measured against the model in an experiment. Any attempt to apply a load larger than σ_u would cause the model to fail instantly as the stress passed through σ_u. The intersection of the 45° line and the ellipse gives the minimum value of σ ($= \sigma_b$) required to cause the model to fail. From the appendix, this occurs when the time t approaches infinity in the limit, so that $\sigma_2 \rightarrow \sigma$, which, from equation (5), gives

(7) $$\sigma = \sigma_b = [Rk_1k_2/(k_1 + k_2)\text{-}1]^{1/2}.$$

Note that for a CS test at some $\sigma > \sigma_b$ failure depends upon the time required for the stress σ_2, to rise to the ellipse along a path normal to the σ-axis. The time depends on

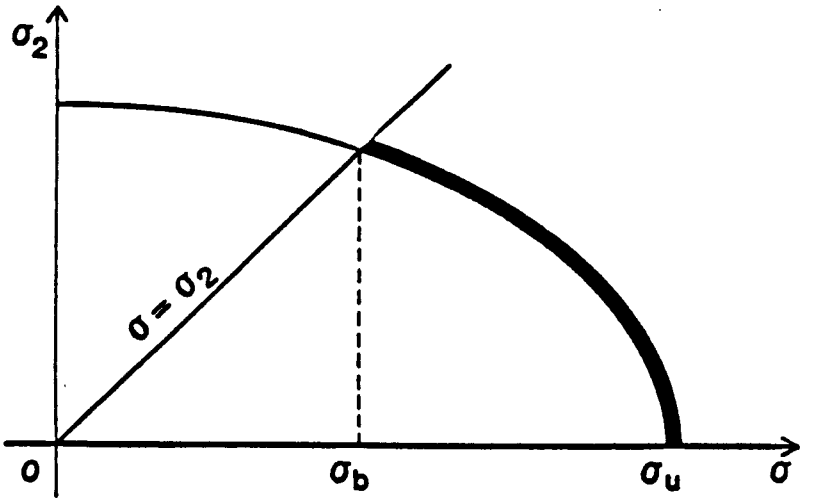

Figure 2.3-2 Yield envelope in terms of the applied stress σ and the stress across the spring of the Voigt model, σ_2. Since $\sigma_2 \leq \sigma$, the state of stress must plot to the right of the line at 45° to the σ-axis. σ_u and σ_b as indicated (see text for discussion).

both elements of the Voigt model through the relaxation time

$$\tau_2 = \eta_2/k_2$$

and the applied stress (see appendix). It is small when the stress is large, and approaches infinity as $\sigma \rightarrow \sigma_b$. Any $\sigma < \sigma_b$ can be sustained indefinitely by the model, because no stress path which does not intersect the ellipse to the right of the 45° line can cause failure. In the limit, a CS test on the model at a stress less than σ_b should reach steady state (in the ideal sense of a constant strain rate) because there will never be sufficient strain energy accumulated in the springs to cause failure. This is the condition at which the "saturation modulus" of Hart et al. (1975) referred to above can, theoretically, be determined. From that point, no further elastic strain occurs, and the only element of the model which is active is the dashpot of the Maxwell model. Similarly, a CDR test in which

$$\sigma = \eta_1 \dot{\varepsilon}_D < \sigma_b$$

will go to a steady state stress.

The stress σ_b thus represents the "fundamental strength" of the model; it is the largest stress which the model can sustain indefinitely without failure. While, as noted, experimental evidence indicates that it is incorrect to suggest that there is a lower limit to the strength of ice (see Section 2.2.4.6.3), the concept has implications for theoretical and experimental work as well as potential utility in applied problems. The point is discussed further in Section 2.3.5.4.

Finally, note that, for the case when the elastic moduli are constant, the fundamental and maximum strengths of the model are related through the ratio of the spring moduli as [from equations (6) and (7)]

$$\sigma_u/\sigma_b = [1 + (k_1/k_2)]^{1/2}.$$

2.3.4.2 Relationships at Failure

2.3.4.2.1 *Introduction*

The DSEC prescribes relationships at failure of the 4-PF model between stress, strain, strain rate and time which are similar to those observed from experiments on ice. This will be illustrated by considering the determination in CS, CSR and CDR tests of both the linear 4-PF model and a non-linear model in which the strain rates of the dashpots are related to the stress through the hyperbolic sine law. It will be apparent that the qualitative results (i.e. the forms of the curves) are independent of the linearity or non-linearity of the stress-strain laws of the model elements.

In developing the arguments below, the solutions for the relationships between strength, strain rate, strain and time for CS and CSR tests are derived in closed form for the linear model (see appendix). In both tests, the stress applied to the model is specified, so that the stress across each of the model elements connected in series is known independently of the deformation. The partitioning of the stress across the elements of the Voigt model can be found from the equilibrium condition above.

Thus, the response of any element of the model to the applied load can be determined without reference to the state of deformation of any other element and it is not necessary to assign specific stress-strain laws (with numerical values of the constants) to the dashpots of the model. In CDR tests, this is not the case. When a constant strain rate ($\dot{\varepsilon}_o$) is applied to the linear model, the strain rate is partitioned across the elements so that the equation

$$\dot{\varepsilon}_o = \dot{\varepsilon}_E + \dot{\varepsilon}_D + \dot{\varepsilon}_V$$

is satisfied. As a result, the stress varies with the deformation according to a rather complicated algebraic expression (see appendix) which requires that a stress-strain relationship and numerical values be assigned to the dashpot of the Maxwell model if the stress is to be determined. For convenience, the solutions were done numerically and the results non-dimensionalized to the same parameters as were used in the case of the CS and CSR tests. The procedures are given in the appendix.

For the non-linear 4-PF model, closed form solutions were derived for the cases of CS and CSR tests, but a numerical solution was required for CDR tests. In addition, it was not practical to non-dimensionalize the parameters of the non-linear model. Instead, numerical values were used. The values were selected based on the results of experimental determinations of the parameters of the linear model for different ice types (see reference in Section 2.3.2). They are clearly approximations, so that the results are not intended to represent any particular type of ice. The values used in the calculations for the non-linear model are given in the appendix.

In the discussion which follows, the term "strength" refers to the stress in a CSR or CDR test at the instant the failure criterion is satisfied. In CS tests, strength is simply the applied stress, which is assumed to be between the strength limits so that "failure" occurs as a function of time. The equations which describe the deformation of both the linear and non-linear models (see appendix) permit the

stress, strain, stress rate, strain rate, and time at "failure" to be calculated for any test. The results of these calculations were used to prepare the curves in the following sections.

2.3.4.2.2 *Strain at Failure*

Figure 2.3-3 is a chart which shows the stress-strain and stress- strain rate relationships for each of the elements of the linear model at the instant of failure under a uniaxial compressive stress for CS, CSR and CD tests. As illustrated in the chart, the elastic strain in the springs of the model must be partitioned in the same manner regardless of the loading path. This is because the strain of the lead spring is determined by the stress at failure (through a 1-dimensional elastic stress-strain law applied to the spring). This, in turn specifies a single value of the strain in the Voigt model which is required to satisfy the DSEC. The proof is given in the appendix for CS and CSR tests; calculations for CDR tests (also in the appendix) give the same result.

A plot of the elastic strain at failure vs. compressive strength (see appendix for elastic moduli) is shown in Figure 2.3-4 in which σ_u is the upper strength limit of the model and ε_u is the strain at that stress. Note that the curve shows relatively little variation over most of the range of possible strengths. However, it passes through a maximum value of the elastic strain at failure at the "fundamental strength " (as indicated in Figure 2.3-4), which is too low to be evident at the scale of the plot.

In order to find the total strain at failure for comparison, it is necessary to include the strain of the dashpot of the Maxwell model. To permit this strain component to be calculated, the coefficient of Newtonian viscosity (η_1) was assumed to have the value required to match the strain rate predicted by the power law at a stress of 1 MPa (see appendix). The curve for the total strain at failure for a CS test

		STRAIN AND STRAIN RATE	CONSTANT STRESS CL. σ_c=CONSTANT	CONSTANT STRESS RATE CLR. $\sigma_c = \dot{\sigma}_o t_f$	CONSTANT DEFORMATION RATE CD. $\epsilon_T = \dot{\epsilon}_o t_f$
MAXWELL MODEL	SPRING	ϵ_{Ef} =	$\frac{\sigma_c}{k_1}$	$\frac{\sigma_c}{k_1} = \frac{\dot{\sigma}_o t_f}{k_1}$	$\frac{\sigma_c}{k_1}$
		$\dot{\epsilon}_{Ef}$ =	0	$\frac{\dot{\sigma}_o}{k_1}$	$\frac{\dot{\sigma}_o}{k_1}$
	DASHPOT	ϵ_{Df} =	$\frac{\sigma_c t}{\eta_1}$	$\int_0^t \frac{\dot{\sigma}_o t}{\eta_1} dt$	$\int_0^t \frac{\sigma}{\eta_1} dt$
		$\dot{\epsilon}_{Df}$ =	$\frac{\sigma_c}{\eta_1}$	$\frac{\sigma_c}{\eta_1}$	$\frac{\sigma_c}{\eta_1}$
VOIGT MODEL		ϵ_{Vf} =	$\frac{\sigma_2}{k_2}$	$\frac{\sigma_2}{k_2}$	$\frac{\sigma_2}{k_2}$
		$\dot{\epsilon}_{Vf}$ =	$\frac{\sigma_c - \sigma_2}{\eta_2}$	$\frac{\sigma_c - \sigma_2}{\eta_2}$	$\frac{\sigma_c - \sigma_2}{\eta_2}$

Figure 2.3-3 Chart showing the relationships between the stress, strain and strain rate in each element of the linear 4-PR model at yield according to the DSEC for three loading paths.

on a model with the same ratio of elastic moduli as was used to calculate the elastic strain at failure is also shown in Figure 2.3-4. The curve for the total strain at failure for CSR and CDR tests (with the same moduli) must lie between the two curves shown. This follows because the strain in the dashpot of the Maxwell model at failure must be greatest for CS tests since the sample is under the peak load for the duration of the test. Figure 2.3-4 shows that, as for the elastic strain, the total strain at failure is also relatively constant over most of the range of possible strengths. The increase in total strain at low strength reflects the increase in time-to-failure (discussed in Section 2.3.2.2.4) which permits the strain in the dashpot of the Maxwell model to become large.

The shape of the curve for the total strain is obviously dependent on the stress-strain law of the lead dashpot. For a non-linear dashpot,in which the strain rate

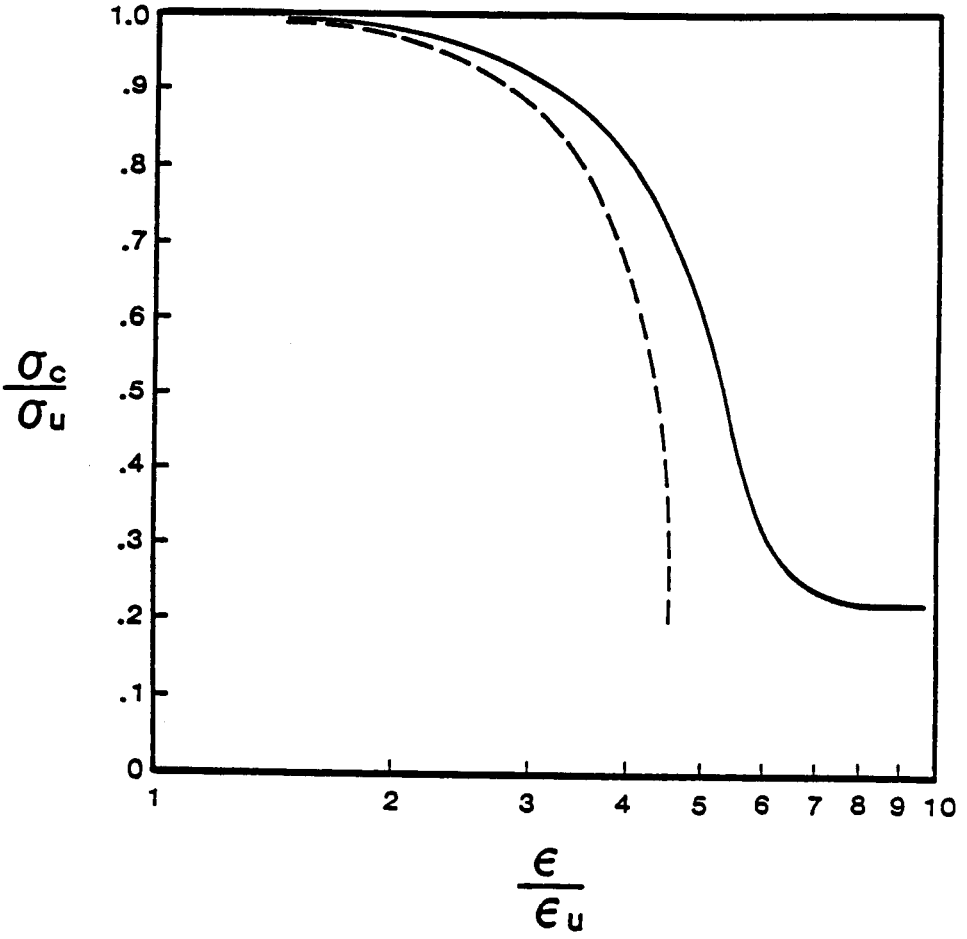

Figure 2.3-4 Stress ratio vs. strain ratio at yield for the linear model. Dashed line is elastic strain and solid line is total strain (see text for discussion).

increases rapidly with increasing stress, the curve for total strain might be anticipated to be straighter than that for the linear model. An example calculated from the non-linear law is shown in Figure 2.3-5. The relevant derivation is given in the appendix.

The results suggest that, over most of the range of strengths, the total strain at failure in CS, CSR and CDR tests should show little variation. Thus, in actual experiments, the normal uncertainties of strain measurement might prevent the details of the curve from being defined, so that the results would suggest that the strain at failure is independent of the strength.

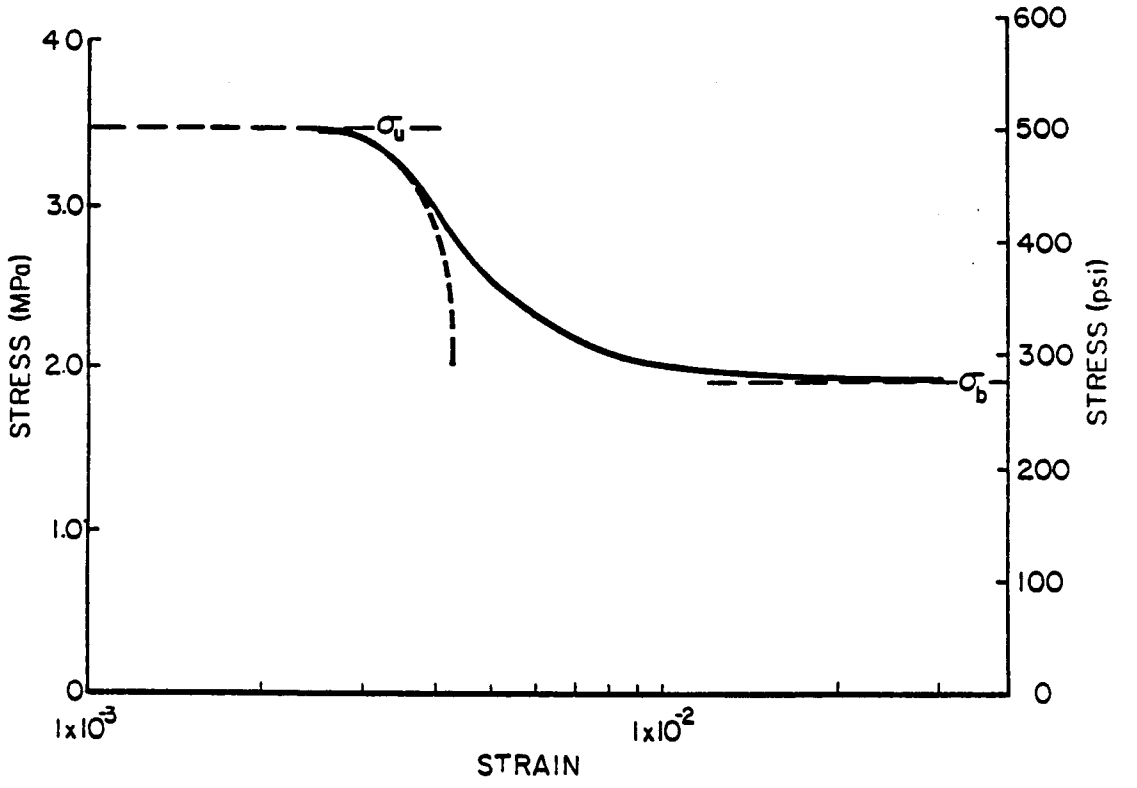

Figure 2.3-5 Stress vs. strain at yield for the non-linear 4-PF model described in the text. Dashed line is elastic strain and solid line is total strain. σ_u and σ_b are the upper and lower strength limits.

2.3.4.2.3 *Strain Rate at Failure*

A second point that can be deduced from the chart in Figure 2.3-3 is that the strain rates at the instant of failure should also be similar for any strength for CS, CSR and CDR tests. This follows because the strain rate of the lead dashpot is fixed by the stress at failure regardless of the form of its stress-strain law. Further, since the strain of the Voigt model must be the same at any strength for any loading path, the partitioning of stress in the Voigt model requires that the stress on the spring (σ_2) be the same at failure, independent of the loading path. Therefore, the stress on the dashpot ($\sigma - \sigma_2$) is also the same, so that the strain rate of the Voigt model is the same. Thus, the differences between strain rates at failure for different loading

paths depends only on the strain rate of the lead spring. This rate, in turn, depends on the rate of change of the stress according to the equation

$$\dot{\varepsilon}_E = (1/k_1)\dot{\sigma}$$

For CS tests, the applied stress is constant so that the strain rate in the lead spring is zero. For CSR and CDR tests the strain rate at failure must therefore be greater, as shown in Figure 2.3-6 for the three loading paths. The limits on the range of possible strengths is indicated by the asymptotes to the upper and lower limits. For stresses below the fundamental strength, the model would simply go to

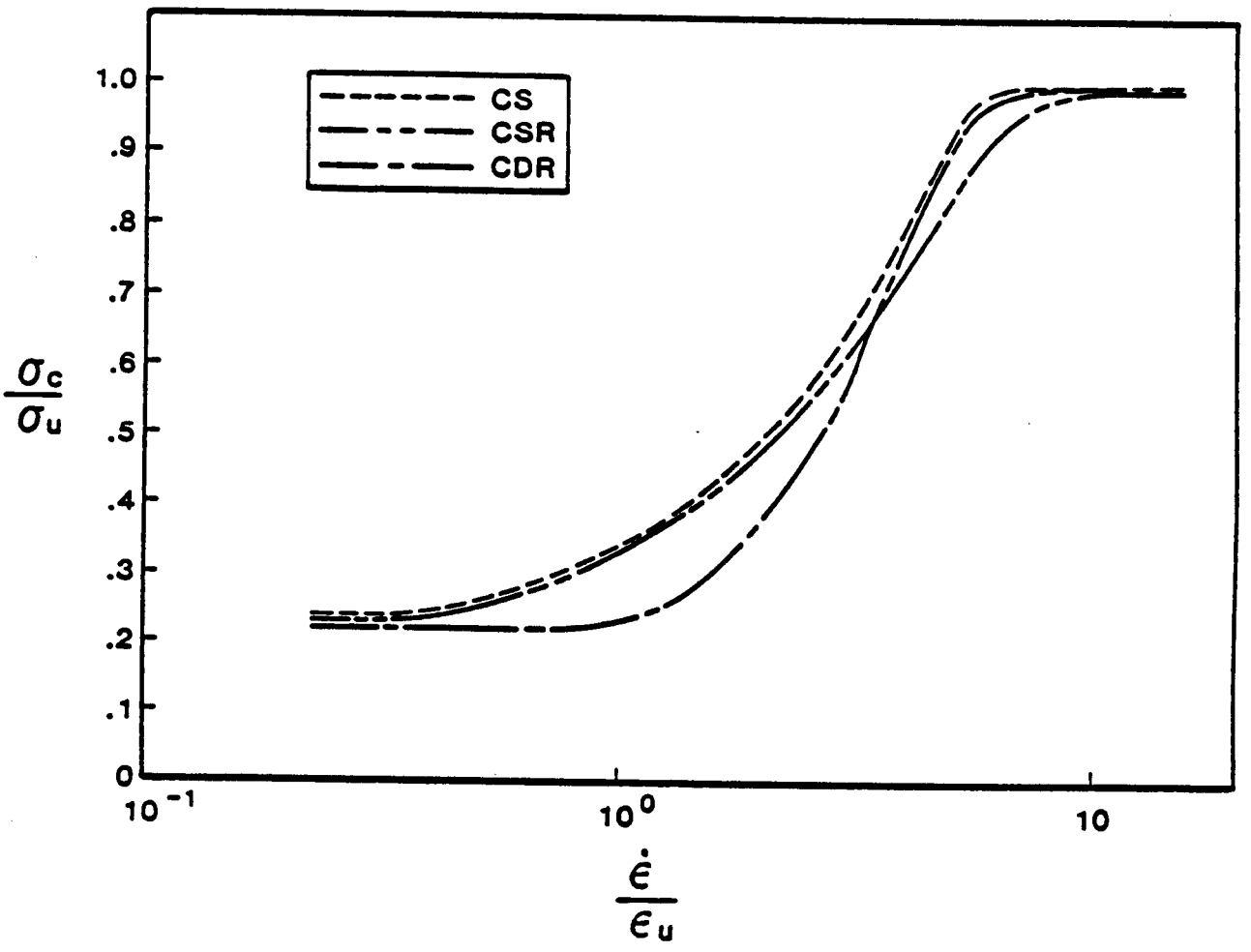

Figure 2.3-6 Stress ratio vs. strain rate ratio at yield for the linear model. Loading paths indicated in key.

steady state creep and the stress-strain rate curve in that range would follow the stress-strain curve for the lead dashpot.

The magnitude of the difference between the curves, and the limited range of strain rates over which failure occurs, reflect the assumption of linearity of the dashpots. This can be seen by comparing Figure 2.3-6 with Figure 2.3-7 which was calculated from the non-linear model. In this example, the curves for the three loading paths could not be separated at the scale of the plot and the range of strain rates at failure is clearly increased.

2.3.4.2.4 *Time-to-Failure*

The time-to-failure as a function of strength for the three tests depends on the rate of loading and the time constants of the dashpot of the Voigt model. The curves for the linear model are shown in Figure 2.3-8 as ratios of σ_c/σ_u and time-to-failure to relaxation time of the dashpot of the Voigt model.

As might have been anticipated from consideration of the loading function, the time-to-failure at any stress is lowest for CS tests, since the model is under the peak stress from the instant of application of stress.

The curves reverse the pattern of the strength vs. strain rate curves and are asymptotic to both the upper and fundamental strengths. Note also that, on the semi-logarithmic plots used here, there are pronounced decreases in the slopes of the curves as the fundamental strength is approached. The rapid increase in the total strain at failure at stresses just above the lower limit (noted in Section 2.3.4.2.2) reflects the increased time-to-failure in this stress range.

For completeness, the comparable relationships for the non-linear model are shown in Figure 2.3-9.

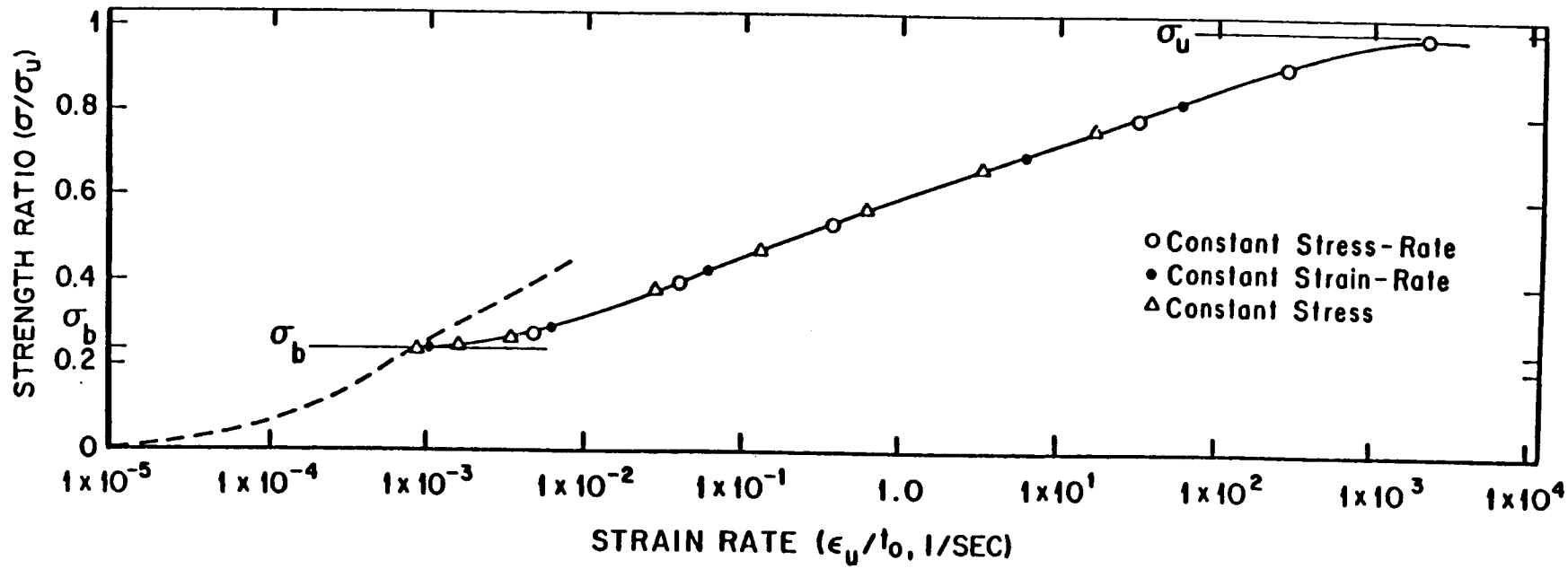

Figure 2.3-7 Stress ratio vs. strain rate at yield for the non-linear 4-PF model. Calculated points for the three loading paths define curves which are too close to draw separately at this scale. σ_u and σ_b are the upper and lower strength limits. Dashed line is the stress vs. strain rate curve for the dashpot of the Maxwell model.

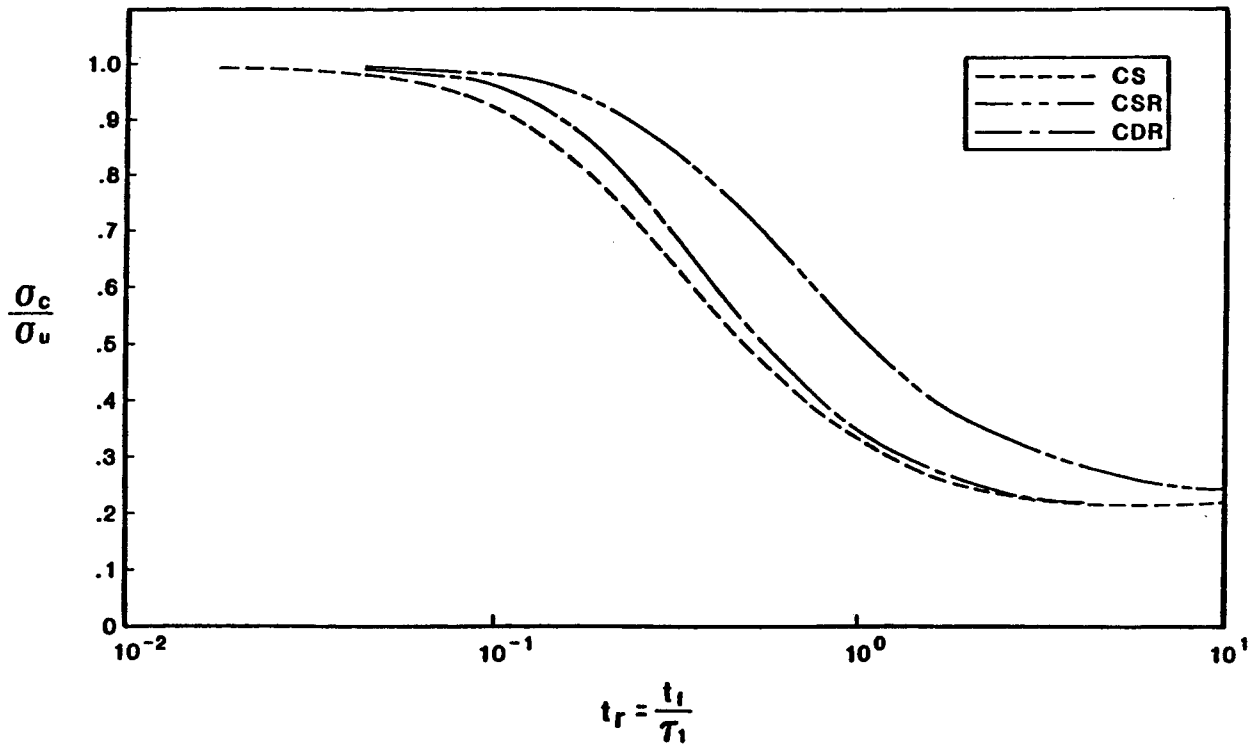

Figure 2.3-8 Stress ratio vs. time ratio at yield for the linear model. Loading paths as indicated in the key.

2.3.4.3 Summary of the Model

The application of the DSEC to the 4-PF model leads immediately to upper and lower limits to the strength of the model. The significance of the limits for studies of ice properties is discussed in the next section.

The relationships between the calculated curves for the three loading paths can be expected to vary depending upon the forms of the stress-strain laws of the individual model elements and the values of the model parameters. However, the model developed here provides the basis for interpretation of the relationships between tests to failure along different loading paths, through curves of the type in Figures 2.3-4 to 9 (note that strength-stress rate curves could be calculated for CSR- and CDR tests).

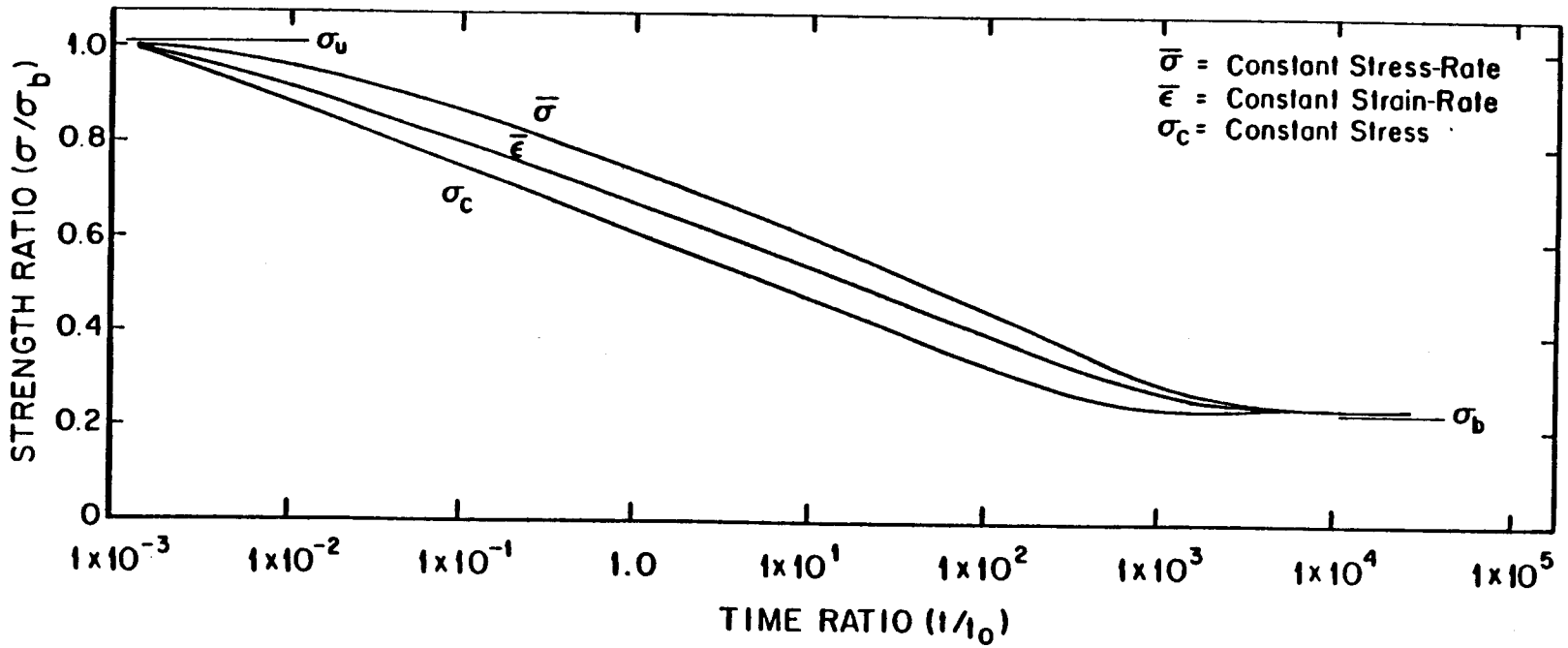

Figure 2.3-9 Strength vs. time-to-yield for the non-linear model. Loading paths as indicated in the key.

For both the linear and non-linear models the elastic strain at failure is the same for the three loading paths for every strength between the limits. The total strain tends to follow the elastic strain, but becomes large near the lower limit. However, over most of the range of strengths, the strain at failure is likely to be about the same for the three loading paths considered here.

Plots of strength vs. strain rate at the instant of failure for the three loading paths show the same trend of increasing strength with rate that is known from experimental data. The transition from the lower to the upper strength limit for the linear model occurs over a change in strain rate of about one order of magnitude of the strain rate, while for the non-linear model the transition takes place over about 5 to 6 orders of magnitude.This illustrates the strong dependence of this relationship on the form of the model.

The strength vs. time-to-failure curves show similar forms for the two models, with (for a given strength) the time increasing from CS to CDR to CSR tests. In addition, the asymptotes at the upper and lower strength limits are apparent.

2.3.5 COMPARISON WITH DATA

2.3.5.1 Introduction

The calculated curves presented in the last section are qualitatively similar to experimental curves for ice in uniaxial compression, but, it is clear that the assumption of a linear model will not permit numerical values for the parameters to be determined from experimental data over more than a limited range of the test variables. However, it may be possible to find reasonable parameters using non-linear models for the dashpots.

Perhaps the greatest use of the results above is in the possibility of establishing a framework for the interpretation of experimental data based on the theoretical upper and lower limits to the strength which result from the application of the

DSEC. As discussed next, based on comparison with experimental data, the limits may define the boundaries of ranges of test parameters across which the deformation mechanisms change.

2.3.5.2 Lower Limit of Strength

The experimental data indicate that there is no lower limit to the strength of ice as the theory predicts (Section 2.3.4). This was shown by Jacka (1984) in experiments on polycrystalline ice, in which CS tests were conducted over time periods of up to 9×10^7 seconds at temperatures from -5° to -32.5°C and stresses in the range of 0.1 to 1.7 MPa. In all cases, the strain rate decreased with time through the experiments, so that steady state creep, in the sense of the model, was never reached. In addition, the strain rate passed through a minimum (the inflection point of the strain-time curve) in most of the tests, with the exception of those at the lowest temperatures and stresses. These were stopped while the strain rate was still decreasing. Jacka's (1984) data for stress vs. time to the minimum strain rate are plotted in Figure 2.3-10, along with similar data from Mellor and Cole (1982). Note the change in slope of the curve at a stress of about 0.5 MPa. Similar data from sea ice samples acquired during this project are shown in Figures 2.2-9 and 10, and show the same change in slope with decreasing stress.

There are numerous studies which provide data to suggest that the slope break in the stress vs. time-to-minimum strain rate curve for CS tests in uniaxial compression is associated with a change in deformation mechanism. St. Lawrence and Cole (1982) conducted CS tests on polycrystalline fresh ice during which cracking rates of the sample were monitored. The results showed that, at low stresses, the dominant deformation mechanism was by recrystallization with no cracking. However, at higher stresses the samples deformed by the growth of numerous small fractures without recrystallization. Duval et al. (1983) also showed

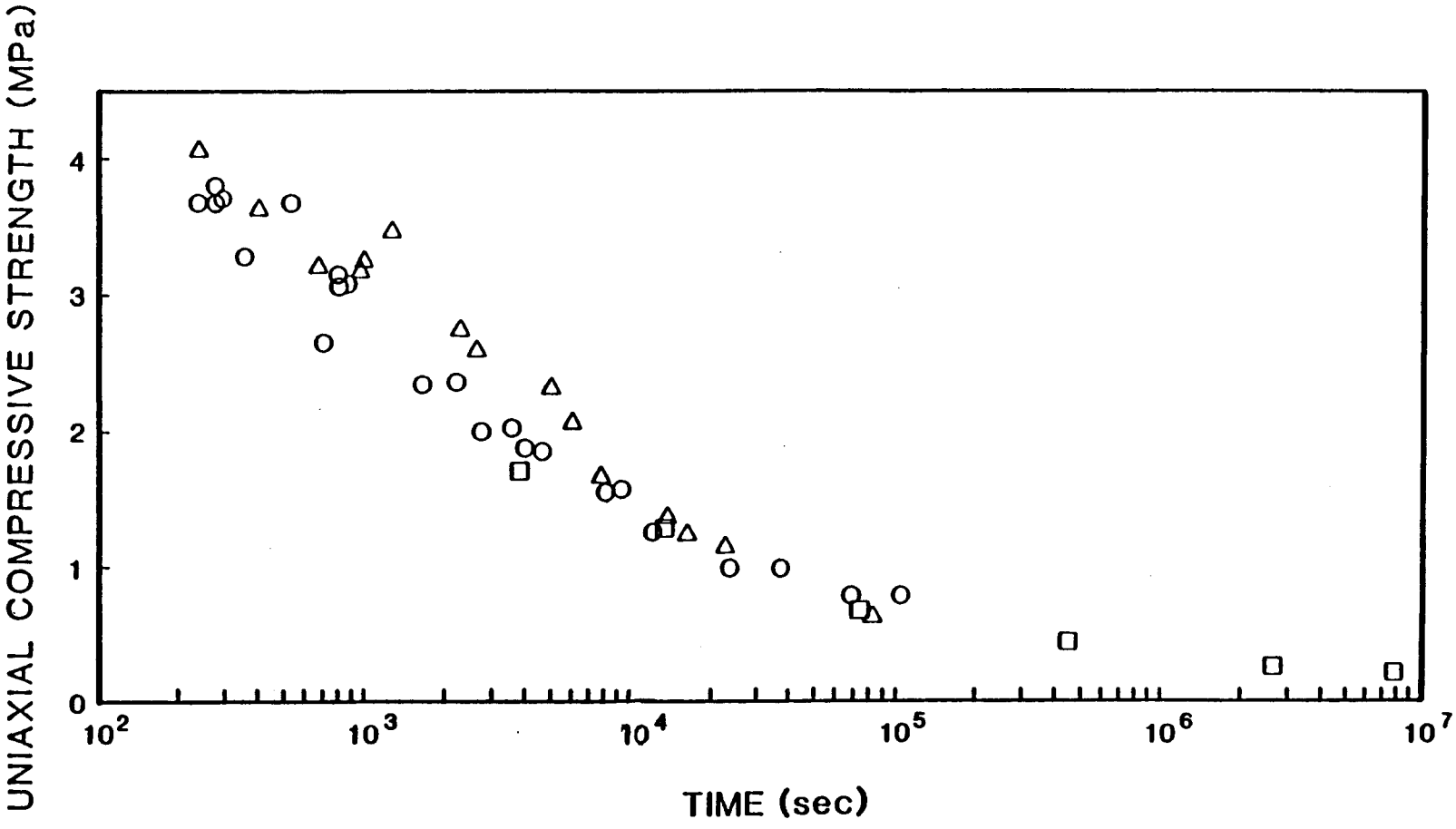

Figure 2.3-10 Uniaxial compressive strength of polycrystalline fresh ice vs. (1) time-to-minimum strain rate for CS tests [circles -- Mellor and Cole (1982); squares-Jacka (1984)], and (2) peak stress in CDR loading [triangles--Mellor and Cole (1982)]. Compared trends in data to Figures 2.3-8 and 2.3-9.

that minimum strain rates occur in CS tests with and without cracking, depending upon the stress level. Jacka and Maccagnan (1984) examined the onset of recrystallization in CS tests, and demonstrated that the process is associated with the minimum strain rate. Finally, in tests on sea ice reported in Section 2.2.4.6.3, failure in CR tests at low stresses always occurred by the progressive growth and coalescence of many small cracks, so that the ice samples turned milky white as deformation proceeded. Tests in which the minimum strain rate was not reached showed no such pervasive cracking. These studies all imply that the slope break in the stress vs. time to minimum strain rate in CS tests is related to the change in deformation mechanism from recrystallization to "brittle creep" (i.e., deformation by propagation of small fractures) leading to failure. A similar conclusion applies to CDR and CSR tests since all three tests types give the same break in slope (Figure 2.3-8), and results from tests at the three paths are included in Figures 2.2-10 and 2.3-10.

2.3.5.3 Upper Strength Limit

The existence of an upper limit to the strength of ice in uniaxial compression seems to be reasonable on physical grounds. As noted, it is simply the smallest stress which will cause "instantaneous" failure of the sample. An upper limit is implied by the results of experimental studies of the strength vs. strain rate relationship for ice from CDR tests either as an asymptote (Mellor and Hawkes, 1972) or as a peak, following which the strength decreases with increasing strain rate [see, for example, Vaudrey (1977)]. The calculated results above show that the DSEC applied to the 4-PF model requires that the strength become asymptotic to an upper limit with increasing rate of deformation or decreasing time to failure, rather than passing through a peak (Figure 2.3-6). Further, this applies to CS and CSR tests as well as CDR tests.

The failure mechanism in the upper range of strengths (i.e., at or beyond the peak) for the sea ice tests was described (Section 2.2.4.6.2) as brittle fracture along one or a few cracks which propagate across the sample, as opposed to the pervasive growth and coalescence of small cracks which lead to failure at lower strengths. The transition between mechanisms is gradual; the number of cracks in the sample at failure decreases with increasing stress. Samples which fail at high stresses tend to retain their initial clarity in the ice between the major fractures, as opposed to the milky white appearance of those failed at lower stresses.

2.3.6 DISCUSSION AND CONCLUSIONS

The comparison between the theory and the data suggests the following preliminary conclusions:

(1) With an appropriate choice of parameters the combination of the 4-PF model and the DSEC can be made to predict the strength and deformational behavior of both polycrystalline fresh ice and sea ice over the range between the upper and lower strength limits. Further, the limits correspond to changes in deformation mechanisms, rather than to limits on the actual strength of the ice.

(2) At stresses below the lower limit, polycrystalline fresh ice deforms by ductile mechanisms of which recrystallization is probably most important. Unfortunately, there are no data available regarding deformation mechanisms of sea ice in this range.

(3) As the upper limit is approached, the failure mechanism for both polycrystalline fresh ice and sea ice becomes true brittle fracture.

(4) Between the limits is a range of stresses in which the failure mechanism for both ice types involves the formation and coalesence of small, stable cracks. No studies have been done to examine the contribution of ductile deformation mechanisms to the total strain within this range. However, whatever the

mechanisms, the process results in a response to stress which (for the bulk sample) can be described as viscoelastic.

Thus, in effect, the model defines the boundaries of three discrete ranges of deformational behavior of ice, each of which may require a different stress-strain law for description.

The values of the upper and lower limits are known approximately for a few temperature ranges. A reasonable upper limit to the uniaxial compressive strength of polycrystalline ice at -7°C is about 9 MPa (Hawkes and Mellor, 1972). A lower limit of about 0.5 MPa at -5°C is suggested from the data in Figure 2.3-10. For sea ice, approximate values can be inferred using the data in Sections 2.2.4.6.3 and 2.2.4.6.4; the upper limit ranges from 2.7 to 6.2 MPA and the lower limit from 0.5 to 1 MPA as the temperature decreases from -5° to -20°C. It is of interest to note that most past work on the uniaxial compressive strength of all types of ice has been done in the lower half of the stress range between the limits.

As suggested in Section 2.3.4.2.5, it is questionable whether it is possible to determine appropriate values of the model parameters from creep tests on ice. This is because such determinations require that some of the measurements be made as the ice deforms in steady state creep which, as noted above, probably does not occur. However, it should be noted that all determinations of the parameters for the commonly cited one-dimensional creep laws (i.e., power, exponential or hyperbolic sine) are made based on the assumption that the ice is deforming in steady state. It is likely that, in future, it will be necessary for parameters to be determined by approximate methods, or by fitting assumed functions to data (i.e., Szyszkowski and Glockner, 1985).

The results above suggest that further experimental work could usefully be directed at studies of the transitions between mechanisms as the upper and lower limits predicted by the model are approached. In addition, the fact that a failure

criterion based on strain energy appears to define that boundaries suggests that energy considerations in brittle fracture and in dynamic recrystallization might be useful in analysis of the problem.

2.3.7 REFERENCES CITED

Day, W. A. (1975). On the Reiner-Weissenberg criterion for yield; Quart. Jour. Mech. and Appl. Math., v. 28, pp. 207-221.

Duval, P., Ashby, M. F. and Anderman, I. (1983). Rate-controlling processes in the creep of polycrystalline ice; J. Phys. Chem., v. 87, pp. 4066-4074.

Flugge, W. (1967). Viscoelasticity; Blaisdell Pub. Co., Waltham, Mass., pp. 127.

Glasstone, S., Laidler, K. J. and Eyring, H. (1941) The Theory of Rate Processes; McGraw-Hill, N.Y.

Hart, E. W., Li, C. Y., Yamada, H. and Wire, G. L. (1975). Phenomenological Theory: A guide to constitutive relations and fundamental deformation properties; in A. S. Argon, ed., Constitutive Equations in Plasticity, M.I.T. Press, Cambridge. Mass., pp. 149-197.

Hawkes, I. and Mellor, M. (1972). Deformation and fracture of ice under uniaxial stress; Jour. Glaciology, v. 11, no. 61, pp. 103-131.

Hutter, K. (1980). A note on rate process theory and creep response of ice; Cold Regions Sci. and Tech., v. 3, pp. 335-336.

Jacka, T. H. (1984). The time and strain required for development of minimum strain rates in ice; Cold Regions Sci. and Tech., v. 8, pp. 261-268.

Jacka, T. H. and Maccagnan, M. (1984). Ice crystallographic and strain rate changes with strain in compression and extension; Cold Regions Sci. and Tech. v. 8, pp. 269-286.

Jellinek, H. H. G. and Brill, R. (1956). Viscoelastic properties of ice; Jour. Appl. Physics, v. 27, pp. 1198-1209.

Krausz, A. S. and Eyring, H. (1975). Deformation Kinetics; John Wiley and Sons, New York, pp. 398.

Lindgren, S. (1970). Thermal ice pressure; IAHR Symposium, Ice and its Action on Hydraulic Structures, Reykjavik, Iceland.

Maser, K. R. (1972). An analysis of the small-scale strength testing of ice; M.I.T. Sea Grant Office, Rept. No. MITSG 72-6, pp. 137.

Mellor, M. (1980). Mechanical properties of polycrystalline ice; in P. Tryde, ed., Physics and Mechanics of Ice; IUTAM Symposium, Copenhagen, 1979, pp. 217-245.

Mellor, M. and Cole, D. M. (1982). Deformation and failure of ice under constant stress or constant strain-rate; Cold Regions Sci. and Tech., v. 5, pp. 201-219.

Mendelson, A. (1968). Plasticity: Theory and Applications; Macmillan Co., New York, pp. 353.

Nevel, D. E. (1976). Creep theory for a floating ice sheet; USA CRREL SR 76-4, pp. 98.

Peyton, H. R. (1966) Sea Ice Strength; Geophysical Inst., U. of Alaska, Report UAG R-182, pp. 273.

Reiner, M. (1960). Plastic yielding in anelasticity; J. Mech. Phys. Solids, v. 8, pp. 2S5-261.

Reiner, M. and Weissenberg, K. (1939). Rheol. Leaflet v. 10, p. 12.

Sinha, N. K. (1978). Rheology of columnar-grained ice: Experimental Mechanics, v. 18, pp. 464-470.

Sinha, N. K. (1979.) Grain boundary sliding in polycrystalline materials; Phil. Mag. A, v. 40, pp. 825-842.

St. Lawrence, W. F. and Cole, D. M. (1982). Acoustic emissions from polyrystalline; Cold Regions Sci. and Tech., v. 5, pp. 183-199.

Szyszkowski, W. and Glockner, P. G. (1985). Modelling the time-dependent behavior of ice; Cold Regions Sci. and Tech., v. 11, pp. 3-21.

Tabata, T. (1958). Studies on the viscoelastic properties of sea ice; in Arctic Sea Ice, U.S. Natl. Acad. Sciences-Natl. Res. Council, Pub. 598, pp. 139-147.

Vaudrey, K. D. (1977). Ice engineering study of related properties of floating ice sheets and summary of elastic and viscoelastic analyses; Naval Civil Eng. Lab., Tech. Rpt. R-860, pp. 79.

2.3.8 APPENDIX

The deformation of the spring-dashpot model of the 4-parameter linear viscoelastic fluid in uniaxial compression is governed by the differential equation

(A-1)
$$\dot{\varepsilon} + \tau_2 \ddot{\varepsilon} = \frac{1}{\eta_1}\sigma + \left(\frac{1}{k_1} + \frac{\tau_2}{\eta_1} + \frac{1}{k_2}\right)\dot{\sigma} + \frac{\tau_2}{k_1}\ddot{\sigma}.$$

This equation can be integrated to give the stress-strain or strain-time curves for each of the three loading programs from which the conditions at failure can be derived, as shown below. Note that the derivations do not include the case of recovery of strain after unloading from a test which was not taken to failure.

CONSTANT STRESS (CS)

For a constant stress σ_c [Note: the symbol-σ_c is used here in place of σ_0 for constant stress for convenience in defining the dimensionless parameters introduced below] applied at $t = 0$, equation (A-1) can be integrated to give the strain-time relationship

(A-2) $$\varepsilon_T = \frac{\sigma_c}{k_1} + \frac{\sigma_c t}{\eta_1} + \frac{\sigma_c}{k_2}\left(1 - e^{-t/\tau_2}\right)$$

where the terms on the right side of the expression correspond (from left to right) to the strain in the spring (ε_E) and dashpot (ε_D) of the Maxwell model, followed by the contribution of the Voigt model (ε_V). Note that the strain in each element depends only on the applied stress and not on the parameters of other elements of the model. This follows because, as noted in the text, equilibrium requires that the stress across each element be the same, so that the applied stress is transmitted uniformly across the elements and each responds as if it were isolated from the remainder of the model. Clearly, ε_E is constant through the test, ε_D increases linearly with time (since ε_D is linearly related to the applied stress), and ε_V goes from zero to a constant as the time goes from zero to infinity. Curves of strain vs time for different stress levels, calculated from equation (A-2), are shown in Figure 2.3-A1.

At failure, the strain energy stored in the two springs of the model must equal the resiliance, or

(A-3) $$R = \frac{\sigma_2}{k_1} + \frac{\sigma_c^2}{k_2}\left(1 - e^{-t_f/\tau_2}\right)$$

where t_f is the time to failure and τ_2 is the relaxation time of the Voigt model. For failure at the upper strength limit (σ_u), $t_f = 0$ and the strain is given by [from equation (4)]

$$\varepsilon_u = \sigma_u/k_1$$

and R is

(A-4) $$R = \sigma_u^2/k_1.$$

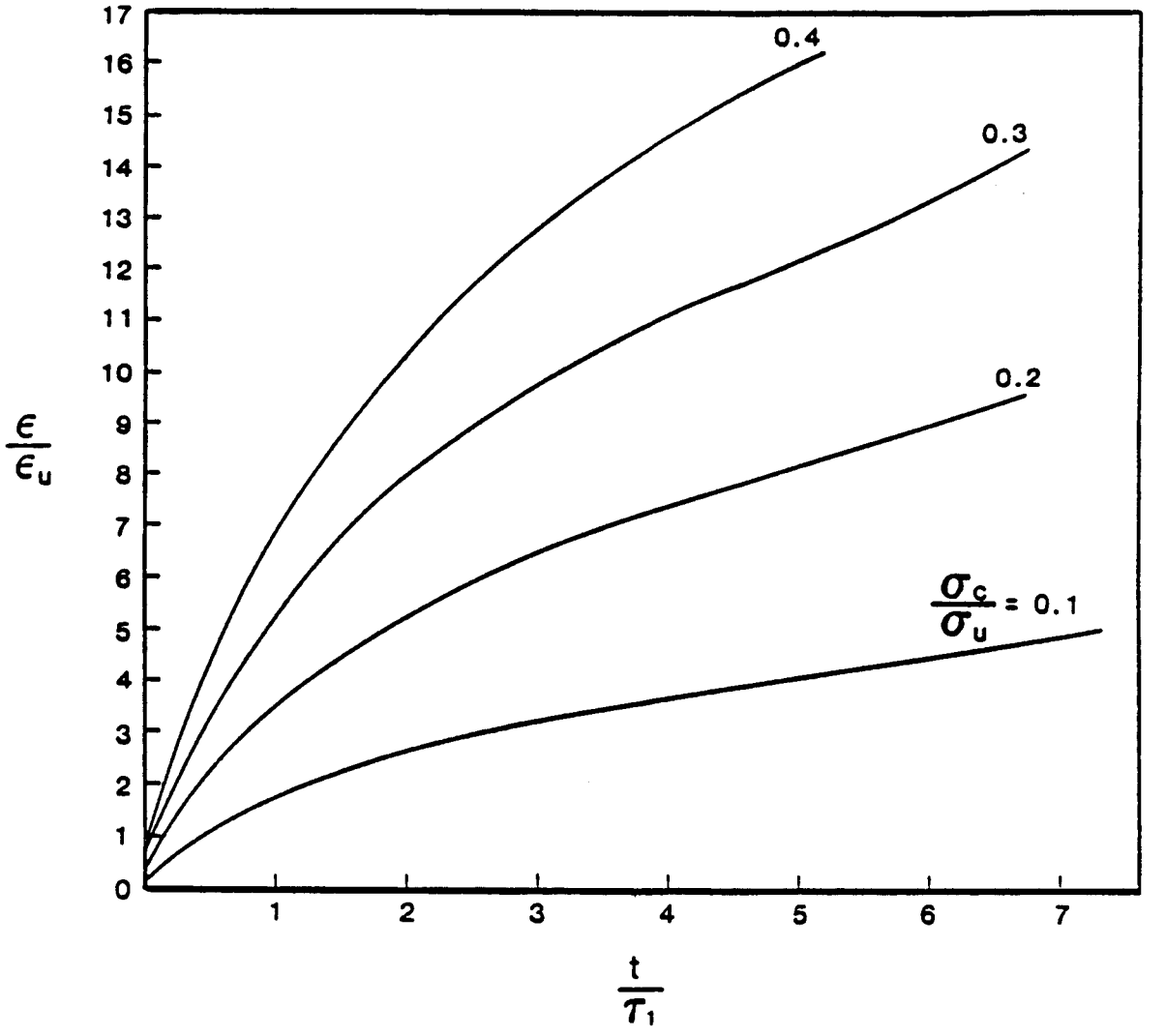

Figure 2.3-A1 Strain ratio vs. time ratio for CS tests at indicated stress ratios for the linear 4-PF model. See text for discussion.

Introducing this relationship, and the dimensionless constants

$$a = \sigma_c/\sigma_u \qquad (0 \le a \le 1),$$

(A-5)
$$b = k_2/k_1 \qquad (0 \le b \le 1),$$

$$\iota_r = \iota_f/\iota_2$$

into equation (A-3) and solving for t_r gives the time-to-failure as a function of the stress and the moduli as

(A-6) $$t_r = -\ln\left\{1-\left[b\left(\frac{1}{a^2}-1\right)\right]^{1/2}\right\}$$

The elastic strain at failure (ε_{Ef}) is the sum of the first and third expressions on the right side of equation (A-2) evaluated at t_f;

(A-7) $$\varepsilon_{Ef} = \frac{\sigma_c}{k_1} + \frac{\sigma_c}{k_2}\left(1-e^{t_r}\right)$$

Substituting for t_r from equation (A-6) and using equations (A-4) and (A-5) then leads to the elastic strain ratio at failure,

(A-8) $$\frac{\varepsilon_{Ef}}{\varepsilon_u} = a + \frac{1}{b^{1/2}}\left(1-a^2\right)^{1/2}$$

To find the total strain at failure, the contribution of the dashpot of the Maxwell model

(A-9) $$\varepsilon_D = \frac{\sigma_c t_f}{\eta_1}$$

is added to equation (A-7). Introducing the definition

(A-10) $$c = \frac{\eta_2}{\eta_1} \quad \left(0 \le c \le 1\right)$$

into equation (A-9), adding to equation (A-8) and using (A-5) then gives the total strain ratio at failure as

$$\frac{e_f}{\varepsilon_u} = \frac{\varepsilon_{Ef} + \varepsilon_D}{\varepsilon_u} = a + \frac{1}{b^{1/2}}\left(1-a^2\right)^{1/2} + \frac{ac}{b}\,t_r$$

Finally, the strain rate at failure is found from the derivative of equation (A-2) which, after rearrangement and substitution of (A-6) and (A-10) leads to

$$\dot{\varepsilon}_f = \frac{\sigma_c}{\eta_1}\left\{1 + \frac{1}{c}\left[1-b^{1/2}\left(\frac{1}{a^2}-1\right)^{1/2}\right]\right\}$$

CONSTANT STRESS RATE (CSR)

For a constant stress rate σ_o, the stress as a function of time is simply

$$\sigma = \sigma_o\, t$$

The stress-strain relationship given by the integral of equation (A-1) for this condition is

(A-11
$$\varepsilon_T = \left\{\frac{t}{k_1} + \frac{1}{\eta_1}\frac{t^2}{2} + \frac{1}{k_2}\left[t-\tau_2\left(1-e^{-t/\tau_2}\right)\right]\right\}\sigma_o$$

in which the terms in brackets correspond (from left to right) to the strain in the dashpot and spring of the Maxwell model, and the Voigt model. Note that, as was the case for CS tests, the strain in each model element depends only on the applied stress. The stress-strain curve is shown in Figure 2.3-A2.

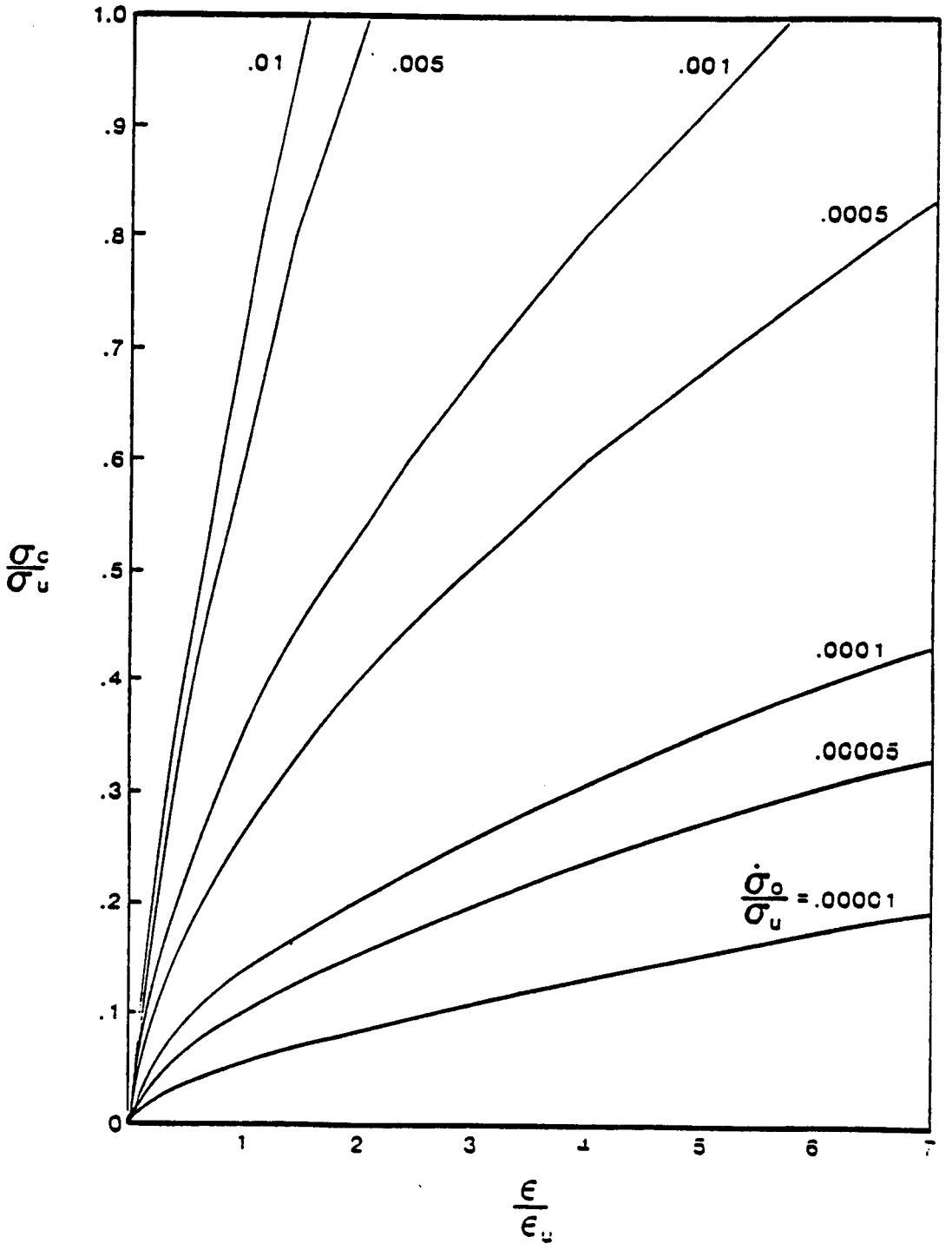

Figure 2.3-A2 Stress ratio vs. strain ratio for CSR tests at stress rates shown on curves. See text for discussion.

The elastic strain at the failure stress σ_c and $t = t_f$ is

(A-12) $$\varepsilon_r = \frac{\sigma_c}{k_1} + \frac{\sigma_c}{k_2}\left|1 - \frac{\tau_2}{t_f}\left(1 - e^{-t_f/\tau_2}\right)\right|$$

and the failure criterion

(A-13) $$R = \frac{\sigma_c^2}{k_1} + \frac{\sigma_c^2}{k_2}\left|1 - \frac{\tau_2}{t_f}\left(1 - e^{-t_f/\tau_2}\right)\right|^2$$

Introducing the definitions from equations (A-4), (A-5) and (A-6) and rearranging leads to

(A-14) $$1 - \frac{1}{t_r}\left(1 - e^{-t_r}\right) = \left|\left(\frac{1}{a^2} - 1\right)b\right|^{1/2}$$

Substitution into equation (A-12) and using (A-4) then gives the elastic strain ratio at failure as

$$\frac{\varepsilon_{Ef}}{\varepsilon_u} = a + \frac{1}{b^{1/2}}\left(1 - a^2\right)^{1/2}$$

which is the same as that for CS tests at the constant stress [equation (A-8)].

The strain rate at failure for CSR tests is found by differentiation of equation (A-11) and substitution of (A-10) and (A-14) to get

$$\dot{\varepsilon}_t = \frac{\sigma_c}{\eta_1}\left\{1 + \frac{1}{c}\left|1 - b^{1/2}\left(\frac{1}{a^2} - 1\right)^{1/2}\right|\right\} + \frac{\sigma_o}{k_1}$$

which differs from the strain rate at failure for CS tests by the addition of the term for the strain rate of the spring of the Maxwell model, as noted in the text.

CONSTANT STRAIN RATE (CDR)

In the case of a constant strain rate ε_o applied to the model, the strain at any time is

$$\varepsilon_t = \varepsilon_o t$$

and equation (A-1) can be integrated to

(A-15) $$\sigma = c_1 e^{c_3 t} + c_2 e^{c_4 t} + \eta_1 \varepsilon_o$$

where

$$c_1 = -\frac{c_4}{c_4 - c_3}\left(\frac{k_1}{c_4} + \eta_1\right)\varepsilon_o,$$

$$c_2 = \frac{c_4}{c_4 - c_3}\left(\frac{k_1}{c_3} + \eta_1\right)\varepsilon_o,$$

$$c_3 = -\frac{1}{2}c_5 + c_6,$$

$$c_4 = -\frac{1}{2}c_5 - c_6,$$

$$c_5 = \frac{k_1}{\eta_2} + \frac{k_1}{\eta_1} + \frac{k_2}{\eta_2},$$

$$c_6 = \left(c_5^2 - 4\frac{k_1}{\eta_1 \eta_2}\right)^{1/2}$$

The form of equation (A-15) reflects the fact that in CDR tests, the stress varies so that the applied strain rate is partitioned between the model elements so that the relationship

$$\dot{\varepsilon}_o = \dot{\varepsilon}_E + \dot{\varepsilon}_D + \dot{\varepsilon}_V$$

is satisfied at all times. Thus, the stress must be a function of all of the model parameters.

The stress-strain relationships for the spring and dashpot of the Maxwell model are

(A-16) $$\varepsilon_E = \frac{\sigma}{k_1}$$

and

(A-17) $$\varepsilon_D = \int \frac{\sigma}{\eta_1} dt$$

respectively. The comparable equation for the Voigt model is found from the equilibrium equation

$$\sigma = \sigma_1 + \sigma_2$$

which, using the stress-strain laws of the spring and dashpot, can be written as the differential equation

$$\dot{\varepsilon}_v + \frac{1}{\tau_2}\varepsilon_v = \frac{\sigma}{\eta_2}$$

The solution is

(A-18) $$\varepsilon_v = \frac{1}{\eta_2}\left[\frac{c_1}{D_1}\left(e^{c_3 t} + e^{-t/\tau_2}\right) + \frac{c_2}{D_2}\left(e^{c_4 t} - e^{-t/\tau_2}\right) + \eta_1 \dot{\varepsilon}_o \tau_2\left(1 - e^{-t/\tau_2}\right)\right]$$

where

$$D_1 = c_3 + \frac{1}{\tau_2}; \quad D_2 = c_4 + \frac{1}{\tau_2}$$

Equations (A-16), (A-17) and (A-18) can be non-dimensionalized to the same parameters as those used for CS and CSR tests, and the conditions at failure can then be calculated after assuming numerical values for the parameters. In this case, the value of k_1 was taken as 9 GPa, following Hawkes and Mellor (1972); η_1 was taken as 5×10^6 to approximate the strain rate at a stress of 1 MPa as would be calculated from the power law for creep with typical parameters (i.e., $n = 3$, $A = 2 \times 10^{-7}$). The values of k_2 and η_2 were then fixed by the choice of the constants b (=0.05) and c (=0.2). The choice of the upper limit of the strength is arbitrary since all of the equations are normalized to its value. The stress-strain curve from equation (A-15) using these values is shown in Figure 2.3-A3.

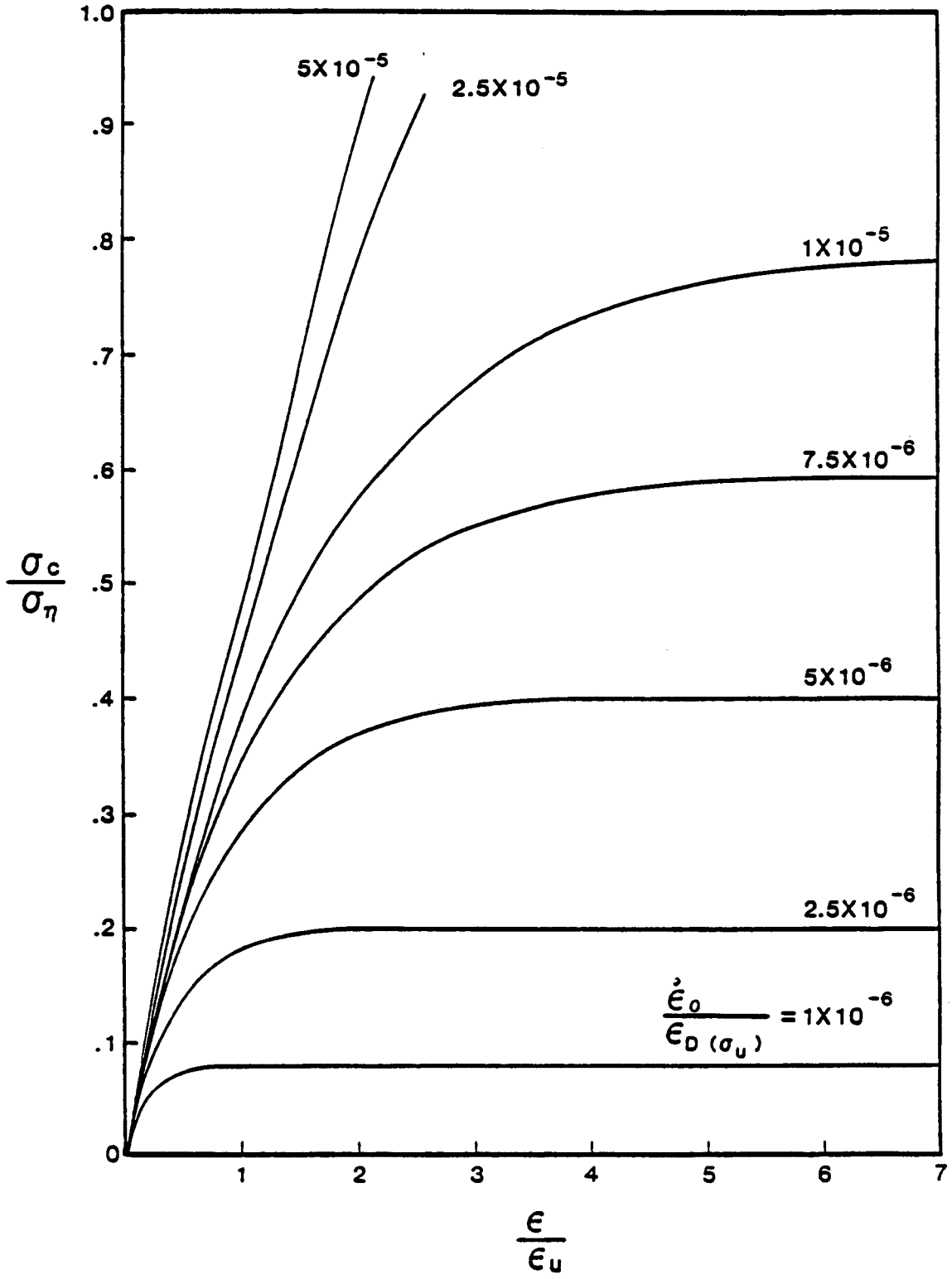

Figure 2.3-A3 Stress ratio vs. strain ratio for CDR tests at strain rates indicated on curves. See text for discussion.

HYPERBOLIC SINE MODEL,

If the strain rate of the dashpots of the Maxwell and Voigt models are represented by the equations

$$\dot{\varepsilon}_D = B \sinh \theta\sigma$$

and

$$\dot{\varepsilon}_V = A \sinh \phi\sigma_2$$

respectively, and k_1 and k_2 are the spring moduli, then the stress-strain law of the model is

$$\varepsilon_T = \frac{\sigma}{k_1} + B \int_o^t \sinh \theta\sigma dt' + A \int_j^t \sinh \phi \left[\sigma - k_2 \varepsilon_V\right] dt'$$

where the primes indicate dummy variables. This equation can be integrated directly to give the strain-time and stress-strain curves for CS and CSR tests as

$$\varepsilon_T = \frac{k_1 + k_2}{k_1 k_2} \sigma_c + Bt \sinh \theta\sigma_c - \frac{2}{\phi k_2} \tanh^{-1}\left(\tanh \frac{\phi\sigma_c}{2} e^{-A\phi k_2 t}\right)$$

and

$$\varepsilon_T = \frac{k_1 + k_2}{k_1 k_2} \dot{\sigma}_o t + \frac{B}{\theta\dot{\sigma}_o}\left(\cosh \theta\sigma_o t - 1\right) - \frac{1}{\phi k_2} \sinh^{-1}\left[\frac{\alpha \sinh(\beta t - \delta) - 1}{\alpha + \sinh(\beta t - \delta)}\right]$$

respectively where $\dot{\sigma}_0$ is the applied constant stress rate in CSR tests.. The constants α, β and δ in the second equation are

$$a = \frac{\dot{\sigma}_o}{Ak_2},$$

$$\beta = \phi k_2 (1 + a^2)^{1/2},$$

$$\delta = sinh^{-1}\ 1/a.$$

The stress-strain curve for CDR tests is found numerically from the equation

$$\sigma = \frac{1}{\theta}\ sinh^{-1}\frac{f(t)}{A} + k_2\ f(t)$$

where

$$f(t) = \dot{\varepsilon}_o t - \frac{\sigma}{k_1} - B\int_o^t sinh\,\theta\sigma\, dt'$$

The curves in Figures 2.3-5, 7 and 9 were found by calculation using values of the parameters which were selected based on data from linear models for different types of ice reported in the literature. The values are given in Table 2.3-A1.

TABLE 2.3-A1

VALUES OF CONSTANTS USED IN CALCULATIONS OF THE RESPONSE TO LOAD THE NON-LINEAR 4-PF MODEL

CONSTANT	VALUE
k_1	3.45 GPa
k_2	0.21 GPa
ϕ	4.06 MPa^{-1}
θ	3.09 Mpa^{-1}
A	5 x 10^{-6} sec^{-1}
B	1 x 10^{-7} sec^{-1}
σ_b	0.86 MPa

2.4 FRACTURE TOUGHNESS OF SEA ICE

by

Lewis H. Shapiro, Ronald C. Metzner, and Jerome B. Johnson

2.4.1 INTRODUCTION

A short series of fracture toughness tests was run in the laboratory using small beams of natural sea ice. The purpose was to obtain a set of data for comparison with the fracture toughness measurement made by Vaudrey (1977) on laboratory-grown saline ice.

2.4.2 SAMPLE DESCRIPTION AND TESTING

Beams used in the study were cut from slabs of sea ice collected from the landfast ice offshore from Barrow, Alaska. The slabs represented a profile of the ice sheet from the surface to a depth of 76 cm. After collection they were packed in insulated boxes, shipped to Fairbanks and stored until sample preparation and testing. The samples were subjected to a limited range of temperature changes during this process (-11° to -16°C) and were tested at -14°C.

The sample beams were 5 x 5 cm in cross section and about 40 cm long. The slit which provided the stress concentration was 1.3 cm deep, and a scalpel was run along the base of the slit to nucleate small cracks from which the main crack could propagate. A total of 30 beams were tested. Loading was done in 4-point bending through a spherical seat (Figure 2.4-1).

The sample beams cut from the uppermost 25 cm of the ice sheet were composed of fine-grained (maximum diameter of a few mm) randomly oriented crystals. The ice over the next 20 cm of depth had a similar appearance in thin section, but contained dispersed sediment and macroscopic inhomogeneities in the form of networks of whitish-colored ice lenses. These were apparently areas of closely

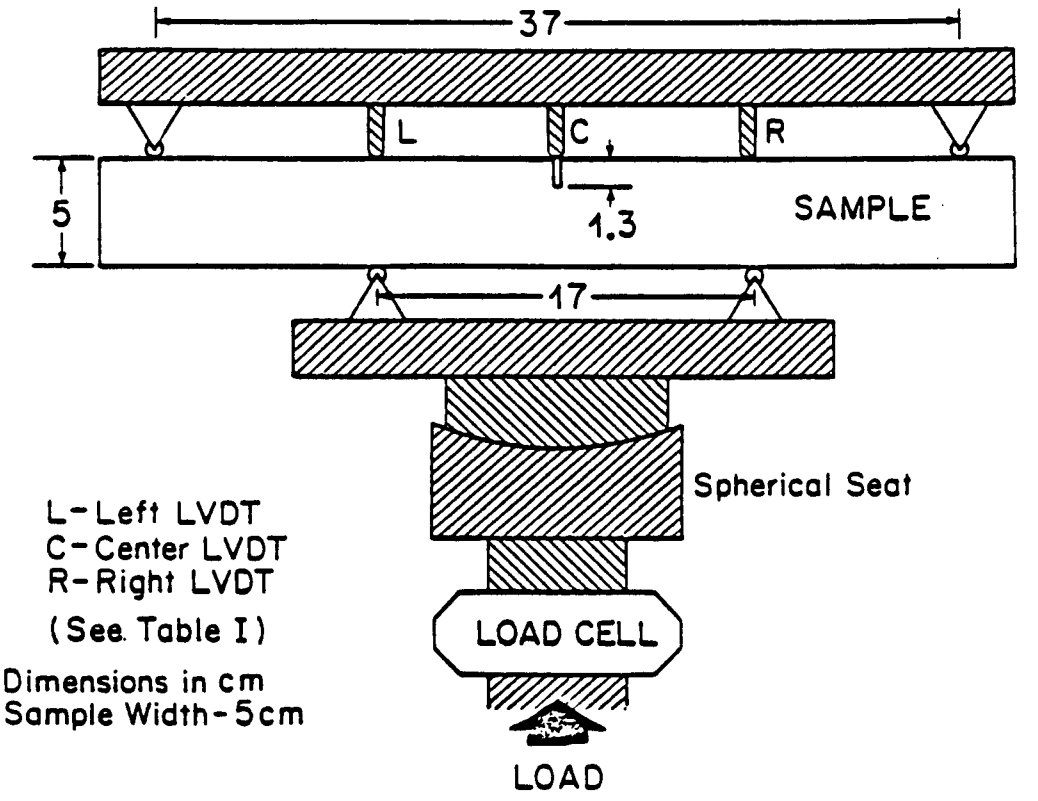

Figure 2.4-1 Schematic diagram of the four-point bending apparatus and sample geometry.

spaced brine channels or large, irregular pockets of trapped brine. The remainder of the samples were composed of elongate crystals from the columnar zone which ranged in size from 0.6 x 1.3 to 2.5 cm at 45-cm depth to 1.3 x 2.5 to 4 cm at 75-cm depth. The c-axes of the crystals showed a weak orientation, and the beams were cut normal to this direction. Thus, the average direction of the long dimension of the grains was aligned parallel to the axis of the sample beams.

The load was applied by a hand-operated hydraulic pump and was measured by a load cell below the spherical seat (Figure 2.4-1). The samples always failed within a small fraction of the possible travel during one stroke of the pump, so that smooth loading curves with respect to time were obtained. Loading rates varied from 550 to 690 kPa/sec. Data were recorded on a chart recorder and scaled by hand.

Beam displacements were measured by LVDT's positioned as shown in Figure 2.4-1. However, there were discrepancies in the displacement measurements which were determined to be due to slight rotations of the samples as the spherical seat aligned them during the initial loading phase. It would have been possible to correct the data to compensate for the errors if the data had been in digital form. However, the need to scale the data by hand from the charts made it impractical to attempt to do so.

Calculation of the fracture toughness (K_{IC})was done using the procedures in Vaudry (1977); that is,

$$K_{IC} = 3Pb^{1/2} (L_1 - L_2) \beta (2wd^2)^{-1}$$

where P is the load, b is the slot depth, L_1 and L_2 are the spacings between load points, w is the sample width, d is the thickness and β is given by

$$\beta = 1.99 - 2.47 (b/d) + 12.97 (b/d)^2 - 23.17 (b/d)^3 + 24.80 (b/d)^4$$

For b/d = 0.25,

$$\beta \approx 1.918$$

so that

$$K_{IC} = 1.97P$$

2.4.3 RESULTS AND CONCLUSIONS

The data are given in Table 2.4-1. Fracture toughness is plotted against brine volume in Figure 2.4-2. The values are comparable to those reported by Vaudry (1977) although, as expected, the scatter in the data points is large.

Four of the 30 samples broke along surfaces away from the slit. The load at failure was low, and these values are not included in the plots. These samples were from the interval which contained the dispersed sediments and lenses of whitish ice described above, and their salinities were abnormally high (Table 2.4-1).

TABLE 2.4-1

RESULTS OF FRACTURE TOUGHNESS TESTS

Sample No.**	Displacement (cm x 10^2) L	C	R	Load (kPa)	K_{IC}*** (kPa$\sqrt{m}$)	Salinity (ppt)	$\sqrt{v}$ ppt
0-5-1	3.18	4.47	4.17	199	62.3	8.2	5.76
0-5-2	3.07	3.43	4.27	229	71.9	8.4	5.83
0-5-3	3.18	3.71	4.24	217	67.9	8.6	5.89
0-5-4	2.51	2.77	2.77	226	70.8	8.7	5.93
0-5-5	2.06	3.33	3.53	195	61.2	8.6	5.89
5-9-1	2.54	3.05	3.35	210	65.8	8.5	5.86
5-9-2	6.86	-	....-	262	82.3	9.5	6.20
5-9-3	5.46	4.27	4.24	270	84.5	9.1	6.06
5-9-4	5.46	4.27	4.24	270	84.5	9.1	6.06
5-9-5	5.03	5.51	3.10	211	66.3	9.0	6.03
9-13-1	3.63	6.15	-	152	47.8	8.3	5.79
9-13-2	2.16	2.79	3.28	283	89.0	8.7	5.93
9-13-3	5.84	-	-	78	24.5	9.1	6.06
9-13-4	2.82	2.49	2.46	215	67.6	8.6	5.89
9-13-5	0.711	6.30	0.813	117	36.8	9.3	6.13
13-17-1	1.40	1.30	1.45	148	46.5	6.3	5.05
13-17-2	1.88	2.46	-	187	58.7	6.6	5.16
13-17-3	2.59	2.92	3.05	226	71.0	7.9	5.65
13-17-4	5.84	8.33	4.09	177	55.6	7.9	5.65
13-17-5	2.18	3.00	3.07	131	41.2	-	-
17-22-1	2.21	3.33	2.92	281	88.1	5.2	4.58
17-22-2	1.88	1.73	1.65	268	84.2	5.3	4.58
17-22-3	1.09	1.30	1.42	260	81.5	5.4	4.67
17-22-4	2.79	2.34	2.11	272	85.5	5.0	4.49
17-22-5	4.06	4.45	3.89	254	79.9	5.9	4.88
22-30-1	-	-	5.26	241	75.6	4.6	4.31
22-30-2	2.06	2.57	3.25	312	97.9	4.9	4.45
22-30-3	3.96	4.50	4.65	265	83.1	4.1	4.07
22-30-4	2.69	3.53	3.15	304	95.4	4.0	4.02
22-30-5	3.58	4.85	5.13	286	89.9	4.2	4.12

*Failed away from the slit.

**The first two numbers of the sample designation refer to the depth range in inches.

***Multiply by 0.910 to convert to psi $\sqrt{in}$.

Apparently the samples contained large inhomogeneities which limited their strength.

The remaining samples broke cleanly along a single crack, with no visible internal cracking in the sample.

Vaudry (1977) determined a least square straight line fit to his results for fracture toughness vs. brine volume for the laboratory grown saline ice tested in his study. That line is shown in Figure 2.4-2 along with a similar line determined from the data of this study. The two lines do not differ significantly. This suggests that the calculated values for fracture energy ($\gamma_c \approx 3 \times 10\text{-}3$ kPa-m) and critical crack length ($c \approx 0.6$ cm) should be the same for both test series. However, the variation of grain size and fabric in the samples used in this study, coupled with the fact that no independent measurements were made of the bending strength or Young's modulus, suggests that such a comparison should be treated with caution. In addition, the

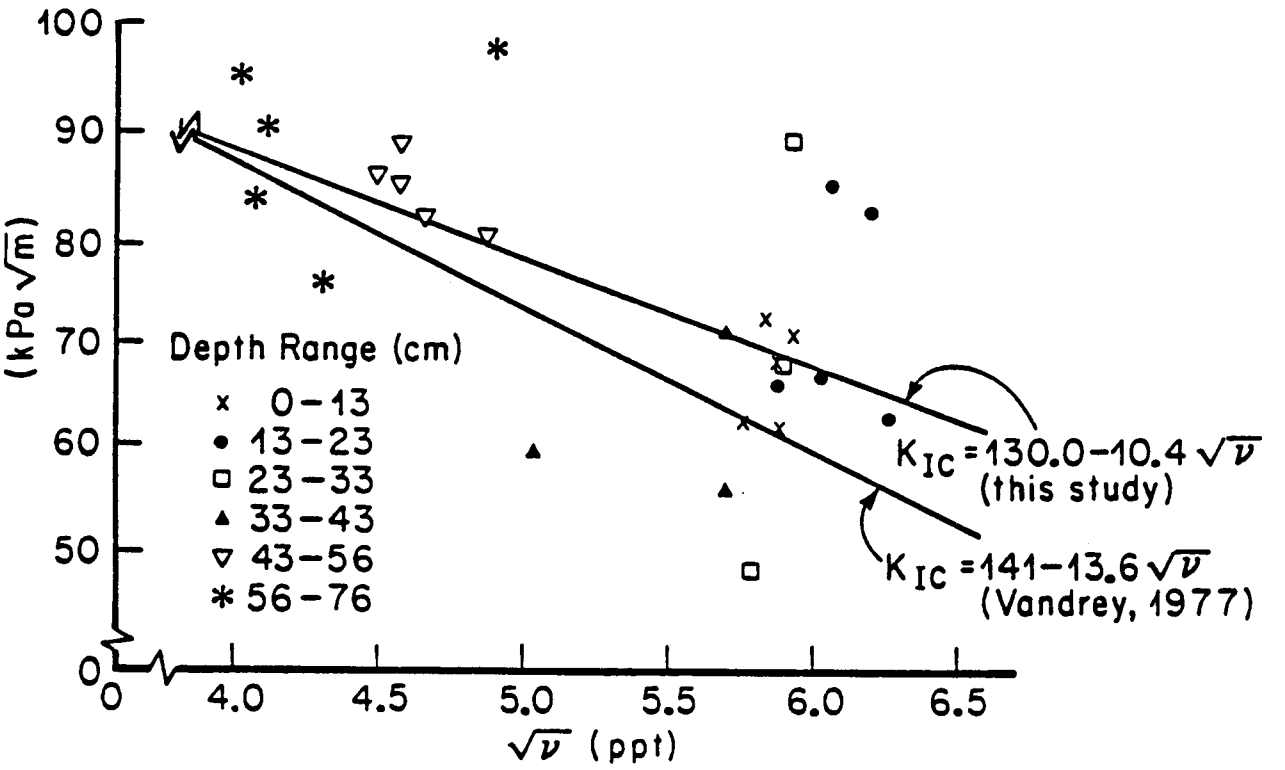

Figure 2.4-2 Fracture toughness vs. square root of brine volume.

similarity of the results of this study and those of Vaudry (1977) and Urabe et al., (1980) implies that there is little to be gained by additional fracture toughness testing of sea ice which is not directed to investigating the influence of specific variables.

2.4.4 REFERENCES CITED

Urabe, N., T. Iwaski, and A. Yoshitake. (1980). Fracture toughness of sea ice; Cold Reg. Sci. and Tech., v. 3, pp. 29-37.

Vaudrey, K. D. (1977). Ice engineering study of related properties of floating ice sheets and summary of elastic and viscoelastic analyses; Naval Civil Eng. Lab., Tech. Rpt. R-860, 79 pp.

2.5 STRAIN TRANSDUCER FOR LABORATORY EXPERIMENTS

by

Lewis H. Shapiro, Ronald C. Metzner, and Jerome B. Johnson

2.5.1 INTRODUCTION

At the time the experimental phase of the program was terminated, it was intended that a series of small-scale uniaxial compression tests on sea ice be conducted in the field in conjunction with the larger-scale experiments described in Section 2.2.4. This would have involved testing samples to failure in compression at high rates of loading, which often results in explosive failure of the samples. Because of the inherent difficulty in attaching resistance wire strain gauges to the surface of ice samples, it would have been necessary to use an extensometer to measure strain during the tests. These are relatively fragile instruments which are also quite expensive. Rather than subject them to possible damage during the testing program we searched for an inexpensive substitute. We found no suitable equipment available commercially and, as a result, undertook the task of designing one. The result was a clip gage in the form of a semi-circular arch (Figure 2.5-1) which can be fabricated for about 1/20 the cost of a commercial extensometer. The characteristics of the gage are described in the following sections.

2.5.2 CLIP-TYPE STRAIN GAGES

Clip gages (Perry and Lissner, 1962) operate on the principle that the true strain of the sample is sensed as the strain across the tips of the gage (e_f), which are attached to the sample. This strain is transformed into bending strain which is measured by wire strain gages mounted on the clip gage. The measured strain (e_b) is then used to determine the true strain (e_f) through a calibration curve. Typically,

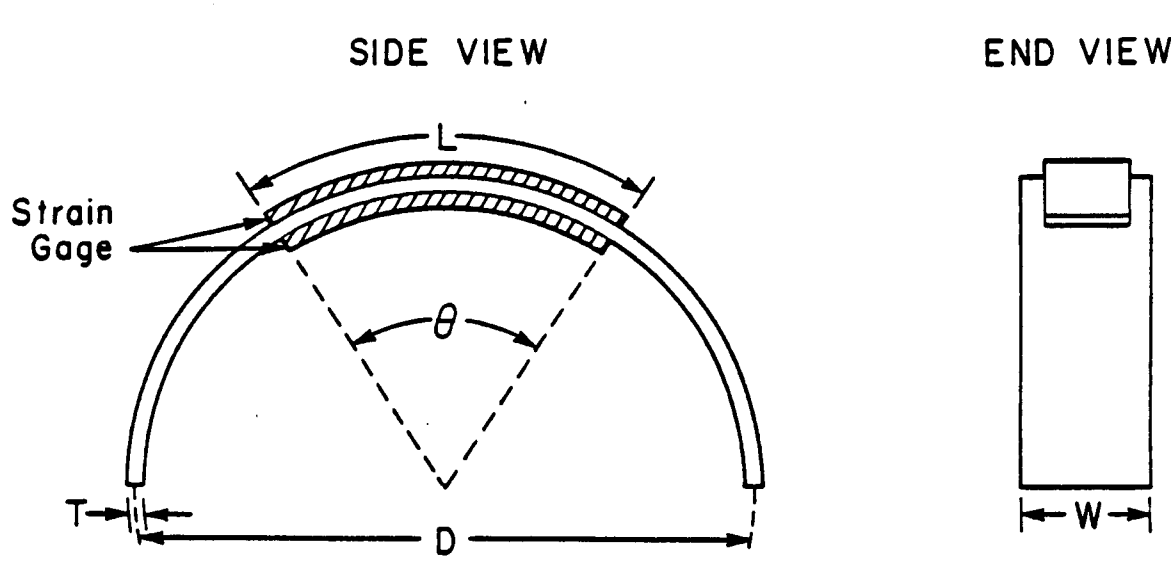

Figure 2.5-1 Schematic diagram of a clip gage in the form of a semi-circular arch. The ends of the arch are attached to the sample so that the sample strain (e_f) is shown as an apparent change in the arch diameter D.

clip gages are made of spring steel or similar material, bent into a channel shape (Figure 2.5-2). In this form they are much less sensitive to the strain in the sample than resistance wire gages attached directly to the sample. Thus, clip gages are normally used in applications in which it is anticipated that the strain will exceed the limits of resistance wire gages. However, for the application we anticipated, it was necessary that the clip gages be capable of monitoring strains in the same range as wire gages. Therefore, we sought alternatives to conventional clip gages, which led to the recognition that the circular arch design might be sufficiently sensitive to strain to serve the desired purpose. To investigate this, we did a series of calculations using a simple finite element model of a circular arch, and fabricated several arches for experimental study. The characteristics of the arches are given in Table 2.5-1.

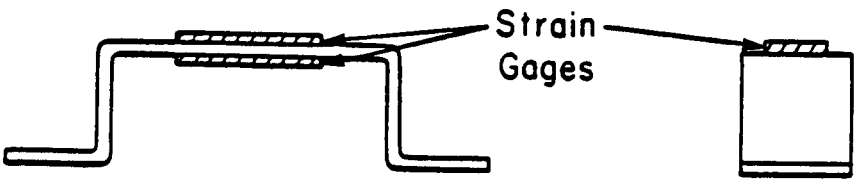

Figure 2.5-2 Schematic diagram of a typical channel-type clip gage.

TABLE 2.5-1 CHARACTERISTICS OF FABRICATED ARCH-TYPE CLIP GAGES

Arch Number	Material	Diameter (D cm)	Thickness (T cm)	Width (W cm)	θ (Deg)	Resistance Gages
1.	Steel (AISI 1020)	2.54	0.0178	0.953	121.8	1/2 bridge, 120ω
2.	Steel (AISI 1020)	2.54	0.0305	0.953	121.8	1/2 bridge, 120ω
2a*	Steel (AISI 1020)	2.54	0.0394	0.953	64.5	1/2 bridge, 350ω
3.	Steel, stainless	5.24	0.0838	1.270	56.4	full bridge, 350ω
4.	Steel, stainless	5.24	0.0838	1.270	56.4	1/2 bridge 350ω
5.	Acrylic Plastic	15.24	0.3175	2.54	20.3	full bridge 120ω
6.	Acrylic Plastic	5.4	0.3175	1.270	56.4	full bridge 350ω

*Arch 2a is Arch 2 with a second set of strain gages fixed on top of the first set to increase the thickness, T.

2.5.3 CALCULATION OF ARCH-GAGE PROPERTIES

The finite element model consisted of a 180° arch represented by 40 connected linear elements. The boundary conditions required the tips of the arch to remain in the plane of the base diameter during deformation. The strain which would be sensed by resistance strain gages fixed to the arch and covering different arc lengths L [= (D/2)] was determined by summing the strain in the individual elements of the model over the desired length. Calculations were done for arches of various dimensions and material properties for several values of e_f and L. The results indicated that (1) small wire gages over the crest of the arch provided the greatest sensitivity, and (2) the sensitivity of the arch gages is linearly related to the ratio of the gage thickness to the diameter (T/D) and independent of the properties of the material from which the arch is constructed.

The calculated effective modulus (M_e) of an arch followed a relationship of the form

$$M_e = AE\,(wD^3)^{-1}$$

where A is a constant (3.48×10^2 in SI units for the values used in the calculations), w is the width of the gage, and E is Young's modulus of the material. The form of the equation is similar to that determined from the solution to a similar (though not identical) problem by Timoshenko and Goodier (1951).

Based on the calculations from the finite element model, it was assumed that the true strain (e_f) and the strain sensed by the gage (e_b) would be related by an expression of the form

$$e_f = f(\theta)\, g(T/D)\, e_b$$

in which g(T/D) is a linear function of the ratio T/D and $f(\theta)$ is a correction factor involving the function $\cos(\theta/2)$ which is required to account for the irregular shape to which the gage bends (Figure 2.5-3).

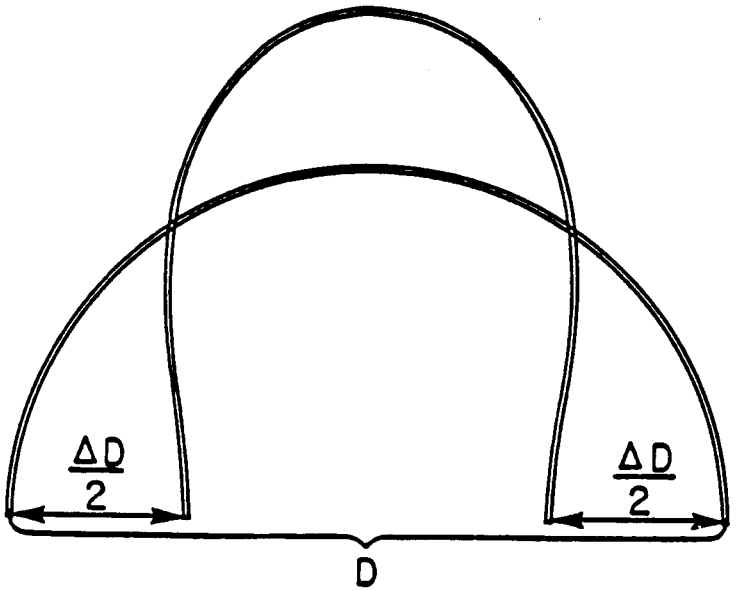

Figure 2.5-3 Bending of an arch clip gage as a result of shortening of the diameter D.

2.5.4 MEASUREMENT OF GAGE RESPONSE

All of the gages listed in Table 2.5-1 were deformed on a traveling stage micrometer which could be advanced in precise increments of 0.001 mm. A standard strain increment and excitation voltage were used for all tests to facilitate comparison of the results. Each arch was mounted on the micrometer and stepped through several increments of a standard strain and the results were averaged to determine the voltage output per unit strain. The degree of linearity was determined by recording the voltage output vs. accumulated strain in tension or compression. Because only a few gages were constructed, the results should be regarded as preliminary, pending additional experiments. However, as described below, the results suggest that the model predictions are, at least, approximately correct.

The results of the experiments showed that all of the gages were linear for strains (e_f) up to at least 2% in both tension and compression (linearity ranged up to 8% in compression for the steel gages). In addition, the sensitivity of the gages was linearly related to the ratio T/D (Figure 2.5-4) and independent of the material used in construction, as predicted by the calculations. Finally, the results of an experiment in which an arch gage was used to track the strain sensed by a resistance strain gage attached to a small beam are shown in Figure 2.5-5. In the experiment, the beam was forced to bend slightly out of plane to simulate the "barrelling" of a test specimen. The linearity of the relationship is apparent.

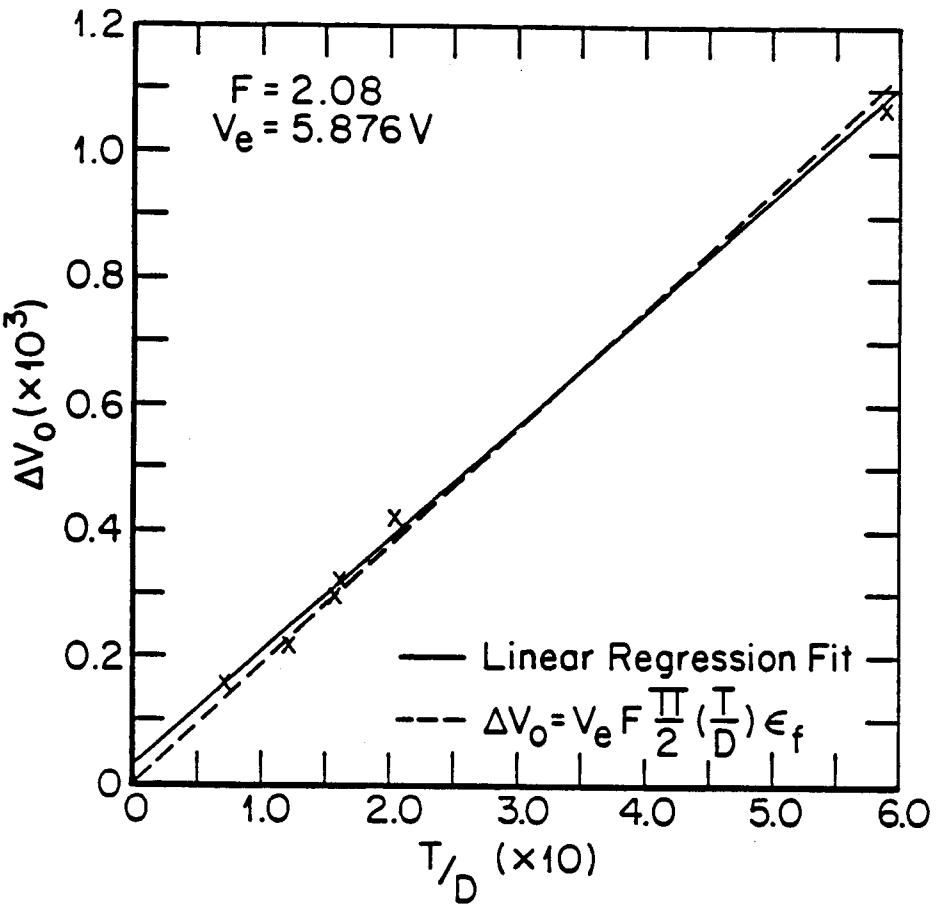

Figure 2.5-4 Voltage output per unit strain vs. thickness to diameter ratio for the six arch gages listed in Table 2.5-1.

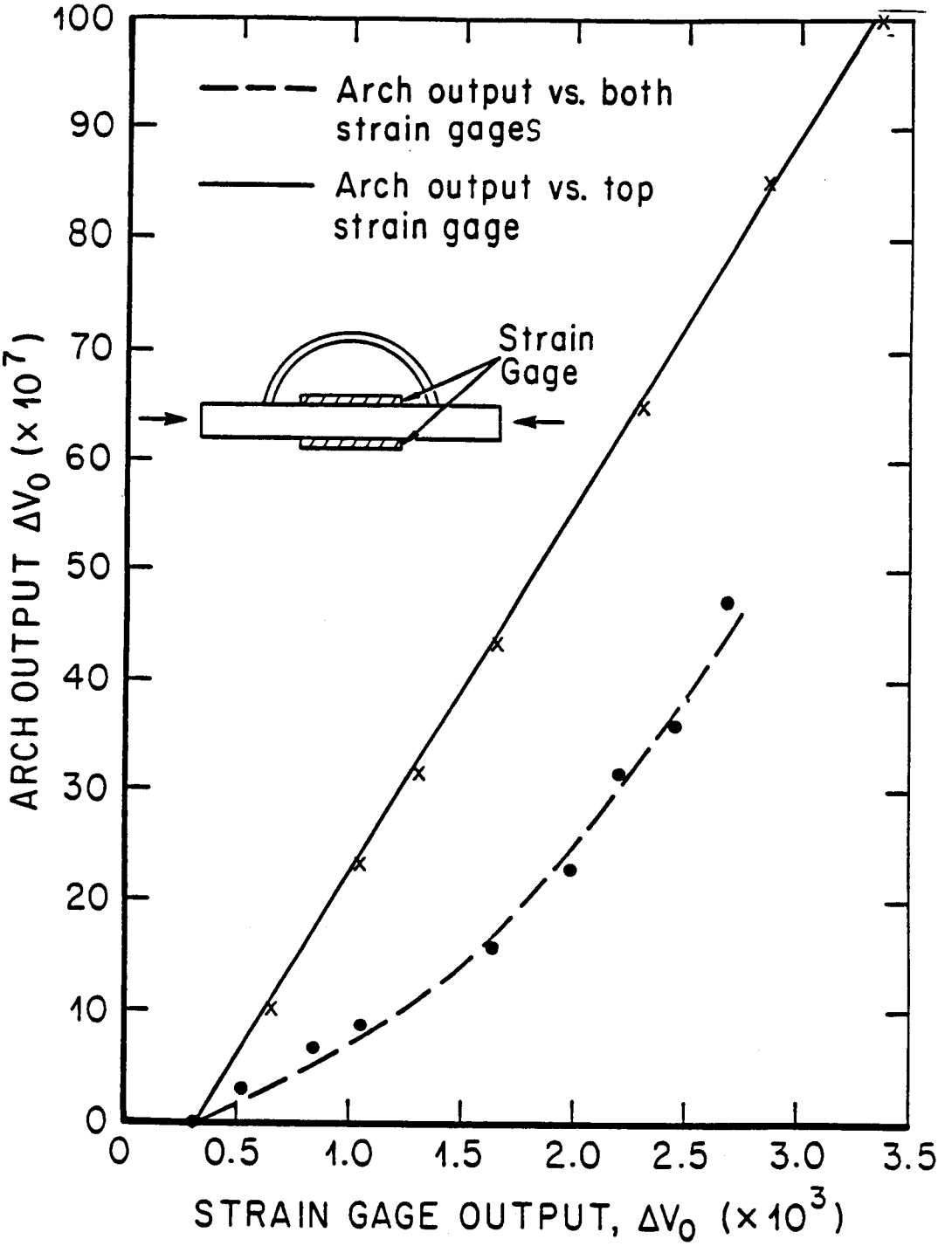

Figure 2.5-5 Plot of arch clip gage output vs. resistance gage output for the bending beam experiment. The arch gage accurately tracked the resistance gage over which it was mounted. The curve for the combined output of both resistance gages reflects the bending of the beam.

2.5.5 DISCUSSION AND CONCLUSIONS

We believe that the use of arch clip gages is practical now, provided that the calibrations are established for the exact conditions under which they are to be used (i.e. method of attachment to the samples, temperature, etc.). However, additional work is needed in several areas to define the general properties of the gages. These include (1) the range of T/D ratios for different materials for which the calculations are valid, (2) the detailed form of the correction factor $f(\theta)$, and (3) the variations in response of the gages for different methods of attachment to the sample.

2.5.6 REFERENCES CITED

Perry, C.C., and Lissner, H.R., 1962, The Strain Gauge Primer, McGraw-Hill, New York, 2nd ed., pp. 332.

Timoshenko, S., and Goodier, J.N., 1951, Theory of Elasticity, McGraw-Hill, New York, 2nd ed., pp.506.

3.
DEFORMATION OF SEA ICE IN THE NEARSHORE ZONE

3.1 FAST ICE SHEET DEFORMATION DURING ICE PUSH AND SHORE ICE RIDE-UP

by

Lewis H. Shapiro, Ronald C. Metzner, Arnold Hanson,* and Jerome B. Johnson

3.1.1 INTRODUCTION

During the course of this project, we had the opportunity to study several ice push events in the Barrow area. The events occurred over the three-year period between 1975 and 1978 and were described and analyzed in Shapiro et al. (1984). This section is a summary of the results presented in that paper.

The study is an extension of the general problem of determining the forces associated with the formation of shore ice pile-ups and grounded pressure ridges. The basic approach used in these studies follows that of Parmenter and Coon (1972) for free-floating pressure ridges, in which the force is calculated from the work required to store the potential energy in the ridge and overcome friction (see for example, Kovacs and Sodhi, 1979; Vivatrat and Kreider, 1981). Other possible energy sinks in the process (i.e., ice fracture, gouging of the sea floor, etc.) are not accounted for. The contributions from these sources are not considered to be large, but neglecting them emphasizes that the forces calculated represent lower limits to the possible forces acting at the ridge site or along the beach. Calculated stresses range up to 3.5×10^5 Pa (Kovacs and Sodhi, 1979) and are thus higher than the estimated maximum stress which can be transmitted through pack ice (approximately 10^5 Pa; Pritchard, 1977). This suggests that shore ice pile-up and ride-up require some mechanism for stress concentration, through which stresses transmitted through the pack ice are amplified at the point of ridging or ice pile-up.

*Deceased.

The mechanism might involve a variety of factors including (1) the initial distribution of stress along the pack ice-landfast ice boundary at the start of the event, (2) the changes in the stress field internal to the landfast ice sheet due to deformation and fracture as the motion proceeds and, (3) the shape of the shoreline and the nature of the bonding between the ice and the shore.

The results of this study provide a description of some of the processes which operate during ice push events, and lead to the suggestion of a model through which numerical studies could be done.

The events which were studied are listed in Table 3.1-1 along with their key characteristics.

3.1.2 SUMMARY OF DATA AND OBSERVATIONS

We can make six generalizations from the observational data:

(1) In ice ride-up events, the length of beach affected is probably significantly shorter than the length of the edge of the fast ice along which the driving forces are applied.

(2) The pack ice through which the driving force is transmitted is likely to be compact, indicating that ridging of thin, weak ice has already occurred at the time of an ice push event. Thus, the stresses transmitted to the fast ice edge and on toward the beach may be greater than those in normal pack ice where thin ice is present. This also implies that ice push or ride-up events are driven by wind stress imparted to the ice over large areas, and that local winds are not alone responsible.

(3) During the spring events the ice sheet was initially driven toward the beach as a unit, closing the shore lead. Then, fractures formed parallel to the direction of the motion (usually at high angles to the shore). During small advances the cracks did not propagate far offshore, but during large advances some of the fractures crossed the entire width of the fast ice sheet. This indicates that the length

TABLE 3.1-1 Ice Pile-up and Ride-Up Events in the Point Barrow Area, 1975-1978

Location	Date	Major Features
Along beach at NARL	July 4-6, 1975	Offshore boundary of fast ice sheet moved shoreward about 250 m. Extensive ice pile-up and ride-up along about 2.5 km of beach.
Along beach at NARL	June 30, 1976	Fast ice sheet moved 15-25 m shoreward. Ice pile-up, ride-up and over-thrusting along the same area as 1975 event.
City of Barrow	Dec. 30, 1977	Ice advanced up the beach on a 725 m front; maximum advance of 35 m. Ice pile-up along the entire front.
Point Barrow	Dec. 30, 1977(?)	Small ice pile-up on Chukchi Sea side of Point Barrow.
Tapkaluk Island	Late January 1978	Ice advanced along a 900 m front and overrode the island in several locations.
Martin Island	Late January 1978	Ice advanced onto island about 55 m along a 215 m front.
Igalik Island	Late January 1978	Ice advanced 105 m and over-rode the island along a 400 m wide front.

of the cracks depends upon the extent of the advance. In addition, the longer fractures separated the ice sheet into segments, each of which advanced through a different distance.

(4) The three winter events at Barrow, Tapkaluk Island and Martin Island show a similar pattern of fractures bounding the segment of the fast ice sheet which advanced. The pattern consists of two fractures; one is approximately perpendicular

to the beach and may show evidence of active compressive and/or shear stresses in the adjacent ice sheet. The second fracture extends from a point at or near the intersection between the first fracture and the beach. At its origin, it is approximately tangent to the beach but it curves offshore with increasing distance. No movement of the ice sheet occurs until these fractures form.

(5) The Igalik Island event, which occurred in winter, was like the spring events at Barrow in that fractures bounding the thrust sheet were at a high angle to the shore and the thrust sheet moved as a plug with little internal fracturing.

(6) The spring events caused extensive bulldozing of the beach gravel into ice-push ridges as much as 1 m high which enhanced the probability of formation of ice pile-ups. In contrast, bulldozing of the beach during the winter events was minor.

3.1.3 DISCUSSION

The cracks bounding the winter thrust sheets at Barrow, Tapkaluk Island, and Martin Island share a geometric configuration which has an analogy in the theory of plasticity. The pattern of two cracks meeting at a right angle at the boundary of a field of deforming material, one curving and tangent to the boundary and the other normal, occurs frequently in slip-line field theory (see for example, Prager and Hodge, 1951). An example is shown in Figure 3.1-1, which is part of the solution to Prandtl's problem for the flow field of a perfectly plastic material squeezed in plane strain between two rigid plates with rough (no-slip) surfaces. The lines indicate the trajectories of the maximum shear stresses and, according to von Mises' criterion, can be viewed as lines along which failure in shear can occur. This interpretation has been used to explain fracture patterns observed in rocks (Varnes, 1962; Cummings, 1976).

If we assume the analogy to apply at least qualitatively to the plane stress problem for an ice sheet in winter, an immediate implication is that the ice was

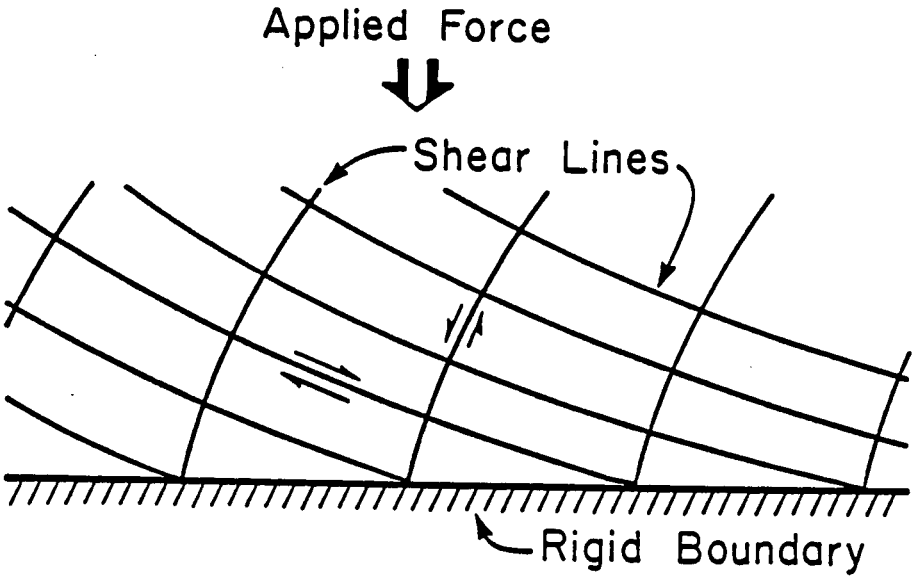

Figure 3.1-1 Example of the relationships between shear lines and a rigid boundary from Prandtl's solution for an infinite slab of a perfectly plastic material compressed between rough, rigid plates (from Prager and Hodge, 1951).

firmly frozen to the beach when the cracks were initiated, in accordance with the requirement that the boundary be rough. There is also the suggestion that the direction of loading was normal to the beach. However, this does not require that the force arising from the interaction between the pack ice and the fast ice be directed normal to the shore. Some deviation can occur, depending upon the value of the effective coefficient of friction at the boundary. Clearly, if this is low, then the normal component of the applied force will be preferentially transmitted.

As noted, in the two spring events at Barrow the edge of the ice sheet was melted back from the shore when the first motion occurred. Thus, movement through several meters was possible before the ice contacted the beach. Subsequently, the advance was irregular with some sections of the leading edge stopped while others continued to move. A similar pattern of displacement apparently developed in the Tapkaluk Island event. Possible patterns of stresses and displacements in the fast

ice sheet resulting from movements of this type were examined using finite-element methods.

The SAP IV structural analysis finite-element program (Bathe et al., 1973) was used to model a fast ice sheet in irregular contact with the shore under a distributed load along its offshore boundary. A two-dimensional array of linearly elastic membrane elements was used to form a 300-element rectangular mesh to represent an ice sheet adjacent to a beach. The state of the ice sheet-beach interface was specified by the boundary conditions along one of the long edges of the rectangle. These determined the lengths of reaches of the boundary along which the ice edge was fixed or free to move in response to the applied loads. The configuration used in most of the calculations consisted of a fixed boundary with central free segments of various lengths.

A uniformly distributed load was applied on the seaward boundary of the ice sheet (the grid boundary opposite the ice-beach interface) for each calculation run. The loading direction was varied to simulate normal loading (load directed normal to the beach), simple shear loading (load directed parallel to the beach) and combined shear and normal loading (load directed at 45° to the beach).

The calculations did not include a mechanism by which fixed node points along the beach could be released and moved according to some criterion in the program. Further, the SAP IV program has no provision for the use of stress-strain laws other than linear elasticity. Therefore, the results of the computations can only be used as indicators of the geometries of the stress and displacement fields at the instant the load is applied. These fields were interpreted on the assumption that stress concentration points and zones of high stress or displacement gradients indicated the points of origin and directions of propagation of fractures in the ice sheet. While a more flexible model would have been useful, the results are adequate for our qualitative interpretations.

The most important results of the calculations are that, for cases of normal loading and combined normal and shear loading, the highest stress concentrations occur (as expected) at the points of transition from the fixed- to free-boundary condition along the ice-beach interface. In addition, the zones of high displacement gradient which trend offshore from these points suggest the formation of shear zones oriented approximately parallel to the line of action of the boundary stresses. Thus, if only part of the ice-beach boundary is free to be displaced, the ice sheet within this segment will tend to advance up the beach as a plug, as would be anticipated for a punch test. The same displacement pattern would also result if the ice sheet was in motion and then stopped along sections of its leading edge due to interaction with the beach or other obstacles. In that case, a crack at a high angle to shore and parallel to the direction of motion would be expected to form.

Examples of this pattern were noted in the 1975 and 1976 events at Barrow and within the thrust sheet at Tapkaluk Island. In these cases, the fractures separated the segments of the ice sheet that moved through different distances.

3.1.4 PROPOSED MODEL

The results of the observations and analysis can be combined to suggest a model for the fracture and displacement of a fast ice sheet during a typical winter ice-push or ice ride-up event (Figure 3.1-2). The ice is assumed to be initially fixed to the beach, and the possible effects of grounded features are ignored. Figure 3.1-2A shows the geometry of the initial cracks which form according to von Mises' criterion. Some minor landward movement all along the front can occur at this time. In the second stage (Figure 3.1-2B), the thrust sheet is pushed up the beach with a tendency to rotate along the curving crack as indicated by the arrows. This results in the formation of compressive features along the high-angle crack. In addition, the normal force transmitted across the curving crack causes onshore movement of

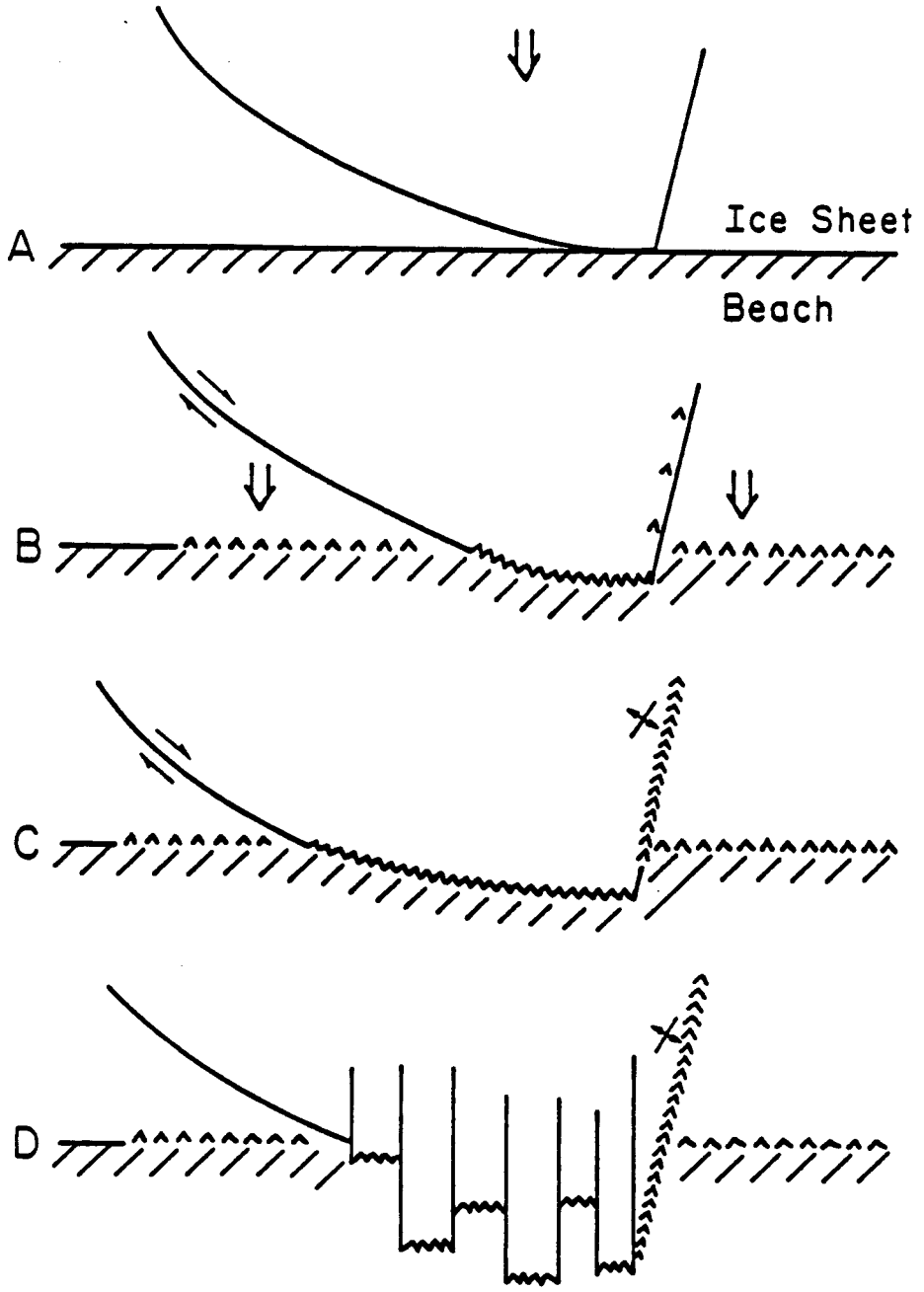

Figure 3.1-2 Proposed model for the fracture and displacement of a fast ice sheet during an ice-push event. See text for discussion.

the wedge of ice between that crack and the shore. Figure 3.1-2C shows the final form of the process if there is little or no differential motion at the leading edge of the thrust sheet as it moves up the beach, or if the total displacement is small. The alternative of segmentation of the thrust sheet as occurred at Tapkaluk Island is shown in Figure 3.1-2D. In this case, compressive features at either side of the diagram may not be present if there is little resistance to movement along the leading edge of the thrust sheet. Instead, plug geometry (as described above) develops rapidly, and motion occurs along the high-angle cracks that bound the plugs. Additional cracks with similar orientation then develop as the movement progresses.

For an ice-push event during break-up, melting along the shore weakens the bond between the ice sheet and the beach. Thus, the first three steps in Figure 3.1-2 do not apply. Instead, cracks at a high angle to the beach form in the early stages of the process and govern subsequent displacement of the ice sheet. A similar process might also be expected to occur for an event during freeze-up, when the ice sheet is not firmly bonded to the beach.

The geometry of the initial stress field at the time when the fractures of Figure 3.1-2A are formed can be assumed to be similar to Prandtl's solution, modified to reflect the distribution of grounded features, the shape of the shoreline and of the pack ice-landfast ice boundary, and the distribution of forces along the latter. The fractures begin at some local stress concentration along the shoreline. If no suitable stress concentration exists, then the stresses are relieved by ridging at the edge of the fast ice, or elsewhere in the fast ice sheet, and no ice advance will occur. After the fractures form or the movement of the thrust sheet begins, the stress distribution will vary in accordance with changes in the boundary conditions and the distribution of new fractures within the thrust sheet. The final form of the thrust sheet (including ice pile-up and ride-up at the beach) will depend upon the sequence of changes and

the magnitudes of the stress variations which occur throughout the process. As a result, the extent to which the local stresses (deduced ex post facto) are representative, of the far-field stresses at the start will vary from event to event.

This model assembles the available information into a pattern; clearly the interpretation will require modification as more data become available. However, even a preliminary model can serve to emphasize questions that can usefully be raised regarding the processes of ice push and ice ride-up. Before proceeding to these, however, we should note that the January 1978 event at Igalik Island does not fit the model because its crack pattern is more similar to a spring event. There are several possible explanations, but none are supported by data. It is possible that the open lead was closer to (or at) the beach here than at other localities along the barrier islands. The resolution of the satellite imagery does not permit this to be evaluated. Alternatively, it is possible that the bonding between the ice sheet and the beach was uniformly weak; thus motion occurred all along the beach when the load was applied, as is postulated during spring events. Subsequently, the low, uniform slope of the island did not resist the motion enough to break the ice sheet up into smaller segments.

3.1.5 CONCLUSIONS

The suggestion that ice pile-up and ride-up represent the result of a stress concentration mechanism is supported by three points: (1) The length of these features along the beach is generally less than that along which pack ice-fast ice interaction occurs; (2) For the case of winter events, the fractures bounding the thrust sheets tend to make the dimensions of the thrust sheet wider at the offshore edge than at the beach, and (3) For an ice sheet advancing as a series of discrete segments, the resistance to the motion (and thus the force) can vary between segments, depending upon local conditions. This emphasizes the need for care in

deducing far-field stresses from those required to form local features. It is likely that such values will be conservative in the sense that they will overestimate the far-field stresses, but the extent to which this is true depends on the contribution of other energy sinks that may not be accounted for in the calculations.

The discussion above addresses a possible sequence of events for breakup of an ice sheet during an ice push event. Other aspects which require study include (1) possible seasonal variation in the efficiency of grounded features in anchoring the ice sheet and thus affecting shoreward ice movement, (2) the influence of the nature of the boundary between the fast ice and the beach, and (3) the nature of the interactions between pack ice and fast ice.

3.1.6 REFERENCES CITED

Cummings, D., 1976. Bull. Geol. Soc. Amer., 88, 720.

Kovacs, A., Sodhi, D. S., and Cox, G.F.N., 1982. CRREL Report 82-31. U.S. Army Cold Reg. Res. and Eng. Lab., Hanover, NH.

Parmerter, R. R. and Coon, M. D., 1972. J. Geophys. Res., 77, 6565.

Prager, W. and Hodge, P. G., Jr., 1951. "Theory of Perfectly Plastic Solids." Wiley, New York.

Pritchard, R. S., 1977. In: "Proceedings, POAC '77", Vol. 1, p. 494, Memorial Univ. of Newfoundland, St. John's.

Shapiro, L. H., Metzner, R. C., Hanson, A. and Johnson, J. B., 1984. In: "The Alaskan Beaufort Sea: Ecosytems and Environments", P. W. Barnes, D. M. Schell, and E. Reimnitz, eds., Academic Press, New York, p. 137.

Varnes, D. J., 1962. U.S. Geol. Survey Prof. Paper 378-B, B-1.

Vivatrat, V. and Kreider, J. R., 1981. In: "Proceedings of the Offshore Technology Conference", p. 471, Houston, TX.

3.2 HISTORICAL REFERENCES TO ICE CONDITIONS ALONG THE BEAUFORT SEA COAST OF ALASKA

by

Lewis H. Shapiro and Ronald C. Metzner

3.2.1 INTRODUCTION

The existing data base describing average and extreme ice conditions along the northern coast of Alaska comes primarily from observations made since the discovery of oil at Prudhoe Bay. This followed from the increase in interest in the area, and the recognition that the adjacent continental shelf would be the subject of further exploration. In this context, the frequency of occurrence of unusual or extreme events involving the ice cover in nearshore areas is of interest. It may be true that the most severe conditions likely to be encountered have occurred since observations have increased. However, this cannot be known until the data base of observations is extended in time.

The purpose of this project was to attempt to extend the data base backward in time through interviews with local residents of the North Slope who had lived in coastal areas in past years. Many of these people were engaged in traditional hunting and trapping activities along the coast, and had both the opportunity and the incentive to carefully observe ice conditions in the area.

3.2.2 PROCEDURES

A pilot program of interviews was conducted involving eight individuals ranging from 55 to 85 years of age. All had lived in different coastal areas in the past, and had long experience traveling offshore along the North Slope over the ice during winter, or in small boats during the summer. In four cases the individual was interviewed (by Mr. K. Toovak of Barrow who collaborated with us on the program)

and responded to questions posed. In the others, the person was supplied with a tape recorder and a list of questions and simply asked to provide background and to respond to the questions. The interviews and commentary were all done in the Inupiaq language. They were translated by Mr. Toovak speaking into a tape recorder while listening to the interview being played on a second recorder and later transcribed. A second series of interviews produced a wealth of historical information, but did not add anything of interest to the objectives of the program. Thus, they were not transcribed, but copies of the tapes (as well as those from the first series of interviews) were given to the Alaska Native Language Center of the University of Alaska for use in the compilation of a dictionary of the Inupiaq language. Copies were also archived with the oral history program at Rasmuson Library at the University.

3.2.3 SUMMARY AND DISCUSSION

A detailed description of the project, including the results and an evaluation of the methodology, was given in Shapiro and Metzner (1979). The major observations were (1) descriptions of ice push events in the Barrow area during winter, (2) the first report of a major ice movement in Harrison Bay during winter (the formation in February of a 1-mile-wide lead, probably along the trend of the 10-m depth contour, and extending from near Cape Halkett toward Thetis Island), and (3) the first report of a major breakup ice-push event near Cape Halkett (in July). Negative information was also useful. As an example, none of the people questioned reported any instances of winter ice-push events driving the ice over the barrier islands along the North Slope. However, an event of this type occurred during the 1977-78 winter along the north side of Elson Lagoon east of Point Barrow (Section 3.1). Thus, the lack of previous observations suggests that this is a rare event.

As anticipated, there was little reference to synoptic relationships between ice motion and weather systems. However, the point was noted that westerly winds in winter form a lead which extends from Cross Island, along the north side of the barrier islands and across Camden Bay. This is apparently a rapid event, because we have two stories of hunting parties trapped on the offshore side of the lead.

Numerous descriptions were given of summer ice conditions, particularly with regard to small boat travel. These included some general rules-of-thumb regarding relationships between wind directions and changes in position of the pack ice edge, and the drift of heavy ice near shore.

Finally, there were a few references to the relationship between marine mammals and summer ice conditions, and to bowhead whale migration and capture in the Prudhoe Bay area.

3.2.4 REFERENCES CITED

Shapiro, L. H. and Metzner, R. C. (1979) Historical references to ice conditions along the Beaufort Sea coast of Alaska; Geophysical Institute Report UAG R-268, pp. 62.

3.3 VIBRATION OF SEA ICE SHEETS

by

Lewis H. Shapiro and Howard F. Bates

3.3.1 INTRODUCTION

This study began as the result of several incidental observations which indicated that long-period (i.e., 6 to 10 minutes) vibrations of an ice sheet may be associated with increasing stress in the ice in nearshore areas. Further, in many cases, the vibrations began on the order of several hours before the effect of the increasing stress was shown by motion of the ice sheet, suggesting that long-period vibrations might be precursors to episodes of ice motion. If so, monitoring ice sheet vibration through a tide gauge under the ice in shallow water (or by tiltmeters on the surface of the ice sheet in deeper water) might provide the basis for a system to warn of impending ice motion, thus enhancing safety in offshore operations.

To investigate the association, we undertook a theoretical study of the process of wave propagation in an ice-covered sea. The purpose was to determine the conditions under which waves of the period observed would propagate, and the possible effect of ice stress on the wave periods. The results were published in three papers (Bates and Shapiro, 1980a, 1981a,b). In addition, the theory was applied to the problem of breaking floating ice sheets by traveling vehicles in Bates and Shapiro (1980b).

3.3.2 BACKGROUND

Observations of ice motion or rising stress levels associated with long-period vibrations came from the following sources:

(1) On two occasions, waves with amplitudes of a few centimeters and periods on the order of 600 seconds were recorded by a tide gauge under the fast ice sheet near Point Barrow. During one of these events, several stress transducers, which

had been implanted in the fast ice sheet for other purposes, recorded a continuously increasing compressive stress with superimposed sinusoidal stress variations in phase with the waves. In addition, sinusoidal patterns of strain variation were also recorded by strain gauges in the ice sheet. The sinusoidal variations apparently resulted from flexing of the ice sheet in response to the waves propagating through the water. The stress levels were below the calibrated range of the transducers (suggesting that the stress reached a maximum of a few kPa) but the pattern was clear. In the other event, no stress transducers were installed in the ice. However, compressive stresses are indicated because the ice sheet advanced about 10 m onto the beach as the waves reached their maximum amplitude, about 12 hours after they were first observed.

(2) Sinusoidal stress variations (with time) had previously been observed on stress transducer data (R. D. Nelson, unpub.), but no supporting tide gauge records were available with which to associate the stress variations.

(3) Hunkins (1962) reported that long-period waves with amplitudes inversely proportional to frequency accompanied winds exceeding 5 m/sec (10 kn) over relatively continuous floating sea ice.

(4) As discussed in Section 3.5.3.3, the University of Alaska sea ice radar system often recorded examples of "flickering" of reflectors on the ice surface for periods of up to several hours prior to movement of the ice sheet. The flickering is interpreted as resulting from vibration of the ice sheet, although the nature of the data do not permit the period or amplitude of the vibration to be determined. As noted in Section 3.5.3.3, not all episodes of ice motion were preceded by flickering, but all episodes of flickering were followed by ice motion.

These observations were interpreted to imply an association between long-period waves in the ice-covered sea and rising stress levels in the. ice sheet. This, in turn, implies that a means must exist by which substantial energy is coupled from the wind through the ice sheet to the water as it produces the stress in the ice. We

hypothesized that the energy might be introduced into the ice-covered sea by the impulsive breaking of ice during the production of pressure ridges. During the breaking of the ice in the ridging process, blocks of ice are abruptly displaced upward and downward, with the energy necessary for this motion supplied by the impulsive release of stored elastic energy. To maintain hydrostatic equilibrium, approximately 8 times the volume of the ice that is displaced upward must be displaced downward. The pumping action represented by the abrupt vertical motion of a substantial volume of ice would then transform a fraction of the released energy into wave motion in the ice-covered sea. Ridging involves the breaking of progressively thicker, stronger ice (i.e., the thinnest, weakest ice breaks and ridges first), so that the process tends to "harden" the pack ice. This increases the stress level in the ice sheet and permits stresses to be transmitted further.

The hypothesis accounts for the observations by providing an energy source for the waves and a mechanism for associating the waves with rising stress levels.

3.3.3 WAVE-PROPAGATION IN AN ICE-COVERED SEA

The basic solution to this problem was first done by Greenhill (1887). He solved the problem for a floating ice sheet modeled as an elastic plate floating on a liquid, for the case of a sinusoidal displacement as a forced response. Later workers who used this formulation were Ewing and Crary (1934), Hunkins (1962) and Wadhams (1973). Nevel (1970a,b) obtained two-dimensional rectangular and cylindrical wave solutions directly from the differential equations of the system.

In our work, we extended the solution to the case where the elastic plate is under in-plane compressive stress and found a general solution for any arbitrary boundary and initial conditions (Bates and Shapiro, 1980a). The basic approach was to model the ice sheet-ocean system as a wave guide. The wave equation was solved in the liquid layer subject to the boundary conditions of a rigid sea floor and the equation of motion of a stressed, floating, linearly elastic plate at the upper surface.

The results show that two bands of gravity waves propagate in the system in response to a plane-wave impulse. The shorter period set are flexural gravity waves, which depend on the elastic properties of the plate. In the longer period waves, to first order, the plate acts as a non-elastic membrane with mass. The two bands join at a critical period which depends upon the elastic modulus of the ice and the magnitude of the compressive stress in the ice sheet. For the values chosen in the calculation (Young's modulus from 6×10^8 to 6×10^9 N/m^2 and stresses from 0 to 70 kPa), the critical period ranges from 11.2 to 23.9 sec; it increases with increasing Young's modulus and decreases with increasing stress. In addition, for the impulsive source, the amplitude of the long-period waves varies inversely with frequency, which agrees with Hunkins (1962) observations noted above.

The results of this work were applied to the problem of breaking floating ice sheets by traveling vehicles (Bates and Shapiro, 1980b). That work suggests optimum speeds for safe travel (or, conversely, for breaking ice) as functions of ice thickness, water depth and compressive stress.

In the solution for the elastic plate, the stress at the critical period is unbounded, suggesting that the problem be reformulated to consider a plate with viscoelastic rather than elastic properties. This was done (with additional support from the National Science Foundation) through the application of the correspondence principle to the elastic solution, and the results were published in Bates and Shapiro (1981a). These showed that the assumption that the plate was viscoelastic forced the stress to remain bounded at the critical period, but did not change other aspects of the elastic solution. In a later paper (Bates and Shapiro, 1981b) the results were shown to be in reasonable agreement with the available experimental data regarding ice sheet deflection under moving loads.

3.3.4 SUMMARY

The results of this study provide a theoretical framework for the observations described above. They verify that long-period waves in the range of observed periods can be excited by impulsive forces, such as might be caused by ridging. The observed rise in stress level is attributed to the increased capacity of the ice to transmit stress as the weaker parts of the ice sheet are absorbed in pressure ridges.

3.3.5 REFERENCES CITED

Bates, H.F. and Shapiro, L.H. (1980a). Long period gravity waves in ice covered seas; J. Geophys. Res. v. 85, p.1095.

_____(1980b). Breaking ice with gravity waves; J. Energy Res. Tech., v. 102, p.148.

_____(1981a). Plane waves in a viscoelastic floating ice sheet; J. Geophys. Res. v. 86, p. 4269.

_____(1981b). Stress amplification under a moving load on a floating ice sheet; J. Geophys. Res. v. 86, p. 6638.

Ewing, M. and Crary, A.P. (1934). Propagation of elastic waves in ice, 2; Physics, v. 5, p. 181.

Greenhill, A.G. (1887). Wave motion in hydrodynamics; Amer. J. Math., v. 9, p. 62.

Hunkins, K. (1962). Water waves in the Arctic Ocean; J. Geophys. Res., v. 67, p. 2477.

Nevel, D.E. (1972). Vibration of a floating ice sheet; Res. Rep. RR 281, U.S. Army Cold Reg. Res. and Eng. Lab., Hanover, N.H.

Wadhams, P. (1973). Attenuation of swell by sea ice; J. Geophys. Res., v. 78, p. 3552.

3.4 COEFFICIENTS OF FRICTION OF SEA ICE ON BEACH GRAVEL

by

Lewis H. Shapiro and Ronald C. Metzner

ABSTRACT

The coefficients of static and kinetic friction of sea ice on unfrozen beach gravel were calculated from measurements made while dragging two large blocks of sea ice [approximate weights 23,300 and 26,400 lbs (10,600 and 12,000 kg)] in short increments up a sloping beach surface. The results of 36 separate experiments yielded values of the coefficients of static and kinetic friction of $\mu_s = 0.50$ and $\mu_k = 0.39$ respectively. These values should be applicable to calculations of the forces required to drive an ice sheet on shore during an ice push event.

3.4.1 INTRODUCTION

The purpose of this note is to present the results of a series of determinations of the coefficients of static and kinetic friction between sea ice and unfrozen beach gravel. The measurements were made by repeatedly dragging large blocks of sea ice along a beach with a bulldozer. The data should be useful for calculations of the forces involved in driving ice sheets on shore during ice push events.

The work was done at the Naval Arctic Research Laboratory at Barrow, Alaska in late June. At the time of the experiments, the beach surface was thawed, and the landfast ice had melted back,leaving a shore lead about 6 ft (2 m) wide. The shoreward edge of the ice was resting on a low berm on the offshore side of the lead and the thickness of the ice was about 4 ft (1.3 m). The extent of melting which had occurred by the time of the experiments [from an initial thickness approaching 6 ft (2 m)] suggested that the temperature of the ice was at the melting point through its entire thickness, although this was not verified by direct measurement.

3.4.2 PROCEDURE

A chain saw was used to cut two blocks from the leading edge of the ice (dimensions are shown schematically in Figure 3.4-1). Note from the figure, that the leading edge of Block #1 was naturally sloped, while that of Block #2 was nearly vertical.

The arrangement of the experiments is illustrated in Figure 3.4-2. A horizontal hole was drilled through the center of each block with a hand auger. A cable was then passed through the hole, and attached to a short length of timber which served to anchor it. The cable extended about 15 meters from the leading edge of the block to a dial dynamometer [Dillon Mfg. Co., 20,000 lbf (44,080 N) x 100 lbf (220.4 N) divisions, 10 inches (0.254 m) diameter dial face, ± 1/2% @ full scale]; a second cable attached the dynamometer to a bulldozer which was used to drag the block.

The experiments were done during a two day period. On the first day the blocks were dragged up the sloping beach from the water line to the beach crest in a series of start-stop movements. The dynamometer was monitored visually as the blocks were dragged; forces were estimated to the nearest 100 lbf (220.4 N). The peak force reached as the block was put in motion after each stop was used to calculate the coefficient of static friction. The motion was then continued through a short distance [maximum about 6 ft (2 m)] at an average velocity of about 1 ft/sec (0.3 m/sec). During the movement, the dynamometer reading fluctuated as the force required to keep the block in motion changed. The mid-point of the range of fluctuation was estimated and used in the calculation of the coefficient of kinetic friction. During the traverses up the beach slope, a total of 15 determinations of the coefficients of friction were made on Block #1 and 21 on Block #2. These experiments were done over the part of the beach which an ice sheet must traverse

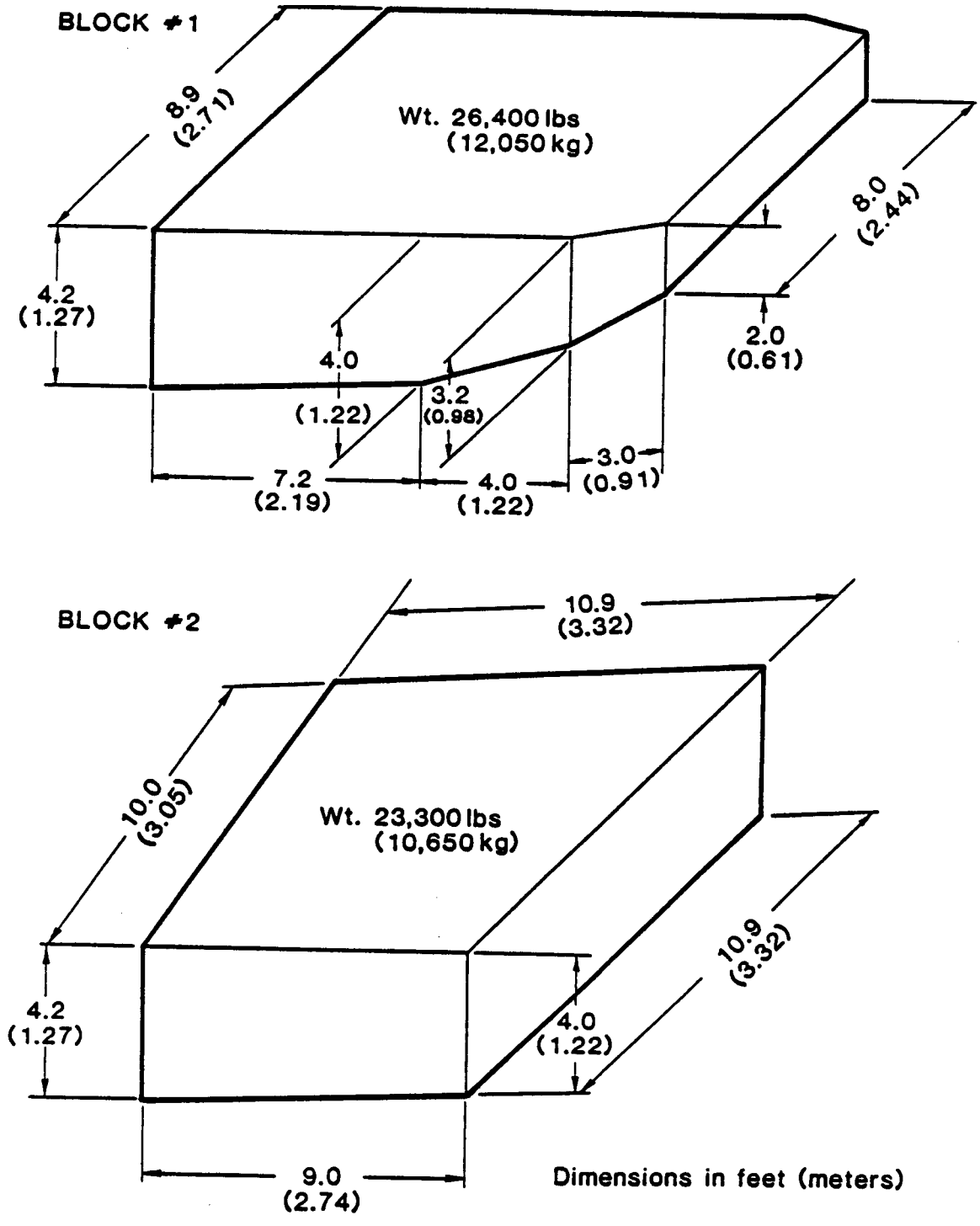

Figure 3.4-1 Geometry and weights of test blocks. The leading face of the blocks is to the right in both cases; note the sloping face of block #1 and the vertical face of block #2. Dimensions in feet (meters).

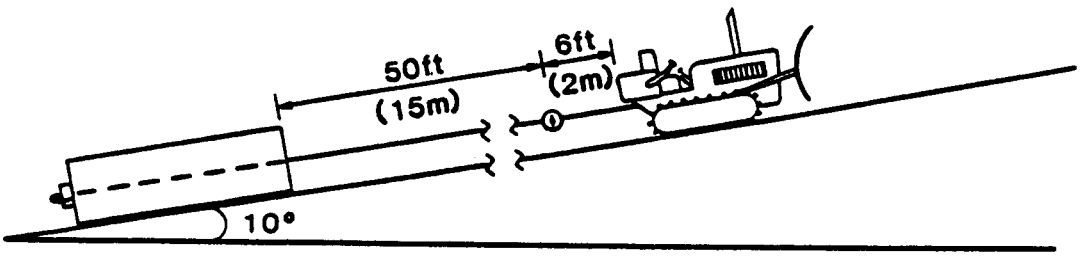

Figure 3.4-2 Schematic of the experimental set-up. Dimension in feet (meters).

during an ice-push event. An additional 15 experiments were done on the second day by dragging Block #2 parallel to the shoreline along the crest of the beach.

To determine the weights of the test blocks, their volumes were calculated from the dimensions and forms shown in Figure 3.4-1. Density measurements were made on samples taken near the top, mid-height and bottom of the blocks, and from a zone of gravel-rich ice which was present in the upper parts of the blocks. Each density measurement was assumed to be representative of a fraction of the block volume, from which an average density was calculated. The result was 58.3 lbs/ft^3 (936 kg/m^2); the high value reflects the approximately 15% of the blocks which were gravel-rich ice. The calculated block weights are shown on Figure 3.4-1. Note that the gravel-rich ice was restricted to the upper parts of the blocks. The basal areas of both blocks were generally free of gravel, so that the experimental results can be taken as representing the coefficients of friction for "clean" ice over unfrozen beach gravel.

The pebble surface of the beach slope was relatively smooth and densely packed on its lower reaches where most of the experiments were done on the first day. However, the surface was rougher and less compact toward the crest of the slope and in the area where the experiments were done on the second day. This is reflected in the results, as discussed in the next section.

The slope of the beach was determined by placing a board about 6 ft (2m) long on the surface and measuring its inclination with a clinometer. Several measurements were made along the slope on which the experiments were done and indicated a uniform inclination of 10°. The slope of the path parallel to the beach, along which Block #2 was dragged on the second day, was assumed to be zero and was not measured.

3.4.3 RESULTS AND DISCUSSION

The values of the coefficients of static and kinetic friction determined from the test results are shown in Figure 3.4-3. These were calculated from the relationship

$$\mu_{s,k} = (\vec{F}\text{-}\vec{W}\sin\beta)/\vec{W}\cos\beta$$

where μ is the coefficient of static (μ_s) or kinetic (μ_k) friction, $\vec{F}$ is the corresponding force, $\vec{W}$ is the block weight and β is the slope angle of the beach. The mean values and standard deviations of the data in Figure 3.4-3 are given in Table 3.4-1. Note that the standard deviations indicate that the data points spread over approximately the same percentage range of the means for the three data sets.

The use of the equation above implies the assumption that the force $\vec{F}$ was applied parallel to the beach slope and along the center lines of the blocks, so that it acted through the centers of gravity of the blocks. If this were true, then no vertical force components were introduced as the blocks were pulled. Deviations from the ideal would enter as the sine of the angle between the force vector and the center line of the block. Calculations indicate that for small angles the resulting percent errors would be of the same order as the angular deviation (i.e., a variance of 5 degrees would result in a 5% error in the calculated coefficients of friction).

Other sources of error arise from possible misreading of the dynamometer dial and from the estimates and approximations used in the calculation of the weights of

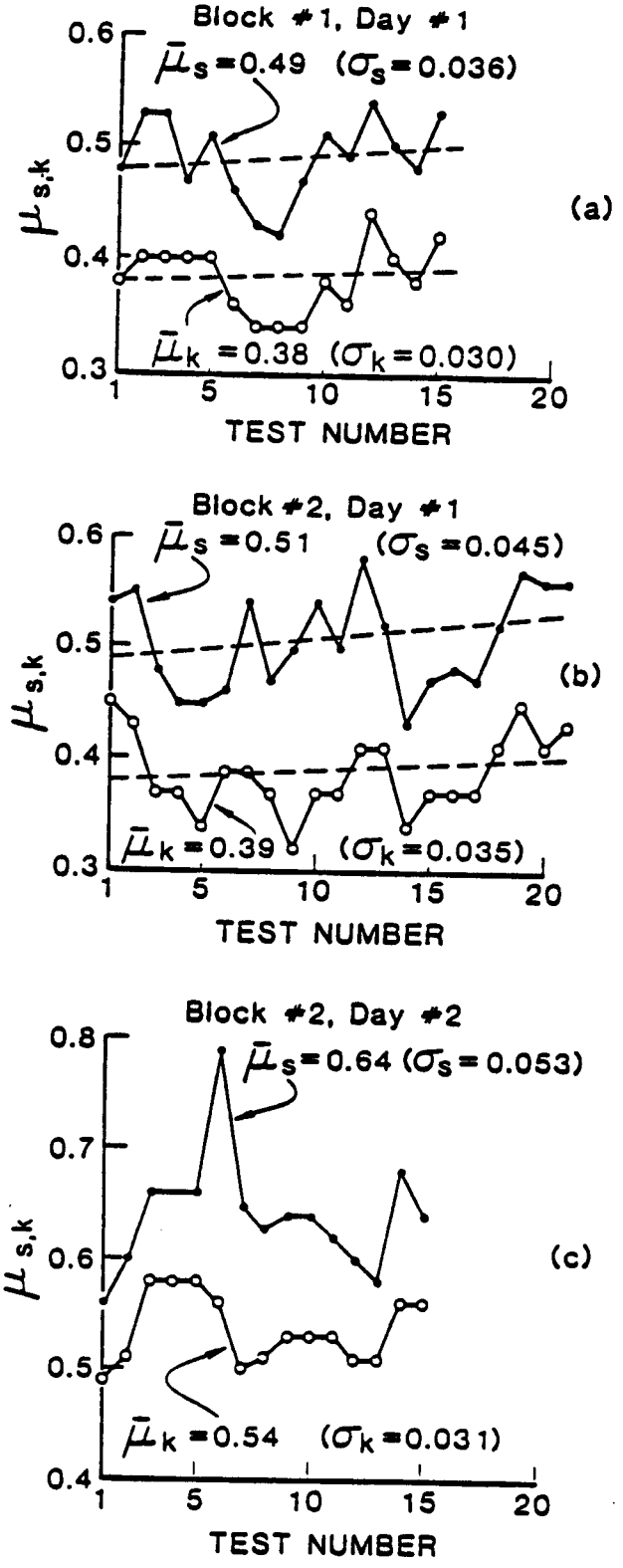

Figure 3.4-3 Plots of $\mu_{s,k}$ vs. test number for the three test series. Dashed lines in (a) and (b) are the results of linear regression calculations. Values of μ_s, μ_k, σ_k from Table 3.4-1 for each data set are indicated in the figure.

TABLE 3.4-1

Values of Coefficients of Friction and Standard Deviations

	μ_s	σ	μ_k	σ
Block #1 (Day 1)	0.49	0.036	0.38	0.030
Block #2 (Day 1)	0.51	0.045	0.39	0.035
All Tests (Day 1)	0.50	0.041	0.39	0.032
Block #2 (Day 2)	0.64	0.053	0.54	0.031

the blocks. The former are likely to be small (i.e., for the magnitudes of the forces involved, the calculated coefficients of friction vary by less than 1% per scale division on the dynamometer dial) and randomly distributed through the data, along with the effects of variations in roughness and texture of the beach surface. Errors in determining the weights of the blocks are linearly related to the calculated coefficients of friction. Calculations assuming "worst case" estimates suggest a maximum possible error of less than 10% in the block weights.

The similarity of the coefficients determined from the experiments on the two blocks on the first day suggests that the difference in the shapes of the leading edges of the blocks was not important. This is probably due to the fact that the shear strength of the unconfined, unfrozen gravel at the surface of the beach was negligible, so that little energy was required to plow the beach and scrape the shallow grooves which were left on the surface behind the blocks.

It might have been anticipated that, with increasing numbers of tests (and the resulting increase in the distance which the blocks had traversed), the coefficients of friction would decrease as the lower surfaces of the blocks were worn smooth by abrasion. Conversely, the increase in surface roughness and the decrease in packing

density of the beach surface with increasing elevation above the water line would be expected to result in an increase in the coefficients. Linear regression of the four data sets from the experiments on the first day (Figure 3.4-3) shows a small increase in the magnitudes of the coefficients with increasing numbers of tests. However, the difference between the largest and smallest values of the coefficients, as calculated from the regression equations, is within the range of scatter of the data. Thus, if changes in test conditions occurred during the experiments on the first day, they were compensating or of little importance.

Note that the coefficients determined for the experiments on Block #2 on the second day are higher than those for both blocks on the first day. We can identify two factors which might be responsible for the discrepancy. First, the increase in roughness and decrease in packing density of the surface of the upper part of the beach (in comparison to the sloping surface where the experiments were done on the first day) would tend to increase the drag on the block. Second, it is possible that the slope was not zero as it was estimated to be (note that an upward slope of as little as 4° would decrease the calculated values of the coefficients of friction by 0.07). Because of these uncertainties, we consider the results of the experiments on the second day to be less reliable than those from the first day. In addition, the values of $\mu_s = 0.50$ and $\mu_k = 0.39$ reflect the interaction of the ice with the lower slope of the beach, and are thus more applicable to the problem of calculating the forces involved in ice-push events.

3.5 NEARSHORE ICE CONDITIONS FROM RADAR DATA, POINT BARROW AREA, ALASKA

by

Lewis H. Shapiro and Ronald C. Metzner

ABSTRACT

From June 1973 to May 1979, the University of Alaska maintained a small radar system to monitor nearshore ice motion and conditions at the Naval Arctic Research Laboratory near Point Barrow, Alaska. The purpose was to support research projects which required that information. In this report, the data acquired are compiled to describe the annual cycle of the ice year in the area. A short open water season can be defined as extending from late July to late September. This is followed by freeze-up, which is characterized by a decreasing frequency of occurrence of drifting pack ice in the area between October and January. The winter season extends from January through May. It is marked by generally stable or slow-drifting pack ice, or by the absence of pack ice offshore from the edge of the fast ice. The onset of breakup in June is characterized by the increasing occurrence of drifting pack ice again. Comparison of the ice cycle with climatologic data indicates no strong correlations with variables other than (possibly) air temperature. As expected, ice activity is greatest during freeze-up and breakup, with rapid changes in the directions and velocity of ice motion. Similar movement patterns occur in winter, but the ice velocities are slower. Data of the type generated by the radar system would be useful for any area in which development of offshore installations is planned. Clearly, a knowledge of the range of possible ice motion patterns and events can provide the basis for improving the design of such installations.

3.5.1 INTRODUCTION

From June 1973 to May 1979, the University of Alaska operated a radar system along the Chukchi Sea Coast at the Naval Arctic Research Laboratory (NARL) approximately 5 km north of Barrow, Alaska (Figure 3.5-1). Support for the installation and operation of the system over this time came from both the University of Alaska Sea Grant program and NOAA/BLM OCSEAP. During its operation the radar was primarily intended to support research projects in the area by monitoring local ice conditions and events. However, efforts were made to operate the system all through the year so that during the period which it was in place, a significant record of local ice conditions and events was obtained. The purpose of this report is to present a synthesis of these observations in the form of a generalized annual ice cycle at Barrow, along with brief descriptions of events and processes to which the radar observations contributed information. Although the data are limited to this particular area, the results may serve as a model for the range of ice conditions which might be encountered elsewhere, particularly along the Chukchi Sea coast of Alaska. In any case, they emphasize the utility of data from monitoring of ice conditions in any area prior to the planning and development of offshore installations. Clearly, a knowledge of the range of possible ice motion patterns and events can provide the basis for improving the design of such installations.

3.5.2 EQUIPMENT AND METHODS

3.5.2.1 Radar System and Data Recording

The radar system used was a 3 cm X-band standard ship's radar of the type which would normally be installed on a small fishing vessel (Sackinger and Rogers, 1974). It was mounted on a tower on the beach at an elevation of about 12 m, which should give a maximum range of about 15-17 km (8-9 NM, based on the rule-of-thumb that the range of the radar in miles is approximately equal to the square root

of twice the height of the antenna in feet). However, the radar was usually operated at a range of 5.6 km (3 NM) (Figure 3.5-1) because no man-made reflectors were deployed on the ice, and this distance proved to be nearly the maximum range from which energy was returned from a sufficient number of natural reflectors for the ice motion to be monitored by tracking "blips" on the radar screen. A discussion of the nature of the reflectors is given in Section 3.5.2.3.

The radar data were displayed on a screen which was photographed (usually at 2.5-minute intervals) as time-lapse motion pictures using a 35-mm camera driven by a timing mechanism. A clock face was included in the picture to give the date and time of the image (Figure 3.5-2). At 2.5-minute intervals between pictures, a standard roll of film lasted approximately 4 days. Generally, film was developed and examined within 2-3 weeks following exposure so that it was possible (in some cases) to "ground truth" the imagery.

The choice of a 35-mm camera for recording the data was dictated by budget considerations; a 35-mm camera was available and the cost of acquiring similar 16 mm equipment (with the time-lapse capability) was too great for available funds. This was unfortunate because, while the 35-mm camera provided data of excellent quality, there was no commercially available equipment (such as analyzer projectors, which were available in 16 mm) with which to analyze 35-mm film. Accordingly, a viewing system was constructed with which the 35-mm film could be scanned so that ice conditions and motion could be characterized qualitatively. However, the resolution of the system was poor and the images did not register repeatedly on the viewing screen. This prevented the equipment from being used for detailed work, such as measuring the displacement and velocity vectors of the ice cover (by tracking the positions of identifiable reflectors on successive frames, as described below) or providing details of the sequence of events in development of the ice cover. For these studies, rolls of film in which events or sequences of interest

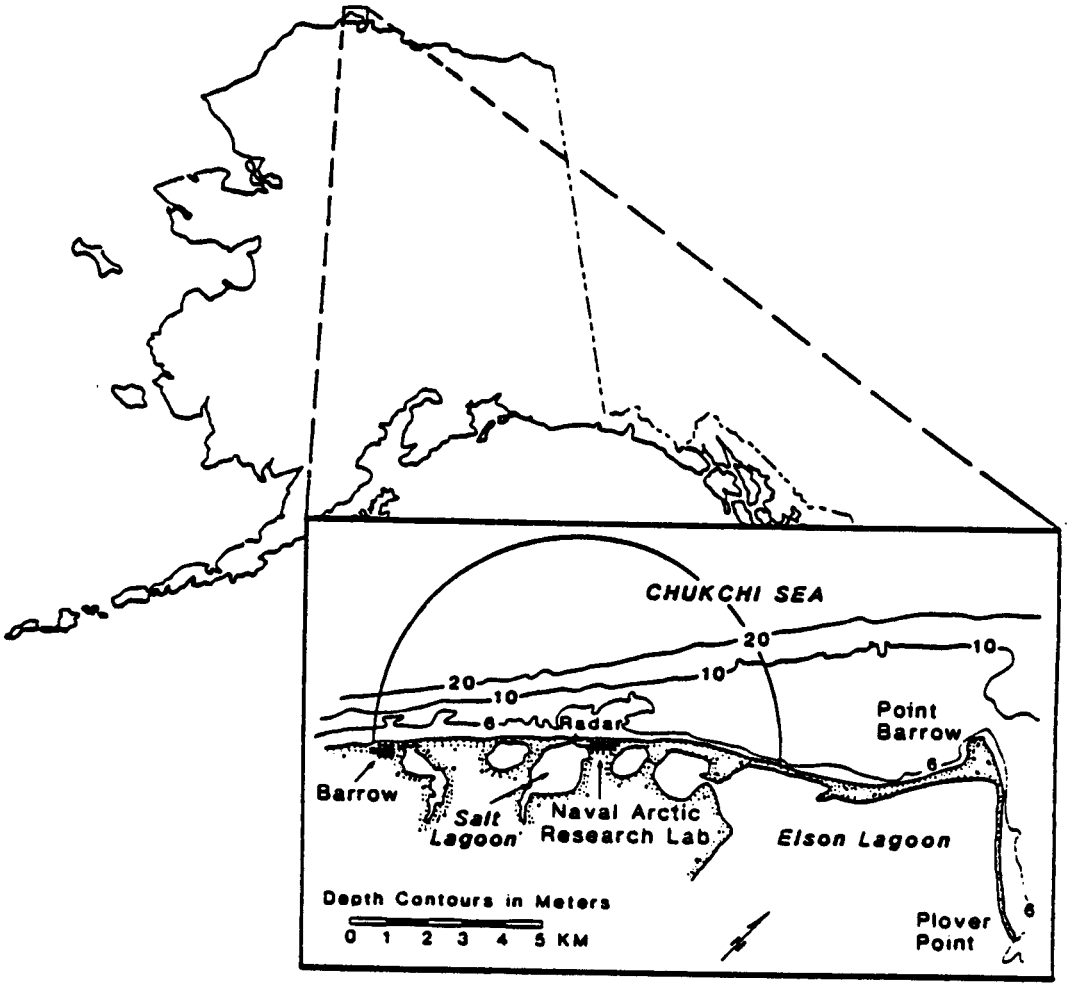

Figure 3.5-1 Map of the Point Barrow area showing the location of the radar site. The arc indicates the field-of-view of the radar when operated at a range of 5.5 km (3 NM).

appeared were reproduced on 16-mm film, for which an analyzer projector was available. Most of the analysis was done using this equipment. If detailed information was required from a short sequence of frames, the 35-mm data were enlarged to 70 mm and studied on a color additive viewer with which accurate registration could be done. However, the cost in time for this procedure was prohibitive, and it was not used as often as would have been desirable.

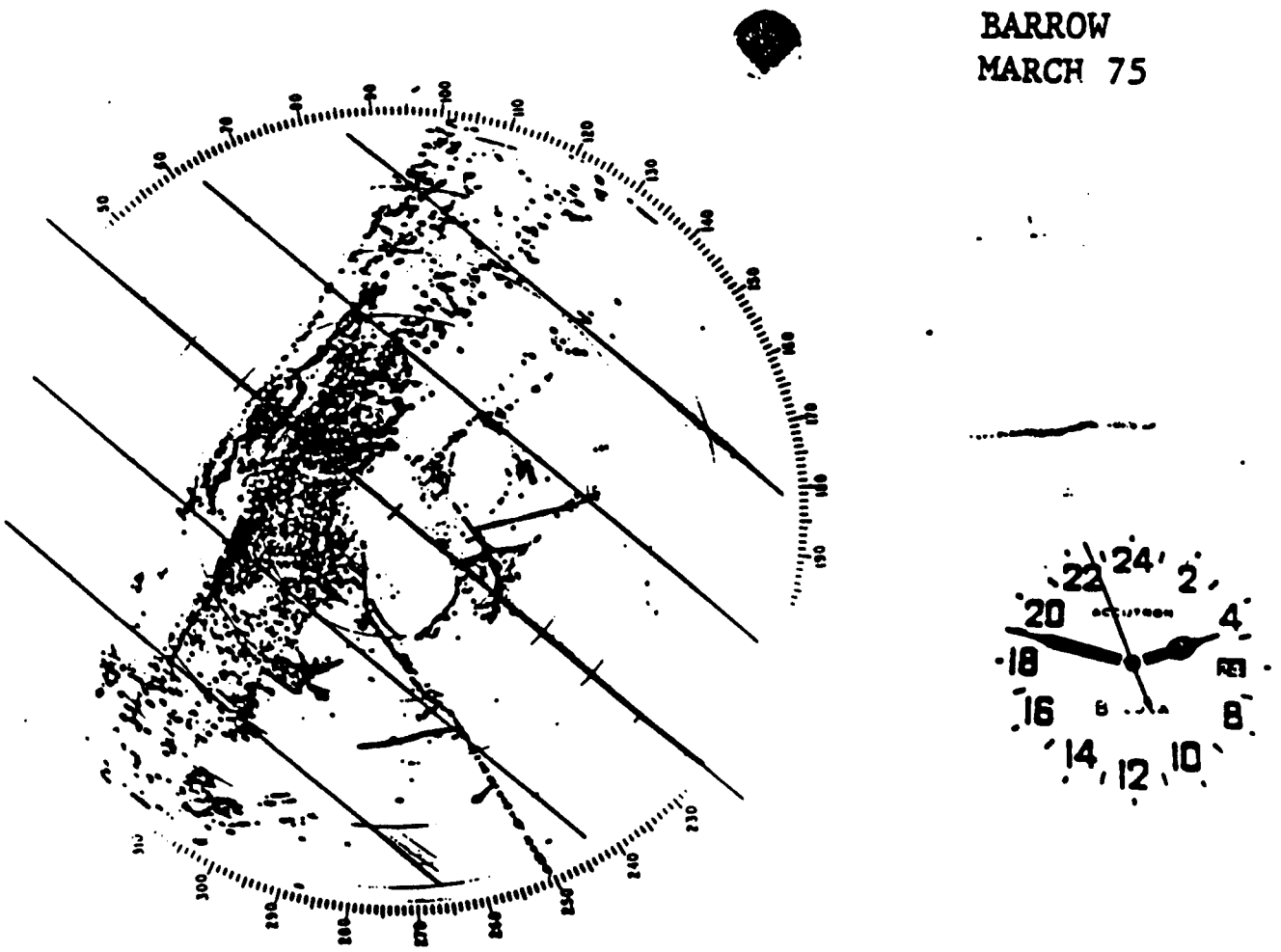

Figure 3.5-2 Typical frame of radar data at 5.5 km (3 NM) range. Spacing between concentric ranging circles is 0.93 km (0.5 NM). Parallel transverse lines are 1.85 km (1 NM) apart.

3.5.2.2 Data Analysis

A total of 387 films were obtained, representing 1550 days, or 71% of the total days that the radar was in place. Table 3.5-1 shows the percentage of possible days of each month for which data were obtained. These range from a low of 38% of all possible days for January to a high of 75% of possible days for May. Unfortunately, the sample is weakest for the late summer and fall, so that relatively little imagery was obtained during the critical freeze-up period. Still, the data range over the

TABLE 3.5-1

TOTAL DAYS OF RADAR COVERAGE BY MONTH AND YEAR

Month	1973	1974	1975	1976	1977	1978	1979	days	%
Jan	--	31	0	12	16	9	23	91	49
Feb	--	29	0	24	27	29	6	115	68
Mar	--	31	26	23	26	30	12	150	81
Apr	--	30	22	30	28	30	30	171	95
May	--	31	31	31	31	25	26	175	94
Jun	27	30	24	30	26	12	--	149	83
Jul	31	30	31	28	13	31	--	164	88
Aug	23	30	29	30	0	1	--	113	61
Sep	22	21	30	21	0	0	--	94	52
Oct	0	21	27	31	7	10	--	96	52
Nov	2	10	30	30	22	26	--	120	67
Dec	24	0	28	20	31	2	--	105	56

entire year and provide the basis for a preliminary characterization of the variation in ice conditions in the area through a calendar year, as described below.

The individual film rolls cover periods of from 2 to 8 days, averaging 3 to 4 days per roll. For convenience, the data characterization was done by film roll, rather than time interval. Each film was scanned and ice conditions and direction of motion (if any) were noted. Unusual events, such as pack ice being driven into contact with, or drawing offshore from, the fast ice were also noted. The results are summarized in Table 3.5-2. In general, there was little variability in the direction of ice motion within any roll of film. As an example, of the 387 film rolls, only 25 examples were found in which the drift direction reversed (i.e., the direction of drift changed from,

say, northeast to southwest along the coast) within the time covered by a film roll. Seventeen of the reversals occurred during breakup or freeze-up.

TABLE 3.5-2

ICE DRIFT DIRECTIONS BY MONTH

Month	Total Films	Drift Direction				
		Northeast	Southwest	In*	Out*	Reversal
Jan	23	5	9	4	4	2
Feb	29	4	3	0	2	0
Mar	38	7	6	4	2	2
Apr	43	3	7	6	5	2
May	44	7	6	3	3	2
Jun	37	14	3	8	5	0
Jul	41	19	12	10	13	4
Aug	28	16	5	6	8	4
Sep	24	11	5	2	3	4
Oct	24	10	12	4	3	1
Nov	30	11	10	8	8	4
Dec	26	3	6	8	8	0

(#) Numbers in each category give the number of films on which pack ice displacement occurred in the direction indicated. Totals may be greater than the number of films since drift in more than one direction occurred on some films.

(*) Headings "In" and "Out" refer to onshore and offshore(respectively) displacements of pack ice normal to the coast or edge of the fast ice.

3.5.2.3 Reflectors

The number of reflectors visible on the radar screen was always sufficient to permit the distribution and motion of the ice to be determined in the entire field-of-view when the radar system was operated at a range of 5.6 km (3 NM) or less. In addition, linear alignments of reflectors representing shear ridges within the fast ice were usually easy to identify. Once in place following freeze-up, the features of the fast ice remained stationary until breakup. Thus, it was always possible to separate fast ice and pack ice on the imagery, because the distribution of reflectors on the fast ice did not change through the winter.

In general the intensity of the energy return from reflectors on the ice surface decreased with increasing distance from the radar. Thus, low ridges, hummocks or discrete floes of multiyear ice at short ranges gave strong reflections, while similar or larger features at a distance gave weaker returns. Exceptions did occur which were probably due to variations in the orientation of reflecting surfaces on the features.

Attempts to determine the nature of the actual reflecting surfaces and their relationship to the intensity of energy return (as shown by the diameter of the blip produced on the radar screen) were unsuccessful. It was not possible to identify particular reflecting surfaces. However, it was often (but not always) possible to dentify a specific floe or ridge as the source of energy for a particular blip shown on the imagery. In this context, it should be noted that the fact that a feature was prominent did not ensure that it would return sufficient energy to produce a prominent signature on the radar screen. As an example, in one instance, a large grounded ridge (sail height in excess of 10 m) located 1.5 km offshore from the radar site was invisible to the radar, although a smaller ridge about 100 m to the southwest gave a strong reflection. Apparently, there was no surface on the larger ridge which was suitably oriented to reflect energy back to the radar antenna. In

contrast, features which were much smaller were often observed at greater distances from the radar. For example, reflectors defining the outlines of individual floes of thin ice in early fall could often be identified at the limit of the field-of-view of the radar. These reflectors were probably from low (less than 1 m high) ridges or hummocks formed during impacts between floes. Thus, there is no basis for associating the intensity of a reflector with the size of the feature which produced it.

The smallest blips which could be discriminated on the data [at 5.6 km (3 NM) scan] had diameters of about 40 m at the scale of the imagery. Clearly, the actual sizes of the reflectors on the ice surface were smaller; the enlarged scale of the blips results from the dispersion of the returned radar energy. The effect of the sizes of the blips on the lower limit of the ice displacement which could be detected is discussed in Section 3.5.2.4.

It would have been desirable to determine the effect of changes in snow cover on the character of the reflectors through the winter. However, this was not possible because of the need to adjust the gain on the radar system periodically, which had the effect of changing the intensity of the reflectors.

3.5.2.4 Measurement of Ice Motion

Ice velocity measurements were made by tracking individual reflectors on sequential frames of the film. The scale of the imagery was provided by the range lines (Figure 3.5-2) and the time by the clock (or by simply counting frames of film since the time interval between exposures was known). In making velocity measurements it was always possible to track the motion of reflectors over at least 1.5-2 km. At the velocities measured, this took sufficient time that the measurements are believed to be accurate to within 0.1 km/hr, so that velocities reported below are given to this precision.

Ridging events were shown by the formation of lines of reflectors. It was usually possible to identify the exact frame on which a particular reflector on a ridge

line appeared, so that the time required for development of a ridge could be determined. An example of the use of this type of data in describing the process of development of the fast ice cover is given in Shapiro (1975a).

It was simple to detect pack ice motion when the data were viewed as time-lapse motion pictures because, even when the movements were slow, the displacements eventually became large enough to be obvious. Smaller displacements of the fast ice were also easy to detect if they occurred rapidly; the apparent "jump" of all of the reflectors in the fast ice was obvious. However, small displacements of the fast ice at low rates were never observed on the radar data although, as described in Section 3.5.4.4, at least two examples of such movements did occur during the time the radar system was operating. There is no quantitative basis for defining a lower limit of the magnitude of displacement of the ice which could be detected. However, experience suggests that displacement of a blip by about one-half its diameter (i.e., 20 m for the smallest detectable blip) should be apparent. Thus, this is assumed to be the approximate lower limit of detectable displacement within the fast ice.

As noted above, a color additive viewer was also used in the interpretation of the data. An example of the results of this type of analysis is given in Section 3.6.4.1 (Figure 3.6-11, showing the displacement vectors of the fast ice during the ice push event of July 1975 superimposed on a map of ice gouges in the sea floor).

3.5.3 CHARACTERISTIC ICE MOTION PATTERNS

3.5.3.1 Introduction

No weather or current monitoring equipment was deployed as part of this project at any time during the operation of the radar system. Local weather data were acquired from the NWS station at Barrow and from the NOAA air monitoring station northeast of NARL for use in interpreting the motion during some events

which were observed in the field (i.e., ice push events, lead formation, etc.). In addition, satellite imagery of the area and regional weather charts were examined regularly. As a result, various qualitative "rules-of-thumb" were developed for interpreting the local patterns of ice distribution and motion. The rules are based primarily on the assumption that pack ice tends to drift at about 30° to the right of the wind direction under "average" conditions (Whitman and McDowell, 1964). However, the actual movement patterns also reflect the shape of the coastline in the area, the topography of the sea floor (which controls the positions of grounded ice ridges within the fast ice), and the local tides and ocean currents. These factors introduce enough variation and complication into the patterns that it was never feasible to try to develop quantitative models relating ice motion to driving forces.

3.5.3.2 Generalized Drift Patterns

The relationship between the orientation of the coastline and wind and ice drift directions (based on the rule-of-thumb given above) is shown in Figure 3.5-3. Details are discussed in Section 3.5.4.6. The purpose here is to describe, in general, the basic movement patterns which have been observed.

The orientation of the coastline requires that most of the observed ice motion in the area (in terms of the duration of observations) be to the northeast or southwest, since these provide the longest path lengths within the radar field-of-view. Clearly, ice drifting at a high angle to the coast will be in view for only limited times before it either leaves the field-of-view of the radar or impacts the edge of the fast ice and stops. However, ice could drift through the area on tracks parallel to the coast for long periods of time. Ice drift along the coast to the northeast is caused by winds from the south to southwest which, in turn, occur when a low pressure system is located over the central Chukchi Sea. With this configuration, the winds tend to drive the pack ice close to shore so that, in general, pack ice drifting to the northeast was close to, or against, the edge of the fast ice. In addition, ice push events observed

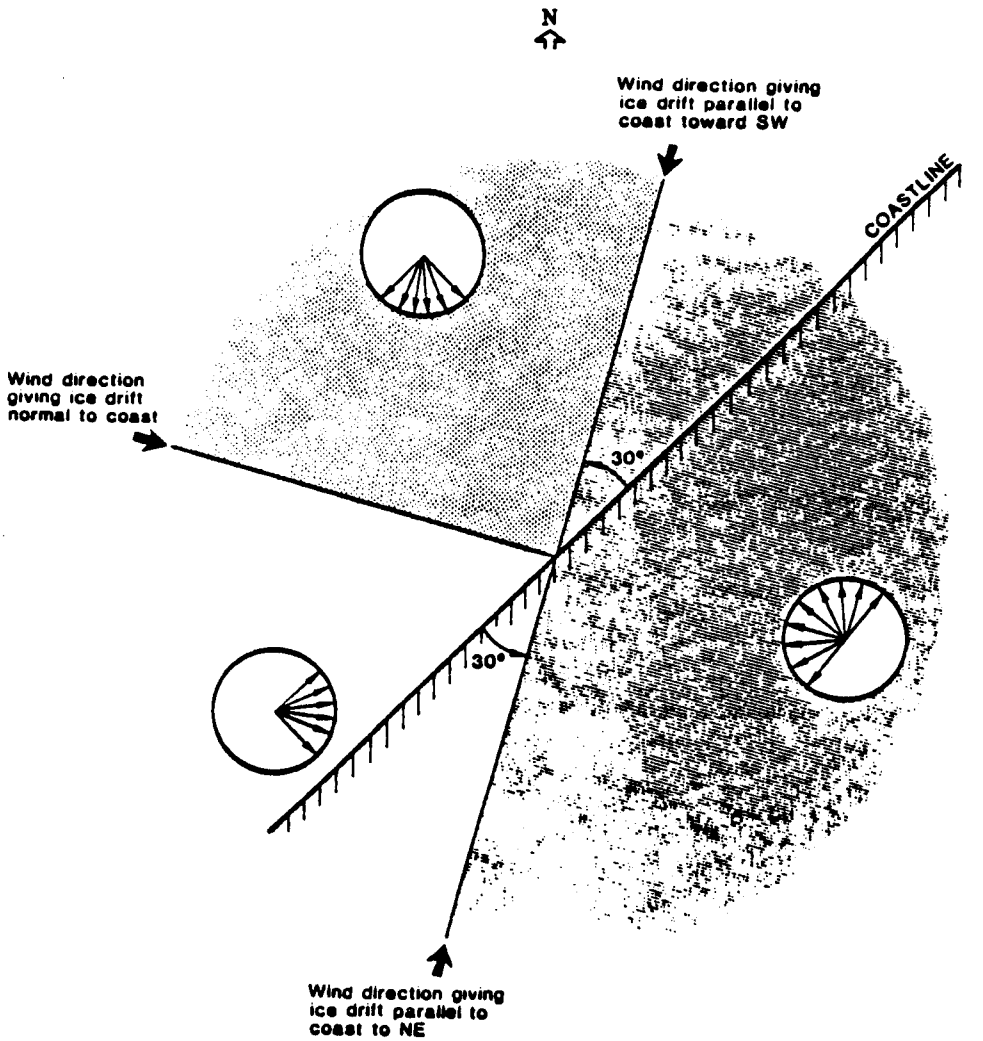

Figure 3.5-3 Schematic diagram illustrating the possible senses of ice motion within the field-of-view of the radar for wind from different directions, assuming that the ice drifts at 30° to the right of the wind direction. Arrows in circles show the range of possible ice movement directions for winds originating in each patterned sector.

in the Barrow area always followed the northward movement of a low pressure system through the Chukchi Sea (Shapiro et al., 1984); the winds from such a system tend to compress the pack ice cover against the coast, so that the stress can be transmitted to the fast ice.

The prevailing winds from the east to northeast (as well as the less common winds from the southeast) tend to move the pack ice offshore,opening a wide flaw

lead. New ice was usually forming in the lead, but it was always smooth, with relatively few reflectors, so that it was usually invisible to the radar.

Northerly to northwesterly winds would push the ice toward the southwest, along the coast. However, this part of the coast is in the lee of Point Barrow with respect to ice drift from the north and northeast (see Figure 3.5-1). Thus, when pack ice as loose floes was observed drifting from the northeast to the southwest, it was often near the limit of the field-of-view of the radar system. Occasionally, floes were found to be drifting to the southwest when the winds were from the northeast. Examination of satellite images suggest that this occurred when pack ice drifted southwestward around Point Barrow and diverged into the nearshore area (from which pack ice had earlier been driven by the offshore sense of the wind) under the influence of internal stresses. Southwesterly movement of a continuous ice sheet was usually observed only when the ice sheet separated from the edge of the fast ice opening a lead. Once the ice sheet drifted out of view, it was usually followed by loose floes drifting along a southwesterly track near the limit of the field-of-view of the radar, as described above.

Drag effects were commonly observed when the pack ice was driven against the edge of the fast ice at a low angle. In these case, forces resulting from the interaction of the pack ice with the edge of the fast ice served to slow the pack ice near the boundary. This produced a velocity gradient so that the pack ice velocity increased with distance from shore. In general, the effect was observable for about 1 km seaward of the fast ice edge. The best example was presented in Shapiro (1975b). More specific descriptions of patterns of ice motion and distribution through a typical year are given in Section 3.5.4.

3.5.3.3 Flickering of Reflectors

One particularly interesting and important phenomenon shown on the radar data is the flickering of reflectors on the pack ice surface prior to motion, when the

data are viewed as time-lapse motion pictures. The flickering occurs for periods of up to several hours prior to movement, and is a reliable precursor. Not all movements were preceded by flickering, but flickering episodes were always followed by movement; the pack ice always moved offshore or compressed against the edge of the fast ice following a period of flickering.

The flickering is caused by the repeated disappearance and reappearance of individual reflectors on sequential frames of the data, with no change in their positions. We interpret this as indicating that the reflectors are vibrating, which rotates the surfaces so that energy is not returned to the radar system continuously. The vibration, in turn, is attributed to the passage of waves through the water which cause the ice sheet to flex to conform to the shape of the water surface. Unfortunately, the nature of the radar data does not permit the period of the waves to be determined.

The observation of flickering was one of the factors which led to the study of ice sheet vibration described in Section 3.3 of this report.

3.5.4 ANNUAL CYCLE

3.5.4.1 Introduction

Based upon the radar data, the ice year can be subdivided into four phases which grade gradually into each other. These phases do not coincide with the four seasons of the year, so that it is proper to assign names to them. Accordingly, we refer to the seasons of open water, freeze-up, winter and breakup. In addition, since the timing of the transition between these seasons probably varies along the coast, we recognize that the data apply only to the area within, or close to, the field-of-view of the radar system. However, we anticipate that similar terminology would apply elsewhere along the coast.

In the following sections, the changes in the ice cover during each season are described, and examples of particular (not necessarily "typical") events from each season are given. Then, the changes in the ice season are discussed briefly in relation to the climatological data for Barrow as summarized in Brower et al, (1977).

3.5.4.2 Open Water Season

The term "open water" is defined here as the complete absence of ice within the field-of-view of the radar. The only months in which this condition was met for any complete roll of film were July, August and September (on 5%, 14% and 21% of the available data for each of these months, respectively). Note that the unusual summer ice conditions of 1975, in which part of the fast ice remained in place all summer so that the condition of no visible ice was never met, were included in the data set. The radar was also operated through the entire summer in that year, so that the data are likely to be biased toward the presence of ice.

The term "open water season" itself is something of a misnomer, because it is not continuous. Ice drifted through the radar field-of-view in every month, appearing and disappearing throughout the season. If the term is defined more loosely as indicating the time when there is no "fast ice" within the field-of-view of the radar, then the season probably extends from late July to late September.

Note that these results give little information about trafficability. Minor quantities of ice grounded in shallow water would negate the classification as "open water" and, clearly, vessels can navigate through the area when drifting ice is present. However, the term is useful as an indicator of local conditions in the sense that it indicates the advance of the seasons.

3.5.4.3 Freeze-up

The results of our observations suggest that the term freeze-up is a misnomer when applied to the formation of the fast ice near Barrow; freezing is a secondary

process in this area. Our observations suggest that a significant percentage of the fast ice consists of floes which drift into the area after forming elsewhere. The percentage of the fast ice cover which formed by freezing was variable from year-to-year, but even where ice did freeze in place, it did so because it was protected by ridges or grounded hummock fields formed from floes which drifted into the area. Observations in other areas suggest that this is a general rule along the coast.

The character of the fast ice varied depending upon the direction from which the ice came, reflecting the nature of the ice itself, and the configuration of the coastline (Figure 3.5-1). When the ice came from the south, it consisted primarily of thin (less than 0.5 m thick) floes of first-year ice as pans which drifted northeastward along the coast. The pattern of movement during this stage suggests that the floes were stopped by a barrier to the north, out of the radar field-of-view, and gradually filled in the nearshore area from north to south. We suggest that the barrier is Point Barrow, and that the process occurs when the bight south of the Point is filled with floes. Subsequently, floes passing through the field-of-view of the radar gradually slow and stop as they encounter the ice "downstream." Some pressure ridging can occur along the floe boundaries during this process as the ice compacts northward. Simultaneously, the streamlines of the pack ice further offshore are deflected to the north, on a trajectory which carries the ice around Point Barrow. This produces the pattern of ridges (as illustrated in Figure 3.5-4) which are aligned along that trajectory. The ridges are dominantly shear ridges and reflect the drag of the drifting pack ice against the ice inshore, which is stationary and continuous with the shore.

The process described above repeats with the addition of new ice, until the fast ice extends out to (approximately) the 20-m depth contour; each ridge in Figure 3.5-4 represents an intermediate stage in the process. Stages may last from minutes to days, but for some time, each ridge is at the offshore boundary of the fast ice.

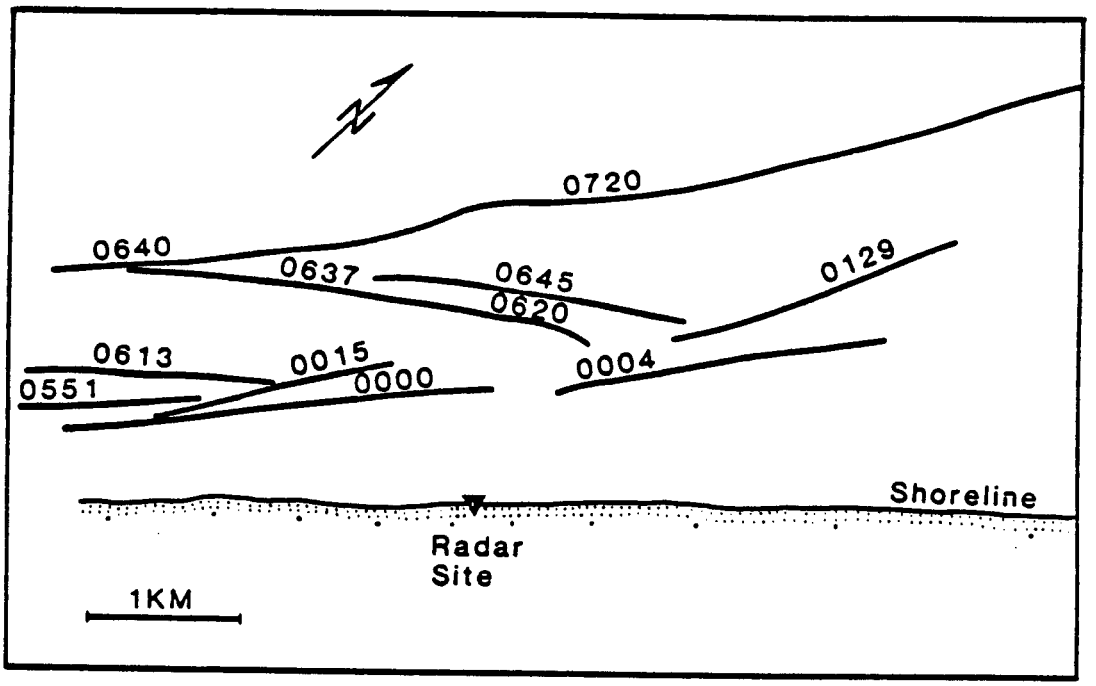

Figure 3.5-4 Pattern of shear ridges in the fast ice which formed during a storm on January 1, 1974 when ice motion was from the southwest, parallel to the coast. Numbers indicate time (hours:min) when ridge formed, starting from an arbitrary time (00:00). Similar patterns developed over the entire freeze-up period of other years when ice motion was primarily from the southwest.

It is not uncommon during freeze-up for the entire fast ice sheet, in some stage of development, to detach from the shore and move offshore leaving open water to the beach. The latest time at which this occurred in any year was December 31 (of 1973), during a major storm [the subsequent process of rebuilding the fast ice sheet during the storm was described by Shapiro (1975a,b)] although, in general, these events were more common earlier in the season. Note that when an event of this type occurred during freeze-up, the "fast ice" sheet always moved off to the north or northeast. Attempts to associate the start of movement of the ice sheet with local winds showed no apparent relationship, suggesting that ocean currents or tides were responsible.

In the 1974-75 winter, the fast ice near Barrow contained an unusually large percentage of multiyear ice floes which dominated the form of the fast ice sheet through that winter. When these floes first entered the field-of-view of the radar system during freeze-up they were moving southeastward from the north-northwest quadrant toward the coast. Many of the floes became grounded (some had sails as high as 3 m in 5 m water depth), although the maximum depth of grounding was not determined. However, multiyear ice floes were common in the fast ice at least to a distance of about 2 km from shore, corresponding to a water depth of 15-20 m. Inshore, the first-year ice of the fast ice was formed by freezing in place between the multiyear ice floes.

The source of the multiyear floes was clearly either the northern Chukchi Sea or the Beaufort Sea, and this was verified by examination of NOAA satellite imagery. The imagery shows that the floes which drifted into the fast ice zone came into the area from the edge of the pack ice north of Point Barrow. The motion could not be tracked in detail from the satellite imagery, but it appears that the floes drifted southwest from north of Point Barrow in diffuse swirls, and then turned back toward the coast along a more southeasterly track as if caught in an eddy.

It is not possible to define the beginning and end of the freeze-up season with any precision. The earliest that fast ice was recorded by the radar (except for 1975 when the fast ice remained in place all summer) was late September. The data on the frequency of observation of ice motion (Figure 3.5-5) indicate a gradual decrease in ice activity throughout the season from a peak in October to a significantly lower level in February. Note that the rise in the curve for January may reflect a bias in the data, since there are fewer observations for January than for any other month (see Table 3.5-1). However, the available data suggest that most of the movement episodes observed during January occurred early in the month. In addition, the latest ice events which caused movement of the fast ice occurred in late December

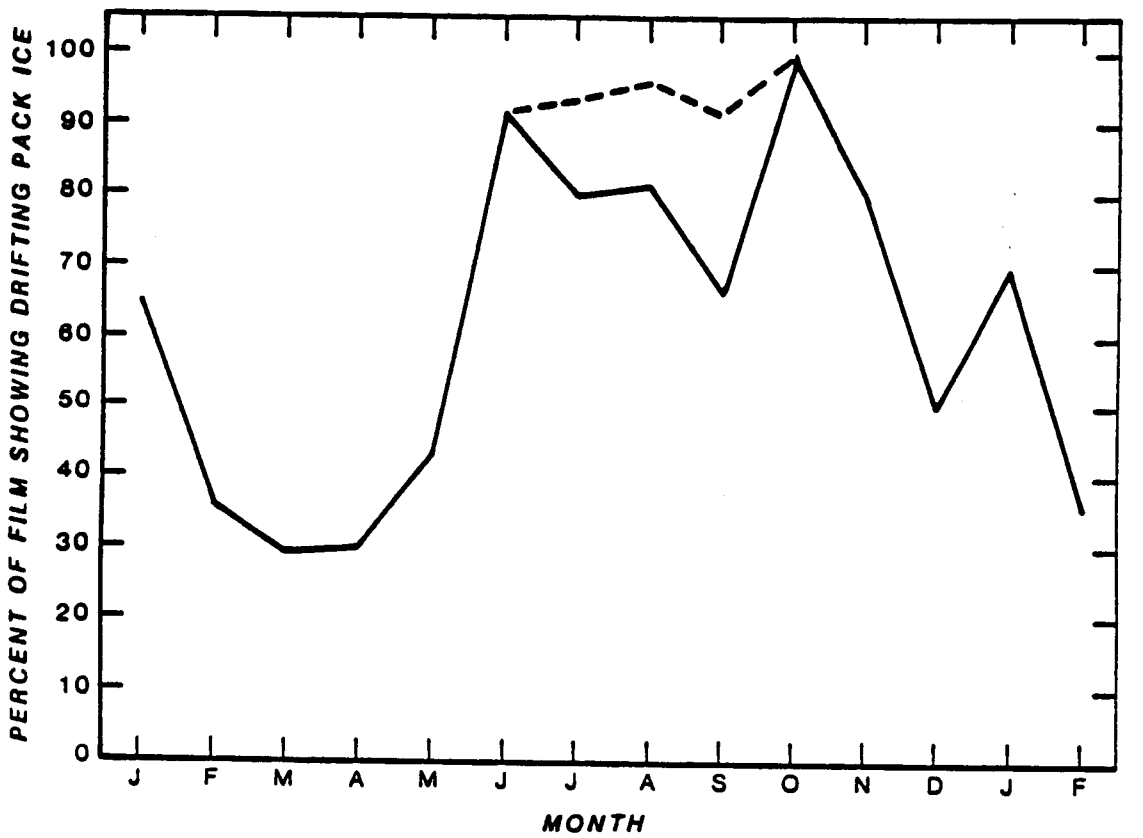

Figure 3.5-5 Percent of films of radar data showing drifting pack ice, plotted by month. Dashed line indicates curve if films with only open water for July, August and September are included. See text for discussion.

and early January. This suggests that the end of the freeze-up period could be taken as, say, mid-January, with the implication that the fast ice is relatively stable from that time until breakup.

3.5.4.4 Winter

The winter season, as shown by the frequency of ice motion (Figure 3.5-5) and the pattern of distribution of the ice, extends from January to May. Its start is defined by the decrease in pack ice motion and the beginning of the season of relative stability of the fast ice sheet. We identify the end of the season with the marked

increase in the occurrence of drifting ice offshore between May and June (Figure 3.5-5). The onset of melting and instability of the fast ice follow in June.

The pattern of ice distribution within the field-of-view of the radar system during winter always included stationary fast ice. Offshore from the fast ice, the most common condition was for the pack ice to be either present but stationary, or absent. By month, between January and May, one of these was the only pattern shown by the-data for (respectively) 57%, 75%, 63%, 58% and 75% of the films (Table 3.5-2). During March, April and May of 1976, 1977 and 1978, they were the only patterns recorded; no drifting ice was observed. On the remainder of the films, the pack ice was in motion for at least part of the time covered by the film. When ice drift was parallel to the edge of the fast ice, the direction was to the northwest or southeast with about equal frequency. Occasionally the pack ice was driven into the edge of the fast ice at a high angle (such impacts occurred on about 10% of the films for this time of year). A spectacular shear ridge formed in March 1974 from such an event (see description below in this section). However, the effects of the impact events were usually confined to the edge of the fast ice. The single exception which occurred during the time the radar operated had minor effects, as described near the end of this section.

The absence of pack ice offshore from the fast ice indicated that the ice was drifting slowly away from the coast under the influence of the prevailing northeast to east winds, leaving a lead in which new ice was forming. Since the ice in the lead was young and thin with no sizable ridges or hummocks it was invisible to the radar. However, in one event (the 1974 ridging event described below) the radar data show the pack ice to advance directly against the edge of the fast ice after a period of more than one day when it was outside of the field-of-view of the radar. At that time, new reflectors appeared on the radar screen near the edge of the fast ice while the edge of the pack ice was still about 2 km away and advancing shoreward. This shows that

thin ice was present in the lead; the appearance of the reflectors indicates that ridging was occurring as this ice was brought into contact with the edge of the fast ice.

The pattern in which stationary pack ice was located offshore from (but in contact with) the fast ice often indicated the presence of a stable extension to the fast ice (Stringer, 1974) rather than continuous pack ice cover. Stable extensions are probably ungrounded masses of pack ice which attach to the fast ice and extend offshore. They are common features in the local area and, since they often extended beyond the limits of the field-of-view of the radar, it was not possible to distinguish them from continuous pack ice cover unless they were observed during flights in the area. It is likely that stable extensions of the fast ice originate as part of the pack ice sheet, but are left behind against the fast ice when the pack ice moves offshore.

As noted, a major impact and ridging event occurred in March 1974, which formed the highest ridge in the radar field-of-view for the entire 6 years that the system was operated; brash ice was piled to an elevation of about 13 m in water depth of 20 m. The event is described in some detail as an illustration of the scope of possible movements in the nearshore area during the winter season.

The event occurred as part of an (at least) 11-day period of pack ice activity; this was the largest number of days of nearly continuous activity recorded by the radar system during the winter season (as defined above). The movements were generally slow (ice velocities ranged from about 0.1 km/hr to less than 0.5 km/hr), with interspersed periods of quiescence. However, even when the ice was not in motion, the reflectors on the surface flickered often, indicating that the ice sheet was vibrating and unstable (see discussion in Section 3.5.3.3). Figure 3.5-6 shows the displacement path of the pack ice in the field-of-view of the radar during the 11-day period. Each leg of the diagram represents the path of the ice during the time indicated on the figure, as calculated by multiplying the average velocity of the ice

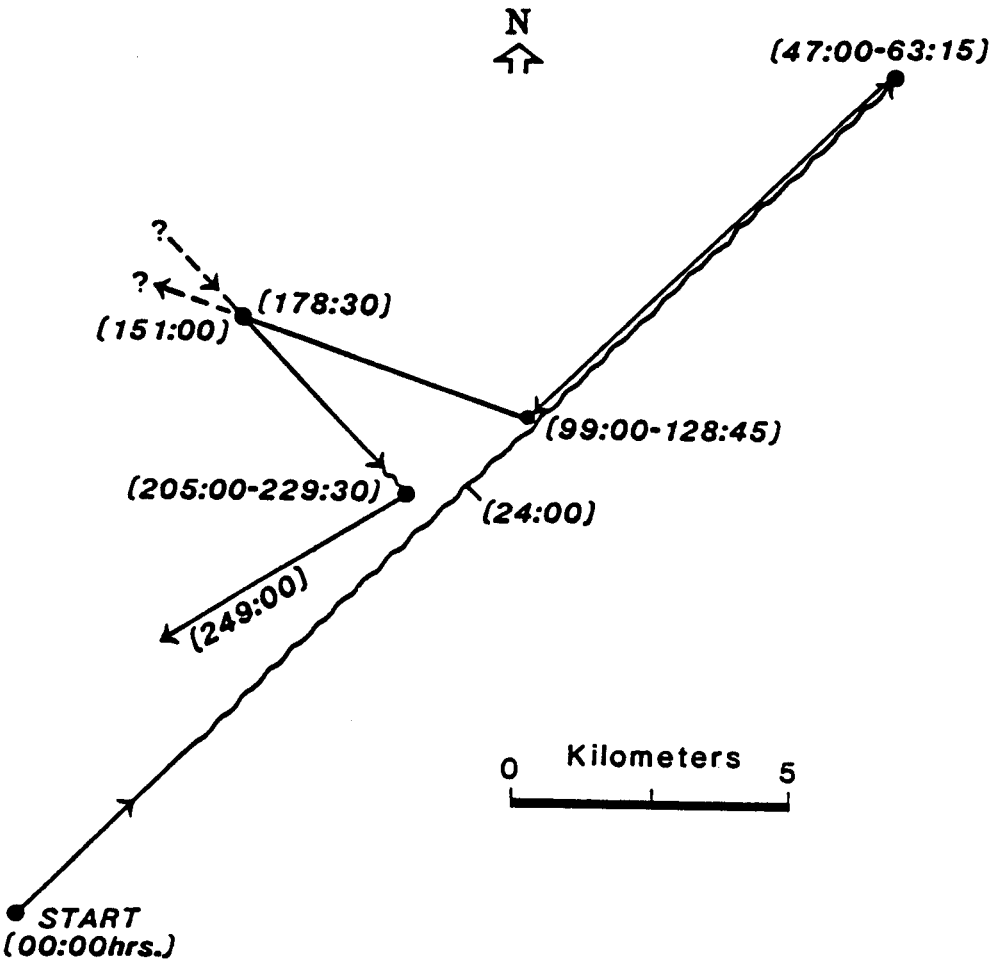

Figure 3.5-6 Displacement path of a hypothetical point on the pack ice surface during the movement episode of March 1974. Distances calculated from ice velocity and time measurements. Arrowheads show the movement direction and numbers in parentheses are cumulative times as hours:minutes. Wavy line segment indicates duration of impact with the fast ice edge. Dashed lines show the path of ice leaving and entering the radar field-of-view.

over the period of movement by the time over which the movement occurred. Thus, ideally the plot would represent the displacement path of some point on the surface of the ice sheet for the time covered by the diagram.

At the start of the event, the ice sheet had been stable for a period of about one month. The first movement was the slow opening of a lead along the edge of the fast

ice. The lead widened from the south end of the radar field-of-view toward the north and reached a width of about 0.6 km before the first movement to the northeast (shown in Figure 3.5-6) occurred. The first impact of the pack ice with the edge of the fast ice, leading to the formation of the shear ridge, occurred 10 hrs after the movement began, and continued until the ice stopped moving 37 hours later (at 47:00 in Figure 3.5-6). The fact that the ridge was developing over this entire time is shown by the nearly continuous appearance of new reflectors along the line of the ridge. In addition, the ridge created a "shadow zone" for the energy from the radar, so that reflectors on the pack ice disappeared as they drifted behind the ridge.

After the movement stopped, the reflectors on the ice surface continued to flicker intermittently until the ice began moving again, but to the southwest, at 63:15 hrs, as shown in Figure 3.5-6. Movement in this direction continued for about 36 hrs, after which the pack ice stopped for about 24 hours. It then flickered for about 5 hours, and then moved off to the northwest at about 0.2 km/hr until the ice edge was out of the field-of-view of the radar, leaving a flaw lead. The pack ice remained out of view for about 28 hours, and then reappeared moving normal to the fast ice edge at about the same velocity at which it departed. During this advance, new reflectors appeared offshore from, but close to, the fast ice boundary, while the pack ice edge was still about 2 km seaward. This is interpreted as showing that the lead was covered by thin ice (as discussed above) which, though less than 24 hours old, was capable of transmitting stress over that distance.

The pack ice advanced until it impacted the fast ice edge. It then continued to compress against the fast ice for several hours, as shown by flickering and slight shoreward motion of reflectors in the pack ice. However, there were no new ridges formed along the edge of the fast ice, and no motion was detected by the radar system within the fast ice during and after the impact. In addition, during the year in which this event occurred, precise surveys were being conducted within the radar field-of-

view, in order to monitor slight movements of the fast ice during the winter. The survey data verify that no movement occurred as a result of the impact. However, it should be noted that in the spring of 1974, numerous grounded ice ridges were distributed throughout the fast ice, so that it might have been more stable than in typical years.

Subsequently, the ice remained stationary for about 18 hours. A lead about 0.1 km wide then opened, separating the pack ice from the fast ice, and the pack ice proceeded to drift to the west-southwest (beginning at 229:30) at about 0.5 km/hr, eventually leaving the field of view. When the sequence of film terminated other floes were drifting at the same velocity to the southwest, parallel to the coast and about 2 km from the edge of the fast ice.

The total displacement of a hypothetical point on the ice surface, as represented by the vector plot in Figure 3.5-6, is more than 35 km in the 11 days represented by the data (not including the motion during the 28 hours that the ice was out of view). In addition, the direction of motion changed 4 times during the event. The implications of movements of this type on possible offshore operations are discussed in Section 3.5.5.

Only two episodes of movement of the fast ice during the winter season were observed during the time the radar system was in operation. In neither case were the displacements large enough to be detected by the radar; they were noted only because observers were present in the area at the time of the events. It is reasonable to assume that other events of this type occurred but were simply not observed.

The first event occurred in March 1976. Strong east to northeast winds forced the pack ice to drift away from the fast ice opening a lead, and also caused tension fractures up to a meter wide to form within the fast ice. This was unexpected, because the width of the fast ice in the Barrow area is too narrow for the wind fetch over the ice to generate stresses high enough to cause fracture. It is possible that the

drag effect of ice ridges within the fast ice increased the wind stress sufficiently for tensile fracture to occur.

The second example of fast ice motion during winter occurred in April 1977 when the pack ice was being compressed against the edge of the fast ice under the influence of southwest winds. Observations were made only near the shoreline, where the effects consisted of audible cracking of the ice and a slight (about 15 cm) rise of the ice sheet where it was driven up along the tide crack.

The fact that no large-scale movements of the fast ice occurred in winter while this program was operating clearly does not mean that such events cannot happen. In fact, there is anecdotal evidence that major ice push events have occurred during the winter months (Shapiro and Metzner, 1979; J. Kelley, pers. comm., 1986), although there is no indication that larger motions of the fast ice in an offshore direction have occurred. At best, the data indicate that these events are simply less likely to take place in winter. The point is discussed further in Section 3.5.5.

3.5.4.5 Breakup

As might be anticipated, breakup is the time of year when the ice cover is most active. As noted above, the start of the breakup process seems to be indicated by the increased occurrence of drifting ice offshore (Figure 3.4-5) and the rapid drop of the frequency of the pattern of no pack ice offshore from the fast ice in June (Table 3.5-2). The frequency of this pattern drops from 75% in May to 32% in June, and then to about 8% in July. The frequency of ice drift from the south also increases in those months, from 15% in May to 38% in June and to 51% in July. Interestingly, the frequency of winds which would tend to give these conditions does not change as much as the drift pattern (see discussion in Section 3.5.4.6).

The fast ice never moved out as a unit during breakup. Instead, by a combination of melting and fracture during movements it was simply reduced to

small, individual floes which drifted off in streams. In general, the lines of reflectors representing grounded ice ridge lines, were the last features to disappear. Eventually, they lose sufficient mass through melting that they float up and drift offshore.

The effects of the impact of the pack ice on the edge of the fast ice are more noticeable during breakup than at other times of year. These effects generally took the form of a pervasive tightening shoreward through both the pack ice and fast ice, following an impact. However, ice push events, in which the fast ice was pushed up the beach, occurred only early in breakup, while the fast ice sheet was continuous, and never after the fast ice had begun to disaggregate. This may reflect the looseness of the ice within the fast ice zone, which might enhance the possibility for piling along the ridge lines, rather than transmission of stress through a continuous ice sheet to the ice along the beach. However, we have no field observations of the process to verify this.

Patterns of ice motion within the radar field of view during breakup were variable, particularly when the pack ice had been reduced to discrete floes. As a result, the patterns are difficult to describe in general. The following discussion and examples illustrate the point.

It was not uncommon for floes inshore from a line of remnants of ice ridges to be moving parallel to the coast, but in the opposite direction from that of the floes offshore from the ridge line. Examples of such patterns were observed in which the motion was in both senses (i.e., inshore floes drifting northeast and offshore floes drifting southwest, and vice-versa). This may reflect the influence of near-shore currents carrying the ice on one side of the ridge in one direction, while the wind pushed the ice on the other side in the opposite direction.

Rapid reversals of direction of ice motion (say, from southwest to northeast) were also common when the pack ice was composed of discrete floes. In some cases,

the reversals occurred as part of a continuous movement, in contrast to reversals during winter, in which the pack ice always came to a halt before changing its direction of motion. When the movements were continuous, they occurred over periods of a few hours. In addition, the floes were often observed to move in patterns of whirls or eddies during these events.

The motion of a continuous pack ice sheet, and its interaction with the fast ice over a 6-day period in late June, 1974 are illustrated in the displacement vector diagram in Figure 3.5-7. This figure was prepared using the same procedures as Figure 3.5-6. The sequence of movements began with the pack ice moving northeast along the coast at a velocity of 2.2 km/hr for about 4.5 hours. It then stopped for about 8 hours, and then moved northeast, but dragging along the edge of the fast ice as indicated by a velocity gradient in the ice which varied from 0.6 km/hr at the edge of the fast ice to 1.2 km/hr about 1 km further offshore. Drift in this direction continued for about 16 hours. Then, over the next 16 hours, the drift direction turned from northeast to north, then to north-northwest, and finally to the northwest. During this time the ice velocity slowed gradually to 0.2 km/hr, and the ice drifted out of the field-of-view of the radar to the northwest. It remained out of view for almost 24 hours, with the exception of a 4-hour period (from 57:30 to 61:30, about midway through the 24 hour period) when floes were visible drifting northeast at 0.5 km/hr at the limit of the field of view. When the pack ice next appeared on the radar screen it was drifting eastward at 2 km/hr on a path which led to impact with the edge of the fast ice (at 71:45). For 12 hours following the impact the pack ice continued to tighten against the edge of the fast ice. Numerous compressive pulses occurred, each of which resulted in a slight shoreward displacement of the reflectors in the pack ice. Subsequently, no movement occurred for about 4 hours, when the reflectors on the pack ice began to flicker. The flickering continued for about 3 hours after which the pack ice began to move northeastward, parallel to the coast at a

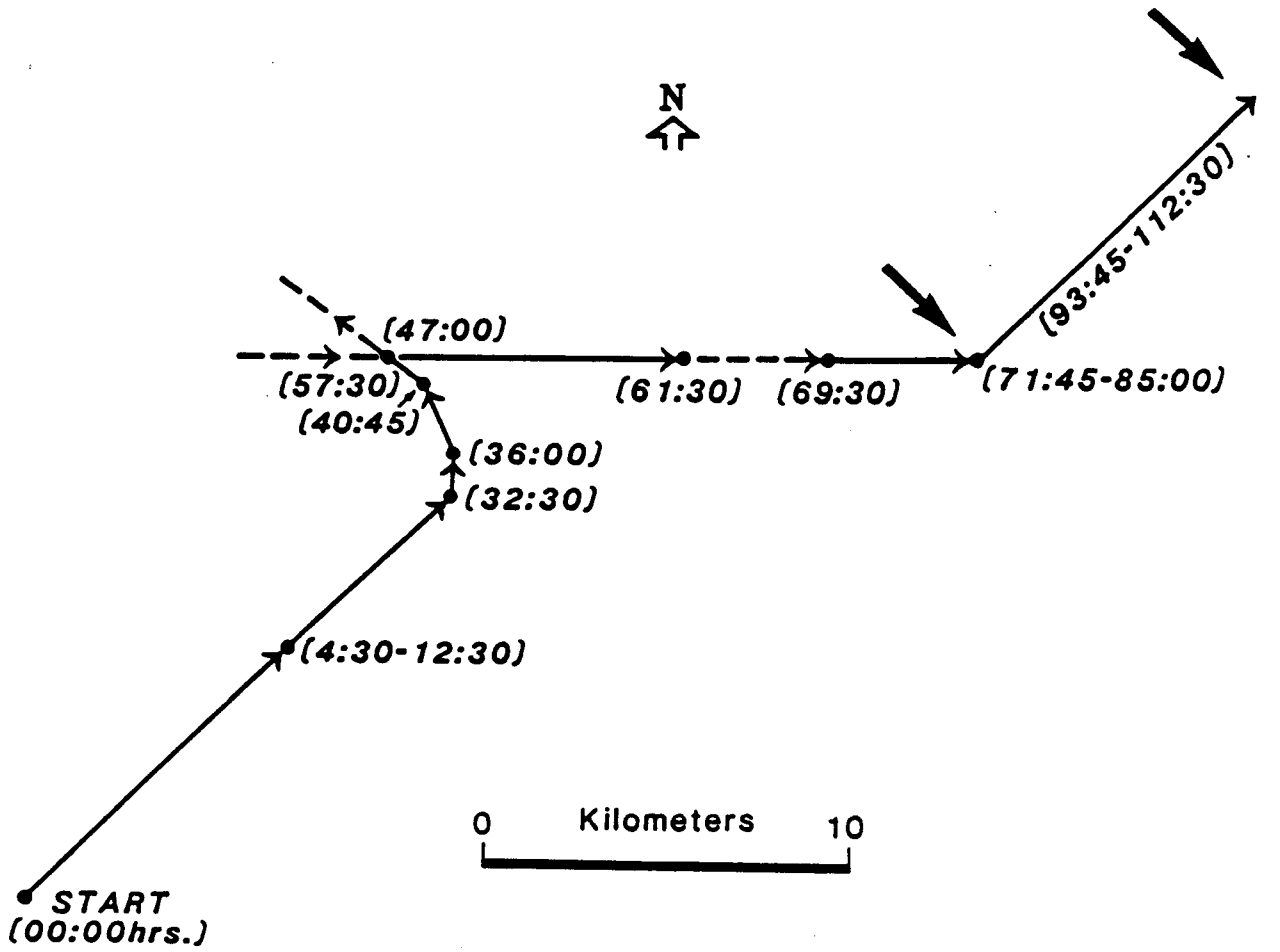

Figure 3.5-7 Displacement path of a hypothetical point on the pack ice surface during the movement episode of June 1974. Distances calculated from ice velocity and time measurements. Arrowheads show the movement direction and numbers in parentheses are cumuulative times as hours:minutes. Dashed lines show the path leaving and entering the radar field-of-view. Bold arrows indicate impact with the fast ice edge followed by compressive pulses or flickering during the times indicates.

velocity of 1.2 km/hr. The movement continued for about 9 hours, when the pack ice stopped and compressed against the coast again. It then remained in place for about 18 hours with no further movement when the film sequence was terminated.

The most unusual movement pattern observed during the breakup season is illustrated schematically in Figure 3.5-8. The figure shows three different velocities

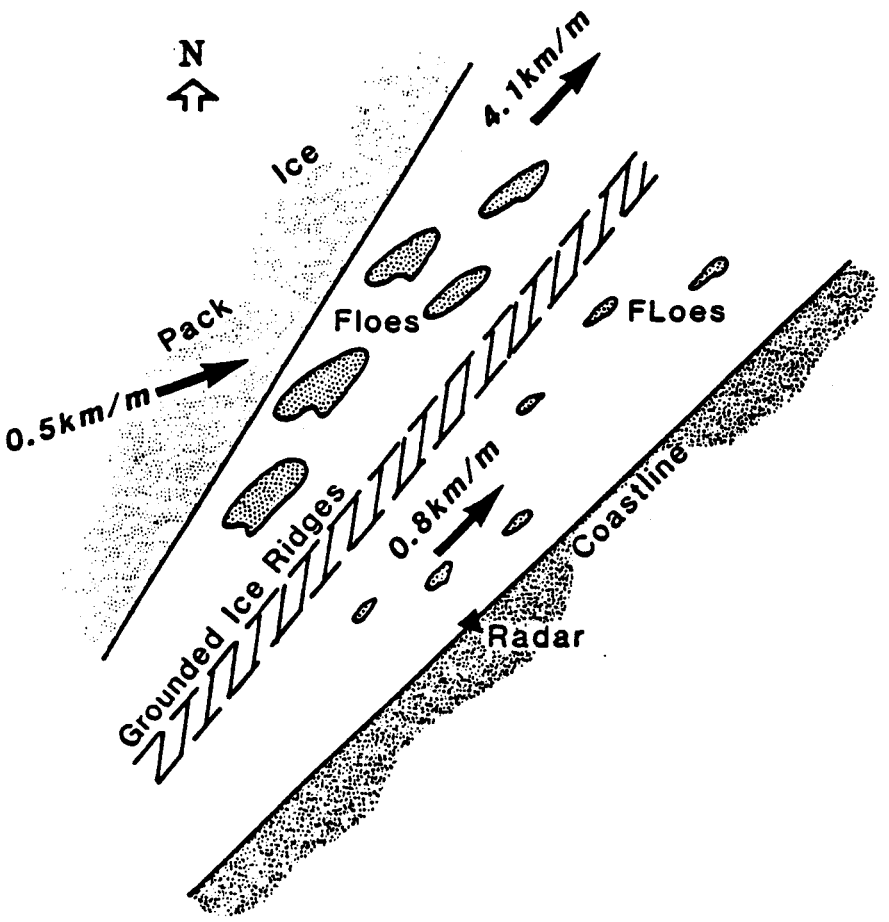

Figure 3.5-8 Schematic diagram of unusual ice movement pattern during breakup. Pack ice moving eastward at 0.5 km/hr as large floes offshore from the line of grounded ice ridges (about 1 km from shore) are moving at about 4.1 km/hr. The velocity of the small floes inshore from the ridges is about 0.8 km/hr. The pack ice ultimately impacted the line of grounded ridges and compressed against it.

and two different directions of ice motion occurring in the small area of the field-of-view of the radar at the same time. Inshore of a line of ice grounded ridges, small, loose floes were drifting northeast along the coast at a velocity of 0.8 km/hr. Offshore from the ridge line, larger floes were drifting northeast at 4.1 km/hr. Then, the edge of the pack ice entered the field-of-view of the radar moving almost due east toward the coast at 0.5 km/hr, crossing the path of the drifting floes. Ultimately the pack ice impacted the line of grounded ridges and compressed against it.

The examples above illustrate the difficulty of characterizing "typical" ice movements or conditions during the breakup season. It is sufficient to conclude that breakup is a time of almost continuous ice activity leading to the disintigration of fast ice.

3.5.4.6 Relationship of the Annual Cycle to Climatic Data

The weather data for the Barrow area, summarized by Brower et al. (1977), were examined for correlation with the seasons of the ice year defined above. As noted earlier, the data sets for the weather and the radar system do not overlap in time. Brower et al. used climatic data for the period from January 1966 to December 1974 in their compilation, while the radar system was operated from June 1973 to May 1979. It is assumed here that both data sets cover sufficient time to be considered as representative. However, the correlations between the climate data and the ice seasons are weak at best; they are discussed here only for the sake of completeness.

Variations in wind direction, storm tracks in the Chukchi Sea and air temperature were considered most likely to be associated with changes in the ice season. The relationship to wind direction is clear from the discussion above regarding the variation of ice drift direction parallel to the coast with the seasons. Storm tracks through the Chukchi Sea generate southerly winds which drive the ice northward and, in addition, they trigger ice push events. Temperature is simply the most reliable , indicator of seasonal change.

All the northerly moving storm tracks in the central Chukchi Sea recorded in Brower et al. (1977) are listed in Table 3.5-3 as the number of storms per month. There are too few events to justify a statistical analysis of the data. However, it appears that storms are least common in the winter months (February, March and April), but are not noticeably more likely to occur consistently at other times of year.

Clearly, there are no major "spikes" in the data which coincide with the changes in season of the ice year.

The data on wind directions are listed in Table 3.5-3 which shows the percentage of time that the wind was from the quadrants indicated in Figure 3.5-3, corresponding to the directions of pack ice motion indicated in the figure. The only suggestive points in the data are for the month of July, in which the frequency of winds from the northeast, east and southeast decreases in favor of winds from the south, southwest and west. This appears to coincide with the increased frequency of

TABLE 3.5-3

CLIMATE DATA BY MONTH (1966-1974) FROM BROWER ET AL. (1977)

	TOTAL NUMBER OF NORTHERLY STORMS	MEAN AIR TEMPERATURE (C)	WIND DIRECTION (%) (*) NE-E-SE	S-SW	W	N-NW
JAN	6	-26	52	20	12	18
FEB	1	-29	53	15	13	18
MAR	2	-27	58	15	10	17
APR	0	-19	62	15	6	15
MAY	6	-7	67	15	6	12
JUN	2	0	60	12	10	17
JUL	5	+3	48	18	15	17
AUG	4	+3	54	15	12	18
SEP	2	-1	S8	15	8	17
OCT	5	-9	62	20	5	12
NOV	4	-25	64	16	7	12
DEC	3	-25	56	18	11	12

(*) NOTE: Percent of time that weather is calm brings the total of these four columns to 100%.

ice motion from the southwest noted above. However, it should be noted that a similar relationship occurs in January and February, so that it is difficult to draw conclusions from the data.

The monthly mean temperatures at Barrow are listed in Table 3.5-3. These indicate some correlation with the ice seasons, in that two of the ice seasons (winter and breakup) begin about 1 month following a sharp change in the mean temperature. In addition, as might be anticipated the open water season occurs during the two warmest months and the month which follows them.

It would be possible to extend the study to attempt to interpret the changes of the ice seasons in terms of the extent and nature of the ice cover (i.e., continuous pack ice cover vs. discrete, drifting floes) which clearly reflect the air temperature. However, that would require extensive examination of satellite imagery, which was beyond the scope of this project.

3.5.5 SUMMARY AND CONCLUSIONS

The descriptions above can be summarized into the following generalizations regarding the seasons of the ice year:

1. The open water season, defined as those months in which no ice was visible in the field-of-view of the radar system for the time represented by at least one roll of film, ranges from late July to late September. However, drifting pack ice or remnants of the fast ice were often visible during these months, so that the radar field-of-view was never totally free of ice for more than a few weeks.

2. The process of freeze-up (in particular, the formation of the fast ice) begins in late September and can extend to about mid-January. The definition of the duration of the season is based upon (1) the observation of the earliest occurrence of fast ice in the area (neglecting the single year when the fast ice remained in place through the

entire summer) and (2) the last observed offshore movement of fast ice and the frequency of observation of drifting pack ice in the field-of-view of the radar.

In the Barrow area, a significant portion of the fast ice is compose of floes which drift into the area. First-year ice which freezes within the fast ice zone forms primarily in sheltered areas between floes or inshore from grounded ice ridges. In three of the years in which our observations were made, the pack ice came from the southwest in the form of floes of first-year ice up to 0.5 m thick. In one year, it originated ice remained in place through the following summer, so that no new floes were introduced during the subsequent freeze-up.

When the fast ice formed from floes drifting into the area from the southwest, it commonly developed in segments which became attached to the offshore boundary of ice already in place. Segments frequently broke loose and drifted off, to be replaced by other floes until the fast ice was built seaward to (approximately) the 20 m depth contour. The offshore edge of each segment was usually marked by a shear ridge which, at some stage, had represented the fast ice-pack ice boundary.

The highest ice velocity measured during the years the radar system operated was 8 km/hr, which occurred during a storm late in the freeze-up season.

3. The winter season extends from mid-January through May. During this time, the pack ice is most commonly either out of the field-of-view of the radar system (i.e., greater than about 5.5 km from shore) or adjacent to the fast ice but stationary. Note that the latter condition may be due to the presence of a local floating extension of the fast ice which could not be distinguished from pack ice without independent observations.

Incursions of pack ice against the fast ice are not uncommon during the winter season and can lead to the formation of ice ridges along the edge of the fast ice. During the course of the project there were no cases of large-scale motion of the fast ice as a result of impacts. However, there is anecdotal evidence that such

movements, in the form of ice push events, have occurred in the past, but there are no reports of the fast ice sheet floating offshore during the winter season.

There was no preferred direction for pack ice motion observed by the radar during the winter, and ice velocities were generally low.

4. The start of the breakup season is indicated by the increase in the occurrence of drifting ice in the field-of-view of the radar in June. Ice motion is dominantly to the north during this season and, as the fast ice deteriorates (primarily through melting) it tends to break into small floes which drift off in that direction. However, examples of a wide range of movement patterns and directions were observed during the course of the project. In addition, in 1975, the fast ice remained in place through the entire summer. In that year, pack ice drift from the north was common through July, August and September. This does not presuppose a cause and effect relationship between the pattern of ice drift from the north and the absence of a true breakup that year. Rather, it suggests that both resulted from an unsual distribution pattern of weather systems during the summer of 1975.

The changes in the ice cover with the seasons, as defined above, may be related to variations in air temperature through the year. However, they cannot be correlated to changes in prevailing wind directions or the passage of storm systems, the only other climate variables examined.

The patterns of ice distribution and motion in the field-of-view of the radar can be interpreted as being driven primarily by the regional wind field, but strongly influenced by the local regime of tide and currents, sea floor topography and the configuration of the coastline. It seems probable that similar influences would operate elsewhere along the coast, reflecting local conditions. Quantitative modeling of ice motion under these conditions would be difficult, because of the number of variables and the range of possible interactions between them. Thus, rules-of-thumb developed from repeated observations may be necessary if local ice

conditions are to be predicted. This, in turn, requires a period of monitoring of local patterns of ice movement and distributions, such as was done for the Barrow area on this project.

Many of the problems of operating a program such as this have been negated by technological advances in recent years. Smaller, portable radar systems are available, and the availability of low-light video equipment for recording images of the radar screen would eliminate many of the difficulties we faced in attempting to interpret the data. In addition, it would make the data available quickly and facilitate ground truth studies.

The range of changes in ice movement direction described in the winter and breakup movement episodes (Figures 3.5-6 and 7) indicates some of the problems which might be encountered in developing offshore installations in exposed coastal areas. An example is provided by suggestions for the design of a tanker terminal for the Chukchi Sea coast of Alaska, using a single-point mooring system mounted on a monopod. The idea is that a ship at the terminal could be positioned so that it was always on the lee side of the structure with respect to moving pack ice. However, the data raise the question of whether a vessel could maneuver near the monopod, given the rate of ice motion and associated problems of clearing ice from around the structure. This is not to suggest that the design is not feasible; instead, it emphasizes the point that knowledge of the pattern of ice motion in the area should be available for consideration during the design stage.

3.5.6 REFERENCES CITED

Sackinger, W. M. and J. C. Rogers, 1974, Dynamics of breakup in shorefast ice: in J. C. Reed and J. E. Sater, eds., The Coast and Shelf of the Beaufort Sea; Arctic Inst. of North America, pp. 367-376.

Shapiro, L. H., 1975a, A preliminary study of the formation of landfast ice at Barrow, Alaska, winter, 1973-1974; U. of Alaska Geo. Inst. Rpt. UAG R-235, 44 pp.

Shapiro, L. H., 1975b, A preliminary study of ridging in landfast ice at Barrow, Alaska, using radar data; Proc. 3rd Int. Conf. on Port and Ocean Eng. under Arctic Conditions (POAC), Fairbanks, Alaska; pp. 417-426.

Shapiro, L. H. and Metzner, R. C., 1979, Historical references to ice conditions along the Beaufort Sea Coast of Alaska; U. of Alaska Geo. Inst. Rpt. UAG R-268, 11 pp. + App.

Shapiro L. H., R. C. Metzner, A. Hanson and J. B. Johnson, 1984, Fast ice sheet deformation during ice-push and shore ice ride-up; in P. W. Barnes, D. M. Schell and E. Reimnitz, eds., The Alaskan Beaufort Sea, Ecosystems and Environments, Academic Press, New York, pp. 137-158.

Stringer, W. J., 1974, Morphology of the Beaufort Sea shorefast ice; in J. C. Reed and J. E. Sater, eds., The Coast and Shelf of the Beaufort Sea; Arctic Inst. of North America, pp. 165-172

Wittman, W. I. and G. P. MacDowell, 1964, Manual of short-term sea ice forecasting; Spec. Pub. 82, U.S. Navy Oceanographic Office, Wash. D.C., 142 pp.

3.6 CORRELATION OF NEARSHORE ICE MOVEMENTS WITH SEA-BED ICE GOUGES

by

Lewis H. Shapiro, Peter W. Barnes,* and Ronald C. Metzner

ABSTRACT

Side-scan sonar surveys of the sea floor were made in consecutive summers (1977 and 1978) in an area within the field-of-view of the University of Alaska sea ice radar system near Barrow, Alaska. The purpose was to interpret changes in ice gouge characteristics in terms of the history of the ice cover in the time before and between the surveys, as recorded by the radar. The survey showed that the principal direction of the gouges in the area is at a high angle to the coast (and to both the isobaths and the predominant direction of ice drift, which are parallel to the coast). We interpret the principal ice gouge orientation as primarily due to the drag of keels of multiyear floes during ice push events. The gouge density is greatest in the area in which most ice ridges occur, which may reflect the incision of keels into the sea floor during ridging. Changes in gouge density between the surveys are interpreted as due to sediment movements during a period of storms following the 1977 survey.

3.6.1 INTRODUCTION

The interaction between ice movement and ridge growth and ice gouging of the sea floor has received little attention because of the difficulty of obtaining data on both the nature of the ice cover and the sea floor for the same area and time frame. The sea floor preserves gouges beyond the ice event(s) which cause them, recording

*U.S. Geological Survey, Branch of Marine Geology, 3435 Deer Creek Road, Palo Alto, CA 94304.

evidence of ice motion which can be studied when the ice melts or moves away. Thus, knowledge of both the history of the ice cover and the evolution of ice gouges from year-to-year at the same location should provide insight into the relationships between ice canopy processes and the resulting disruption of the sea floor, as well as the seasonal timing of gouging events. The opportunity for such a study was presented by the presence of the University of Alaska sea ice radar system at Barrow. The radar monitored ice conditions relatively continuously and the results could be coupled with the results of summer studies of ice gouging within the radar field-of-view.

A bathymetric survey of the area within the the field-of-view of the University of Alaska sea ice radar system at NARL (Figure 3.6-1) had been conducted by two of the authors (L.H.S. and R.C.M.) in September 1976. The purpose was to supply bathymetric data to aid in the interpretation of ice motion and ridging patterns in the area. Data were acquired by a continuous recording fathometer installed on a 14-foot Boston Whaler; the position of the vessel was monitored by the radar system as the survey was made. The records were examined by E. Riemnitz of the U.S.G.S. who pointed out that numerous ice gouges were visible on the data, although the records were too coarse for accurate gouge depths to be measured. In addition, since the fathometer only measured the depth below the boat, the area sampled was small and the orientation of the gouges could not be determined. However, a preliminary analysis of the distribution of ice gouges-with-depth was made from the data, and the systematic aspect of the pattern suggested that further work in the area might be useful.

Subsequently, more detailed ice gouge surveys were conducted during the summers of 1977 and 1978 using a precision fathometer and a side-scan sonar The data from these surveys, along with the results of the study of local ice motion using the radar data (Section 3.5) form the basis for this report.

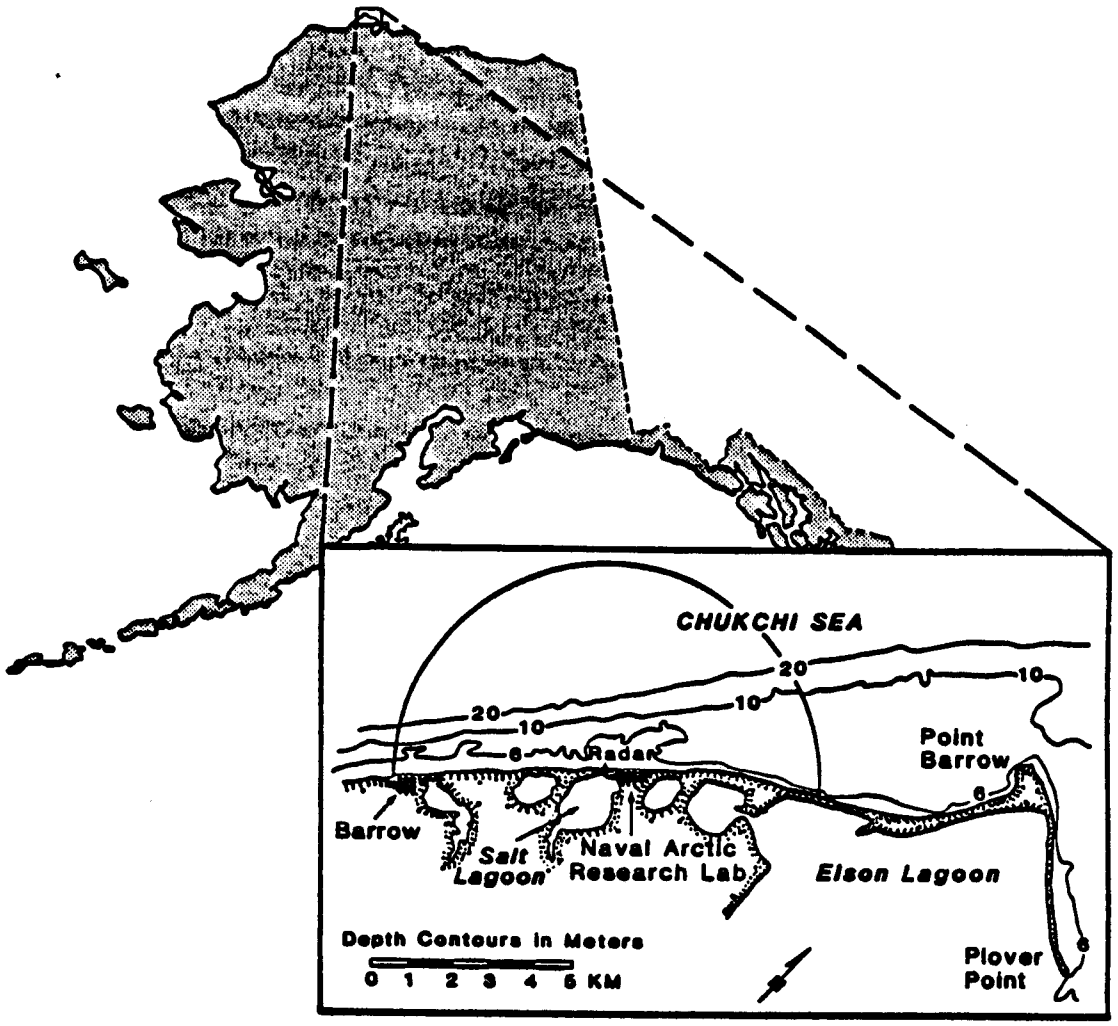

Figure 3.6-1 Map of the location of the survey area showing the field-of-view of the University of Alaska sea ice radar system and the boundaries of the survey area.

3.6.2 METHODS AND EQUIPMENT

The first survey using this instrumentation was conducted in September 1977; the second was done in August 1978. The surveys covered about 6 sq km within the field-of-view of the radar (Figures 3.6-2 and 3) with overlapping side-scan sonar data.

The vessel used in the 1977 survey was a 16-foot skiff with the side-scan sonar tow fish suspended from the bow and the fathometer on an outrigger along the side.

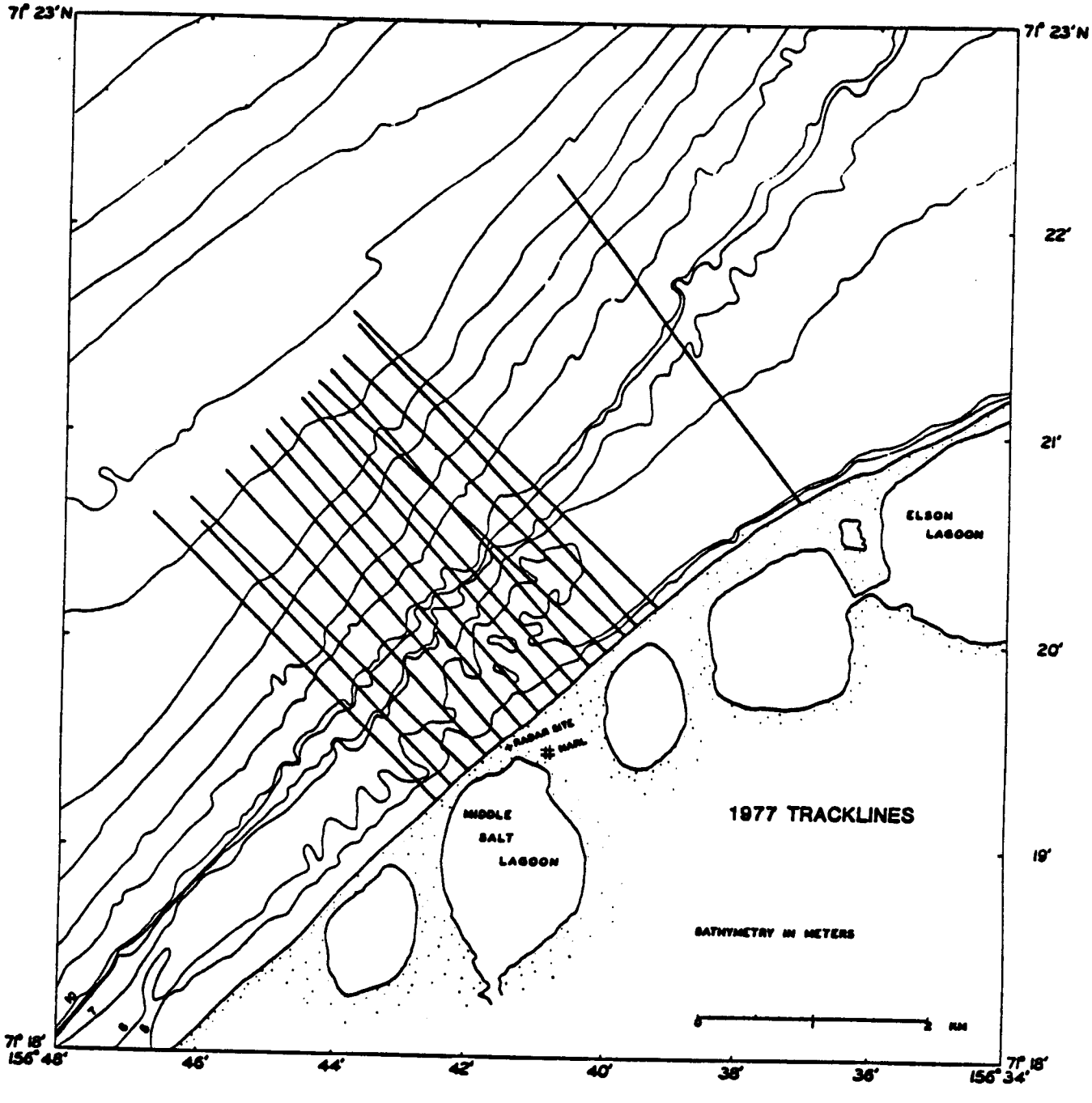

Figure 3.6-2 Tracklines of the 1977 side-scan sonar survey.

The tracklines were navigated by installing range markers at 200-m intervals along the beach on a nominal heading of 310° T. Due to strong coastal currents, problems were encountered on the vessel in maintaining the alignment of the markers at distances of more than 1.5 km from shore. However, a radar reflector was mounted

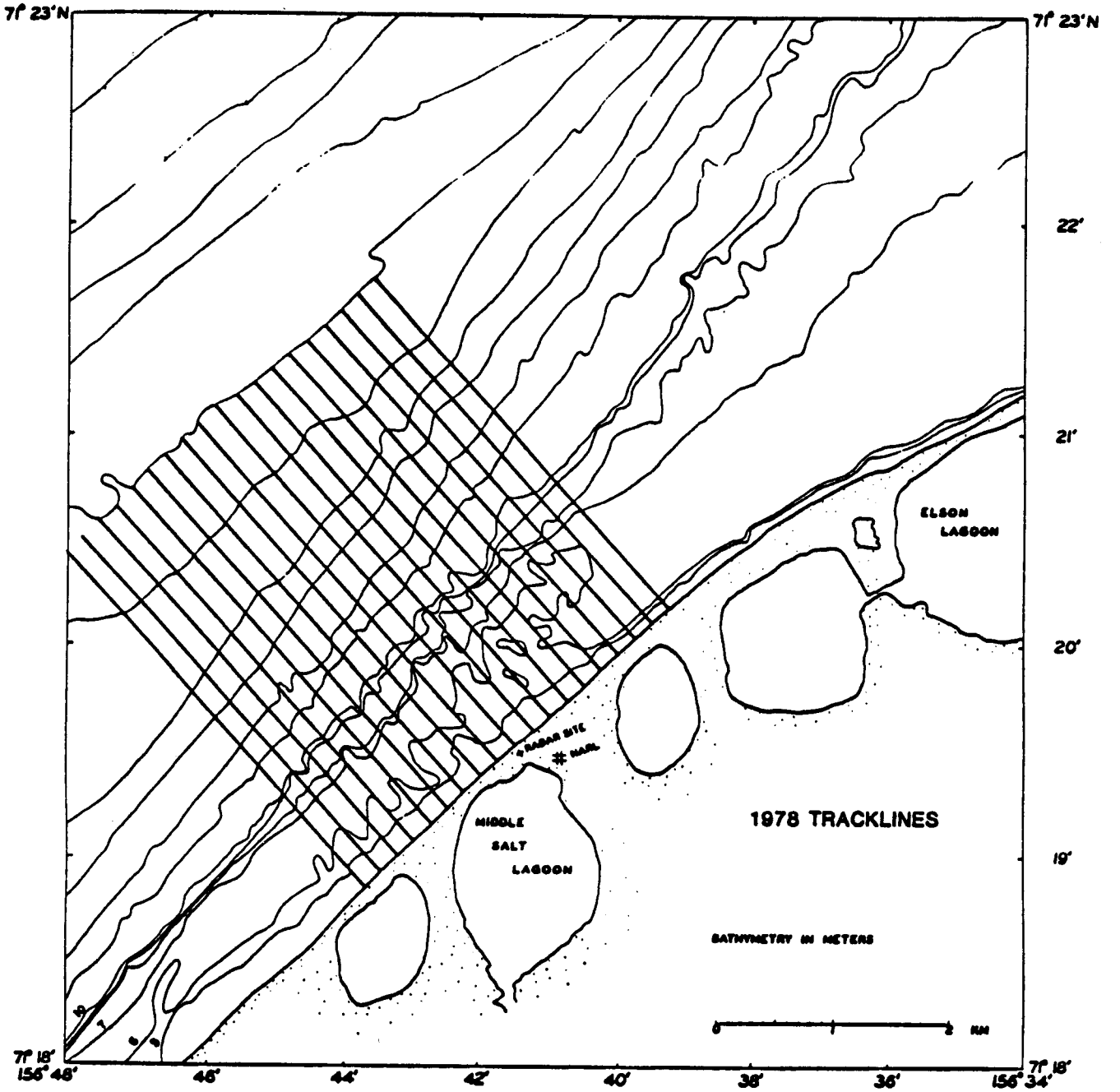

Figure 3.6-3 Tracklines of the 1978 side-scan sonar survey.

on the vessel and the radar screen was photographed at 1.5-minute intervals, providing a time-lapse motion picture of the path of the vessel. The positioning data from the range markers were probably more accurate within 1 km of shore, while the radar data were more accurate seaward. Positions along the tracklines were

determined from the radar data with the radar clock synchronized with the clock used to mark the records of the survey vessel. The 1977 survey speeds generally ranged between 5 and 6 kt

The 1978 survey was run at a speed of about 5 knots using a 42-foot vessel with a narrow beam fathometer and towing a side-scan sonar fish. The tracklines were navigated with a precision range system which gave position accuracies within 10 m, although range markers were again set up at 200-m intervals along the beach for close inshore navigation. The ranges were maintained using equi-distant baselines for the two range stations set up on the beach along a known baseline.

The fathometer used in both years recorded at a scale of 1 cm equals 1 m. At this scale, depth differences of greater than 10 cm were usually resolvable. No corrections to depth were made to the fathogram records for tides or changes in the velocity of sound with depth, although the transducer depth (25 cm) was compensated for. Thus, the absolute depths observed in the surveys might be subject to sea level correction although the comparative gouge depth observations are quite accurate.

Sonographs were obtained on a wet paper, dual helix recorder which scanned the sea floor for approximately 125 m on either side of the vessel. System vagaries and problems associated with record interpretation have been dealt with at length (Belderson, 1973; Toimil, 1978; Barnes and others, 1984). With the 250-m swath width of the sonographs and the 200-m spacing of tracklines used in the survey, the nominal overlap of sonographs should have been 25 m, so that a mosaic of the sonographs of the survey area could be constructed. However, in the 1977 survey speed variations along the trackline, variation in record quality due to sea state and tow depth limitations, and problems encountered in compensating for the surface current all interacted to hinder the creation of the hoped for mosaic.

In the 1978 survey, the navigation was improved and the vessel was larger, which allowed for more even coverage of the survey area. However, the record quality was poor and it was not possible to correlate the results with the 1977 survey in detail.

3.6.3 OBSERVATIONS

The number of linear traces made by ice gouging the sea floor was counted on the sonographs for each 0.5-km segment of trackline. The resulting value, corrected for orientation and scale problems (Barnes and McDowell, 1978), was used to describe the density (in terms of number of gouges per 0.5 km of trackline) in the survey area. The gouge densities for the two survey years are shown in Figures 3.6-4 and 5.

Gouge densities were generally higher in 1977 than in 1978 in all water depths within the survey area. However, the distribution pattern was similar in both years; the maximum gouge densities were found in a narrow band between 5-m and 20-m water depths, with the highest densities at about 7-m to 8-m depths. This agrees with the observations of Toimil (1978) in the Barrow area. Note that the highest gouge densities were found within the area of highest density of prominent lines of grounded ice ridges as mapped from the radar imagery of the area for the years from 1973 to 1978 (Figure 3.6-6).

The maximum depth of ice gouge incision below the sea floor was determined from the fathograms for each of the 0.5-km segments in each year (Figures 3.6-7 and 8). The maximum gouge depths inshore of the 10-m isobath and seaward of the 30-m isobath are generally less than 1 m. Peak values exceeding 2 m occur in the vicinity of the 20-m isobath. It is interesting to note that the most numerous gorges occur inshore of the zone of deepest gouge incision. Comparison of figures 3.6-7 and 8 shows that, with the exception of a small area centered 2 km west of the radar site, the depth of gouge incision decreased between 1977 and 1978.

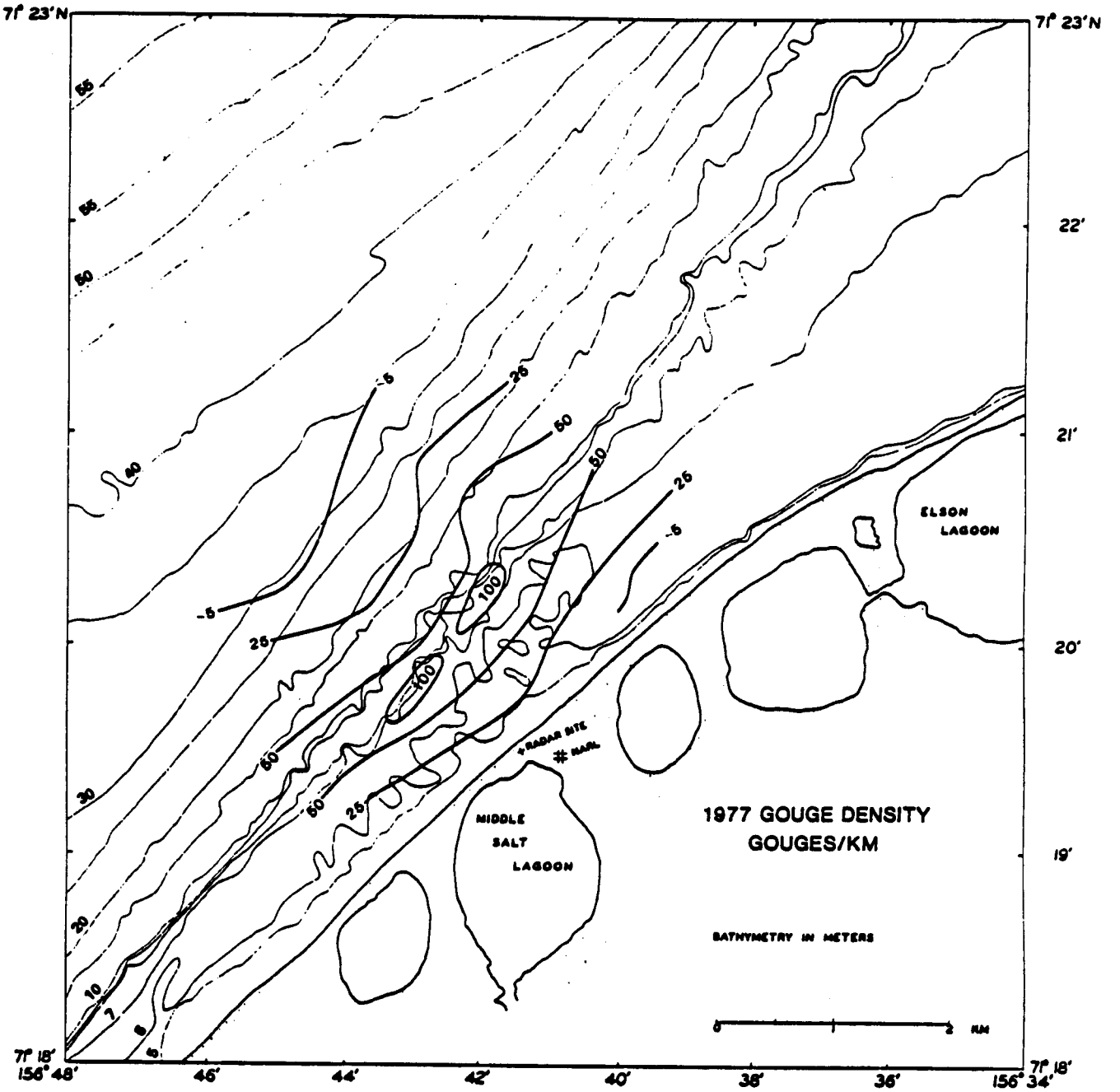

Figure 3.6-4 Density of ice gouges in 1977.

The principal orientation of ice gouges in each of the 0.5-km segments was also determined using the techniques outlined in Barnes and others (1978) and Barnes and others (1984). The results are shown in Figures 3.6-9 and 10. It is apparent that the principal gouge orientation was at a high angle to the coastline and to the

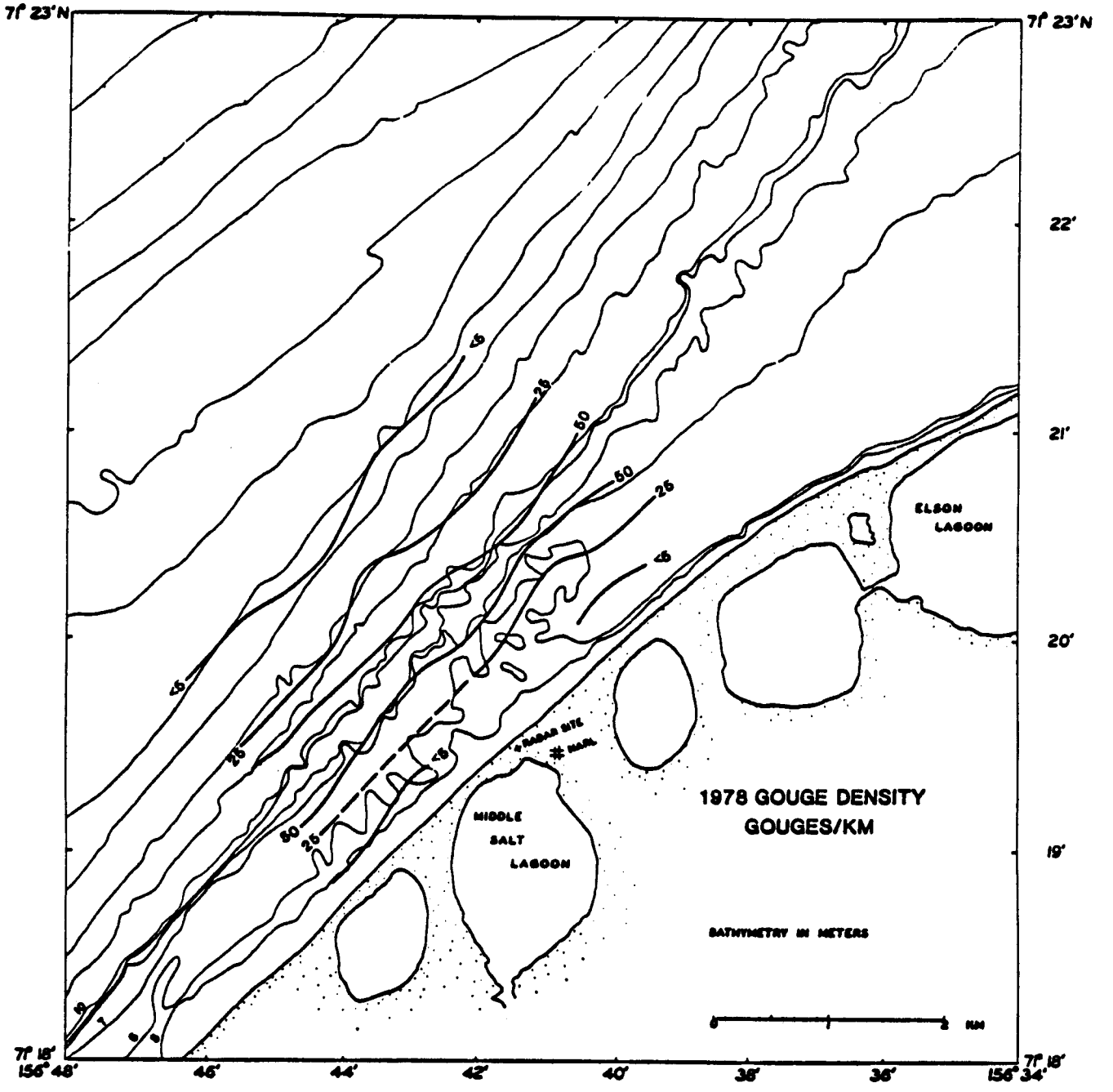

Figure 3.6-5 Density of ice gouges in 1978.

isobaths over the entire survey area in both years. This is in marked contrast to the results of other surveys along the northern coast of Alaska, where the principal trends tend to be parallel to the coastline and the isobaths (Toimil, 1978; Barnes et al., 1984).

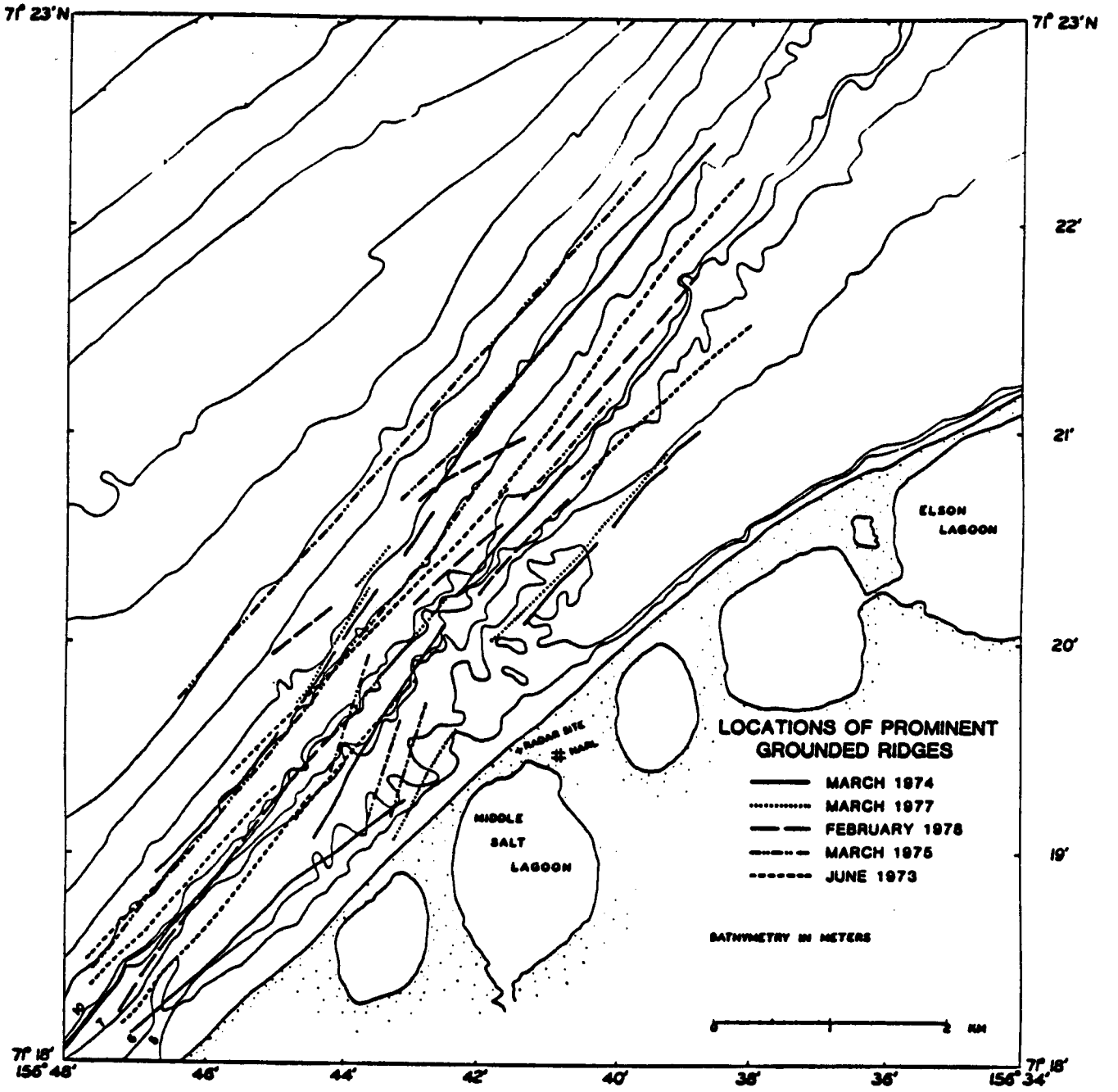

Figure 3.6-6 Locations of prominent grounded ice ridges in the field-of-view of the radar system.

3.6.4 DISCUSSION

3.6.4.1 Ice Gouge Orientation and Ice Motion

Ice gouges record the ice motion direction during gouging events and may not reflect the general pattern of ice drift in an area. This is true particularly if, in

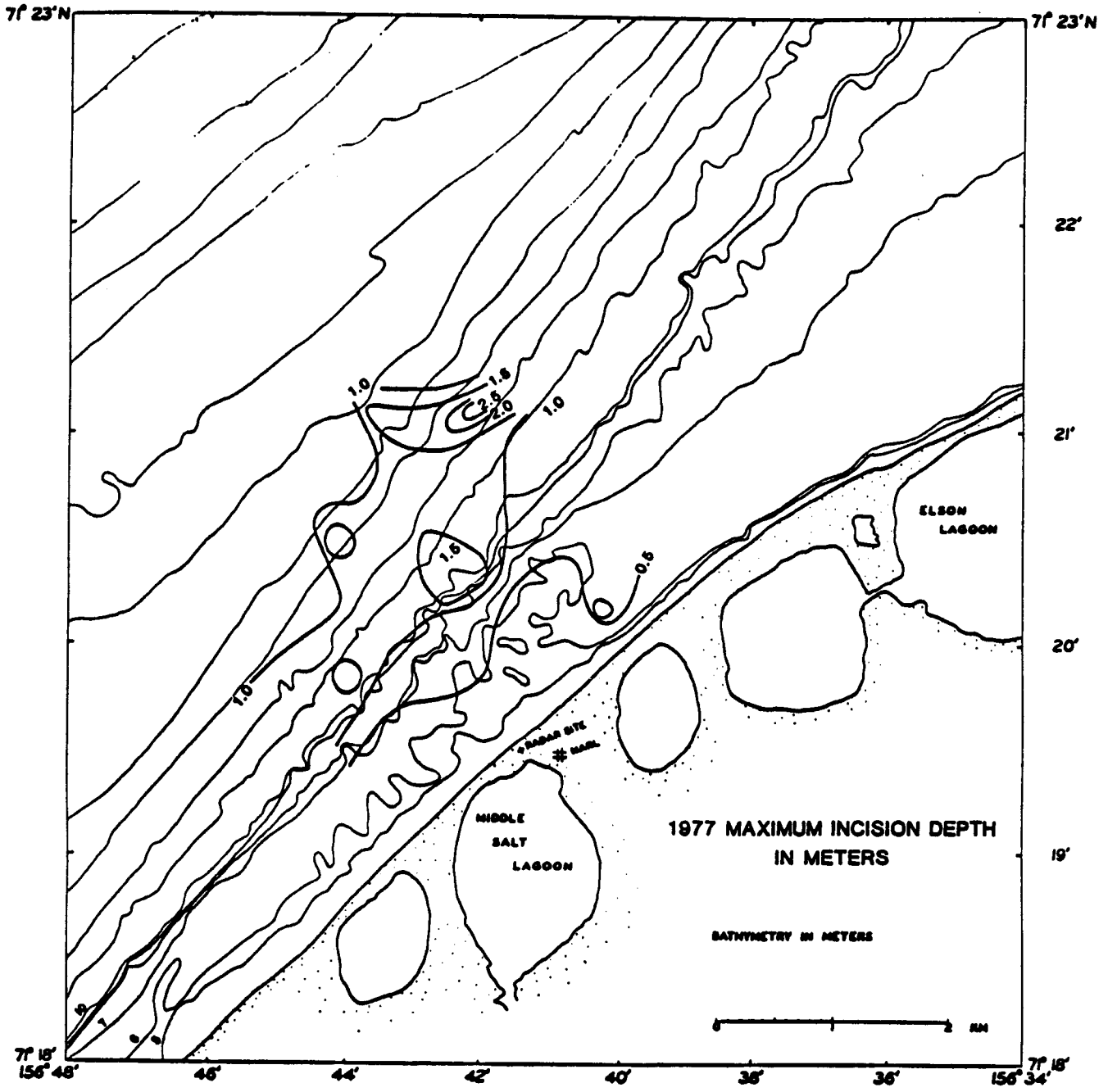

Figure 3.6-7 Maximum ice gouge incision depth, 1977.

general, the ice does not have sufficient draft to reach the sea floor. Gouges inshore from the (approximately) 20-m isobath probably form mainly during freeze-up (October-November) and breakup (July). During the winter the fast ice is generally (but not always) stationary and the motion needed to generate gouges is absent.

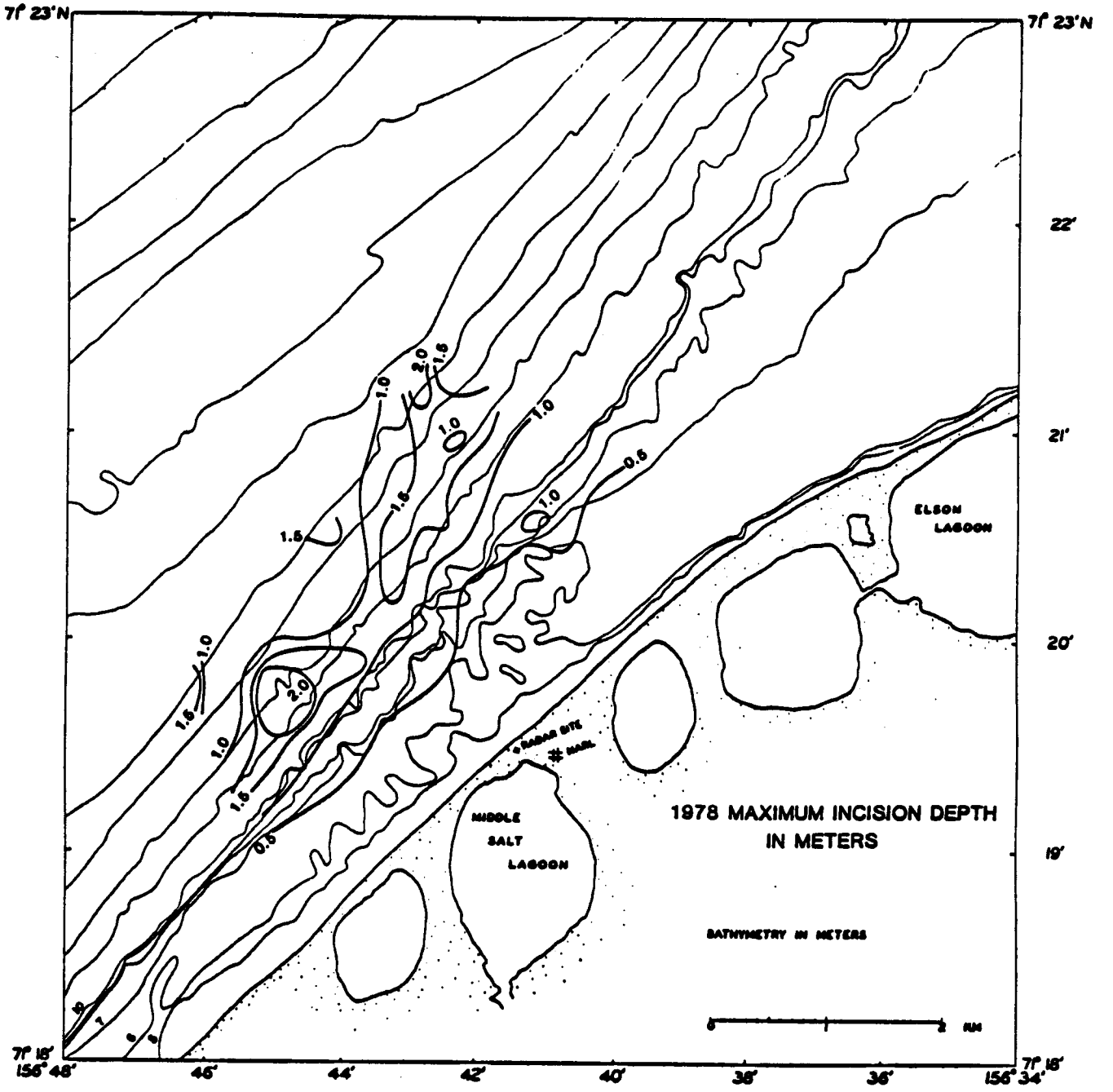

Figure 3.6-8 Maximum ice gouge incision depth, 1978.

This suggests that the ice gouge density, depth and orientation in the study area should primarily reflect the patterns of ice motion during freeze-up and breakup. However, as described below (and in Section 3.5.4), the dominant drift directions of the ice in the area are parallel to the coast during both freeze-up and breakup. Thus,

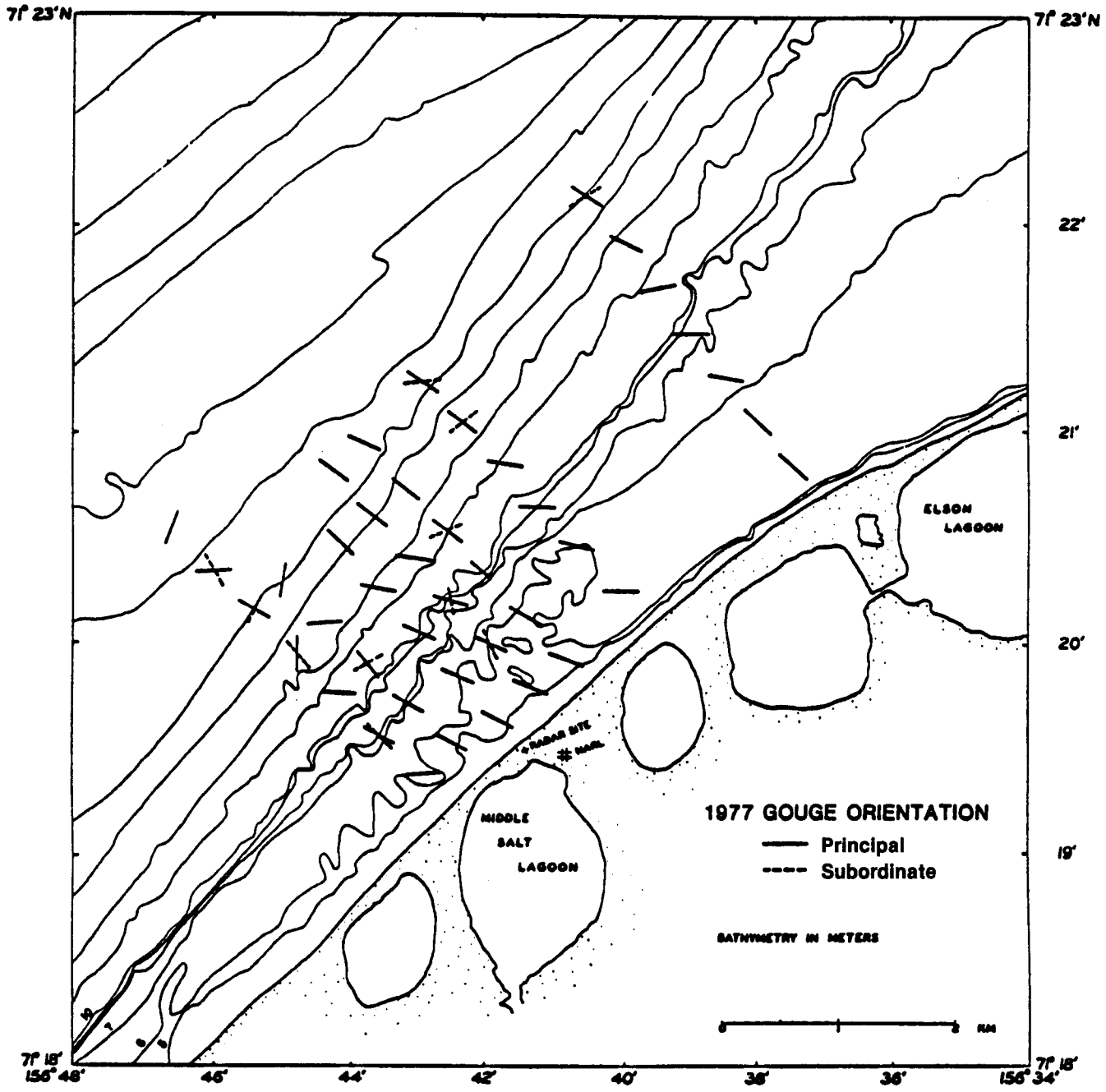

Figure 3.6-9 Principal orientation of ice gouges, 1977.

assuming that the gouges reflect the drag of deep keels in the ice cover, the principal gouge orientations would be expected to also be aligned parallel to the coast. The fact that the principal gouge orientations are at a high angle to both the coast and the isobaths suggests that they reflect "unusual" movements of the ice cover. Two

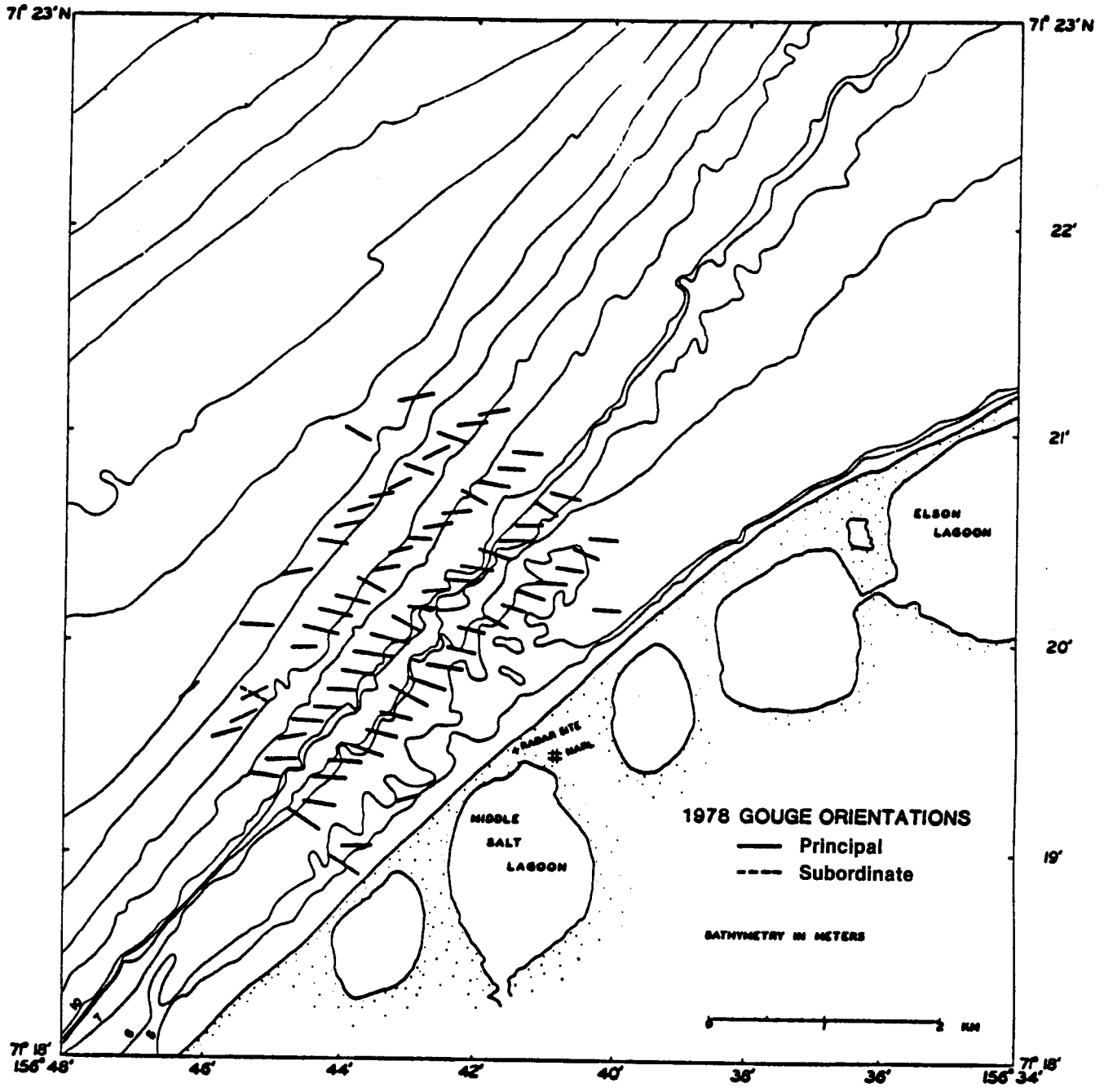

Figure 3.6-10 Principal orientation of ice gouges, 1978.

possible patterns of movement which could be responsible for the observed gouge pattern are developed in the following discussion.

As noted in Section 3.5.4.3, the term "freeze-up" is a misnomer for the mechanism by which the fast ice in the study area develops, because it suggests

general freezing of the ice sheet in place. In fact, in most years the fast ice sheet probably consists of pack ice which drifts into the area from the southwest, having formed further south in the Chukchi Sea. Freezing in place occurs only in the spaces between floes. The pack ice from the southwest generally includes only floes of thin (i.e., less than 0.5 m thick), young ice, and ridges formed from them are not likely to have the deep keels required for gouging of the sea floor, other than in shallow water near the beach or possibly during grounding on shoals. In addition, minor ice-push events frequently occur during freeze-up. In these events, the pack ice is driven into the edge of the developing fast ice sheet at a high angle, pushing it shoreward. The shoreward movement of first-year ridge keels incorporated in the fast ice could result in additional gouging but, in general, it does not seem probable that first-year ice alone was responsible for the extent and depth of gouging in the area. Instead, the most prominent gouge orientations shown in Figures 3.6-9 and 10 were probably created by the keels of multiyear floes, as described next.

In 1974, the pack ice which drifted into the area during freeze-up consisted primarily of multiyear ice floes which, from study of satellite imagery, can be shown to have originated in the Beaufort Sea, and drifted southwestward around Point Barrow. Some of the floes then turned and drifted into the field-of-view of the radar at a high angle to the beach. Ultimately, the floes grounded, possibly producing gouges as they slowed after contacting the sea floor. In addition, they may have subsequently been driven further shoreward by floes arriving behind them, extending the gouges. Field studies showed that the freeboards of some of the floes were up to 3 m in water depths as shallow as 5 m, indicating that they were grounded. Once in place, the floes sheltered the inshore area, permitting first-year ice to freeze in the interstices, thereby solidifying the fast ice sheet.

The drift of thick multiyear ice floes along the track described above (which, of course, may also occur at other times of year than freeze-up) clearly provides one

mechanism for producing gouges at a high angle to the coast. It may be particularly important in water depths greater than those usually covered by fast ice, because it is not likely that first-year ice ridge keels could form gouges in deep water.

There are few data available on the frequency with which the source of floes for the fast ice varies from northeast or southwest. For the five freeze-up seasons through which the radar system operated, the floes came from the southwest during three years, from the northwest in one year, and in one season (summer 1975) most of the fast ice stayed in place through the summer. However, these few years are probably not representative of the actual frequencies, and the few air photos we have seen of the fast ice in the study area for other years indicate that a southwesterly source for the fast ice is more common. No studies have been done to determine how often multiyear ice enters the area from north of Point Barrow at other times of year, although satellite imagery might provide information to examine this question.

Ice push events provide a second possible mechanism for producing gouges at a high angle to the shoreline. As noted in Shapiro et al. (1984) and in Section 3.1 above, the passage of a storm northward through the central Chukchi Sea generates southwesterly winds which tighten the pack ice against the fast ice along the coast of Alaska, forcing the latter toward the shore. If an ice push event results, grounded first-year and multiyear ice keels within the fast ice can be dragged over the sea floor, creating or lengthening gouges. The magnitude of the displacement in any ice push event probably varies with the time of year, the state of the ice, and the duration of the driving force. However, the typical displacement direction of the ice (as shown by the radar data) is similar to the principal gouge orientation directions shown in Figures 3.6-9 and 10.

A major ice push event occurred in July 1975 as the result of the passage of such a storm system [the details are given in Shapiro et al. (1984)]. The fast ice sheet was still intact at the time, although surface melting had reduced its thickness by about

50% to 1 m. The pattern of motion of the fast ice during the 1975 event is illustrated in Figure 3.6-11 which shows displacement vectors of prominent reflectors in the fast ice sheet (as mapped from the radar data) superimposed on the map of ice gouge orientations from the 1977 survey. The similarity between the orientation of the displacement vectors and the principal gouge orientation is apparent from the figure. As noted above, the fast ice sheet in 1975 included numerous grounded multiyear floes which would have been dragged across the sea floor during the event.

3.6.4.2 ICE GOUGE DENSITY AND DEPTH

The maximum gouge densities in both surveys occur within the zone of most intense ridging activity (Figures 3.6-4, 5 and 6), implying that most of the gouges are due to the incision of keels during ridging events. In addition, the low density of grooves in the area inshore from about 5 m water depth in either year (Figures 3.6-4 and 5) emphasizes the vigorous wave and current reworking of the sea floor in these depths which obliterates the gouges.

Gouge densities were higher in the 1977 survey than in the 1978 survey, particularly in the inshore segments of the survey area (Figures 3.6-4 and 5). In 1977, densities of from 50 to in excess of 100 gouges per 0.5 km of trackline were common in water depths from 8 to 15 meters. In contrast, densities observed in the 1978 survey were generally less than 50 gouges per 0.5 km of trackline. In particular, there was a marked decrease in gouge density in the area of the survey inshore from about 8 m (Figures 3.6-4 and 5). We suggest that the difference in the gouge densities between the two surveys reflects the timing of the surveys and the nature of the ice and storm events between the surveys.

Freeze-up following the September 1977 survey was late and followed more than a month of stormy weather which, based upon the records from the NWS station at Barrow, began shortly after the survey. During this period, waves and coastal

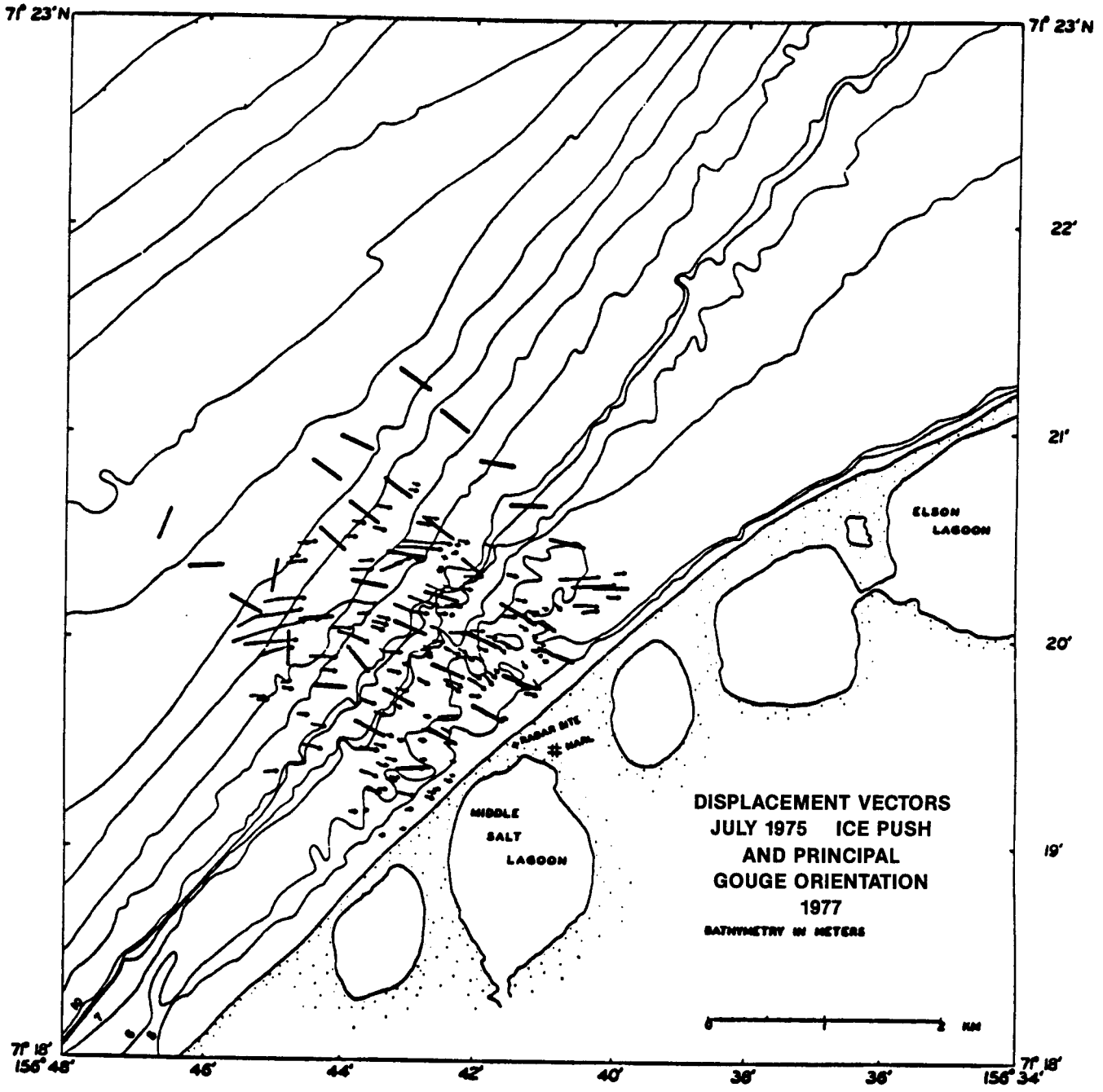

Figure 3.6-11 Displacement vectors from the 1975 ice-push event (small arrows) superimposed on principal ice gouge orientations mapped in the 1977 survey (from Figure 3.6-9).

currents probably reworked the sea floor, infilling and eroding the ice gouge morphology (Barnes and Reimnitz, 1979). The radar data show that the first emplacement of fast ice which remained through the winter was in late October.

Subsequently, there were five separate pack ice incursions into the near shore zone which produced minor ice push events. However, the floes which formed the fast ice were all first-year ice from the southwest. Thus, it is probable that gouging due to ice push was relatively minor and new gouges formed during freeze-up were restricted to incision of keels during ridging. The fast ice was stable through the winter, no ice-push events occurred during breakup in 1978, and the fast ice was gone by mid-July, shortly before the survey in early August. As a result, during the time between the surveys there was ample opportunity for gouges in the sea floor to be reworked by nearshore waves and currents while few new gouges would have been formed. The gouges formed during the ice push event of July 1975 and in the winter of 1975-76 would still have been prominent features at the time of the 1978 survey, although somewhat subdued by reworking during the storms in the fall of 1977.

3.6.5 CONCLUSIONS

The principal direction of the ice gouges in the area of the side-scan sonar surveys along the Chukchi Sea coast near Point Barrow is at a high angle to the beach and isobaths, and to the dominant direction of ice drift in the area as shown by radar data. The principal gouge orientations can be interpreted to have been caused primarily by two processes. The first is the repeated occurrence of ice push events in which the fast ice is pushed toward the shore by impact of the pack ice. Ice push occurs during both freeze-up and breakup, but is more common in the latter. During these events, keels of multiyear floes or, possibly, grounded first-year ice ridges are dragged over the sea floor,creating the gouges.

The second process is probably responsible for the gouges at a high angle to the beach in water depths greater than those normally covered by fast ice, as well as some of the gouges in shallower water. It occurs when multiyear ice drifts

southwestward toward the coast during freeze-up. The source of the floes is either the Beaufort or northern Chukchi Sea.

The gouge density is greatest in the area in which most ice ridges occur. It may be related to the incision of keels into the sea floor during ridging as well as to drag during ice push events. We attribute the change in gouge density between the two surveys to reworking of the bottom sediments by waves and currents during the storms which followed the 1977 survey.

The maximum gouge incisions are located in a zone just offshore from the zone of maximum gouge density. This probably reflects the drift of larger, heavier floes into the near shore area, which are stopped as they reach shallow water.

The pervasive onshore ice push and ice gouge events documented here suggest that this process may be important in bringing material to the beach, as first suggested by Hume and Schalk (1976). However, the supply of material from ice push events may be inconsequential when compared to the volume removed during reworking by waves and currents, or by man.

3.6.6 REFERENCES CITED

Barnes, P. W., and Reimnitz, E., 1979, Ice gouge obliteration and sediment redistribution event: 1977-1978, Beaufort Sea, Alaska; U. S. Geol.Survey, Open-File Report, 79-848, 22p.

Barnes, P.W., McDowell, D.M., and Reimnitz, E., 1978, Ice gouging characteristics: their changing patterns from 1975-1977, Beaufort Sea, Alaska:.U.S. Geological Survey Open-File Report 78-730, 42p.

Barnes, P.W., Rearic, D.M. and Reimnitz, E., 1984, Ice gouge characteristics and their relation to ice gouging and ice dynamics; in O.W. Barnes,D.M. Schell and E. Reimnitz (eds.), The Alaskan Beaufort Sea-Ecosystems and Environment: Academic Press, San Francisco, California, p.85-212.

Hume, J.D., and Schalk, M., 1976, The effects of ice on the beach and nearshore, Point Barrow, Arctic Alaska, Review Geography de Montreal,v. 30, p. 105-114.

Shapiro, L. H., Metzner, R. C., Hanson, A., and Johnson, J. B. (1984)Fast ice sheet deformation during ice-push and shore ice ride-up; in Barnes, P. W., Schell, D. M. and Reimnitz, E., The Alaskan Beaufort Sea, Ecosystems and Environments, Academic Press Inc., New York, pp.137-157.

Toimil, L.J., 1978, Ice gouge microrelief on the floor of the eastern Chukchi Sea, Alaska: a reconnaissance survey; U.S. Geological Survey Open-File Report, 78-693, 94p.

REMOTE SENSING DATA ACQUISITION, ANALYSIS, AND ARCHIVAL

by

William J. Stringer

Geophysical Institute
University of Alaska Fairbanks
Fairbanks, Alaska 99775-0800

Final Report
Outer Continental Shelf Environmental Assessment Program
Research Unit 663

November 1988

ACKNOWLEDGMENTS

This study was funded in part by the Minerals Management Service, Department of the Interior, through an interagency agreement with the National Oceanic and Atmospheric Administration, Department of Commerce, as part of the Outer Continental Shelf Environmental Assessment Program.

TABLE OF CONTENTS

BACKGROUND

The current Alaskan OCS leasing schedule includes areas in the northern Bering Sea, and throughout the Chukchi and Beaufort seas. Sea ice in these areas not only poses a potential hazard to manmade structures and exploration activities such as drill ship operations, but is also a factor in pollutant transport and in the distribution and migration behavior of marine mammals. Remotely sensed imagery has been utilized in the Outer Continental Shelf Environmental Assessment Program for many purposes, but the most useful data to date have been those related to the forms, seasonal distribution and movement of sea ice. These data have also been used to estimate the concentration and distribution of suspended particulate matter, verify the presence of specific circulation features, and map the distribution of water temperature for use in other studies such as investigations of fish behavior. These data provide an excellent record of historical or baseline conditions which otherwise could not be available. Archival of satellite imagery has been considered a necessary part of providing a data base from which to assess specific environmental problems in view of outer continental shelf oil and gas development. The acquisition and archival of satellite imagery by this research unit provides convenient and economical access to this data base by OCSEAP investigations. While a decade ago satellite imagery was fairly inexpensive, a single 1:1,000,000 scale Landsat color image now costs $350, a single black and white Landsat print is $50, and a black and white AVHRR image is $44. Currently, the archive contains 20,000 AVHRR transparencies and various products (black and white single band prints and transparencies, color prints and transparencies, enlargements, etc., from 13,000 Landsat scenes, with a conservatively estimated replacement cost of around $3.5M for these photographic products alone, at current prices. In addition, the archive contains approximately 200 Landsat images in digital tape format and about the same amount of AVHRR digital tapes. These currently cost $660 and $80, respectively. Currently for AVHRR, the emphasis is on acquisition of digital tapes so that this particular part of the archive is showing the greatest relative growth. Furthermore, the archive contains images of both types not found in the national data base. This has resulted from a number of factors but chiefly because the institution maintaining the archive also acquires Landsat imagery directly from the satellite and deals directly with the Alaskan receiving station for AVHRR imagery. For this reason also, these data can

be made available to OCSEAP users in a timely fashion. Thus this archive provides an extensive timely and economical access to these sources of data without the need to establish multiple channels of data flow from the sources of imagery.

In addition to acquisition and archive, the research unit maintains the equipment required to enhance the imagery and aid its analysis by OCSEAP investigators. Thus, color-coded ocean surface temperature maps have been generated and provided to OCSEAP investigators in the field within hours of their acquisition by the satellite, and retrospective data showing water surface temperature distributions from earlier years have been digitally enhanced and provided to OCSEAP management.

Finally, the research unit undertakes studies based on this extensive data set which have been identified by OCSEAP management as needed by other research units or as useful to OCSEAP/MMS for environmental assessment considerations. A number of such studies have been performed during this contract. Most were small, however, with one major study - on polynyi size, location.

OBJECTIVES

The stated objectives of this study were:

1. To acquire, analyze and archive remotely sensed imagery, including that based on infrared and microwave data, for the Alaska OCS areas, particularly those covered with seasonal sea ice. The Synthetic Aperture Radar (SAR) imagery shall be included as soon as it becomes available.

2. To provide imagery and special products to other OCSEAP investigators, and MMS and NOAA staffs.

3. Identify and describe sea ice distribution patterns and phenomena, such as building of ridges, movement of ice floes and islands, ice "breakout" through the Bering Strait, processes of freeze-up, and formation of leads and polynyi. The objective shall be accomplished in close cooperation with (or in support of) other OCSEAP investigations.

RESULTS

1. Acquisition and Archival of Remotely Sensed Imagery

A. AVHRR Imagery. In recent years, the value of this data set to OCSEAP studies has increased considerably. This is in part due to improvements in the quality of these data, partly due to advances in digital image processing and partly due to the types of studies conducted by OCSEAP. For the first two years of this three year contract period, we continued to acquire and archive AVHRR photographic positive transparencies of visible and thermal wavelength images on a daily basis. Some discretion was used taking into account the best data for the time of year.

During January of this year, NOAA closed its photographic laboratory at NOAA/NESDIS CDA Station (just outside Fairbanks), where photographic AVHRR products were being produced. At the same time, the host institution to RU 663 had developed a digital image capability so that much higher resolution multispectral AVHRR data products could be produced by RU 663 using AVHRR digital tapes. Therefore, it was determined to develop a new approach to archiving AVHRR data. First, a great quantity of facsimile AVHRR products were available from the weather service. While data from one or two of the six daily satellite passes had been archived previously, now data from all passes could be saved. While not the same quality as the previously archived transparencies, some useful information can be taken directly from them and, in addition, they can be used as a means of determining which digital tapes would be cloud-free in an investigator's area of interest. This is extremely important as the digital tapes are expensive. Therefore, the facsimiles were added to the archive and an additional archive of digital AVHRR tapes was initiated. This tape archive includes tapes identified by OCSEAP investigators as useful to their activities and tapes archived because they are largely cloud-free and represent good representations of conditions at various points in time. The archived tapes contain visual, near infrared and thermal infrared data and can be digitally analyzed and displayed in a multi-color format. In addition, products specific to a particular investigator can be produced. Tapes of AVHRR scenes found to be of interest to OCSEAP which have not been previously archived have been purchased by RU 663 from NOAA in Washington, D.C. and placed in the tape archive. Thus, AVHRR imagery has been obtained in three formats: positive photographic transparency, suitable for analysis or reproduction, positive paper

facsimiles suitable for data selection (i.e. tape acquisition) and some analysis purposes, and magnetic tape. Appendix 1 describes lists of the positive transparencies, facsimile prints, and digital tapes acquired under the contract and submitted separately to NOAA/OCSEAP. Catalogue lists are necessary because choices were made and data were not archived for all dates.

B. Landsat Imagery. The host institution to this contract maintains a Landsat "Quick-Look" program under which Landsat imagery is acquired for scientific purposes. The image-producing equipment is located at the NOAA/NESDIS CDA Station where AVHRR imagery is acquired. Landsat has been purchased from the federal government by the EOSAT Corporation which is operating the satellite as a profit-making venture. We could not hope to maintain a useful archive by purchasing these images at their current prices. However, by special arrangement with EOSAT, the University of Alaska is permitted to acquire and archive these images for the purpose of scientific studies. The data is acquired through the cooperation of NOAA which operates the CDA Station and the University of Alaska, whose equipment and personnel transform the raw data into imagery. Although we have a number of Landsat images in digital tape format, only a few have been acquired through this contract. Almost all Landsat acquisitions under this contract have been in hard copy paper print and negative transparency format. We have two routes which can be used to perform digital image analysis on this imagery if we do not possess a digital tape: 1) we can purchase it at a rate of $660 per copy, or 2) we can digitize a hard copy print at a cost of around $50 (for time on an image scanner). This second route produces a somewhat lower quality image but in many instances - particularly where a number of images are to be analyzed - the value of the quantity available exceeds the loss of data quality. Appendix 2 describes Landsat images acquired and archived during this contract; a complete list was submitted separately to NOAA/OCSEAP.

C. Side-Looking Airborne Radar. We have maintained in our archive side-looking airborne radar imagery obtained by OCSEAP approximately ten years ago at the time that OCSEAP included a research unit for that purpose. In addition, we have added to this file a small quantity of side-looking airborne radar acquired by the Ice Centre Environment Canada as it is requested by investigators. We do not actively acquire these data because of their high cost relative to the demand for them. However, we can and have obtained these data from the Canadian archive as the need arises.

D. Aerial Photography. Our archive maintains file copies of the photographs obtained under the joint NASA/Alaska high altitude aerial photography program under which the entire state of Alaska was photographed at 1:125,000 scale in color infrared photography and selected portions of the state were re-photographed at 1:62,500 scale. Some areas such as the trans-Alaska pipeline corridor and the Beaufort Sea coast were photographed more than once during the life of the program. During this contract various copies of these photographs have been supplied to OCSEAP and MMS as they represent historical benchmarks in the development of the Alaskan coastal zone.

E. Passive Microwave Imagery. For several years NASA has operated the multi-channel passive microwave SMMR which provides low resolution (30 x 30 km) all-weather monitoring of ice in the polar ice caps. These data are available from NASA Goddard in raw format or gridded onto 10 km pixels. There have been no requests for these data by OCSEAP investigators. However, one of our students has acquired the data set for Alaska between 1983 and 1987. (Thus this data set contains 900 images of Alaska and the adjacent oceans on a two-day interval between 1983 and 1987.) These data are available for OCSEAP investigators, if the need arises. This instrument is aboard Nimbus 7, and all but one of the frequency bands have failed. Since the most useful data are derived form multi-frequency algorithms, the data set is essentially no longer being expanded.

Last year, a similar multi-channel microwave radiometer was launched aboard the most recent vehicle of the Defense Meteorological Satellite Program. These data are held for a period of months and then released to the World Data Center for Ice and Snow in Boulder, Colorado. We have been in contact with the data center and anticipate no problem in obtaining these data if they are desired by OCSEAP investigations.

F. NOAA/Navy Ice Charts. These charts are produced weekly by the NOAA/Navy joint ice center, Suitland, Maryland. They contain comprehensive ice data including ice edge information based on passive microwave imagery. We have continued to obtain these charts as they become available. The charts cover the entire Alaskan study area and are filed in chronological order since 1972. We have found these charts to be useful for statistical studies of several ice edge location (but not highly detailed) studies of the nearshore environment.

G. SAR Imagery. These data are not yet available. The launch of ERS-1 carrying the first civilian synthetic aperture radar since Seasat (1978) is scheduled for October, 1990. It will be followed by a Japanese and a Canadian SAR later in that decade. The host institution to this contract will be the location of the Alaskan SAR receiving station. These data should provide cloud-free, year round images of sea ice and a measure of sea state in the Beaufort, Chukchi and Bering seas.

2. Provision of Imagery and Special Products to Other OCSEAP Investigators, and MMS and NOAA Staffs

During the last three years, we have responded to a number of data requests. These requests and our response to them follow this introduction. As will be seen, their requests range from provision of a representative satellite image from historical files to production of timely data sets consisting of products derived from satellite imagery using extensive interactive computer programs.

Our capability was considerably enhanced during the last part of this contract by the development of an interactive digital image analysis laboratory by the University of Alaska Fairbanks. This laboratory represents a total investment of approximately $800K. This facility has greatly expanded our capability to provide special products in fulfillment of our contractual obligations.

From January 1 - March 31, 1986 we were engaged in three major activities: 1) a study of temporal changes in the Yukon Delta in response to a request from RU 660 (Martin, Envirosphere); 2) participation in the Chukchi Sea Update Meeting; and 3) provision of remote sensing imagery to OCSEAP management.

During the period April 1 - June 30, 1986, the principal investigator participated in seal reconnaissance flights by RU 667 (Frost, Lowry, and Burns) out of Prudhoe Bay in mid-June. These flights were conducted at 300' altitude which made possible very detailed low altitude oblique photography. We were fortunate that clear sky conditions made Landsat imagery available from this period so that the photography obtained (approximately 450 photographs) can be used as "ground truth" for the Landsat imagery. Also during this period, we completed our Yukon Delta work for Martin (RU 087) and began preparation of the results in a format suitable for publication in an appropriate

journal. John Brueggeman (RU 625) also contacted us concerning ice analysis using satellite imagery to support 1979 whale studies. Following the Chukchi Sea Update meeting in Anchorage this spring, Spaulding (RU 676) requested a copy of our digital Chukchi Sea ice edge data. This was provided with documentation.

During the period July 1 - September 30, 1986, we completed preparation of the results of our Yukon Delta study with Martin (RU 087) for publication in an appropriate journal. We also performed analysis of ice conditions in conjunction with whale sightings in the Bering Sea for John Brueggeman (RU 625). For OCSEAP management, we provided satellite imagery to document sea surface conditions at the time of an oceanographic cruise in the Chukchi Sea. Data requested included both ocean temperature and sediment plume distributions.

During the period October 1 - December 31, 1986, we continued to provide ice-related data which could be used in conjunction with Brueggeman's whale sightings in the Bering sea. This study occupied the bulk of our activities during this quarter. The whale sightings (about 3,000) have been coded in terms of latitude and longitude. The objective of our efforts was to provide data which could be used to determine whether a meaningful statistical relationship could be found between these sightings and ice parameters such as concentration, type (thickness) and ice edge location (including polynya boundaries). For OCSEAP management, we provided enhanced AVHRR imagery in the vicinity of Kotzebue Sound and in the Beaufort Sea.

From January 1 to March 31, 1987, we continued to provide assistance to RU 625 (J. Brueggeman). We created a program to distinguish whether a given station is within or outside a polynya from the digitized data. All 3,000 of Brueggeman's whale/no whale data were tested for correlation with polynyas.

During the period April 1 - June 30, 1987, Everett Tornfelt of the Anchorage MMS Office requested a data search and copies of appropriately selected imagery, which was accomplished.

During the period July 1, 1987 - September 30, 1987, Walter Johnson, Sathy Naidu and Jim Raymund (RU 690) conducted a cruise aboard the Surveyor in the Chukchi Sea between September 17 and October 8. This RU provided support to that effort by monitoring NOAA AVHRR satellite images as they became available during

this time and producing high quality photographic prints of the scenes which may be of value to their study. A high-resolution SPOT image was also acquired showing suspended sediment in the vicinity of Kotzebue. Also during this quarter, we provided Dale Kinney of MMS with "Width and Persistence of the Chukchi Polynya," and Statistical Description of the Summertime Ice Edge in the Chukchi Sea." Mr. Dick Ragle wanted information regarding ice conditions and related hazards in Stephanson Sound and Prudhoe Bay.

During the period October 1 - December 31, 1987, we attended and participated in the OCSEAP Arctic Information Transfer/Update Meetings held in Anchorage. We presented two papers - "Arctic Remote Sensing," which is a review of remote sensing techniques as they apply to the Alaskan OCSEAP needs; and "A Study of Possible Meteorological Influences of Polynya Size," which describes our research on polynyas. Following the presentation of the papers, there was a very helpful discussion with other OCSEAP investigators and OCSEAP and MMS staff. We have formulated our plans for further work based on these discussions.

From January 1 - March 31, 1988 our activities were largely concentrated in two areas: data acquisition and data analysis. There were no requests for data assistance during this quarter.

During the period April 1 - June 30, 1988, we responded to a request for image data showing the "West Dock" area of Prudhoe Bay at various stages of the West Dock Causeway. This request caused us to consider the possibility of registering low resolution AVHRR imagery to higher resolution Landsat imagery in order to fix the location of features visible on the AVHRR imagery. This was done successfully and the resulting product forwarded to our contract monitor. We also received a verbal request for thermal imagery in support of fisheries studies later in the summer in the nearshore areas of the Beaufort Sea.

From July 1 - September 30, 1988, the development of a digital image analysis capability made possible a number of projects providing assistance to OCSEAP investigators which included: analysis of AVHRR images for use in fisheries study; response to a request from MMS to examine data to determine the relative feasibility of various routes of whale migration from Mackenzie Bay to Barrow; and responding to a

request from Dale Kinney of MMS to produce images to provide data for studies attempting to correlate the presence of ocean mammals with open-water areas in sea ice.

3. Performance of Studies Related to the Needs of the Outer Continental Shelf Environmental Assessment Program

A. Studies Resulting in Published Papers. Following a request for data assistance from RU 660 (Martin) (see section 2 above), we found that we had done a significant amount of research on the question of change in the vicinity of the mouth of the Yukon River. The material that had been produced was published as "Landsat Determined Geographic Change," in *Photogrammetric Engineering and Remote Sensing*. An abstract of this paper is included here as Appendix 3.

OCSEAP has long held an interest in ice motions through Bering Strait in terms of its influence on marine mammal migration and the possible transport of pollutants. We were able to work cooperatively with T. Kozo to produce "Mesoscale Nowcasting of Sea Ice Movement Through the Bering Strait with a Description of Major Driving Forces," submitted for publication in *Monthly Weather Review*. An abstract is included as Appendix 4.

One of the parameters often listed as important to models of pollutant transport in ice infested water is the distribution of sizes of ice floes. Earlier this year we submitted a manuscript entitled "Summertime Distribution of Floe Sizes in the Western Nearshore Beaufort Sea," to the *Journal of Geophysical Research*. It has been reviewed and is being revised according to suggestions. An abstract of the manuscript is included here as Appendix 5.

The flooding of rivers on Alaska's North Slope marks the beginning of the transition from winter to summer in the Beaufort Sea. The flood waters exit the river tributaries and spread upon the adjacent fast ice. The timing and extent of this springtime event have had a bearing on a number of regulatory decisions regarding petroleum development activities in this region. Over the past several years we have conducted a number of small studies related to springtime river flooding. Last year we assembled this material into a manuscript which has been submitted to *Arctic and Alpine Research*. An abstract is included here as Appendix 6.

B. Studies Resulting in Published Reports. Sea ice is seldom removed from the Chukchi Sea even in summertime. The ice edge in summer is usually located in the Northern part of the sea with its configuration controlled at least in part by bathymetrically steered currents. However, the ice edge location is variable both from year to year and within each year. This variability has a significant influence on the operation of drillships and other petroleum-related activities. We reported the results of a study of this ice edge behavior in the *Chukchi Sea Information Update,* published by OCSEAP in June 1987 (pp. 33-41).

Remote sensing is a particularly valuable tool to science in the Arctic because of the relative inaccessibility of the region. In the past few years there has been a significant increase in the quantity and quality of sensors available for arctic studies. Upon request, we performed a review of these sensors and their utility to OCSEAP studies. The results were presented at the November 1987 Arctic Information/Update meeting and published in the OCSEAP publication, *Alaska OCS Region 1987 Arctic Information Transfer Meeting,* June 1988 under the title, "Arctic Remote Sensing."

Because of the extensive shallow nearshore waters in the vicinity of Prudhoe Bay, causeways have been utilized for a variety of purposes including seawater intake facilities, docks, and drilling platforms. There has been considerable interest in the influence these structures exert on their physical and biological surroundings. Using satellite imagery we observed at least one occasion when a modification of the thermal regime was detectable. This was presented to OCSEAP and subsequently published as "The Causeway Effect: Modification of Nearshore Thermal Regime Resulting from Causeways," and published in *Beaufort Sea Information Update,* April 1988.

Recently there has been increased interest in the role of polynyas on the behavior of marine mammals. As a result of this interest, this research unit has conducted an extensive analysis of polynyas in the Alaskan nearshore region. Some preliminary results thought to be of particular interest at the time were presented as "A Study of Possible Meteorological Influences on Polynya Size," and published in *Alaska OCS Region 1987 Arctic Information Transfer Meeting,* June 1988.

C. Studies Reported in This Final Report. We have been conducting a major study of polynyas in the seas adjacent to Alaska. In particular, we have measured the areal extent of these polynyas versus time for six study years. Following that, we have calculated correlation statistics between the polynya extent and regional winds. These results are reported in Appendix 7.

APPENDIX 1

Description of NOAA/AVHRR Positive Transparencies, Facsimile Prints, and Digital Tapes Acquired and Archived Under the Contract

NOAA/AVHRR transparencies for the period January 1986 through January 20, 1988 are listed by date and orbit number and categorized according to presence or absence of clouds in four regions: the Beaufort Sea, the Chukchi Sea, the Bering Sea, and the Gulf of Alaska. This imagery is predominantly thermal infrared band from the last week in October through mid-March and visible band imagery for the remainder of the year. No transparencies were available from Gilmore Tracking Station after January 20, 1988.

NOAA facsimile prints are listed for the period January 1986 through February 1989. They are listed by date and orbit number and categorized according to presence or absence of clouds in nine regions: USSR, Beaufort Sea, Chukchi Sea, Bering Sea, Interior Alaska, Gulf of Alaska, Cook Inlet, Southeast, and Canada. After January 20, 1988, the facsimile prints are a replacement for transparencies.

NOAA digital tapes are listed for the period September 1974 through February 1989. This is not daily acquisition. Approximately 175 tapes are archived from numerous sources. All are listed by date, satellite number, and orbit number. Additional information varies depending on the source of the imagery. It may contain qualitative descriptions of cloud-free areas on the imagery or information useful if the imagery is to be used on the ADVAL image analysis system.

There is some overlap in the listings between the record kept at the Geodata Center and that kept by ADVAL.

All of the image products are archived at the Geophysical Institute's Geodata Center.

APPENDIX 2

Description of Landsat Images Acquired and Archived Under the Contract

Between January 8, 1986 and March 3, 1989, we archived 1,103 Landsat scenes of Alaska. They are sorted by Grid, Path, Row, and Date. Additional information is given on percent cloud cover and bands, and for some scenes quality of the image is recorded.

Most Landsat imagery has been obtained from the University of Alaska Quick Look program and is archived as photographic prints at the Geodata Center.

APPENDIX 3

Landsat-Determined Geographic Change

by

W. J. Stringer, J. E. Groves, and C. Olmsted
Geophysical Institute
University of Alaska Fairbanks
Fairbanks, Alaska 99775-0800

ABSTRACT

Geomorphic changes in the Yukon River Delta occurring over a 35-year span have been detected through comparison of a recent Landsat image with earlier maps compiled from aerial photography. Island formation or growth and channel migration were found to have taken place with a calculated location precision of around 200 m. Geographic control of the Landsat image was established through digitization of surveyed control points used for control of aerial photography for mapping. Tide stage considerations were found to be useful in these low-lying areas, even though the astronomical tide range here is relatively small.

(Submitted to *Photogrammetric Engineering and Remote Sensing*.)

APPENDIX 4

Mesoscale Nowcasting of Sea Ice Movement Through the Bering Strait with a Description of Major Driving Forces

by

Thomas L. Kozo
VANTUNA Research Group
Occidental College
Los Angeles, California 90041

William J. Stringer and Lenora J. Torgerson
Geophysical Institute
University of Alaska Fairbanks
Fairbanks, Alaska 99775-0800

ABSTRACT

Surface atmospheric pressure data from a triangular station network surrounding the Bering Strait are used to calculate hypothetical geostrophic wind velocities. Net daily Strait sea ice movement is derived from visible and infrared NOAA satellite imagery for November through May, 1974 to 1984. These historical ice-motion data and network wind-velocity data are used to develop an empirical 12-hr advance forecast (nowcast) sea ice movement model with all-weather capabilities. A necessary outgrowth of this study has been the identification and classification of three modes of ice movement and two modes of ice immobilization according to their major driving forces. The first ice-movement mode is from the Chukchi Sea to the Bering Sea requiring a minimum northeasterly geostrophic wind of 12 m s^{-1}. The second and third modes represent ice movement from the Bering Sea to the Chukchi Sea. Mode 2 is driven by a preexisting north-flowing ocean current that offsets weak winds from the northeast. Mode three is large movement due to a combination of southwesterly winds and north-flowing ocean current. The first immobilization mode (maximum duration one week) is an apparent balance between northerly wind stress, current stress from the south, and internal ice stresses. The second immobilization mode (least common) is due to double, solid sea ice arches forming across the Strait. These arches remained intact under strong northeasterly geostrophic winds (20–26 m s^{-1}) and can last up to 4 weeks.

(Submitted to *Monthly Weather Review.*)

APPENDIX 5

Summertime Distribution of Floe Sizes in the Western Nearshore Beaufort Sea

by

William J. Stringer
Geophysical Institute
University of Alaska Fairbanks
Fairbanks, Alaska 99775-0800

ABSTRACT

The areal extent of ice floes has been measured from Landsat imagery of the summertime Beaufort Sea, spanning the five months between break-up and freeze-up. In general, the distribution of floe areas was found to obey a power law: $N(S) = N_1 S^{\lambda}$, where the counted number of floes per unit floe size interval, N(S), is related to the number of floes in the particular distribution at unit floe size, (N_1), the floe size, (S), and λ, a parameter found here to range between -1.33 and -2.06. The value of λ decreased from -1.33 in May to -2.06 in August and then increased to nearly -1.47 in September. An exponential relationship with λ was found among the values of N_1 from the various distributions: $N_1(\lambda) = N_O e^{-14.4\lambda}$. This relationship appears to hold regardless of the seasonal variation of λ. Thus, floe size distributions were found to obey $N(S) = N_O(e^{-14.4}S)^{\lambda}$, with a value $N_O = 1.23 \times 10^{-6}$, where N_O is the projected number of floes per unit floe size at unit floe size for $\lambda = 0$.

Although not observed, a value of $\lambda = -1$ was found by theoretical considerations to produce a floe size distribution in which the apparent distribution of floe size is the same regardless of the scale at which it is viewed. Based on the observed variation of λ with season, it is hypothesized that such a distribution might appear earlier in the year than the observing period reported here.

(Submitted to *Journal of Geophysical Research.*)

APPENDIX 6

The Timing of Snowmelt Flooding of Alaska's Major North Slope Rivers--An Anomalous Occurrence

by

William J. Stringer
Geophysical Institute
University of Alaska Fairbanks
Fairbanks, Alaska 99775-0800

ABSTRACT

Six milestones associated with snowmelt flooding of a major Alaskan North Slope river during breakup have been identified and their dates of occurrence estabished for a 14-year period using satellite imagery. The most reliably measured milestone is over-ice flooding, which occurs when river snowmelt floodwaters spread out upon oceanic fast ice at the river's mouth. On the average, for the Sagavanirktok River, this occurs on May 25 with a standard deviation of 8 days. However, the pattern of dates for this event suggests bimodality, with the primary mode having an average date of May 27 and a standard deviation of only 3 days, and the secondary mode occurring nearly a month earlier. Time series analysis yields a trend toward earlier dates of over-ice flooding in agreement with the concept of a climatic warming. However, the statistical reliability of this result is low.

(Submitted to *Arctic and Alpine Research.*)

APPENDIX 7

A Study of Possible Meteorological Influences on Polynya Size

This report describes in outline form the results of a comprehensive study of polynyi, areas of open water occurring in the otherwise ice-covered wintertime Bering and Chukchi Seas. The data used were images obtained by the Advanced Very High Resolution Radiometer aboard the NOAA series satellites. Polynya boundaries were traced directly from satellite imagery using a digitizing table. A computer program was used to rectify the image distortion and calculate the extent of each polynya. This yielded tables of polynya extent for all cloud-free days for six one-year study periods.

The first objective was to document the locations of recurring polynyi in the U.S. portions of the Outer Continental Shelf. This was accomplished and the results appear in this report in map format. The second objective was to develop a statistical picture of the extent of these polynyi over a number of years. This was accomplished also and the results appear here in summary form and more completely in a comprehensive report on file with OCSEAP management in Anchorage, Alaska. The third objective was to attempt to relate polynya extent with environmental parameters whose measured values were readily available. These results are quite extensive but unfortunately, largely ambiguous. For this reason they are only described here in general terms while the complete results are detailed in the file report. The remainder of this summary describes the rationale for the various statistical approaches taken in our approach to this third objective, and an assessment of the results.

If one examines wintertime satellite images of the Bering and Chukchi Seas, the most prominent class of features related to sea ice to be seen is the scattering of polynyi generally located along coasts. If a sequence of images is viewed, these polynyi can be seen to expand and contract over periods of several days to weeks. Often groups of polynyi appear to open in phase giving the impression that some general regional forcing is responsible for their formation. There are two large scale regional forcing agents that are external to the ice, winds and ocean currents, and one, ice stress, that is internal to the ice. Clearly ice stress is ultimately related to winds and currents but the force can be transmitted distances sufficiently large that locally it may be the only apparent force acting on the ice. Furthermore, the application of these forces is modified by Coriolis acceleration.

The extensive tabulation of polynya extent we had compiled invited an attempt to correlate polynya extent with these forcing agents. However, of the three, only winds are measured with regularity and on anything like a comprehensive basis. Thus, winds were the only data set available for correlation studies. Even these data are not ideally suited for correlation with polynyi since none of the observing stations are adjacent to the polynya sites, and in many locations orographic configurations cause wind measurements to be only locally valid. On the other hand, this region is known for large storms generally associated with ice motions. It was thought that even scalar winds might be a measure of general ice forcing events related to polynya openings, and although strong correlations might not be found, some relationship might be found. As will be seen, this was not the case. Generally speaking, the correlations found were weak and the confidence levels low. Initial failures at farther straightforward correlations led to attempts to find more and more exotic relationships involving thresholding, running average, delayed correlations, and even application of less rigorous correlation techniques such as ranking.

INTRODUCTION

A polynya is rigorously defined as an irregularly shaped opening enclosed by ice which may contain brash ice or uniform ice markedly thinner than the surrounding ice (Stringer, Barnett, and Godin, 1984). Polynyi are frequently described in the literature as non-linear open water areas surrounded by sea ice without mention of whether an attempt was made to clearly differentiate the open water from thin ice or if such a distinction was possible. Polynyi are important for the understanding of climatic, oceanographic, and biological phenomena in the Arctic.

Dey, Moore, and Gregory (1979) describe the use of AVHRR thermal infrared imagery for monitoring and mapping sea ice freeze-up and break-up and a method of rectifying AVHRR images. Dey (1980) describes the use of thermal infrared images for monitoring North Water, a polynya located in Northern Baffin Bay, for the months of November-January. They concluded that AVHRR thermal infrared images are admirably suited for generalized statistical analysis of sea ice and that boundaries between first-and multiyear ice and open water can be mapped more reliably than boundaries between open water and thin ice.

Smith and Rigby (1981) state that the timing of freeze-up and formation of polynyi, the size of polynyi at maximum ice cover, and the pattern of sea ice break-up and disappearance are important factors for understanding ecological relationships.

Using AVHRR visible and infrared imagery, Landsat imagery, and weekly ice composition maps from the Ice Climatology and Applications Division of the Canadian Atmospheric Environment Service, they studied 16 polynyi in the Canadian Archipelago from July to November, 1975-1977, and they reported broad dates for formation and disappearance of the polynyi.

Stringer (1982) measured the width and persistence of the Chukchi Polynya using Landsat and AVHRR imagery. A qualitative correlation was found between average ice motion away from the coast and the mean vector wind for all months except perhaps July. Carleton (1980) mapped the recurring polynyi south of the Pt. Hope/Cape Thompson area using Landsat imagery. He was able to differentiate between open water and thin ice. He calculated areas for both the open water and thin ice regions and related their total size to the climatic factors of wind and temperature.

Smith and Rigby suggest that polynyi are formed by the effects of wind and temperature, or from the effects of upwelling, currents and tides. Treating a similar and somewhat related subject, Rogers (1978) correlated the distance of the summertime ice edge from Barrow with thawing degree days and components of the geostrophic wind. This report describes the results of a study performed to determine whether polynya area could be correlated with meteorological conditions in a manner similar to the relationships found between these factors and the location of the ice edge.

DATA AND ANALYSIS

The Geophysical Institute Geodata Center includes a collection of AVHRR images from 1974 to the present. Thus, it appeared feasible to document the dates of appearance and disappearance of polynyi for the Bering and Chukchi Seas as well as to quantitatively determine the polynya areas and relate these areas to climatological data.

Nineteen polynyi locations were originally identified and named. A twentieth, the Anadyr Gulf polynya was added to the years of 1975, 1979, and 1983 for the months January through April and January 1986. The names and locations of the polynyi are given in Figure 1 and Table 1. At the conclusion of this study, it became obvious that a few of the original nineteen polynyi sites ought to be revised. The revisions are given in Figure 2 and Table 2.

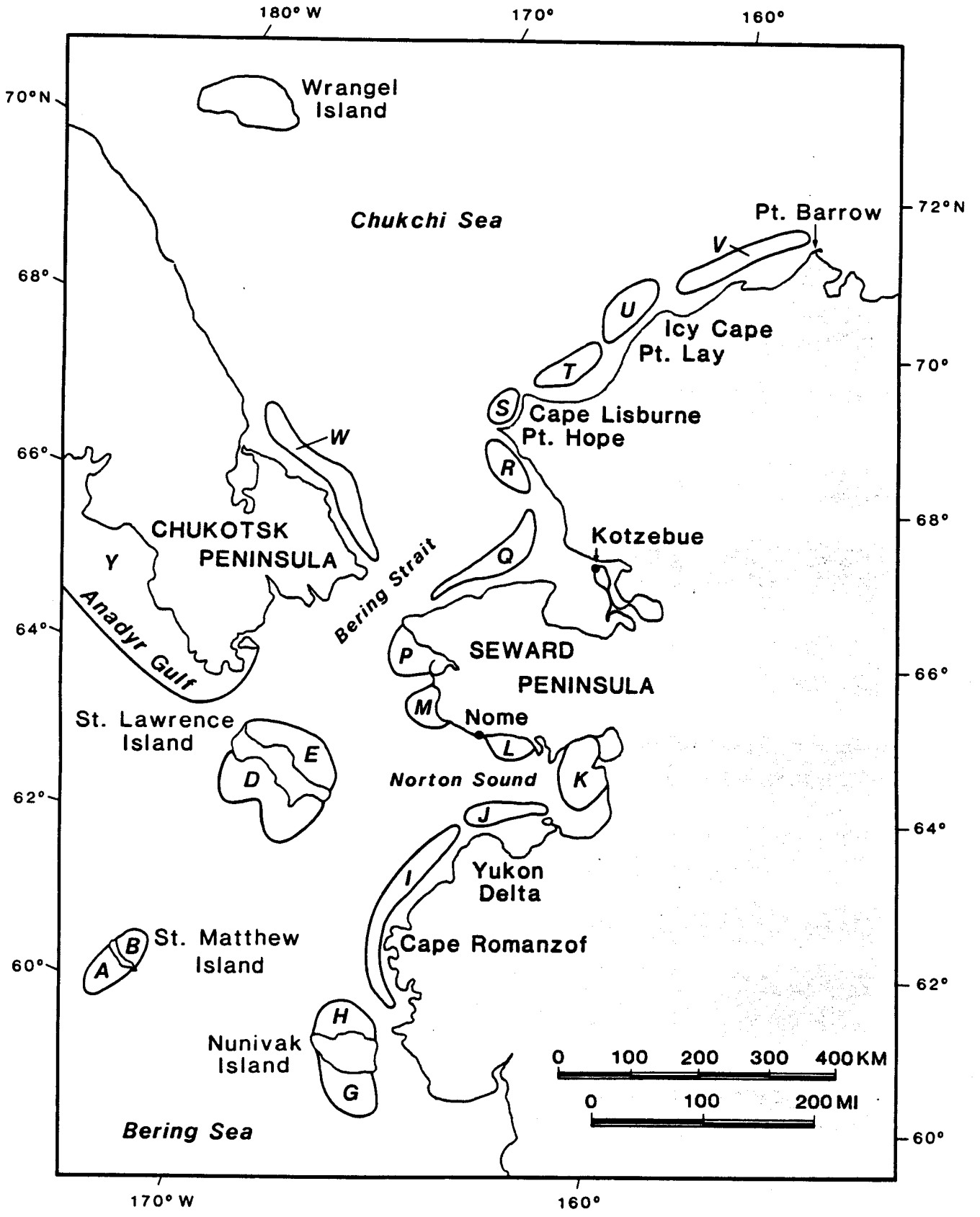

Figure 1. Preliminary Identification of Polynyi for Statistical Studies.

Table 1a. Preliminary Identification of Polynyi for Statistical Studies.

Location of Polynyi	Coded Designation on Alaska Base Map	Median Size (km^2) by Month Averaged Over Six Years						
		Jan.	Feb.	Mar.	Apr.	May	Jun	Jul
St. Matthew Island Polynya, South	A	OPEN	402	1050	1920	OPEN	OPEN	OPEN
St. Matthew Island Polynya, North	B	0	0	0	0	OPEN	OPEN	OPEN
St. Lawrence Island Polynya, South	D	3280	1940	2740	5050	OPEN	OPEN	OPEN
St. Lawrence Island Polynya, North	E	0	0	0	0	OPEN	OPEN	OPEN
Nunivak Island Polynya, South	G	3000	1160	2440	23400	OPEN	OPEN	OPEN
Nunivak Island Polynya, North	H	0	0	126	39200	OPEN	OPEN	OPEN
Cape Romanzof Polynya	I	796	883	1880	27800	OPEN	OPEN	OPEN
Yukon Delta Polynya	J	0	0	0	225	OPEN	OPEN	OPEN
Norton Sound Polynya	K	1290	1070	2080	6140	15400	OPEN	OPEN
Nome Polynya	L	322	164	1400	5070	15400	OPEN	OPEN
Seward Peninsula Polynya, South	M	1670	613	1720	1260	7880	OPEN	OPEN
Seward Peninsula Polynya, North	P	1620	833	1740	1270	7600	OPEN	OPEN
Kotzebue Sound Polynya	Q	2720	0	0	194	0	OPEN	OPEN
Cape Thompson-Pt. Hope Polynya*	R	218	140	510	216	60	250	OPEN
Pt. Hope-Cape Lisburne Polynya	S	80	0	18	55	247	5630	OPEN
Cape Lisburne to Pt. Lay Polynya**	T	283	0	515	590	5470	8820	OPEN
Pt. Lay to Icy Cape Polynya**	U	0	0	188	530	7040	8980	OPEN
Icy Cape to Pt. Barrow Polynya**	V	417	0	0	153	5290	53	488
Chukotsk Peninsula Polynya	W	0	0	0	0	0	OPEN	
Anadyr Gulf Polynya	Y	4950	3140	4490	6180			

* Carleton (1980)
** Chukchi Polynya (Stringer, 1982)

Table 1b. Preliminary Identification of Polynyi for Statistical Studies.

Location of Polynyi	Coded Designation on Alaska Base Map	Average Size (km²) by Month Averaged Over Six Years						
		Jan.	Feb.	Mar.	Apr.	May	Jun	Jul
St. Matthew Island Polynya, South	A	975	467	2310	2200	OPEN	OPEN	OPEN
St. Matthew Island Polynya, North	B	0	0	94	123	OPEN	OPEN	OPEN
St. Lawrence Island Polynya, South	D	4250	1900	4320	13900	24700	OPEN	OPEN
St. Lawrence Island Polynya, North	E	0	297	2790	260	797	OPEN	OPEN
Nunivak Island Polynya, South	G	2870	1830	2800	26100	OPEN	OPEN	OPEN
Nunivak Island Polynya, North	H	38	520	2040	11000	OPEN	OPEN	OPEN
Cape Romanzof Polynya	I	1250	2750	4600	8640	OPEN	OPEN	OPEN
Yukon Delta Polynya	J	280	1810	1230	4380	OPEN	OPEN	OPEN
Norton Sound Polynya	K	1820	3160	4500	7730	13200	OPEN	OPEN
Nome Polynya	L	800	1820	3810	5280	10600	OPEN	OPEN
Seward Peninsula Polynya, South	M	3510	2000	2370	2880	7680	OPEN	OPEN
Seward Peninsula Polynya, North	P	3200	2140	2120	2940	6260	OPEN	OPEN
Kotzebue Sound Polynya	Q	1630	2690	932	607	267	166	OPEN
Cape Thompson-Pt. Hope Polynya*	R	1700	2320	1550	1030	569	5080	OPEN
Pt. Hope-Cape Lisburne Polynya	S	360	1880	182	159	4480	11600	OPEN
Cape Lisburne to Pt. Lay Polynya**	T	1700	3320	1150	2420	11500	12500	OPEN
Pt. Lay to Icy Cape Polynya **	U	1970	2920	1330	2240	10800	12200	OPEN
Icy Cape to Pt. Barrow Polynya **	V	2160	2290	1310	2150	9480	7770	1340
Chukotsk Peninsula Polynya	W	964	471	511	0	145	OPEN	
Anadyr Gulf Polynya	Y	7540	3340	5950	11600			

* Carleton (1980)
** Chukchi Polynya (Stringer, 1982)

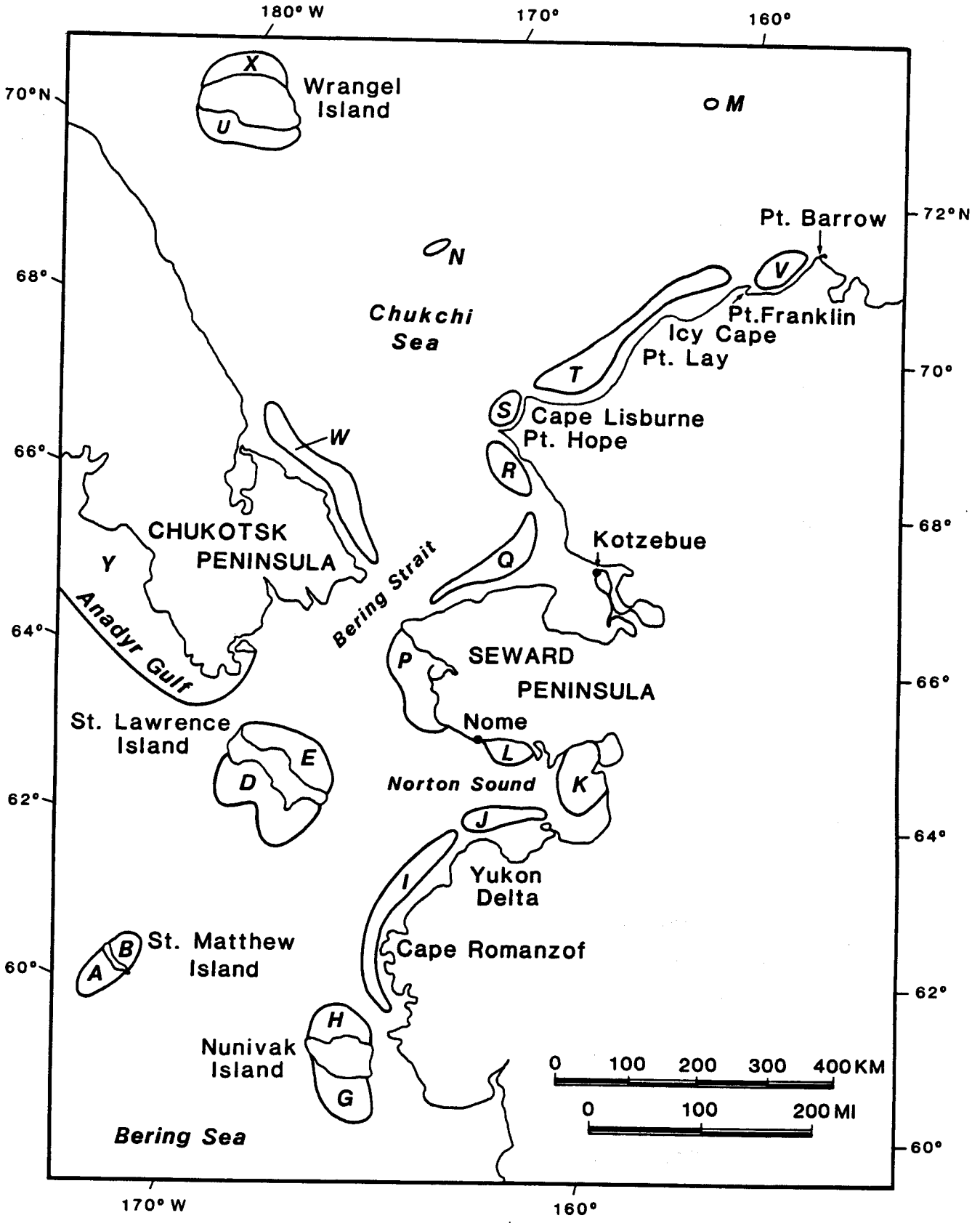

Figure 2. Final Catalog of Recurrent Polynyi in the Chukchi and Bering Seas.

Table 2a. Final Catalog of Recurrent Polynyi in the Chukchi and Bering Seas

Location of Polynyi	Coded Designation on Alaska Base Map	Median Size (km^2) by Month Averaged Over Six Years						
		Jan.	Feb.	Mar.	Apr.	May	Jun	Jul
St. Matthew Island Polynya, South	A	OPEN	402	1050	1920	OPEN	OPEN	OPEN
St. Matthew Island Polynya, North	B	0	0	0	0	OPEN	OPEN	OPEN
St. Lawrence Island Polynya, South	D	3280	1940	2740	5050	OPEN	OPEN	OPEN
St. Lawrence Island Polynya, North	E	0	0	0	0	OPEN	OPEN	OPEN
Nunivak Island Polynya, South	G	3000	1160	2440	23400	OPEN	OPEN	OPEN
Nunivak Island Polynya, North	H	0	0	126	39200	OPEN	OPEN	OPEN
Cape Romanzof Polynya	I	796	883	1880	27800	OPEN	OPEN	OPEN
Yukon Delta Polynya	J	0	0	0	225	OPEN	OPEN	OPEN
Norton Sound Polynya	K	1290	1070	2080	6140	15400	OPEN	OPEN
Nome Polynya	L	322	164	1400	5070	15400	OPEN	OPEN
Katie's Polynya	M							
Herald Shoal Polynya	N							
Seward Peninsula Polynya	P							
Kotzebue Sound Polynya	Q	2720	0	0	194	0	OPEN	OPEN
Cape Thompson-Pt. Hope Polynya*	R	218	140	510	216	60	250	OPEN
Pt. Hope-Cape Lisburne Polynya	S	80	0	18	55	247	5630	OPEN
Cape Lisburne to Pt. Franklin Polynya**	T							OPEN
Pt. Franklin to Pt. Barrow Polynya**	V							OPEN
Chukotsk Peninsula Polynya	W	0	0	0	0	0	OPEN	
Wrangel Island Polynya, South	U							
Wrangel Island Polynya, North	X							
Anadyr Gulf Polynya	Y	4950	3140	4490	6180			

* Carleton (1980)
** Chukchi Polynya (Stringer, 1982)

Table 2b. Final Catalog of Recurrent Polynyi in the Chukchi and Bering Sea

Location of Polynyi	Coded Designation on Alaska Base Map	Average Size (km²) by Month Averaged Over Six Years						
		Jan.	Feb.	Mar.	Apr.	May	Jun	Jul
St. Matthew Island Polynya, South	A	975	467	2310	2200	OPEN	OPEN	OPEN
St. Matthew Island Polynya, North	B	0	0	94	123	OPEN	OPEN	OPEN
St. Lawrence Island Polynya, South	D	4250	1900	4320	13900	24700	OPEN	OPEN
St. Lawrence Island Polynya, North	E	0	297	2790	260	797	OPEN	OPEN
Nunivak Island Polynya, South	G	2870	1830	2800	26100	OPEN	OPEN	OPEN
Nunivak Island Polynya, North	H	38	520	2040	11000	OPEN	OPEN	OPEN
Cape Romanzof Polynya	I	1250	2750	4600	8640	OPEN	OPEN	OPEN
Yukon Delta Polynya	J	280	1810	1230	4380	OPEN	OPEN	OPEN
Norton Sound Polynya	K	1820	3160	4500	7730	13200	OPEN	OPEN
Nome Polynya	L	800	1820	3810	5280	10600	OPEN	OPEN
Katie's Polynya	M							
Herald Shoal Polynya	N							
Seward Peninsula Polynya	P							
Kotzebue Sound Polynya	Q	1630	2690	932	607	267	166	OPEN
Cape Thompson-Pt. Hope Polynya*	R	1700	2320	1550	1030	569	5080	OPEN
Pt. Hope-Cape Lisburne Polynya	S	360	1880	182	159	4480	11600	OPEN
Cape Lisburne to Pt. Franklin Polynya **	T							
Pt. Franklin to Pt. Barrow Polynya**	V							
Chukotsk Peninsula Polynya	W	964	471	511	0	145	OPEN	
Wrangel Island Polynya, South	U							
Wrangel Island Polynya, North	X							
Anadyr Gulf Polynya	Y	7540	3340	5950	11600			

* Carleton (1980)
** Chukchi Polynya (Stringer, 1982)

Six polynyi were collectively identified as North Coast Polynyi because they form off the north facing coasts of St. Matthew, St. Lawrence, and Nunivak Islands and off the Yukon Delta, Seward Peninsula, and Chukotsk Peninsula. They occur less frequently than polynyi adjacent to coasts facing south. They appear to arise from a reversal of winds from the North or Northeast, the predominant wind directions in winter over that part of the Bering Sea north of St. Matthews Island (Brower et al., 1977; Overland, 1981; Wilson et al., 1984). Many polynyi form on the north, south, and eastern coast of the Chukotsk Peninsula. However, as the emphasis in this report was on polynyi occurring in Alaskan waters, only two polynyi were identified here.

The original intention was to digitize polynya areal extent from as many years' AVHRR data as possible. The images were processed from January through May on a daily basis. Tables were prepared which display these measurements. In those cases where an area could not be measured, each polynya was designated as frozen (0), obscured by cloud cover (C), not available (N), fused with the main body of open water (O), or observable, but not capable of being digitized (P).

The numerical areal data contained in the tables were used to calculate monthly summary statistics for all 20 polynyi for all six years. In these calculations the numerical data were used in combination with the non-numerical "presence" designation to produce monthly time series plots for all 20 polynyi for all six years. The "presence" observations were converted to quantitative measurements by interpolating between digitized area determinations.

Each polynya boundary was digitized at least twice. This was to serve two purposes: first, it was desirable to learn how accurately one could reproducibly determine the area of a given polynya under both optimal conditions and under marginal conditions. Second, it allows one to differentiate between genuine daily area fluctuations and variability due to the digitizing method.

Throughout this study, only correlations whose confidence level were 95% or greater were considered significant.

RESULTS

Description of the Data Base and the Organization Plan for Analysis:

Four polynyi were selected for special scrutiny from the twenty studied for all years. These are the St. Lawrence (South) Polynya, the Norton Sound Polynya, the Kotzebue Polynya, and the Chukchi Polynya. The reasons for selecting these polynyi are as follows:

The St. Lawrence (South) Polynya (D; Table 1, Figure 1) is located in the central Bering Sea. It has been studied in connection with the effect polynya formation has on the salt balance of seawater and on the generation of sea ice (McNutt, 1981; Schumacher, Aagaard, Pease, and Trip, 1983). Recently, it has been of interest as whale habitat (Brueggeman, 1982).

The Norton Sound Polynya (K; Table 1, Figure 1) is often a prominent wintertime feature of Norton Sound. Its size is more constrained than that of the other polynyi, because Norton Sound has a well defined area of 36700 km^2. It frequently assumes a characteristic shape determined in part by the configuration of the Sound. A conspicuous feature of this polynya is that the pattern of ice cover remaining within Norton Sound appears to duplicate the shape of the summer sediment plume from the Yukon River described by Dean (Dean, McRoy, Ahlnas, and George, 1987). It is possible that the shape of the Norton Sound Polynya may therefore be influenced in part by outflow from the Yukon River.

The Kotzebue Sound Polynya (Q; Table 1, Figure 1) is located in the Chukchi Sea immediately north of the Seward Peninsula. It is a North Coast Polynya. Like all North Coast Polynyi (and unlike all typical polynyi which one may expect to view daily), this polynya is present only occasionally and for short periods. Its occurrence is a potential indicator for the unusual meteorological conditions which create North Coast Polynyi.

The Chukchi Polynya forms off the Chukchi Sea coast of Alaska from Cape Lisburne to Pt. Barrow. The polynya is often present as a series of small individual polynyi, rather than a single continuous feature. Therefore, this polynya was divided into three roughly equal segments in the hope that one might discern some pattern in their formation (T, U, and V; Table 1, Figure 1).

In theory, using available AVHRR imagery, one should be able to document changes in polynya area over periods as short as only a few hours as more than one orbit passes over Alaska in a day, and during some periods, there have been more than one NOAA satellite in orbit. In practice, only one acceptable image is available

per day. In those rare cases where more than one image was available per day, evidence exists that polynya area can increase markedly in the course of only a few hours. However, there is insufficient imagery to document how unusual or common these events are.

Median monthly values of polynya areas were determined. This is because median values are not unduly influenced by a few arbitrarily large values at one end of the data set - for instance, if the polynya opens into the ice-free ocean - and tend to de-emphasize the influence of continuous strings of data (provided they are short compared to the entire data set). As part of the analysis procedure tables were compiled which list median values and the maximum polynya area observed on a monthly basis for each of the years investigated.

Total open water sums were calculated for the Chukchi and Bering Seas for the months January through April for all six years, because it seemed worthwhile to consider the polynyi not only individually, but also in terms of their total contribution to the open water area of the Bering and Chukchi Seas. These calculations are reported both in absolute terms and as percentages of the areas of the Bering and Chukchi Seas. Individual polynya areas, median polynya areas, and the summed polynya area totals are discussed on a monthly basis in the section: Statistical Analysis of Monthly Changes in Polynya Area. Tables were compiled recording monthly summary statistics for all twenty polynyi for each month of the six years.

Daily time series plots comparing daily polynya area variation with the climatic variables; temperature, wind component from the North, Northeast and East, and barometric pressure difference between Barrow and Nome are discussed in the section: Statistical Analysis of Daily Changes in Polynya Area. Daily time series plots were made for all six years and for January 1986 for the Chukchi Polynya group (T, U, and V and the sum T + U + V) which compared daily polynya areas with temperature and wind components at Barrow and the barometric pressure difference between Barrow and Nome. Daily time series plots were compiled for all six years and January 1986 for the polynyi of Kotzebue Sound (Q and R) which compared daily polynya areas with temperature and wind components at Kotzebue. Daily time series plots were compiled for all six years and January 1986 for the Norton Sound Polynya (K) and for all six years for the Yukon Delta Polynya (J) which compared daily polynya area and temperature at Nome and barometric pressure difference between Barrow and Nome. Daily time series plots were made comparing the timing

of the presence of St. Lawrence Island Polynya, South (D) with that of St. Lawrence Island Polynya, North (E) for all six years.

A descriptive analysis of climatic events during 1975 which might be responsible for unusual polynya formation in that year is given in section: Descriptive Analysis of Polynya Formation in 1975.

Use of Thermal Infrared Analysis of the temperature structure of the Chukchi Polynya is described in the section: Thermal Infrared Analysis of the Chukchi Polynya.

Finally, using the information gained during the statistical analyses, a revised catalog of sites of recurrent polynyi formation is given in the section: A Catalog of Recurrent Polynya Formation observed in the Bering and Chukchi Seas.

STATISTICAL ANALYSIS OF MONTHLY CHANGES IN POLYNYA AREA

Discussion of the Statistical Analysis of the Monthly Data Base

Any attempt to relate polynya size to climatic conditions is limited by the scarcity of recording weather stations in the study area. Four synoptic weather stations exist in the Bering-Chukchi region; Barrow, Kotzebue, Nome and St. Paul. Weather records are kept on a less rigorous schedule at Cape Lisburne, Wales, Cape Romanzof and Unalakleet. The first attempt to relate polynya size to climatic conditions involved the correlation of the polynya median areas with climatic variables obtained at the four synoptic weather stations. The polynyi and the synoptic weather stations were paired as follows: Chukchi Polynya (T)-Barrow; Kotzebue Polynya (Q)-Kotzebue; Norton Sound (K)-Nome; St. Lawrence Island Polynya South (D)-St. Paul. The relationship between the Chukchi Polynya and the Barrow climatic variables were studied especially intensively.

Potential temperature effects were investigated using average temperature, median temperature and heating degree days. Heating degree days were used as a measure of temperature integrated over time. They are a compiled climatological statistic and therefore readily available. Potential wind effects were investigated using average wind speed, resultant wind speed, and wind component are in miles per hour. Resultant wind speed is the vector sum of the wind directions and speed divided by the number of observations. The wind component was calculated from wind resultant direction and resultant speed.

Linear correlation coefficients (Pearson) were obtained to determine if linear relationships existed between average monthly temperature, degree days, resultant

wind speed, average wind speed, and wind component with median polynya size and median polynya area. Relationships were tested by month, by year and among all the area measurements taken together.

A nonparametric measure of correlation based on ranks, Kendalls Tau, was calculated to determine if large polynya areas were paired with high temperatures or low degree days or if analogous pairing occurred with any of the wind related variable. Kendall's Tau was calculated for the above climatic variables and median polynya size and area combining all years, on a yearly basis, and on a monthly basis.

The Student's *t* probability distribution was utilized to test whether the correlation coefficients were significantly different from zero. Both the linear and rank correlation coefficients were considered significant if the significance levels were equal to or exceeded the 95% confidence level.

The Chukchi Polynya (T) and Barrow Climatic Variables

Graphs were prepared displaying the monthly variation of heating degree days, average temperature, and wind component with polynya extent for the six years investigated. Wind component is much more variable than the temperature variables These charts have not been reproduced here because of their extensive number. However, no obvious consistent relationships were found, although occasional direct correlations were to be seen.

Linear and rank correlations found by combining data from all six years suggest that large polynyi are associated with high temperatures and low heating degree days. These linear correlations have an absolute value of approximately 0.6 and the rank correlations have values of approximately 0.5. However, no significant correlations were observed among the wind related variables.

Linear and rank correlations found by combining the data by year were compiled. These correlations also suggest that large polynyi are associated with warmer temperatures. Some years had linear and rank correlations as high as 0.9. No significant linear or rank correlations were found with any of the wind related variables.

Linear and rank correlations found by combining the data by month were also compiled. These correlations support the conclusion that large polynya area is associated with warmer temperatures or low heating degree days. Some months had no linear or rank correlation between polynya extent and temperature or heating degree days. No conclusive relationship was found between polynya area and any of the wind-related variables on a monthly basis.

The above results suggest that the apparent high correlation between the temperature variables and polynyi observed for individual years is probably due to the fact that the temperature becomes warmer and more open water appears as the seasons change from winter to summer. If temperature and open water in polynyi were more significantly related, one would have expected a high correlation using the combined data set. It also suggests that other factors in addition to temperature influence polynya size.

Such an additional factor could be the Alaska Current which travels northward along the Bering and Chukchi Coasts in the summer. It has been shown to have a major effect on the timing and pattern of meltback of the ice edge in the Chukchi Sea (Paquette and Bourke, 1981, Stringer and Groves, 1985). Coachman and Aagaard (1981) describe bottom current flow reversals off Cape Lisburne for the winter of 1976-77. From December through March, frequent current reversals from north to south were observed. Coachman and Aagaard advance this as evidence that the current regime is different in the winter than it is in the summer. It is possible that this reversing current pattern could have as profound an effect on the presence of open water in polynyi in winter as the movement of the Alaska Current has on meltback of the ice edge in summer. However, adequate current measurements do not exist to test this hypothesis.

The Kotzebue Polynya (Q) and Kotzebue Climatic Variables

Figures were prepared displaying the monthly variation of average temperature and wind component from the Northeast with polynya extent for the six year and bimonthly wind component from the Northeast during that time. No obvious consistent relationships were evident.

Linear and rank correlation coefficients were determined for the climatic variables and polynya area obtained by combining all six years. Linear and rank correlation coefficients were obtained for both temperature and wind related variables. The linear and rank correlation coefficients had an absolute value of 0.6.

Linear and rank correlations were obtained between the climatic variables and median polynya area and size combing the data by year. The temperature related variables do not appear to have much influence on this polynya. In the cases where a relationship can be detected, it suggests large polynya area is associated with warmer temperatures. The effect of the wind related variables on this polynya is not clear.

Linear and rank correlations were obtained for average temperature, median temperature and wind component combining twelve two week periods for all the years. Fewer significant correlations were found than were found combining monthly periods for all the years. Thus, refining temporal resolution does not improve correlations.

The Norton Sound Polynya (K) and the Nome Climatic Variables

Figures were prepared showing the monthly variation of average temperature wind component from the Northeast, and wind component from the East with polynya extent for six years. These were examined for evidence of obvious consistent causal relationships. None were obvious.

Linear and Kendall rank correlations were obtained by combining the data for all six years for median polynya area and size and correlating these against the climatic variables: average temperature, degree days, wind component (calculated as wind from the Northeast and East), average wind speed, and resultant wind speed. These correlations implied a large polynya was associated with warmer temperatures. The linear and rank correlation coefficients had an absolute value of approximately 0.7. The wind components had essentially identical negative correlations with polynya area. These linear and rank correlations ranged from -0.3 to -0.4.

Rank and linear correlations were determined between climatic variables and median polynya area and size by year. The size of the Norton Sound Polynya was much more strongly correlated with temperature using the combined data set than was the case in individual years. Few linear and no rank correlations were found between the wind components and polynya area.

Kozo (1987) performed an analysis of 1964-1968 surface winds, pressures and temperatures at three weather stations around Norton Sound. He states that surface wind histograms at Nome and Unalakleet do not show the true large scale wind distribution which would be the major factor in surface pollutant and ice movement in Norton Sound. He offers this as evidence that time series data of winds from Nome should not be used in offshore oil spill trajectory models. This may explain why the correlation coefficients (both linear and ranked) did not show a more pronounced relationship with polynya size.

The St. Lawrence Island Polynya, South (D) and St. Paul Island Climatic Variables

Figures were prepared showing the monthly variation of average temperature and wind component from the northeast polynya extent for six years.

Linear and Kendall rank correlations were calculated for polynya area and the climatic variables: average temperature, degree days, wind component (calculated as wind from the Northeast), average wind speed, and resultant wind speed by combining data for all six years. A wind from the Northeast might be expected to open a polynya on the south side of St. Lawrence Island.

No linear correlations were found for either of the temperature variables. Negative linear correlations (-0.6 to -0.8) were found for average wind speed and wind component and polynya area. This would suggest that winds were more likely to be responsible for freezing polynyi than opening them. Rank correlations were found for the temperature variables and polynya area which suggest large polynyi are associated with warmer temperatures. The rank correlations had an absolute value of approximately 0.45.

There was not sufficient data to warrant calculating correlations by year for the St. Lawrence Island Polynya.

Investigation of Possible Anomalous Polynya Formation in 1975

1975 was an unusual year among the six studied in that unusually large polynyi were formed early in that year. In order to determine whether 1975 meteorological data were anomalous, contingency analyses were run to compare the temperature and wind component distributions by month among the six years. No significant differences were found among the years.

The conclusions which must be drawn from the above observations (if 1975 casual relationships were actually significantly different in some manner from the other five years) are: 1) the weather data recorded at the three synoptic weather stations either did not contain the appropriate variable to demonstrate this difference or the format in which the data was reported by the synoptic stations did not exhibit correlation; 2) another manipulation of the synoptic data such as pressure differences between two different synoptic stations might yield relationships; 3) more meaningful weather data might be obtained at sites other than the four synoptic stations.

1975 was selected for a descriptive analysis in the subsection: Descriptive Analysis of Polynya Formation in 1975.

STATISTICAL ANALYSIS OF DAILY CHANGES IN POLYNYA AREA

The Chukchi Polynya Group (T, U, and V) and the Barrow Climatic Variables

One hundred and forty time series plots were made comparing variation in daily polynya area for the individual polynyi, Cape Lisburne to Pt. Lay Polynya (T), Pt. Lay to Icy Cape Polynya (U), and Icy Cape to Pt. Barrow Polynya (V) and their sum (T + U + V) known as the Chukchi Polynya and the climatic variables, temperature, wind component from the North, wind component from the Northeast and wind component from the East at Barrow and barometric pressure difference between Barrow and Nome. This barometric pressure difference was selected as a possible indicator of storm conditions and of current flow in the Chukchi Sea in the region where the Chukchi Polynya forms.

Each plot was individually inspected to see if a sufficient relationship existed between polynya area and climatic variable to justify a cross-correlation analysis or if an especially dramatic change in a climatic variable signaled a dramatic change in polynya area.

The only apparent relationship observed was between temperature and polynya area. As daily temperatures increased, daily polynya area tended to increase. This tendency was indicated earlier with the correlation studies of the monthly data.

Seven and thirteen day moving average plots of the wind components were prepared for comparison with polynya area to determine if polynya area was influenced by sustained winds. Some of the thirteen day moving average plots suggested that there might be a relationship for this period of sustained wind, but it was not prominent.

Seven and thirteen day moving average plots of the barometric pressure difference between Nome and Barrow were also compared with daily polynya area plots. No relationship was detectable for either average.

None of the moving average plots suggested cross-correlations would be instructive.

Histograms were made from the six years of daily climatic data recorded as wind components and barometric pressure difference and the 99th and 95th percentiles determined in an effort to identify extreme conditions.

Suitable time series plots of polynya area were selected. These were then examined individually to determine if any extreme wind component or barometric pressure difference was associated with a significant polynya formation event or if any threshold wind velocity existed. Whether considering the Chukchi Polynya

System as a whole or in its constituent parts, there appears to be no consistent relationship between extreme winds and polynya area for wind component from the East or the Northeast. Likewise, no relationship was found for barometric pressure difference.

The best conclusion that can be drawn on a qualitative basis is that the Chukchi Polynya system is generally related to winds. The two years, 1975 and 1976, which had the most extreme winds had the largest polynya area. It is also suggested that sustained winds over a one week or two week period have more effect on polynya size than an extreme wind of one or two days duration.

The Polynyi of Kotzebue Sound (Q) and (R) and the Kotzebue Climatic Variables

Fifty six time series plots were made comparing daily polynya area for Kotzebue Sound Polynya (Q) and Cape Thompson-Pt. Hope Polynya (R) with daily temperature and wind components from the East, Northeast and North.

Each plot was individually inspected to see if a sufficient apparent relationship existed between polynya area and climatic variable to justify a cross-correlation analysis or if an especially dramatic change in a climatic variable signaled a dramatic change in polynya area. These are instantaneous relationships because they relate one day's wind or temperature on that day's polynya area.

No relationships were found between any of the climatic variables and polynya area except a possible qualitative one between temperature (positive) and the wind components from the East (positive) and North (negative) for the area of the Kotzebue Sound Polynya (Q) in 1976.

Seven and thirteen day moving average plots of the wind components were prepared for comparison with polynya area to determine if polynya areas were influenced by sustained winds. No relationship was obvious between East or Northeast wind components and polynya area. A possible relationship was detected between wind component from the North at both seven and thirteen days and polynya area for both Kotzebue Sound Polynyi.

Cross-correlations were performed for the seven and thirteen day moving average plots of wind component from the North and Polynya area for 1975 and 1976 for the Kotzebue Sound Polynya (Q). The 1976 wind component analysis showed a positive relationship between wind from the South and polynya area. The most significant lag was for -1 or 2 days for a moving average of seven days. The cross-correlation coefficient was 0.48. The 1975 cross-correlations were not significant. The 1976 finding suggests that a sustained wind from the South for a week may be

more influential in the formation of the Kotzebue Sound Polynya than instantaneous winds or sustained wind over two weeks.

Histograms were made from the six years of daily climatic data recorded as wind components in an effort to determine extreme conditions. The 95th and 99th percentiles were recorded in a table. Analysis of this table showed that no generalizations could be made about the association of extreme wind from any direction and polynya size.

The Kotzebue Sound Polynya (Q) and the Cape Thompson-Point Hope Polynya (R) constitute a North and South Coast Polynyi pair in that they are located on opposite (north-south) sides of Kotzebue Sound. If polynya extent is related to forcings directed along that axis, these polynyi should exhibit a tendency toward an anti-correlation. Figure 3 shows the daily variation of the extent of these two polynyi during 1976. The extent of the Kotzebue Sound Polynya is shown as a dotted line while the Pt. Hope-Cape Lisburne polynya is shown as a dotted line while the Pt. Hope-Cape Lisburne polynya is shown as a solid line. During this time the major openings and closing of these two polynyi can be seen to be anti-correlated.

The Norton Sound Polynyi (J, K and L) and the Nome Climatic Variables

Sixty-five time series plots were made comparing daily polynya area for the Norton Sound Polynya (K) and the Yukon Delta Polynya (J) with daily temperatures, wind components from the East, Northeast, and North and barometric pressure difference between Barrow and Nome.

Seven and thirteen day moving average plots of the wind components were made for comparison with polynya area to determine if polynya area were influenced by sustained winds.

Histograms were made from the six years of daily climatic data recorded as wind components in an effort to determine extreme conditions. The 95th and 99th percentiles were recorded in a table. Likewise these extreme values were examined with the appropriate time series plot to determine if any extreme wind component values were associated with a significant polynya event or if any threshold velocity existed.

The Norton Sound Polynya (K)

Each daily plot was individually inspected to see if a sufficient relationship existed between polynya area and climatic variable to justify a cross-correlation analysis or if an especially dramatic change in a climatic variable signaled a

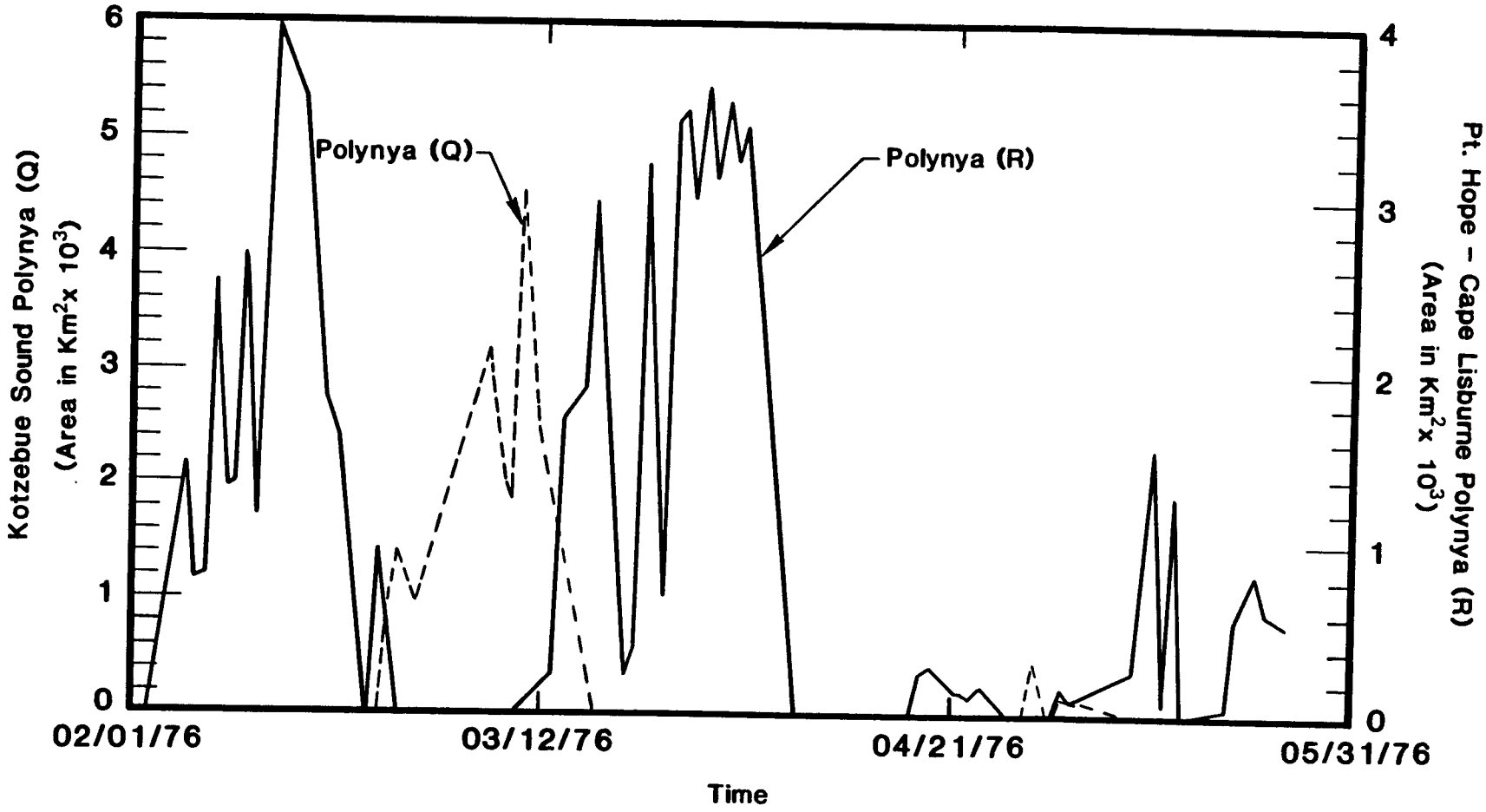

Figure 3. Daily area variation of the Kotzebue Sound Polynya (Q) and the Pt. Hope – Cape Lisburne Polynya (R) in 1976 showing the tendency of the North Coast Polynya (Q) to form when the south coast facing Polynya (R) is closed and vice versa.

dramatic change in polynya area. Four years' data revealed a relationship between temperature and polynya area where higher temperatures were associated with larger polynya area. There appears to be no significant relationship with the other variables

Inspection of the seven and thirteenth day moving average plots revealed some apparent direct relationships between temperature and polynya area at both the seven and thirteen day moving averages. Apparent direct relationships between wind components and polynya area were found at both the seven and thirteen day averages.

Cross-correlations were performed between polynya area and temperature. The coefficients varied between 0.7 for a one day lag to 0.50 for a nine to thirteen day lag.

The only consistent conclusion one can derive is that the Norton Sound Polynya (K) tends to be large during warmer temperatures. There also may be some correlation between large polynya area and wind component from the East, North, or Northeast both in the sustained situation and at threshold values.

The Yukon Delta Polynya (J)

The Yukon Delta Polynya is a North Coast Polynya. It was selected with the other Norton Sound polynyi for a cross-correlation study because, like the other Norton Sound polynyi, it has a well-defined site and there was a long run of continuous area measurements available in 1976.

Each daily plot was individually inspected to determine whether a sufficiently strong relationship existed between polynya area and climatic variable to justify a cross-correlation analysis or if an especially dramatic change in a climatic variable signaled a dramatic change in polynya area. It is difficult to draw conclusions from these daily plots as the Yukon Delta Polynya forms much less frequently than other polynyi. Nevertheless, some associations were seen for both the sustained and the threshold effects.

The data suggest that the Yukon Delta Polynya is associated with extreme wind components from the South or Southwest. A one to two day lag with a cross correlation coefficient of approximately 0.5 behind the observation of peak polynya area was observed for the wind component from the South. Low barometric pressure at Barrow with respect to Nome may also be a factor. However, the Yukon Delta Polynya forms so infrequently it has not been possible to get a sufficiently large sample to statistically prove these theories.

The St. Lawrence Polynyi (D and E) and the St. Paul Island Climatic Variables

As the St. Lawrence Polynyi do not have long runs of continuous polynya area measurements, and there is no synoptic weather station closer than St. Paul Island to provide a meaningful and continuous climatic data base set, no daily time series were compiled for these polynyi. Polynya (D) is a south coast polynya, while Polynya (E) is a North Coast Polynya. Polynya (D) and Polynya (E) do not form at the same time and tend to be anti-correlated. Presumably this is because the means of formation for the Polynyi are different or are even related to reversals of phenomena related to their presence. Figure 4 shows the daily extent of these two polynyi during 1975. The extent of the St. Lawrence Island North polynya is shown as a solid line while the St. Lawrence Island South polynya is shown as a dotted line. This figure illustrates the tendency toward anti-correlation between these polynyi. (Note that the previous example of an anti-correlated pair of polynyi involved two polynyi located at opposite sides of a bay while in this example the two polynyi are on opposite sides of an island).

DESCRIPTIVE ANALYSIS OF POLYNYA FORMATION IN 1975

1975 was selected as a year for more intensive study because so many large polynyi formed that spring. The approaches considered for relating polynya formation to climatic events were 1) an attempt to relate the 700 mb pressure maps published in *Monthly Weather Review* (Taubensee, 1975) with polynya formation, and 2) an attempt to relate daily weather changes at Barrow, Kotzebue and Nome with some of the more dramatic polynya formation events in 1975.

The result of this intensive study is a suggestion that the causes for formation of polynyi are complex and probably cannot be fully described by atmospheric conditions alone, but may require oceanographic measurements such as current velocities, sea surface temperatures, etc.

An unusual meteorological condition was found in March 1975 associated with an atypically large area for the Chukchi polynya. This appeared to be a region of high pressure which may form anywhere over the Alaskan landmass or north of Alaska or the MacKenzie Delta. This condition persisted for more than two weeks, an unusual event for March. During that time we saw the formation of polynyi in atypical locations such as the North Coast Polynyi or of atypical size for the time of the year.

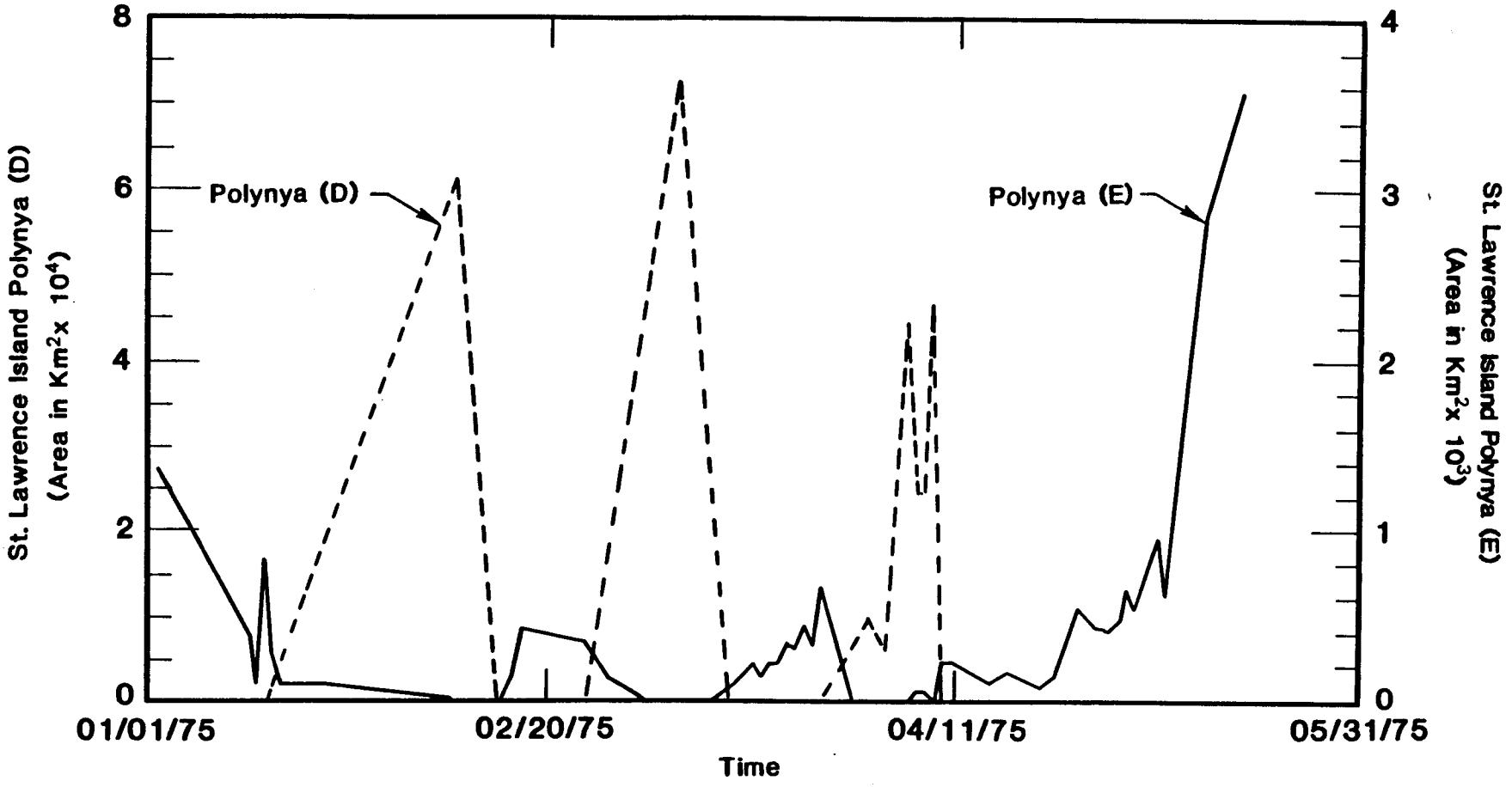

Figure 4. Daily area variation of the St. Lawrence Island Polynyi (D and E) in 1975 showing the tendency of the North Coast Polynya (E) to form when the south coast facing Polynya (D) is closed and vice versa

A CATALOG OF RECURRENT POLYNYA FORMATION OBSERVED IN THE BERING SEA AND CHUKCHI SEA

Stirling and Cleator (1981) describe the location and approximate dates of presence of recurrent polynyi in the Canadian Arctic. A similar description of the location and times of presence of twenty-one polynyi in the Bering and Chukchi Seas has been compiled. These descriptions derive from a study of six years of the size of polynyi in the months January through June. Good descriptions are possible for the typical size and shape of each polynya as well as for range of break-up dates. However, no data are given for the first time of formation other than that may be implied from average advance and retreat of the ice edge within the Bering and Chukchi Seas. Figure 2 displays the revised polynya formation sites as suggested by this study; Table 2 records the names of the sites.

THERMAL INFRARED ANALYSIS OF THE CHUKCHI POLYNYA (T+U+V)

Thermal infrared analysis of the temperature structure of two polynyi in the Chukchi Sea using a series of AVHRR images have allowed limited confirmation of the recurrent formation of these polynyi.

The Chukchi Polynya (T + U + V) forms off the coast of Alaska from Cape Lisburne to Pt. Barrow. The Polynya is often present as small individual polynyi, not as a single continuous feature.

Examination of computer printouts of the Chukchi Polynya for the purpose of assembling a series of illustrations of how the polynya forms revealed that our original division of the Chukchi Polynya into three segments was not representative of a realistic description of the mechanism of formation of this Polynya. A division of the Chukchi Polynya in two halves at Pt. Franklin seems more correct. First, the polynya segment (V) seems to form independently of T and U. Evidence for this was obtained from the thermal infrared analysis of a series of nine AVHRR images of the Chukchi Polynya for the period March 13 through March 21, 1987. The thermal structure of the polynya south of Icy Cape was different from that north of Ice Cape.

SUMMARY OF RESULTS

1) The sites for the formation of twenty-two recurrent polynyi were identified. These sites have been located on a map, and written descriptions of the

time of formation and area extent are given where sufficient information exists for such descriptions.

2) Extensive tabulations of daily polynya area are available for twenty polynyi spanning the months January through June for six years (1974, 1975, 1976, 1977, 1979, 1983). These are available through OCSEAP project management as they are too extensive to report in this format.

3) Extensive statistical analysis attempting to relate polynya size to climatic variables has been performed. These met with mixed success. There is weak evidence for involvement of wind in formation of some polynyi, while others are weakly related to temperature.

4) The necessity for the compilation of a database of climatic measurements obtained near the polynyi formation sites in close conjunction with observable changes in polynya size has been suggested. Current synoptic weather stations are not able to provide such data.

5) The necessity for the compilation of an oceanographic database of measurements such as current velocities, sea surface temperature, etc., near the polynyi formation sites in close conjunction with observable changes in polynya size has been suggested as a possible source of data helping explain polynya formation.

6) Thermal infrared analysis of AVHRR imagery was found to be a useful tool in studying the internal structure of polynyi and for verifying the physical dimensions of the polynya.

7) It has been demonstrated that North Coast Polynyi form independently and in a somewhat anti-correlated manner from South Coast Polynyi in the cases of the St. Lawrence Island Polynyi, North and South, (D and E) and of the Kotzebue Sound Polynya (Q) and the Cape Thompson-Pt. Hope Polynya (R). This suggests that the formation of these two polynyi may be related to reversals of some parameter we could not measure such as oceanic currents.

8) An unusual meteorological condition in March 1975 leading to an atypically large area for the Chukchi Polynya in March is described.

REFERENCES

Brower, W. A., et al., 1977. Climatic atlas of the Outer Continental Shelf waters and coastal regions of Alaska, Arctic Environmental Information and Data Center, Anchorage, Alaska, and the U.S. National Climatic Center, Asheville, NC, 28801, 3 vols.

Brueggeman, J. J., 1982. Early spring distribution of Bowhead whales in the Bering Sea, *J. Wildlife Management, 46(4)*, 1036-1044.

Carleton, A. M., 1980. Polynya Development in the Cape Thompson-Pt. Hope Region, *Arctic and Alpine Res.*, 12(2), 205-214.

Coachman, L. K. and K. Aagaard, 1981. Reevaluation of water transports in the vicinity of the Bering Strait; The Eastern Bering Sea shelf: Oceanography and Resources, Vol. 1 (1981), D. W. Hood and J. A. Calder, eds., Office of Marine Pollution, U.S. National Oceanographic and Atmospheric Admin., Washington, D. C., pp. 95-110.

Dean, K. G., C. P. McRoy, K. Ahlnas and T. H. George, 1987. Satellite observations of the Northern Bering Sea, Proceedings POAC'87, Vol. 1, 149-157.

Dey, B., H. Moore and A. Gregory, 1979. Monitoring and mapping sea ice breakup and freezeup of Arctic Alaska from Satellite Data, *Arctic and Alpine Res., 11(2)*, 229-242.

Dey, B., 1980. Applications of satellite thermal IR images for monitoring north water during periods of polar darkness, *J. Glaciol., 25(83)*, 425-438.

Kozo, T. L., 1987. Mesoscale meteorology of the Norton Sound region, Proceedings POAC'87, Vol. III, 163-182.

McNutt, L., 1981. Remote sensing analysis of ice growth and distribution in the Eastern Bering Sea; The Eastern Bering Sea Shelf: Oceanography and Resources, Vol. 1 (1981), D. W. Hood and J. A. Calder, eds., Office of Marine Pollution, U.S. National Oceanographic and Atmospheric Administration, Washington, D.C., pp. 141-165.

Overland, J. E., 1981. Marine climatology of the Bering Sea; The Eastern Bering Sea Shelf: Oceanography and Resources, Vol. 1 (1981), D. W. Hood and J. A. Calder, eds., Office of Marine Pollution, U.S. National Oceanographic and Atmospheric Administration, Washington, D.C. pp. 15-22.

Paquette, R. G. and R. H. Bourke, 1981. Ocean circulation and fronts as related to ice meltback in the Chukchi Sea, *J. Geophys. Res., 86(C5)*, 4215-4230.

Rogers, J. C., 1978. Meteorological factors affecting interannual variability of summertime ice extent in the Beaufort Sea, *Monthly Weather Review, 106(6)*, 890-897.

Schumacher, J. D., K. Aagaard, C. H. Pease, and R. B. Tripp, 1983. Effects of shelf polynya on flow and water properties in the Northern Bering Sea. *J. Geophys. Res., 88(C5)*, 2723-2732.

Smith, M. and B. Rigby, 1981. Distribution of polynyas in the Canadian Arctic: Polynyas in the Canadian Arctic, Stirling, I. and H. Cleator, eds., Occasional Paper No. 45, Canadian Wildlife Service, pp. 7-27.

Stirling, I. and H. Cleator, 1981. Polynyas in t he Canadian Arctic, Occasional Paper No. 45, Canadian Wildlife Service, pp. 5-6.

Stringer, W. J., 1982. Width and persistence of the Chukchi polynya, Geophysical Institute, University of Alaska Fairbanks, NOAA-OCS Contract No. 81-RAC00147, October 1, 1982.

Stringer, W. J., D. G. Barnett, and R. H. Godin, 1984. Handbook for sea ice analysis and forecasting, Geophysical Institute, University of Alaska Fairbanks, Contract No. N00228-81-C-H553.

Stringer, W. J. and J. E. Groves, 1985. Statistical description of the summertime ice edge in the Chukchi Sea, Geophysical Institute, University of Alaska Fairbanks, U.S. Department of Energy Contract No. DE-AC21-83MC20037, November 8, 1985.

Taubensee, R. E., 1975. Weather and circulation of March 1975, *Monthly Weather Review, 103(6)*, 562-566.

Wilson, J. G., A. L. Comiskey, R. W. Lindsay, and V. L. Long, 1984. Regional meteorology of the Bering Sea during MIZEX-West, February and March, 1983, NOAA/ERL Pacific Marine Environmental Laboratory, Seattle, Washington 98115.

U.S. DEPARTMENT OF COMMERCE
NATIONAL OCEANIC AND ATMOSPHERIC ADMINISTRATION
NATIONAL OCEAN SERVICE

Alaska Office
Federal Bldg., U.S. Courthouse, Room A13
222 W. Eighth Ave., #56
Anchorage, Alaska 99513-7543

FOURTH-CLASS MAIL
POSTAGE AND FEES PAID
U.S. Department of Commerce
Permit Number G-19

SPECIAL FOURTH CLASS
CLASS OF POSTAL SERVICE

UNIV OF ALASKA/INFO SERVICES
ARCTIC ENV INFO AND DATA CTR
707 A STREET
ANCHORAGE, AK 99501